Modélisation numérique et expérimentale des structures mixtes acier- béton et bois- béton

Quang Huy Nguyen

UNIVERSITÉ DE RENNES 1

INSA INSTITUT NATIONAL DES SCIENCES APPLIQUÉES RENNES

Mémoire d'Habilitation à Diriger des Recherches

de l'Université de Rennes 1

présenté par

NGUYEN Quang Huy

Maître de Conférences de l'INSA de Rennes

Modélisation numérique et expérimentale des structures mixtes acier-béton et bois-béton

Soutenue le 22 Avril 2016 à L'INSA de Rennes devant le jury composé de:

Prof. CAMPIAN Cristina	Technical University of Cluj-Napoca	Rapporteur
Prof. KOTRONIS Panagiotis	École centrale de Nantes	Rapporteur
Prof. TAERWE Luc	Ghent University	Rapporteur
Prof. BURSI Oreste Salvotore	University of Trento	Examinateur
Prof. FERRIER Emmanuel	Université de Lyon 1	Examinateur
Prof. HJIAJ Mohammed	INSA de Rennes	Examinateur
Prof. LIMAM Ali	INSA de Lyon	Examinateur

INSA de Rennes

Laboratoire de Génie Civil et Génie Mécanique (LGCGM)

H D R

à mes parents
à Mai Lan
à Cua
à Mymy

REMERCIEMENTS

Les travaux exposés dans ce mémoire de HDR émergent d'un travail collectif de plusieurs personnes que je ne saurai citer de façon exhaustive. Ces personnes que je remercie du fond du cœur, m'ont aidé à produire des résultats et à m'orienter dans mes réflexions, elles ont partagé avec moi des responsabilités et m'ont soutenu et motivé dans les moments difficiles. J'espère n'oublier personne dans cette page de remerciements.

Mes premiers remerciements s'adressent au Professeur Mohammed Hjiaj pour bien des raisons tant tu as contribué à mes activités de recherche et à mon évolution professionnelle durant ces dix dernières années. Je n'oublierai jamais le coup de fil que tu m'a passé en mai 2005 me demandant de venir faire une thèse avec toi. Cela a été un tournant dans ma carrière professionnelle. Je te dois énormément tant sur le plan scientifique que personnel, pour m'avoir suivi et soutenu pendant de nombreuses années.

Je tiens à remercier mes collègues, Hugues, Samy, Maël, Fred, David, Christian, Quentin, pour votre compétence, votre disponibilité, et pour l'ambience de travail chaleureuse que vous contribuez tous à créer dans les bureaux et sur la dalle d'essai. J'adresse un remerciement tout particulier au Professeur Jean-Marie Aribert et Alain Lachal qui ont su me faire profiter de leur expérience et de leur savoir faire. Mes remerciements vont aussi à nos secrétaires Nathalie et Jacqueline pour votre dévouement sans faille au sein du laboratoire et du département.

Un très grand merci à tous les doctorants ayant participé aux travaux présentés dans cette HDR : Van Anh Lai, Manuel Manthey, Van Toan Tran et Pisey Keo. Je remercie aussi Philippe Le Grognec et Enzo Martinelli, Jean-Marc Battini, Olivia Mirza, Nguyen Xuan Huy avec qui j'ai collaboré pour les travaux présentés ici.

Je remercie très vivement Cristina Mihaela Campian, Panagiotis Kotronis, Luc Taerwe (qui ont la tâche de rapporteurs), Oreste Salvotore Bursi, Emmanuel Ferrier, Ali Limam pour m'avoir fait l'honneur de participer à mon jury et d'évaluer mon travail.

En dernier lieu dans cette longue liste de remerciements, mes pensées se tournent vers mes parents, mon épouse Mai Lan et nos deux enfants Cua et Mymy pour leur patience, leur amour et leurs encouragements. Merci infiniment !

TABLE DES MATIÈRES

LISTE DES FIGURES

LISTE DES TABLEAUX

INTRODUCTION GÉNÉRALE

Ce mémoire synthétise l'ensemble des travaux de recherche que j'ai menés au sein de l'équipe GEOSAX du laboratoire LGCGM après ma nomination en octobre 2010 à l'INSA de Rennes sur un poste de Maître de Conférences. L'essentiel de ces travaux concerne la modélisation expérimentale, théorique et numérique des structures mixtes et hybrides (acier-béton et bois-béton) et s'intéresse aux développements des outils numériques et des méthodes de dimensionnement destinés à ces structures.

Ma thèse de doctorat, effectuée à l'INSA de Rennes et l'université de Wollongong (Australie) de 2005 à 2009, contient déjà la plupart des ingrédients qui seront le fil conducteur de ma carrière de chercheur. Durant ma thèse, j'ai travaillé sur des problématiques de la modélisation du comportement des poutres mixtes acier-béton avec la prise en compte des effets différés du béton. L'objectif principal de ma thèse a été de développer des outils numériques, à savoir des modèles éléments finis, pour l'analyse du comportement non-linéaire des poutres mixtes acier-béton avec glissement à l'interface. Ceci m'a donné l'occasion de démarrer mes travaux avec un profil de recherche à caractère numérique. Entre 2009 et 2010, en étant qu'ingénieur d'études au laboratoire LGCGM, j'ai eu l'opportunité de participer à une expérimentation en vraie grandeur sur un assemblage à brides circulaires boulonnées. Cette première expérience a permis d'ajouter à mon profil initial un volet expérimental qui s'avère indispensable pour une recherche en Ingénierie Structurale.

Mes activités de recherche se sont articulées autour de trois thèmes. Le premier thème, qui est dans la continuité de ma thèse, porte sur la modélisation des poutres multicouches de Timoshenko. Il s'agit des développements des modèles éléments finis sophistiqués de type poutre multicouche servant à des analyses du comportement mécanique en flexion, du comportement vibratoire et du comportement au flambement des poutres/poteaux mixtes avec prise en compte de la déformation de cisaillement. Le second thème est l'étude expérimentale et numérique du comportement des planchers mixtes bois-béton sous sollicitations accidentelles. Les travaux de ce thème ont été menés dans le cadre d'un contrat de thèse CIFRE avec AIA Ingénierie. Enfin, le troisième thème des mes activités de recherche porte sur l'étude pré-normative des structures hybrides béton-acier. Il s'agit de structures de nouvelle génération dans lesquelles des profilés aciers sont noyés dans le béton afin d'améliorer les performances des structures classiques en béton armé. Les travaux ont été réalisés dans le cadre du projet européen RFCS SMARTCOCO dont j'assure la coordination à

l'INSA de Rennes, et trois thèses de doctorat que je co-encadre (dont deux soutenues et une en cours).

Organisation du document

Ce mémoire est composé de trois parties. La première partie du document est dédiée à la présentation de mes parcours professionnels et du rapport d'activités depuis que je suis à l'INSA de Rennes. Elle fait le bilan exhaustif de mes activités de recherche, d'encadrement, d'enseignement, et de responsabilités administratives assumées. Ensuite, la seconde partie du mémoire est consacrée à la présentation des travaux de recherche qui sont divisés en trois thèmes. Cette partie est rédigée dans un style didactique, sans jamais trop entrer dans les détails techniques. Une sélection des articles publiés est présentée dans la troisième partie de ce document, qui permettra aux lecteurs d'avoir accès à ces détails.

Partie I

Présentation générale du candidat

PARCOURS PROFESSIONNEL ET RAPPORT D'ACTIVITÉS

.1 Curriculum Vitae

.1.1 État Civil

Nom & Prénom :	**NGUYEN Quang Huy**
Date et lieu de naissance :	06 Novembre 1981 au Vietnam
Nationalité :	Franco-Vietnamienne
Situation familiale :	Marié, 2 enfants
Fonction actuelle :	**Maître de Conférences** à l'INSA de Rennes
Adresse professionnelle :	Département Génie Civil et Urbain, INSA de Rennes, 20, Avenue des Buttes de Coësmes, Rennes, France
Téléphone :	+ 33 2 23 23 83 94
Email :	qnguyen@.insa-rennes.fr

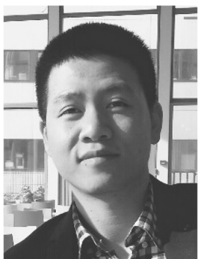

.1.2 Formation et titres universitaires

2005-2009 : INSA de Rennes et Université de Wollongong (Australie)

- Doctorat en Génie Civil (**double diplôme**) : Thèse en cotutelle internationale entre l'INSA de Rennes et l'Université de Wollongong (Australie).
- Titre : *Modélisation du comportement non-linéaire des poutres mixtes acier-béton avec prise en compte des effets différés.*
- Directeurs de Recherche : Prof. Mohammed Hjiaj (INSA de Rennes) ; Prof. Brian Uy (University of New South Wales, Australia) ; Prof. Alex Remennikov (University of Wollongong, Australia).
- Thèse défendue le 13 juillet 2009 à l'INSA de Rennes avec la mention très honorable (mention la plus élevée à l'INSA de Rennes).
- Jury : Sherif El-Tawil, University of Michigan, USA (Rapporteur) ; Vincent de Ville de Goyet, Université de Liège, BE (Rapporteur) ; Ahmed Elghazouli, Imperial College, UK (Rapporteur) ; Jean-Pierre Jaspart, Université de Liège, BE ((Rapporteur) ; Jean-Marie Aribert (Président du Jury).

2004-2005 : INSA de Rennes

- Diplôme de Master Recherche en Ingénierie Mécanique et Génie Civil.
- Mémoire : Modélisation et simulation du comportement élasto-plastique avec endommagement anisotrope de l'argilite.
- Mention : Bien (1^{er}/36)

2002-2005 : Diplôme d'Ingénieur en Génie Civil et Urbanisme de l'INSA de Rennes

.1.3 Parcours professionnel

- **2010-2015** : Maître de Conférences à l'INSA de Rennes.
- **2009-2010** : Ingénieur d'études à l'INSA de Rennes.
- **2008-2009** : ATER au département GCU de l'INSA de Rennes.

.2 Activités de Recherche à caractère numérique

.2.1 Modélisation du comportement des éléments mixtes multicouches (acier-béton ou bois-béton) avec glissement d'interface (2005-2015)

Cet axe de recherche consiste à développer des outils numériques sophistiqués et performants, reposant sur les développements les plus récents de la mécanique non linéaire, afin de mieux cerner le comportement complexe des éléments mixtes multicouches (glissement à l'interface, effets différés, fissuration et couplage). Ces outils devraient pouvoir être utilisés dans diverses études paramétriques dont l'objectif est d'améliorer les règles de dimensionnement des poutres, poteaux et ossatures mixtes (acier-béton et bois-béton). Les développements suivants ont été réalisés depuis ma présence au sein du laboratoire LGCGM de l'INSA de Rennes :

- Matrice de raideur exacte pour les poutres (Bernoulli et Timoshenko) mixtes multicouches avec glissement d'interface : analyse élastique et visco-élastique (effets différés du béton) : **4 publications de rang A** [23, 29, 39, 40].
- Modèle éléments finis pour l'analyse du comportement non-linéaire matériel et géométrique des éléments multicouches avec glissement d'interface : **6 publications de rang A** [3, 19, 24, 36, 42].
- Solution semi-analytique pour l'analyse des effets du fluage et du retrait du béton sur le comportement des poutres mixtes acier-béton avec interaction partielle : **4 publica-**

tions de rang A [37, 38].

- Solution analytique pour le calcul des charges critiques de flambement (élastique et plastique) des poteaux multicouches avec glissement d'interface : **2 publications de rang A** [16, 17].
- Solution analytique pour la vibration libre des poutres multicouches avec glissement d'interface : **1 publication de rang A** [41].
- Modèle élasto-plastique endommageable du béton avec identification du modèle CEB FIP, fissuration, tension-stiffening.
- Modèle viscoélastique-plastique du béton pour le couplage des effets du temps et la fissuration : **1 publication de rang A** [34].
- Modèle thermo-mécanique couplé pour l'analyse des planchers mixtes bois-béton.

.2.2 Optimizing the seismic Performance of steel and steel and concrete structures by Standardizing material quality control (2009-2011)

Ce projet européen est financé par le Fond de Recherche pour le Charbon et l'Acier (RFCS). Le montant est de 172 500 €. L'INSA est leader pour le workpackage 9 (07/2007 - 06/ 2010). L'objectif est de prendre en compte de la variabilité des propriétés mécaniques de l'acier pour le dimensionnement des structures en acier et mixtes en zone sismique. Le but final recherché est une norme de production de l'acier qui garantit une production d'acier de qualité. Les participants sont Riva Acciaio S.p.A. (Italie), Université de Liège (Belgique), RWTH Aachen (Allemagne), University of Thessaly R.C. (Grèce), Arcelor-Mittal (Luxembourg), Università di Pisa (Italie). Les responsables internes du projet sont le Prof. Mohammed Hjiaj et le Dr. Hugues Somja.

Entre 2009 et 2011, j'ai été contributeur ponctuel à ce projet. Mes implications dans ce projet sont :

- Étudier le critère de ruine des structures en acier et mixtes en zone sismique.
- Déterminer la résistance d'un assemblage poutre-poteau et des fondations.
- Développer en Fortran un post-traitement pour la vérification de la ruine après une analyse dynamique non-linéaire, par éléments finis, des structures en acier et mixtes (code éléments finis FINELG).
- Déterminer le facteur de comportement (facteur q) en fonction de la rotation plastique ultime.

.2.3 Ductilité des ossatures mixtes (2010-2011)

Cet axe a permis de développer des outils numériques pour l'étude de la capacité de rotation des rotules plastiques dans les poteaux mixtes. L'objectif a été de déterminer cette capacité de rotation en prenant en compte les aspects de voilement local élasto-plastique. Les développements se sont faits dans le cadre du stage de Master Recherche de Tran Van Dang que j'ai co-dirigé avec le Dr. Hugues Somja. Le résultat de cette recherche a fait l'objet d'une publication (rang A) dans le journal "Earthquake Engineering and Structural Dynamics" (voir [43]).

.2.4 Comportement des assemblages à brides circulaires boulonnées (2010-2011)

Cette action de recherche a eu pour objectif de mettre au point des méthodes pratiques de calcul de la résistance statique d'assemblages par brides circulaires. Les méthodes développées se basent sur des modèles analytiques prenant en compte le contact entre platines, les déformations élasto-plastiques et la précontrainte des boulons. Les développements se sont faits dans le cadre de deux stages de Master Recherche de Kevin Moreau et Gwendal Jouan que j'ai co-dirigés avec le Prof. Mohammed Hjiaj et Dr. Maël Couchaux.

.3 Activités de Recherche à caractère expérimental

.3.1 Essai sur des assemblages de tubes ronds à brides boulonnées (2009-2010)

Cette action de recherche a été menée dans le cadre d'un projet de recherche expérimentale entre l'INSA de Rennes et le Centre Technique Industriel de la Construction Métallique (CTICM). Ce projet a eu pour objectif l'étude expérimentale du comportement en flexion de deux profils creux circulaires, reliés entre eux par un assemblage à brides boulonnées fonctionnant essentiellement dans le domaine élastique. L'un des objectifs principaux de cette action de recherche était de clarifier l'influence de la précontrainte dans les boulons et éventuellement les défauts de planéité des brides sur le comportement de l'assemblage. Le comportement à l'état limite ultime de ce type d'assemblage a été également étudié. Un essai sur une poutre de 7.5 mètre de long (cf. Figure 1) a été effectué en Novembre 2009 au sein du Laboratoire Génie Civil et Génie Mécanique de l'INSA de Rennes.

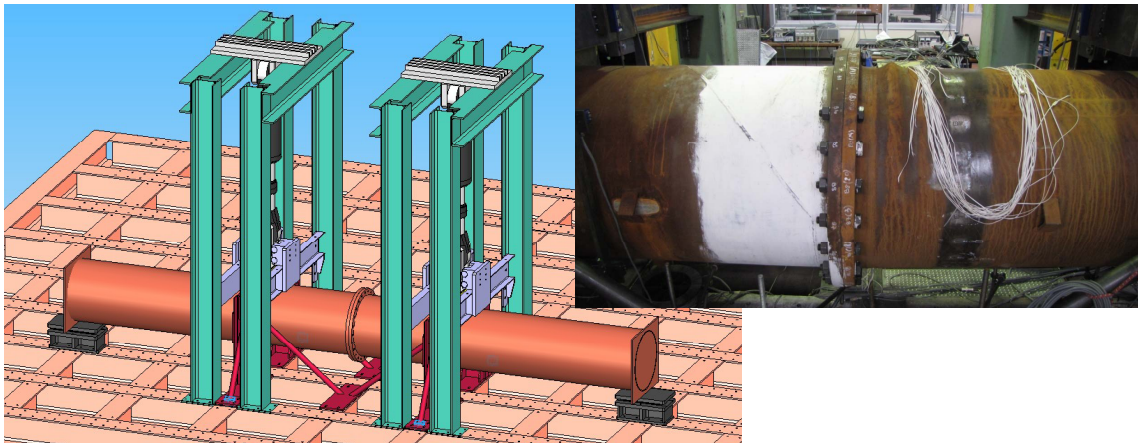

Figure 1 – Essai réalisé sur un assemblage à brides circulaires boulonnées

.3.2 Caractérisation du comportement statique et cyclique des planchers mixtes bois-béton (2011-2014)

Cette action de recherche a été conduite dans le cadre d'un partenariat entre l'INSA de Rennes et l'entreprise AIA Ingénierie (Angers). Le montant du volet expérimental a été de 60 000 €HT. J'ai été le pilote, pour l'INSA de Rennes, de ce projet.

Description : Le procédé de construction dénommé "Système mixte Bois-Béton" ou SBB, destiné à la réalisation de planchers (neuf ou réhabilitation), est développé par la société AIA Ingénieries depuis 1999 et a fait l'objet d'un brevet. Ce projet a eu pour but de caractériser le comportement des planchers mixtes bois-béton en situation d'usage dite accidentelle, sous incendie d'une part, et sous situation sismique d'autre part. L'objectif principal était de proposer des méthodes de dimensionnement au séisme et à l'incendie, reposant sur une base scientifique, rigoureuses et validées par des campagnes expérimentales exhaustives. La première partie du projet s'est appuyée sur une campagne d'essais Push-Out cycliques réalisée à l'INSA de Rennes (12 spécimens). Celle-ci a permis de déterminer la résistance maximale cyclique et *d'obtenir l'avis technique du CSTB en décembre 2012*. Les essais au feu ont été réalisés au laboratoire Efectis.

Cette action a fait l'objet d'une thèse que j'ai co-encadrée et d'une publication dans un ouvrage "Materials and Joints in Timber Structures" édité par la RILEM (voir Annexe 10).

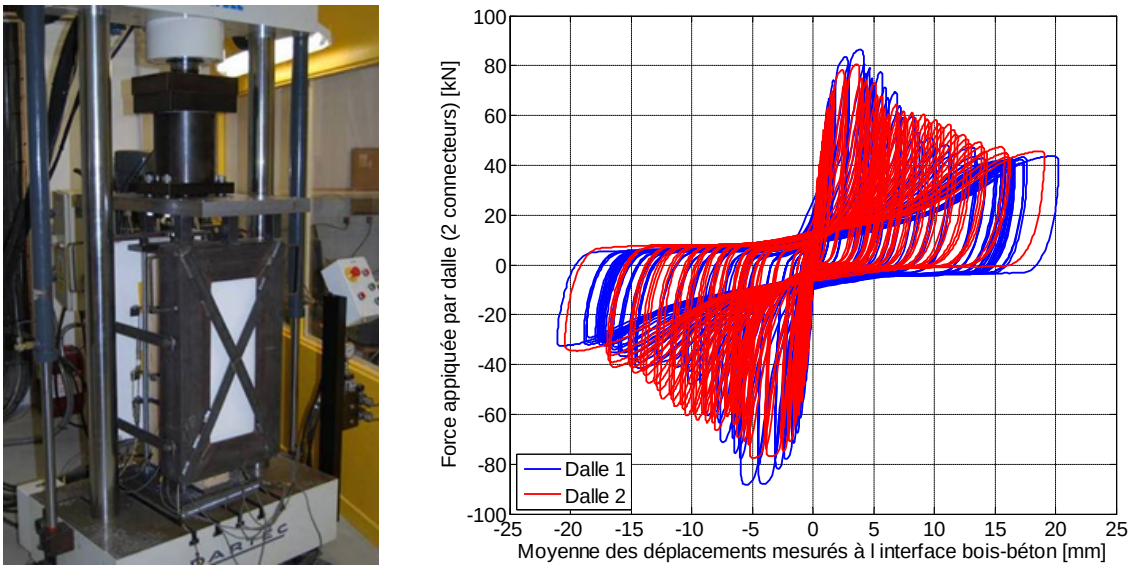

Figure 2 – Montage expérimental et résultats des essais cycliques des spécimens SBB

.3.3 Caractérisation du comportement des façades mixtes bois-béton sous sollicitations quasi-statiques (2012-2013)

Cette action de recherche a été réalisée dans le cadre d'un projet de recherche expérimentale avec l'entreprise AIA Ingénierie (Angers). le montant du volet expérimental a été de 13 860 €HT. J'ai été responsable interne de ce projet.

Une campagne d'essais (16 spécimens) a été réalisée à l'INSA de Rennes avec pour objectif, la caractérisation du comportement des connecteurs SBB de façades mixtes Bois-Béton sous sollicitations quasi-statiques (voir Figure 3). Dans ce système de connexion, la peau du béton est séparée de l'ossature bois par une lame d'air variant de 2cm à 4cm qui affecte la rigidité et la résistance de la connexion. Afin d'optimiser le développement des façades, il a été nécessaire de connaître les propriétés de la connexion du système sous actions mécaniques dans le sens vertical du bois. Le comportement de la connexion suivant le sens transversal du bois a dû être également caractérisé afin de tenir compte de la dilatation thermique du béton qui engendre une sollicitation perpendiculaire aux fibres du bois.

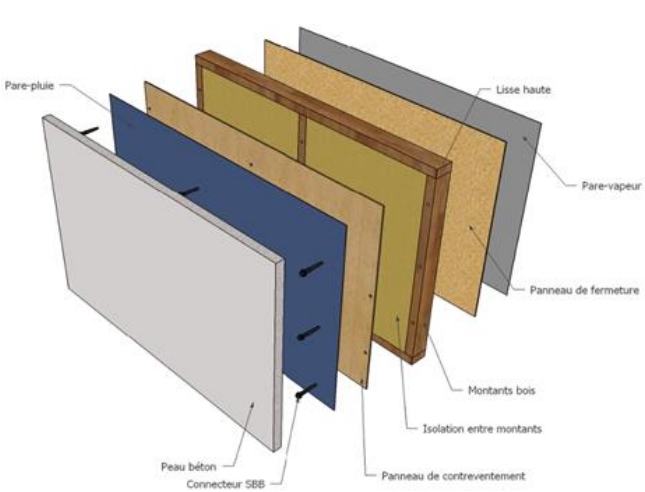

Figure 3 – Composition d'une façade mixte bois-béton et montage expérimental

.3.4 Projet Européen SMARTCOCO : SMART COmposite COnstruction (2012-2015)

Ce projet européen est financé par le Fond de Recherche pour le Charbon et l'Acier (RFCS). Le montant total est de 1 300 000 €dont 315 635 €pour le budget INSA. Les participants sont l'Université de Liège (Belgium) ; l'Imperial College (Royaune Uni) ; Besix (Belgium) ; Arcelormittal (Luxemburg) ; Plumiecs (Belgium). Je suis **responsable technique** pour la partie INSA de ce projet.

Description : L'objectif est de développer des règles de dimensionnement de structures en béton armé renforcées par des profilés métalliques en traitant les cas les plus courants :

- Poteaux ou murs en béton armé contenant plusieurs profilés noyés ;
- Connections de planchers béton minces en béton armé aux poteaux par des clés de cisaillement constituées de tronçons de poutres métalliques ;
- Éléments acier noyés dans le béton en général, et notamment les cadres de renforcement métalliques autour des ouvertures dans les noyaux centraux ;
- Renforts de poteaux en béton armé par un profilé acier sur un niveau, renforts dans les murs dans les zones de discontinuité, etc.

Ce type de structure ne rentre pas dans le cadre des normes de dimensionnement existantes comme les Eurocodes 2 et 4. Les règles de dimensionnement sont développées sur base des études numériques et expérimentales à l'échelle 1. L'INSA de Rennes participe aux études expérimentales, numériques et analytiques sur des éléments hybrides de type

poteau, assemblage poteau-poutre et clef de cisaillement. J'ai mené à bien une lourde campagne d'essai de 7 corps d'épreuve de mur hybride et 4 corps d'épreuve d'assemblage hybride (voir Figure 4).

Figure 4 – Montage expérimental des essais du projet SMARTCOCO

Trois thèses de doctorat ont été lancées sur les problématiques de ce projet. Les résultats obtenus ont fait l'objet de 3 publications que j'ai présentées dans des conférences internationales. Par ailleurs, j'ai rédigé 3 rapports de recherche dans le cadre du projet RFCS.

.4 Activités de Recherche à caractère pré-normatif

Cette action de recherche est liée directement au projet Européen SMARTCOCO mentionné au paragraphe .3.4. L'objectif des travaux dans cet axe de recherche est de participer à un effort international européen destiné à développer une norme de dimensionnement pour des structures hybrides acier-béton. Cet objectif nécessite des travaux de grande ampleur à moyen et long terme. Dans le cadre du projet SMARTCOCO, une méthode de dimensionnement a été proposée par l'INSA de Rennes (dont je suis l'acteur principal) pour des éléments hybrides suivants :

- Murs/Poteaux en béton armé renforcés par plusieurs profilés métalliques noyés : 1 publication [35].
- Poteaux élancés en béton armé renforcés par plusieurs profilés métalliques noyés : **1 publication de rang A** [25].
- Assemblage entre poteau béton armé et poutre métallique (ou mixte) par clef de cisaillement noyé dans le poteau.

.5 Encadrement doctoral et scientifique

.5.1 Thèses

T1. Van-Anh LAI (***01/10/2009 -14/12/2012***). Nonlinear analysis of steel-concrete beams taking into account the shear deformability of the steel joist. Bourse MENRT. **Taux d'encadrement 65%**.

T2. Manuel MANTHEY (***01/03/2012 -03/09/2015***). Comportement des poutres mixtes bois-béton sous sollicitations accidentelles (sismique et incendie). Bourse CIFRE. **Taux d'encadrement 65%**.

T3. Van Toan TRAN (***01/10/2011 -27/11/2015***). Étude numérique et expérimentale des murs en béton armé renforcés par plusieurs profilés métalliques totalement enrobés. Bourse du Gouvernement Vietnamien. **Taux d'encadrement 65%**.

T4. Pisey KEO (***01/10/2011 -27/11/2015***). Modélisation du comportement des poteaux hybrides acier-béton. Bourse de l'Ambassade de France au Cambodge. **Taux d'encadrement 40%**.

T5. Viet Phuong NGUYEN (***thèse en cours***). Experimental and numerical studies of RCS hybrid joints under static loading. Bourse du Gouvernement Vietnamien. **Taux d'encadrement 65%**.

T6. Dang Dung LE (***thèse en cours***). Seismic performance of a nouvel RCS hybrid joint. Bourse du Gouvernement Vietnamien. **Taux d'encadrement 50%**.

.5.2 Masters Recherche

MR1. Van Dang TRAN (***2010***). Étude de la capacité de rotation des poteaux mixtes. **Taux d'encadrement 80%**.

MR2. Kevin MOREAU (***2010***). Étude des assemblages de tubes cylindriques par brides boulonnées en construction métallique. **Taux d'encadrement 50%**.

MR3. Gwendal JOUAN (***2010***). Développement d'un modèle analytique de type poutre rendant compte du comportement de platines circulaires en contact avec application au cas particulier des assemblages par brides circulaires boulonnées. **Taux d'encadrement 50%**.

MR4. Sach Nam NGUYEN (***2011***). Exact free vibration analysis of Timoshenko composite beams with partial interaction. **Taux d'encadrement 100%**.

MR5. Sreyleak DIM (***2013***). Dimensionnement d'un nouveau type d'assemblage poutre-poteau pour des structures hybrides. **Taux d'encadrement 100%**.

MR6. Tuan Toan NGUYEN (***2013***). Méthode d'analyse élastique avec redistribution des portiques mixtes avec prise en compte de la fissuration et la plasticité. **Taux d'encadrement 100%**.

.6 Responsabilités scientifiques

- 2011-2014 : responsable scientifique du projet industriel SBB au niveau interne de l'INSA de Rennes. Budget 60 000 €. (voir paragraphe .3.2).
- 2012-2015 : coordinateur interne du projet Européen RFCS SMARTCOCO pour l'INSA de Rennes. Budget 315 635 €. (voir paragraphe .3.4).

.7 Rayonnement

.7.1 Collaborations scientifiques internationales

2014 INSAR-UWS Collaboration on Application of Hybrid Structures under Elevated Temperatures. Partenaire : University of Western Sydney - Australia. UWS IRIS grant project. Budget 15 000 AU$.

2013-2015 INSAR-UTC Research Collaboration. Experimental study of RCS joint under cyclic loading. Partenaire : University of Transport and Communications Hanoi, Vietnam. NAFOSTED grant project. Budget 500 000 000 VND.

.7.2 Participation à des comités scientifiques/techniques

Depuis 2013 je suis impliqué dans le Comité Technique "Composites Structures TC 11" de la Convention Européenne de la Construction Métallique en tant que membre actif (corresponding member) désigné, pour la France, par le Chairman du Comité Prof. Riccardo ZANDONINI. Ce comité a pour vocation d'initier des actions de recherche concertées entre partenaires européens pour promouvoir la construction mixte acier-béton, en se concentrant sur les points techniques qui nécessitent de trouver des solutions. Il s'agit autant de conceptions nouvelles, proposées par les partenaires industriels très actifs dans ce comité, que de points techniques de la norme méritant des développements.

.7.3 Expertise d'articles (Peer review)

J'ai été "reviewer" pour les journaux internationaux suivants :

- Journal of Structural Engineering (ASCE) : 17 fois
- Finite Elements in Analysis and Design : 1 fois
- Engineering Structures : 1 fois.
- Steel and Composite Structures, An International Journal : 2 fois.

.8 Prix et distinctions

2014 : Prime d'Encadrement Doctoral et de Recherche (PEDR).

.9 Productions scientifiques

Mes références bibliographiques sont listées ci-dessous. Elles peuvent se synthétiser numériquement de la façon suivante (du 01/09/2007 au 15/02/2016) :

- 19 articles dans des revues internationales à comité de lecture (Rang A).
- 17 articles en conférences internationales avec comité de lecture et actes.
- une communication par affiche dans un congrès international.
- 2 communications avec actes dans des congrès nationaux .
- 1 livre scientifique.
- 2 rapports de recherche.

.9.1 Publications dans des revues internationales à comité de lecture

J1. Q-H. Nguyen, M Hjiaj, B Uy and S. Guezouli. Analysis of composite beams in the hogging moment regions using a mixed finite element formulation. *Journal of Constructional Steel Research* 2009 ; 65(3) : 737-748. `(5-Year IF 1.699) 23 citations` http://dx.doi.org/10.1016/j.jcsr.2008.07.026.

J2. J-M. Battini, **Q-H. Nguyen** and M. Hjiaj. Non-linear finite element analysis of composite beams with interlayer slips. *Computers and Structures* 2009 ; 87(13-14) : 904-912. `(5-Year IF 2.528) 36 citations` http://dx.doi.org/10.1016/j.compstruc.2009.04.002.

J3. Q-H. Nguyen, M. Hjiaj and J-M. Aribert. A space-exact beam element for time-dependent analysis of composite members with discrete shear connection. *Journal of Constructional Steel Research* 2010 ; 66 :1330-1338. `(5-Year IF 1.699) 13 citations` http://dx.doi.org/10.1016/j.jcsr.2010.04.007.

J4. Q-H. Nguyen, M Hjiaj and B. Uy. Time-dependent analysis of composite beams with continuous shear connection based on a space-exact stiffness matrix. *Engineering Structures* 2010 ; 32(9) : 2902-2911. `(5-Year IF 2.152) 16 citations` http://dx.doi.org/10.1016/j.engstruct.2010.05.009.

J5. S. Guezouli, M. Hjiaj and **Q-H. Nguyen**. Local Buckling influence on the moment redistribution for continuous composite beams in bridges. *The Baltic Journal for Road and Bridges Engineering* 2010 ; 5(4) : 207-217.(5-Year IF 0.70) 4 citations https://doi.org/10.3846/bjrbe.2010.29.

J6. **Q-H. Nguyen**, E. Martinelli and M. Hjiaj. Derivation of the "exact" stiffness matrix for a two-layer Timoshenko composite beam element with partial interaction. *Engineering Structures* 2011 ; 33(2) : 298-307. (5-Year IF 2.152) 41 citations http://dx.doi.org/10.1016/j.engstruct.2010.10.006.

J7. **Q-H. Nguyen**, M. Hjiaj and S. Guezouli. Exact finite element model for shear-deformable two-layer beams with discrete shear connection. *Finite Element Analysis and Design* 2011 ; 47(7) : 718-727. (5-Year IF 1.967) 17 citations http://dx.doi.org/10.1016/j.finel.2011.02.003.

J8. P. Le Grognec, **Q-H. Nguyen** and M. Hjiaj. Exact buckling solution for two-layer Timoshenko beams with interlayer slip. International *Journal of Solids and Structures* 2012 ; 49 : 143-150. (5-Year IF 2.483) 16 citations http://dx.doi.org/10.1016/j.ijsolstr.2011.09.020.

J9. **Q-H. Nguyen**, M Hjiaj and P. Le Grognec. Analytical approach for free vibration analysis of two-layer Timoshenko beams with interlayer slip. *Journal of Sound and Vibration* 2012 ; 331 : 2902-2911. (5-Year IF 2.223) 14 citations http://dx.doi.org/10.1016/j.jsv.2012.01.034.

J10. E. Martinelli, **Q-H. Nguyen** and M. Hjiaj. Dimensionless formulation and comparative study of analytical models for composite beams in partial interaction. *Journal of Constructional Steel Research* 2012 ; 75 : 21-31. (5-Year IF 1.699) 9 citations http://dx.doi.org/10.1016/j.jcsr.2012.02.016.

J11. M. Hjiaj, J-M. Battini and **Q-H. Nguyen**. Large displacement analysis of shear deformable composite beams with interlayer slips. *International Journal of Non-Linear Mechanics* 2012 ; 47(8), 895-904. (5-Year IF 1.870) 14 citations http://dx.doi.org/10.1016/j.ijnonlinmec.2012.05.001.

J12. S. Nofal, H. Somja, M. Hjiaj and **Q-H. Nguyen**. Effects of material variability on the ductility of composite beams and overstrength coefficients. *Earthquake Engineering and Structural Dynamics* 2013 ; 42(7) : 953-972. (5-Year IF 2.500) 4 citations http://dx.doi.org/10.1002/eqe.2253.

J13. S. Guezouli, A. Lachal and **Q-H. Nguyen**. Numerical investigation of internal force transfer mechanism in push-out tests. *Engineering Structures* 2013 ; 52 :140-152. (5-Year IF 2.152) 7 citations http://dx.doi.org/10.1016/j.engstruct.2013.02.021.

J14. **Q-H. Nguyen**, V-A. Lai, M. Hjiaj. Force-based FE for large displacement inelastic analysis of two-layer Timoshenko beams with interlayer slips. *Finite element analysis and design* 2014 ; 85 :1-10. (5-Year IF 1.967) 3 citations http://dx.doi.org/10.1016/j.finel.2014.02.007.

J15. P. Le Grognec, **Q-H. Nguyen** and M. Hjiaj. Plastic bifurcation analysis of a two-layer shear-deformable beam-column with partial interaction. *International Journal of Non-Linear Mechanics* 2014 ; 67 : 85-94. (5-Year IF 1.870) 3 citations http://dx.doi.org/10.1016/j.ijnonlinmec.2014.08.010.

J16. P. Keo, H. Somja, **Q-H. Nguyen** and M. Hjiaj. Simplified design method for slender hybrid columns. *Journal of Constructional Steel Research* 2015 ; 110 :101-120. (5-Year IF 1.699) 2 citations http://dx.doi.org/10.1016/j.jcsr.2015.03.006.

J17. P. Keo, **Q-H. Nguyen**, H. Somja and M. Hjiaj. Geometrically nonlinear analysis of hybrid beam-column with several encased steel profiles in partial interaction. *Engineering Structures* 2015. 100 :66-78. (5-Year IF 2.152) 1 citation http://dx.doi.org/10.1016/j.engstruct.2015.05.030.

J18. P. Keo, M. Hjiaj, **Q-H. Nguyen** and H. Somja. Derivation of the exact stiffness matrix of shear-deformable multi-layered beam element in partial interaction. *Finite Elements in Analysis and Design* 2016. 112 :40-49. (5-Year IF 1.967) 0 citation http://dx.doi.org/10.1016/j.finel.2015.12.004.

J19. Q-H. Nguyen and M. Hjiaj. Nonlinear time-dependent behavior of composite steel-concrete beams. *Journal of Structural Engineering ASCE* 2016 (**in press**)(5-Year IF 1.910). http://dx.doi.org/10.1061/(ASCE)ST.1943-541X.0001432

J20. XH. Nguyen, **Q-H. Nguyen**, DD. Le and O. Mirza. Experimental study on seismic performance of new RCS connection. *Engineering Structures* (5-Year IF 2.152). **Paper under review**.

.9.2 Communications internationales avec comité de lecture et actes (proceedings)

C1. Q-H. Nguyen, M. Hjiaj, B. Uy. Time effects analysis of composite beams using a mixed F. E. formulation. *International Conference on Structural Engineering, Mechanics and Computation* (SEMC 2007), Cape Town, South Africa, 10-12 September 2007.

C2. Q-H. Nguyen, M. Hjiaj, B. Uy. Calibration of a mixed finite element model for the monotonic analysis of continuous composite beams. *International Conference on Modern Design, Construction and Maintenance of Structures* (MDCMS 2007), Hanoi, Vietnam, 10-12 December 2007.

C3. Q-H. Nguyen, M. Hjiaj, B. Uy and S. Guezouli. A class of finite elements for nonlinear analysis of composite beams. *Composite Construction VI Conference* (CCVI), Colorado, USA, 20-24 July 2008.

C4. Q-H. Nguyen, M. Hjiaj, B. Uy and S. Guezouli. Nonlinear F.E. analysis of composite beams. *5th European Conference on Steel and Composite Structures*, Graz, Austria, 3-5 Septembre 2008.

C5. S. Guezouli, M. Hjiaj, **Q-H. Nguyen**. Connection degree in composite continuous beams : Influence on the bending moment capacity. *5th European Conference on Steel and Composite Structures*, Graz, Austria, 3-5 Septembre 2008.

C6. M. Hjiaj, D-L. Dao, **Q-H. Nguyen**, V-T. Nguyen, G. de Saxcé. A variational stress update algorithm for the non-associated Drucker-Prager model with isotropic hardening. *International Conference on Computational Solid Mechanics*, 27-30 November 2008, Hochiminh City, Vietnam, pp. 175-184.

C7. Q-H. Nguyen, M. Hjiaj and B. Uy. Analysis of elastic-perfectly plastic composite beams using equilibrium elements. *9th International Conference on Steel Concrete Composite and Hybrid Structures*, 8-10 July 2009. Leeds, UK, pp. 669-674 (ISBN 9789810830687).

C8. Q-H. Nguyen, M. Hjiaj and J-M. Battini. Geometrically non-linear finite element analysis of two-layer composite beams with interlayer slip. *IV European Conference on Computational Mechanics*, Palais des Congrès, Paris, France, May 16-21, 2010.

C9. Q-H. Nguyen, M. Hjiaj and B. Uy. Closed-form solution for two-layer composite shear deformable beams with interlayer. *4th International Conference on Steel & Composite Structures*, 21-23 July 2010, Sydney, Australia.

C10. S. Nofal, **Q-H. Nguyen**, H. Somja and M. Hjiaj. Overstrength demands for joints in composite frames with account of actual European steel production. *6th European Conference on Steel and Composite Structures*. Budapest, Hungary. 31 August - 2 September 2011.

C11. M. Hjiaj, **Q-H. Nguyen** and J-M Battini. Geometrically nonlinear analysis of shear deformable composite members with partial interaction. *10th International Conference on Advances in Steel Concrete Composite and Hybrid Structures*. Singapore, 2 - 4 July 2012 (ISBN : 978-981-07-2615-7).

C12. Q-H. Nguyen, M. Hjiaj and P. Le Grognec. Analytical expressions of buckling loads for two-layer Timoshenko members with interlayer slips. *International conference on advances in computational mechanics*. August 14-16, 2012, HoChiMinh City, Vietnam (ISBN : 978-604-908-577-2).

C13. M. Manthey, **Q-H. Nguyen**, H. Somja, J. Duchêne and M. Hjiaj. Experimental Study of the

Composite Timber-Concrete SBB Connection under Monotonic and Reversed-Cyclic Loadings. *Materials and Joints in Timber Structures*. 2014 ; S. Aicher, H. W. Reinhardt and H. Garrecht, Springer Netherlands. 9 : 433-442. http://dx.doi.org/10.1007/978-94-007-7811-5_39

C14. Q-H. Nguyen, V-T. Tran and M. Hjiaj. Development of design method for composite columns with several encased steel profiles under combined shear and bending. *7th European Conference on Steel and Composite Structures*. Napoli, Italia, September 10-12, 2014.

C15. P. Keo, M. Hjiaj, **Q-H. Nguyen** and H. Somja. Nonlinear analysis of hybrid steel-concrete beam with interlayer slips. *11th World Congress on Computational Mechanics*. 20-25 July 2014, Barcelona, Spain.

C16. Q-H. Nguyen, M. Hjiaj, X.H. Nguyen and D.D Le. Finite Element analysis of a hybrid RCS beam-column connection. *The 3rd International Conference CIGOS 2015 on « Innovations in Construction »*. Paris, France, 11-12 May 2015.

C17. Q-H. Nguyen, X.H. Nguyen, D.D Le and O. Mirza. Experimental investigation on seismic response of exterior RCS beam-column connection. *11th International Conference on Advances in Steel Concrete Composite and Hybrid Structures*. Beijing, China, 3-5 December 2015.

.9.3 Communications internationales par affiche

C18. P. Keo, H. Somja, **Q-H. Nguyen** and M. Hjiaj. Design of slender hybrid columns. *IABSE Workshop "Hybrid2014 by iabse.ch" Exploring the Potential of Hybrid Structures for Sustainable Construction*. Hybrid 2014, Jun 2014, Fribourg, Switzerland.

.9.4 Communications nationales avec actes

C19. Q-H. Nguyen, M. Hjiaj et B. Uy. Méthode semi-analytique pour les effets du temps dans les poutres mixtes acier-béton. *XXVIe Rencontres Universitaires de Génie Civil*. 4 au 6 juin 2008, Nancy.

C20. Q-H. Nguyen, M. Hjiaj and E. Martinelli. Closed-form solution for Timoshenko composite beams with partial interaction. *XXVIIIe Rencontres Universitaires de Génie Civil*. 2 au 4 juin 2010, La Bourboule.

.9.5 Ouvrages scientifiques

O1. Q-H. Nguyen. Modélisation du comportement des poutres mixtes acier-béton : Avec prise en compte de la non-linéarité matérielle et des effets différés du béton. *Presses Académiques Francophones*. 2014 (ISBN 978-3-8381-8989-5). https://www.presses-academiques.com/pabooknguyen2014

.9.6 Rapports de recherche

R1. H. Degée, T. Bogdan, A. Plumier, N. Popa, L-G. Cajot, J-M. De Bel, P. Mengeot, M. Hjiaj, **Q-H. Nguyen**, H. Somja, A. Elghazouli, D. Bompa. RFCS SMARTCOCO project : SMART COmposite COnstruction. Mid-Term Report, 2013.

R2. Q-H. Nguyen. RFCS SMARTCOCO project : SMART COmposite COnstruction. WP6.1 Resistance to combined bending and shear of composite wall with three encased steel profiles. Test report, 2015.

.10 Activités pédagogiques

Mes enseignements à l'INSA de Rennes depuis 2010 sont listés ci-dessous :

- **Béton Armé I** : 3ème année, 12h cours magistraux + 8h travaux dirigés. http://fr.slideshare.net/nguyenmlan/cours-ba-i
- **Béton Armé II** : 4ème année, 24h cours magistraux + 24h travaux dirigés + Mini projet. http://fr.slideshare.net/nguyenmlan/cours-ba-ii
- **Béton Armé III** : 4ème année, 24h travaux dirigés + Mini projet.
- **Mécanique 3** : 2ème année, 20h travaux dirigés.
- **Mécanique 4** : 2ème année, 28h travaux dirigés.

.11 Responsabilités administratives

- **2010-2012** : Responsable pédagogique de la 3ème année élève-ingénieur du département Génie Civil et Urbain de l'INSA de Rennes.
- **Depuis 2012** : Responsable pédagogique de la 4ème année élève-ingénieur du département Génie Civil et Urbain de l'INSA de Rennes.

En tant que responsable d'année, je suis chargé de :

- faire l'emploi du temps ;
- préparer les contrats d'aménagement d'études pour les étudiants ;
- organiser des réunions pédagogiques, des conférences et des visites de chantier ;
- préparer le jury de fin d'année.

Partie II

Présentation des travaux de recherche

THÈME 1

MODÉLISATION DES POUTRES MULTICOUCHES DE TIMOSHENKO : INTERACTION PARTIELLE, NON-LINÉARITÉ MATÉRIELLE, INSTABILITÉ ET GRAND DÉPLACEMENT

1.1 Introduction

De nos jours, les structures multicouches sont largement utilisées dans le secteur du Bâtiment car, à l'étape de leur fabrication, elles offrent la possibilité de réaliser une structure adaptée, en terme de comportement, à sa future utilisation. Elles permettent d'obtenir des associations de comportement très variées adaptées aux multiples applications. Elles offrent des avantages considérables sur les plans mécaniques, économiques et architecturaux. La connexion entre les couches de la section constituées de matériaux différents est généralement faite, soit par collage, soit au moyen d'organes de liaison, appelés connecteurs. C'est cette connexion, qui assure l'action composite d'une section faite de matériaux différents. Le rôle majeur de la connexion est d'empêcher, ou tout au moins de limiter, le glissement tendant à se produire à l'interface des matériaux sous l'effet des actions extérieures et de transmettre les efforts entre les couches constituées de différents matériaux. Les structures multicouches étudiées dans mes travaux sont des éléments de type poutre (Figure 1.1).

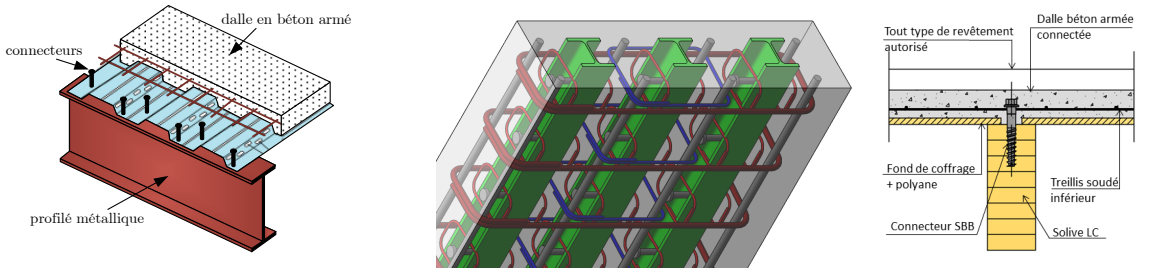

Poutre mixte acier-béton | Poteau hybride acier-béton | Poutre mixte bois-béton

Figure 1.1 – Exemple des poutres multicouches

La présence du glissement à l'interface des couches rend l'analyse des poutres multicouches plus complexe. Plusieurs modèles théoriques caractérisés par différents niveaux de complexité ont été proposés et sont actuellement disponibles dans la littérature. La première formulation pour les poutres mixtes acier-béton (à deux couches) avec interaction par-

tielle a été développée par Newmark et al. (1951) [32]. Dans cette formulation, la théorie élastique des poutres d'Euler-Bernoulli est adoptée. Depuis, sur base de cette formulation, plusieurs chercheurs ont développé des modèles analytiques pour l'analyse du comportement statique et dynamique des poutres multicouches dans le domaine linéaire (voir par exemple [9, 12, 18, 20, 37, 45]) ainsi que dans le domaine non-linéaire. En outre, plusieurs modèles numériques basés sur les mêmes hypothèses cinématiques ont été développés pour étudier le comportement non-linéaire des poutres multicouches avec glissement à l'interface (voir par exemple [2, 3, 11, 26, 36, 47, 51]).

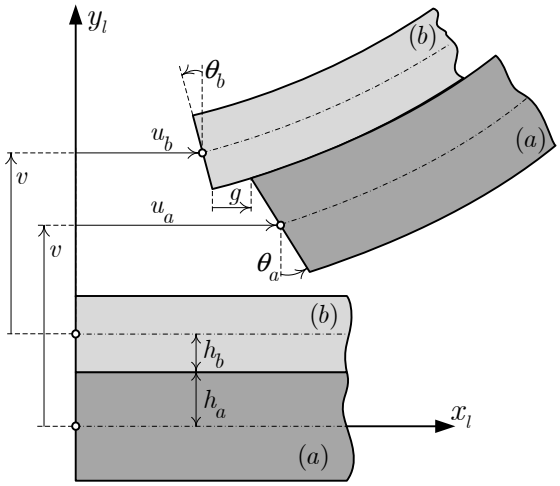

Figure 1.2 – Cinématique d'une poutre Timoshenko à deux couches

Au-delà des différentes formulations alternatives proposées dans la littérature sur la base des hypothèses cinématiques d'Euler-Bernoulli [32], le plus important progrès dans la théorie des poutres multicouches en interaction partielle est de prendre en compte la déformation de cisaillement de la section transversale. Il s'agit de considérer que chaque couche se comporte comme une poutre de Timoshenko. La Figure 1.2 illustre la cinématique d'une poutre de Timoshenko à deux couches. Rappelons qu'une cinématique de type Timoshenko impose à chaque couche initialement droite une rotation qui lui est propre et qui est distincte de la rotation locale de la fibre neutre.

Après ma thèse de doctorat en 2009, en menant une étude bibliographique, j'ai trouvé qu'il y avait très peu de travaux de recherche dans la littérature traitant le problème de déformation de cisaillement dans les poutres courtes multicouches. On peut citer ici les

travaux de Murakami (1984) [30], de Ranzi and Zona (2007) [46], de Xu et Wu (2007) [54], de Schnabl et al. (2007) [49]. Par suite, je me suis lancé dans cet axe de recherche. L'objectif principal est de développer des outils numériques afin d'analyser le comportement mécanique en flexion, du comportement vibratoire et du comportement au flambement des poutres multicouches avec prise en compte de la déformation de cisaillement des couches.

1.2 Présentation du problème

L'objet de l'étude est une poutre mixte [1] plane, initialement droite, de longueur L_0, constituée éventuellement de sections transversales de matériaux différents, avec des connecteurs de cisaillement à l'interface qui sont supposés répartis le long de l'interface (Figure 1.3). Dans la configuration de référence, la couche i ($i = a, b$) occupe un volume Ω_i de section transversale constante A_i, de moment quadratique I_i, de hauteur $2h_i$, et de masse par unité de longueur m_i.

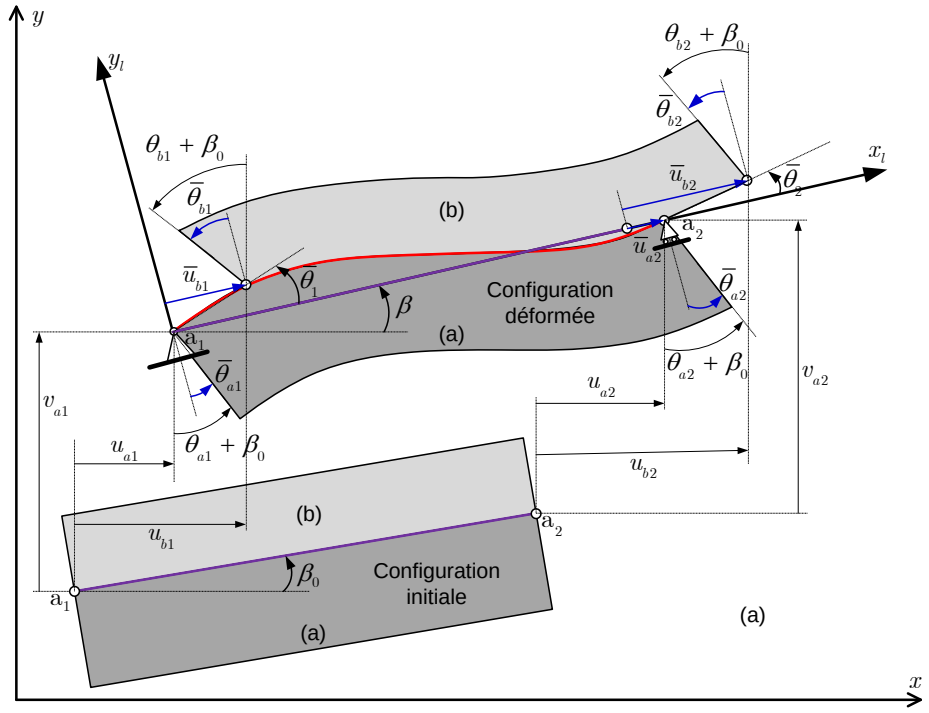

Figure 1.3 – Degré de liberté d'une poutre à deux couches dans le repère global et le repère local

1. Pour des raisons de clarté, je ne présente ici que le cas des poutres à deux couches

1.3 Poutres multicouches de Timoshenko en grand déplacement

1.3.1 Formulation corotationnelle

Afin de résoudre le problème de la non-linéarité géométrique, la formulation corotationnelle est choisie car elle est basée sur les hypothèses de grands déplacements mais petites déformations qui sont tout à fait adaptées à des poutres mixtes (acier-béton, bois-béton, bois-bois). L'idée de base est de décomposer le mouvement de l'élément en deux parties. La première partie est un mouvement de corps rigide et la deuxième est une déformation pure. Le système d'axes corotationnel utilisé gère les rotations et translations de l'élément. La déformation est toujours mesurée au niveau du repère de référence local de l'élément, puisque les grands déplacements et les grandes rotations sont contenus dans le mouvement du système d'axes corotationnel qui suit toujours le mouvement de l'élément. Lorsqu'on considère la déformation calculée comme petite, le modèle linéaire devient valable. L'avantage principal de la formulation corotationnelle par rapport à la formulation Lagrangienne Totale est que la non-linéarité matérielle peut être traitée à part en petite transformation dans le repère local, indépendamment de la non-linéarité géométrique. Il est important de souligner que la méthode corotationnelle est maintenant bien connue depuis plusieurs années. Cependant, lorsque l'on considère les poutres multicouches avec glissement à l'interface, il est nécessaire de sélectionner pertinemment les variables cinématiques locales et globales. A ma connaissance, avant nos travaux de recherche publiés depuis 2009, une telle formulation n'existait pas dans la littérature.

En se basant sur les notations définies sur la Figure 1.3, les déplacements nodaux et les rotations nodales dans le repère local $(x_l; y_l)$ sont reliés à ceux du repère global $(x; y)$ par les relations cinématiques suivantes :

$$\overline{\theta}_{ij} = \theta_{ij} - (\beta - \beta_0) \;\text{ avec }\; i = a, b \;\text{ et }\; j = 1, 2 \tag{1.1}$$

$$\overline{u}_{a2} = L_n - L_0 \tag{1.2}$$

$$\overline{u}_{b1} = g_1 \cos\left(\frac{\overline{\theta}_{a1} + \overline{\theta}_{b1}}{2}\right) \tag{1.3}$$

$$\overline{u}_{b2} = L_n - L_0 + g_2 \cos\left(\frac{\overline{\theta}_{a2} + \overline{\theta}_{b2}}{2}\right) \tag{1.4}$$

où L_0 et L_n sont, respectivement, la longueur initiale et celle à l'état déformé ; $g_j (j = 1, 2)$

est le glissement à l'interface défini dans le repère global :

$$g_j = \frac{u_{bj} - u_{aj}}{\cos\left(\frac{\overline{\theta}_{aj}+\overline{\theta}_{bj}}{2}\right) + \beta} \tag{1.5}$$

Notons $\mathbf{p}_g = [u_{a1}\ \ u_{b1}\ \ v_{a1}\ \ \theta_{a1}\ \ \theta_{b1}\ \ u_{b2}\ \ u_{b2}\ \ v_{a2}\ \ \theta_{a2}\ \ \theta_{b2}]^{\mathrm{T}}$ le vecteur des déplacements nodaux dans le repère global ; et $\mathbf{p}_l = \left[\overline{u}_{a2}\ \ \overline{u}_{b1}\ \ \overline{\theta}_{a1}\ \ \overline{\theta}_{b1}\ \ \overline{\theta}_{a2}\ \ \overline{\theta}_{b2}\right]^{\mathrm{T}}$ le vecteur des déplacements nodaux dans le repère local. Comme on peut le voir, à partir des équations de la cinématique corotationnelle (1.1)-(1.4), le vecteur $\mathbf{p}_l$ peut être exprimé comme fonction de $\mathbf{p}_g$:

$$\mathbf{p}_l = \mathbf{p}_l\left(\mathbf{p}_g\right) \tag{1.6}$$

Une fois le vecteur $\mathbf{p}_l$ obtenu à partir de $\mathbf{p}_g$, il est utilisé pour déterminer le vecteur des forces nodales $\mathbf{f}_l$ et la matrice de raideur $\mathbf{K}_l$. Il est à noter que $\mathbf{f}_l$ et $\mathbf{K}_l$ dépendent seulement de la déformation de l'élément local qui est géométriquement linéaire.

En dérivant l'équation (1.23) on obtient

$$\delta\mathbf{p}_l = \mathbf{B}_{lg}\delta\mathbf{p}_g \tag{1.7}$$

où $\mathbf{B}_{lg}$ est la matrice de transformation entre le repère local et le repère global. Finalement, en écrivant l'égalité des travaux virtuels dans les deux repères, on obtient le vecteur des forces nodales $\mathbf{f}_g$ et la matrice de raideur $\mathbf{K}_g$ dans le repère global :

$$\mathbf{f}_g = \mathbf{B}_{lg}^{\mathrm{T}}\mathbf{f}_l \tag{1.8}$$

$$\mathbf{K}_g = \mathbf{B}_{lg}^{\mathrm{T}}\mathbf{K}_l\mathbf{B}_{lg} + \left.\frac{\partial\left(\mathbf{B}_{lg}^{\mathrm{T}\mathbf{f}_l}\right)}{\partial\mathbf{p}_g}\right|_{\mathbf{f}_l} \tag{1.9}$$

1.3.2 Résultats essentiels

Les articles ci-dessous, fournis en annexe du présent rapport, font la synthèse du travail et des résultats obtenus :

Annexe 1 : M. Hjiaj, J-M. Battini and **Q-H. Nguyen**. Large displacement analysis of shear deformable composite beams with interlayer slips. *International Journal of Non-Linear Mechanics* 2012 ; 47(8), 895-904. `(5-Year IF 1.870) 14 citations` http://dx.doi.org/10.1016/j.ijnonlinmec.2012.05.001.

Annexe 2 : **Q-H. Nguyen**, V-A. Lai, M. Hjiaj. Force-based FE for large displacement inelastic analysis of two-layer Timoshenko beams with interlayer slips. *Finite element analysis and design* 2014 ; 85 :1-10. (5-Year IF 1.967) 3 citations http://dx.doi.org/10.1016/j.finel.2014.02.007.

Annexe 3 : P. Keo, **Q-H. Nguyen**, H. Somja and M. Hjiaj. Geometrically nonlinear analysis of hybrid beam-column with several encased steel profiles in partial interaction. *Engineering Structures* 2015. 100 :66-78. (5-Year IF 2.152) 1 citation http://dx.doi.org/10.1016/j.engstruct.2015.05.030.

Enfin, le détail de la démarche et des résultats peut être trouvé dans les thèses de Van-Anh LAI (soutenue le 14/12/2012) et de Pisey Keo (soutenue le 27/12/2015) que j'ai co-encadrées.

1.4 Matrice de raideur exacte de l'élément local linéaire

1.4.1 Conditions de compatibilité dans le repère local

Considérons un élément de poutre mixte à deux couches dans le repère local comme le montre la Figure 1.2. On suppose que les couches peuvent glisser l'une par rapport à l'autre mais qu'il n'y a pas de séparation entre elles. Comme mentionné dans l'introduction, dans ce travail, la théorie de la déformation de cisaillement au premier ordre (first-order shear deformation theory) de Timoshenko est appliquée pour chaque couche. Par conséquent, dans le système local, deux couches ont le même déplacement transversal mais les rotations et les courbures sont différentes. Sur la base de l'hypothèse des petits déplacements dans le système local, les relations de compatibilité s'écrivent :

$$\varepsilon_i = u_i' \tag{1.10}$$

$$\gamma_i = v - \theta_i' \tag{1.11}$$

$$\kappa_i = \theta_i' \tag{1.12}$$

$$g = u_b - u_a + h_a\theta_a + h_b\theta_b \tag{1.13}$$

où : ε_i, γ_i et κ_i sont respectivement la déformation axiale, la distorsion et la courbure au centre de gravité de la couche "i" ; g désigne le glissement à l'interface.

1.4.2 Équations d'équilibre

Les équations d'équilibre qui sont compatibles avec l'hypothèse cinématique indiquée au paragraphe 1.4.1 peuvent être obtenues à l'aide du principe des travaux virtuels s'écrivant :

$$\int_{L_0} \left[\sum_{i=a,b} (N_i \delta u_i' + M_i \delta \theta_i' + T_i \delta (v' - \delta \theta_i)) + D_{sc} \delta g \right] \mathrm{d}x - \int_{L_0} p_y \delta v \mathrm{d}x - \mathbf{f}_l^{\mathrm{T}} \delta \mathbf{p}_l \tag{1.14}$$

où : N_i, M_i et T_i sont respectivement l'effort axial, le moment fléchissant et l'effort tranchant calculés au centre de gravité de la couche "i" ; p_y est la charge répartie le long de l'élément ; D_{sc} représente l'effort de cisaillement à l'interface ; δu_i, δv et $\delta \theta_i$ désignent un champ des déplacements cinématiquement admissibles satisfaisant les conditions aux limites. En réalisant une intégration par parties, on obtient les équations d'équilibre comme suit :

$$N_a' - D_{sc} = 0 \tag{1.15}$$

$$N_b' + D_{sc} = 0 \tag{1.16}$$

$$M_i' - T_i + h_i D_{sc} = 0 \tag{1.17}$$

$$T_a' + T_b' - p_y = 0 \tag{1.18}$$

avec les conditions aux limites statiques suivantes : $N_a(L_0) = \mathbf{f}_l(1)$; $N_b(0) = -\mathbf{f}_l(2)$; $N_b(L_0) = \mathbf{f}_l(3)$; $M_a(0) = -\mathbf{f}_l(4)$; $M_b(0) = -\mathbf{f}_l(5)$; $M_a(L_0) = \mathbf{f}_l(6)$; $M_b(L_0) = \mathbf{f}_l(7)$.

1.4.3 Fonctions d'interpolation exactes

La matrice de raideur exacte, dans le cas d'un comportement élastique linéaire, peut être obtenue en utilisant des fonctions d'interpolation exactes qui, quant à elles, sont déduites de la solution analytique du problème aux limites. En combinant les équations fondamentales, à savoir les équations d'équilibre, de compatibilité et les lois constitutives, on obtient une équation différentielle d'ordre 5 de la seule variable D_{sc} :

$$\frac{EI}{k_{sc}GA} \partial_x^5 D_{sc} - \left(\frac{EI}{GA} \beta^2 + \frac{1}{k_{sc}} \right) \partial_x^3 D_{sc} + \mu^2 \partial_x D_{sc} = \frac{h p_y}{E_a I_a + E_b I_b} \tag{1.19}$$

La solution analytique de cette équation différentielle peut être exprimée sous la forme :

$$D_{sc} = C_1 \mathrm{e}^{\lambda_1 x} + C_2 \mathrm{e}^{-\lambda_1 x} + C_3 \mathrm{e}^{\lambda_2 x} + C_4 \mathrm{e}^{-\lambda_2 x} + C_5 + D_{sc}^0 \tag{1.20}$$

où C_i $(i = 1, 5)$ sont des constantes d'intégration et D^0_{sc} désigne la solution particulière qui dépend de p_y.
Nota : Pour des raisons de clarté, le détail du développement mathématique et les paramètres non définis ici sont donnés en Annexe III.

En substituant D_{sc} par l'expression analytique (1.20) dans les équations fondamentales du problème, on peut déterminer les expressions analytiques de toutes les variables cinématiques. Finalement, le champ des déplacements peut être exprimé en fonction des déplacements nodaux $\mathbf{p}_l$ et la solution particulière s'écrit comme suit :

$$u_a(x) = \mathbf{a}_{u_a}(x)\,\mathbf{p}_l + u^0_a(x) \tag{1.21}$$

$$u_b(x) = \mathbf{a}_{u_b}(x)\,\mathbf{p}_l + u^0_b(x) \tag{1.22}$$

$$v(x) = \mathbf{a}_v(x)\,\mathbf{p}_l + v^0(x) \tag{1.23}$$

$$\theta_a(x) = \mathbf{a}_{\theta_a}(x)\,\mathbf{p}_l + \theta^0_a(x) \tag{1.24}$$

$$\theta_b(x) = \mathbf{a}_{\theta_b}(x)\,\mathbf{p}_l + \theta^0_b(x) \tag{1.25}$$

$$g(x) = \mathbf{a}_g(x)\,\mathbf{p}_l + g^0(x) \tag{1.26}$$

où $\mathbf{a}_\clubsuit(x)$ désigne la fonction d'interpolation exacte de la variable cinématique $\clubsuit$.

1.4.4 Résultats essentiels

Les articles ci-dessous, fournis en annexe du présent rapport, font la synthèse du travail et des résultats obtenus :

Annexe 4 : Q-H. Nguyen, E. Martinelli and M. Hjiaj. Derivation of the "exact" stiffness matrix for a two-layer Timoshenko composite beam element with partial interaction. *Engineering Structures* 2011 ; 33(2) : 298-307. `(5-Year IF 2.152) 41 citations` http://dx.doi.org/10.1016/j.engstruct.2010.10.006.

Annexe 5 : Q-H. Nguyen, M. Hjiaj and S. Guezouli. Exact finite element model for shear-deformable two-layer beams with discrete shear connection. *Finite Element Analysis and Design* 2011 ; 47(7) : 718-727. `(5-Year IF 1.967) 16 citations` http://dx.doi.org/10.1016/j.finel.2011.02.003.

Annexe 6 : P. Keo, M. Hjiaj, **Q-H. Nguyen** and H. Somja. Derivation of the exact stiffness matrix of shear-deformable multi-layered beam element in partial interaction. *Finite Elements in Analysis and Design* 2016. 112 :40-49. `(5-Year IF 1.967) 0 citation` http://dx.doi.org/10.1016/j.finel.2015.12.004.

1.5 Flambement élastique/plastique des poutres mixtes de Timoshenko

Parmi les travaux de recherche sur les poutres mixtes en interaction partielle existant dans la littérature, le problème du flambement a été peu étudié. Concernant l'étude analytique générale du flambement des poutres à deux couches avec glissement à l'interface, on peut citer les travaux de référence suivants : [5, 12, 14, 27, 48, 54]. La plupart des études analytiques adopte l'hypothèse cinématique d'Euler-Bernoulli. Schnabl et Planinc (2011) [48] ont récemment utilisé l'hypothèse cinématique de Timoshenko afin de prendre en compte l'effet de la déformation de cisaillement sur la charge critique de flambement des poutres mixtes. Toutefois, dans leur article, les équations fondamentales du problème ont été développées mais aucune expression analytique de la charge critique de flambement n'a été reportée. Xu et Wu (2007) [54] ont également proposé un modèle analytique considérant l'hypothèse cinématique de Timoshenko pour chaque couche. En imposant une hypothèse cinématique supplémentaire, à savoir l'égalité de rotation des couches, ils ont développé une solution analytique pour la charge de flambement dans le cas d'une poutre simplement appuyée. Cette hypothèse supplémentaire leur a permis de simplifier la résolution du problème. Néanmoins, cette hypothèse est à notre avis trop forte car, avec l'hypothèse cinématique de Timoshenko pour chaque couche, les rotations doivent être naturellement différentes (voir Figure 1.2).

A ma connaissance, jusqu'à 2012 aucune expression analytique des charges critiques de flambement n'a été développée dans le contexte des poutres mixtes en interaction partielle avec prise en compte de la déformation de cisaillement, de la plasticité des matériaux et des différentes conditions aux limites cinématiques. Je me suis lancé dans cet axe de recherche en collaborant avec le Prof. Hjiaj de l'INSA de Rennes et le Dr. Le Grognec de l'école des Mines de Douai.

1.5.1 Formulation théorique

Considérons une poutre élasto-plastique à deux couches soumise à un effort de compression conduisant au flambement comme le montre la Figure 1.4. Dans le domaine élastique, le matériau de la couche m est supposé isotrope et défini par le tenseur d'ordre $\mathbf{D}^m$ dont les

composants dans une base orthonormée sont :

$$D^m_{ijkl} = \frac{E_m \nu_m}{(1+\nu_m)(1-2\nu_m)} \delta_{ij}\delta_{kl} + G_m \left(\delta_{ik}\delta_{jl} + \delta_{il}\delta_{kj}\right) \tag{1.27}$$

où δ_{ij} est le symbole de Kronecker. Dans le domaine plastique, on se place dans le contexte des matériaux standards généralisés avec le choix du critère de von Mises et d'un écrouissage isotrope linéaire :

$$f(\boldsymbol{\Sigma}, A) = \sqrt{\frac{3}{2}\boldsymbol{\Sigma}^d : \boldsymbol{\Sigma}^d} - \sigma_0^m - A \qquad\qquad A = H_m p \tag{1.28}$$

où $\boldsymbol{\Sigma}$ représente le second tenseur des contraintes de Kirchhoff dont le déviateur est $\boldsymbol{\Sigma}^d$; p est la déformation plastique équivalente ; et σ_0^m and H_m sont respectivement le seuil initial de contrainte et le module d'écrouissage isotrope.

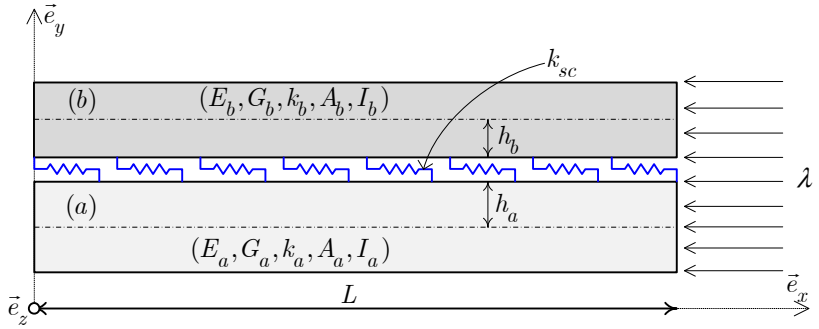

Figure 1.4 – Poutre mixte de Timoshenko en compression pure

Dans la présente formulation théorique, les deux hypothèses suivantes sont adoptées concernant la bifurcation plastique :

1. La poutre est supposée être plastifiée avant le point critique de bifurcation. Le seuil initial σ_0^m $(m = a, b)$ est supposé être suffisamment petit pour que la déformation plastique se développe avant atteindre la charge critique de flambement, de telle sorte que le phénomène de flambage se produit dans le régime plastique.
2. La bifurcation plastique survient à la valeur critique du module tangent et la post-bifurcation (à charge croissante) s'effectue avec décharge naissante.

Avec ces deux hypothèses, la charge critique $\lambda_c = \lambda_T$ et le mode de flambement $\mathbf{X}$

s'obtiennent par la résolution de l'équation de bifurcation suivante :

$$\forall\ \delta\mathbf{U}, \qquad \int_{\Omega} \nabla^T \delta\mathbf{U} : \mathbf{K}\left(\lambda_T\right) : \nabla\mathbf{X} d\Omega = 0 \tag{1.29}$$

qui fait intervenir le tenseur tangent nominal $\mathbf{K}$ qui peut être le tenseur tangent élastique nominal $\mathbf{K}^e$ ou élastoplastique nominal $\mathbf{K}^p$ selon le comportement considéré.

L'écriture explicite de l'équation de bifurcation nécessite la connaissance des modules nominaux. À partir des lois d'état et d'évolution, on aboutit à l'expression du tenseur tangent élastoplastique matériel :

$$\mathbf{D}^p = \frac{\partial\boldsymbol{\Sigma}}{\partial\mathbf{E}} = \mathbf{D} - \frac{\mathbf{D} : \frac{\partial f}{\partial\boldsymbol{\Sigma}} \otimes \frac{\partial f}{\partial\boldsymbol{\Sigma}} : \mathbf{D}}{H + \frac{\partial f}{\partial\boldsymbol{\Sigma}} : \mathbf{D} : \frac{\partial f}{\partial\boldsymbol{\Sigma}}} \tag{1.30}$$

Le tenseur tangent élastoplastique nominal peut être écrit comme suit :

$$\mathbf{K}^p = \frac{\partial\boldsymbol{\Pi}}{\partial\mathbf{F}} = \mathbf{F} \cdot \frac{\partial\boldsymbol{\Sigma}}{\partial\mathbf{E}} \cdot \mathbf{F}^T + (\mathcal{I} \cdot \boldsymbol{\Sigma})^T = \mathbf{F} \cdot \mathbf{D}^p \cdot \mathbf{F}^T + (\mathcal{I} \cdot \boldsymbol{\Sigma})^T \tag{1.31}$$

où : $\mathbf{E}$ est le tenseur des déformations de Green-Lagrange ; $\mathbf{F}$ est le gradient des déformations ; $\boldsymbol{\Pi} = \mathbf{F}.\boldsymbol{\Sigma}$ est le premier tenseur des contraintes de Kirchhoff ; et $\mathcal{I}$ représente le tenseur unité ($\mathcal{I}_{ijkl} = \delta_{il}\delta_{kj}$).

En supposant un comportement pré-critique avec un état de contrainte uniaxial

$$\boldsymbol{\Pi} = -P\mathbf{e}_x \otimes \mathbf{e}_x = \begin{bmatrix} -P & 0 & 0 \\ 0 & 0 & 0 \\ 0 & 0 & 0 \end{bmatrix} \qquad (P > 0) \tag{1.32}$$

et des déformations pré-critiques faibles (ce qui est fréquemment vérifié en pratique) :

$$\|\nabla\mathbf{U}\| \ll 1 \tag{1.33}$$

le tenseur des contraintes $\boldsymbol{\Sigma}$ s'écrit :

$$\boldsymbol{\Sigma} = \mathbf{F}^{-1}.\boldsymbol{\Pi} \approx \boldsymbol{\Pi} \tag{1.34}$$

Par conséquent, le tenseur $\mathbf{D}^p$ se simplifie comme suit :

$$\mathbf{D}^p = \mathbf{D} - \frac{\mu^2}{H+3\mu}\left(\mathbf{I} - 3\mathbf{e}_x \otimes \mathbf{e}_x\right) \otimes \left(\mathbf{I} - 3\mathbf{e}_x \otimes \mathbf{e}_x\right) \tag{1.35}$$

Les composantes de $\mathbf{D}^p$ dans la base orthonormée $(\mathbf{e}_x, \mathbf{e}_y, \mathbf{e}_z)$ sont :

$$\begin{array}{ll} D^p_{xxxx} = \Lambda + 2\mu - \frac{4\mu^2}{H+3\mu} & D^p_{yyzz} = \Lambda - \frac{\mu^2}{H+3\mu} \\ D^p_{yyyy} = \Lambda + 2\mu - \frac{\mu^2}{H+3\mu} & D^p_{xxzz} = \Lambda + \frac{2\mu^2}{H+3\mu} \\ D^p_{zzzz} = \Lambda + 2\mu - \frac{\mu^2}{H+3\mu} & D^p_{xxyy} = \Lambda + \frac{2\mu^2}{H+3\mu} \\ D^p_{xyxy} = D^p_{xzxz} = D^p_{yzyz} = \mu & \end{array} \tag{1.36}$$

où Λ et μ sont les coefficients de Lamé. Les autres composantes sont nulles ou déterminées à partir de l'équation (1.36) en utilisant les propriétés de symétrie du tenseur $\mathbf{D}^p$ ($D^p_{ijkl} = D^p_{klij} = D^p_{jikl} = D^p_{ijlk}$).

Le tenseur tangent élastoplastique nominal $\mathbf{K}^p$ devient :

$$\mathbf{K}^p \approx \frac{\partial \mathbf{\Sigma}}{\partial \mathbf{E}} + (\mathcal{I}.\mathbf{\Sigma})^T = \mathbf{D}^p - P\mathbf{e}_i \otimes \mathbf{e}_x \otimes \mathbf{e}_x \otimes \mathbf{e}_i \tag{1.37}$$

En outre, en traitant le cas des poutres qui est unidimensionnel, des hypothèses complémentaires sur la nature des contraintes permettent de remplacer le tenseur 3D $\mathbf{D}^p$ par un tenseur réduit $\mathbf{C}^p$ défini comme suit :

$$\begin{array}{c} C^p_{ijkl} = D^p_{ijkl} + \frac{D^p_{ijyy}\left(D^p_{yyzz}D^p_{zzkl} - D^p_{zzzz}D^p_{yykl}\right) + D^p_{ijzz}\left(D^p_{zzyy}D^p_{yykl} - D^p_{yyyy}D^p_{zzkl}\right)}{D^p_{yyyy}D^p_{zzzz} - D^p_{yyzz}D^p_{zzyy}} \\ (i,j) \neq (y,y),(z,z) \qquad (k,l) \neq (y,y),(z,z) \end{array} \tag{1.38}$$

On retient les seules valeurs utiles qui sont :

$$C^p_{xxxx} = E_T \qquad C^p_{xyxy} = C^p_{xzxz} = C^p_{yzyz} = \mu = G \tag{1.39}$$

où : E_T est le module élastoplastique tangent calculé par $\frac{1}{E_T} = \frac{1}{E} + \frac{1}{H}$.

Finalement, l'équation de bifurcation d'une poutre s'écrit :

$$\forall\ \delta\mathbf{U}, \qquad \int_\Omega \nabla^T \delta\mathbf{U} : \left(\mathbf{C}^p - P_c\mathbf{e}_i \otimes \mathbf{e}_x \otimes \mathbf{e}_x \otimes \mathbf{e}_i\right) : \nabla\mathbf{X} d\Omega = 0 \tag{1.40}$$

Quant à une poutre mixte à deux couches, l'analyse de bifurcation 3D permet d'aboutir au système d'équations différentielles suivant pour les cinq champs modaux inconnus

(deux déplacements longitudinaux $\mathcal{U}_a$, et $\mathcal{U}_b$, deux rotations Θ_a et Θ_b et le déplacement transversal $\mathcal{V}$) :

$$E_{Ta}A_a\mathcal{U}_{a,xx} - k_{sc}\mathcal{G} = 0 \tag{1.41}$$

$$E_{Tb}A_b\mathcal{U}_{b,xx} + k_{sc}\mathcal{G} = 0 \tag{1.42}$$

$$k_aG_aA_a\left(\Theta_{a,x} - \mathcal{V}_{,xx}\right) + k_bG_bA_b\left(\Theta_{b,x} - \mathcal{V}_{,xx}\right) + \lambda_T\mathcal{V}_{,xx} = 0 \tag{1.43}$$

$$E_{Ta}I_a\Theta_{a,xx} + k_aG_aA_a\left(\mathcal{V}_{,x} - \Theta_a\right) + k_{sc}h_a\mathcal{G} = 0 \tag{1.44}$$

$$E_{Tb}I_b\Theta_{b,xx} + k_bG_bA_b\left(\mathcal{V}_{,x} - \Theta_b\right) + k_{sc}h_b\mathcal{G} = 0 \tag{1.45}$$

où $\mathcal{G} = \mathcal{U}_a - h_a\Theta_a - \mathcal{U}_b - h_b\Theta_b$ représente la composante modale du glissement à l'interface. La résolution de ces équations mène à tout un ensemble de solutions explicites pour diverses conditions aux limites :

– Extrémités bi-articulées :

$$\lambda_T = \frac{\frac{\pi^2\overline{E_TI}_\infty}{L^2}\left(\frac{\pi^2\widetilde{E_TI}^2\overline{GA}}{L^2\overline{E_TI}_\infty\widetilde{GA}^2} + \frac{\overline{E_TI}}{\overline{E_TI}_\infty} + \frac{k_{sc}\widetilde{E_TI}^2\widehat{E_TI}_\infty\overline{GA}}{\widehat{E_TA}\widehat{E_TI}\overline{E_TI}_\infty\widetilde{GA}^2} + \frac{k_{sc}L^2}{\pi^2\widehat{E_TA}}\right)}{\frac{\pi^4\widetilde{E_TI}^2}{L^4\widetilde{GA}^2}\left(1 + \frac{k_{sc}L^2\widehat{E_TI}_\infty}{\pi^2\widehat{E_TA}\widetilde{E_TI}}\right) + \left(1 + \frac{\pi^2}{L^2}\overline{\left(\frac{E_TI}{GA}\right)}\right)\left(1 + \frac{k_{sc}L^2}{\pi^2\widehat{E_TA}}\right) + \frac{k_{sc}\bar{h}^2}{\widetilde{GA}}} \tag{1.46}$$

– Extrémités bi-encastrées :

$$\lambda_T = \frac{\frac{\pi^2\overline{E_TI}_\infty}{L^2}\left(\frac{16\pi^2\widetilde{E_TI}^2\overline{GA}}{L^2\overline{E_TI}_\infty\widetilde{GA}^2} + \frac{4\overline{E_TI}}{\overline{E_TI}_\infty} + \frac{4k_{sc}\widetilde{E_TI}^2\widehat{E_TI}_\infty\overline{GA}}{\widehat{E_TA}\widehat{E_TI}\overline{E_TI}_\infty\widetilde{GA}^2} + \frac{k_{sc}L^2}{\pi^2\widehat{E_TA}}\right)}{\frac{16\pi^4\widetilde{E_TI}^2}{L^4\widetilde{GA}^2}\left(1 + \frac{k_{sc}L^2\widehat{E_TI}_\infty}{4\pi^2\widehat{E_TA}\widetilde{E_TI}}\right) + \left(1 + \frac{4\pi^2}{L^2}\overline{\left(\frac{E_TI}{GA}\right)}\right)\left(1 + \frac{k_{sc}L^2}{4\pi^2\widehat{E_TA}}\right) + \frac{k_{sc}\bar{h}^2}{\widetilde{GA}}} \tag{1.47}$$

– Extrémités encastrées-libre :

$$\lambda_T = \frac{\frac{\pi^2\overline{E_TI}_\infty}{L^2}\left(\frac{\pi^2\widetilde{E_TI}^2\overline{GA}}{16L^2\overline{E_TI}_\infty\widetilde{GA}^2} + \frac{\overline{E_TI}}{4\overline{E_TI}_\infty} + \frac{k_{sc}\widetilde{E_TI}^2\widehat{E_TI}_\infty\overline{GA}}{4\widehat{E_TA}\widehat{E_TI}\overline{E_TI}_\infty\widetilde{GA}^2} + \frac{k_{sc}L^2}{\pi^2\widehat{E_TA}}\right)}{\frac{\pi^4\widetilde{E_TI}^2}{16L^4\widetilde{GA}^2}\left(1 + \frac{4k_{sc}L^2\widehat{E_TI}_\infty}{\pi^2\widehat{E_TA}\widetilde{E_TI}}\right) + \left(1 + \frac{\pi^2}{4L^2}\overline{\left(\frac{E_TI}{GA}\right)}\right)\left(1 + \frac{4k_{sc}L^2}{\pi^2\widehat{E_TA}}\right) + \frac{k_{sc}\bar{h}^2}{\widetilde{GA}}} \tag{1.48}$$

où

$$\begin{array}{ll}
\bar{h} = h_a + h_b & \widehat{E_TA} = \frac{E_{Ta}A_aE_{Tb}A_b}{E_{Ta}A_a + E_{Tb}A_b} \\
\overline{E_TI} = E_{Ta}I_a + E_{Tb}I_b & \overline{E_TI}_\infty = \overline{E_TI} + \bar{h}^2\widehat{E_TA} \\
\overline{GA} = k_aG_aA_a + k_bG_bA_b & \widetilde{GA} = \sqrt{k_aG_aA_ak_bG_bA_b} \\
\widehat{E_TI} = \bar{h}^2\left(\frac{h_a^2}{E_{Ta}I_a} + \frac{h_b^2}{E_{Tb}I_b}\right)^{-1} & \widehat{GA} = \bar{h}^2\left(\frac{h_a^2}{k_aG_aA_a} + \frac{h_b^2}{k_bG_bA_b}\right)^{-1} \\
\widehat{E_TI}_\infty = \widehat{E_TI} + \bar{h}^2\widehat{E_TA} & \overline{\left(\frac{E_TI}{GA}\right)} = \frac{E_{Ta}I_a}{k_aG_aA_a} + \frac{E_{Tb}I_b}{k_bG_bA_b} \\
 & \widetilde{E_TI} = \sqrt{E_{Ta}I_aE_{Tb}I_b}
\end{array} \tag{1.49}$$

1.5.2 Résultats essentiels

Ces expressions générales qui ont été exploitées dans divers cas particuliers (dont les deux cas extrêmes de deux poutres : solidaires d'une part et déconnectées dans la direction longitudinale d'autre part) ont donné les résultats attendus. Elles permettent également de retrouver la solution de Bernoulli, en faisant tendre les raideurs de cisaillement transverse vers l'infini.

Les articles ci-dessous, fournis en annexe du présent rapport, font la synthèse du travail et des résultats obtenus :

Annexe 7 : P. Le Grognec, **Q-H. Nguyen** and M. Hjiaj. Exact buckling solution for two-layer Timoshenko beams with interlayer slip. International *Journal of Solids and Structures* 2012 ; 49 : 143-150. `(5-Year IF 2.483) 16 citations` http://dx.doi.org/10.1016/j.ijsolstr.2011.09.020.

Annexe 8 : P. Le Grognec, **Q-H. Nguyen** and M. Hjiaj. Plastic bifurcation analysis of a two-layer shear-deformable beam-column with partial interaction. *International Journal of Non-Linear Mechanics* 2014 ; 67 : 85-94. `(5-Year IF 1.870) 3 citations` http://dx.doi.org/10.1016/j.ijnonlinmec.2014.08.010.

1.6 Vibration libre des poutres mixtes de Timoshenko

L'objet de cette partie des mes travaux concerne la vibration libre des poutres mixtes de Timoshenko en interaction partielle pour laquelle on dispose encore de peu de solutions analytiques, contrairement au cas des poutres mixtes d'Euler-Bernoulli dont la solution analytique est bien connue [1, 13, 15]. A notre connaissance, il y a deux modèles disponibles dans la littérature. Le premier a été développé par Berczyński and Wróblewski (2005) [4] qui ont adopté l'hypothèse cinématique de Timoshenko pour chaque couche. Ils ont abouti à une équation différentielle d'ordre 12 pour la détermination des fréquences propres. Néanmoins, la solution analytique n'a pas été donnée. Le deuxième modèle a été proposé par Wu et al. (2007) [53] qui ont abouti à des formules analytiques des fréquences propres mais en se limitant au cas où la rotation de la section, autrement dit le cisaillement transversal, est identique dans les deux couches. Cette hypothèse semble à notre avis trop forte, notamment dans le cas où il y a une grande différence entre la rigidité de cisaillement des deux couches. Dans l'objectif d'avoir un modèle plus général que celui de Wu et al. (2007) [53], nous avons développé un modèle analytique pour la vibration libre des poutres mixtes de Timoshenko qui se base sur les mêmes hypothèses que le modèle de Berczyński

and Wróblewski (2005) [4].

1.6.1 Équations principales du problème

En utilisant le principe de Hamilton, le problème de vibration libre des poutres mixtes peut être formulé comme suit :

$$\int_{t_1}^{t_2} (\delta T - \delta U)\, \mathrm{d}t = 0 \tag{1.50}$$

où U représente l'énergie élastique totale de la poutre :

$$U = \sum_{i=a,b} \frac{1}{2} \int_L \left(EA_i \left(u_{i,x}\right)^2 + EI_i (\theta_{i,x})^2 + GA_i (\theta_i + v_{,x})^2 \right) \mathrm{d}x + \frac{1}{2} \int_L k_{sc}\, g^2 \mathrm{d}x \tag{1.51}$$

et T désigne l'énergie cinétique de la poutre :

$$T = \frac{1}{2} \int_L m\, \dot{v}^2 \mathrm{d}x \tag{1.52}$$

En substituant les équations (1.51) et (1.52) dans (1.50) et en faisant une intégration par partie, on obtient :

$$\begin{aligned}
\int_{t_1}^{t_2} \int_L \Big\{ & \left(EA_a u_{a,xx} - k_{sc} g\right) \delta u_a + \left(EA_b u_{b,xx} + k_{sc} g\right) \delta u_b + \\
& \Big[EI_a \theta_{a,xx} + GA_a (v_{,x} + \theta_a) + h_a k_{sc} g \Big] \delta\theta_a + \\
& \Big[EI_b \theta_{b,xx} + GA_b (v_{,x} + \theta_b) + h_b k_{sc} g \Big] \delta\theta_b + \\
& \Big[GA_a (v_{,xx} + \theta_{a,x}) + GA_b (v_{,xx} + \theta_{b,x}) - m\ddot{v} \Big] \delta v \Big\} \mathrm{d}x \mathrm{d}t \\
& = \int_{t_1}^{t_2} \left[N_a \delta u_a + N_b \delta u_b + M_a \delta\theta_a + M_b \delta\theta_b + \left(T_a + T_b\right) \delta v \right]_0^L \mathrm{d}t
\end{aligned} \tag{1.53}$$

Il est à noter que selon le principe d'Hamilton les variations δu_i, $\delta\theta_i$ et δv doivent être égales à zéro à t_1 et t_2. Comme δu_i, $\delta\theta_i$ and δv sont arbitraires, l'équation (1.53) équivaut à :

$$EA_a u_{a,xx} - k_{sc} g = 0 \tag{1.54a}$$

$$EA_b u_{b,xx} + k_{sc} g = 0 \tag{1.54b}$$

$$EI_a \theta_{a,xx} + GA_a (v_{,x} + \theta_a) + h_a k_{sc} g = 0 \tag{1.54c}$$

$$EI_b\theta_{b,xx} + GA_b(v_{,x} + \theta_b) + h_b k_{sc} g = 0 \tag{1.54d}$$

$$GA_a(v_{,xx} + \theta_{a,x}) + GA_b(v_{,xx} + \theta_{b,x}) - m\ddot{v} = 0 \tag{1.54e}$$

Ces équations représentent les équations différentielles principales du mouvement en vibration libre d'une poutre mixte de Timoshenko. En combinant ces cinq équations, on aboutit à une équation différentielle d'ordre 8 impliquant seulement le déplacement transversal v :

$$v_{,xxxxxxxx} - \xi_1 v_{,xxxxxx} + \xi_2 v_{,xxxx} - \xi_3 \ddot{v}_{,xxxxxx} + \xi_4 \ddot{v}_{,xxxx} - \xi_5 \ddot{v}_{,xx} + \xi_6 \ddot{v} = 0 \tag{1.55}$$

où

$$\xi_1 = k_{sc}\left(\frac{1}{EA} + \frac{h_a^2}{EI_a} + \frac{h_b^2}{EI_b}\right) + \frac{GA}{EI} \tag{1.56}$$

$$\xi_2 = \frac{k_{sc} GA\,(EI_a + EI_b + h^2 EA)}{EA EI_a EI_b} \tag{1.57}$$

$$\xi_3 = \frac{m}{GA_\infty} \tag{1.58}$$

$$\xi_4 = \frac{m}{GA_\infty}\left[\frac{GA_a}{EI_a} + \frac{GA_b}{EI_b} + k_{sc}\left(\frac{1}{EA} + \frac{h_a^2}{EI_a} + \frac{h_b^2}{EI_b}\right)\right] \tag{1.59}$$

$$\xi_5 = \frac{m\,k_{sc}}{GA_\infty EA}\left(\frac{GA_a}{EI_a} + \frac{GA_b}{EI_b}\right) + \frac{m\,GA}{EI_a EI_b}\left[k_{sc}\left(\frac{h_a^2}{GA_a} + \frac{h_b^2}{GA_b}\right) + 1\right] \tag{1.60}$$

$$\xi_6 = \frac{m\,k_{sc} GA}{EA\,EI_a EI_b} \tag{1.61}$$

Les paramètres non définis ici peuvent être trouvés en Annexe III.

1.6.2 Solution analytique

Selon la méthode de séparation des variables, la solution générale de l'équation différentielle (1.55) peut être exprimée sous la forme :

$$v(x,t) = \sum_n \phi_n(x)\varphi_n(t) \tag{1.62}$$

où ϕ_n représente les modes propres qui dépendent des conditions aux limites ; et φ_n désigne les fonctions du temps de la vibration libre. En substituant l'équation (1.62) dans (1.55), on obtient :

$$\left(\frac{\mathrm{d}^8\phi_n}{\mathrm{d}x^8} - \xi_1\frac{\mathrm{d}^6\phi_n}{\mathrm{d}x^6} + \xi_2\frac{\mathrm{d}^4\phi_n}{\mathrm{d}x^4}\right)\varphi_n - \left(\xi_3\frac{\mathrm{d}^6\phi_n}{\mathrm{d}x^6} - \xi_4\frac{\mathrm{d}^4\phi_n}{\mathrm{d}x^4} + \xi_5\frac{\mathrm{d}^2\phi_n}{\mathrm{d}x^2} - \xi_6\phi_n\right)\frac{\mathrm{d}^2\varphi_n}{\mathrm{d}t^2} = 0 \tag{1.63}$$

d'où les équations différentielles ordinaires suivantes :

$$\frac{\mathrm{d}^2\varphi}{\mathrm{d}t^2} + w_n^2\varphi_n = 0 \tag{1.64}$$

$$\frac{\mathrm{d}^8\phi_n}{\mathrm{d}x^8} - (\xi_1 - w_n^2\xi_3)\frac{\mathrm{d}^6\phi_n}{\mathrm{d}x^6} + (\xi_2 - w_n^2\xi_4)\frac{\mathrm{d}^4\phi_n}{\mathrm{d}x^4} + w_n^2\xi_5\frac{\mathrm{d}^2\phi_n}{\mathrm{d}x^2} - w_n^2\xi_6\phi_n = 0 \tag{1.65}$$

L'équation (1.64) représente la vibration harmonique dont la solution est de la forme :

$$\varphi_n(t) = e^{\mathrm{i}w_n t} \tag{1.66}$$

En résolvant son équation caractéristique, la solution générale de l'équation différentielle (1.65) peut être écrite sous la forme :

$$\phi_n(x) = c_1\sin(\lambda_1 x) + c_2\cos(\lambda_1 x) + c_3\mathrm{e}^{\lambda_2 x} + c_4\mathrm{e}^{-\lambda_2 x} + c_5\mathrm{e}^{\lambda_3 x} + c_6\mathrm{e}^{-\lambda_3 x} + c_7\mathrm{e}^{\lambda_4 x} + c_8\mathrm{e}^{-\lambda_4 x} \tag{1.67}$$

où c_i $(i = 1, 2, ..., 8)$ sont des constantes d'intégration qui seront déterminées par les conditions aux limites.

1.6.3 Résultats essentiels

La solution analytique développée pour le problème de vibration libre des poutres mixtes de Timoshenko est tout à fait originale. L'article ci-dessous, fourni en annexe du présent rapport, fait la synthèse du travail et des résultats obtenus :

Annexe 9 : Q-H. Nguyen, M Hjiaj and P. Le Grognec. Analytical approach for free vibration analysis of two-layer Timoshenko beams with interlayer slip. *Journal of Sound and Vibration* 2012 ; 331 : 2902-2911. `(5-Year IF 2.223) 14 citations` http://dx.doi.org/10.1016/j.jsv.2012.01.034.

1.7 Bilan et Perspectives

L'ensemble de mes travaux de recherche sur la modélisation des poutres multicouches de Timoshenko s'appuie sur le développement de deux outils bien distincts : une méthode de résolution analytique et un modèle par éléments finis. La démarche employée pour résoudre analytiquement le problème de poutres multicouches avec glissement à l'interface (en flexion, en vibration libre et en flambement) s'appuie sur la théorie des poutres

de Timoshenko et sur le modèle de Newmark et al. (1951) [32] pour la cinématique de glissement à l'interface. En adoptant des lois constitutives linéaires, on a abouti à une solution analytique des équations du problème de flexion en petit déplacement conduisant à une matrice de rigidité exacte de poutres multicouches de Timoshenko. Cette matrice de raideur a été introduite dans un programme d'éléments finis permettant d'analyser, de façon exacte et avec un nombre minimal d'éléments, le comportement en flexion de poutres multicouches avec la prise en compte de l'interaction partielle et des déformations de cisaillement transversal. Dans l'hypothèse de faibles déformations pré-critiques, on a trouvé des expressions simples de la charge critique. Toutefois, ces expressions explicites de la charge de flambement ne sont applicables que pour des poutres/poteaux mixtes (à deux couches). Une perspective immédiate est de générer ces expressions pour le cas de poutres multicouches. La solution analytique du problème de vibration libre a été pour l'instant développée en négligeant l'inertie de rotation des composants. Il serait intéressant de voir l'influence de cette dernière sur les fréquences propres de poutres multicouches de Timoshenko.

Le développement d'un programme d'éléments finis "maison" a été motivé par la nécessité de disposer de méthodes numériques performantes pour faire face aux singularités les plus sévères. A l'issus de mes travaux de thèse, des modèles éléments finis ont été développés dans l'optique de simuler le comportement élastoplastique des poutres multicouches de Timoshenko en grandes transformations. Ces modèles sont basés sur la formulation corotationnelle. Toutefois, les modèles éléments finis développés se sont limités pour l'instant à des analyses statiques. Une perspective envisageable est d'étendre le programme d'élément fini "maison" pour la dynamique non linéaire des poutres multicouches de Timoshenko.

THÈME 2

COMPORTEMENT DES PLANCHERS MIXTES BOIS-BÉTON SOUS SOLLICITATIONS SISMIQUES ET D'INCENDIE

2.1 Position du problème

Les planchers mixtes bois-béton sont une solution pertinente en construction neuve comme en réhabilitation. Les planchers mixtes bois-béton sont des éléments porteurs horizontaux constitués d'un ensemble d'éléments qui participent tous à la résistance du plancher. Ce sont des dalles en béton armé solidarisées à des poutres en bois au moyen d'organes mécaniques appelés connecteurs. Le rôle majeur de ces derniers est de permettre de se rapprocher d'un fonctionnement monolithique de la section mixte, en limitant le glissement qui tend à se produire à l'interface bois-béton sous l'effet des actions extérieures et en transmettant les efforts entre les deux matériaux constituant la section mixte. En d'autres termes, la section mixte vise à se comporter comme un élément structurel unique.

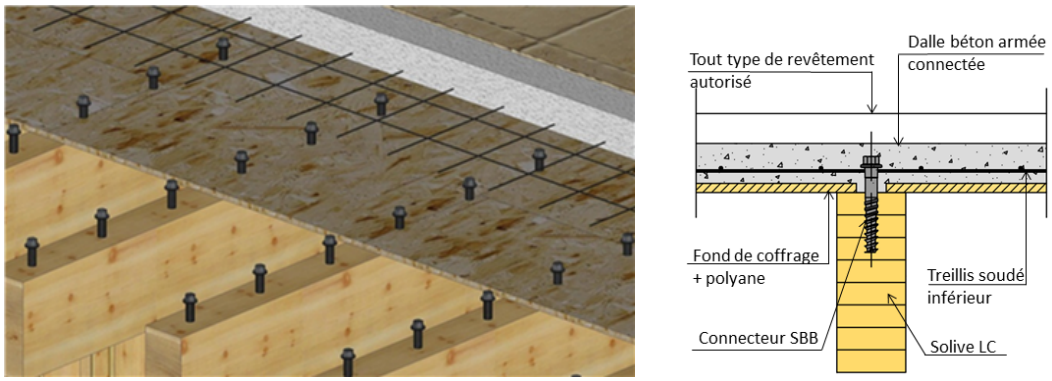

Figure 2.1 – Schéma de principes de plancher mixte SBB®

La connexion est assurée majoritairement par des dispositifs mécaniques visant à limiter le glissement à l'interface bois-béton. Parmi ceux-ci, les solutions suivantes peuvent être citées : tirefonds, vis, tirefonds à ailette, tubes métalliques, ferrure en âme, entaille dans la poutre bois. Dans le cas particulier des planchers mixtes SBB®, des tirefonds métalliques de diamètre importants (de 21 mm à 26 mm) sont utilisés (Figure 2.1). Il s'agit du système SBB® développé par l'entreprise AIA Ingénierie. Ce système dispose depuis 2000 d'un Avis Technique CSTB (référence 3/12-732) permettant son utilisation dans les bâtiments

qui ne doivent pas être vérifiés sous actions sismiques. L'INSA de Rennes a été sollicité par l'entreprise AIA Ingénierie d'Angers en 2011 afin de caractériser le comportement sous séisme du système SBB®. Dans ce contexte, deux campagnes expérimentales dont j'étais responsable scientifique ont été menées à l'INSA de Rennes. 24 essais Push-Out ont été réalisés à température ambiante sous chargement statique et cyclique alterné sur le système de connexion mixte bois-béton SBB®.

Concernant le comportement des planchers mixtes bois-béton sous conditions accidentelles de séisme et d'incendie, il y a très peu de recherches qui ont été menées dans la littérature. Cet axe de recherche vise une meilleure connaissance des phénomènes affectant le comportement mécanique et thermomécanique de la connexion bois-béton. Il porte sur l'étude expérimentale et la modélisation du comportement des planchers mixtes sous sollicitations sismiques et d'incendie. Il constitue l'objectif principal du projet de recherche industriel avec l'entreprise AIA Ingénierie d'Angers et la thèse CIFRE de Manuel Manthey (2015) [28] que j'ai co-encadrée.

2.2 Comportement des planchers mixtes bois-béton sous séisme

Dans le cas courant d'une poutre mixte bois-béton sur deux appuis soumise à une charge uniformément répartie, la poutre mixte fléchit. La réponse de la section mixte induit un glissement à l'interface des deux éléments (bois et béton) connectés. Ce glissement relatif est empêché par les connecteurs qui sont sollicités en cisaillement afin de reprendre l'effort de glissement. La caractérisation du comportement de la connexion est à la base du dimensionnement des poutres mixtes bois-béton. Il est nécessaire de connaître la résistance au cisaillement de la connexion et sa rigidité afin de pouvoir dimensionner une poutre mixte bois-béton. Ce sont de ces paramètres que dépend la distribution des contraintes dans la section mixte ou encore la répartition et le nombre de connecteurs le long de la poutre. Les propriétés mécaniques de la connexion sont en général caractérisées par des essais Push-Out.

2.2.1 Essais Push-Out sous chargement statique et cyclique alterné

Il est à noter que les travaux expérimentaux concernant les connexions mixtes bois-béton sous sollicitations cycliques alternées sont quasiment inexistants dans la littérature. Par conséquent, l'étude de la réponse hystérétique de la connexion SBB® passe inévitablement par une campagne expérimentale. Ainsi nous avons mené une série d'essais au premier

semestre 2012 au laboratoire LGCGM de l'INSA de Rennes. Les objectifs des essais Push-Out sous chargement statique et cyclique alterné sont :

- la caractérisation de la résistance au cisaillement de la connexion ;
- la capacité de déformation de la connexion d'un système bois-béton sous sollicitations cycliques alternées.
- la détermination de la ductilité, du coefficient d'amortissement visqueux et de la dissipation d'énergie de la connexion ;
- l'évaluation la perte de résistance au cisaillement sous trois cycles consécutifs de même amplitude.

Tableau 2.1 – Description des éprouvettes testées

N° essai	**Type d'essai**	**Nombre d'essais**	**Connecteur SBB**	**Classe Poutre-Bois**	**Dimensions poutre-bois [mm]**	**Epaisseur Dalle [cm]**	**Ferraillage Dalle**
26-170 S	Statique	6	26-170 (2x2)	GL24h	112x347*	7	1,89cm²/ml
26-170 C	Cyclique	6	26-170 (2x2)	GL24h	112x347*	7	1,89cm²/ml
26-250 S	Statique	6	26-250 (2x2)	GL24h	112x440*	7 + renformis 11x6	1,89cm²/ml
26-250 C	Cyclique	6	26-250 (2x2)	GL24h	112x440*	7 + renformis 11x6	1,89cm²/ml

Le tableau 2.1 présente un récapitulatif des 24 essais réalisés. Les spécimens d'essai sont composés d'un tronçon de solive bois auquel deux dalles en béton sont connectées via deux connecteurs par dalle, soit quatre connecteurs par éprouvette. Des armatures de renfort ont été placées aux extrémités des dalles à l'endroit où le chargement est appliqué. La Figure 2.2 illustre le dispositif expérimental des essais Push-Out qui a été conçu et réalisé par nous-même au Laboratoire LGCGM. La partie intérieure des éprouvettes, constituée par la solive bois (1), repose sur le plateau fixe de la presse (3). Lors des essais, la solive bois (1) est maintenue en place. Le vérin, qui exerce un effort de compression, agit sur les dalles béton (2) de l'éprouvette. Afin d'appliquer uniformément les efforts sur les dalles béton (2), une cage métallique (4) constituée de cornières et de barres de contreventement a été fabriquée. Le maintien en place de la solive bois est obtenu par serrage d'une plaque métallique (5) épaisse à l'aide de tiges métalliques (6) vissées sur le plateau de la presse.

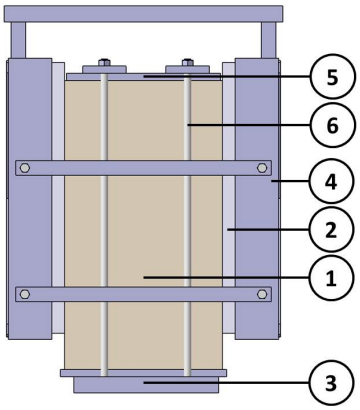

Vue de face

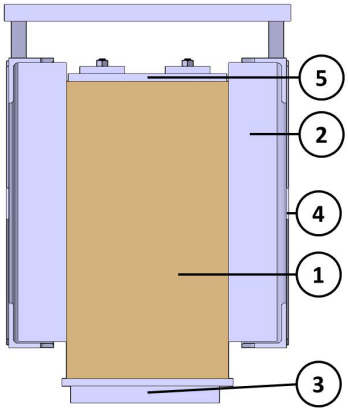

Vue de face (coupe)

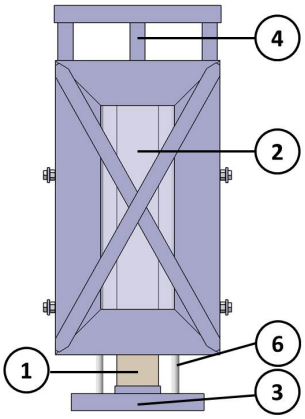

Vue de côté

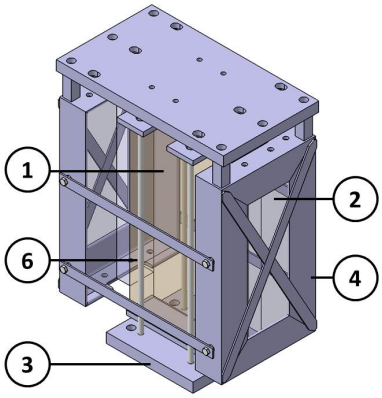

Vue ISO

Spécimen 26 - 170

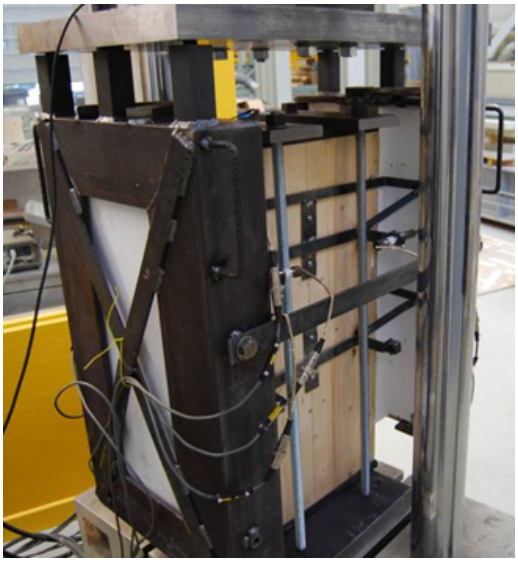

Spécimen 26 - 250

Figure 2.2 – Montage expérimental des essais Push-Out

Synthèse de l'exploitation des résultats expérimentaux

Il apparait clairement que le système SBB® présente un comportement ductile, qui devrait permettre d'envisager son usage comme élément dissipatif, en classe DCM ou DCH selon la configuration envisagée. Lorsque le système SBB® est utilisé comme élément non dissipatif, par exemple pour réaliser la liaison diaphragme-éléments verticaux, cette ductilité, même si elle n'est pas directement utilisée, confère au SBB® une grande robustesse et permet d'utiliser la résistance F_u, une fois la distribution statistique des résultats expérimentaux prise en compte conformément à l'Eurocode 0. Le comportement cyclique caractéristique de la connexion SBB® est représenté sur la Figure 2.3. Le tableau 2.2 fait la synthèse des résultats obtenus pour les essais Push - Out sous chargement cyclique alterné.

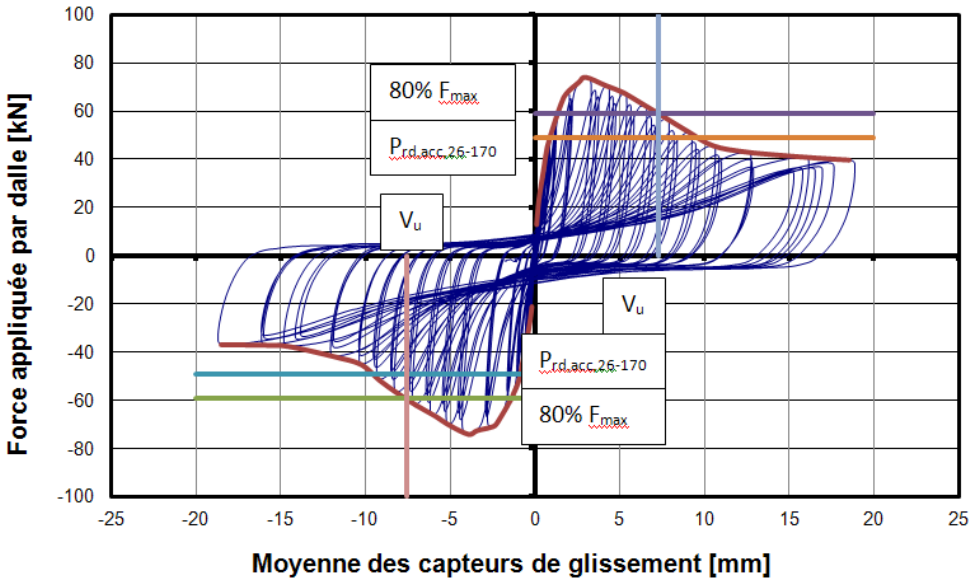

Figure 2.3 – Comportement caractéristique de la connexion sous sollicitations cycliques alternées.

2.2.2 Justification des planchers mixtes bois-béton sous séisme

En conception parasismique, les planchers doivent remplir le rôle de diaphragme horizontal. En fonction de la rigidité en plan du diaphragme, comparée aux rigidités latérales des systèmes verticaux de contreventement, le diaphragme peut être classé comme rigide, semi - rigide ou souple. Il s'agit d'une simplification pour le calcul, un diaphragme n'est

TABLEAU 2.2 – Synthèse de l'exploitation des résultats expérimentaux.

		SBB 26-170 dans Gl24h		SBB 26-250 dans Gl24h	
		Compression	Traction	Compression	Traction
NF EN 12512	F_y [daN]	-2617 (moyenne) -1832 (valeur de calcul au sens de l'EC 0)	2867 (moyenne) 1972 (valeur de calcul au sens de l'EC0)	-2947 (moyenne) -2243 (valeur de calcul au sens de l'EC0)	2573 (moyenne) 2256 (valeur de calcul au sens de l'EC0)
	s_y [mm]	-0,62	0,77	-1,00	1,02
	F_u [daN]	-3054 (moyenne) -2420 (valeur de calcul au sens de l'EC0)	3135 (moyenne) 2483 (valeur de calcul au sens de l'EC0)	-3212 (moyenne) -2869 (valeur de calcul au sens de l'EC0)	2715 (moyenne) 2436 (valeur de calcul au sens de l'EC0)
	s_u [mm]	-7,76	7,89	-9,29	8,70
	Rapport $\frac{s_u}{s_y}$	12,51	10,25	9,29	8,53
Eurocode 8, § 8.3 (3)	Classe de ductilité	DCH	DCH	DCM*	DCM*

* : bornée aux structures de classe de ductilité DCM de par l'article 8.3(3) de l'Eurocode 8 - 1 (2005, [38])

jamais strictement rigide ou parfaitement souple. L'hypothèse de diaphragme rigide (au sens de l'Eurocode 8-1) nous permet de prendre uniquement en compte les déformations dues à la connexion entre le diaphragme et les éléments de contreventement verticaux. In extenso, le plancher est supposé suffisamment rigide pour que les déformations dues à la flexion et au cisaillement du plancher soient jugées négligeables. Dans le cas des planchers mixtes bois-béton, la fonction diaphragme est assurée par la dalle béton, coulée en place sur l'ensemble de la surface du plancher. L'Eurocode 8-1 ne donne une définition que pour les diaphragmes rigides, à l'article 4.3.1(4), « Le diaphragme est considéré comme rigide si, lorsqu'il est modélisé avec sa flexibilité en plan effective, ses déplacements horizontaux n'excèdent en aucun point les déplacements résultant de l'hypothèse du diaphragme rigide de plus de 10% des déplacements horizontaux absolus correspondants dans la situation sismique de calcul ». Cette démarche est assez lourde à mettre en oeuvre car elle nécessite le développement de deux modèles numériques de l'ouvrage sous séisme, un modèle avec un plancher rigide et un modèle avec le plancher modélisé avec sa rigidité en plan réelle. Les déplacements obtenues avec les deux modélisations doivent ensuite être comparées afin de juger si le diaphragme est, ou non, rigide.

Bien que la rigidité d'un diaphragme est fonction de sa portée et de son élancement, l'Eurocode 8-1 article 5.10(1) assure qu'une dalle pleine de béton d'épaisseur d'au moins

7 cm, armée dans les deux directions horizontales en respectant les sections minimales de l'Eurocode 2 - 1 (2005, [51]) article 9.3.1.1(1) et correctement connectée aux éléments verticaux peut être considérée comme rigide. Newcombe et al. (2010) [31] ont réalisé une campagne expérimentale portant sur la rigidité en plan des planchers mixtes bois-béton. Des planchers à échelle 1 : 3 (éprouvettes de 3 m x 3 m) ont été soumis à des sollicitations cycliques alternées dans leur plan afin d'évaluer leur comportement sous séisme. Il a été observé que les déformations situées au niveau de la liaison entre le plancher et les éléments verticaux de contreventement étaient bien supérieures aux déformations dans le plan du plancher et que par conséquent les planchers bois - béton pouvaient être considérés comme rigide. L'épaisseur des planchers testés était de 25 mm (échelle 1 : 3), ces planchers intégraient des treillis soudés de dimensions réduites. A noter qu'un platelage de 7 mm avait été mis en place ainsi que des poutres de dimensions 150 x 45 mm (espacées de 500 mm). La connexion bois-béton était assurée par un système de connexion à encoches + vis (5,3 mm x 80 mm). 5 essais ont été menés avec 5 liaisons différentes entre le plancher bois-béton et les éléments verticaux de contreventement. Les liaisons testées entre le plancher et les éléments verticaux sont de deux natures, soit une connexion entre une poutre bois de rive et les solives bois du plancher mixte, soit une connexion entre une poutre bois de rive et la dalle béton du plancher mixte.

Dans le cadre des planchers SBB®, il existe plusieurs méthodes pour lier le plancher bois-béton aux éléments de contreventement verticaux. Les liaisons aux voiles en béton armé s'opèrent généralement entre la dalle béton et le voile béton. Ce cas se rapporte donc à un dimensionnement traditionnel qui se rencontre en construction béton armé. Les liaisons entre les planchers bois - béton et un mur à ossature bois (MOB) peuvent s'opérer par des poutres de rive connectées à la dalle béton via des connecteurs SBB®. Dans ce dernier cas, les connecteurs SBB® doivent alors permettre la transmission des efforts sismiques du diaphragme horizontal aux éléments de contreventement verticaux. Les essais en cisaillement de la connexion sous chargement cyclique alternée montrent que la connexion SBB® offre une bonne ductilité sous chargement cyclique alternée. Une fois la résistance maximale atteinte, un endommagement de la connexion est observé au fur et à mesure que les déplacements imposés s'accroissent. Cependant la connexion conserve une capacité résistante non négligeable. Un autre point important est que les cycles effectués à un même déplacement (3 cycles par amplitude de déplacement) ne présentent pas d'affaiblissement important en résistance et en rigidité. Les essais ont également démontrés la symétrie de la loi de comportement du système. L'exploitation des

résultats expérimentaux présentée au tableau 2.2 a permis de conclure que la connexion SBB® satisfaisait aux exigences des classes DCM (SBB 26 - 250 avec renformis non ferraillé) et DCH (SBB 26 - 170) au sens de l'Eurocode 8-1. Bien que le critère dissipatif ne soit pas requis pour la liaison des diaphragmes avec les éléments de contreventement verticaux, le bon comportement de la connexion sous sollicitations cycliques alternées est rassurant. D'une part, la ruine fragile du système est évitée et d'autre part, il a été montré que la connexion SBB® présentait une grande robustesse.

2.2.3 Résultats essentiels

Les travaux menés sur le comportement des planchers mixtes bois-béton dans le cadre du projet de recherche avec l'entreprise AIA Ingénierie d'Angers ont contribué au renouvellement de l'Avis Technique sur le système bois-béton SBB® auprès du CSTB. Le comportement sous chargement statique monotone de la connexion a permis de caractériser avec précision les propriétés mécaniques de la connexion mise en place dans du lamellé collé. De plus, l'emploi du procédé a pu être justifié en zone sismique en France métropolitaine (dans toutes zones géographiques où l'action verticale sismique n'est pas à prendre en compte).

L'article ci-dessous, fourni en annexe du présent rapport, fait la synthèse du travail et des résultats obtenus :

Annexe 10 : M. Manthey, **Q-H. Nguyen**, H. Somja, J. Duchêne and M. Hjiaj. Experimental Study of the Composite Timber-Concrete SBB Connection under Monotonic and Reversed-Cyclic Loadings. *Materials and Joints in Timber Structures*. 2014 ; S. Aicher, H. W. Reinhardt and H. Garrecht, Springer Netherlands. 9 : 433-442. http://dx.doi.org/10.1007/978-94-007-7811-5_39

2.3 Modélisation du comportement des planchers mixtes bois-béton sous incendie

Cet axe de recherche vise à apporter une meilleure compréhension des phénomènes observés lors des essais au feu des planchers mixtes bois-béton réalisés au Laboratoire Efectis dans le cadre du développement du procédé SBB® de l'entreprise AIA Ingénierie. Le détail de ces essais peut être trouvé dans la thèse de Manuel Manthey (2015) [28]. L'analyse est menée via la confrontation des résultats expérimentaux à des modélisations numériques (thermiques et thermomécaniques couplées). Deux échelles sont à considérer : le compor-

tement global du plancher bois-béton sous condition d'incendie et le comportement de la connexion à hautes températures. Plusieurs modèles numériques ont été réalisés sous Abaqus©, aussi bien des modèles thermiques que des modèles thermomécaniques. Les modèles thermiques ont permis d'estimer les champs de température obtenus, notamment au droit de la connexion, pour les différentes configurations de plancher SBB®. Les modèles thermomécaniques réalisés ont pour objet de simuler les essais au feu (sur le plancher et Push-out). A l'échelle du plancher deux phénomènes déterminant du comportement au feu du système ont été identifiés :

- la dilatation différentielle des matériaux bois et béton, qui entraîne des efforts internes dans le plancher notamment sur la connexion (facteurs d'importance : portée du plancher, espacement de la connexion, temps d'exposition à l'incendie. . .) ;
- la réduction des sections bois et béton qui entraîne une diminution de la rigidité effective du plancher. De plus, la modification des sections entraîne une évolution du glissement à l'interface bois-béton au cours de l'incendie et donc modifie les efforts repris par la connexion. L'échauffement des matériaux induit également une altération des propriétés mécaniques de ceux-ci.

2.3.1 Modélisation thermique des sections mixtes bois-béton

La modélisation thermique des sections mixtes bois-béton permet de juger de l'échauffement des différents éléments constituant la section mixte. Il est ainsi possible d'identifier les configurations de plancher avec un échauffement important de la connexion. Un échauffement trop important de la connexion entraîne une dégradation de ses propriétés et peut mettre en péril le caractère mixte de la section bois-béton. Dans le cas extrême où la connexion n'est plus effective, la stabilité structurelle doit être justifiée avec les éléments bois et béton déconnectés. Les propriétés thermiques des matériaux ont été définies selon les Eurocodes, à savoir l'Eurocode 5-1-2 pour le bois, l'Eurocode 2-1-2 pour le béton et l'Eurocode 4-2 pour l'acier du connecteur. L'utilisation du logiciel Abaqus© a permis d'utiliser des lois de comportement non linéaires évoluant avec la température. L'objectif des modèles thermiques est d'établir en fonction du temps les champs de température dans la section bois, la section béton et le connecteur SBB®.

Géométrie et conditions aux limites du modèle

Le modèle est constitué de 3 à 4 éléments : la solive bois, la dalle béton, le connecteur et éventuellement le platelage OSB. Pour le modèles thermique, les armatures n'ont pas été

modélisées. En ce qui concerne les connecteurs, une modélisation simplifiée du connecteur en deux cylindres coaxiaux a été retenue. Les autres éléments (solives, dalle, platelage) ont été retranscrits avec leur géométrie exact. Dans ce modèle, les éléments finis de type C3D8RT (disponible dans la bibliothèque des éléments d'Abaqus©) ont été utilisés pour les différentes pièces. Il s'agit d'éléments cubiques à huit noeuds, couplés thermomécaniquement, avec pour chaque noeud trois degrés de liberté en translation et un degré de liberté pour la température.

Pour les modélisations des essais Push-Out sous incendie, le maillage a été adapté afin d'obtenir des nœuds correspondant aux points de mesure des thermocouples des essais. L'ensemble de la section est initialisé à une température de 20°C. Les conditions aux limites sont précisées la Figure 2.4. Il s'agit de modéliser d'une part l'échauffement de la section en sous-face par l'incendie et d'autre part le rafraichissement de la section en face supérieure.

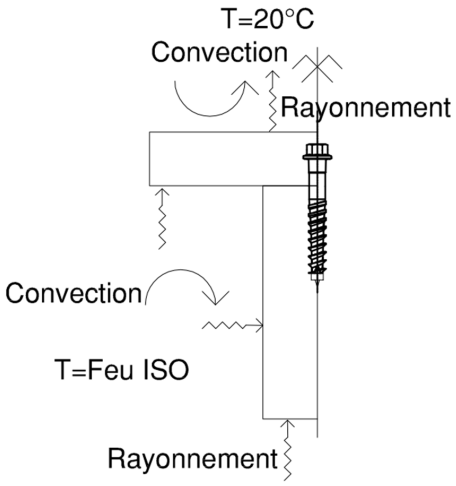

Figure 2.4 – Conditions aux limites pour la modélisation thermique des poutres mixtes bois-béton.

Confrontation des résultats numériques aux résultats expérimentaux

Le modèle thermique est appliqué aux trois configurations testées lors des essais Push-out sous incendie dans le cadre de la thèse CIFRE de Manuel Menthay (2015) [28] (Figure 2.5). Les résultats des modélisations thermiques sont précisés sur la Figure 2.6. Dans la partie gauche de la figure, les isothermes dans les éléments bois, béton et la connexion sont

présentées sur des vues éclatées avec des échelles des températures spécifiques propres à chaque élément. Dans la partie droite, les températures modélisées le long du connecteur sont précisées à différents instants de l'incendie. L'allure des températures modélisées dans le connecteur met en avant la difficulté d'associer une température au connecteur à un instant d'incendie donné. Dans les trois configurations, la répartition de la température au sein du connecteur varie significativement selon la hauteur, dans le cas extrême de la configuration n°2 la température varie d'environ 50°C entre le haut et le bas du connecteur à 60 minutes d'incendie. Pour les trois configurations, l'échauffement du connecteur se produit par le béton et le point le plus froid du connecteur se situe au pied de celui-ci. C'est la configuration avec le renformis béton qui conduit aux températures les plus importantes et la configuration avec le panneau OSB qui limite au maximum l'échauffement du connecteur.

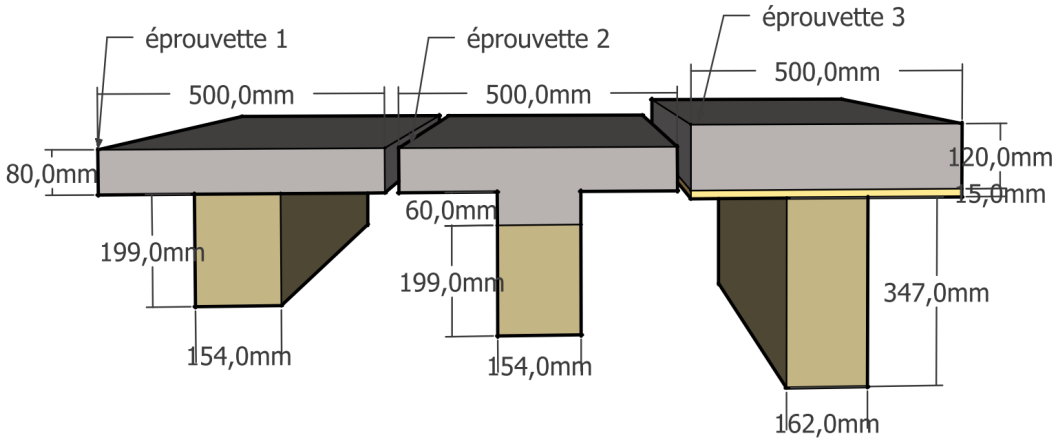

(1) de base ; (2) avec renformis ; (3) avec panneau OSB

Figure 2.5 – Trois configurations d'essais Push-out sur la connexion bois-béton sous incendie.

Les résultats numériques obtenus ont mis en évidence la capacité du modèle thermique proposé à reproduire les températures atteintes expérimentalement au sein de sections mixtes bois-béton. Ce modèle a été ensuite utilisé pour déterminer la distribution des températures dans 9 autres sections de poutre mixte bois-béton dimensionnées selon les critères préconisés actuellement pour le dimensionnement au feu des poutres mixtes bois-béton SBB®. Le détail des résultats peut être trouvé dans la thèse de Manuel Menthay (2015) [28].

Isothermes obtenues dans les sections mixtes bois - béton modélisées

Profil des températures obtenues dans le connecteur en différents instants de l'incendie

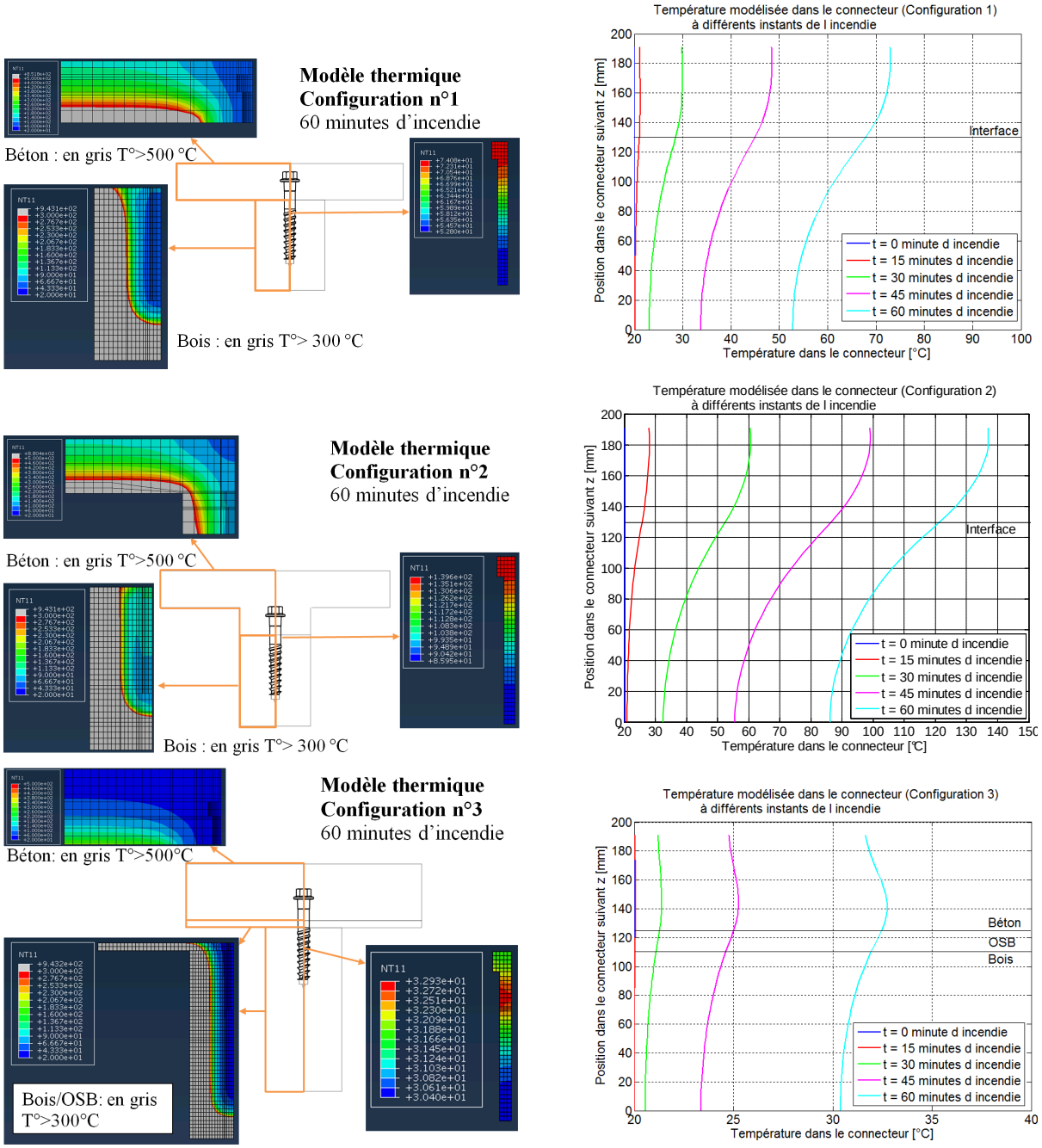

Figure 2.6 – Isothermes obtenues dans les sections mixtes bois-béton modélisées et profil des températures obtenues dans le connecteur en différents instants de l'incendie.

2.3.2 Modélisation thermomécanique couplée de poutres mixtes bois-béton

Afin de simuler l'essai du plancher bois-béton testé sous incendie au laboratoire EFECTIS en 2011 [8], nous avons fait un modèle thermomécanique couplé à l'aide du logiciel Abaqus©. Les résultats numériques sont comparés aux mesures expérimentales. Par ailleurs, le modèle a été réalisé suivant différentes hypothèses afin de juger de l'importance de la prise en compte de la dilatation thermique du béton dans le comportement global de la poutre mixte sous incendie.

2.3.2.1 Comportement thermomécanique des matériaux

Il existe des lois complexes de comportement au feu des matériaux. Dans le cas du bois certains modèles cherchent à décrire avec précision le comportement thermo-hygro-chimico-mécanique du matériaux, de même pour le béton. Dans le cadre de ce travail de recherche, les modèles utilisés sont des modèles plus rapides à mettre en oeuvre et nécessitant moins de paramètres d'entrée. Il s'agit en grande partie des modèles théoriques proposés dans les Eurocodes afin de se rattacher au contexte normatif.

Béton

Les propriétés mécaniques du béton en fonction de la température sont issues de l'Eurocode 2-1-2. Le modèle "concrete damage plasticity" est utilisé. Il a été défini en ajoutant la dépendance des différents paramètres à la température. La Figure 2.7 illustre la loi de comportement et l'évolution du coefficient de dilatation thermique du béton en fonction de la température.

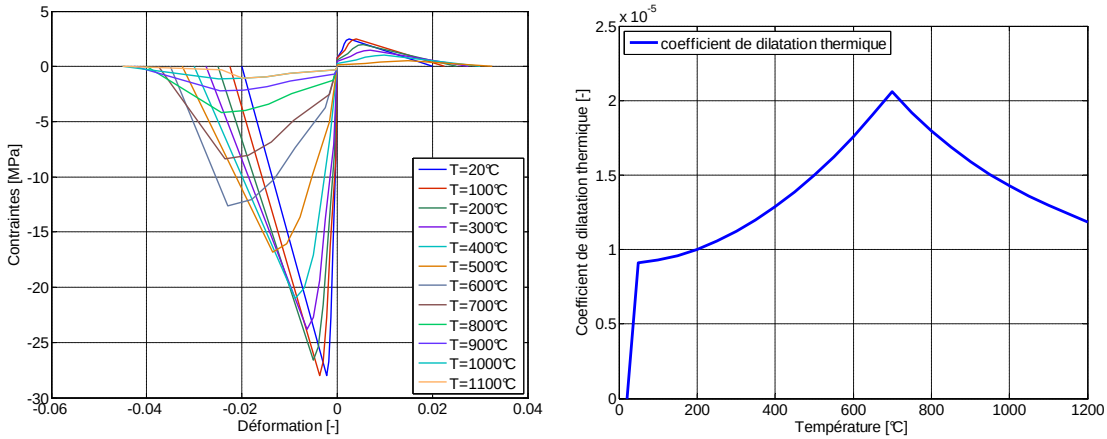

Figure 2.7 – Comportement thermomécanique du béton pour une sollicitation uniaxiale.

Bois

Les altérations des propriétés mécaniques du bois en fonction de la température sont introduites d'après les spécifications de l'Annexe B de l'Eurocode 5-1-2 pour les résineux. Au-delà de 300°C, le bois est carbonisé et le charbon est supposé n'avoir aucune résistance mécanique. Les propriétés mécaniques du bois sont prises suivant la norme NF EN 14080 [33]. On adopte ici pour le bois une loi de comportement élastoplastique avec écrouissage linéaire isotrope. Cette loi favorise la convergence du modèle. Le tableau 2.3 précise les coefficients de réduction des propriétés mécaniques retenus en fonction de la température pour le matériau bois. On ne peut pas parler de dilatation thermique α_T pour le matériau bois au sens où on l'entend pour les matériaux béton ou acier. Les dimensions de l'élément bois varient selon l'évaporation ou non de l'eau contenue dans le bois. Or sous incendie, l'augmentation de température est trop rapide pour permettre l'évaporation de l'eau contenue dans le bois. Par conséquent il est courant de considérer un coefficient de dilatation thermique α_T nul pour le matériau bois.

TABLEAU 2.3 – Coefficient de réduction des propriétés mécaniques en fonction de la température pour le matériau bois.

Température du bois	Paramètres Eurocode 5-1-2 (hypothèse d'un bois résineux)			
	En compression		En traction	
θ [°C]	$\frac{E_{0,g,\theta}}{E_{0,g,mean}}$	$\frac{f_{c,0,g,\theta}}{f_{c,0,g,k}}$	$\frac{E_{0,g,\theta}}{E_{0,g,mean}}$	$\frac{f_{t,0,g,\theta}}{f_{t,0,g,k}}$
20	1,0	1,0	1,0	1,0
100	0,35	0,25	0,50	0,65
300	0	0	0	0

Acier des connecteurs SBB® et des armatures

On adopte ici une loi de comportement élastoplastique avec écrouissage linéaire isotrope pour l'acier en ajoutant la dépendance des différents paramètres à la température. La loi de comportement introduite est symétrique en traction et compression. Les coefficients minorateurs pris en compte pour les autres températures sont ceux de l'Eurocode 2-1-2. Ils sont rappelés au tableau 2.4.

TABLEAU 2.4 – Coefficient de réduction des propriétés mécaniques en fonction de la température pour le matériau acier.

Température de l'acier	Paramètres Eurocode 2-1-2 (Hypothèses : Acier de classe N et laminé à chaud)		
θ [°C]	$\frac{f_{sy,\theta}}{f_{yk}}$	$\frac{f_{sp,\theta}}{f_{yk}}$	$\frac{E_{s,\theta}}{E_s}$
20	1,00	1,00	1,00
100	1,00	1,00	1,00
200	1,00	0,81	0,90
300	1,00	0,61	0,80
400	1,00	0,42	0,70
500	0,78	0,36	0,60
600	0,47	0,18	0,31
700	0,23	0,07	0,13
800	0,11	0,05	0,09
900	0,06	0,04	0,07
1000	0,04	0,02	0,04
1100	0,02	0,01	0,02
1200	0,00	0,00	0,00

2.3.2.2 Géométrie et maillage

La géométrie des éléments respecte celle de l'éprouvette testée sous incendie en 2011 chez Efectis [8] (Figure 2.8). Il s'agit d'un plancher mixte bois-béton de 5,35m x 3m, simplement appuyé (portée entre appuis de 4,90m). Le spécimen d'essai a été soumis à un chargement (2 charges ponctuelles, pour une charge totale de 240 kN) induisant des sollicitations sous combinaisons accidentelles identiques à celles du cas réel.

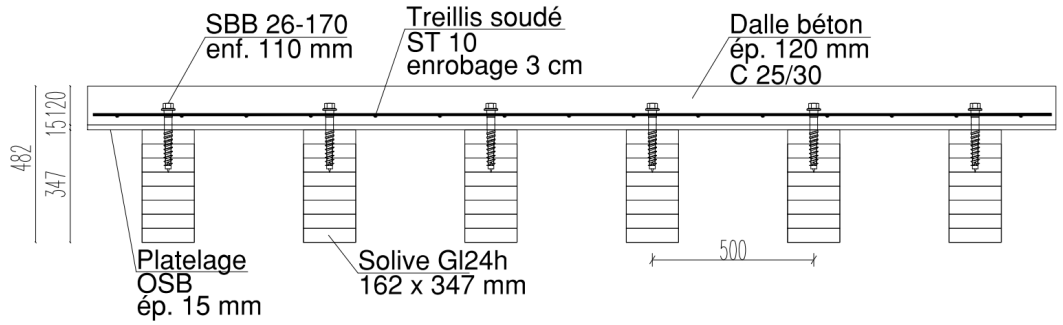

Figure 2.8 – Géométrie du plancher testé en 2011 chez Efectis [8].

Pour l'élément bois, les armatures et le béton, les géométries exactes des éléments ont été entrées dans le modèle. Les connecteurs ont été modélisés de manière simplifiée par deux cylindres coaxiaux (un pour le fût et un pour la tête du connecteur). Le panneau OSB n'a pas été explicitement modélisé, une "lame d'air" a été laissée entre le bois et le béton. Les conditions limites en sous-face de l'élément béton prennent en compte l'influence du platelage sur la température en modélisant une température ISO réduite le temps où le platelage reste en place. Au-delà de 30 minutes d'incendie, le platelage est totalement consumé et son influence n'est plus prise en compte.

Le type d'élément fini retenu pour l'ensemble des objets de ce modèle est celui nommé C3D8RT dans le logiciel Abaqus. Il s'agit d'un élément cubique à huit noeuds, couplé thermomécaniquement, avec pour chaque noeud trois degrés de liberté en translation et un degré de liberté pour la température. Le tableau 2.5 présente le nombre d'éléments, de noeuds et de variables qui constituent le modèle réalisé. La distinction est faite entre les éléments propres aux objets modélisés et les éléments générés par le programme pour modéliser les contacts entre les objets.

Tableau 2.5 – Taille du modèle thermomécanique réalisé.

Nombre total d'éléments	111 467
Éléments solides définissant les objets modélisés	56 813
Éléments générés pour le contact	54 654
Nombre total de nœud	231 199
Nombre total de variables constituant le modèle	507 451

2.3.2.3 Conditions aux limites

Les conditions aux limites du modèle traduisent les conditions lors de l'essai. Par symétrie, seule la moitié d'une poutre mixte a été modélisée. Concernant les chargements, les poids propres des éléments bois et béton sont pris en compte via des charges surfaciques placées respectivement sur le dessus des éléments correspondants. Ces chargements évoluent avec la température selon la combustion des éléments bois et béton. Le chargement vertical appliqué lors des essais par le vérin est modélisé quant-à-lui comme une charge surfacique appliquée sur une surface localisée de l'élément béton. Les détails des conditions aux limites "mécaniques" et "chargement" du modèle sont présentés à la Figure 2.9.

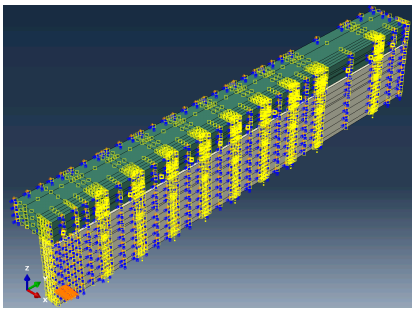

Poutre bois : appui rotulé

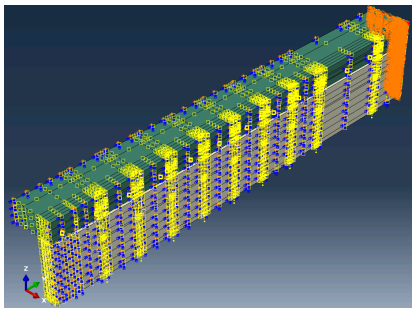

Symétrie de la poutre suivant le plan XZ

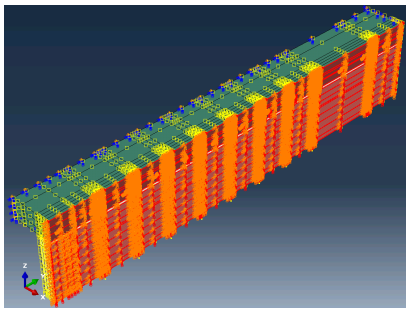

Symétrie 1 de la poutre suivant le plan ZY

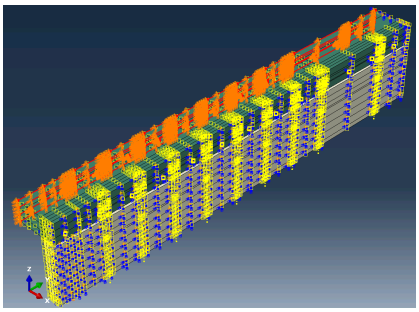

Symétrie 2 de la poutre suivant le plan ZY

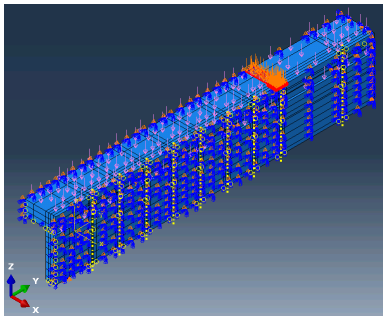

Charge appliquée par le vérin

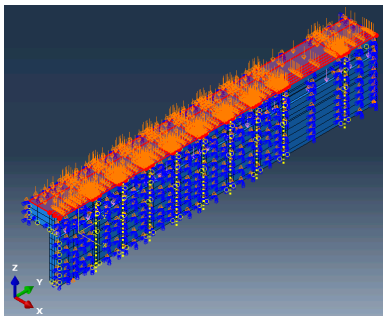

Poids propre de la dalle béton

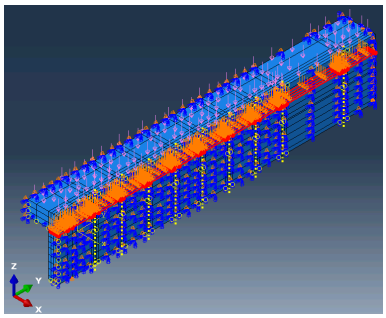

Poids propre de la poutre bois

Figure 2.9 – conditions aux limites ”mécaniques” et ”chargement” du modèle thermomécanique couplé.

La montée en température est modélisée conformément à la configuration expérimentale. Elle agit en sous-face du plancher mixte sur la poutre bois et en sous face de la dalle béton. Dans le modèle thermomécanique, les conditions aux limites thermiques sont des surfaces où sont appliquées des radiations et des convections entre l'air ambiant et le spécimen d'essai (Figure 2.10). En d'autres termes, l'air ambiant du laboratoire à 20°C est modélisé au-dessus du plancher et la montée en température des gaz selon la norme ISO 834-1 (feu iso) est appliquée en sous-face du plancher. Lors de l'essai, un platelage bois était présent en sous face de la dalle béton. Pendant les 30 premières minutes de l'incendie il a joué le rôle d'isolant thermique au profit de la dalle béton, puis apès il s'est consumé et a

perdu son rôle d'isolant. Afin de retranscrire au mieux ce phénomène, le platelage n'a pas été directement modélisé en tant qu'élément dans le modèle numérique mais la condition limite de montée en température en sous-face de la dalle béton a été prise en compte.

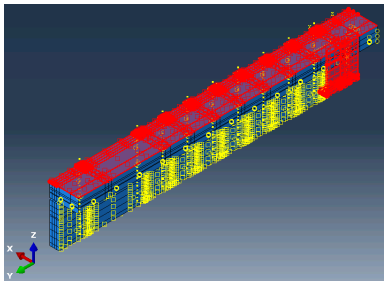

Température ambiante (20°C)

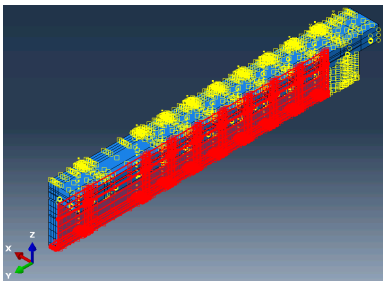

Montée en température des gaz selon l'ISO 834 - 1

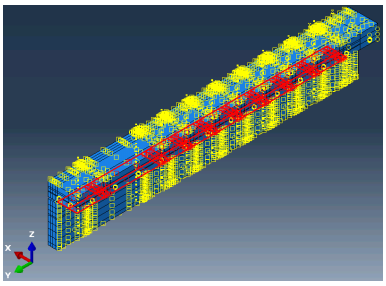

Montée en température des gaz selon l'ISO 834 - 1 modifiée pour prendre en compte le platelage

Figure 2.10 – conditions aux limites "thermique" du modèle thermomécanique couplé.

2.3.2.4 Résultats marquants

Le modèle a été réalisé avec et sans dilatation thermique des matériaux afin de qualifier l'influence de la dilatation gênée sur le comportement de la poutre mixte. Lors de l'essai de tenue au feu du plancher mixte, les grandeurs mesurées étaient thermiques (thermocouples dans le béton) et mécaniques (variation de la déformée de la dalle béton à mi - portée). Il a bien été vérifié que les températures mesurées et modélisées étaient proches. La Figure 2.11 présente les variations de flèches à mi-portée mesurées en quatre points lors de l'essai. Malheureusement, la flèche initiale due au chargement n'a pas été mesurée. Seule la variation de flèche durant l'incendie a été mesurée. Les résultats numériques pour la variation de flèche à mi-portée sont également tracés sur cette figure. Les résultats du modèle intégrant la dilatation thermique des matériaux présentent l'allure la plus proche des résultats expérimentaux. Le modèle sans dilatation thermique, qui lui ne traduit que la perte de matière et l'affaiblissement mécanique des éléments avec la température ne présente pas la même allure que celle observée expérimentalement. Néanmoins l'écart en terme de variation de flèche modélisée à 60 minutes d'incendie reste réduit, de l'ordre de 5 mm. Il convient par ailleurs de rappeler qu'à l'Eurocode, les exigences en situation d'incendie sont en termes de contraintes et non en termes d'amplitudes des déformées.

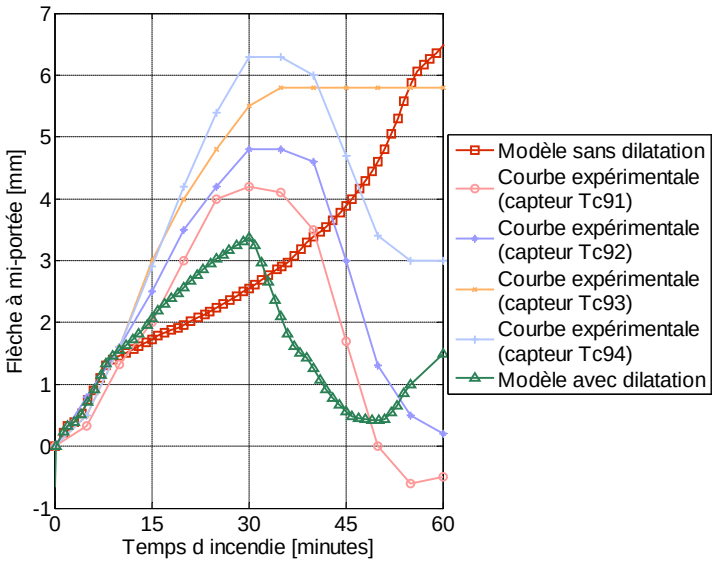

Figure 2.11 – Variation des flèches de la poutre à mi-portée sous incendie.

L'impact de la dilatation gênée des matériaux est plus sensible sur la sollicitation des connecteurs que sur la déformée globale de la poutre. Comme en témoigne la Figure 2.12 où les glissements obtenus pour chaque modèle sont comparés. Il convient de rappeler ici que seule la moitié de la poutre est modélisée par symétrie. Pour la poutre à température ambiante, uniquement chargée mécaniquement, les glissements au droit de chaque connecteur, avec moins de 0,25 mm, restent faibles. Dans la modélisation à 60 minutes d'incendie, mais sans prise en compte de la dilatation thermique des matériaux, les glissements augmentent pour se rapprocher de 0,30 mm maximum. Par contre la modélisation avec prise en compte de la dilatation thermique des matériaux voit les glissements augmenter significativement. Au centre de la poutre, les effets de la dilatation thermique gênée sont les plus faibles. Ils augmentent au fur et à mesure que les connecteurs s'éloignent du centre de la poutre, jusqu'à atteindre environ 3,5 mm pour le connecteur le plus proche de l'appui. La connexion par tire-fonds métalliques présente ici l'avantage d'avoir un comportement ductile qui permet de ne pas craindre une rupture de la connexion sous les efforts supplémentaires dus à la dilatation thermique du béton.

Enfin, le détail de la démarche et des résultats du modèle thermomécanique couplé des poutres mixtes bois-béton peuvent être trouvé dans la thèse de Manuel Menthay (2015) [28].

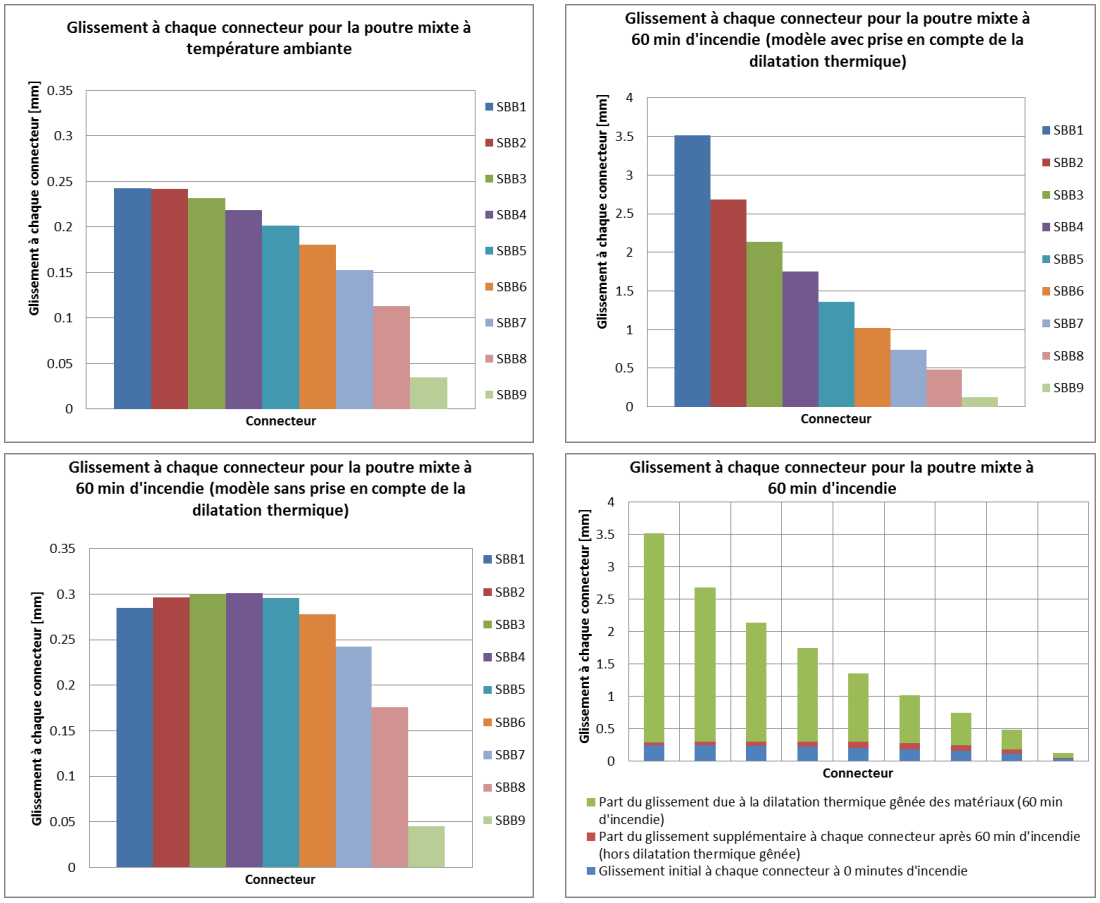

Figure 2.12 – Répartition des glissements au droit de chaque connecteur bois-béton du modèle thermomécanique couplé de poutre sous incendie.

2.4 Bilan et perspectives

Mes travaux de recherche sur les structures bois-béton reposent sur la modélisation expérimentale et numérique du comportement de planchers mixtes bois-béton connectés par des tire-fonds métalliques SBB® de l'entreprise AIA Ingénierie. 24 essais Push Out ont été réalisés sur le système de connexion SBB®. 12 essais Push Out ont été effectués sous chargement cyclique alterné et 12 autres sous chargement statique monotone. Les essais ont montré un comportement ductile de la connexion et une bonne résistance mécanique du système. Les essais sous chargement cyclique ont permis de s'assurer de la capacité du système à dissiper de l'énergie et de quantifier la perte de résistance de la connexion sous chargement alterné. Cette étude expérimentale a abouti à l'obtention de l'Avis Technique du procédé SBB® auprès du CSTB concernant son emploi en zone sismique en France métropolitaine. Les modèles thermiques et thermomécaniques couplés réalisés sous Abaqus©

ont permis de confirmer l'échauffement limité des connecteurs bois-béton en situation d'incendie ainsi que de quantifier les dégradations de rigidité et de résistance de ces derniers. Les confrontation entre les résultats de la modélisation numérique des essais à ceux obtenus expérimentalement s'est avérée globalement satisfaisante.

La modélisation numérique des essais permet d'isoler l'influence de la dilatation thermique gênée du béton sur l'amplitude des glissements à l'interface bois-béton. Un des phénomènes mis en avant dans ce travail de recherche est l'importance de la dilatation gênée du béton sur les sollicitations des connecteurs bois-béton. Dans certaines configurations, cette influence est telle qu'elle peut permettre l'apparition du phénomène de "thermal bowing action". C'est à dire que la dilatation gênée du béton vient s'ajouter aux sollicitations des connecteurs dues aux charges gravitaires et ainsi peut conduire au soulèvement de la poutre mixte. Finalement, les résultats ont mis en évidence que le comportement mixte des planchersbois-béton SBB® peut être assuré en situation d'incendie sous réserve de sections suffisantes.

Plusieurs perspectives sont envisagées à l'issue du projet de recherche SBB® de l'entreprise AIA Ingénierie. Une perspective évidente est d'étendre le procédé SBB® à d'autres types d'éléments structuraux que le plancher (par exemple dans les voiles mixtes bois-béton). Une autre perspective d'étude est l'aspect environnemental des planchers mixtes bois-béton qui pourrait être quantifié par une Analyse du Cycle de Vie permettant la comparaison de ce système aux systèmes de constructions traditionnelles (analyse pressentie comme favorable par rapport à un plancher classique en béton armé).

THÈME 3

ÉTUDE PRÉ-NORMATIVE DES STRUCTURES HYBRIDES BÉTON-ACIER

3.1 Contexte et objectifs généraux

L'intérêt des solutions mixtes acier-béton est connu de longue date. Dans le cadre des ouvrages d'art métalliques, la prise en compte de l'effet bénéfique de la présence éventuelle d'une dalle de béton sur la flexion de l'ouvrage est évidente. Il en est de même pour le comportement des poutres de bâtiments lorsqu'elles supportent un plancher en béton armé. La mixité acier-béton permet aussi, en enrobant les éléments acier par le béton dans les poteaux mixtes, de leur donner une meilleure tenue au feu. La structure mixte dans sa définition classique, à savoir celle d'une charpente métallique optimisée par la prise en compte du béton environnant, a fait objet de nombreux travaux de recherche et est à ce jour assez bien maîtrisée. Les résultats de ces travaux ont été transcrits en normes d'application, telles que l'Eurocode 4 et l'Eurocode 8 (chapitre 7). L'axe ingénierie structurale de l'équipe GEOSAX du LGCGM a d'ailleurs largement contribué aux recherches dans le domaine et au développement de ces normes.

De nos jours, les structures en béton armé renforcées par des profilés métalliques noyés localement ou globalement sont souvent utilisées dans les bâtiments de grande hauteur. On parle des structures de la nouvelle génération nommées "structures hybrides" béton-acier. Les systèmes structurels couverts sont en fait assez variés, par exemple :

- Les poteaux/voiles en béton armé renforcés par plusieurs profilés acier totalement enrobés ;
- Les poteaux en béton armé renforcés par des profilés sur un seul étage, sans continuité dans les poteaux des étages inférieurs et supérieurs ;
- Les assemblages poteau béton armé / poutre acier (ou mixte) par des profilés noyés dans le poteau ;
- Les renforts par clés de cisaillement dans les zones de nœud des structures en béton armé ;
- ...

Si les structures mixtes sont relativement maîtrisées, les structures hybrides béton-acier le sont beaucoup moins, et quasiment absentes de la réglementation européenne actuelle. En effet, avec la présence des profilés métalliques noyés dans le béton, les éléments structu-

raux hybrides ne sont ni des éléments de structures béton armé, au sens de l'Eurocode 2, ni des éléments mixtes au sens de l'Eurocode 4. Bien que les configurations soient variées, de nombreux verrous scientifiques sont communs aux différents éléments hybrides, parce qu'ils sont liés aux mécanismes de transmission des forces entre le béton et les profilés métalliques. Pour les connexions linéiques et surfaciques en cisaillement, la combinaison des résistances dues au frottement, à l'adhérence chimique, aux résistances de connecteurs mécaniques a été très peu étudiée dans la littérature. Concernant les zones de transfert local, il est possible de trouver différents schémas dans la littérature. Néanmoins, ils sont définis pour des configurations particulières. Il manque un modèle général ainsi que des règles générales pour définir les détails constructifs qui éviteront les concentrations de contraintes importantes dans certains endroits de la structure.

L'objectif de mes travaux de recherche dans cette thématique est de participer à un effort international européen destiné à développer une méthode de dimensionnement pour les éléments hybrides béton-acier (Projet RFCS SMARTCOCO, Comité technique TC11). Cet objectif nécessite des travaux de grande ampleur à moyen et long terme, et est commun à l'axe ingénierie structurale de l'équipe GEOSAX du LGCGM.

Les travaux présentés dans ce qui suit ont été réalisés dans le cadre du projet européen RFCS SMARTCOCO (2012-2015) dont je suis le responsable scientifique pour l'INSA de Rennes.

3.2 Dimensionnement des poteaux hybrides béton-acier au second ordre

3.2.1 Position du problème

Dans les immeubles de grande hauteur, lorsque le renforcement des poteaux béton par barres HA n'est pas suffisant pour résister aux charges appliquées, une solution possible, qui permet de garder le même équarrissage des poteaux, consiste à les renforcer par un ou plusieurs profilés métalliques noyés. La Figure 3.1 montre un exemple de l'utilisation de poteaux hybrides dans la construction. Ces poteaux, nommés "poteaux hybrides", sont usuellement sollicités par une force de compression importante combinée à une flexion selon leur axe fort s'ils participent au contreventement de la structure. En général, ces poteaux sont élancés et par conséquent le calcul de leur résistance doit être effectué au

second ordre. Malheureusement, pour ce type de poteaux, ni les règles de l'Eurocode 2, ni celles de l'Eurocode 4 ne sont applicables car ils ne respectent pas les domaines de validité des méthodes des Eurocodes.

Figure 3.1 – Poteaux hybrides utilisés en Chine : immeuble "East Pacific Center"

Comme l'objectif de mes travaux dans la thématique des structures hybrides est de développer un modèle de calcul s'insérant dans la réglementation actuelle, la démarche est la suivante. Il faut d'abord évaluer la pertinence des méthodes proposées dans les Eurocodes 2 et 4 et ensuite développer des méthodes de dimensionnement qui semblent les mieux adaptées à un contexte normatif.

3.2.2 Résultats essentiels

A l'occasion des travaux de recherche développés dans la thèse de Pisey KEO (2015) [23] que j'ai co-encadrée, nous avons réalisé une étude paramétrique très conséquente sur 1140 cas différents de poteaux hybrides. Il est apparu que les poteaux hybrides se comportaient plutôt de façon similaire à celle des poteaux en béton armé, et que dès lors, la méthode de l'Eurocode 2 était plus pertinente. Sur base de cette étude paramétrique, une méthode simplifiée a été proposée. Cette méthode est une version améliorée de celle de l'Eurocode 2 pour les poteaux hybrides dans laquelle nous intégrons les effets d'une plastification partielle ou complète des profilés lorsque les déformations augmentent, notamment sous l'effet du fluage de béton.

L'article ci-dessous, fourni en annexe du présent mémoire, fait la synthèse du travail et des résultats obtenus :

Annexe 12 : P. Keo, H. Somja, **Q-H. Nguyen** and M. Hjiaj. Simplified design method for slender hybrid columns. *Journal of Constructional Steel Research* 2015 ; 110 :101-120. `(5-Year IF 1.699) 2 citations` http://dx.doi.org/10.1016/j.jcsr.2015.03.006.

Le modèle par éléments finis crée pour réaliser cette étude, sur base de l'élément fini de type poutre mixte que j'ai développé dans ma thèse, est détaillé dans l'article suivant (fourni en annexe) :

Annexe 6 : P. Keo, M. Hjiaj, **Q-H. Nguyen** and H. Somja. Derivation of the exact stiffness matrix of shear-deformable multi-layered beam element in partial interaction. *Finite Elements in Analysis and Design* 2016. 112 :40-49. `(5-Year IF 1.967) 0 citation` http://dx.doi.org/10.1016/j.finel.2015.12.004.

3.2.3 Perspectives

L'approche, à l'instar des méthodes des Eurocodes, ne traite que de l'amplification non-linéaire, dans le plan, pour une sollicitation de flexion composée. Elle devrait être étendue, pour être complète, à l'étude du déversement, et au cas de la flexion composée déviée. Ces objectifs devraient être inclus dans un nouveau projet européen RFCS, faisant suite au projet SMARTCOCO.

3.3 Murs en béton armé renforcés par plusieurs profilés métalliques totalement enrobés

Cet axe de recherche porte sur l'étude analytique, numérique et expérimentale du comportement des murs hybrides béton-acier soumis à des sollicitations de flexion composée. Les travaux ont été réalisés dans le cadre du Workpakage 6.1 du projet RFCS SMARTCOCO (2012-2015) et de la thèse de Van Toan Tran (2015) [52]. La figure 3.2 illustre le mur hybride béton-acier étudié.

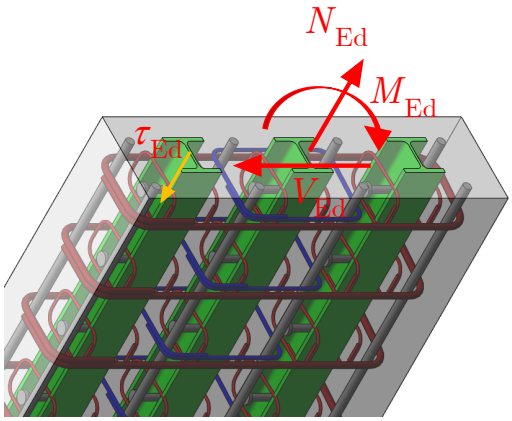

Figure 3.2 – Description du mur hybride étudié

3.3.1 Développement d'une méthode de dimensionnement pour les murs hybrides

Comme expliqué au paragraphe 3.1, lorsqu'un mur en béton armé est renforcé par plus d'un profilé acier, il ne rentre plus dans le cadre des éléments en béton armé traités par les normes "béton" actuelles (telles que l'Eurocode 2 ou l'ACI218) ni des éléments mixtes traités par par les normes "mixte acier-béton" actuelles (telles que l'Eurocode 4 ou l'AISC2010). Comme nous l'avons vu précédemment pour les poteaux/murs hybrides, la question qui peut se poser est : peut-on le considérer simplement comme un élément béton armé au sens de l'Eurocode 2 (ou de l'ACI318) ou comme un élément mixte acier-béton au sens de l'Eurocode 4 (ou de l'AISC 2010). Pour ce type d'élément hybride acier-béton, les lacunes dans les connaissances sont principalement liées au problème de transfert de force entre le béton et les profilés métalliques. Dans le cas où l'interaction complète entre le béton et les profilés est assurée (par l'adhérence, le frottement et/ou des connecteurs tels que des goujons de cisaillement ou des raidisseurs à plaques), les profilés en acier peuvent être considérés comme des armatures et donc leur résistance en flexion et au cisaillement peut être évaluée en utilisant les normes pour le béton armé. Par ailleurs, pour évaluer la résistance en flexion, le concept de section mixte au sens de l'Eurocode 4 ou de l'AISC 2010 peut également être utilisé. En revanche, la résistance à l'effort tranchant de la section hybride ayant plus d'un profilé métallique enrobé n'est pas encore explicitement traitée par ces normes.

Dans cette étude, nous avons proposé une méthode de calcul permettant d'évaluer la résistance des murs hybrides soumis à des sollicitations de flexion composée. Cette méthode

est, bien entendu, basée sur les méthodes existantes telles que celles de l'Eurocode 2 et de l'Eurocode 4. Il est à noter que dans cette méthode, une attention particulière est portée à l'évaluation de la résistance à l'effort tranchant et au cisaillement longitudinal car la prévention vis-à-vis de la ruine par cisaillement est une des préoccupations majeures pour le dimensionnement d'un tel élément structurel.

3.3.1.1 Modèle de calcul de la connexion

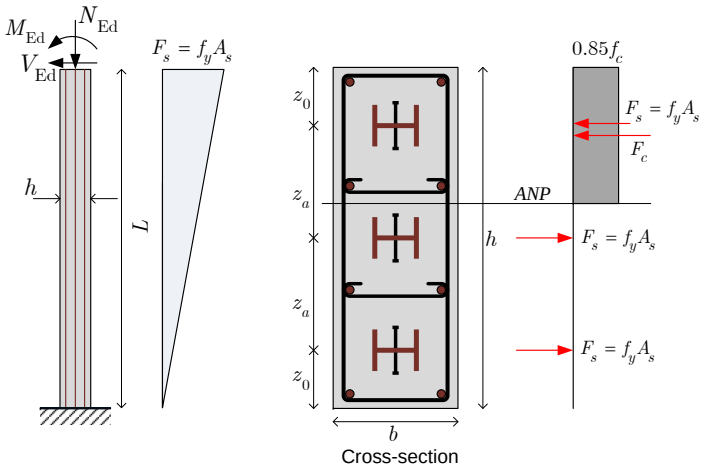

Figure 3.3 – Effort normal : profilé et section

Concernant la connexion à l'interface acier-béton, un modèle simple de calcul du nombre de connecteurs pour assurer l'interaction complète entre l'acier et le béton est proposé. Ce modèle est basé sur le concept de l'Eurocode 4 pour le calcul de la connexion dans une poutre mixte acier-béton. La démarche de ce modèle est comme suit. En considérant une interaction acier-béton complète, le moment plastique de la section "hybride" transversale peut être calculé à l'aide de la distribution des efforts proposée dans l'Eurocode 4, et présentée à la Figure 3.3. Par conséquent, les goujons à mettre en place doivent être capables de transférer la totalité de l'effort de traction du profilé au béton. Ainsi, l'effort de cisaillement à l'interface profil-béton, noté V_L, agissant sur les goujons compris entre la section où le moment plastique de flexion est atteint et la section où le moment de flexion s'annule, est

$$V_L = F_S(x = L/2) - F_S(x = 0) = A_s f_y \tag{3.1}$$

où A_s est l'aire du profil et f_y est la limite élastique du profil. Dès lors, le nombre minimal

des goujons nécessaires pour assurer l'interaction complète est calculé comme suit :

$$n_{min} = \frac{V_L}{P_{Rd}} \tag{3.2}$$

où P_{Rd} désigne la résistance en cisaillement d'un goujon dont l'expression est donnée dans l'Eurocode 4 6.6.3.1(1).

3.3.1.2 Résistance en flexion

Dans le modèle de dimensionnement proposé, la résistance en flexion de la section hybride ayant une connexion complète est évaluée à l'aide de la courbe d'interaction M-N qui est établie par deux méthodes : méthode des 3 pivots de l'Eurocode 2 et celle de moment plastique de l'Eurocode 4.

3.3.1.3 Résistance à l'effort tranchant

Afin d'évaluer la résistance à l'effort tranchant des murs hybrides, un modèle bielle-tirant a été développé. Ce modèle s'appuie sur le concept du treillis de Morsch qui consiste à modéliser le mur par un treillis comportant des bielles de béton et des tirants d'acier. La Figure 3.4 illustre le concept du modèle bielle-tirant pour les murs hybrides.

Dans ce modèle, la section totale est divisée en deux sous-sections comme le montre la Figure 3.4. La sous-section 2 est une section béton armé pure dont la résistance à l'effort tranchant peut être calculée selon l'Eurocode 2. La sous-section 1 quant-à-elle est évaluée à l'effort tranchant à l'aide du modèle bielle-tirant que nous avons développé dans le cadre du projet européen RFCS SMARTCOCO (2012-2015). Le point original dans ce modèle est que la contribution de la résistance au cisaillement des profilés à la résistance globale de la section est prise en compte.

3.3.1.4 Résultats essentiels

L'article ci-dessous, fourni en annexe du présent rapport, fait la synthèse du travail et des résultats obtenus :

Annexe 11 : Q-H. Nguyen, V-T. Tran and M. Hjiaj. Development of design method for composite columns with several encased steel profiles under combined shear and bending. *7th European Conference on Steel and Composite Structures*. Napoli, Italia, September 10-12, 2014.

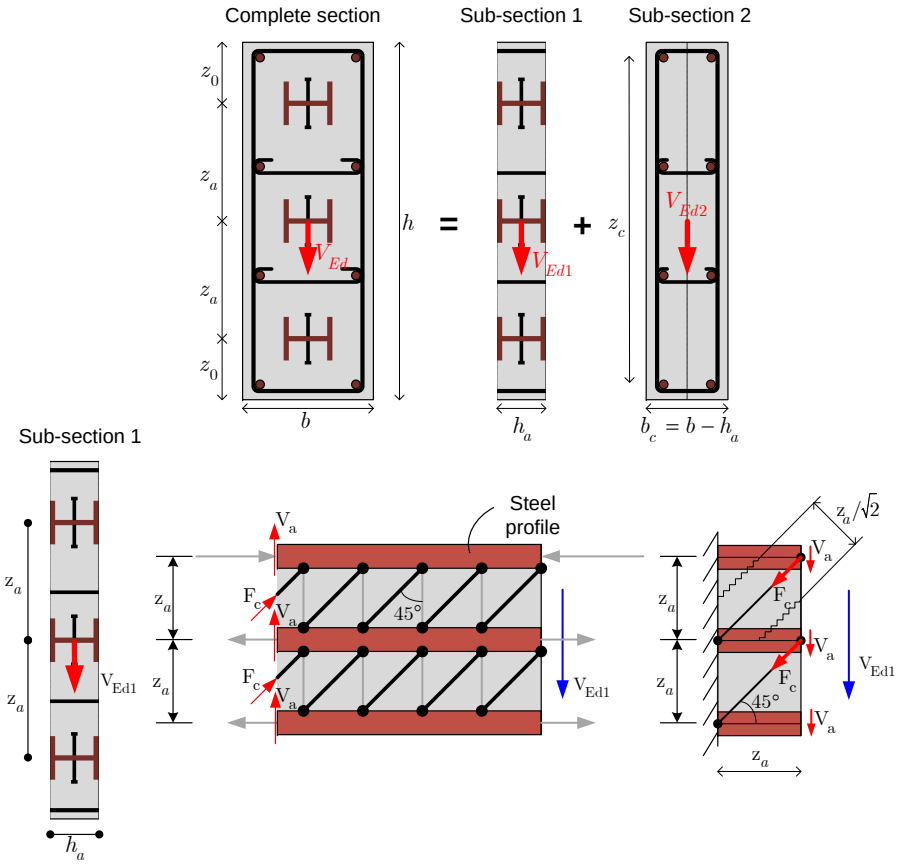

Figure 3.4 – Modèle bielle-tirant développé pour les murs hybrides

3.3.2 Étude expérimentale du comportement des murs hybrides en flexion

Dans le cadre du Workpakage 6.1 du projet européen RFCS SMARTCOCO (2012-2015), j'ai réalisé en 2015 une campagne d'essais sur les murs hybrides en flexion dont les objectifs principaux sont :

- d'évaluer les contributions de l'adhérence, du frottement et de la connexion à l'interface acier-béton sur la résistance des spécimens ;
- d'évaluer la contribution du confinement du béton produit par les étriers sur la résistance des spécimens ;
- de mettre en évidence différents mécanismes de transfert des efforts à la rupture tels que le mécanisme de type bielle-tirant.
- de calibrer la méthode de dimensionnement développée (présentée au paragraphe 3.3.1).

Tableau 3.1 – Description des corps d'épreuve

Nom du corps d'épreuve	Description
ARC	Béton armé pur, spécimen de référence;
BW	Spécimen hybride avec 3 profilés, sans connecteurs;
BWHC	Comme BW, avec haut confinement du béton par les étriers;
CW	Spécimen hybride avec 3 profilés, avec des goujons comme connecteurs;
CWHC	Comme CW, avec haut confinement du béton par les étriers;
DW	Spécimen hybride avec 3 profilés, avec des raidisseurs comme connecteurs;
DWHC	Comme DW, avec haut confinement du béton par les étriers;

Corps d'épreuve	Profilé en acier	Armature longitudinale	Cadres	Espacement des cadres	Connecteur	Espacement des connecteurs
ARC		8 HA20	HA14	20 cm		
BW	3 HEB100	8 HA20	HA14	20 cm		
BW-HC	3 HEB100	8 HA20	HA14	10 cm		
CW	3 HEB100	8 HA20	HA14	20 cm	50 Nelson S3L16-75	20 cm
CW-HC	3 HEB100	8 HA20	HA14	10 cm	50 Nelson S3L16-75	20 cm
DW	3 HEB100	8 HA20	HA14	20 cm	34 Plaques 80x40x10	30 cm
DW-HC	3 HEB100	8 HA20	HA14	10 cm	34 Plaques 80x40x10	30 cm

Sept corps d'épreuve (à l'échelle 1) ont été dimensionnés (avec le modèle de calcul présenté au paragraphe 3.3.1), conçus et testés au laboratoire LGCGM de l'INSA de Rennes. Un pré-dimensionnement a été d'abord réalisé en s'appuyant sur la capacité des vérins hydrauliques du laboratoire. Ce pré-dimensionnement a conduit à des spécimens de 5m de longueur de section $90 \times 25\ cm^2$. La description des corps d'épreuve est présentée au tableau 3.1. La figure 3.5 montre la configuration du spécimen et du dispositif d'essai.

3.3.2.1 Résultats essentiels

Les résultats expérimentaux obtenus ont été traités et analysés avec pour objectif essentiel la mise en évidence des différents mécanismes de transfert de charge et de ruine des murs hybrides soumis à la flexion simple. Le comportement global représenté par la relation entre la charge appliquée et la flèche à mi-travée est présenté à la Figure 3.6. On a observé que parmi les sept corps d'épreuve testés, seul le corps d'épreuve A-RC a été ruiné par flexion. Les autres corps d'épreuve ont été ruinés par une combinaison de flexion et cisaillement transversal.

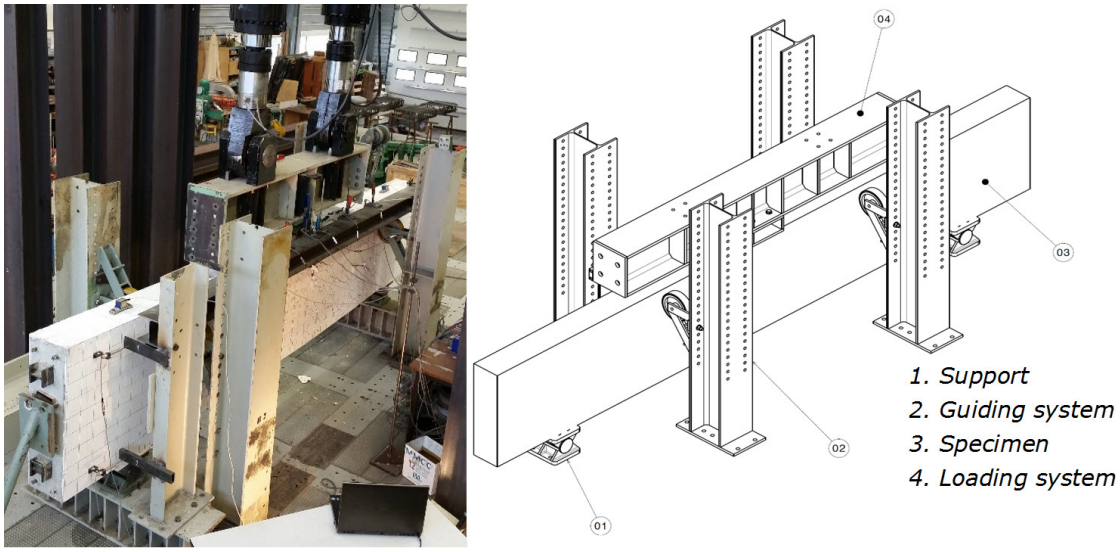

Figure 3.5 – Configuration d'un essai

L'analyse de la capacité portante des corps d'épreuve met en évidence la contribution non négligeable des profilés noyés à la résistance globale et à la rigidité initiale des corps d'épreuve. En effet, le fait de renforcer le mur béton armé par trois profilés HEA100 produit une augmentation de 2,03 à 2,51 fois la capacité portante (voir Figure 3.7). Cependant, les résultats ont montré que le confinement du béton dû au doublement du nombre d'étriers ne joue pas significativement sur la capacité portante. Les différences observées entre les charges ultimes obtenues proviennent des différentes valeurs de résistance en compression du béton mesurées pour chaque corps d'épreuve au jour de l'essai. De plus, il est constaté que les corps d'épreuve avec connecteurs (goujon ou raidisseur) ont un comportement plus ductile que les corps d'épreuve sans connecteur.

En analysant les contraintes, calculées à partir des déformations mesurées à l'aide de jauges électriques et en adoptant des lois de comportement du béton et de l'acier déterminées expérimentalement par des essais de caractérisation, on a pu constater que les armatures longitudinales étaient plastifiées par flexion en premier suivies par la plastification du profilé le plus tendu. L'analyse en section a montré que jusqu'à 60% de la capacité portante, l'hypothèse cinématique de Bernoulli restait valable pour des murs hybrides. Enfin, l'analyse des fissures a mis en évidence une inclinaison des bielles de béton comprise entre 41° et 51° (Figure 3.8). Ceci a permis de valider le choix de bielles à 45° dans le modèle bielle-tirant que nous avons proposé pour évaluer la résistance à l'effort tranchant

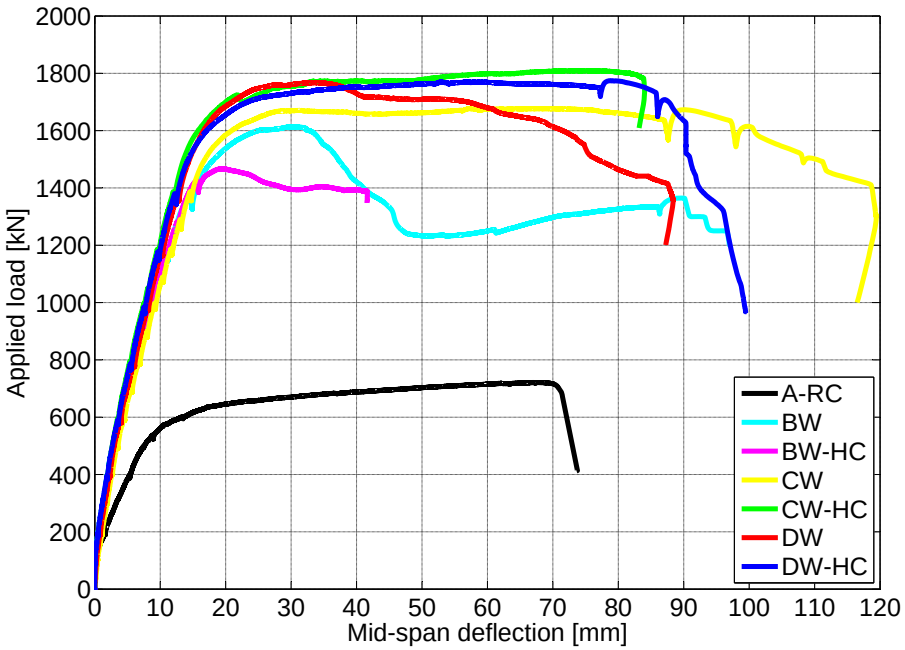

Figure 3.6 – Courbes "charge-flèche"

des murs hybrides.

Enfin, le détail des analyses et des résultats expérimentaux peuvent être trouvés dans la thèse de Van Toan Tran (2015) [52] que j'ai co-encadrée.

3.3.3 Modélisation numérique du comportement des murs hybrides en flexion

Suite à l'étude expérimentale des murs hybrides, une étude numérique a été réalisée. L'objectif principal de cette étude numérique a été de construire un modèle EF fiable, capable de prédire correctement la charge ultime, le déplacement maximal, les distributions de contraintes et de déformations et surtout les modes de ruine des murs hybrides testés dans le cadre du Workpakage 6.1 du projet européen RFCS SMARTCOCO (2012-2015). Ce modèle a été utilisé par la suite pour une étude paramétrique permettant de calibrer le modèle de dimensionnement proposé. Un modèle élément fini 3D a été développé à l'aide du logiciel Abaqus. Le modèle EF développé a pris en compte plusieurs aspects qui conditionnent le comportement global des murs hybrides, à savoir l'interaction partielle entre les profilés métalliques et le béton, le contact entre les composants, le comportement

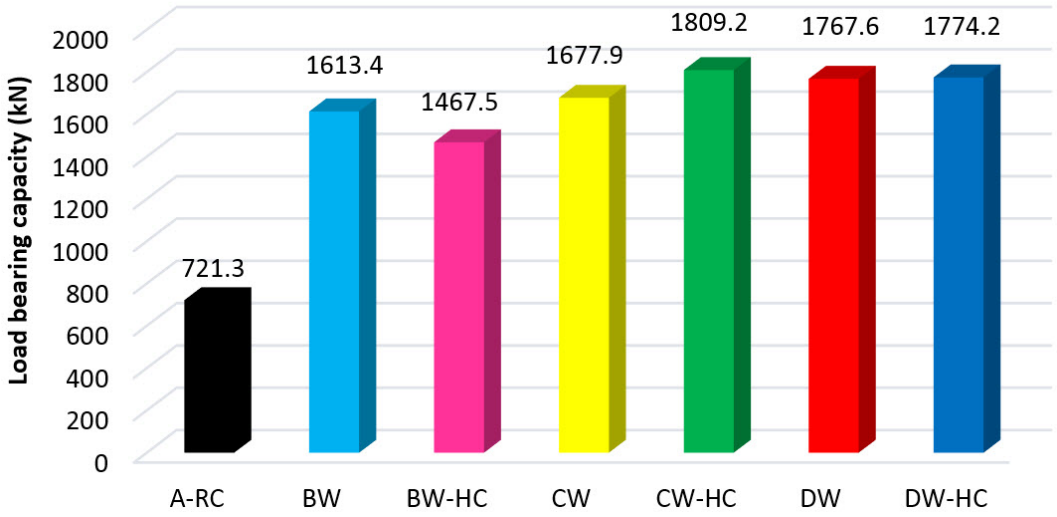

Figure 3.7 – Capacité portante des corps d'épreuve

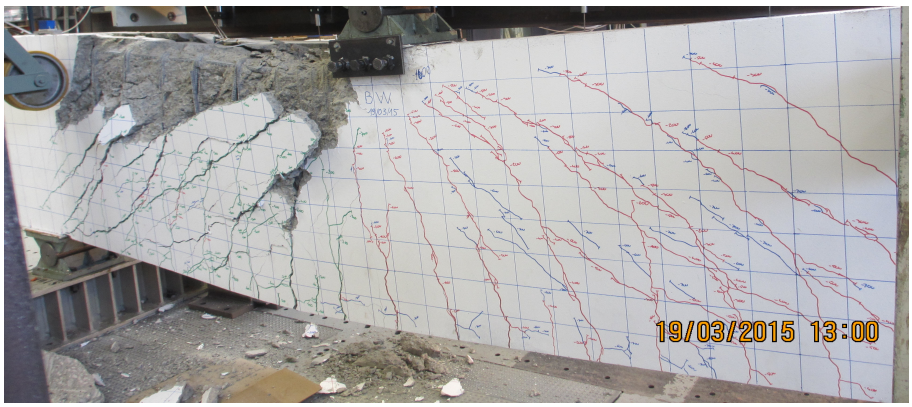

Figure 3.8 – Photo du corps d'épreuve BW après l'essai

nonlinéaire matériel, notamment le béton.

3.3.3.1 Géométrie et maillage

Étant donné que les corps d'épreuve testés sont symétriques en géométrie et chargement, seulement la moitié des spécimens a été modélisée. Les géométries exactes des éléments ont été introduites dans le modèle. Des éléments solides C3D8R à 8 nœuds ont été utilisés pour le béton, les profilés et les connecteurs. Quant aux armatures, des éléments treillis T3D2 à deux nœuds ont été utilisés. La Figure 3.9 présente le maillage et les types d'élément utilisés pour le béton, les armatures, le profilé et les connecteurs.

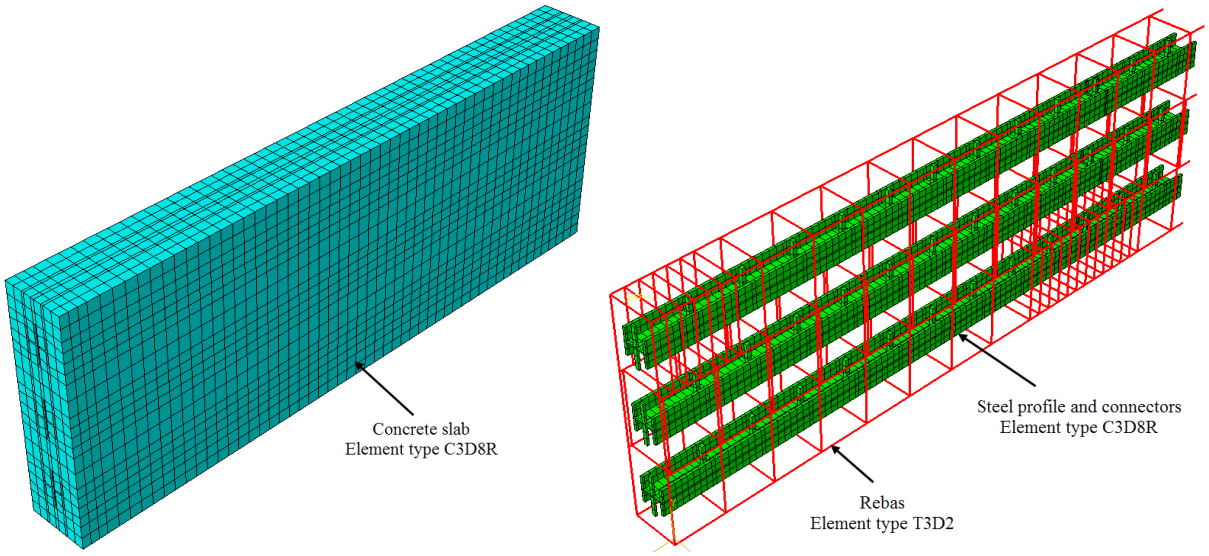

Figure 3.9 – Maillage et types d'élément utilisé

3.3.3.2 Loi de comportement des matériaux

Le modèle "Concrete Damaged Plasticity" disponible dans la bibliothèque des lois de comportement des matériaux d'Abaqus a été adopté pour le béton. Il est à noter que c'est un des modèles plus pertinent pour la modélisation des structures en béton. Les paramètres du modèle ont été choisis de façon pouvoir reproduire la courbe contrainte-déformation en compression de l'EC2 (Figure 3.10). Concernant l'acier des profilés, des armatures et de connecteurs, une loi de comportement élastoplastique avec écrouissage linéaire isotrope a été adoptée.

3.3.3.3 Interaction et conditions aux limites

Les armatures sont supposées totalement ancrées dans le béton donc l'interaction entre les armatures et le béton a été modélisée par l'option "embedded constraint" d'Abaqus. il s'agit d'imposer une liaison parfaite entre eux, c'est-à-dire les mêmes déplacements et rotations entre les nœuds communs à l'interface. Quant à l'interface profil-béton et connecteur-béton des éléments de contact rigide surface-à-surface avec frottement ont été utilisés. Les conditions aux limites du modèle traduisent les conditions lors de l'essai.

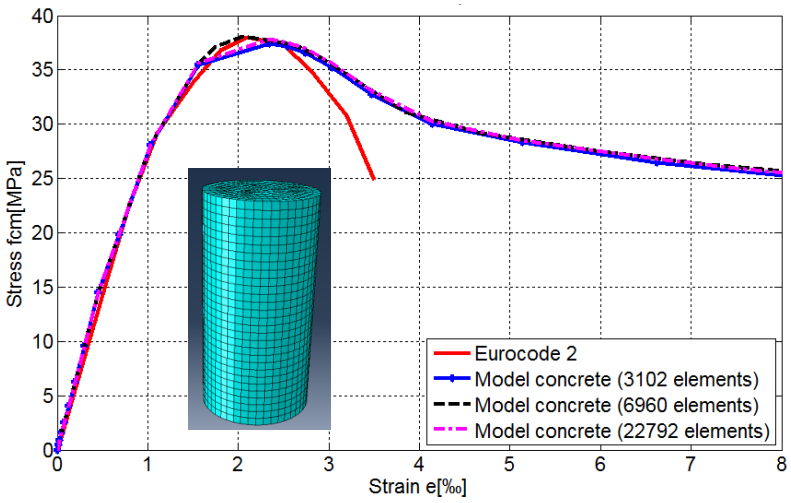

Figure 3.10 – Courbe contrainte-déformation du béton en compression introduite dans le modèle EF

3.3.3.4 Résultats essentiels

Une confrontation des résultats numériques aux résultats expérimentaux a été faite afin de valider le modèle EF 3D. Dans ce mémoire, j'ai décidé de présenter seulement les résultats du corps d'épreuve CW (dont la description est faite au tableau 3.1). Les résultats numériques ont montré que le modèle EF développé est capable de prédire de façon assez précise le comportement (global et local) des murs hybrides en flexion (Figures 3.11). Ces résultats ont permis également de valider le modèle de calcul de la connexion présenté au paragraphe 3.3.1.1.

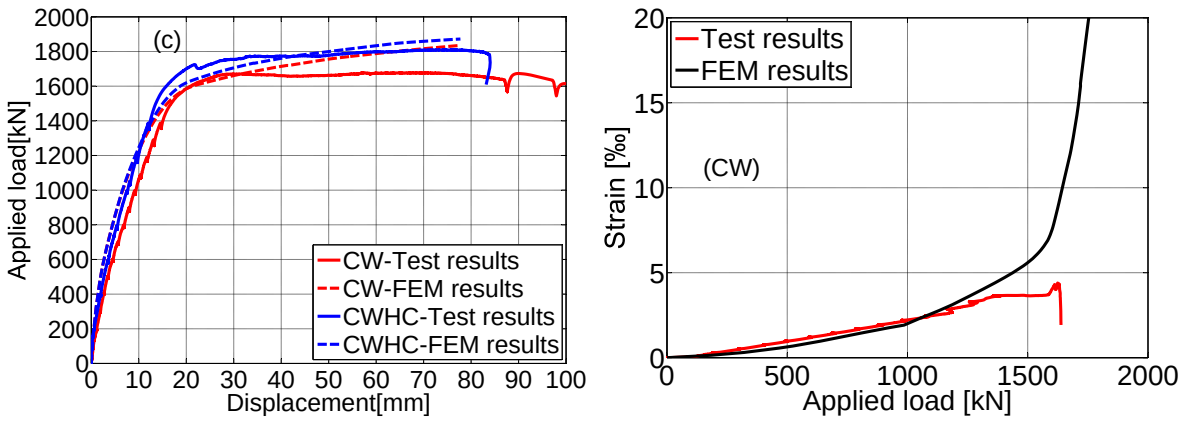

Figure 3.11 – Confrontation numérique-expérimentale au niveau global et local

Enfin, le détail des résultats peut être trouvé dans la thèse de Van Toan Tran (2015) [52] que j'ai co-encadrée.

3.3.4 Perspectives

La travail réalisé jusqu'à présent se limite au comportement des murs hybrides sous sollicitations statiques. La poursuite de ce travail consisterait à étudier le comportement des murs hybrides sous sollicitations sismiques et d'incendie. Cela devrait être inclu dans un nouveau projet européen RFCS, faisant suite au projet SMARTCOCO.

3.4 Nouvel assemblage hybride poteau BA / poutre acier

3.4.1 Position du problème

Les ossatures mixtes (RCS) constituées de poteaux béton armé (RC) et poutres métalliques (S) ont été largement utilisées dans le secteur du Bâtiment au cours de ces 30 dernières années. Les ossatures RCS possèdent plusieurs avantages à la fois du point de vue économique et du point de vue structurel par rapport aux ossatures traditionnelles en acier ou en béton armé [10]. Par conséquent, de nombreux programmes de recherche ont été menés pour étudier l'interaction entre les composants acier et les composants béton dans les ossatures RCS. Un grand défi dans la conception des ossatures RCS en zone sismique est la connexion entre le poteau béton armé et la poutre métallique, nommée désormais *assemblage RCS*.

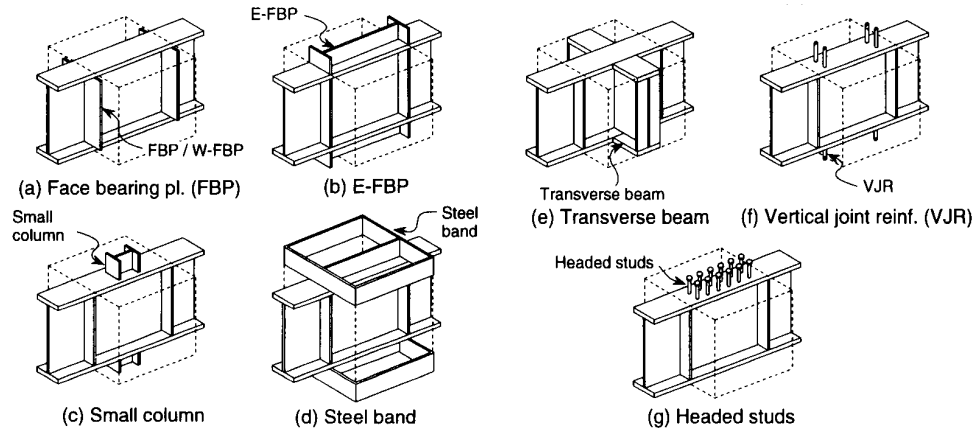

Figure 3.12 – Types d'assemblage RCS traités dans le modèle de Kanno et Deierlein (1996) [22]

Afin d'identifier le comportement des assemblages RCS sous chargement monotone et cyclique, une campagne d'essais sur plusieurs types d'assemblage RCS a été menée à l'Université du Texas [7, 50]. Sur base de cette étude, des règles de dimensionnement pour les assemblages RCS (intérieurs et extérieurs) dans les bâtiments situés dans des zones de sismicité faible à modérée ont été mises au point par "The American Society of Civil Engineers" [44]. Un examen approfondi de ces règles de dimensionnement réalisé par Kanno et Deierlein (1996) [21] a montré que, pour certaines configurations, les résistances calculées étaient non-conservatives. En conséquence, ils ont proposé un modèle de calcul plus rafiné et plus précis pour les assemblages hybrides présentés à la Figure 3.12. Dans leur modèle, les améliorations majeures sont la prise en compte des raideurs et résistances fournies par tous les composants de l'assemblage.

Un nouveau type d'assemblage RCS, composé d'un profil acier soudé à la poutre métallique et totalement noyé dans le poteau béton armé, a récemment été proposé dans le cadre du projet européen RFCS SMARTCOCO (2012-2015). Ce nouvel assemblage, appelé par la suite *assemblage hybride*, est illustré à la Figure 3.13. L'avantage principal de cet assemblage hybride est d'offrir une connexion poteau-poutre assez simple du point de vue constructif. Cependant, aucune règle de dimensionnement existante n'est applicable pour ce type d'assemblage. L'objectif de mes travaux de recherche dans ce thème est de développer une méthode de calcul pour cet assemblage en se basant sur les normes européennes (Eurocodes) et américaines (ACI218, AISC2010) et en réalisant des études expérimentales et numériques.

3.4.2 Étude expérimentale du comportement de l'*assemblage hybride* sous chargements statique et cyclique

Dans le cadre du projet européen RFCS SMARTCOCO (2012-2015), nous avons proposé une méthode de calcul pour estimer la résistance de l'*assemblage hybride* étudié. Cette méthode s'appuie principalement ; d'une part, sur les règles de dimensionnement de l'assemblage métallique de l'Eurocode 3 (pour la transmission des efforts de la poutre au profilé noyé), et d'autre part, sur le mécanisme local de type bielle-tirant dans les assemblages béton armé (pour la transmission des efforts du profil noyé au béton. Le détail de ma méthode peut être trouvée dans [6]. Cette méthode a été ensuite utilisée pour concevoir 4 corps d'épreuve (à l'échelle 1) pour la campagne d'essais sur l'assemblage hybride sous chargement monotone. Cette campagne expérimentale fait partie des tâches

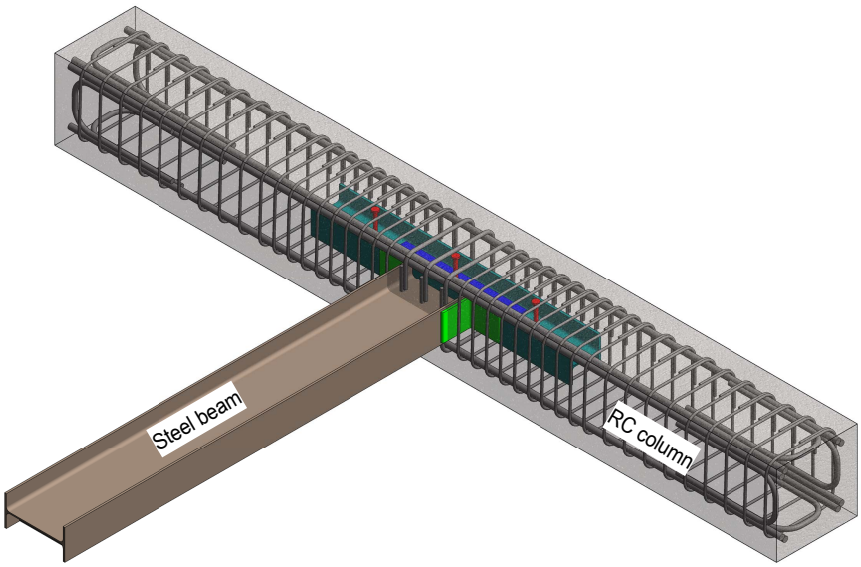

Figure 3.13 – Nouvel assemblage hybride

du Workpakage 7 du SMARTCOCO dont les essais ont eu lieu au laboratoire LGCGM durant le premier trimestre 2016.

Dans le cadre du projet de recherche que j'ai fait avec les chercheurs de l'Université de Transport et de Communications (UTT) de Hanoï, Vietnam, en 2014 nous avons mené une campagne expérimentale avec le même type d'assemblage mais sous chargement cyclique. La Figure 3.14 montre le montage expérimental des essais statiques réalisés à l'INSA de Rennes et des essais cycliques réalisés à l'UTT de Hanoï. L'article ci-dessous, fourni en annexe du présent mémoire, fait la synthèse du travail et des résultats obtenus :

Annexe 13 : Q-H. Nguyen, X.H. Nguyen, D.D Le and O. Mirza. Experimental investigation on seismic response of exterior RCS beam-column connection. *11th International Conference on Advances in Steel Concrete Composite and Hybrid Structures*. Beijing, China, 3-5 December 2015.

3.4.3 Modélisation du comportement de l'*assemblage hybride*

Pour calibrer et valider une méthode de dimensionnement, des recherches à caractère expérimental sont indispensables. Cependant, les essais expérimentaux restent coûteux et de ce fait le nombre d'essais possibles est limité. Par conséquent, en association avec l'approche expérimentale, le recours à la modélisation numérique, notamment avec la méthode des

Figure 3.14 – Essais de l'*assemblage hybride* sous chargement statique et cyclique

éléments finis, est nécessaire. En effet, par rapport à l'expérimentation, la modélisation numérique permet d'apporter des données importantes qui ne peuvent être obtenues par l'expérimentation. Pour cette raison, en parallèle avec l'étude expérimentale du comportement de l'assemblage hybride, une étude numérique a été réalisée. Un modèle élément fini 3D a été développé à l'aide du logiciel Abaqus. Le modèle EF développé a pris en compte plusieurs aspects qui conditionnent le comportement global de l'*assemblage hybride*, à savoir l'interaction partielle entre les profilés métalliques et le béton, le contact entre les composants, le comportement nonlinéaire matériel, notamment le béton. Ce modèle a servi à une étude paramétrique où les principaux paramètres étudiés sont la longueur du profil noyé et la classe de résistance du béton. Les résultats des premières modélisations ont montré que la longueur du profil noyé a une influence majeure sur le comportement d'un tel assemblage. L'article ci-dessous, fourni en annexe du présent mémoire, fait la synthèse des résultats obtenus :

Annexe 14 : Q-H. Nguyen, M. Hjiaj, X.H. Nguyen and D.D Le. Finite Element analysis of a hybrid RCS beam-column connection. *The 3rd International Conference CIGOS 2015 on « Innovations in Construction »*. Paris, France, 11-12 May 2015.

Il est à noter que les travaux de recherche relatifs à cet axe sont en cours avec le démarrage en 2015 de deux thèses de doctorat (Viet Phuong Nguyen et Dang Dung Le) que je co-encadre.

CONCLUSION GÉNÉRALE

Ce mémoire d'Habilitation à Diriger des Recherches est l'occasion de dresser un bilan de ma trajectoire professionnelle et de mes activités de recherche. C'est surtout, au travers d'un exercice de style, l'occasion de faire le tri dans les questionnements qui m'ont accompagné durant ces cinq dernières années et recenser ceux qui me guideront à l'avenir. Ce document a été écrit dans un style didactique, sans jamais trop entrer dans les détails techniques. Une sélection des articles publiés peut être trouvée en annexe, qui permettra aux lecteurs d'avoir accès à ces détails. Je remercie donc ceux qui ont pris le temps de lire ce manuscrit, et j'espère que cette lecture aura été intéressante.

Depuis le début de ma carrière professionnelle, j'évolue dans le domaine de la modélisation expérimentale, théorique et numérique des structures mixtes acier-béton et bois-béton. L'enjeu est à chaque fois le même : conduire une résolution du problème qui permette de disposer de résultats, d'une part suffisamment précis pour qu'ils soient exploitables dans un cas industriel et d'autre part suffisamment originaux pour qu'ils contribuent à la connaissance scientifique du domaine. Mes travaux de recherche se concrétisent par une activité de publications et s'appuient sur des projets de recherche européens et industriels, et des collaborations scientifiques nationales et internationales.

Le co-encadrement de doctorants a toujours fait partie de mes priorités car il est le moyen de partager, de transmettre mes connaissances scientifiques et mon goût pour le monde de la recherche. J'attache une attention particulière non seulement à l'encadrement mais aussi à l'accompagnement des doctorants dans leur projet professionnel. On retrouve cette volonté aussi bien en enseignement, que dans mes responsabilités collectives à l'INSA de Rennes (responsable pédagogique de 3ème et 4ème année). A travers ce mémoire, je pense avoir montré que je réunis les conditions d'autonomie, de maturité, de vision stratégique et de capacité à l'encadrement de jeunes chercheurs pour prétendre passer l'Habilitation à Diriger les Recherches (HDR) et c'est pour cette raison que je propose, par le présent rapport, ma candidature à ce diplôme national.

RÉFÉRENCES

[1] C Adam, R Heuer, and A Jeschko. Flexural vibrations of elastic composite beams with interlayer slip. *Acta Mechanica*, 125(1-4) :17–30, 1997.

[2] A Ayoub and FC Filippou. Mixed formulation of nonlinear steel-concrete composite beam element. *Journal of Structural Engineering-ASCE*, 126(3) :371–381, 2000.

[3] Jean-Marc Battini, Quang-Huy Nguyen, and Mohammed Hjiaj. Non-linear finite element analysis of composite beams with interlayer slips. *Computers & Structures*, 87 :904 – 912, 2009. doi : http://dx.doi.org/10.1016/j.compstruc.2009.04.002.

[4] S Berczyński and T Wróblewski. Vibration of steel-concrete composite beams using the timoshenko beam model. *Journal of vibration and control*, 11(6) :829–848, 2005.

[5] B Cas, M Saje, , and I Planinc. Buckling of layered wood columns. *Advances in Engineering Software*, 38(8-9) :586–597, 2007.

[6] H Degée, T Bogdan, A Plumier, N Popa, L-G Cajot, J-M De Bel, P Mengeot, M Hjiaj, QH Nguyen, H. Somja, A Elghazouli, and D Bompa. Rfcs smartcoco project : Smart composite construction. Technical report, Mid-Term Report, 2013.

[7] G Deierlein, TM Sheikh, JA Yura, and JO Jirsa. Beam-column moment connections for composite frames : Part 2. *Journal of Structural Engineering, ASCE*, 115(11) : 2877–2896, 1989.

[8] Efectis. Rapport d'essai n°11-u-427 concernant un plancher porteur constitué de solives en bois lamellé-collé connectées à une dalle en béton armé. Technical report, EFECTIS GROUPE, 2011.

[9] C Faella, E Martinelli, and E Nigro. Steel and concrete composite beams : "exact" expression of the stiffness matrix and applications. *Computers and Structures*, 80 : 1001–1009, 2002.

[10] Griffis Lawrence G. Some design considerations for composite-frame structures. *Engineering Journal*, 23(2) :59–64, 1986.

[11] N Gattesco. Analytical modelling of nonlinear behaviour of composite beams with deformable connection. *Journal of Constructional Steel Research*, 52, 1999.

[12] UA Girhammar and KA Gopu. Composite beam-column with interlayer slip exact analysis. *Journal of Structural Engineering, ASCE*, 119(4) :2095–2111, 1993.

[13] UA Girhammar and D Pan. Dynamic analysis of composite members with interlayer slip. *International Journal of Solids and Structures*, 30(6) :797–823, 1993.

[14] UA Girhammar and DH Pan. Exact static analysis of partially composite beams and beam-columns. *International Journal of Mechanical Sciences*, 49(2) :239–255, 2007.

[15] UA Girhammar, D Pan, and A Gustafsson. Exact dynamic analysis of composite beams with partial interaction. *International Journal of Mechanical Sciences*, 49, 2007.

[16] Philippe Le Grognec, Quang-Huy Nguyen, and Mohammed Hjiaj. Exact buckling solution for two-layer timoshenko beams with interlayer slip. *International Journal of Solids and Structures*, 49(1) :143 – 150, 2012. doi : http://dx.doi.org/10.1016/j.ijsolstr.2011.09.020.

[17] Philippe Le Grognec, Quang-Huy Nguyen, and Mohammed Hjiaj. Plastic bifurcation analysis of a two-layer shear-deformable beam-column with partial interaction. *International Journal of Non-Linear Mechanics*, 67 :85 – 94, 2014. doi : http://dx.doi.org/10.1016/j.ijnonlinmec.2014.08.010.

[18] M Heinisuo. An exact finite element technique for layered beam. *Computers and Structures*, 30(3) :615–622, 1988.

[19] Mohammed Hjiaj, Jean-Marc Battini, and Quang-Huy Nguyen. Large displacement analysis of shear deformable composite beams with interlayer slips. *International Journal of Non-Linear Mechanics*, 47(8) :895 – 904, 2012. doi : http://dx.doi.org/10.1016/j.ijnonlinmec.2012.05.001.

[20] B Jurkiewiez, S Buzon, and JG Sieffert. Incremental viscoelastic analysis of composite beams with partial interaction. *Computers and Structures*, 83(21-22) :1780–1791, 2005.

[21] R Kanno and G Deierlein. Seismic behavior of composite (rcs) beam-column joint assemblies. *Composite Construction in Steel and Concrete III, ASCE*, pages 236–249, 1996.

[22] R Kanno and G Deierlein. Design model of joints for rcs frames. *Composite Construction in Steel and Concrete IV, ASCE*, pages 947–958, 2000.

[23] Pisey Keo, Mohammed Hjiaj, Quang-Huy Nguyen, and Hugues Somja. Derivation of the exact stiffness matrix of shear-deformable multi-layered beam element in partial interaction. *Finite Elements in Analysis and Design 2016 (in press).*

[24] Pisey Keo, Quang-Huy Nguyen, Hugues Somja, and Mohammed Hjiaj. Geometrically nonlinear analysis of hybrid beam-column with several encased steel profiles in partial interaction. *Engineering Structures*, 100 :66 – 78, 2015. doi : http://dx.doi.org/10.1016/j.engstruct.2015.05.030.

[25] Pisey Keo, Hugues Somja, Quang-Huy Nguyen, and Mohammed Hjiaj. Simplified design method for slender hybrid columns. *Journal of Constructional Steel Research*, 110 :101 – 120, 2015. doi : http://dx.doi.org/10.1016/j.jcsr.2015.03.006.

[26] P Krawczyk and B Rebora. Large deflections of laminated beams with interlayer slips - part 2 : finite element development. *Engineering with Computers*, 24(1) : 33–51, 2007.

[27] A Kryžanowski, S Schnabl, G Turk, and I Planinc. Exact slip-buckling analysis of two-layer composite columns. *International Journal of Solids and Structures*, 46 (14-15) :2929–2938, 2009.

[28] Manuel Manthey. *Comportement des poutres mixtes bois-béton sous sollicitations accidentelles*. Thèse de doctorat, INSA de Rennes, 2015.

[29] Enzo Martinelli, Quang-Huy Nguyen, and Mohammed Hjiaj. Dimensionless formulation and comparative study of analytical models for composite beams in partial interaction. *Journal of Constructional Steel Research*, 75 :21 – 31, 2012. doi : http://dx.doi.org/10.1016/j.jcsr.2012.02.016.

[30] H Murakami. A laminated beam theory with interlayer slip. *Journal of Applied Mechanics*, 51, 1984.

[31] MP Newcombe, WA van Beerschoten, D Carradine, S Pampanin, and AH Buchanan. In-plane experimental testing of timber-concrete composite floor diaphragms. *Journal of structural engineering*, 136(11) :1461–1468, 2010.

[32] MN Newmark, CP Siess, and IM Viest. Tests and analysis of composite beams with incomplete interaction. *Proceedings of Society of Experimental Stress Analysis*, 9(1) : 75–92, 1951.

[33] NF-EN-14080. Structure en bois - bois lamellé collé et bois massif reconstitué - exigences. Technical report, Paris, AFNOR, 2013.

[34] Quang-Huy Nguyen and Mohammed Hjiaj. Nonlinear time-dependent behavior of composite steel-concrete beams. *Journal of Structural Engineering ASCE 2016 (in press)*.

[35] Quang-Huy Nguyen, Van Toan Tran, and Mohammed Hjiaj. Development of design method for composite columns with several encased steel profiles under combined shear and bending. *7th European Conference on Steel and Composite Structures September 10-12, 2014*.

[36] Quang-Huy Nguyen, Mohammed Hjiaj, Brian Uy, and Samy Guezouli. Analysis of composite beams in the hogging moment regions using a mixed finite element formulation. *Journal of Constructional Steel Research*, 65(3) :737 – 748, 2009. doi : http://dx.doi.org/10.1016/j.jcsr.2008.07.026.

[37] Quang-Huy Nguyen, Mohammed Hjiaj, and Jean-Marie Aribert. A space-exact beam element for time-dependent analysis of composite members with discrete shear connection. *Journal of Constructional Steel Research*, 66(11) :1330 – 1338, 2010. doi : http://dx.doi.org/10.1016/j.jcsr.2010.04.007.

[38] Quang-Huy Nguyen, Mohammed Hjiaj, and Brian Uy. Time-dependent analysis of composite beams with continuous shear connection based on a space-exact stiffness matrix. *Engineering Structures*, 32(9) :2902 – 2911, 2010. doi : http://dx.doi.org/10.1016/j.engstruct.2010.05.009.

[39] Quang-Huy Nguyen, Mohammed Hjiaj, and Samy Guezouli. Exact finite element model for shear-deformable two-layer beams with discrete shear connection. *Finite Elements in Analysis and Design*, 47(7) :718 – 727, 2011. doi : http://dx.doi.org/10.1016/j.finel.2011.02.003.

[40] Quang-Huy Nguyen, Enzo Martinelli, and Mohammed Hjiaj. Derivation of the exact stiffness matrix for a two-layer timoshenko beam element with partial interaction.

Engineering Structures, 33(2) :298 – 307, 2011. doi : http://dx.doi.org/10.1016/j.engstruct.2010.10.006.

[41] Quang-Huy Nguyen, Mohammed Hjiaj, and Philippe Le Grognec. Analytical approach for free vibration analysis of two-layer timoshenko beams with interlayer slip. *Journal of Sound and Vibration*, 331(12) :2949 – 2961, 2012. doi : http://dx.doi.org/10.1016/j.jsv.2012.01.034.

[42] Quang-Huy Nguyen, Mohammed Hjiaj, and Van-Anh Lai. Force-based {FE} for large displacement inelastic analysis of two-layer timoshenko beams with interlayer slips. *Finite Elements in Analysis and Design*, 85 :1 – 10, 2014. doi : http://dx.doi.org/10.1016/j.finel.2014.02.007.

[43] Srour Nofal, Hugues Somja, Mohammed Hjiaj, and Quang-Huy Nguyen. Effects of material variability on the ductility of composite beams and overstrength coefficients. *Earthquake Engineering & Structural Dynamics*, 42(7) :953–972, 2013. doi : http://dx.doi.org/10.1002/eqe.2253.

[44] The ASCE Task Committee on Design Criteria for Composite Structures in Steel and Concrete. Guidelines for design of joints between steel beam and reinforced concrete columns. *Journal of Structural Engineering, ASCE*, 120(8) :2330–2357, 1994.

[45] G Ranzi, MA Bradford, and B Uy. Analytical solutions for the time-dependent behaviour of composite beams with partial interactions. *International Journal of Solids and Structures*, 43(13) :3770–3793, 2006.

[46] Z Ranzi and A Zona. A steel-concrete composite beam model with partial interaction including the shear deformability of the steel component. *Engineering Structures*, 29 (11) :3026–41, 2007.

[47] MR Salari and E Spacone. Analysis of steel-concrete composite frames with bond-slip. *Journal of Structural Engineering-ASCE*, 127(11) :1243–1250, 2001.

[48] S Schnabl and I Planinc. The effect of transverse shear deformation on the buckling of two-layer composite columns with interlayer slip. *International Journal of Non-Linear Mechanics*, 46(3) :543–553, 2011.

[49] S Schnabl, M Saje, G Turk, and I Planinc. Analytical solution of two-layer beam taking into account interlayer slip and shear deformation. *Journal of Structural Engineering-ASCE*, 133(6) :886–94, 2007.

[50] TM Sheikh, GG Deierlein, JA Yura, and JO Jirsa. Beam-column moment connections for composite frames : Part 1. *Journal of Structural Engineering, ASCE*, 115(11) : 2858–2876, 1989.

[51] E Spacone and S El-Tawil. Nonlinear analysis of steel-concrete composite structures : state-of-the-art. *Journal of Structural Engineering-ASCE*, 130(2) :1901–1912, 2004.

[52] Van Toan Tran. *Étude numérique et expérimentale des murs en béton armé renforcés par plusieurs profilés métalliques totalement enrobés*. Thèse de doctorat, INSA de Rennes, 2015.

[53] YF Wu, RQ Xu, and WQ Chen. Free vibrations of the partial-interaction composite members with axial force. *Journal of Sound and Vibration*, 299, 2007.

[54] R Xu and Y Wu. Static, dynamic, and buckling analysis of partial interaction composite members using timoshenko's beam theory. *International Journal of Mechanical Sciences*, 49, 2007.

Partie III

Selection des articles publiés

ANNEXE 1

M. Hjiaj, J-M. Battini and **Q-H. Nguyen**. Large displacement analysis of shear deformable composite beams with interlayer slips. *International Journal of Non-Linear Mechanics* 2012 ; 47(8), 895-904. (5-Year IF 1.870) http://dx.doi.org/10.1016/j.ijnonlinmec.2012.05.001.

International Journal of Non-Linear Mechanics 47 (2012) 895–904

Contents lists available at SciVerse ScienceDirect

International Journal of Non-Linear Mechanics

journal homepage: www.elsevier.com/locate/nlm

Large displacement analysis of shear deformable composite beams with interlayer slips

Mohammed Hjiaj [a,*], Jean-Marc Battini [b], Quang Huy Nguyen [a]

[a] Structural Engineering Research Group/LGCGM, INSA de Rennes, 20 avenue des Buttes de Coësmes, CS 70839, 35708 Rennes Cedex 7, France
[b] Department of Civil and Architectural Engineering, KTH, Royal Institute of Technology, SE-10044 Stockholm, Sweden

ARTICLE INFO

Article history:
Received 11 October 2011
Received in revised form
29 April 2012
Accepted 1 May 2012
Available online 16 May 2012

Keywords:
Co-rotational method
Finite elements
Shear deformation
Layered beams
Interlayer slips

ABSTRACT

This paper presents a novel geometric non-linear finite element formulation for the analysis of shear deformable two-layer beams with interlayer slips. We adopt the co-rotational approach where the motion of the element is decomposed into two parts: a rigid body motion which defines a local coordinate system and a small deformational motion of the element relative to this local coordinate system. The main advantage of this approach is that the transformation matrices relating local and global quantities are independent to the choice of the geometrical linear local element. The effect of transverse shear deformation of the layers is taken into account by assuming that each layer behaves as a Timoshenko beam element. The layers are assumed to be continuously connected and partial interaction is considered by considering a continuous relationship between the interface shear flow and the corresponding slip. In order to avoid curvature and shear locking phenomena, the local linear element is formulated using "exact" displacement shape functions derived from the closed-form solution of the governing equations of a two-layer beam element. Finally, three numerical applications are presented in order to assess the performance of the proposed formulation.

1. Introduction

For the last few decades, composite members and structures have been increasingly used in both buildings and bridges. Steel–concrete composite beams and nailed timber members are two of the possible technical solutions based on coupling two layers made out of different materials with the aim of optimizing their mechanical behavior within a unique member. Reinforced concrete is inexpensive, massive and stiff with a poor behavior in tension and a fairly good ability to resist compressive actions. On the other hand, steel members are lightweight, easy to assemble, strong under tensile forces but they have a low buckling resistance. The behavior of composite members depends to a large extend on the type of shear connection. Rigid shear connectors develop full composite action between the layers. Consequently, conventional principles of analysis of composite members can be employed. In most cases, connectors are flexible and relative displacements occur at the interface of the two layers resulting in a so-called partial interaction. Whereas the transverse separation is often small and can be neglected [9], interface slips influence the behavior of two-layer composite beams and must be considered. Two typical examples are steel–concrete beams and nailed timber members. These composite structures with interlayer slips may develop non-linear geometrical and material behavior, even for small deformations. This is especially the case if the composite beam is subjected to both axial and transversal loads or/and to thermomechanical loading (fire).

Several theoretical models, characterized by different levels of approximation, have been proposed for the geometrically linear analysis of elastic composite structures. The first formulation of an elastic theory for composite beams with partial interaction is commonly attributed to Newmark et al. [10]. They adopted the Euler–Bernoulli kinematical hypotheses for both concrete slab and steel profile; and considered a continuous and linear relationship between the relative interface displacements (slips) and the corresponding interface shear stresses. In their paper, a closed-form solution is provided for a simply supported elastic composite beams. Since then, this model was extensively used by many authors to formulate analytical models for the static response of linear elastic [11–15,4,16] as well as linear-viscoelastic [17–21] continuous composite beams with arbitrary support and loading conditions. A key extension of Newmark's model has been proposed in [31–34] by considering more general kinematic assumptions where relative transverse displacement (uplift) is permitted. The most significant advance in the theory of two-layer beams in partial interaction moved recently toward the introduction of shear flexibility of both layers according to the well-known Timoshenko's theory [39]. In [40], the exact expression of the

* Corresponding author.
E-mail address: mohammed.hjiaj@insa-rennes.fr (M. Hjiaj).

0020-7462/$ - see front matter © 2012 Elsevier Ltd. All rights reserved.
http://dx.doi.org/10.1016/j.ijnonlinmec.2012.05.001

stiffness matrix has been developed for the two-layer elastic Timoshenko composite beam with interlayer slip. Besides these analytical works, several numerical models, mostly F.E. formulations, based on the basic assumptions of the Newmark's model have been developed to investigate the inelastic behavior of composite beams with partial interaction (see e.g. [22–26]. A locking-free strain-based formulation for the linear static analysis of two-layer planar beams with interlayer slip has been proposed by Schnabl et al. [8]. The derivation relies on a modification of the principle of virtual work to include constraining equations that remove the displacement field vector from the principle of virtual work. Zona et al. [6] have investigated F.E. formulations for two models derived by coupling, using a shear-deformable connection, an Euler–Bernoulli beam with a Timoshenko beam and two Timoshenko beams. It has been recognized that to avoid both curvature and shear locking, high order polynomials must be used.

In contrast with the large body of the literature devoted to materially non-linear problems, a limited number of contributions dealt with geometric non-linearity. These contributions consider composite beams made of two Euler–Bernouilli layers. Linearized buckling loads have been computed by Girhammar and Gopu [12] using a modified second-order theory for two-layered beams with longitudinal slips. Exact expressions for buckling length coefficients of elastic composite beams with particular boundary conditions have been derived by Girhammar and Pan [16]. A theory for two-layered one-dimensional elastic member including both connector and geometric non-linearities has been presented by Wheat et al. [35]. Pi et al. [36] have proposed a total Lagrangian beam/column element for the fully non-linear analysis of steel–concrete composite beams and columns considering a monolithic element with an additional degree of freedom to the deformed beam axis added in order to describe small interlayer slips. A geometrically non-linear mixed finite element formulation was recently proposed by Tort and Hajjar [37] for the analysis of rectangular concrete-filled steel tube beam-columns including the slip between the steel and concrete components. Their model considers fibre-based distributed plasticity approach and was developed within the co-rotational framework. This approach was also considered by Battini et al. [30] for the development of beam-column element using the exact local elastic stiffness matrix. In Saje et al. [27], a large displacement total Lagrangian formulation for composite beam in partial interaction was developed. Each layer was considered separately and internal constraints are applied, using Lagrange multipliers, to enforce contact between the layers. The formulation by Saje et al. [27] was afterwards applied to the bucking analysis of layered wood columns (see [38]). Krawczyk et al. [28,29] developed a non-linear formulation which borrows concepts of the co-rotational approach. In their formulation, shear locking is eliminated by incorporating an additional hierarchical mode for interpolation of the element transverse displacement and membrane locking is alleviated by using the assumed strain method. More recently, Ranzi et al. [7] have proposed a fully non-linear kinematical model for planar composite beams including longitudinal partial interaction as well as vertical uplift. A reduced formulation, useful for solving practical structural problem, was afterwards derived considering that rotations remain moderate and deformations are small. In the contributions cited above, Bernoulli beam theory is adopted for each layer.

The purpose of this paper is to present a new non-linear finite element formulation for the analysis of shear-deformable two-layer composite planar beams with interlayer slips. A co-rotational description is used, which means that the motion of the element is decomposed into two parts: a rigid body motion which defines a local coordinate system and a small deformational motion of the element relative to this local coordinate system. The geometrical non-linearity induced by the large rigid-body motion is incorporated in the transformation matrices relating local and global internal force vectors and tangent stiffness matrices, whereas the deformational response, captured at the level of the local coordinate system, is assumed small and is modeled using a geometrical linear element. The main advantage of this approach is that the transformation matrices relating local and global quantities are independent to the choice of the geometrical linear local element. This means that for elements with the same number of nodes and degrees of freedom the transformation matrices are the same. A second advantage of this approach is the separation between geometrical and material non-linearities, if any. These two properties are very interesting since different geometrical linear finite element formulations, including or not material non-linearity, can be used as local formulations and automatically transformed into geometrical non-linear formulations.

In the present work, the local formulation is based on the exact solution of the governing equations for shear deformable composite beams with flexible shear connection. As a result, shear and curvature locking encountered in low order polynomial finite elements are both avoided (see [7]). This formulation does not requires an internal node and is therefore consistent with the co-rotational format. The features of the formulation presented in this paper are as follows: (i) longitudinal partial interaction and shear deformation of the layers are considered, providing therefore a general description of the stresses and strains in the layers; (ii) the small strain and large rotations formulation, which is an accurate representation of most structural behavior; (iii) exact local stiffness matrix used, providing accurate and stable results. The present model provides an efficient tool for non-linear buckling analysis of two-layer shear deformable beam with arbitrary support and loading conditions. The main contribution of the present paper is the incorporation of shear deformation of the layers which allows for a more general treatment of composite beams with interlayer slip. This extension adds complexity to the treatment of large displacement of layered beams within a co-rotational formulation. Indeed, the independent shearing of the different layers results in independent cross-section rotation of the layers and so in extra degree of freedom which necessarily modifies the FE formulation itself. The present formulation addresses all these issues and therefore goes beyond that developed in [30] which was restricted to shear-free Bernoulli kinematics.

The organization of the paper is as follows. In Section 2, the local formulation is presented. Section 3 is devoted to the co-rotational framework and the derivation of the transformation matrices. Section 4 addresses issues related to eccentric nodes and forces. Three numerical examples are presented in Section 5 in order to assess the performance of the formulation and support the conclusions in Section 6.

2. Local linear element

During the past recent years, finite element formulations for shear deformable composite beams with deformable shear connection have been proposed [1–3]. It has been recognized that low order displacement-based finite element model exhibit shear and curvature locking, particularly for short element with stiff shear connection. To avoid these problems, shape functions for the generalized displacement must be selected such the inconsistencies in the strain field representation are avoided [1–3]. Ranzi et al. [1–3] have developed several high order beam elements (up to 21 DOF) for both beam model that includes shear deformability of only one layer (EB-T model) as well as beam

model that account for the shear deformability of both layers (T–T model). To avoid locking problems in two nodes beam elements, we employ the exact local stiffness matrix based on the closed-form solution of the governing equations of a two-layer shear deformable beam with interlayer slip (see [40]). It is worth pointing out that this exact stiffness matrix can handle three two-layer beam models according to the beam theory adopted for each layer. To keep the paper self-contained, the main steps of the derivation of the exact local stiffness matrix are recalled in this section.

2.1. Field equations

The present section introduces the field equations describing the mechanical behavior of a shear-deformable two-layer composite beam with partial shear interaction in small displacements. Variables subscripted with *a* refer to the layer *a* and those with *b* are related to the layer *b*. Quantities with subscript *sc* are associated with the interface connection.

2.1.1. Equilibrium

The equilibrium equations are derived by considering a differential element dx located at an arbitrary position x (see Fig. 1).

- Equilibrium equations for layer *a*:

$$\partial_x N_a + D_{sc} = 0 \tag{1}$$

$$\partial_x T_a + V_{sc} = 0 \tag{2}$$

$$\partial_x M_a + T_a - h_a D_{sc} = 0 \tag{3}$$

- Equilibrium equations for layer *b*:

$$\partial_x N_b - D_{sc} = 0 \tag{4}$$

$$\partial_x T_b - V_{sc} + p_y = 0 \tag{5}$$

$$\partial_x M_b + T_b - h_b D_{sc} = 0 \tag{6}$$

where
- $\partial_x^i \bullet = \mathrm{d}^i \bullet / \mathrm{d}x^i$;
- h_i is the distance between the centroid of the layer "i" and the layers interface;
- N_i, T_i, M_i (i=a,b) are the axial forces, the shear forces and bending moments at the centroid of layer "i";
- D_{sc} is the shear bond force per unit length;
- V_{sc} is the uplift force per unit length;
- p_y is the applied external load per unit length.

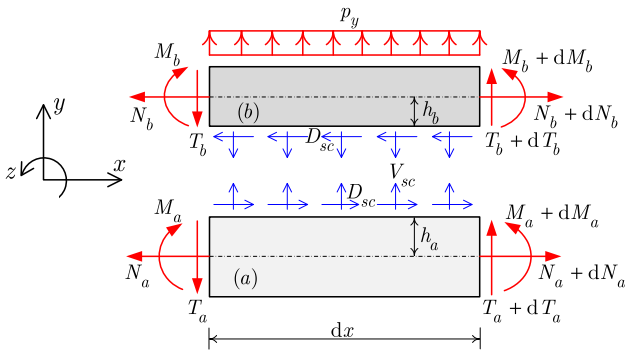

Fig. 1. Free body diagram of an infinitesimal two-layer composite beam segment.

Eqs. (1)–(6) can be written in the following matrix form:

$$\hat{\partial}\boldsymbol{D} + \boldsymbol{V}_{sc} + \boldsymbol{P}_e = \boldsymbol{0} \tag{7}$$

in which

$$\boldsymbol{D} = [N_a \;\; N_b \;\; M_a \;\; M_b \;\; T_a \;\; T_b \;\; D_{sc}]^{\mathrm{T}},$$

$$\boldsymbol{V}_{sc} = [0 \;\; -V_{sc} \;\; 0 \;\; 0 \;\; V_{sc} \;\; 0]^{\mathrm{T}},\ \boldsymbol{P}_e = [0 \;\; 0 \;\; 0 \;\; 0 \;\; p_y \;\; 0]^{\mathrm{T}}$$

and the differential operators $\hat{\partial}$ is given as

$$\hat{\partial} = \begin{bmatrix} \partial_x & 0 & 0 & 0 & 0 & 0 & 1 \\ 0 & \partial_x & 0 & 0 & 0 & 0 & -1 \\ 0 & 0 & \partial_x & 0 & 1 & 0 & -h_a \\ 0 & 0 & 0 & \partial_x & 0 & 1 & -h_b \\ 0 & 0 & 0 & 0 & \partial_x & 0 & 0 \\ 0 & 0 & 0 & 0 & 0 & \partial_x & 0 \end{bmatrix}$$

2.2. Compatibility

The transverse displacement for layers *a* and layer *b* are assumed to be the same. For each layer, the plane sections are supposed to remain plane, but not normal to the neutral axis (Timoshenko's assumption). Consequently, both the layer *a* and layer *b* does not have the same rotation and curvature. Based on the above assumptions, the axial, shear and flexural (curvature) deformations at any section are related to the beam displacements as follows (Fig. 2):

$$\varepsilon_i = \partial_x u_i \tag{8}$$

$$\gamma_i = \partial_x v - \theta_i \tag{9}$$

$$\kappa_i = \partial_x \theta_i \tag{10}$$

where

- i=a,b;
- ε_i and u_i are the axial strain and the longitudinal displacement at the centroid of layer "i", respectively;
- γ_i is the shear strain of layer "i";
- v is the transverse displacement;
- θ_i and κ_i are the cross-section rotation and curvature of layer "i", respectively.

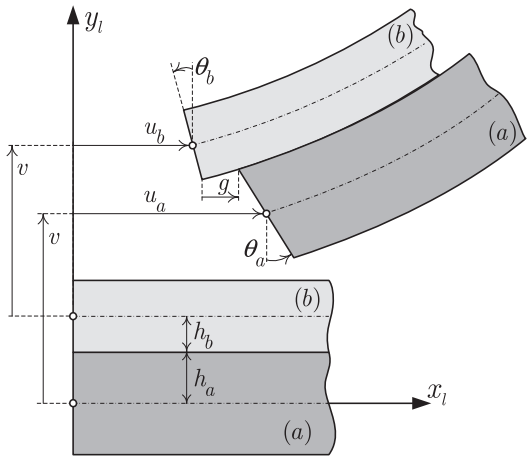

Fig. 2. Kinematics of a shear-deformable two-layer beam with interlayer slip.

The interlayer slip g along the interface can be expressed as follows:

$$g = u_b - u_a + h_a\theta_a + h_b\theta_b \tag{11}$$

Eqs. (8)–(10) can be written in the following matrix form:

$$\boldsymbol{e} = \hat{\partial}^{\mathrm{T}}\boldsymbol{d} \tag{12}$$

in which

$$\boldsymbol{e} = [\varepsilon_a \;\; \varepsilon_b \;\; \kappa_a \;\; \kappa_b \;\; \gamma_a \;\; \gamma_b \;\; g]^{\mathrm{T}}$$

and

$$\boldsymbol{d} = [u_a \;\; u_b \;\; \theta_a \;\; \theta_b \;\; v_a \;\; v_b]^{\mathrm{T}}.$$

2.3. Constitutive relations

The generalized stress–strain relationships for the transverse sections of the two layers are simply obtained by integrating over each cross-section the appropriate uniaxial constitutive model. For a linear elastic material, these relationships lead to the following generalized relationships:

$$N_i = \int_{A_i} \sigma \, \mathrm{d}A = E_i A_i \varepsilon_i \tag{13}$$

$$T_i = \int_{A_i} \tau \, \mathrm{d}A = k_i^s G_i A_i \gamma_i \tag{14}$$

$$M_i = -\int_{A_i} y\sigma \, \mathrm{d}A. \tag{15}$$

where E_i, G_i, A_i and I_i are the elastic modulus, the shear modulus, the area and the second moment of area of the layer "i"; k_i^s is the shear stiffness factor that depends on the cross-sectional shape of layer "i". The above relations must be completed by the relationship between the shear bond force D_{sc} and the interlayer slip g

$$D_{sc} = k_{sc} g \tag{16}$$

where k_{sc} is the shear bond stiffness.

The constitutive relations can be expressed in matrix form as follows:

$$\mathbf{D} = \mathbf{k}\mathbf{e} \tag{17}$$

where

$$\mathbf{k} = \begin{bmatrix} E_aA_a & 0 & 0 & 0 & 0 & 0 & 0 \\ 0 & E_bA_b & 0 & 0 & 0 & 0 & 0 \\ 0 & 0 & E_aI_a & 0 & 0 & 0 & 0 \\ 0 & 0 & 0 & E_bI_b & 0 & 0 & 0 \\ 0 & 0 & 0 & 0 & k_a^sG_aA_a & & 0 \\ 0 & 0 & 0 & 0 & 0 & k_b^sG_bA_b & 0 \\ 0 & 0 & 0 & 0 & 0 & 0 & k_{sc} \end{bmatrix} \tag{18}$$

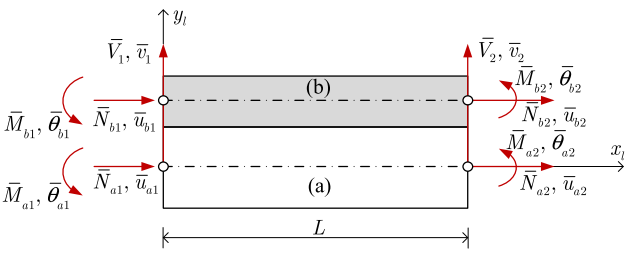

Fig. 3. Nodal forces and displacements of a composite beam element.

2.3.1. The exact stiffness matrix

The field equations (7) and (12) and the constitutive relationships ((13)–(15)) are now combined together into a single fifth-order differential equation relating the longitudinal shear stress (shear bond force) D_{sc} to the external loading p_y

$$\frac{EI}{k_{sc}GA}\partial_x^5 D_{sc} - \left(\frac{EI}{GA}\beta^2 + \frac{1}{k_{sc}}\right)\partial_x^3 D_{sc} + \mu^2 \partial_x D_{sc} = \frac{hp_y}{E_aI_a + E_bI_b} \tag{19}$$

with

- $h = h_a + h_b$,
- $\dfrac{1}{EI} = \dfrac{1}{E_aI_a} + \dfrac{1}{E_bI_b}$,
- $\dfrac{1}{GA} = \dfrac{1}{k_a^sG_aA_a} + \dfrac{1}{k_b^sG_bA_b}$,
- $\alpha = \dfrac{h_a}{E_aI_a} - \dfrac{h_b}{E_bI_b}$,
- $\beta^2 = \dfrac{1}{EA} + \dfrac{h_a^2}{E_aI_a} + \dfrac{h_b^2}{E_bI_b}$,
- $\mu^2 = \beta^2 - EI\,\alpha^2$.

The differential equation (19) involves a single unknown variable: the shear bond force distribution $D_{sc}(x)$. By taking the limit $GA \to \infty$, which corresponds to the Euler–Bernoulli assumption for both layers, Eq. (19) reduces to the governing equation of the Newmark's model [10]

$$\partial_x^3 D_{sc} - k_{sc}\mu^2 \partial_x D_{sc} = \frac{hk_{sc}p_y}{E_aI_a + E_bI_b}$$

It worth mentioning that Eq. (19) describes also the behavior of two-layer beams where one of the layers obeys the Bernoulli kinematic assumptions. The solution of the fifth-order differential Eq. (19) can be expressed as

$$D_{sc} = C_1 e^{\lambda_1 x} + C_2 e^{-\lambda_1 x} + C_3 e^{\lambda_2 x} + C_4 e^{-\lambda_2 x} + C_5 + D_{sc}^0 \tag{20}$$

in which C_i (i=1,5) are constants of integration and

$$D_{sc}^0 = -\frac{hp_y}{\mu^2(E_aI_a + E_bI_b)}x \tag{21}$$

is a particular solution, corresponding to the case of uniformly distributed transverse load p_y. By back substituting the above expression into the field equations, the analytical expression for all variables can be obtain in terms of 10 constants of integration. These constants are determined in terms of nodal displacements using kinematic boundary conditions (Fig. 3) (Details are given in [40]). Finally, the displacement field can be expressed in term of the nodal displacements $\mathbf{p}_l$ and the particular solution as follows:

$$u_a(x) = \mathbf{a}_{u_a}(x)\mathbf{p}_l + u_a^0(x) \tag{22}$$

$$u_b(x) = \mathbf{a}_{u_b}(x)\mathbf{p}_l + u_b^0(x) \tag{23}$$

$$v(x) = \mathbf{a}_v(x)\mathbf{p}_l + v^0(x) \tag{24}$$

$$\theta_a(x) = \mathbf{a}_{\theta_a}(x)\mathbf{p}_l + \theta_a^0(x) \tag{25}$$

$$\theta_b(x) = \mathbf{a}_{\theta_b}(x)\mathbf{p}_l + \theta_b^0(x) \tag{26}$$

$$g(x) = \mathbf{a}_g(x)\mathbf{p}_l + g^0(x) \tag{27}$$

where

$$\mathbf{p}_l = [\bar{u}_{a1} \;\; \bar{u}_{b1} \;\; \bar{v}_1 \;\; \bar{\theta}_{a1} \;\; \bar{\theta}_{b1} \;\; \bar{u}_{a2} \;\; \bar{u}_{b2} \;\; \bar{v}_2 \;\; \bar{\theta}_{a2} \;\; \bar{\theta}_{b2}]^{\mathrm{T}} \tag{28}$$

and $\mathbf{a}_{u_a}(x)$, $\mathbf{a}_{u_b}(x)$, $\mathbf{a}_{\theta_a}(x)$, $\mathbf{a}_{\theta_b}(x)$ and $\mathbf{a}_v(x)$ are the "exact" displacement interpolation functions derived from the analytical solution of the governing equations. The superimposed dash used for the

components of the displacement vector $\mathbf{p}_l$ indicates that these quantities pertain to the local coordinate system (see Section 3). Having at hand the "exact" displacement interpolation functions, the exact expression for the stiffness matrix can be obtained by using the principle of virtual displacements

$$\int_0^L \delta\mathbf{e}^{\mathrm{T}}\mathbf{D}\,\mathrm{d}x = \delta\mathbf{p}_l^{\mathrm{T}}\mathbf{f}_l + \int_0^L \delta v\, p_y\,\mathrm{d}x \tag{29}$$

where $\delta\mathbf{e}$ is "virtual" strain field deduced from the virtual displacements; $\mathbf{D}$ is the associated internal force vector; $\mathbf{f}_l$ is nodal force vector.

The substitution of Eqs. (17) and (22)–(27) in Eq. (29) and the fact that the latter must hold for arbitrary $\delta\mathbf{p}_l$ leads to

$$\mathbf{K}_l\mathbf{p}_l = \mathbf{f}_l + \mathbf{f}_l^0 \tag{30}$$

where

$$\mathbf{K}_l = \int_0^L \left(\hat{\partial}^{\mathrm{T}} \begin{bmatrix} \mathbf{a}_{u_a}(x) \\ \mathbf{a}_{u_b}(x) \\ \mathbf{a}_{\theta_a}(x) \\ \mathbf{a}_{\theta_b}(x) \\ \mathbf{a}_v(x) \\ \mathbf{a}_v(x) \\ \mathbf{a}_g(x) \end{bmatrix}\right)^{\mathrm{T}} \mathbf{k} \left(\hat{\partial}^{\mathrm{T}} \begin{bmatrix} \mathbf{a}_{u_a}(x) \\ \mathbf{a}_{u_b}(x) \\ \mathbf{a}_{\theta_a}(x) \\ \mathbf{a}_{\theta_b}(x) \\ \mathbf{a}_v(x) \\ \mathbf{a}_v(x) \\ \mathbf{a}_g(x) \end{bmatrix}\right) \mathrm{d}x \quad \text{and } \mathbf{f}_l^0 = \int_0^L \mathbf{a}_v^{\mathrm{T}}(x) p_y\,\mathrm{d}x \tag{31}$$

is the exact stiffness matrix. In this paper, internal loading is not considered and therefore $\mathbf{f}_l^0 = \mathbf{0}$.

3. Co-rotational framework

The two-layered beam is allowed to have arbitrarily large displacements and rotations at the global level but strains remain small. As with any co-rotational formulation three ingredients are required. They are (i) the choice of a local co-rotating frame, (ii) the relations between global and local variables, and (iii) a variationally consistent internal force vector and tangent stiffness matrix.

3.1. Beam kinematics

The idea of the co-rotational approach is to decompose the motion of the element into rigid body and pure deformational parts, through the use of a local coordinate system (x_l,y_l) which continuously rotates and translates with the element, see Figs. 4 and 5. The origin of the local coordinate system is taken at node a_1 and the x_l-axis of the local coordinate system is defined by the line connected the nodes a_1 and a_2. The y_l-axis is perpendicular to the x_l-axis so that the result is right handed orthogonal coordinate system. The motion of the element

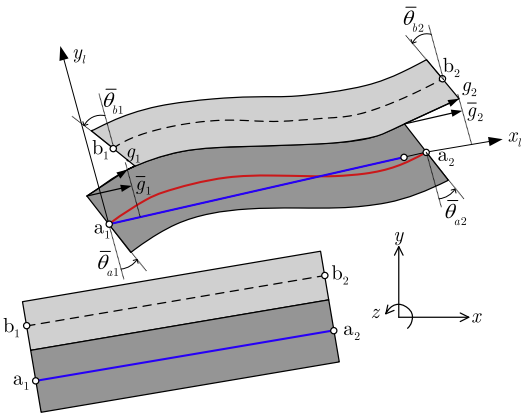

Fig. 4. Co-rotational kinematics: slips.

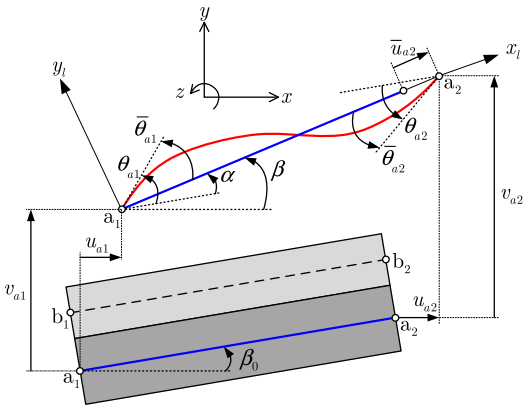

Fig. 5. Co-rotational kinematics: displacements and rotations.

from the original undeformed configuration to the actual deformed one can thus be separated in two parts. The first one, which corresponds to the rigid motion of the local frame, is described by the translation of the node a_1 and the rigid rotation α of the axes. The deformational part of the motion is always small relative to the local co-ordinate system and a geometrical linear element, as the one defined in Section 2, can then be reused. The co-rotational method for 2D beams is known for many years. However, when considering composite beams with interlayer slips, it is necessary to select pertinent kinematical local and global variables. This requires the reformulation of local stiffness matrix and the derivation of appropriate transformation matrices.

The notations used in this section are defined in Figs. 4 and 5. The coordinates of the nodes a_1 and a_2 in the global coordinate system (x,y) are (x_{a1},y_{a1}) and (x_{a2},y_{a2}). As mentioned before, the element has 10 degrees of freedom and the following variables have been selected to describe the motion of the composite member: the global displacements and rotations of the nodes a_1 and a_2, the global rotations of the nodes b_1 and b_2 and the slips g_1,g_2 between the two beams at the two end nodes. Relations between global and local variables are necessary to calculate deformations and establish the relation between local and global forces. The vector of global displacements is defined by

$$\mathbf{p}_g = [u_{a1}\ \ v_{a1}\ \ \theta_{a1}\ \ \theta_{b1}\ \ g_1\ \ u_{a2}\ \ v_{a2}\ \ \theta_{a2}\ \ \theta_{b2}\ \ g_2]^{\mathrm{T}} \tag{32}$$

The global slips g_1,g_2 are defined as perpendicular to the average end cross-section rotations defined by

$$\theta_i = \frac{\theta_{ai}+\theta_{bi}}{2}, \quad i = 1,2 \tag{33}$$

The co-rotating frame rotates with each element as the structure deforms. The current angle α of the co-rotating frame (rigid body rotation) with respect to the global coordinate system is obtained using

$$\sin\alpha = c_o s - s_o c \tag{34}$$

$$\cos\alpha = c_o c + s_o s \tag{35}$$

with

$$c_o = \cos\beta_o = \frac{1}{l_o}(x_{a2}-x_{a1}) \tag{36}$$

$$s_o = \sin\beta_o = \frac{1}{l_o}(y_{a2}-y_{a1}) \tag{37}$$

$$c = \cos\beta = \frac{1}{l_n}(x_{a2}+u_{a2}-x_{a1}-u_{a1}) \tag{38}$$

$$s = \sin\beta = \frac{1}{l_n}(y_{a2}+v_{a2}-y_{a1}-v_{a1}) \tag{39}$$

and

$$l_o = [(x_{a2}-x_{a1})^2+(y_{a2}-y_{a1})^2]^{1/2} \tag{40}$$

$$l_n = [(x_{a2}+u_{a2}-x_{a1}-u_{a1})^2+(y_{a2}+v_{a2}-y_{a1}-v_{a1})^2]^{1/2} \tag{41}$$

The components of $\mathbf{p}_l$ are computed according to

$$\overline{u}_{a1} = 0 \tag{42}$$

$$\overline{v}_1 = 0 \tag{43}$$

$$\overline{v}_2 = 0 \tag{44}$$

$$\overline{u}_{a2} = l_n - l_o \tag{45}$$

$$\overline{\theta}_{a1} = \theta_{a1} - \alpha \tag{46}$$

$$\overline{\theta}_{b1} = \theta_{b1} - \alpha \tag{47}$$

$$\overline{\theta}_{a2} = \theta_{a2} - \alpha \tag{48}$$

$$\overline{\theta}_{b2} = \theta_{b2} - \alpha \tag{49}$$

$$\overline{u}_{b1} = \overline{g}_1 - h_a\,\overline{\theta}_{a1} - h_b\,\overline{\theta}_{b1} \tag{50}$$

$$\overline{u}_{b2} = \overline{g}_2 + \overline{u}_{a2} - h_a\,\overline{\theta}_{a2} - h_b\,\overline{\theta}_{b2} \tag{51}$$

where local slips $\overline{g}_1$ and $\overline{g}_2$ defined by (see Eq. (9))

$$\overline{g}_i = \overline{u}_{bi} - \overline{u}_{ai} + h_a\,\overline{\theta}_{ai} + h_b\,\overline{\theta}_{bi}, \quad i = 1,2 \tag{52}$$

are calculated using (see Eq. (33))

$$\overline{g}_i = g_i \cos\overline{\theta}_i, \quad \overline{\theta}_i = \frac{\overline{\theta}_{ai}+\overline{\theta}_{bi}}{2}, \quad i = 1,2 \tag{53}$$

3.2. Element formulation

Once the local displacements have been calculated using Eqs. (42)–(53), the local internal force vector $\mathbf{f}_l$ and the local tangent stiffness matrix $\mathbf{K}_l$ can be computed using the linear element defined in Section 2. Then, the global internal force vector $\mathbf{f}_g$ and the global tangent stiffness matrix $\mathbf{K}_g$, consistent with $\mathbf{p}_g$, are obtained using a change of variables, performed in three steps, between the global quantities and the local ones. The idea is the following one: let us consider that the internal force vector $\mathbf{f}_i$ and tangent stiffness matrix $\mathbf{K}_i$ are consistent with the displacement vector $\mathbf{p}_i$ such as

$$\delta\mathbf{f}_i = \mathbf{K}_i\delta\mathbf{p}_i \tag{54}$$

and that $\mathbf{p}_i$ is related to another displacement vector $\mathbf{p}_j$ through

$$\delta\mathbf{p}_i = \mathbf{B}_{ij}\delta\mathbf{p}_j \tag{55}$$

Then, by equating the virtual work in the two systems, the internal force vector $\mathbf{f}_j$ consistent with $\mathbf{p}_j$ is defined by

$$\delta\mathbf{p}_j^{\mathrm{T}}\mathbf{f}_j = \delta\mathbf{p}_i^{\mathrm{T}}\mathbf{f}_i \tag{56}$$

which, using Eq. (55), gives

$$\mathbf{f}_j = \mathbf{B}_{ij}^{\mathrm{T}}\mathbf{f}_i \tag{57}$$

The expression of the tangent stiffness matrix $\mathbf{K}_j$, consistent with $\mathbf{p}_j$ is obtained by differentiation of Eq. (57) and by introducing Eq. (54). It is obtained

$$\mathbf{K}_j = \mathbf{B}_{ij}^{\mathrm{T}}\mathbf{K}_i\mathbf{B}_{ij} + \mathbf{H}_{ij}, \quad \mathbf{H}_{ij} = \left.\frac{\partial(\mathbf{B}_{ij}^{\mathrm{T}}\mathbf{f}_i)}{\partial\mathbf{p}_j}\right|_{\mathbf{f}_i} \tag{58}$$

The element formulation is obtained using the following three successive change of variables:

$$\mathbf{f}_l\mathbf{K}_l \rightarrow \mathbf{f}_e\mathbf{K}_e \rightarrow \mathbf{f}_a\mathbf{K}_a \rightarrow \mathbf{f}_g\mathbf{K}_g$$

The different internal force vectors and tangent stiffness matrices are consistent with the following displacement vectors:

$$\mathbf{p}_l = [\overline{u}_{a1}\ \overline{u}_{b1}\ \overline{v}_1\ \overline{\theta}_{a1}\ \overline{\theta}_{b1}\ \overline{u}_{a2}\ \overline{u}_{b2}\ \overline{v}_2\ \overline{\theta}_{a2}\ \overline{\theta}_{b2}]^{\mathrm{T}} \tag{59}$$

$$\mathbf{p}_e = [\overline{u}_{a2}\ \overline{\theta}_{a1}\ \overline{\theta}_{b1}\ \overline{\theta}_{a2}\ \overline{\theta}_{b2}\ \overline{g}_1\ \overline{g}_2]^{\mathrm{T}} \tag{60}$$

$$\mathbf{p}_a = [\overline{u}_{a2}\ \overline{\theta}_{a1}\ \overline{\theta}_{b1}\ \overline{\theta}_{a2}\ \overline{\theta}_{b2}\ g_1\ g_2]^{\mathrm{T}} \tag{61}$$

$$\mathbf{p}_g = [u_{a1}\ v_{a1}\ \theta_{a1}\ \theta_{b1}\ g_1\ u_{a2}\ v_{a2}\ \theta_{a2}\ \theta_{b2}\ g_2]^{\mathrm{T}} \tag{62}$$

The first change of variables between $\mathbf{p}_l$ and $\mathbf{p}_e$ is based on the linear equations (42)–(44), (50) and (51). Then, the transformation matrices giving $\mathbf{f}_e$ and $\mathbf{K}_e$ as a function of $\mathbf{f}_l$ and $\mathbf{K}_l$ are easily obtained as

$$\mathbf{H}_{le} = \mathbf{0} \tag{63}$$

$$\mathbf{B}_{le} = \begin{bmatrix} 0 & 0 & 0 & 0 & 0 & 0 & 0 \\ 0 & -h_a & -h_b & 0 & 0 & 1 & 0 \\ 0 & 0 & 0 & 0 & 0 & 0 & 0 \\ 0 & 1 & 0 & 0 & 0 & 0 & 0 \\ 0 & 0 & 1 & 0 & 0 & 0 & 0 \\ 1 & 0 & 0 & 0 & 0 & 0 & 0 \\ 1 & 0 & 0 & -h_a & -h_b & 0 & 1 \\ 0 & 0 & 0 & 0 & 0 & 0 & 0 \\ 0 & 0 & 0 & 1 & 0 & 0 & 0 \\ 0 & 0 & 0 & 0 & 1 & 0 & 0 \end{bmatrix} \tag{64}$$

For the second change of variables between $\mathbf{p}_e$ and $\mathbf{p}_a$, the transformation matrices giving $\mathbf{f}_a$ and $\mathbf{K}_a$ as a function of $\mathbf{f}_e$ and $\mathbf{K}_e$ can be obtained using Eq. (53) as

$$\mathbf{B}_{ea} = \begin{bmatrix} 1 & 0 & 0 & 0 & 0 & 0 & 0 \\ 0 & 1 & 0 & 0 & 0 & 0 & 0 \\ 0 & 0 & 1 & 0 & 0 & 0 & 0 \\ 0 & 0 & 0 & 1 & 0 & 0 & 0 \\ 0 & 0 & 0 & 0 & 1 & 0 & 0 \\ 0 & -\frac{g_1}{2}\sin\overline{\theta}_1 & -\frac{g_1}{2}\sin\overline{\theta}_1 & 0 & 0 & \cos\overline{\theta}_1 & 0 \\ 0 & 0 & 0 & -\frac{g_2}{2}\sin\overline{\theta}_2 & -\frac{g_2}{2}\sin\overline{\theta}_2 & 0 & \cos\overline{\theta}_2 \end{bmatrix} \tag{65}$$

and

$$\mathbf{H}_{ea} = \mathbf{H}_{ea1}f_e(6) + \mathbf{H}_{ea2}f_e(7) \tag{66}$$

with

$$\mathbf{f}_e = [f_e(1)f_e(2)f_e(3)f_e(4)f_e(5)f_e(6)f_e(7)]^{\mathrm{T}} \tag{67}$$

$$\mathbf{H}_{ea1} = \begin{bmatrix} 0 & 0 & 0 & 0 & 0 & 0 & 0 \\ 0 & -\frac{g_1}{4}\cos\overline{\theta}_1 & -\frac{g_1}{4}\cos\overline{\theta}_1 & 0 & 0 & -\frac{1}{2}\sin\overline{\theta}_1 & 0 \\ 0 & -\frac{g_1}{4}\cos\overline{\theta}_1 & -\frac{g_1}{4}\cos\overline{\theta}_1 & 0 & 0 & -\frac{1}{2}\sin\overline{\theta}_1 & 0 \\ 0 & 0 & 0 & 0 & 0 & 0 & 0 \\ 0 & 0 & 0 & 0 & 0 & 0 & 0 \\ 0 & -\frac{1}{2}\sin\overline{\theta}_1 & -\frac{1}{2}\sin\overline{\theta}_1 & 0 & 0 & 0 & 0 \\ 0 & 0 & 0 & 0 & 0 & 0 & 0 \end{bmatrix} \tag{68}$$

and

$$\mathbf{H}_{ea2}=\begin{bmatrix} 0 & 0 & 0 & 0 & 0 & 0 & 0 \\ 0 & 0 & 0 & 0 & 0 & 0 & 0 \\ 0 & 0 & 0 & 0 & 0 & 0 & 0 \\ 0 & 0 & 0 & -\frac{g_2}{4}\cos\overline{\theta}_2 & -\frac{g_2}{4}\cos\overline{\theta}_2 & 0 & -\frac{1}{2}\sin\overline{\theta}_2 \\ 0 & 0 & 0 & -\frac{g_2}{4}\cos\overline{\theta}_2 & -\frac{g_2}{4}\cos\overline{\theta}_2 & 0 & -\frac{1}{2}\sin\overline{\theta}_2 \\ 0 & 0 & 0 & 0 & 0 & 0 & 0 \\ 0 & 0 & 0 & -\frac{1}{2}\sin\overline{\theta}_2 & -\frac{1}{2}\sin\overline{\theta}_2 & 0 & 0 \end{bmatrix} \tag{69}$$

The third change of variables is from $\mathbf{p}_a$ to $\mathbf{p}_g$ and is performed using Eqs. (45)–(49). After some algebraic manipulations (see e.g. [5]), the transformation matrices giving $\mathbf{f}_g$ and $\mathbf{K}_g$ as a function of $\mathbf{f}_a$ and $\mathbf{K}_a$ are obtained as

$$\mathbf{B}_{ag}=\begin{bmatrix} -c & -s & 0 & 0 & 0 & c & s & 0 & 0 & 0 \\ -s/l_n & c/l_n & 1 & 0 & 0 & s/l_n & -c/l_n & 0 & 0 & 0 \\ -s/l_n & c/l_n & 0 & 1 & 0 & s/l_n & -c/l_n & 0 & 0 & 0 \\ -s/l_n & c/l_n & 0 & 0 & 0 & s/l_n & -c/l_n & 1 & 0 & 0 \\ -s/l_n & c/l_n & 0 & 0 & 0 & s/l_n & -c/l_n & 0 & 1 & 0 \\ 0 & 0 & 0 & 0 & 1 & 0 & 0 & 0 & 0 & 0 \\ 0 & 0 & 0 & 0 & 0 & 0 & 0 & 0 & 0 & 1 \end{bmatrix} \tag{70}$$

and

$$\mathbf{H}_{ag}=\frac{\mathbf{z}\mathbf{z}^{\mathrm{T}}}{l_n}f_a(1)+\frac{1}{l_n^2}(\mathbf{r}\mathbf{z}^{\mathrm{T}}+\mathbf{z}\mathbf{r}^{\mathrm{T}})(f_a(2)+f_a(3)+f_a(4)+f_a(5)) \tag{71}$$

with

$$\mathbf{r}=[-c\ \ -s\ \ 0\ \ 0\ \ 0\ \ c\ \ s\ \ 0\ \ 0\ \ 0]^{\mathrm{T}} \tag{72}$$

$$\mathbf{z}=[s\ \ -c\ \ 0\ \ 0\ \ 0\ \ -s\ \ c\ \ 0\ \ 0\ \ 0]^{\mathrm{T}} \tag{73}$$

and c, s defined in Eqs. (38) and (39).

4. Eccentric nodes and forces

Due to the choice of the interface slips at the end cross-sections as degrees of freedom, see Eq. (32), the boundary conditions require a special treatment. This is particularly the case if external loads are applied at the end section of the upper beam. The case developed in this section presents both an eccentric node and two eccentric forces. This case, see Fig. 6, will be used in the numerical applications in Section 5. All possible cases of eccentric nodes and forces can be dealt in the similar way and the present formulation is thus very general.

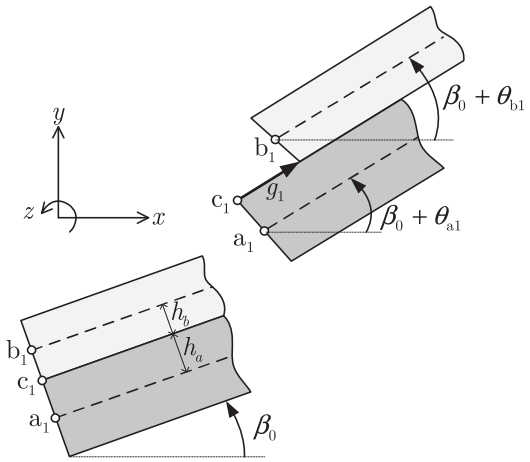

Fig. 6. Eccentric nodes and forces.

4.1. Eccentric nodes

Let us first consider, see Fig. 6, that prescribed displacement or rotation are applied at node c1. This situation requires a rigid link between the nodes a1 and c1 and a change of degrees of freedom from $\mathbf{p}_g$ to $\mathbf{p}_c$ with

$$\mathbf{p}_g=[u_{\mathrm{a1}}\ \ v_{\mathrm{a1}}\ \ \theta_{\mathrm{a1}}\ \ \theta_{\mathrm{b1}}\ \ g_1\ \ u_{\mathrm{a2}}\ \ v_{\mathrm{a2}}\ \ \theta_{\mathrm{a2}}\ \ \theta_{\mathrm{b2}}\ \ g_2]^{\mathrm{T}} \tag{74}$$

$$\mathbf{p}_c=[u_{\mathrm{c1}}\ \ v_{\mathrm{c1}}\ \ \theta_{\mathrm{a1}}\ \ \theta_{\mathrm{b1}}\ \ g_1\ \ u_{\mathrm{a2}}\ \ v_{\mathrm{a2}}\ \ \theta_{\mathrm{a2}}\ \ \theta_{\mathrm{b2}}\ \ g_2]^{\mathrm{T}} \tag{75}$$

The position of the node c1 in the deformed configuration is given by

$$u_{\mathrm{c1}}+x_{\mathrm{c1}}=u_{\mathrm{a1}}+x_{\mathrm{a1}}-h_{\mathrm{a}}\sin(\beta_o+\theta_{\mathrm{a1}}) \tag{76}$$

$$v_{\mathrm{c1}}+y_{\mathrm{c1}}=v_{\mathrm{a1}}+y_{\mathrm{a1}}+h_{\mathrm{a}}\cos(\beta_o+\theta_{\mathrm{a1}}) \tag{77}$$

which, after differentiation, gives

$$\begin{bmatrix}\delta u_{\mathrm{c1}}\\ \delta v_{\mathrm{c1}}\end{bmatrix}=\begin{bmatrix}\delta u_{\mathrm{a1}}\\ \delta v_{\mathrm{a1}}\end{bmatrix}-\begin{bmatrix}\cos(\beta_o+\theta_{\mathrm{a1}})\\ \sin(\beta_o+\theta_{\mathrm{a1}})\end{bmatrix}h_{\mathrm{a}}\delta\theta_{\mathrm{a1}} \tag{78}$$

The internal force vector and tangent stiffness matrix consistent with $\mathbf{p}_c$ are then obtained, see Section 3.2, using the transformation matrix $\mathbf{B}_{gc}$. This gives

$$\delta\mathbf{p}_g=\mathbf{B}_{gc}\delta\mathbf{p}_c,\quad \mathbf{f}_c=\mathbf{B}_{gc}^{\mathrm{T}}\mathbf{f}_g\ \ \mathbf{K}_c=\mathbf{B}_{gc}^{\mathrm{T}}\mathbf{K}_g\mathbf{B}_{gc}+\mathbf{H}_{gc} \tag{79}$$

with

$$\mathbf{B}_{gc}=\begin{bmatrix} 1 & 0 & \cos(\beta_o+\theta_{\mathrm{a1}})h_{\mathrm{a}} & 0 & 0 & 0 & 0 & 0 & 0 & 0 \\ 0 & 1 & \sin(\beta_o+\theta_{\mathrm{a1}})h_{\mathrm{a}} & 0 & 0 & 0 & 0 & 0 & 0 & 0 \\ 0 & 0 & 1 & 0 & 0 & 0 & 0 & 0 & 0 & 0 \\ 0 & 0 & 0 & 1 & 0 & 0 & 0 & 0 & 0 & 0 \\ 0 & 0 & 0 & 0 & 1 & 0 & 0 & 0 & 0 & 0 \\ 0 & 0 & 0 & 0 & 0 & 1 & 0 & 0 & 0 & 0 \\ 0 & 0 & 0 & 0 & 0 & 0 & 1 & 0 & 0 & 0 \\ 0 & 0 & 0 & 0 & 0 & 0 & 0 & 1 & 0 & 0 \\ 0 & 0 & 0 & 0 & 0 & 0 & 0 & 0 & 1 & 0 \\ 0 & 0 & 0 & 0 & 0 & 0 & 0 & 0 & 0 & 1 \end{bmatrix} \tag{80}$$

and the only non-zero term in the matrix $\mathbf{H}_{gc}$ is

$$\mathbf{H}_{gc(3,3)}=-\sin(\beta_o+\theta_{\mathrm{a1}})h_{\mathrm{a}}f_g(1)+\cos(\beta_o+\theta_{\mathrm{a1}})h_{\mathrm{a}}f_g(2) \tag{81}$$

4.2. Eccentric forces

Let us now consider, that, in the same problem, two external force vectors $\mathbf{f}_{a1}$ and $\mathbf{f}_{b1}$ defined by

$$\mathbf{f}_{a1}=[f_{a1}(1)\ f_{a1}(2)\ f_{a1}(3)]^{\mathrm{T}}\quad \mathbf{f}_{b1}=[f_{b1}(1)\ f_{b1}(2)\ f_{b1}(3)]^{\mathrm{T}} \tag{82}$$

are applied at the nodes a1 and b1. $f_{a1}(1)$,$f_{b1}(1)$ are horizontal forces, $f_{a1}(2)$,$f_{b1}(2)$ are vertical forces and $f_{a1}(3)$,$f_{b1}(3)$ are moments. These loads require a special treatment since the degrees of freedom of the element are $\mathbf{p}_c$, see Eq. (75). The idea is to calculate the loads applied at node c1 which perform the same external virtual work.

For the load $\mathbf{f}_{a1}$, it gives

$$[\delta u_{\mathrm{c1}}\ \ \delta v_{\mathrm{c1}}\ \ \delta\theta_{\mathrm{a1}}]\ \mathbf{f}_{c1}=[\delta u_{\mathrm{a1}}\ \ \delta v_{\mathrm{a1}}\ \ \delta\theta_{\mathrm{a1}}]\mathbf{f}_{a1} \tag{83}$$

Using Eq. (78), it is obtained

$$\mathbf{f}_{c1}=\begin{bmatrix} 1 & 0 & 0 \\ 0 & 1 & 0 \\ \cos(\beta_o+\theta_{\mathrm{a1}})h_{\mathrm{a}} & \sin(\beta_o+\theta_{\mathrm{a1}})h_{\mathrm{a}} & 1 \end{bmatrix}\mathbf{f}_{a1} \tag{84}$$

Differentiation of Eq. (84) gives the stiffness correction term $\mathbf{K}_{sc}$ associated to $[u_{c1}\ v_{c1}\ \theta_{a1}]$, which must be subtracted from the tangent stiffness matrix of the structure, as

$$\mathbf{K}_{sc}=\begin{bmatrix}0&0&0\\0&0&0\\0&0&A\end{bmatrix},\quad A=-\sin(\beta_o+\theta_{a1})h_a f_{a1}(1)+\cos(\beta_o+\theta_{a1})h_a f_{a1}(2) \tag{85}$$

For the load $\mathbf{f}_{b1}$, the calculations are a little bit more complicated since the slip g_1 is involved. The external virtual work equation is

$$[\delta u_{c1}\ \ \delta v_{c1}\ \ \delta\theta_{a1}\ \ \delta\theta_{b1}\ \ \delta g_1]\ \mathbf{f}_{c1}=[\delta u_{b1}\ \ \delta v_{b1}\ \ \delta\theta_{b1}]\mathbf{f}_{b1} \tag{86}$$

The position of the node b1 in the deformed configuration is given by (see Fig. 6)

$$u_{b1}+x_{b1}=u_{c1}+x_{c1}+g_1\cos(\beta_o+\theta_1)-h_b\sin(\beta_o+\theta_{b1}) \tag{87}$$

$$v_{b1}+y_{b1}=v_{c1}+y_{c1}+g_1\sin(\beta_o+\theta_1)+h_b\cos(\beta_o+\theta_{b1}) \tag{88}$$

which, after differentiation, gives

$$\begin{bmatrix}\delta u_{b1}\\ \delta v_{b1}\end{bmatrix}=\begin{bmatrix}\delta u_{c1}\\ \delta v_{c1}\end{bmatrix}+\begin{bmatrix}-\sin(\beta_o+\theta_1)\\ \cos(\beta_o+\theta_1)\end{bmatrix}\frac{g_1}{2}\delta\theta_{a1}-\begin{bmatrix}\cos(\beta_o+\theta_{b1})h_b+\sin(\beta_o+\theta_1)\frac{g_1}{2}\\ \sin(\beta_o+\theta_{b1})h_b-\cos(\beta_o+\theta_1)\frac{g_1}{2}\end{bmatrix}\delta\theta_{b1}+\begin{bmatrix}\cos(\beta_o+\theta_1)\\ \sin(\beta_o+\theta_1)\end{bmatrix}\delta g_1 \tag{89}$$

By introducing Eq. (89) in Eq. (86), it is obtained

$$\mathbf{f}_{c1}=\begin{bmatrix}1&0&0\\0&1&0\\-\sin(\beta_o+\theta_1)\frac{g_1}{2}&\cos(\beta_o+\theta_1)\frac{g_1}{2}&0\\-\cos(\beta_o+\theta_{b1})h_b-\sin(\beta_o+\theta_1)\frac{g_1}{2}&-\sin(\beta_o+\theta_{b1})h_b+\cos(\beta_o+\theta_1)\frac{g_1}{2}&1\\\cos(\beta_o+\theta_1)&\sin(\beta_o+\theta_1)&0\end{bmatrix}\mathbf{f}_{b1} \tag{90}$$

Differentiation of Eq. (90) gives the stiffness correction term $\mathbf{K}_{sc}$ associated to $[u_{c1}\ v_{c1}\ \theta_{a1}\ \theta_{b1}\ g_1]$, which must be subtracted from the tangent stiffness matrix of the structure, as

$$\mathbf{K}_{sc}=\begin{bmatrix}0&0&0&0&0\\0&0&0&0&0\\0&0&A&A&B\\0&0&A&C&B\\0&0&B&B&0\end{bmatrix} \tag{91}$$

with

$$A=-\cos(\beta_o+\theta_1)\frac{g_1}{4}f_{b1}(1)-\sin(\beta_o+\theta_1)\frac{g_1}{4}f_{b1}(2) \tag{92}$$

$$B=-\tfrac{1}{2}\sin(\beta_o+\theta_1)f_{b1}(1)+\tfrac{1}{2}\cos(\beta_o+\theta_1)f_{b1}(2) \tag{93}$$

$$C=[\sin(\beta_o+\theta_{b1})h_b-\cos(\beta_o+\theta_1)\frac{g_1}{4}]f_{b1}(1)-[\cos(\beta_o+\theta_{b1})h_b+\sin(\beta_o+\theta_1)\frac{g_1}{4}]f_{b1}(2) \tag{94}$$

5. Numerical examples

In this section results of the analysis of shear deformable composite beams with partial interaction are presented in order to investigate the effect of shear deformability on the geometrically non-linear behavior of composite members.

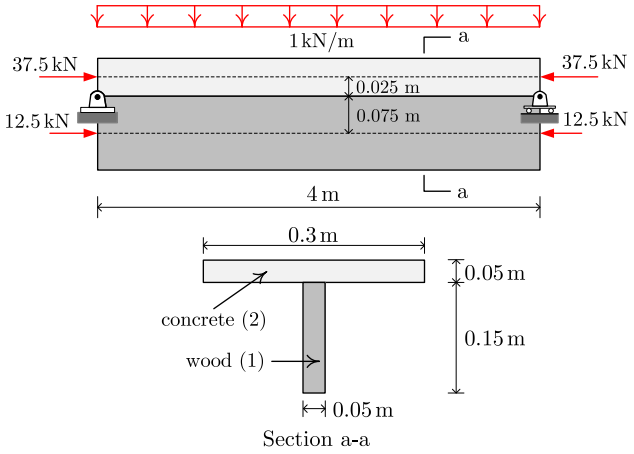

Fig. 7. Example 1: beam with axial and transversal loads.

Table 1
Example 1: numerical results.

		Present	[29]	Present/[29]
Without Shear def.	v_{max} (downwards) (mm)	9.249	9.276	0.997
	$F_{max}=k_{sc}\times g_{max}$ (kN/m)	13.798	13.865	0.995
With Shear def.	v_{max} (downwards) (mm)	9.938	9.851	1.009
	$F_{max}=k_{sc}\times g_{max}$ (kN/m)	13.987	14.022	0.998

5.1. Example 1: beam with axial and transversal loads

We consider a simply-supported wood–concrete composite beam with a span length of 4 m loaded both by axial and transversal loads (see Fig. 7). This example has been analyzed by Krawczyk and Rebora [29] using a different non-linear finite element formulation. The wood cross-section is rectangular (50 mm width and 150 mm hight). The concrete slab is 300 mm wide and 5 mm thick. The material parameters used for the calculation are: $E_1=8$ GPa, $G_1=0.4$ GPa, $E_2=12$ GPa and $G_2=5$ GPa. The shear stiffness k_{sc} is taken equal to 50 MPa. For this problem, a non-linear analysis is required even for small traversal displacement. Two analyses have been performed using the proposed model. The first one does not consider shear deformation (Bernoulli formulation) whereas in the second one shear deformation is taken into account. The calculations are performed with 20 elements. The maximum deflection v_{max} as well as the maximum longitudinal shear force F_{max} are presented, for both analyses, in Table 1. It can be seen that very good agreement with (29) is obtained.

5.2. Example 2: non-linear response of pinned laminated beam

The laminated beam presented in Fig. 8 is pinned at both ends and loaded with a uniform transverse load. The end restraints enforce zero vertical and axial displacements for both layers at the level of the shear connection. Both a slender beam with $h=0.05$ m and a short beam with $h=0.2$ m are considered. The material parameters used for the calculation are: $E_1=10$ GPa, $E_2=1$ GPa; $\nu_1=\nu_2=0.3$. The shear stiffness k_{sc} is taken equal to 1 GPa. The calculations were performed with 40 elements. The load–deflection curves for both beams are given in Figs. 9 and 10 where v is the transverse displacement at the mid-span. It can be observed that both the cases exhibit geometrical non-linear behavior at small deflections. For the slender beam both Bernoulli and Timoshenko analyses give almost identical results, but for the

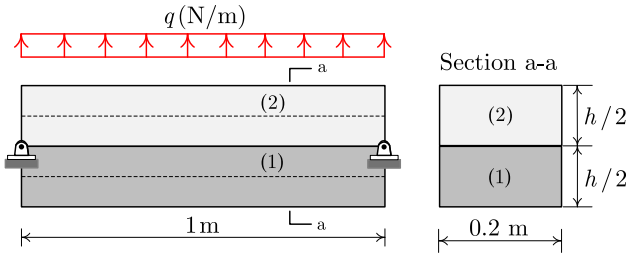

$k_{sc} = 1\,\text{GPa}$; $E_1 = 10\,\text{GPa}$; $E_2 = 1\,\text{GPa}$; $\upsilon_1 = \upsilon_2 = 0.3$

Fig. 8. Example 2: non-linear response of pinned laminated beam.

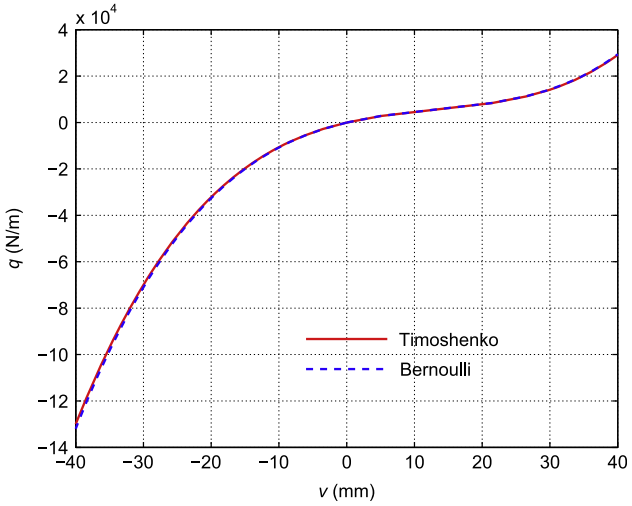

Fig. 9. Example 2: non-linear response for $h=0.05$ m.

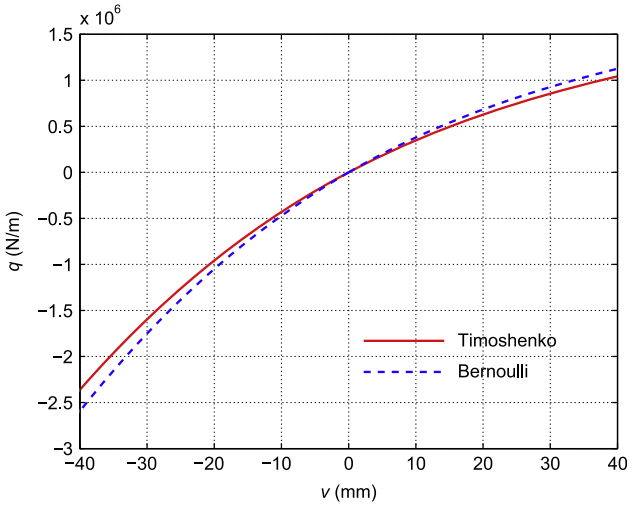

Fig. 10. Example 2: non-linear response for $h=0.2$ m.

short beam significant differences are obtained: for the applied loads $q=1\times10^6$ and $q=-2\times10^6$ the differences for vertical displacement v are 12% and 7%, respectively.

5.3. *Example 3: non-linear buckling*

The non-linear buckling behavior of the beam depicted in Fig. 11 is investigated. The material parameters used for the

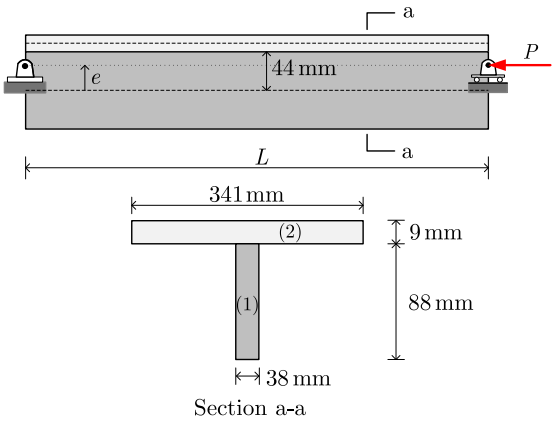

Fig. 11. Example 3: non-linear buckling.

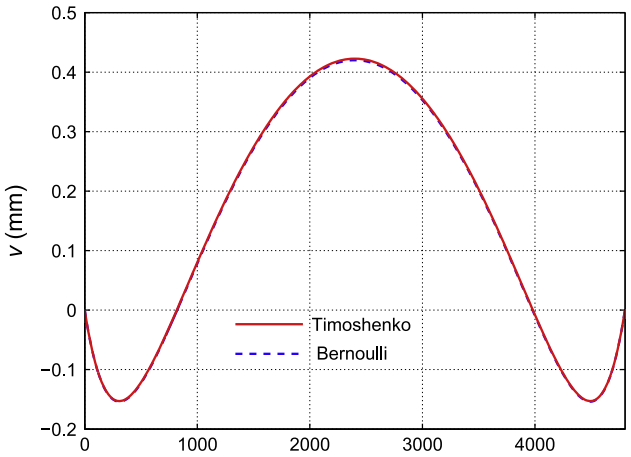

Fig. 12. Example 3: deflection pattern for the slender beam.

calculation are: $E_1=7.84$ GPa, $E_2=4.9$ GPa; $\nu_1=\nu_2=0.3$ and $k_{sc}=49$ MPa. Due to the lack of symmetry in the structure, small lateral displacements are present even for low values of the compressive load P. This problem was analyzed with $L=2400$ mm in [30] using a local Bernoulli formulation. It has been shown that a small change in e can result in a very different buckling load. This example is now analyzed with $L=4800$ mm, $e=16$ mm (slender beam) and $L=600$ mm, $e=2.7$ mm (short beam) in order to evaluate the influence of the shear deformations on the overall behavior of short composite beams. The deflection patterns computed for $P=7\times10^3$ (slender beam) and $P=2\times10^5$ (short beam) and using 40 elements are shown in Figs. 12 and 13, respectively. It can be observed that for the slender beam, Timoshenko and Bernoulli formulations give almost identical results. However, for the short beam, a difference of 14% for the deflection at the middle of the beam is observed.

6. Conclusion

In this paper, a new finite element formulation for the large displacement analysis of two-layer shear deformable composite planar beams with interlayer slips has been presented. The element has two nodes and five degrees of freedom at each node. A co-rotational description has been adopted and the element is obtained using rather simple transformation matrices between local and global quantities where the local quantities (internal

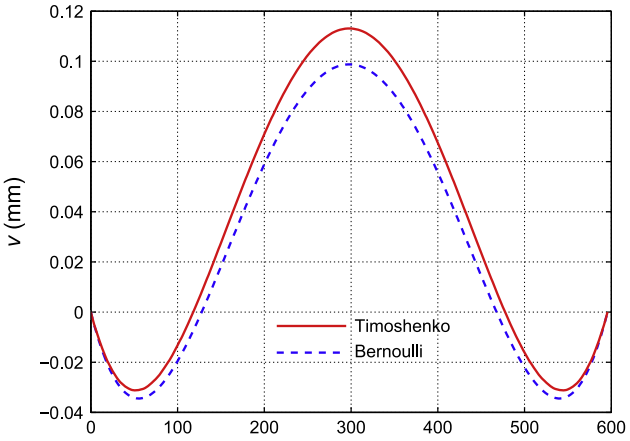

Fig. 13. Example 3: deflection pattern for the short beam.

force vector and tangent stiffness matrix) are derived using a geometrical linear formulation. The main advantage of the present approach is that the transformation matrices between local and global quantities are independent to the choice on the local linear element. This means that, using the present co-rotational framework, different geometrical linear elements can be easily transformed into non-linear ones. In the present work, a formulation based on the exact local stiffness matrix has been used [40]. This exact stiffness matrix is derived from the closed-form solution of the governing equations of the problem. The influence of both shear-flexibility and partial interaction can be covered by the present model, which is based on rather general kinematic assumption within the framework of beam theory. The performance of the element has been assessed using three numerical applications. The influence of shear-flexibility on the overall non-linear behavior of composite beams has been investigated. It has been shown that for slender beam, the effect of shear-flexibility on the deflection is not pronounced and Timoshenko and Bernoulli formulations give identical results. However, for short beams the deflection increases with shear-flexibility (14% with a length-to-depth ratio equal to 6).

References

[1] A. Dall'Asta, A. Zona, Non-linear analysis of composite beams by a displacement approach, Computers and Structures 80 (2002) 2217–2228.
[2] A. Ayoub, A two-field mixed variational principle for partially connected composite beams, Finite Elements in Analysis and Design 37 (2001) 929–959.
[3] M.R. Salari, E. Spacone, P.B. Shing, D.M. Frangopol, Nonlinear analysis of composite beams with deformable shear connectors, Journal of Structural Engineering, ASCE 124 (1998) 1148–1158.
[4] G. Ranzi, M.A. Bradford, B. Uy, A direct stiffness analysis of a composite beam with partial interaction, International Journal for Numerical Methods in Engineering 61 (2004) 657–672.
[5] M.A. Crisfield, Non-Linear Finite Element Analysis of Solids and Structures, Essentials, vol. 1, Wiley, Chichester, 1991.
[6] A. Zona, G. Ranzi, Finite element models for nonlinear analysis of steel–concrete composite beams with partial interaction in combined bending and shear, Finite Elements in Analysis and Design 47 (2011) 98–118.
[7] G. Ranzi, A. Dall'Asta, L. Ragni, A. Zona, A geometric nonlinear model for composite beams with partial interaction, Engineering Structures 32 (2010) 1384–1396.
[8] S. Schnabl, M. Saje, G. Turk, I. Planinc, Locking-free two-layer Timoshenko beam element with interlayer slip, Finite Elements in Analysis and Design 43 (2007) 705–714.
[9] H. Robinson, K.S. Naraine, Slip and uplift effects in composite beams, in: Proceedings of the Engineering Foundation Conference on Composite Construction (ASCE), 1988, pp. 487–497.
[10] M.N. Newmark, C.P. Siess, I.M. Viest, Tests and analysis of composite beams with incomplete interaction, Proceedings of the Society for Experimental Stress Analysis 9 (1) (1951) 75–92.
[11] M. Heinisuo, An exact finite element technique for layered beam, Computer and Structures 30 (3) (1988) 615–622.
[12] U.A. Girhammar, K.A. Gopu, Composite beam-column with interlayer slip exact analysis, Journal of Structural Engineering (ASCE) 119 (4) (1993) 2095–2111.
[13] C. Faella, E. Martinelli, E. Nigro, Steel and concrete composite beams: "exact" expression of the stiffness matrix and applications, Computers and Structures 80 (2002) 1001–1009.
[14] F. Wu, D.J. Oehlers, M.C. Griffith, Partial-interaction analysis of composite beam/column members, Mechanics of Structures and Machines 30 (3) (2002) 309–332.
[15] R. Seracino, C.T. Lee, T.C. Lim, J.Y. Lim, Partial interaction stresses in continuous composite beams under serviceability loads, Journal of Constructional Steel Research 60 (2004) 1525–1543.
[16] U.A. Girhammar, D.H. Pan, Exact static analysis of partially composite beams and beam-columns, International Journal of Mechanical Sciences 49 (2007) 239–255.
[17] M.A. Bradford, R.I. Gilbert, Composite beams with partial interaction under sustained loads, Journal of Structural Engineering (ASCE) 118 (7) (1992) 1871–1883.
[18] R.I. Gilbert, M.A. Bradford, Time-dependent behavior of continuous composite beams at service loads, Journal of Structural Engineering ASCE 121 (2) (1995) 319–327.
[19] G. Ranzi, M.A. Bradford, Analytical solutions for the time-dependent behaviour of composite beams with partial interaction, International Journal of Solids and Structures 43 (13) (2006) 3770–3793.
[20] B. Jurkiewiez, S. Buzon, J.G. Sieffert, Incremental viscoelastic analysis of composite beams with partial interaction, Computers and Structures 83 (21–22) (2005) 1780–1791.
[21] Q.H. Nguyen, M. Hjiaj, B. Uy, Time-dependent analysis of composite beams with partial interaction based on a time-discrete exact stiffness matrix, Engineering Structures 32 (9) (2010) 2902–2911.
[22] N. Gattesco, Analytical modelling of nonlinear behaviour of composite beams with deformable connection, Journal of Constructional Steel Research 52 (1999) 195–218.
[23] M.R. Salari, E. Spacone, Analysis of steel–concrete composite frames with bond-slip, Journal of Structural Engineering (ASCE) 127 (11) (2001) 1243–1250.
[24] A. Ayoub, F.C. Filippou, Mixed formulation of nonlinear steel–concrete composite beam element, Journal of Structural Engineering (ASCE) 126 (3) (2000) 371–381.
[25] E. Spacone, S. El-Tawil, Nonlinear analysis of steel–concrete composite structures: state-of-the-art, Journal of Structural Engineering (ASCE) 130 (2) (2004) 1901–1912.
[26] Q.H. Nguyen, M. Hjiaj, B. Uy, S. Guezouli, Analysis of composite beams in the hogging moment regions using a mixed finite element formulation, Journal of Constructional Steel Research 65 (3) (2009) 737–748.
[27] M. Saje, B. Čas, I. Planinc, Non-linear finite element analysis of composite planar frames with an interlayer slip, Computers and Structures 82 (2004) 1901–1912.
[28] P. Krawczyk, F. Frey, Large deflections of laminated beams with interlayer slips. Part 1: model development, Engineering Computations 24 (1) (2007) 17–32.
[29] P. Krawczyk, B. Rebora, Large deflections of laminated beams with interlayer slips - part 2: finite element development, Engineering Computations 24 (1) (2007) 33–51.
[30] J.M. Battini, Q.H. Nguyen, M. Hjiaj, Non-linear finite element analysis of composite beams with interlayer slips, Computers and Structures 87 (13–14) (2009) 904–912.
[31] A.O. Adekola, Partial interaction between elastically connected elements of a composite beam, International Journal of Solids and Structures 4 (1968) 1125–1135.
[32] F. Gara, G. Ranzi, G. Leoni, Displacement-based formulations for composite beams with longitudinal slip and vertical uplift, International Journal for Numerical Methods in Engineering 65 (2006) 1197–1220.
[33] H. Murakami, A laminated beam theory with interlayer slip, Journal of Applied Mechanics 51 (1984) 551–559.
[34] A. Kroflič, I. Planinc, M. Saje, G. Turk, B. Čas, Non-linear analysis of two-layer timber beams considering interlayer slip and uplift, Engineering Structures 32 (2010) 1617–1630.
[35] D.L. Wheat, J.M. Calixto, Non-linear analysis of two-layered wood members with interlayer slip, ASCE Journal of Structural Engineering 120 (6) (1994) 1909–1929.
[36] Y.L. Pi, M.A. Bradford, B. Uy, Second order nonlinear analysis of composite steel–concrete members. I: theory, ASCE Journal of Structural Engineering 132 (5) (2006) 751–761.
[37] C. Tort, J.F. Hajjar, Mixed finite element for three-dimensional nonlinear dynamic analysis of rectangular concrete-filled steel tube beam-columns, ASCE Journal of Engineering Mechanics 136 (11) (2010) 1329–1339.
[38] B. Čas, M. Saje, I. Planinc, Buckling of layered wood columns, Advances in Engineering Software 38 (2007) 586–597.
[39] S. Schnabl, M. Saje, G. Turk, I. Planinc, Analytical solution of two-layer beam taking into account interlayer slip and shear deformation, Journal of Structural Engineering (ASCE) 133 (6) (2007) 886–894.
[40] Q.H. Nguyen, E. Martinelli, M. Hjiaj, Derivation of the exact stiffness matrix for a two-layer Timoshenko beam element with partial interaction, Engineering Structures 33 (2) (2011) 298–307.

ANNEXE 2

Q-H. Nguyen, V-A. Lai, M. Hjiaj. Force-based FE for large displacement inelastic analysis of two-layer Timoshenko beams with interlayer slips. *Finite element analysis and design* 2014; 85 :1-10. (5-Year IF 1.967) http://dx.doi.org/10.1016/j.finel.2014.02.007.

Finite Elements in Analysis and Design 85 (2014) 1–10

Contents lists available at ScienceDirect

Finite Elements in Analysis and Design

journal homepage: www.elsevier.com/locate/finel

Force-based FE for large displacement inelastic analysis of two-layer Timoshenko beams with interlayer slips

Quang-Huy Nguyen [a,*], Mohammed Hjiaj [a], Van-Anh Lai [b]

[a] Structural Engineering Research Group, INSA de Rennes, France
[b] University of Transport Technology, Viet Nam

ARTICLE INFO

Article history:
Received 4 December 2013
Received in revised form
21 February 2014
Accepted 24 February 2014
Available online 25 March 2014

Keywords:
Two-layer beam/column
Partial interaction
Shear flexibility
Force-based formulation
Large displacement
Elastoplastic buckling

ABSTRACT

This paper presents a novel finite element model for the fully material and geometrical nonlinear analysis of shear-deformable two-layer composite planar beam/column members with interlayer slips. We adopt the co-rotational approach where the motion of the element is decomposed into two parts: a rigid body motion which defines a local co-ordinate system and a small deformational motion of the element relative to this local co-ordinate system. The main advantage of this approach is that the transformation matrices relating local and global quantities are independent from the choice of the geometrical linear local element. The effect of transverse shear deformation of the layers is taken into account by assuming that each layer behaves as a Timoshenko beam element. The layers are assumed to be continuously connected and partial interaction is considered by adopting a continuous relationship between the interface shear flow and the corresponding slip. In order to avoid curvature and the shear locking phenomena, the local linear element is derived from the force-based formulation. The present model provides an efficient tool for the elastoplastic buckling analysis of two-layer shear deformable beam/column with arbitrary support and loading conditions. Finally, two numerical applications are presented in order to assess the performance of the proposed formulation.

1. Introduction

Two-layer composite members are often used in civil engineering. Two typical examples are steel–concrete beams and nailed timber members. For these applications, a complete shear layer interaction cannot be obtained and a relative displacement of adjacent layers occurs. Whereas the transverse separation is often small and can be neglected; the slip tangent to the interface surface influences the behavior of the composite beam and must be considered.

Several theoretical models, characterized by different levels of approximation, have been proposed for the geometrically linear analysis of elastic composite structures. To the best knowledge of the authors, the earliest and most cited work on the partial interaction of composite beams is due to Newmark et al. in 1951 [1] and it is based on the small deformation elastic analysis considering Euler–Bernoulli's beam theory for representing the deformation of beam layers. Since then, this model was extensively used by many authors to formulate analytical models for the static response of linear elastic [2–7] as well as linear-viscoelastic [8–12] of composite beams with arbitrary support and loading conditions. In addition, several numerical models based on the same basic assumptions have been developed to investigate the behavior of composite beams with partial interaction in the nonlinear range (for material nonlinearities, see e.g. [13–17], and for geometric nonlinearities, see e.g. [18–20]). The most significant advances in the theory of two-layer beams in partial interaction moved recently toward the introduction of shear flexibility of both layers according to the well-known Timoshenko theory (see e.g. [21–35]).

The two-layer members with interlayer slips may develop nonlinear geometrical and material behavior, even for small deformations. In contrast with the large body of literature devoted to material nonlinear and geometrical linear problems of shear deformable layered beam/columns in partial interaction, only a few numerical models which consider both material and geometrical nonlinearities, the interlayer slip and cross-section shear flexibility can be found in the literature. Recently, Hozjan et al. [36] developed a FE model for two-layer beam/column based on the shear-stiff Reissner beam theory. This model takes into account the exact geometrical (Total Lagrangian approach) and material nonlinearities as well as finite slip between the layers. However, the transverse shear deformation is neglected. They developed the fundamental equations of the problem which exactly account for the equilibrium between the contact surfaces of the layers in the deformed state as well as for the tangential separation of layers at the edges. These equations were then cast into the discretized weak form by the modified principle of virtual work using the unconventional finite element technique.

* Corresponding author. Tel.: +33 2 23 23 83 94.
E-mail address: qnguyen@insa-rennes.fr (Q.-H. Nguyen).

http://dx.doi.org/10.1016/j.finel.2014.02.007
0168-874X/

The purpose of this paper is to present a novel finite element model for the fully material and geometrical nonlinear analysis of shear-deformable two-layer composite planar beams with interlayer slips. The effect of transverse shear is taken into account using Timoshenko's beam theory. A co-rotational description is used, which means that the motion of the element is decomposed into two parts: a rigid body motion which defines a local co-ordinate system and a small deformational motion of the element relative to this local co-ordinate system. The geometrical nonlinearity induced by the large rigid-body motion, is incorporated in the transformation matrices relating local and global internal force vectors and tangent stiffness matrices whereas the deformational response, captured at the level of the local co-ordinate system, is assumed to be small and modeled using a geometrical linear element. The main advantage of the co-rotational approach is that the transformation matrices relating local and global quantities are independent to the choice of the local linear geometrical element. A second advantage of this approach is the separation between geometrical and material nonlinearities. The local formulation is based on the force-based approach. This choice is motivated by the fact that shear and curvature locking can be avoided. Furthermore, force-based EF is known for being more effective in dealing with material nonlinear problems [13]. The present model provides an efficient tool for elastoplastic buckling analysis of two-layer shear deformable beam with arbitrary support and loading conditions. The main contribution of the present paper is the incorporation of shear deformation of the layers which allows for a more general treatment of two-layer beams with interlayer slip. This extension adds complexity to the treatment of large displacement of layered beams within a co-rotational formulation. Indeed, the independent shearing of the different layers results in independent cross-section rotation of the layers and so in extra degree of freedom which necessarily modifies the FE formulation itself.

2. Problem definition

Let us consider a planar composite beam element with two layers of possibly different cross-sections and materials and including shear connectors at the interface which are uniformly distributed along the longitudinal direction, as shown in Fig. 1. It is assumed that the interlayer slip can occur at the interface but there is no uplift. In order to take into account the transverse shear effect, the first-order shear deformation beam theory of Timoshenko is used.

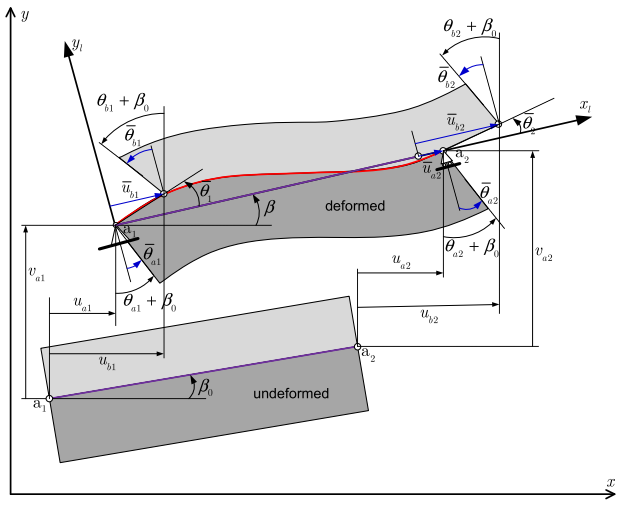

Fig. 1. Degree of freedom in the global and local co-ordinate systems.

The co-ordinates of the nodes a_1 and a_2 in the global co-ordinate system (x,y) are (x_{a1},y_{a1}) and (x_{a2},y_{a2}), respectively. For instant, these nodes are chosen to be at the layer interface in order to derive easily the kinematic relationships between the global nodal displacements and the local ones. The general case of eccentric nodes will be treated in Section 3.3.

The element has 10 global degrees of freedom in the fixed global co-ordinate system (x,y) (cf. Fig. 1). The vectors of global nodal displacements and forces are defined by

$$\mathbf{p}_g = \begin{bmatrix} u_{a1} & u_{b1} & v_{a1} & \theta_{a1} & \theta_{b1} & u_{a2} & u_{b2} & v_{a2} & \theta_{a2} & \theta_{b2} \end{bmatrix}^{\mathrm{T}} \tag{1}$$

Due to the presence of the three rigid body modes in the global co-ordinate system, the corresponding element stiffness matrix is singular. Consequently, in general there is no flexibility matrix associated with this global system. For this reason, the proposed force-based element is formulated in the local system (x_l,y_l) without rigid body modes which translates and rotates with the element as the deformation proceeds. In this local system, the element has seven degree of freedoms and the vector of local displacements is defined as

$$\mathbf{p}_l = \begin{bmatrix} \overline{u}_{a2} & \overline{u}_{b1} & \overline{u}_{b2} & \overline{\theta}_{a1} & \overline{\theta}_{b1} & \overline{\theta}_{a2} & \overline{\theta}_{b2} \end{bmatrix}^{\mathrm{T}} \tag{2}$$

where $\overline{u}_{a2}$ is the axial displacement of layer a; $\overline{\theta}_{m1}$ and $\overline{\theta}_{m2}$ $(m=a,b)$ are the end rotations of layer m. These relative displacements correspond to the minimum number of geometric variables necessary to describe the deformation modes of the element.

3. Co-rotational formulation

In our work, a co-rotational (CR) approach is adopted to take into account geometric nonlinearity. This approach is a priori based on the kinematic assumptions: displacements and rotations may be arbitrarily large, but deformations must be small. The main advantage of this approach is that the formulation of the element in the local basic system is completely independent of the transformation, i.e. in the local system the element can be formulated as geometrically linear and the geometric nonlinearity can be introduced in the transformation.

3.1. Co-rotational kinematics for composite beams with partial interaction

The idea of the co-rotational approach is to decompose the motion of the element into rigid body and pure deformational parts, through the use of a local basic system (x_l,y_l) which continuously rotates and translates with the element (see Fig. 1). The origin of the local co-ordinate system is taken at node a_1 and the x_l-axis of the local co-ordinate system is defined by the line connecting the nodes a_1 and a_2. The y_l-axis is perpendicular to the x_l-axis so that the result is a right handed orthogonal co-ordinate system. The motion of the element from the original undeformed configuration to the actual deformed one can thus be separated in two parts. The first one, which corresponds to the rigid motion of the local frame, is described by the translation of the node a_1 and the rigid rotation of the axes. The deformational part of the motion is always small relative to the local co-ordinate system and a geometrical linear element will be used. The co-rotational method for 2D beams is known for many years. However, when considering composite beams with interlayer slips, it is necessary to select pertinent kinematical local and global variables.

According to the notations defined in Fig. 1, the components of the local displacement vector $\mathbf{p}_l$ can be computed from those of

the global vector $\mathbf{p}_g$ as

$$\overline{\theta}_{a1} = \theta_{a1} - (\beta - \beta_0) \tag{3}$$

$$\overline{\theta}_{b1} = \theta_{b1} - (\beta - \beta_0) \tag{4}$$

$$\overline{\theta}_{a2} = \theta_{a2} - (\beta - \beta_0) \tag{5}$$

$$\overline{\theta}_{b2} = \theta_{b2} - (\beta - \beta_0) \tag{6}$$

$$\overline{u}_{a2} = l_n - l_0 \tag{7}$$

$$\overline{u}_{b1} = g_1 \cos \overline{\theta}_1 \tag{8}$$

$$\overline{u}_{b2} = \overline{u}_{a2} + g_2 \cos \overline{\theta}_2 \tag{9}$$

where l_0 and l_n are, respectively, the undeformed and the deformed element length defined as

$$l_0 = \sqrt{(x_{a2} - x_{a1})^2 + (y_{a2} - y_{a1})^2} \tag{10}$$

$$l_n = \sqrt{(x_{a2} + u_{a2} - x_{a1} - u_{a1})^2 + (y_{a2} + v_{a2} - y_{a1} - v_{a1})^2} \tag{11}$$

g_1 and g_2 denote the global slips at interface which are assumed to be perpendicular to the average cross-section rotations. Therefore, they are defined by

$$g_i = \frac{(u_{bi} - u_{ai})}{\cos(\overline{\theta}_i + \beta)} \text{ with } \overline{\theta}_i = \frac{\overline{\theta}_{ai} + \overline{\theta}_{bi}}{2} \text{ and } i = 1, 2 \tag{12}$$

3.2. Element formulation

As can be seen from Eqs. (3)–(12), the local displacement can be expressed as functions of global ones, i.e.

$$\mathbf{p}_l = \mathbf{p}_l(\mathbf{p}_g) \tag{13}$$

Then $\mathbf{p}_l$ is used to compute the internal force vector $\mathbf{f}_l$ and the stiffness matrix $\mathbf{K}_l$ in the local co-ordinate system (see Section 4). Note that $\mathbf{f}_l$ and $\mathbf{K}_l$ depend only on the definition of the local strains and not on the particular form of Eq. (13). The transformation matrix $\mathbf{B}_{lg}$ between the local and global displacements is defined by

$$\delta\mathbf{p}_l = \mathbf{B}_{lg}\, \delta\mathbf{p}_g \tag{14}$$

and is obtained by differentiation of Eq. (13). The global internal force vector $\mathbf{f}_g$ and the global tangent stiffness matrix $\mathbf{K}_g$, consistent with $\mathbf{p}_g$, can be obtained by equating the internal virtual work in both the global and the local systems, i.e.

$$\mathbf{f}_g = \mathbf{B}_{lg}^{\mathrm{T}} \mathbf{f}_l, \quad \mathbf{K}_g = \mathbf{B}_{lg}^{\mathrm{T}} \mathbf{K}_l \mathbf{B}_{lg} + \mathbf{H}_{lg}, \quad \mathbf{H}_{lg} = \left. \frac{\partial(\mathbf{B}^{\mathrm{T}} \mathbf{f}_l)}{\partial \mathbf{p}_g} \right|_{\mathbf{f}_l} \tag{15}$$

For the sake of clarity and in order to give explicitly the expression of transformation matrices, the transformation between the local quantities and the global ones is presented here through two consecutive changes of variables only

$$\mathbf{p}_l \rightarrow \mathbf{p}_a = \begin{bmatrix} \overline{\theta}_{a1} & \overline{\theta}_{b1} & \overline{\theta}_{a2} & \overline{\theta}_{b2} & \overline{u}_{a2} & g_1 & g_2 \end{bmatrix}^{\mathrm{T}} \rightarrow \mathbf{p}_g \tag{16}$$

For the first change of variables between $\mathbf{p}_l$ and $\mathbf{p}_a$, the transformation matrices giving $\mathbf{f}_a$ and $\mathbf{K}_a$ as a function of $\mathbf{f}_l$ and $\mathbf{K}_l$ can be obtained using Eqs. (8) and (9).

$$\mathbf{B}_{la} = \begin{bmatrix} 1 & 0 & 0 & 0 & 0 & 0 & 0 \\ 0 & 1 & 0 & 0 & 0 & 0 & 0 \\ 0 & 0 & 1 & 0 & 0 & 0 & 0 \\ 0 & 0 & 0 & 1 & 0 & 0 & 0 \\ 0 & 0 & 0 & 0 & 1 & 0 & 0 \\ -\frac{g_1}{2}\sin\overline{\theta}_1 & -\frac{g_1}{2}\sin\overline{\theta}_1 & 0 & 0 & 0 & \cos\overline{\theta}_1 & 0 \\ 0 & 0 & -\frac{g_2}{2}\sin\overline{\theta}_2 & -\frac{g_2}{2}\sin\overline{\theta}_2 & 1 & 0 & \cos\overline{\theta}_2 \end{bmatrix} \tag{17}$$

and

$$\mathbf{H}_{la} = \mathbf{H}_{la1}\mathbf{f}_l(2) + \mathbf{H}_{la2}\mathbf{f}_l(3) \tag{18}$$

where

$$\mathbf{H}_{la1} = \begin{bmatrix} -\frac{g_1}{4}\cos\overline{\theta}_1 & -\frac{g_1}{4}\cos\overline{\theta}_1 & 0 & 0 & 0 & -\frac{1}{2}\sin\overline{\theta}_1 & 0 \\ -\frac{g_1}{4}\cos\overline{\theta}_1 & -\frac{g_1}{4}\cos\overline{\theta}_1 & 0 & 0 & 0 & -\frac{1}{2}\sin\overline{\theta}_1 & 0 \\ 0 & 0 & 0 & 0 & 0 & 0 & 0 \\ 0 & 0 & 0 & 0 & 0 & 0 & 0 \\ 0 & 0 & 0 & 0 & 0 & 0 & 0 \\ -\frac{1}{2}\sin\overline{\theta}_1 & -\frac{1}{2}\sin\overline{\theta}_1 & 0 & 0 & 0 & 0 & 0 \\ 0 & 0 & 0 & 0 & 0 & 0 & 0 \end{bmatrix} \tag{19}$$

and

$$\mathbf{H}_{la2} = \begin{bmatrix} 0 & 0 & 0 & 0 & 0 & 0 & 0 \\ 0 & 0 & 0 & 0 & 0 & 0 & 0 \\ 0 & 0 & -\frac{g_2}{4}\cos\overline{\theta}_2 & -\frac{g_2}{4}\cos\overline{\theta}_2 & 0 & 0 & -\frac{1}{2}\sin\overline{\theta}_2 \\ 0 & 0 & -\frac{g_2}{4}\cos\overline{\theta}_2 & -\frac{g_2}{4}\cos\overline{\theta}_2 & 0 & 0 & -\frac{1}{2}\sin\overline{\theta}_2 \\ 0 & 0 & 0 & 0 & 0 & 0 & 0 \\ 0 & 0 & 0 & 0 & 0 & 0 & 0 \\ 0 & 0 & -\frac{1}{2}\sin\overline{\theta}_2 & -\frac{1}{2}\sin\overline{\theta}_2 & 0 & 0 & 0 \end{bmatrix} \tag{20}$$

The second change of variables from $\mathbf{p}_a$ to $\mathbf{p}_g$ is performed using Eqs. (3)–(7) and (12). After some algebraic manipulations, the transformation matrices giving $\mathbf{f}_g$ and $\mathbf{K}_g$ as a function of $\mathbf{f}_a$ and $\mathbf{K}_a$ are obtained as

$$\mathbf{B}_{ag} = \begin{bmatrix} \frac{-s}{l_n} & 0 & \frac{c}{l_n} & 1 & 0 & \frac{s}{l_n} & 0 & \frac{-c}{l_n} & 0 & 0 \\ \frac{-s}{l_n} & 0 & \frac{c}{l_n} & 0 & 1 & \frac{s}{l_n} & 0 & \frac{-c}{l_n} & 0 & 0 \\ \frac{-s}{l_n} & 0 & \frac{c}{l_n} & 0 & 0 & \frac{s}{l_n} & 0 & \frac{-c}{l_n} & 1 & 0 \\ \frac{-s}{l_n} & 0 & \frac{c}{l_n} & 0 & 0 & \frac{s}{l_n} & 0 & \frac{-c}{l_n} & 0 & 1 \\ -c & 0 & -s & 0 & 0 & c & 0 & s & 0 & 0 \\ \frac{-1}{c_1} & \frac{-1}{c_1} & 0 & \frac{\Delta u_1 s_1}{2c_1^2} & \frac{\Delta u_1 s_1}{2c_1^2} & 0 & 0 & 0 & 0 & 0 \\ 0 & 0 & 0 & 0 & 0 & \frac{-1}{c_2} & \frac{-1}{c_2} & 0 & \frac{\Delta u_2 s_2}{2c_2^2} & \frac{\Delta u_2 s_2}{2c_2^2} \end{bmatrix} \tag{21}$$

with

$$c_i = \cos\left(\frac{\theta_{ai} + \theta_{bi}}{2} + \beta_0\right), \quad s_i = \sin\left(\frac{\theta_{ai} + \theta_{bi}}{2} + \beta_0\right), \quad \Delta u_i = u_{bi} - u_{ai}, \quad i = 1, 2 \tag{22}$$

and

$$\mathbf{H}_{ag} = \frac{(\mathbf{r}\mathbf{z}^{\mathrm{T}} + \mathbf{z}\mathbf{r}^{\mathrm{T}})}{l_n^2} \sum_{i=1}^{4} \mathbf{f}_a(i) + \frac{\mathbf{z}\mathbf{z}^{\mathrm{T}}}{l_n} \mathbf{f}_a(5) + \mathbf{H}_{ag1}\mathbf{f}_l(6) + \mathbf{H}_{ag2}\mathbf{f}_l(7) \tag{23}$$

with

$$\mathbf{r} = \begin{bmatrix} -c & 0 & -s & 0 & 0 & c & 0 & s & 0 & 0 \end{bmatrix}^{\mathrm{T}} \tag{24}$$

$$\mathbf{z} = \begin{bmatrix} s & 0 & -c & 0 & 0 & -s & 0 & c & 0 & 0 \end{bmatrix}^{\mathrm{T}} \tag{25}$$

$$\mathbf{H}_{ag1}=\frac{1}{4c_1^3}\begin{bmatrix} 0 & 0 & 0 & -2c_1s_1 & -2c_1s_1 & 0 & 0 & 0 & 0 & 0\\ 0 & 0 & 0 & -2c_1s_1 & -2c_1s_1 & 0 & 0 & 0 & 0 & 0\\ 0 & 0 & 0 & 0 & 0 & 0 & 0 & 0 & 0 & 0\\ -2c_1s_1 & 2c_1s_1 & 0 & \Delta u_1(2-c_1^2) & \Delta u_1(2-c_1^2) & 0 & 0 & 0 & 0 & 0\\ -2c_1s_1 & 2c_1s_1 & 0 & \Delta u_1(2-c_1^2) & \Delta u_1(2-c_1^2) & 0 & 0 & 0 & 0 & 0\\ 0 & 0 & 0 & 0 & 0 & 0 & 0 & 0 & 0 & 0\\ 0 & 0 & 0 & 0 & 0 & 0 & 0 & 0 & 0 & 0\\ 0 & 0 & 0 & 0 & 0 & 0 & 0 & 0 & 0 & 0\\ 0 & 0 & 0 & 0 & 0 & 0 & 0 & 0 & 0 & 0\\ 0 & 0 & 0 & 0 & 0 & 0 & 0 & 0 & 0 & 0 \end{bmatrix} \tag{26}$$

$$\mathbf{H}_{ag2}=\frac{1}{4c_2^3}\begin{bmatrix} 0 & 0 & 0 & 0 & 0 & 0 & 0 & 0 & 0 & 0\\ 0 & 0 & 0 & 0 & 0 & 0 & 0 & 0 & 0 & 0\\ 0 & 0 & 0 & 0 & 0 & 0 & 0 & 0 & 0 & 0\\ 0 & 0 & 0 & 0 & 0 & 0 & 0 & 0 & 0 & 0\\ 0 & 0 & 0 & 0 & 0 & 0 & 0 & 0 & 0 & 0\\ 0 & 0 & 0 & 0 & 0 & 0 & 0 & 0 & -2c_2s_2 & -2c_2s_2\\ 0 & 0 & 0 & 0 & 0 & 0 & 0 & 0 & -2c_2s_2 & -2c_2s_2\\ 0 & 0 & 0 & 0 & 0 & 0 & 0 & 0 & 0 & 0\\ 0 & 0 & 0 & 0 & 0 & -2c_2s_2 & 2c_2s_2 & 0 & \Delta u_2(2-c_2^2) & \Delta u_2(2-c_2^2)\\ 0 & 0 & 0 & 0 & 0 & -2c_2s_2 & 2c_2s_2 & 0 & \Delta u_2(2-c_2^2) & \Delta u_2(2-c_2^2) \end{bmatrix} \tag{27}$$

3.3. General finite element with eccentric nodes

The element formulation which is developed just now uses the displacements at the interface of the layers as degree of freedom. However, in general the kinematic and static boundary conditions would be arbitrary. In order to make the present formulation able to cover any case of prescribed displacements, a change of degrees of freedom at the global level must be performed.

Let us consider the general case where the prescribed displacements are applied at the nodes $\hat{a}_1$, $\hat{a}_2$, $\hat{b}_1$ and $\hat{b}_2$ which are located randomly over the cross-section of the element ends as illustrated in Fig. 2. The new global displacement vector $\mathbf{p}_e$ is defined as

$$\mathbf{p}_e=\begin{bmatrix} u_{\hat{a}1} & u_{\hat{b}1} & v_{\hat{a}1} & \theta_{a1} & \theta_{b1} & u_{\hat{a}2} & u_{\hat{b}2} & v_{\hat{a}2} & \theta_{a2} & \theta_{b2} \end{bmatrix}^{\mathrm{T}} \tag{28}$$

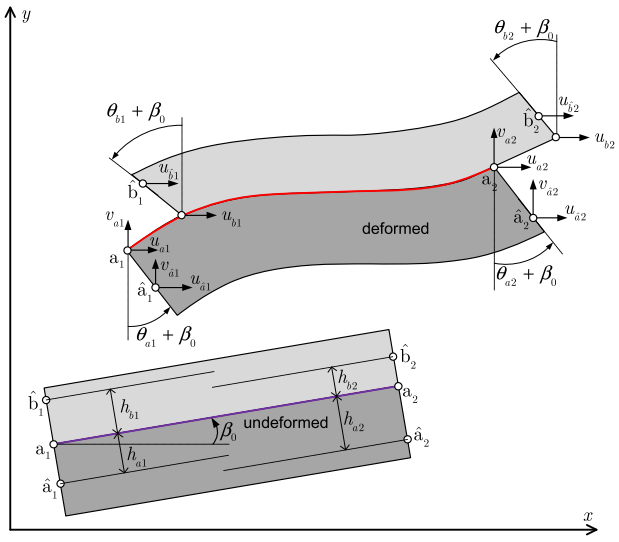

Fig. 2. Degrees of freedom of general element with eccentric nodes.

According to the scheme in Fig. 2, the components of $\mathbf{p}_g$ can be expressed by the ones of $\mathbf{p}_e$ as

$$\begin{aligned} u_{b1}+x_{a1}&=u_{\hat{b}1}+x_{\hat{b}1}+h_{b1}\ \sin(\theta_{b1}+\beta_0)\\ u_{a1}+x_{a1}&=u_{\hat{a}1}+x_{\hat{a}1}-h_{a1}\ \sin(\theta_{a1}+\beta_0)\\ v_{a1}+y_{a1}&=v_{\hat{a}1}+y_{\hat{a}1}+h_{a1}\ \cos(\theta_{a1}+\beta_0)\\ u_{b2}+x_{a2}&=u_{\hat{b}2}+x_{\hat{b}2}+h_{b2}\ \sin(\theta_{b2}+\beta_0)\\ u_{a2}+x_{a2}&=u_{\hat{a}2}+x_{\hat{a}2}-h_{a2}\ \sin(\theta_{a2}+\beta_0)\\ v_{a2}+y_{a2}&=v_{\hat{a}2}+y_{\hat{a}2}+h_{a2}\ \cos(\theta_{a2}+\beta_0) \end{aligned} \tag{29}$$

The transformation matrices giving $\mathbf{f}_e$ and $\mathbf{K}_e$ as a function of $\mathbf{f}_g$ and $\mathbf{K}_g$ are then obtained

$$\mathbf{B}_{ge}=\begin{bmatrix} 1 & 0 & 0 & -h_{a1}c_{a1} & 0 & 0 & 0 & 0 & 0 & 0\\ 0 & 1 & 0 & 0 & h_{b1}c_{b1} & 0 & 0 & 0 & 0 & 0\\ 0 & 0 & 1 & -h_{a1}s_{a1} & 0 & 0 & 0 & 0 & 0 & 0\\ 0 & 0 & 0 & 1 & 0 & 0 & 0 & 0 & 0 & 0\\ 0 & 0 & 0 & 0 & 1 & 0 & 0 & 0 & 0 & 0\\ 0 & 0 & 0 & 0 & 0 & 1 & 0 & 0 & -h_{a2}c_{a2} & 0\\ 0 & 0 & 0 & 0 & 0 & 0 & 1 & 0 & 0 & h_{b2}c_{b2}\\ 0 & 0 & 0 & 0 & 0 & 0 & 0 & 1 & -h_{a2}s_{a2} & 0\\ 0 & 0 & 0 & 0 & 0 & 0 & 0 & 0 & 1 & 0\\ 0 & 0 & 0 & 0 & 0 & 0 & 0 & 0 & 0 & 1 \end{bmatrix}$$

$$\begin{aligned} \text{with}\quad c_{a1}&=\cos(\theta_{a1}+\beta_0)\\ s_{a1}&=\sin(\theta_{a1}+\beta_0)\\ c_{b1}&=\cos(\theta_{b1}+\beta_0)\\ c_{a2}&=\cos(\theta_{a2}+\beta_0)\\ s_{a2}&=\sin(\theta_{a2}+\beta_0)\\ c_{b2}&=\cos(\theta_{b2}+\beta_0) \end{aligned} \tag{30}$$

and the only nonzero terms in the matrix $\mathbf{H}_{ge}$ are

$$\begin{aligned} \mathbf{H}_{ge}(3,3)&=h_{a1}s_{a1}\mathbf{f}_g(1)-h_{a1}c_{a1}\mathbf{f}_g(3)\\ \mathbf{H}_{ge}(4,4)&=-h_{b1}s_{b1}\mathbf{f}_g(2)\\ \mathbf{H}_{ge}(9,9)&=h_{a2}s_{a2}\mathbf{f}_g(6)-h_{a2}c_{a2}\mathbf{f}_g(8)\\ \mathbf{H}_{ge}(10,10)&=-h_{b1}c_{b1}\mathbf{f}_g(7) \end{aligned} \tag{31}$$

4. Local force-based finite element formulation

4.1. Kinematics

Consider a typical straight two-node layered beam element in the local system (x_l, y_l) as shown in Fig. 2. The centroidal axis of the layer a is taken as the beam reference axis. The layers can slip one on the other but no separation can occur at the interlayer. It is also assumed that the cross-sections do not distort in their own planes. The shear deformation is taken into account by considering the first-order shear deformation theory of Timoshenko for each layer. Therefore, in the local system, two layers have the same transversal displacement but different rotations and curvatures. In the local system, rotations and displacements are considered to be small. Based on the above assumptions, the axial, shear and flexural deformations at the layer centroid are related to the displacements as follows:

$$\mathbf{u}(x,y)=\begin{bmatrix} u_a(x,y)\\ u_b(x,y)\\ v(x,y) \end{bmatrix}=\begin{bmatrix} u_a(x)-y\theta_a(x)\\ u_b(x)-y\theta_b(x)\\ v(x) \end{bmatrix} \tag{32}$$

where $u_a(x)$ and $v(x)$ are, respectively, the axial and the transverse displacement of the reference axis; $\theta_i(x)$ is the rotation of the cross-section $i(=a$ or $b)$.

The interlayer slip $g(x)$ is defined as the relative axial displacement at the interface of layer b compared to layer a

$$g(x) = u_b(x) - u_a(x) \tag{33}$$

For the sake of simplicity, (x) is now omitted in all functions of x. As the deformations are assumed to be small compared to unity in the local co-ordinate, the quadratic part of the Green–Lagrange tensor is negligible compared to the linear part. One obtains

$$\begin{aligned}
&\varepsilon_{a,xx} = u_a' - y\theta_a' \\
&\gamma_{a,xy} = v' - \theta_a \\
&\varepsilon_{b,xx} = u_b' - y\theta_b' \\
&\gamma_{b,xy} = v' - \theta_b
\end{aligned} \tag{34}$$

where the prime denotes the differentiation with respect to x. We denote $\hat{\mathbf{e}}$ vector of generalized section strains which is related to the cross-section deformations by the kinematic relations as

$$\hat{\mathbf{e}}(\mathbf{d}) = \begin{bmatrix} u_a' \\ \theta_a' \\ v' - \theta_a \\ u_b' \\ \theta_b' \\ v' - \theta_b \\ u_b - u_a \end{bmatrix} \tag{35}$$

The conjugate internal force (stress resultant) vector $\mathbf{D}$ can be defined as

$$\mathbf{D} = \begin{bmatrix} N_a & M_a & T_a & N_b & M_b & T_b & D_{sc} \end{bmatrix}^{\mathrm{T}} \tag{36}$$

where N_i, M_i and T_i are, respectively, the axial force, the bending moment and the shear force of the layer $i(=a \text{ or } b)$ at a given cross-section of co-ordinate x

$$\begin{aligned}
&N_i = \int_{Ai} \sigma_{i,xx}\, \mathrm{d}A_i \\
&M_i = -\int_{Ai} y\sigma_{i,xx}\, \mathrm{d}A_i \\
&T_i = \int_{Ai} \tau_{i,xy}\, \mathrm{d}A_i
\end{aligned} \tag{37}$$

and D_{sc} is the bond force at the interface.

4.2. Equilibrium equations

The equations of equilibrium which are consistent with the kinematic hypothesis stated in Section 4.2, can be obtained from the Principle of Virtual Work which is written as

$$\int_L \mathbf{D}^{\mathrm{T}} \hat{\mathbf{e}}(\delta\mathbf{d}) \mathrm{d}x - \mathbf{f}_l^{\mathrm{T}}\, \delta\mathbf{p}_l = 0 \tag{38}$$

where $\hat{\mathbf{e}}(\delta\mathbf{d})$ is the vector of generalized section strains derived from the virtual displacement field $\delta\mathbf{d}$ via the compatibility Eq. (35); $\mathbf{f}_l = \begin{bmatrix} \overline{Q}_1 & \overline{Q}_2 & \overline{Q}_3 & \overline{Q}_4 & \overline{Q}_5 & \overline{Q}_6 & \overline{Q}_7 \end{bmatrix}^{\mathrm{T}}$ is the vector of end forces conjugated to the vector of local displacements $\mathbf{p}_l$ (see Fig. 1). Note that for simplicity's sake, the element distributed loads (body forces) are omitted in the above expression.

Eq. (38) is rewritten in the expanded form as

$$\int_L \left[\sum_{i=a,b} (N_i \delta u_i' + M_i\, \delta\theta_i' + T_i(\delta v' - \delta\theta_i)) + D_{sc}(\delta u_b - \delta u_a) \right] \mathrm{d}x - \mathbf{f}_l^{\mathrm{T}}\, \delta\mathbf{p}_l = 0 \tag{39}$$

Applying integration by parts, the above equation is rewritten as

$$\begin{aligned}
&\int_L \left[(N_a' + D_{sc})\delta u_a + (N_b' - D_{sc})\delta u_b + (M_a' + T_a)\delta\theta_a + (M_b' + T_b)\delta\theta_b + (T_a' + T_b')\delta v \right] \mathrm{d}x \\
&= \left[N_a\, \delta u_a + N_b\, \delta u_b + M_a\, \delta\theta_a + M_b\, \delta\theta_b + (T_a + T_b)\delta v \right]_0^L - \mathbf{f}_l^{\mathrm{T}}\, \delta\mathbf{p}_l
\end{aligned} \tag{40}$$

The above equation must be fulfilled for all kinematically admissible variations δu_i, δv and $\delta\theta_i$ $i(=a \text{ or } b)$ satisfying the essential boundary conditions $\delta u_a(0) = \delta v(0) = \delta v(L)$ resulting in the following equilibrium equations being obtained:

$$\left.\begin{aligned}
&N_a' + D_{sc} = 0 \\
&N_b' - D_{sc} = 0 \\
&M_a' + T_a = 0 \\
&M_b' + T_b = 0 \\
&T_a' + T_b' = 0
\end{aligned}\right\} \text{ in } [0, L] \tag{41}$$

with the following natural boundary conditions:

$$\begin{aligned}
&N_a(L) = \overline{Q}_1; \quad N_b(0) = -\overline{Q}_2; N_b(L) = \overline{Q}_3 \\
&M_a(0) = -\overline{Q}_4; \quad M_b(0) = -\overline{Q}_5; M_a(L) = \overline{Q}_6; \quad M_b(L) = \overline{Q}_7
\end{aligned} \tag{42}$$

4.3. Force interpolation functions

In a force-based FE formulation, the internal forces are expressed in term of end forces by using force interpolation functions. For the regular beam which is statically determinate, the force interpolation functions, obtained from equilibrium, represent the exact distribution of internal forces along the beam. However, the composite beam in partial interaction is internally indeterminate. This can be seen from the equilibrium equation (41) where there are only five equations for seven unknowns. The exact distribution of internal forces is indeed not available, except for some special cases with linear elastic behavior [25]. The number of compatibility conditions is equal to the degree of indeterminacy. However, in our case, the number of compatibility conditions is infinity because of continuous problem. Therefore, some approximations are required to overcome this indeterminacy. In the present formulation, the axial force N_b and the bending moment M_b are treated as redundant forces and are linearly interpolated. Moreover, N_b and M_b must satisfy the natural boundary conditions (42) thus they can be expressed as

$$\begin{aligned}
&N_b = \left(\frac{x}{L} - 1\right)\overline{Q}_2 + \frac{x}{L}\overline{Q}_3 \\
&M_b = \left(\frac{x}{L} - 1\right)\overline{Q}_5 + \frac{x}{L}\overline{Q}_7
\end{aligned} \tag{43}$$

Substituting these expressions into the equilibrium equation (41) and then applying the natural boundary conditions (42), one obtains a relation between internal forces $\mathbf{D}$ and end forces $\mathbf{p}_l$ which can be written in matrix form as

$$\mathbf{D} = \mathbf{b}\mathbf{p}_l \tag{44}$$

where

$$\mathbf{b} = \frac{1}{L}\begin{bmatrix}
L & L-x & L-x & 0 & 0 & 0 & 0 \\
0 & 0 & 0 & x-L & 0 & x & 0 \\
0 & 0 & 0 & -1 & 0 & -1 & 0 \\
0 & x-L & \frac{x}{L} & 0 & 0 & 0 & 0 \\
0 & 0 & 0 & 0 & x-L & 0 & x \\
0 & 0 & 0 & 0 & -1 & 0 & -1 \\
0 & -1 & -1 & 0 & 0 & 0 & 0
\end{bmatrix} \tag{45}$$

is the matrix of force interpolation functions. Note that in this approach the equilibrium equations are satisfied pointwise (strong form). This is in contrast to the displacement-based formulation where the equilibrium equations are satisfied in the average sense (weak form).

4.4. Section constitutive relations

The relation between internal forces $\mathbf{D}$ and generalized strains $\mathbf{e}$ depends on the material properties and the cross-section geometry of the beam. For two-layer beam in partial interaction

with nonlinear material behavior, this relation can be expressed in general form as

$$\mathbf{D} = \Omega(\mathbf{e}) \tag{46}$$

where Ω represents a general function that permits the computation of internal forces for given generalized strains. The linearization of Eq. (46) is obtained using the tangent section stiffness matrix which is given as

$$\mathbf{k}_t = \begin{bmatrix} \mathbf{k}_{a,t} & \mathbf{0} & 0 \\ \mathbf{0} & \mathbf{k}_{b,t} & 0 \\ 0 & 0 & k_{sc,t} \end{bmatrix} \tag{47}$$

where $k_{sc,t}$ is the tangent shear bond stiffness; $\mathbf{k}_{i,t}$ denotes the tangent section stiffness of layer $i(=a \text{ or } b)$, given as

$$\mathbf{k}_{i,t} = \begin{bmatrix} \int_{Ai} E_{i,t}\, \mathrm{d}A & -\int_{Ai} E_{i,t} y\, \mathrm{d}A & 0 \\ -\int_{Ai} E_{i,t} y\, \mathrm{d}A & \int_{Ai} E_{i,t} y^2\, \mathrm{d}A & 0 \\ 0 & 0 & \int_{Ai} k_i^s E_{i,t}\, \mathrm{d}A \end{bmatrix} \tag{48}$$

with

$$E_{i,t} = \frac{\partial \sigma_{i,xx}}{\partial \varepsilon_{i,xx}}$$

$$G_{i,t} = \frac{\partial \tau_{i,xy}}{\partial \gamma_{i,xy}}$$

and k_i^s is the shear factor that depends on the cross-section shape of layer i.

The section tangent flexibility matrix $\mathbf{f}_t$, necessary in the force-based formulation, is obtained by inverting the tangent section stiffness matrix $\mathbf{k}_t$. Finally, the linearized force–deformation relation for two-layer beam in partial interaction can be expressed as

$$\mathbf{e}^j \simeq \mathbf{e}^{j-1} + \Delta\mathbf{e}^j = \mathbf{e}^{j-1} + \mathbf{f}_t^{j-1}(\mathbf{D}^j - \hat{\mathbf{D}}^{j-1}) \tag{49}$$

where j denotes the element current Newton–Raphson state; $\hat{\mathbf{D}}^{j-1}$ denotes the section resisting forces obtained through the strain driven constitutive equations at the state $j-1$. In the present formulation, to evaluate the integrals of Eq. (48) for cross-sections with arbitrary geometry, they are subdivided into regions of regular shapes, over which the Gauss–Lobatto quadrature integration rule is employed. Note that this method is more accurate that the fiber method which usually uses the midpoint integration rule [37].

4.5. Weak form of compatibility equations

The weak form of the compatibility between the deformations derived from the implicit element displacements equation (35) and the corresponding deformations derived from the internal forces via the constitutive law equation (46) may be expressed as

$$\int_L \left\{ \sum_{i=a,b} \left[\delta N_i u_i' + \delta M_i \theta_i' + \delta T_i (v' - \theta_i)\right] + \delta D_{sc}(u_b - u_a) - \delta\mathbf{D}^{\mathrm{T}}\mathbf{e} \right\} \mathrm{d}x = 0 \tag{50}$$

where $\delta\mathbf{D} = [\,\delta N_a \;\; \delta M_a \;\; \delta T_a \;\; \delta N_b \;\; \delta M_b \;\; \delta T_b \;\; \delta D_{sc}\,]^{\mathrm{T}}$ are the weighting functions that satisfy the differential equations of equilibrium (41) and they are chosen as $\delta\mathbf{D} = \mathbf{b}\,\delta\mathbf{p}_l$ with $\mathbf{b}$ defined in Eq. (45).

Applying integration by parts and considering the kinematic boundary conditions, the above equation is rewritten as

$$\delta\mathbf{f}_l^{\mathrm{T}}\mathbf{p}_l = \int_L \delta\mathbf{D}^{\mathrm{T}}\mathbf{e}\, \mathrm{d}x + \int_L \begin{bmatrix} \delta N_a' + \delta D_{sc} \\ \delta N_b' - \delta D_{sc} \\ \delta M_a' + \delta T_a \\ \delta M_b' + \delta T_b \\ \delta T_a' + \delta T_b' \end{bmatrix}^{\mathrm{T}} \begin{bmatrix} u_a \\ u_b \\ \theta_a \\ \theta_b \\ v \end{bmatrix} \mathrm{d}x \tag{51}$$

This equation is satisfied for all statically admissible variations $\delta\mathbf{D}$. Therefore, the second term on the right hand side of Eq. (51) is equal to zero. Furthermore, substituting from Eq. (44) into Eq. (51), the following expression is obtained:

$$\delta\mathbf{f}_l^{\mathrm{T}}\mathbf{p}_l = \delta\mathbf{f}_l^{\mathrm{T}} \int_L \mathbf{b}^{\mathrm{T}}\mathbf{e}\, \mathrm{d}x \tag{52}$$

Since $\delta\mathbf{f}_l$ is a vector of arbitrary virtual forces, Eq. (52) must be valid for all values of $\delta\mathbf{f}_l$. Therefore, this equation may be simplified in the following form:

$$\mathbf{p}_l = \int_L \mathbf{b}^{\mathrm{T}}\mathbf{e}\, \mathrm{d}x \tag{53}$$

This equation, which represents element compatibility equations, allows for the determination of the element end displacements in term of section deformations along the element.

4.6. Linearization of the element compatibility equation

Using the linearized force–deformation relation (49) and Eq. (44), Eq. (53) can be expanded about the current element state j as follows:

$$\mathbf{F}_t^{j-1}\,\Delta\mathbf{f}_l^j = \Delta\mathbf{p}_l^j + \tilde{\mathbf{p}}_l^{j-1} \tag{54}$$

where

$$\mathbf{F}_t^{j-1} = \int_L \mathbf{b}^{\mathrm{T}}\mathbf{f}_t^{j-1}\mathbf{b}\, \mathrm{d}x \tag{55}$$

is the element tangent flexibility matrix; and

$$\tilde{\mathbf{p}}_l^{j-1} = \mathbf{p}_l^{j-1} - \int_L \mathbf{b}^{\mathrm{T}}(\mathbf{e}^{j-1} + \mathbf{f}_t^{j-1}(\mathbf{D}^{j-1} - \hat{\mathbf{D}}^{j-1}))\, \mathrm{d}x \tag{56}$$

represents the element nodal displacements due to the lack of compatibility at the element level.

In order to use the present formulation in the general co-rotational framework, the flexibility matrix $\mathbf{F}_t^{j-1}$ must be inverted to obtain the element stiffness matrix $\mathbf{K}_t^{j-1}$ at the end of the last iteration. As the present local formulation is derived for the element with rigid body modes therefore $\mathbf{F}_t^{j-1}$ can be directly inverted and Eq. (54) can be rewritten as

$$\mathbf{K}_t^{j-1}\,\Delta\mathbf{p}_l^j = \Delta\mathbf{f}_l^j - \tilde{\mathbf{f}}_l^{j-1} \tag{57}$$

where

$$\tilde{\mathbf{f}}_l^{j-1} = \left[\mathbf{F}_t^{j-1}\right]^{-1}\tilde{\mathbf{p}}_l^{j-1} = \mathbf{K}_t^{j-1}\tilde{\mathbf{p}}_l^{j-1} \tag{58}$$

4.7. Nonlinear state determination algorithm

In a standard displacement-based formulation, the state determination is a strain-driven process, i.e., the stresses are obtained from the strains which are computed from the element displacements through the deformation shape functions. This is a sharp contrast with force-based formulation where there are no interpolation functions to relate the section deformations to the deformation field inside the element to the end node displacements. Therefore, the state determination procedure for a force-based element is not straightforward and more complicated. In the present model, the state determination procedure

developed for regular beam/column developed by Spacone et al. [37] is employed and extended in large displacement. The nonlinear system of equations is iteratively solved by Newton–Raphson's method using three imbricated loops at different levels (structural level, element level and cross-section level).

5. Validation and numerical examples

5.1. A simply-supported composite beam

The main objective of this numerical example is to analyze the effect of geometrical nonlinearity on the beam deflection in the elastic range as well as in plastic range. To do so, we consider a simply-supported steel–concrete beam. The beam has a span length of 2800 mm loaded by a single concentrated force at mid-span. The steel section of the beam is IPE 330. The slab is 800 mm wide and 100 mm thick, longitudinally reinforced by 5 steel bars of 14 mm diameter at the mid-depth. The geometric characteristics and the material properties of the beam are shown in Fig. 3.

The von Mises plasticity model with combined isotropic and kinematic hardening is adopted for steel. An extensive description for formulation constitutive rate equations of this model can be found in [38,39]. As to the constitutive law of concrete, for the sake of simplicity it is assumed that the shear and tension/compression behaviors are uncoupled and therefore the 1D constitutive law is used. The elastic linear shear behavior is adopted while the 1D elasto-plastic model developed in [40] is used for concrete in tension/compression. The connection is modeled by an elastic-perfectly plastic model. Table 1 presents the constitutive model parameters which are used for the computer analysis. Note that, in this table, all symbols are defined in the corresponding cited references.

The numerical integrations over the layer cross-section are performed using 5 Gauss–Lobato points. The same number of the Gauss–Lobato point is used for the numerical integrations over the element length.

In order to assess the performance of the present force-based formulation, the results will be compared with the ones obtained with the classical displacement-based formulation (see [39]). Figs. 4 and 5 show the comparisons between the global load/deflection responses obtained by linear and nonlinear geometric analyses. For the sake of clarity in these figures, the following notations are used for the legends of the curves: E means element; D means the displacement-based model; F means the force-based model; ML means material linearity; MN means material nonlinearity; GL means geometric

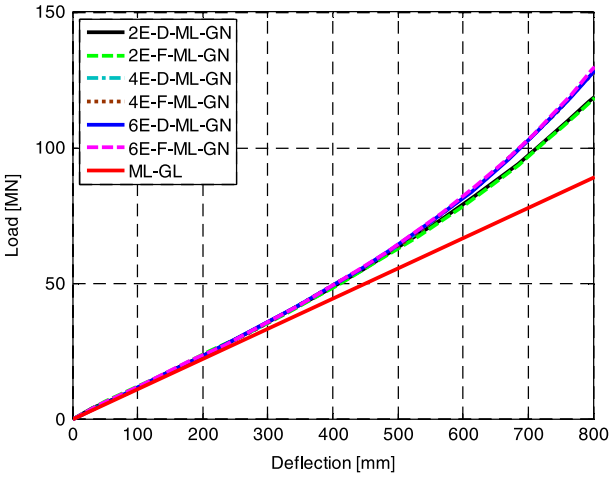

Fig. 4. Elastic load/deflection curves.

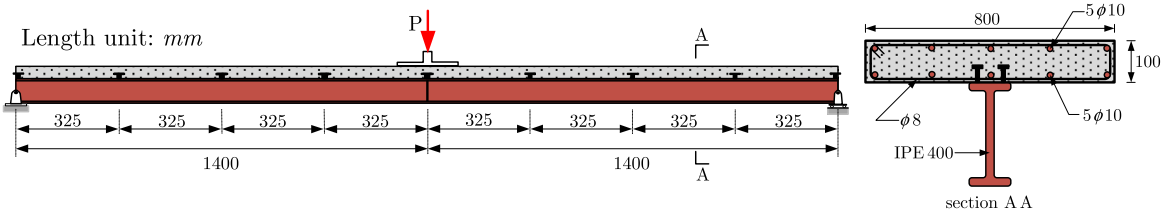

Fig. 3. Geometrical characteristics of studied simply-supported beam.

Table 1
Input values of the constitutive models utilized for computer analysis.

Steel model [38]						
f_y (MPa)	E (MPa)	υ	b	c(MPa)	k_1 (MPa)	k_2 (MPa)
300	200,000	0.3	0.26	2000	17,000	21

Concrete model [40]								
f_c(MPa)	E_c(MPa)	ε_c(%)	υ	G_{cl}(kN/m)	$l_{eq,c}$(mm)	f_t(MPa)	G_{ft}(N/m)	$l_{eq,t}$(mm)
34.7	31,200	2	0.2	30	100	3	60	35

Connector model	
D_y (N/m)	E_{sc}(MPa)
200	300

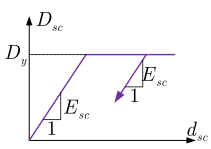

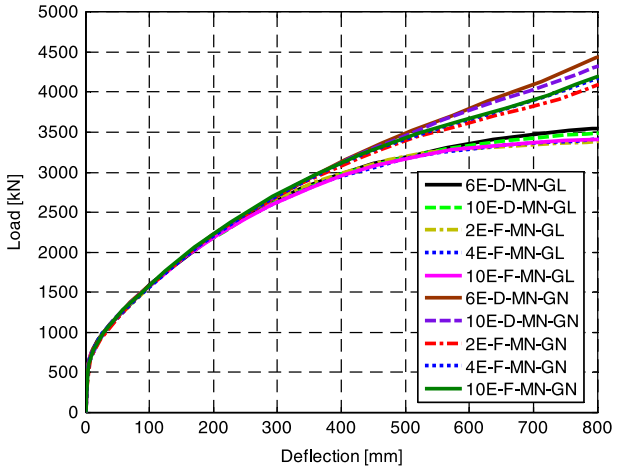

Fig. 5. Elasto-plastic load/deflection curves.

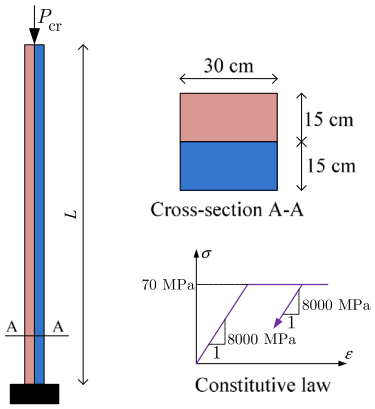

Fig. 6. Geometrical, material and loading data of the two-layer column.

linearity and GN means geometric nonlinearity. It can be observed from Fig. 4 that, the same number of element force-based and displacement-based models gives almost the same elastic load/deflection curves. This is to confirm the well-known conclusion that in elastic range the force and displacement approaches are equivalent because the force field is linearly related to displacement field. Regarding the geometrical nonlinearity, it starts to affect significantly the beam deflection as the deflection exceeds 400 mm (about $L/7$). For instance, we can observe that the deflection increases by about 100 mm (20%) at a load level of 50,000 kN. However, it can be seen from Fig. 5 that such beam behaves elastically up to a load equal to 500 kN. Therefore, the elastic deflection of the composite steel–concrete beam can be computed by neglecting the effect of geometrical nonlinearity.

In the case where all materials have an elasto-plastic behavior, load/deflection curves for different numbers of displacement-based and force-based elements are shown in Fig. 5. It is shown that a mesh of 4 force-based elements gives almost the same curve of the one of 10 force-based. It is to say that only 4 force-based elements are required to obtain the converged nonlinear response of the beam. However, 10 displacement-based elements do not give yet the converged solution. This is to say that when the material nonlinearity is considered, the force-based model produces a better global load/deflection response. The improved accuracy of the force-based solution is related to the fact that the equilibrium is satisfied in strict sense even in the plastic range. Furthermore, once again we can conclude from Fig. 5 that in this example the beam can be considered in large displacement when the deflection exceeds 14% beam length.

5.2. Buckling of a two-layer column

The buckling behavior of the two-layer column depicted in Fig. 6 is investigated. The column is clamped at one end and subjected to a compression force at the other end. For simplicity purposes, the layers are made from the same material and they have the same cross-section dimension as indicated in Fig. 6. An elastic perfectly plastic behavior is assumed for each layer.

Due to the geometric and material nonlinearities, the finite element problem is numerically solved in an incremental way. A specific technique is implemented within this numerical procedure, following [41], in order to detect the bifurcation points along the fundamental equilibrium path. At the end of each increment, it must be checked whether one has gone across one or several critical points. The detection of critical points is based on the singularity of the tangent stiffness matrix, which may be factorized following the Crout formula $\mathbf{K}_g = \mathbf{LdL}^T$, where $\mathbf{L}$ is a lower triangular matrix with unit diagonal elements and $\mathbf{d}$ is a diagonal matrix. Since the number of negative eigenvalues of $\mathbf{K}_g$ is equal to the number of negative diagonal elements (pivots) of $\mathbf{d}$, the critical points are determined by counting the negative pivot number and comparing its value between the successive increments.

5.2.1. Elastic buckling

The elastic buckling force of the two-layer column is now investigated. The material parameters used for the calculation are: $E = 8000$ MPa and $G = 3200$ MPa. For this numerical example, the column length of 1 m is considered. In order to access the accuracy of the present FE model, the numerical buckling load, computed with 10 and 100 elements will be compared with the analytical solution developed by Le Grocgnec et al. [30] for three values of connection stiffness: $k_{sc} = 1$ MPa (no bond); $k_{sc} = 1000$ MPa; $k_{sc} = 1,000,000$ MPa (perfect bond). The results are given in Table 2. It can be seen that with 10 elements the relative error in buckling load is about 2.68% in the case of no bond and goes down to 1.95% in the case of perfect bond. These relative differences are significantly improved with a mesh of 100 elements. The proposed model is thus accurate in predicting the buckling load of composite column in partial interaction taking into account the shear flexibility of the layers.

5.2.2. Elastoplastic buckling

The influence of the material nonlinearity on the critical buckling load of the two-layer column depicted in Fig. 6 is now investigated. For the sake of simplicity it is assumed that the shear behavior is linear elastic given by $\tau = G\gamma$ while the tension/compression behavior is elastic perfectly plastic as shown in Fig. 6. The constitutive law of connection is taken to be linear. Fig. 7 displays the evolution of the ratio elastoplastic buckling load and plastic load versus the slenderness of the column for different values of connection stiffness. The plastic load is defined as $P_{pl} = (A_a + A_b)\sigma_y$ where $\sigma_y = 70$ MPa being the yield strength. The slenderness of the column is defined as $\lambda = L\sqrt{A/I}$ where $A = A_a + A_b$ is the total area and $I = I_a + I_b$ is the total inertia moment of the cross-section with respect to its centroid. It can be observed that for the slenderness smaller than 30 and for any value of connection stiffness the column bucks after reaching the yield strength of the cross-section. As an elastic perfectly plastic model was adopted for the material law, the buckling load is thus equal to the plastic load. Furthermore, it clearly appears that for the slenderness greater than 30 buckling load the buckling load hardly depends on the connection stiffness. For instant, with a slenderness of 60 the buckling load decreases about 68% from no bond to perfect bond.

Table 2
Comparison of elastic buckling load between the present numerical model and analytical solution.

k_{sc}[MPa]	$P_{cr}^{analytical}$[kN]	$P_{cr}^{numerical}$ [kN] (relative error [%])	
		10 elements	100 elements
1	3307	3396 (2.68%)	3338 (0.94%)
1000	9831	10,040 (2.13%)	9901 (0.71%)
1,000,000	12,619	12,865 (1.95%)	12,698 (0.63%)

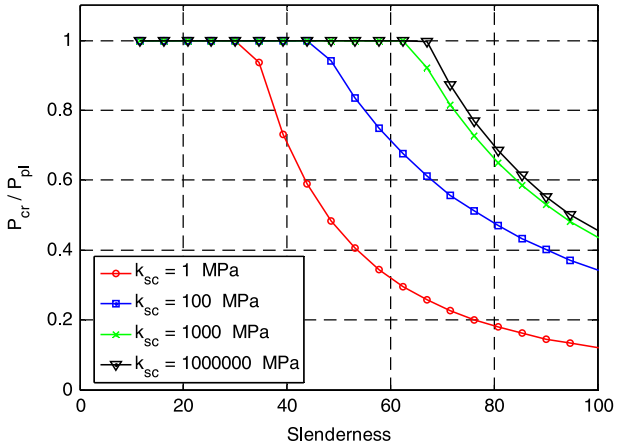

Fig. 7. Elastoplastic buckling load versus slenderness for different connection stiffnesses.

6. Conclusion

In this paper, novel geometric nonlinear FE formulation for the analysis of two-layer beams/columns with interlayer slips has been derived. A co-rotational description has been adopted and the element is obtained using rather simple transformation matrices between local and global quantities where the local quantities are derived using a geometrical linear formulation. The main advantage of the present approach is that the transformation matrices between local and global quantities are independent to the choice on the local linear element. This means that, using the present co-rotational framework, different geometrical linear elements can be easily transformed into nonlinear ones. The local element has been derived using force-based formulation. The effect of transverse shear of cross-sections was taken into account using Timoshenko's beam theory. Two numerical examples have been carried out in order to validate and investigate the performance of the proposed FE model. It has been shown that our results are in good agreement with the ones obtained with the existing displacement-based FE model in terms of the load/deflection curve of composite beam and with the analytical model in terms of elastic buckling load of composite column. The numerical results showed that in the case of full material and geometrical linearities the force-based element performed better the load/deflection response than the classical displacement-based element. Furthermore, it has been seen that the connection stiffness plays a very important role on the elasto-plastic buckling load of slender columns.

References

[1] N.M. Newmark, C.P. Siess, I.M. Viest, Tests and analysis of composite beams with incomplete interaction, Proc. Soc. Exp. Stress Anal. 8 (1) (1951) 75–92.
[2] M. Heinisuo, An exact finite element technique for layered beams, Comput. Struct. 30 (3) (1988) 615–622.
[3] U. Girhammar, V. Gopu, Composite beam–columns with interlayer slip – exact analysis, J. Struct. Eng. 119 (4) (1993) 1265–1282.
[4] C. Faella, E. Martinelli, E. Nigro, Steel and concrete composite beams with flexible shear connection: "exact" analytical expression of the stiffness matrix and applications, Comput. Struct. 80 (11) (2002) 1001–1009.
[5] Y.F. Wu, D.J. Oehlers, M.C. Griffith, Partial-interaction analysis of composite beam/column members, Mech. Struct. Mach. 30 (3) (2002) 309–332.
[6] G. Ranzi, M.A. Bradford, B. Uy, A direct stiffness analysis of a composite beam with partial interaction, Int. J. Numer. Methods Eng. 61 (5) (2004) 657–672.
[7] U.A. Girhammar, D.H. Pan, Exact static analysis of partially composite beams and beam-columns, Int. J. Mech. Sci. 49 (2) (2007) 239–255.
[8] D. Oehlers, M.A. Bradford, Composite steel and concrete structural members: fundamental behaviourElsevier, Oxford: Pergamon, 1995.
[9] G. Ranzi, M.A. Bradford, Analytical solutions for the time-dependent behaviour of composite beams with partial interaction, Int. J. Solids Struct. 43 (13) (2006) 3770–3793.
[10] B. Jurkiewiez, S. Buzon, J.G. Sieffert, Incremental viscoelastic analysis of composite beams with partial interaction, Comput. Struct. 83 (21–22) (2005) 1780–1791.
[11] Q.-H. Nguyen, M. Hjiaj, B. Uy, Time-dependent analysis of composite beams with continuous shear connection based on a space-exact stiffness matrix, Eng. Struct. 32 (9) (2010) 2902–2911.
[12] Q.-H. Nguyen, M. Hjiaj, J.-M. Aribert, A space-exact beam element for time-dependent analysis of composite members with discrete shear connection, J. Constr. Steel Res. 66 (11) (2010) 1330–1338.
[13] M.R. Salari, S. Enrico, P.B. Shing, M.F. Dan, Nonlinear analysis of composite beams with deformable shear connectors, J. Struct. Eng. 124 (10) (1998) 1148–1158.
[14] M. Salari, E. Spacone, Analysis of steel–concrete composite frames with bond-slip, J. Struct. Eng. 127 (11) (2001) 1243–1250.
[15] A. Ayoub, F. Filippou, Mixed formulation of nonlinear steel–concrete composite beam element, J. Struct. Eng. 126 (3) (2000) 371–381.
[16] A. Ayoub, A force-based model for composite steel–concrete beams with partial interaction, J. Constr. Steel Res. 61 (3) (2005) 387–414.
[17] Q.H. Nguyen, M. Hjiaj, B. Uy, S. Guezouli, Analysis of composite beams in the hogging moment regions using a mixed finite element formulation, J. Constr. Steel Res. 65 (3) (2009) 737–748.
[18] J.-M. Battini, Q.-H. Nguyen, M. Hjiaj, Non-linear finite element analysis of composite beams with interlayer slips, Comput. Struct. 87 (13–14) (2009) 904–912.
[19] M. Hjiaj, J.-M. Battini, Q.-H. Nguyen, Large displacement analysis of shear deformable composite beams with interlayer slips, Int. J. Non-linear Mech. 47 (8) (2012) 895–904.
[20] G. Ranzi, A. Dall'Asta, L. Ragni, A. Zona, A geometric nonlinear model for composite beams with partial interaction, Eng. Struct. 32 (5) (2010) 1384–1396.
[21] H. Murakami, A laminated beam theory with interlayer slip, J. Appl. Mech. 51 (3) (1984) 551–559.
[22] G. Ranzi, A. Zona, A steel–concrete composite beam model with partial interaction including the shear deformability of the steel component, Eng. Struct. 29 (11) (2007) 3026–3041.
[23] S. Schnabl, M. Saje, G. Turk, I. Planinc, Locking-free two-layer Timoshenko beam element with interlayer slip, Finite Elem. Anal. Des. 43 (9) (2007) 705–714.
[24] S. Schnabl, M. Saje, G. Turk, I. Planinc, Analytical solution of two-layer beam taking into account interlayer slip and shear deformation, J. Struct. Eng. 133 (6) (2007) 886–894.
[25] Q.-H. Nguyen, E. Martinelli, M. Hjiaj, Derivation of the exact stiffness matrix for a two-layer Timoshenko beam element with partial interaction, Eng. Struct. 33 (2) (2011) 298–307.
[26] E. Martinelli, Q.H. Nguyen, M. Hjiaj, Dimensionless formulation and comparative study of analytical models for composite beams in partial interaction, J. Constr. Steel Res. 75 (0) (2012) 21–31.
[27] Q.-H. Nguyen, M. Hjiaj, P. Le Grognec, Analytical approach for free vibration analysis of two-layer Timoshenko beams with interlayer slip, J. Sound Vib. 331 (12) (2012) 2949–2961.
[28] S. Schnabl, I. Planinc, The influence of boundary conditions and axial deformability on buckling behavior of two-layer composite columns with interlayer slip, Eng. Struct. 32 (10) (2010) 3103–3111.
[29] S. Schnabl, I. Planinc, The effect of transverse shear deformation on the buckling of two-layer composite columns with interlayer slip, Int. J. Non-linear Mech. 46 (3) (2011) 543–553.
[30] P. Le Grognec, Q.-H. Nguyen, M. Hjiaj, Exact buckling solution for two-layer Timoshenko beams with interlayer slip, Int. J. Solids Struct. 49 (1) (2012) 143–150.
[31] P. Krawczyk, B. Rebora, Large deflections of laminated beams with interlayer slips: Part 2: finite element development, Eng. Comput. 24 (1) (2007) 33–51.
[32] B. Čas, M. Saje, I. Planinc, Non-linear finite element analysis of composite planar frames with an interlayer slip, Comput. Struct. 82 (23–26) (2004) 1901–1912.
[33] A. Zona, G. Ranzi, Finite element models for nonlinear analysis of steel–concrete composite beams with partial interaction in combined bending and shear, Finite Elem. Anal. Des. 47 (2) (2011) 98–118.
[34] B. Cas, M. Saje, I. Planinc, Buckling of layered wood columns, Adv. Eng. Softw. 38 (8–9) (2007) 586–597.

[35] Q.-H. Nguyen, M. Hjiaj, S. Guezouli, Exact finite element model for shear-deformable two-layer beams with discrete shear connection, Finite Elem. Anal. Des. 47 (7) (2011) 718–727.
[36] T. Hozjan, M. Saje, S. Srpčič, I. Planinc, Geometrically and materially non-linear analysis of planar composite structures with an interlayer slip, Comput. Struct. 114–115 (0) (2013) 1–17.
[37] E. Spacone, F.C. Filippou, F.F. Taucer, Fiber beam–column model for nonlinear analysis of R/C frames. Part I: formulation, Earthq. Eng. Struct. Dyn. 25 (7) (1996) 711–742.
[38] R. Mahnken, Improved implementation of an algorithm for non-linear isotropic/kinematic hardening in elastoplasticity, Commun. Numerical Methods Eng. 15 (10) (1999) 745–754.
[39] V.A. Lai, Nonlinear analysis of steel–concrete beams taking into account the shear deformability of the steel joist, in: Proceedings of the GCU2012, INSA of Rennes.
[40] Q.-H. Nguyen, Modélisation numérique du comportement des poutres mixtes acier-béton, in Génie CivilInstitut National des Sciences Appliquées des Rennes: Rennes, France, 2008.
[41] E. Riks, An incremental approach to the solution of snapping and buckling problems, Int. J. Solids Struct. 15 (7) (1979) 529–551.

ANNEXE 3

P. Keo, **Q-H. Nguyen**, H. Somja and M. Hjiaj. Geometrically nonlinear analysis of hybrid beam-column with several encased steel profiles in partial interaction. *Engineering Structures* 2015. 100 :66-78. (5-Year IF 2.152) http://dx.doi.org/10.1016/j.engstruct.2015.05.030.

Engineering Structures 100 (2015) 66–78

Contents lists available at ScienceDirect

Engineering Structures

journal homepage: www.elsevier.com/locate/engstruct

Geometrically nonlinear analysis of hybrid beam–column with several encased steel profiles in partial interaction

Pisey Keo, Quang-Huy Nguyen, Hugues Somja, Mohammed Hjiaj *

Université Européenne de Bretagne – INSA de Rennes, LGCGM/ Structural Engineering Research Group, 20 avenue des Buttes de Coësmes, CS 70839, F-35708 Rennes Cedex 7, France

ARTICLE INFO

Article history:
Received 4 November 2014
Revised 13 May 2015
Accepted 19 May 2015
Available online 12 June 2015

Keywords:
Co-rotational method
Finite elements
Hybrid beam
Interlayer slips

ABSTRACT

This article presents a new co-rotational finite element for the large displacement analysis of hybrid steel–concrete beam/column with several encased steel profiles. The advantage of using the co-rotational approach is that the geometrical linear finite element formulation can be reused and automatically be transformed into geometrical nonlinear formulation. The exact stiffness matrix derived from the analytical solution of the governing equations for hybrid beam with longitudinal partial interaction is used for the local formulation. As a result, internal nodes used to avoid curvature locking encountered in low order polynomial finite elements are not required. Finally, five numerical applications are presented in order to illustrate the performance of the proposed formulation.

1. Introduction

The driving force behind employing hybrid/mixed systems is to combine the best attributes of steel and concrete to improve structural performance, erection time, economy of construction and occupant satisfaction in a way that might not be possible using only one of the materials and its associated construction techniques. The advantages of Steel Reinforced Concrete (SRC) constructions over Reinforced Concrete (RC) constructions are: greater ductility, more compact cross-section, reduced creep deformation, and faster concrete casting [1]. Those over Steel construction are: multiple roles of concrete as structural, fireproofing and buckling-restraining elements, higher stiffness, and greater damping. To make more effective use of floor areas of high rise concrete buildings, especially in the lower storeys, the number of columns need to be as minimum as possible and their cross-section dimensions should be kept as small as possible. These lower-storey columns are heavily loaded and require well-detailed concentrated reinforcement to develop the necessary stiffness and buckling resistance. This often results in congestion in these heavily reinforced members, resulting in laborious construction. To achieve strength and stiffness whilst keeping the same column size over the floors for aesthetic considerations, the use of high strength construction materials is an option. The main disadvantage is the material cost and in some situations (very heavily loaded structures) it is no longer an effective solution and other alternative must be found. The use of Steel Reinforced Concrete columns with multiple steel shapes (hybrid columns) seems to be a viable alternative considering the flexibility that one has in designing such member. The overall behavior of such member strongly depends on the stress transfer mechanism between the steel and the concrete encasement which may be accomplished by either bond, shear connectors or plate bearings. On the other hand, the detailing in transition zones between classical reinforced concrete and composite must be carefully carried out to avoid damage due to curved stress flows. To investigate the nonlinear behavior of hybrid columns with multiple embedded steel profiles, a geometrically nonlinear multi-layered beam/column element with partial interaction is developed. The development of formulation is based on the extension of previous works on the behavior of composite beam with interlayer slip. Most of the work on composite beam with partial interaction is restricted to the case of two layers (see for among others [2–18]) and multi-layered beams have received less attention. Ranzi [19] proposed two types of displacement-based elements to evaluate locking problems in partial interaction of multi-layered beams based on Euler–Bernoulli kinematics. For classical polynomial shape functions, it is shown that the element with an internal node describing the axial displacement of the layer, well characterizes the partial interaction behavior of multi-layered beam while the element without internal node suffers from the curvature locking problems. Sousa [20] developed the analytical formulation and derived the exact stiffness for partially connected multi-layered composite beams.

In contrast with the large body of literature devoted to materially nonlinear but geometrical linear problems of two-layered

* Corresponding author.
E-mail address: mohammed.hjiaj@insa-rennes.fr (M. Hjiaj).

http://dx.doi.org/10.1016/j.engstruct.2015.05.030
0141-0296/

beam/columns in partial interaction, only a limited number of contributions have addressed the geometrically nonlinear behavior of layered beams. Assuming Euler–Bernoulli kinematics for each layer, linearized buckling loads have been computed by Girhammar and Gopu [5] using a modified second-order theory for two-layered beams with longitudinal slips. Hereafter, Girhammar and Pan [6] derived the exact expressions for buckling length coefficients of elastic composite beams with particular boundary conditions. A fully nonlinear analysis of steel–concrete composite beams and columns has been proposed by Pi et al. [21] considering Bernoulli kinematics for each layer. They proposed a monolithic element where an additional degree of freedom to the deformed beam axis was added in order to describe small interlayer slips was considered. Ranzi et al. [22] have proposed a fully nonlinear kinematical model for planar composite beams including longitudinal partial interaction as well as vertical uplift. The co-rotational framework approach was considered by Battini et al. [23] and Hjiaj et al. [24] for the development of shear rigid [23] and shear deformable [24] beam–column element using the exact local elastic stiffness matrix. Sousa et al. [25] developed a materially nonlinear displacement-based finite element model based on a total Lagrangian description considering large displacements, small strains and moderate rotations. A large displacement FE model for two-layer beam/column based on shear-rigid Reissner beam theory has been proposed by Hozjan et al. [26]. This model takes into account the exact geometrical and material nonlinearities as well as finite slip between the layers. Recently, Nguyen et al. [27] have presented a novel finite element model for the fully material and geometrical nonlinear analysis of shear-deformable two-layer composite planar beams with interlayer slips using the co-rotational approach.

This paper aims to present a new nonlinear finite element formulation for the large displacement analysis of hybrid planar beam/column with several encased steel profiles taking into account the slips occurring at each steel–concrete interface. The co-rotational framework is adopted and the motion of the element is decomposed into rigid body motion and a deformational part using a local co-rotational frame, which continuously translates and rotates with the element, but does not deform with it [28]. In comparison with the total and the updated Lagrangian formulations, a co-rotational element formulation has several relative advantages: (1) the co-rotational formulation is accurate and has good convergence properties for problems with large displacements and large rotations but small strains and (2) the treatment of geometric nonlinearity is effectively undertaken at the level of discrete nodal variables with the transformation matrix between the local and global nodal entities being independent of the assumptions made for the local element. Thus many existing high-performance elements can be reused at the core of a co-rotational element formulation, and the resulting formulation can be employed to solve large displacement and large rotation problems.

In the present work, the exact stiffness matrix derived from the analytical solution of the governing equations for hybrid beam with interlayer slips is used for the local formulation. As a result, internal nodes used to avoid curvature locking encountered in low order polynomial finite elements are not required. Therefore, this formulation is consistent with the co-rotational format. The features of the formulation presented in this paper are as follows: (i) longitudinal partial interactions of the layers are considered which provide a general description of the stresses and strains in the layers; (ii) the small strain and large rotation formulation is developed which is an accurate representation of most structural behavior; and (iii) exact local stiffness matrix are used which provide accurate and stable results. The present model provides, therefore, an efficient tool for elastic nonlinear buckling analysis of hybrid beam–column with arbitrary support and loading conditions.

The rest of the paper is organized as follows. Section 2 deals with the co-rotational framework, the derivation of the transformation matrices and issues related to eccentric nodes and forces. In Section 3, the local formulation is presented. Five numerical examples are analyzed in Section 4 in order to assess the performance of the formulation and support the conclusions drawn in Section 5.

2. Co-rotational framework

We consider a hybrid beam with n embedded layers experiencing arbitrarily large displacement and rotations with respect to the global frame but strains are assumed to remain small. The main ingredients of a co-rotational formulation are: (i) the choice of co-rotating frame, (ii) the derivation of the relationships between the local variables and the global ones, and (iii) a variationally consistent internal force vector and the tangent stiffness matrix.

2.1. Beam kinematics

The co-rotational description of the motion of a deformable body find its roots in the polar decomposition theorem [29] which states that the total deformation of a continuous body can be decomposed into a rigid body motion and pure deformations. In finite element implementations, this decomposition is performed by defining a local reference system attached to the element, which translates and rotates with the element, but does not deform with it. With respect to the moving frame, local deformational displacements are defined and the geometrical nonlinearity induced by element large rigid-body motion is incorporated into the transformation matrix relating local and global displacements.

The origin of the co-rotational frame is taken at the node c_i which corresponds to the centroid of the concrete cross-section. The x_l-axis of the local coordinate system is defined by the line connecting c_i and c_j. The y_l-axis is orthogonal to the x_l-axis so that the result is right handed orthogonal coordinate system. The motion of the element from the original undeformed configuration to the actual deformed one can thus be separated into two parts. The first one, which corresponds to the rigid motion of the local frame, is the translation of the node c_i and the rigid rotation α of the x_l-axis. The second one refers to the deformations in the co-rotational element frame which remain small with respect to local frame. The strains and element internal nodal forces are calculated from these relative deformations. As a consequence, the linear beam theory defined in Section 3 can be used for describing the relative deformations, endowing the method with significant advantages in computational speed and programming simplicity.

The notations used in this section are defined in Figs. 1 and 2. All variables subscripted with "s_k" belong to the embedded steel element "s_k" and those with "c" belong to the surrounding concrete component. The coordinates of the nodes c_i and c_j in the global coordinate system (x, y) are (x_{c_i}, y_{c_i}) and (x_{c_j}, y_{c_j}), respectively. The element has $2(n+3)$ degrees of freedom: global displacements and rotations of the nodes (c_i and c_j) and slips (g_{ki}, g_{kj}) between the embedded steels "s_k" and the surrounding concrete component "c" at both ends of the element. As the steel elements are surrounded by the concrete component, uplift cannot occur. Thus, the rotations of each constituent at the end nodes are equal (Bernoulli's assumption) and the slips (g_{ki}, g_{kj}) are perpendicular to the end cross-sections.

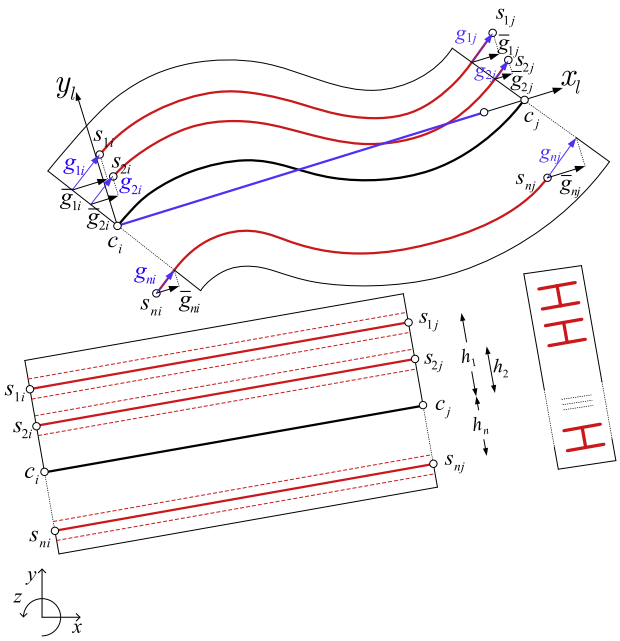

Fig. 1. Co-rotational kinematic: slips.

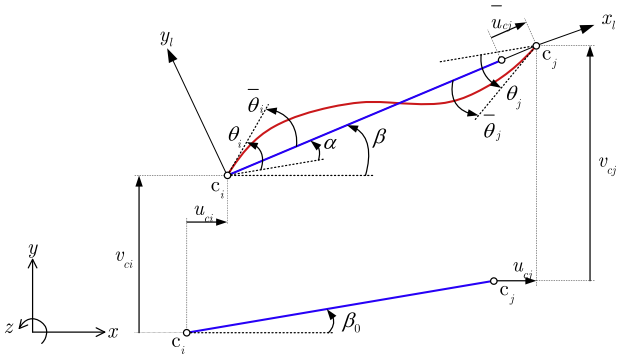

Fig. 2. Co-rotational kinematic: displacement and rotations.

The vectors of global and local displacements are respectively defined by Eqs. (1) and (2)

$$\mathbf{p}_g = \left[u_{ci}\ \ v_{ci}\ \ \theta_i\ \ g_{1i}\ \ g_{2i}\ \ \cdots\ \ g_{ni}\ \ u_{cj}\ \ v_{cj}\ \ \theta_j\ \ g_{1j}\ \ g_{2j}\ \ \cdots\ \ g_{nj}\right]^{\mathrm{T}} \tag{1}$$

$$\mathbf{p}_l = \left[\bar{u}_{s1i}\ \ \bar{u}_{s2i}\ \ \cdots\ \ \bar{u}_{sni}\ \ \bar{u}_{ci}\ \ \bar{v}_i\ \ \bar{\theta}_i\ \ \bar{u}_{s1j}\ \ \bar{u}_{s2j}\ \ \cdots\ \ \bar{u}_{snj}\ \ \bar{u}_{cj}\ \ \bar{v}_j\ \ \bar{\theta}_j\right]^{\mathrm{T}} \tag{2}$$

The rigid rotation of the x_l-axis, α is obtained using the geometrical relation:

$$\sin\alpha = c_o\, s - s_o\, c \tag{3}$$

$$\cos\alpha = c_o\, c + s_o\, s \tag{4}$$

with

$$c_o = \cos\beta_o = \frac{1}{l_o}(x_{cj} - x_{ci}) \tag{5}$$

$$s_o = \sin\beta_o = \frac{1}{l_o}(y_{cj} - y_{ci}) \tag{6}$$

$$c = \cos\beta = \frac{1}{l_n}(x_{cj} + u_{cj} - x_{ci} - u_{ci}) \tag{7}$$

$$s = \sin\beta = \frac{1}{l_n}(y_{cj} + v_{cj} - y_{ci} - v_{ci}) \tag{8}$$

l_o and l_n being the element length in initial and deformed configuration, respectively:

$$l_o = \left[(x_{cj} - x_{ci})^2 + (y_{cj} - y_{ci})^2\right]^{1/2} \tag{9}$$

$$l_n = \left[(x_{cj} + u_{cj} - x_{ci} - u_{ci})^2 + (y_{cj} + v_{cj} - y_{ci} - v_{ci})^2\right]^{1/2} \tag{10}$$

Based on the definition of the co-rotating frame, the components of the local displacements $\mathbf{p}_l$ are computed according to:

$$\bar{u}_{ci} = 0 \tag{11}$$

$$\bar{v}_i = 0 \tag{12}$$

$$\bar{v}_j = 0 \tag{13}$$

$$\bar{u}_{cj} = l_n - l_o \tag{14}$$

$$\bar{\theta}_i = \theta_i - \alpha \tag{15}$$

$$\bar{\theta}_j = \theta_j - \alpha \tag{16}$$

$$\bar{u}_{ski} = -\bar{g}_{ki} - h_k\,\bar{\theta}_i \tag{17}$$

$$\bar{u}_{skj} = -\bar{g}_{kj} + \bar{u}_{cj} - h_k\,\bar{\theta}_j \tag{18}$$

where local slips $\bar{g}_{kl}$ are defined in local element formulation (see Section 3) and determined by

$$\bar{g}_{kl} = g_{kl}\cos\bar{\theta}_l, \quad l = i,j; \quad k = 1,2,\ldots,n \tag{19}$$

2.2. Element formulation

A key step in the co-rotational method is to establish the relationship that relates the local variables to the global ones. This is accomplished by performing a change of variables, in three steps, between the global quantities and the local ones. The second stage is to remove the rigid body motions from the element displacement field which is achieved by calculating the local displacements using Eqs. (11)–(19).

Let us consider two different coordinate systems with subscript i and j. Assume that the internal force vector $\mathbf{f}_i$ and tangent stiffness matrix $\mathbf{K}_i$ are consistent with the displacement vector $\mathbf{p}_i$ such that

$$\delta\mathbf{f}_i = \mathbf{K}_i\,\delta\mathbf{p}_i \tag{20}$$

Consider now that $\mathbf{p}_i$ is related to the displacement vector $\mathbf{p}_j$ through

$$\delta\mathbf{p}_i = \mathbf{B}_{ij}\,\delta\mathbf{p}_j \tag{21}$$

Then, by equating the virtual work in both systems, the internal force vector $\mathbf{f}_j$ consistent with $\mathbf{p}_j$ is defined by

$$\mathbf{f}_j = \mathbf{B}_{ij}^{\mathrm{T}}\mathbf{f}_i \tag{22}$$

The expression of the tangent stiffness matrix $\mathbf{K}_j$, consistent with $\mathbf{p}_j$ is obtained by differentiating Eq. (22) and combining the outcome with Eqs. (20) and (21):

$$\mathbf{K}_j = \mathbf{B}_{ij}^{\mathrm{T}}\mathbf{K}_i\mathbf{B}_{ij} + \mathbf{H}_{ij} \quad \mathbf{H}_{ij} = \left.\frac{\partial(\mathbf{B}_{ij}^{\mathrm{T}}\mathbf{f}_i)}{\partial\mathbf{p}_j}\right|_{\mathbf{f}_i} \tag{23}$$

From the idea described above, the element formulation can be obtained using three successive changes of variables and four different displacement vectors:

$$\mathbf{p}_l = \left[\bar{u}_{s1i}\ \ \bar{u}_{s2i}\ \ \cdots\ \ \bar{u}_{sni}\ \ \bar{u}_{ci}\ \ \bar{v}_i\ \ \bar{\theta}_i\ \ \bar{u}_{s1j}\ \ \bar{u}_{s2j}\ \ \cdots\ \ \bar{u}_{snj}\ \ \bar{u}_{cj}\ \ \bar{v}_j\ \ \bar{\theta}_j\right]^{\mathrm{T}} \tag{24}$$

$$\mathbf{p}_e = \left[\bar{u}_{cj}\ \ \bar{\theta}_i\ \ \bar{\theta}_j\ \ \bar{g}_{1i}\ \ \bar{g}_{2i}\ \ \cdots\ \ \bar{g}_{ni}\ \ \bar{g}_{1j}\ \ \bar{g}_{2j}\ \ \cdots\ \ \bar{g}_{nj}\right]^{\mathrm{T}} \tag{25}$$

$$\mathbf{p}_a = \left[\bar{u}_{cj}\ \ \bar{\theta}_i\ \ \bar{\theta}_j\ \ g_{1i}\ \ g_{2i}\ \ \cdots\ \ g_{ni}\ \ g_{1j}\ \ g_{2j}\ \ \cdots\ \ g_{nj}\right]^{\mathrm{T}} \tag{26}$$

$$\mathbf{p}_g = [\,u_{ci} \;\; v_{ci} \;\; \theta_i \;\; g_{1i} \;\; g_{2i} \;\; \cdots \;\; g_{ni} \;\; u_{cj} \;\; v_{cj} \;\; \theta_j \;\; g_{1j} \;\; g_{2j} \;\; \cdots \;\; g_{nj}\,]^{\mathrm{T}} \tag{27}$$

The first change of variables between $\mathbf{p}_l$ and $\mathbf{p}_e$ is based on the linear equations (Eqs. (11)–(13), (17) and (18)). Then, the transformation matrices giving $\mathbf{f}_e$ and $\mathbf{K}_e$ as function of $\mathbf{f}_l$ and $\mathbf{K}_l$ are easily obtained. For the second change of variables from $\mathbf{p}_e$ to $\mathbf{p}_a$, the transformation matrices giving $\mathbf{f}_a$ and $\mathbf{K}_a$ as function of $\mathbf{f}_e$ and $\mathbf{K}_e$ are derived using Eq. (19). The third change of variables from $\mathbf{p}_a$ to $\mathbf{p}_g$ is performed using Eqs. (14)–(16). After some algebraic manipulations (see e.g. [28]), the transformation matrices giving $\mathbf{f}_g$ and $\mathbf{K}_g$ as function of $\mathbf{f}_a$ and $\mathbf{K}_a$ are obtained. The transformation matrices are given in Appendix A.

2.3. Eccentric nodes and forces

The boundary conditions for composite and hybrid beams may be complicated to define and depend strongly on how the member is connected to the rest of the structures. In general, one could distribute the external load among the different constituent according to some rules among which, the relative stiffness. This would lead to the same axial displacement of each constituent at the beginning of the load step. Another option is to assume no slip at the beam end and the load is applied at an arbitrary point within the cross-section. This section presents the possibility to deal with those options in the proposed formulation.

The choice of the slips as the degrees of freedom is indispensable for the robustness of the formulation. Due to this choice (see Eq. (1)) the boundary conditions require a special treatment in case external concentrated loads are not applied to the node located at the centroid of the beam cross-section (origin of the local frame) but somewhere else on the cross-section.

2.3.1. Eccentric nodes

Let us first consider (see Fig. 3) that prescribed displacement or rotation are applied at node m_i. This situation requires a rigid link between the nodes c_i and m_i and a change of degrees of freedom from $\mathbf{p}_g$ to $\mathbf{p}_{\mathrm{m}}$ with

$$\mathbf{p}_g = [\,u_{\mathrm{ci}} \;\; v_{\mathrm{ci}} \;\; \theta_i \;\; g_{1i} \;\; g_{2i} \;\; \cdots \;\; g_{ni} \;\; u_{cj} \;\; v_{cj} \;\; \theta_j \;\; g_{1j} \;\; g_{2j} \;\; \cdots \;\; g_{nj}\,]^{\mathrm{T}} \tag{28}$$

$$\mathbf{p}_m = [\,u_{\mathrm{mi}} \;\; v_{\mathrm{mi}} \;\; \theta_i \;\; g_{1i} \;\; g_{2i} \;\; \cdots \;\; g_{ni} \;\; u_{cj} \;\; v_{cj} \;\; \theta_j \;\; g_{1j} \;\; g_{2j} \;\; \cdots \;\; g_{nj}\,]^{\mathrm{T}} \tag{29}$$

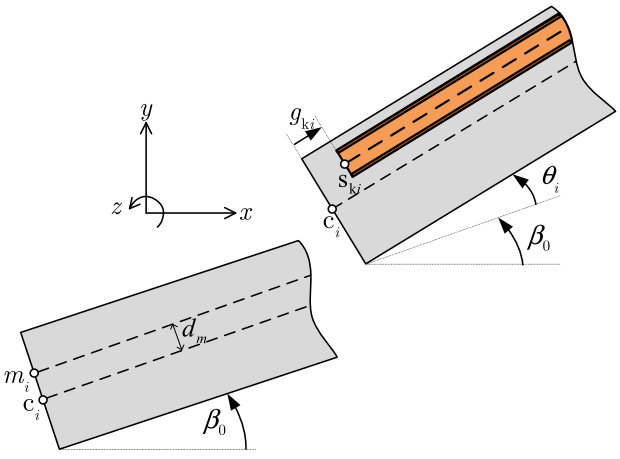

Fig. 3. Eccentric nodes and forces.

The displacements of the node m_i can easily be obtained as

$$\begin{bmatrix} u_{\mathrm{mi}} \\ v_{\mathrm{mi}} \end{bmatrix} = \begin{bmatrix} u_{ci} \\ v_{ci} \end{bmatrix} + \begin{bmatrix} \cos\theta_i - 1 & -\sin\theta_i \\ \sin\theta_i & \cos\theta_i - 1 \end{bmatrix} \begin{bmatrix} -\sin\beta_o \\ \cos\beta_o \end{bmatrix} d_{\mathrm{m}} \tag{30}$$

which, after differentiation, gives

$$\begin{bmatrix} \delta u_{\mathrm{mi}} \\ \delta v_{\mathrm{mi}} \end{bmatrix} = \begin{bmatrix} \delta u_{\mathrm{ci}} \\ \delta v_{\mathrm{ci}} \end{bmatrix} - \begin{bmatrix} \cos(\beta_o + \theta_i) \\ \sin(\beta_o + \theta_i) \end{bmatrix} d_{\mathrm{m}}\, \delta\theta_i \tag{31}$$

The internal force vector and tangent stiffness matrix consistent with $\mathbf{p}_m$ are then obtained, see Section 2.2, using the transformation matrix $\mathbf{B}_{gm}$. This gives

$$\delta\mathbf{p}_g = \mathbf{B}_{gm}\,\delta\mathbf{p}_m \quad \mathbf{f}_m = \mathbf{B}_{gm}^{\mathrm{T}}\mathbf{f}_g \quad \mathbf{K}_m = \mathbf{B}_{gm}^{\mathrm{T}}\mathbf{K}_g\mathbf{B}_{gm} + \mathbf{H}_{gm} \tag{32}$$

with

$$\mathbf{B}_{gm\,(k,k)} = 1 \quad k = 1, 2, \ldots, 2n+6 \tag{33}$$

$$\mathbf{B}_{gm\,(1,3)} = \cos(\beta_o + \theta_i)\, d_{\mathrm{m}} \tag{34}$$

$$\mathbf{B}_{gm\,(2,3)} = \sin(\beta_o + \theta_i)\, d_{\mathrm{m}} \tag{35}$$

and the only non zero term in the matrix $\mathbf{H}_{gm}$ is

$$\mathbf{H}_{gm\,(3,3)} = -\sin(\beta_o + \theta_i)\, d_{\mathrm{m}} f_g(1) + \cos(\beta_o + \theta_i)\, d_{\mathrm{m}} f_g(2) \tag{36}$$

2.3.2. Eccentric forces

Let us now consider that two external force vectors $\mathbf{f}_{ci}$ and $\mathbf{f}_{ski}$ defined by

$$\mathbf{f}_{\mathrm{ci}} = [f_{\mathrm{ci}}(1) \;\; f_{\mathrm{ci}}(2) \;\; f_{\mathrm{ci}}(3)\,]^{\mathrm{T}}; \quad \mathbf{f}_{\mathrm{ski}} = [f_{\mathrm{ski}}(1) \;\; f_{\mathrm{ski}}(2) \;\; f_{\mathrm{ski}}(3)\,]^{\mathrm{T}} \tag{37}$$

are applied at the nodes c_i and s_{ki}. $f_{ci}(1), f_{\mathrm{ski}}(1)$ are horizontal forces (in the local frame), $f_{ci}(2), f_{\mathrm{ski}}(2)$ are vertical forces and $f_{ci}(3), f_{\mathrm{ski}}(3)$ are moments. These loads require a special treatment since the degrees of freedom of the element are $\mathbf{p}_m$, see Eq. (29). The idea is to calculate the loads applied at node m_i which perform the same external virtual work.

For the load $\mathbf{f}_{\mathrm{mi}}$, it gives

$$[\,\delta u_{\mathrm{mi}} \;\; \delta v_{\mathrm{mi}} \;\; \delta\theta_i\,]\,\mathbf{f}_{\mathrm{mi}} = [\,\delta u_{\mathrm{ci}} \;\; \delta v_{\mathrm{ci}} \;\; \delta\theta_i\,]\,\mathbf{f}_{\mathrm{ci}} \tag{38}$$

Using Eq. (31), one gets

$$\mathbf{f}_{\mathrm{mi}} = \begin{bmatrix} 1 & 0 & 0 \\ 0 & 1 & 0 \\ \cos(\beta_o + \theta_i)\, d_{\mathrm{m}} & \sin(\beta_o + \theta_i)\, d_{\mathrm{m}} & 1 \end{bmatrix} \mathbf{f}_{\mathrm{ci}} \tag{39}$$

Differentiating Eq. (39) gives the stiffness correction term $\mathbf{K}_{sm}$ associated to $[\,u_{\mathrm{mi}} \;\; v_{\mathrm{mi}} \;\; \theta_i\,]$, which must be subtracted from the tangent stiffness matrix of the structure, as

$$\mathbf{K}_{sm} = \begin{bmatrix} 0 & 0 & 0 \\ 0 & 0 & 0 \\ 0 & 0 & A \end{bmatrix}; \quad A = -\sin(\beta_o + \theta_i)\, d_{\mathrm{m}} f_{\mathrm{ci}}(1) + \cos(\beta_o + \theta_i)\, d_{\mathrm{m}} f_{\mathrm{ci}}(2) \tag{40}$$

In the case external loads are applied to a embedded section $\mathbf{f}_{\mathrm{ski}}$, the calculations are more complicated since the slip g_{ki} is involved. Equating the external virtual work performed by both force vectors gives

$$[\,\delta u_{\mathrm{mi}} \quad \delta v_{\mathrm{mi}} \quad \delta\theta_i \quad \delta g_{\mathrm{ki}}\,]\,\mathbf{f}_{\mathrm{mi}} = [\,\delta u_{\mathrm{ski}} \quad \delta v_{\mathrm{ski}} \quad \delta\theta_i\,]\,\mathbf{f}_{\mathrm{ski}} \tag{41}$$

The displacements of the node s_{ki} can be obtained as (see Fig. 3)

$$\begin{bmatrix} u_{\mathrm{ski}} \\ v_{\mathrm{ski}} \end{bmatrix} = \begin{bmatrix} u_{\mathrm{mi}} \\ v_{\mathrm{mi}} \end{bmatrix} + \begin{bmatrix} \cos\theta_i - 1 & -\sin\theta_i \\ \sin\theta_i & \cos\theta_i - 1 \end{bmatrix} \begin{bmatrix} -\sin\beta_o \\ \cos\beta_o \end{bmatrix} h_{\mathrm{m}} + \begin{bmatrix} \cos(\beta_o + \theta_i) \\ \sin(\beta_o + \theta_i) \end{bmatrix} g_{ki} \tag{42}$$

with $h_{\mathrm{m}} = h_{\mathrm{k}} - d_{\mathrm{m}}$. After differentiation, it gives

$$\begin{bmatrix}\delta u_{ski}\\ \delta v_{ski}\end{bmatrix}=\begin{bmatrix}\delta u_{mi}\\ \delta v_{mi}\end{bmatrix}-\begin{bmatrix}\cos(\beta_o+\theta_i)h_m+\sin(\beta_o+\theta_i)g_{ki}\\ \sin(\beta_o+\theta_i)h_m-\cos(\beta_o+\theta_i)g_{ki}\end{bmatrix}\delta\theta_i+\begin{bmatrix}\cos(\beta_o+\theta_i)\\ \sin(\beta_o+\theta_i)\end{bmatrix}\delta g_{ki} \tag{43}$$

By inserting Eq. (43) into Eq. (41), one obtains

$$\mathbf{f}_{mi}=\begin{bmatrix}1 & 0 & 0\\ 0 & 1 & 0\\ -\cos(\beta_o+\theta_i)h_m-\sin(\beta_o+\theta_i)g_{ki} & -\sin(\beta_o+\theta_i)h_m+\cos(\beta_o+\theta_i)g_{ki} & 1\\ \cos(\beta_o+\theta_i) & \sin(\beta_o+\theta_i) & 0\end{bmatrix}\mathbf{f}_{ski} \tag{44}$$

Differentiating Eq. (44) gives the stiffness correction term $\mathbf{K}_{ssk}$ associated to $[u_{mi}\ v_{mi}\ \theta_i\ g_{ki}]$, which must be subtracted from the tangent stiffness matrix of the structure, as

$$\mathbf{K}_{ssk}=\begin{bmatrix}0 & 0 & 0 & 0\\ 0 & 0 & 0 & 0\\ 0 & 0 & A & B\\ 0 & 0 & B & 0\end{bmatrix} \tag{45}$$

with

$$A=[\sin(\beta_o+\theta_i)h_m-\cos(\beta_o+\theta_i)g_{ki}]f_{ski}(1)-[\cos(\beta_o+\theta_i)h_m+\sin(\beta_o+\theta_i)g_{ki}]f_{ski}(2) \tag{46}$$

$$B=-\sin(\beta_o+\theta_i)f_{ski}(1)+\cos(\beta_o+\theta_i)f_{ski}(2) \tag{47}$$

3. Local linear element formulation

The purpose of this section is to derive the stiffness matrix $\mathbf{K}_l$ in the local coordinate system based on the kinematic assumptions pertaining to Bernoulli multi-layered beams in partial interaction. During the past decades, several finite element formulations for two-layered beams have been proposed, see for instance [8–15,23–25]. It has been found that curvature locking phenomenon occur in low order Bernoulli displacement-based finite element models particularly for short element with stiff shear connector. In order to avoid locking problem in two-noded beam element, the local stiffness matrix is constructed based on the exact solution of the governing equations of a multi-layered beam with deformable shear connectors. To keep the paper self-contained, the derivation of the exact stiffness matrix is summarized in this section.

3.1. Field equations

The present section introduces the field equations for multi-layered beam with partial interaction in small displacements. The surrounding concrete component as well as all embedded steel elements are assumed to deform according to Bernoulli kinematics. The interface connection between the embedded elements and the surrounding concrete component is modeled by continuously distributed spring.

3.1.1. Equilibrium

The equilibrium equations are derived by considering the free body diagram of a differential element dx located at an arbitrary position x (see Fig. 4). The equilibrium equations are resumed as follow:

$$\partial_x N_{sk}=-D_{sck},\quad k=1,2,\ldots,n \tag{48}$$

$$\partial_x N_c=\sum_{k=1}^{n}D_{sck} \tag{49}$$

$$\partial_x M=-V-\sum_{k=1}^{n}D_{sck}h_k \tag{50}$$

$$\partial_x V=-p_y \tag{51}$$

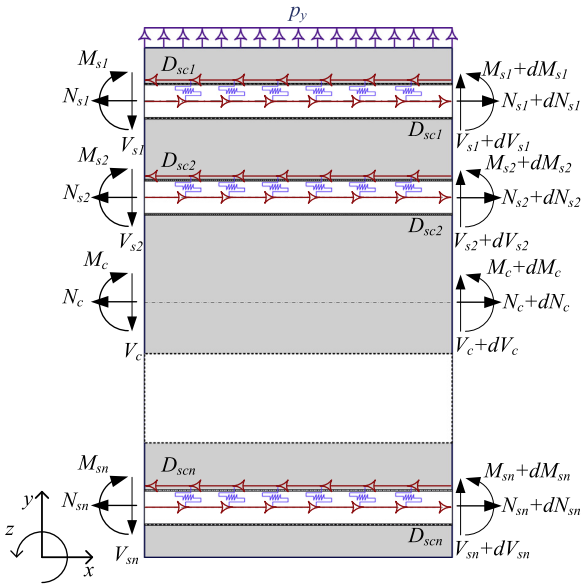

Fig. 4. Free body diagrams of an element at an arbitrary position x.

where

- $\partial_x^i \bullet = \mathrm{d}^i \bullet / \mathrm{d}x^i$;
- $h_k = y_{sk} - y_c$ $(k = 1,2,\ldots,n)$ is the distance between the centroid of the embedded steel element "k" and of the surrounding concrete component;
- N_i, V_i, M_i $(i = s1, s2, \ldots, sn, c)$ are respectively the axial force, the shear force and bending moment at the centroid of layer "i";
- D_{sck} $(k = 1,2,\ldots,n)$ is the slip force per unit length of embedded layer "k";
- $V = \sum V_i$ is the sum of shear forces of each component;
- $M = \sum M_i$ is the sum of bending moments at centroid of each component.

Equilibrium equations Eqs. (48)–(50) can be written in the following matrix form:

$$\hat{\partial}\mathbf{D}-\hat{\partial}_{sc}\mathbf{D}_{sc}-\mathbf{P}_e=0 \tag{52}$$

3.1.2. Compatibility

The steel elements being embedded in concrete, uplift cannot occur, and therefore the surrounding concrete section and all embedded layers have the same transverse displacement. For each constituent, plane sections remain plane and normal to beam axis after deformation. The kinematic variables consist of axial and transversal displacements, cross-section rotation, curvature, and interface slips. Based on the above assumptions, the axial and flexural deformations at any cross-section are as follows (Fig. 5):

$$\epsilon_i=\partial_x u_i,\quad i=s1,s2,\ldots,sn,c \tag{53}$$

$$v_c=v_{sk}=v,\quad k=1,2,\ldots,n \tag{54}$$

$$\theta=\partial_x v \tag{55}$$

$$\kappa=\partial_x^2 v \tag{56}$$

The slip corresponds to the difference between the axial displacement of embedded element and the surrounding concrete component at the interface. It can be seen in Eq. (57) that the slip between embedded steel and surrounding concrete is independent of the connector position. Thus, the slips at the top and bottom of each embedded element are the same.

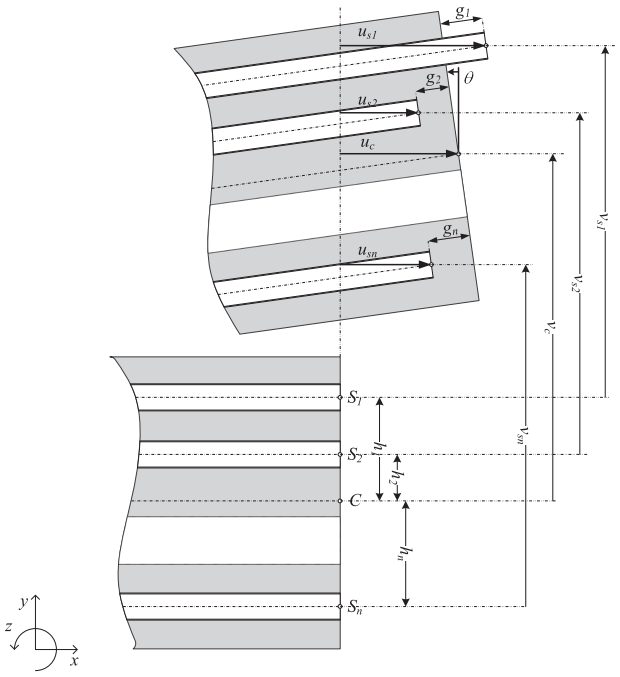

Fig. 5. Kinematic of hybrid beam–column.

$$g_k = u_c - u_{sk} - h_k\,\theta, \quad k = 1, 2, \ldots, n \tag{57}$$

where $h_k = y_{sk} - y_c$ is the distance between centroid of the embedded elements and the surrounding concrete component; k represents an embedded element. The above kinematic relationships can be cast in the following compact matrix form:

$$\mathbf{e} = \hat{\partial}\mathbf{d} \tag{58}$$

$$\mathbf{g} = \hat{\partial}_{sc}^{\mathrm{T}}\mathbf{d} \tag{59}$$

3.1.3. Constitutive relations

The generalized stress–strain relationships for the transverse sections of multi-layer beam are simply obtained by integrating over each cross-section the appropriate uniaxial constitutive model. For a linear elastic material, these relationships lead to the following generalized relationships:

$$N_i = \int_{A_i} \sigma\,\mathrm{d}A_i = (EA)_i\,\epsilon_i, \quad i = s1, s2, \ldots, sn, c \tag{60}$$

$$M_i = -\int_{A_i} y\,\sigma\,\mathrm{d}A_i = (EI)_i\,\kappa \tag{61}$$

where

- $(EA)_i = E_i A_i$ is the axial stiffness of each component;
- $(EI)_i = E_i I_i$ is the flexural stiffness of each component;
- $(EI)_0 = \sum_{k=1}^{n} E_{sk} I_{sk} + E_c I_c$.

The above relations must be completed by the relationship between the shear bond D_{sck} and the slip g_k:

$$D_{sck} = K_{sck}\,g_k, \quad k = 1, 2, \ldots, n \tag{62}$$

where K_{sck} is the shear bond stiffness. The constitutive relations can be expressed in matrix form as follows:

$$\mathbf{D} = \mathbf{K}\mathbf{e} \tag{63}$$

and

$$\mathbf{D}_{sc} = \mathbf{K}_{sc}\,\mathbf{g} \tag{64}$$

3.2. The exact stiffness matrix

Combining the kinematic relations Eqs. (53)–(56) with the elastic law Eqs. (60)–(62) and inserting the outcome into the equilibrium equations Eqs. (48)–(50) produce the following set of differential equations:

$$(EA)_{sk}\,\partial_x^2 u_{sk} = -K_{sck}\,g_k, \quad k = 1, 2, \ldots, n \tag{65}$$

$$(EA)_c\,\partial_x^2 u_c = \sum_{k=1}^{n} K_{sck}\,g_k \tag{66}$$

$$(EI)_0\,\partial_x^3 v = -V(x) - \sum_{k=1}^{n} K_{sck}\,g_k\,h_k \tag{67}$$

Taking the derivative of the slip distribution relation Eq. (57) and making use of Eqs. (65)–(67), one arrives at the following coupled second-order system of differential equations in term of slips as follow:

$$\partial_x^2\mathbf{g} - \Lambda\mathbf{g} = \frac{V(x)}{(EI)_0}\mathbf{h} \tag{68}$$

where

$$\Lambda = \begin{bmatrix} K_{sc1}\left[\frac{1}{(EA)_{sc1}} + \frac{h_1^2}{(EI)_0}\right] & K_{sc2}\left[\frac{1}{(EA)_c} + \frac{h_1 h_2}{(EI)_0}\right] & \cdots & K_{scn}\left[\frac{1}{(EA)_c} + \frac{h_1 h_n}{(EI)_0}\right] \\ K_{sc1}\left[\frac{1}{(EA)_c} + \frac{h_1 h_2}{(EI)_0}\right] & K_{sc2}\left[\frac{1}{(EA)_{sc2}} + \frac{h_2^2}{(EI)_0}\right] & \cdots & K_{scn}\left[\frac{1}{(EA)_c} + \frac{h_2 h_n}{(EI)_0}\right] \\ \vdots & \vdots & \ddots & \vdots \\ K_{sc1}\left[\frac{1}{(EA)_c} + \frac{h_1 h_n}{(EI)_0}\right] & K_{sc2}\left[\frac{1}{(EA)_c} + \frac{h_2 h_n}{(EI)_0}\right] & \cdots & K_{scn}\left[\frac{1}{(EA)_{scn}} + \frac{h_n^2}{(EI)_0}\right] \end{bmatrix} \tag{69}$$

in which,

$$\frac{1}{(EA)_{sck}} = \frac{1}{(EA)_c} + \frac{1}{(EA)_{sk}}, \quad k = 1, 2, \ldots, n \tag{70}$$

A diagonalization of the matrix Λ will uncouple the above system of differential equations Eq. (68) and will produce a set of n second-order ordinary equations. It must be pointed out that the distribution of the shear force $V(x)$ must be known before hand. The latter can be related, through equilibrium Eq. (51), to the external loads. Let Λ_v and Λ_λ respectively be the matrix collecting the eigenvectors and the eigenvalues of Λ:

$$\Lambda_\lambda = \Lambda_v^{-1}\,\Lambda\,\Lambda_v. \tag{71}$$

Next, we insert the vector $\mathbf{g}$ obtained by pre-multiplying the vector $\tilde{\mathbf{g}}$ by the matrix Λ_v:

$$\mathbf{g} = \Lambda_v\tilde{\mathbf{g}} \tag{72}$$

into Eq. (72) and make use of Eq. (71) to produce an uncoupled differential equation system in n variables $\tilde{g}_k$:

$$\partial_x^2\tilde{\mathbf{g}} - \Lambda_\lambda\tilde{\mathbf{g}} = \frac{V(x)}{(EI)_0}\bar{\mathbf{h}} \tag{73}$$

where $\bar{\mathbf{h}} = \Lambda_v^{-1}\mathbf{h}$ which corresponds to n ordinary differential equations as follow:

$$\partial_x^2\tilde{g}_k - \lambda_k\tilde{g}_k = \frac{V\bar{h}_k}{(EI)_0}, \quad k = 1, 2, \ldots, n \tag{74}$$

Assuming no internal element loading which produces a constant shear force and considering that all λ_k are strictly positive, the solution of Eq. (74) can be expressed as:

$$\tilde{g}_k = C_{2k-1}\,e^{\sqrt{\lambda_k}x} + C_{2k}\,e^{-\sqrt{\lambda_k}x} + P_k, \quad k = 1, 2, \ldots, n \tag{75}$$

where P_k is a constant related to the shear force and correspond to the particular solution for non homogeneous differential equations Eq. (74). The expression of P_k is as follow:

$$P_k = -\frac{V\bar{h}_k}{\lambda_k(EI)_0} = -\frac{C_{2n+6}\bar{h}_k}{\lambda_k(EI)_0}, \quad k = 1,2,\ldots,n \tag{76}$$

where C_{2n+6} is the shear force at the left hand side of the beam. All $\tilde{g}_k$ are collected in a vector so the analytical solution can be written in a matrix form:

$$\tilde{\mathbf{g}} = \mathbf{X}_{\tilde{g}}\mathbf{C} \tag{77}$$

with

$$\tilde{\mathbf{g}} = [\,\tilde{g}_1 \quad \tilde{g}_2 \quad \cdots \quad \tilde{g}_n\,]^{\mathrm{T}} \tag{78}$$

$$\mathbf{X}_{\tilde{g}} = \begin{bmatrix} e^{\sqrt{\lambda_1}x} & e^{-\sqrt{\lambda_1}x} & 0 & 0 & \cdots & 0 & 0 & 0 & 0 & 0 & 0 & -\frac{\bar{h}_1}{\lambda_1(EI)_0} \\ 0 & 0 & e^{\sqrt{\lambda_2}x} & e^{-\sqrt{\lambda_2}x} & \cdots & 0 & 0 & 0 & 0 & 0 & 0 & -\frac{\bar{h}_2}{\lambda_2(EI)_0} \\ \vdots & \vdots & \vdots & \vdots & \ddots & \vdots & \vdots & \vdots & \vdots & \vdots & \vdots & \vdots \\ 0 & 0 & 0 & 0 & \cdots & e^{\sqrt{\lambda_n}x} & e^{-\sqrt{\lambda_n}x} & 0 & 0 & 0 & 0 & -\frac{\bar{h}_n}{\lambda_n(EI)_0} \end{bmatrix} \tag{79}$$

and

$$\mathbf{C} = [\,C_1 \quad C_2 \quad \cdots \quad C_{2n+6}\,]^{\mathrm{T}} \tag{80}$$

Having at hand the analytical expression for $\tilde{g}_k$, it is straightforward to derive the slip distributions g_k using Eq. (72):

$$\mathbf{g} = \mathbf{X}_g\mathbf{C} \tag{81}$$

in which

$$\mathbf{X}_g = \Lambda_v\mathbf{X}_{\tilde{g}} \tag{82}$$

By back substituting the above expression into the governing equations Eqs. (66), (67) and making use Eq. (57), the analytical expressions for the displacement u_c, u_{sk} $(k = 1,2,\ldots,n)$ and v are obtained. Making use of the kinematic relationships Eqs. (55), (56), the analytical expressions for the cross-section rotation and the curvature can be established. All these kinematic variables depend on $2n+6$ constants of integration and are given in the following compact form:

$$u_c = \mathbf{X}_{u_c}\mathbf{C} \tag{83}$$

$$u_{sk} = \mathbf{X}_{u_{sk}}\mathbf{C}, \quad k = 1,2,\ldots,n \tag{84}$$

$$v = \mathbf{X}_v\mathbf{C} \tag{85}$$

$$\theta = \mathbf{X}_\theta\mathbf{C} \tag{86}$$

$$\kappa = \mathbf{X}_\kappa\mathbf{C} \tag{87}$$

The coefficients $C_{1\ldots2n+6}$ are constants of integration that will be determined by enforcing the kinematic boundary conditions at the beam ends (see Fig. 6). Once the displacement fields are defined, the nodal forces can be obtained by making use of the constitutive relations Eqs. (63), (64) and the kinematic relationships Eqs. (58), (59).

$$N_{sk} = \mathbf{Y}_{N_{sk}}\mathbf{C}, \quad k = 1,2,\ldots,n \tag{88}$$

$$N_c = \mathbf{Y}_{N_c}\mathbf{C} \tag{89}$$

$$M = \mathbf{Y}_M\mathbf{C} \tag{90}$$

$$V = \mathbf{Y}_V\mathbf{C} \tag{91}$$

It can be cast in a compact form as:

$$\mathbf{Q} = \mathbf{Y}\mathbf{C} \tag{92}$$

where

$$\mathbf{Q} = \left[\,\bar{N}_{s1,0} \quad \cdots \quad \bar{N}_{c,0} \quad \bar{V}_0 \quad \bar{M}_0 \quad \bar{N}_{s1,L} \quad \cdots \quad \bar{N}_{c,L} \quad \bar{V}_L \quad \bar{M}_L\,\right]^{\mathrm{T}} \tag{93}$$

$$\mathbf{Y} = \left[\,-\mathbf{Y}_{N_{s1,0}} \quad \cdots \quad -\mathbf{Y}_{N_{c,0}} \quad -\mathbf{Y}_{V_0} \quad -\mathbf{Y}_{M_0} \quad \mathbf{Y}_{N_{s1,L}} \quad \cdots \quad \mathbf{Y}_{N_{c,L}} \quad \mathbf{Y}_{V_L} \quad \mathbf{Y}_{M_L}\,\right]^{\mathrm{T}} \tag{94}$$

The direct stiffness method is used to derive the exact stiffness of the multi-layered beam element with partial interaction. The nodal displacements can be then written as the following:

$$\mathbf{q} = \mathbf{X}\mathbf{C} \tag{95}$$

where

$$\mathbf{q} = \left[\,\bar{u}_{s1,0} \quad \bar{u}_{s2,0} \quad \cdots \quad \bar{u}_{sn,0} \quad \bar{u}_{c,0} \quad \bar{v}_0 \quad \bar{\theta}_0 \quad \bar{u}_{s1,L} \quad \bar{u}_{s2,L} \quad \cdots \quad \bar{u}_{sn,L} \quad \bar{u}_{c,L} \quad \bar{v}_L \quad \bar{\theta}_L\,\right]^{\mathrm{T}} \tag{96}$$

$$\mathbf{X} = \left[\,\mathbf{X}_{s1,0} \quad \cdots \quad \mathbf{X}_{c,0} \quad \mathbf{X}_{\theta,0} \quad \mathbf{X}_{s1,L} \quad \cdots \quad \mathbf{X}_{c,L} \quad \mathbf{X}_{\theta,L}\,\right]^{\mathrm{T}} \tag{97}$$

The nodal displacements being independent, so the matrix $\mathbf{X}$ is invertible. Thus, the constants C_i are obtained in function of the nodal displacements q_i.

$$\mathbf{C} = \mathbf{X}^{-1}\mathbf{q} \tag{98}$$

Introducing Eq. (98) into Eq. (92), one obtains:

$$\mathbf{K}_e\mathbf{q} = \mathbf{Q} \tag{99}$$

where

$$\mathbf{K}_e = \mathbf{Y}\mathbf{X}^{-1} \tag{100}$$

represents the exact stiffness of the element.

4. Numerical examples

The purpose of this section is to assess the capability of the proposed formulation in reproducing the nonlinear behavior of hybrid beams with interlayer slips and to investigate the influence of the shear connection stiffness on the geometric nonlinear effects. The

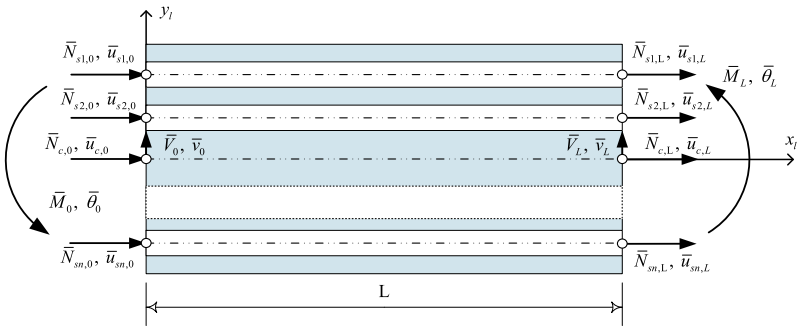

Fig. 6. Nodal forces and displacements of a hybrid beam element.

analysis of the performance and the accuracy of the present formulation is carried out considering five meaningful examples.

4.1. Example 1: Buckling load of mega column

The mega column depicted in Fig. 7 is studied here where full interaction is assumed by taking a large shear connector stiffness $K_{sc} = 10$ GPa. Restraints are applied in order to avoid bucking about the y-axis. The limit loads obtained with different meshes are presented in Table 1. A very good agreement compared to the analytical solution, Euler's buckling load $\frac{\pi^2 EI}{L^2}$, is obtained. A further investigation on the effect of the shear connection stiffness on the critical load has been carried out. The critical load is obtained by performing the nonlinear analysis using 10 elements. It can be seen from Fig. 8 that the critical load obtained from the FE analysis using the proposed formulation (P_{cr}) is lower than Euler's critical load ($P_{cr,E}$) for low shear connection stiffness. The magnitude of P_{cr} increases with increasing value of shear connection stiffness. However, P_{cr} remains constant for a shear connection stiffness K_{sc} beyond a critical value (about 10^6 kPa).

4.2. Example 2: Simply supported steel-reinforced concrete beam subjected to uniformly distributed load

Consider a concrete beam of breath 10 cm and depth 20 cm (see Fig. 9) reinforced by two steel plates of equal thickness 2 mm attached, using shear connectors, to the top and bottom surfaces of the concrete beam. The latter is subjected to a uniformly

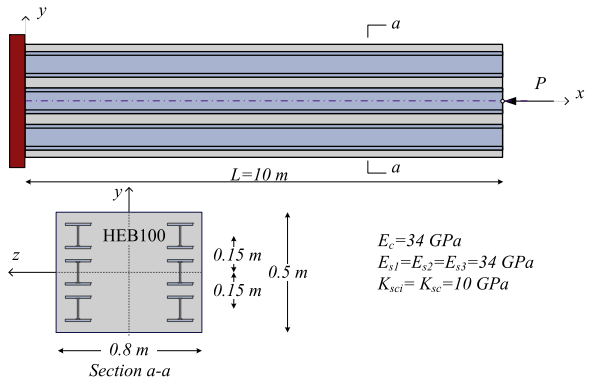

Fig. 7. Example 1. Buckling of mega column.

Table 1
Example 1. Numerical results.

	1 elements	2 elements	4 elements	10 elements
Present/analytical	1.2173	1.0534	1.0139	1.0031

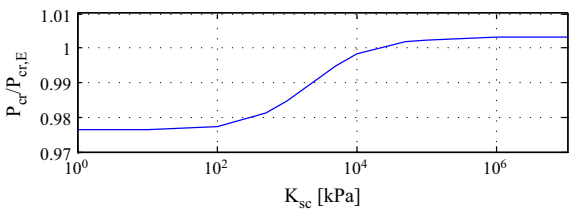

Fig. 8. Example 1. Ratio between the predicted ultimate load and the Euler buckling load in function of shear connection stiffness.

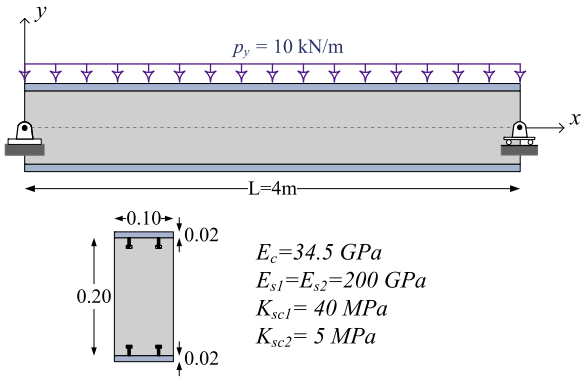

Fig. 9. Example 2. Three-layered beam with transversal loads (dimension in [m]).

distributed load p_y of intensity 10 kN/m. The elastic modulus adopted for steel and concrete are 200,000 MPa and 34,500 MPa, respectively. The stiffness of the shear connection is taken equal to 40 MPa for the top layer and 5 MPa for the bottom layer. Such distribution of the shear connection stiffness breaks the symmetry of the problem. The geometrically linear analysis of this beam problem was performed by Sousa [20] using the exact flexibility matrix. To assess the capabilities of our formulation we perform both a linear analysis with a single exact finite element and a large displacement analysis with 20 elements. For the former analysis, the exact stiffness is derived based on a linear shear force distribution (replacing V with $-p_y x + C_{2n+6}$ in Eq. (76)) so that the distributed load is considered without any approximation. Excellent agreement for geometrically linear analysis with the results in [20] is obtained. For the nonlinear analysis, the distributed load is replaced with concentrated nodal forces. As expected larger slips occur at the interface between the bottom steel plate and the core beam (see Fig. 10 for distributed load $p_y = 10$ kN/m). The maximum deflection v_{max} occurring at mid-span of the beam along with the slips at the beam ends are tabulated in Table 2 in function of the magnitude of the distributed load p_y. It can be seen that the

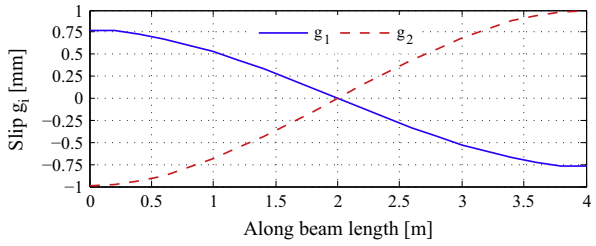

Fig. 10. Example 2. Slips between concrete and steel beams.

Table 2
Example 2. Numerical results.

	p_y (kN/m)	10	400	1000	1500
GLA	$\|v_{max}\|$ (m)	0.0109	0.4351	1.0878	1.6317
	$\|g_1\|$ (mm)	0.7782	31.1287	77.8218	116.7328
	$\|g_2\|$ (mm)	1.0021	40.0829	100.2074	150.3110
GNA	$\|v_{max}\|$ (m)	0.0109	0.4131	0.8470	1.0580
	$\|g_1\|$ (mm)	0.7759	29.5281	61.6088	78.0717
	$\|g_2\|$ (mm)	1.0000	38.6770	82.7453	106.9416

GLA: Geometrically linear analysis.
GNA: Geometrically nonlinear analysis.

sandwich beam behaves linearly below 600 kN/m. Beyond that load, the nonlinear behavior become significantly apparent. One can observe that for a large amplitude of the loading, the magnitude of the transverse displacement and the slips at the beam ends given by the geometrically nonlinear analysis are significantly below the one predicted by a geometrically linear analysis. This behavior is similar to what is observed in non-linear bending of simply supported beams of constant homogenous cross-section carrying uniformly distributed load (see [30]). In such a problem, the large displacement produces axial forces which increase the stiffness of the system requiring larger loads for the same displacement. To illustrate this behavior, the nonlinear load–deflection curve is compared to the linear one (see Fig. 11) where v_{max} is the transverse displacement at the mid-span.

The effect of the degree of interaction on the deflection of the beam has been investigated by considering different levels of the shear connection stiffness expressed in terms of dimensionless parameters k_1 and k_2 given by the following expression:

$$k_i = \sqrt{K_{sci}\left(\frac{1}{(EA)_{sci}} + \frac{h_i^2}{(EI)_0}\right)}L, \quad i = 1,2 \tag{101}$$

where the subscript "$i = 1$" represents the interface at top surface of concrete and "$i = 2$" the one at bottom surface. A high value of k_i corresponds to a stiff connection. In this case, the sandwich beam is subjected to a uniform distributed load $p_y = 2$ MN/m. Fig. 12 shows the maximum value of deflection for a variety of dimensionless stiffnesses of the shear connections. It can be seen that the deflection is significantly reduced when the stiffness of the connector increases. It can be observed that beyond a critical value of k_2 (about 25), the displacement does not increases anymore whatsoever the value of k_1 is (asymptotic behavior).

4.3. Example 3: Hybrid beam with 3 embedded sections subjected to axial and transversal loads

Consider a pinned hybrid beam consisting of a concrete beam of breath b and depth h (see Fig. 12) reinforced by three steel profiles. Equally spaced stud connectors are welded on both side of each steel beam flanges. The details of the geometrical and material characteristics are reported in Fig. 13. The beam is subjected to both axial and transversal loads. Each layer of the hybrid beam is loaded by an axial force. The position of the centroid of the steel beam at mid-height of the hybrid section coincides with the centroid of the concrete section. For this problem, a nonlinear analysis is required in order to take into account the second-order effect induced by the axial loads. The numerical results for the slips and the deflection at several locations are provided in Table 3. These results have been obtained with a mesh consisting of 20 elements. The slips between the surrounding concrete and the steel beams are illustrated in Fig. 14.

One can observe that although the hybrid section is symmetric, the slip distribution at top steel profile is not symmetric with respect to the one at bottom steel profile. As a result of the interaction between bending moment and normal forces, the slip at mid-height of the cross-section is not equal to zero. Indeed, two axial forces are applied at each cross-section centroid (at mid-height), one at the steel section (steel node) and another one at the concrete section (concrete node). These two axial forces accompanied by the bending moment produce different axial displacements of both nodes which result the non-zero slip (g_2) along the beam length.

On the other hand, for the same problem the deformed shape, depicted in Fig. 15, of the hybrid beam with partial interaction is

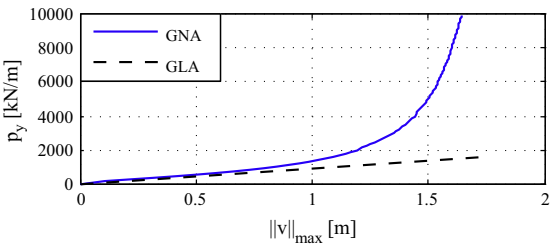

Fig. 11. Example 2. Load–deflection curve.

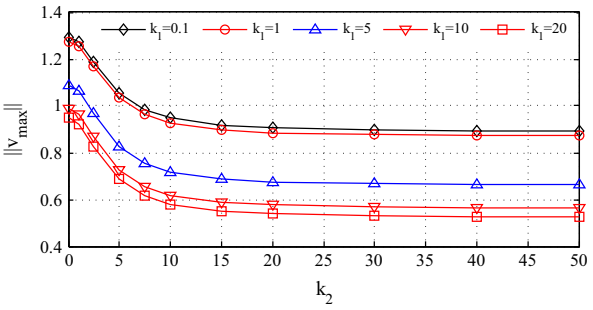

Fig. 12. Example 2. Maximum vertical displacement in function of shear connection stiffness.

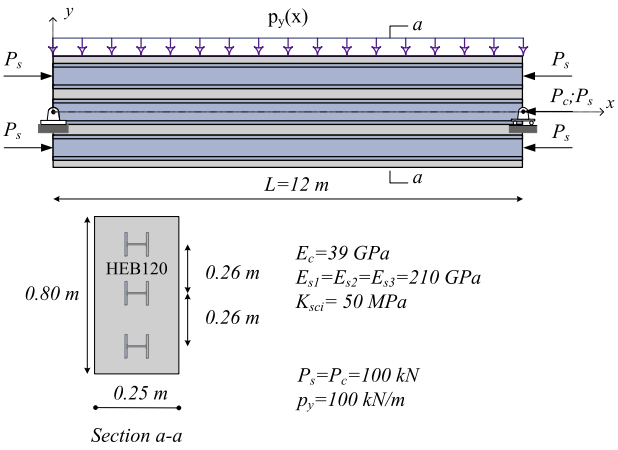

Fig. 13. Example 3. Beam with axial and transversal loads.

Table 3
Example 3. Numerical results.

	$x = 0$ m	$x = 3$ m	$x = 6$ m
v_C (mm)	0	−43.3902	−60.8698
g_1 (mm)	2.8225	1.6484	0.0000
g_2 (mm)	0.7447	0.2580	0.0000
g_3 (mm)	−1.3331	−1.1324	0.0000

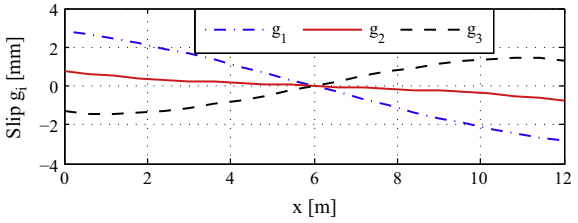

Fig. 14. Example 3. Slips between concrete and steel beams.

On the other hand, for the same problem the deformed shape, depicted in Fig. 15, of the hybrid beam with partial interaction is

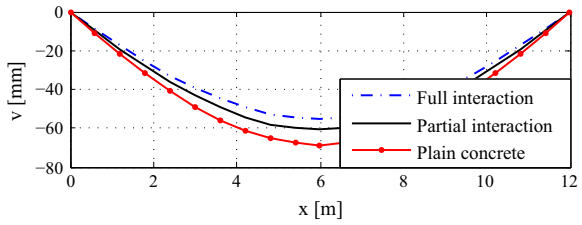

Fig. 15. Example 3. Deformed shape of the beam.

compared to the one of the hybrid beam with full interaction (without slips) and to the one without the embedded steel sections (plain concrete section with longitudinal holes). It is evident that with full interaction, the deflection at mid-span of the hybrid beam is lower than the one with partial interaction. As expected, the deflection of plain concrete beam is larger than the one of the hybrid beam with partial interaction.

4.4. Example 4: Pinned–pinned mega column with non symmetric section

The investigation of second-order effect of slender mega column shown in Fig. 16 subjected to eccentric load is performed here. Restraints are applied in order to avoid bucking about the y-axis. The section being symmetric with respect to the y-axis, half of the column section can be considered. The actual load is then the computed load multiplied by two. The load–deflection curves for various load locations are shown in Fig. 17. The critical load is equal to 196.58 MN. Surprisingly, the deflection shape depends on the eccentricity. Indeed, for an eccentricity equal to 0.15 mm, the column deforms according to a W-shape pattern for compressive load $P = 160$ MN. At this loading point, it is worth to mention that the deflection shape progressively changes (including the sign), due to the nonlinear interaction between the deflection and the compressive force. The various deflection patterns are illustrated in Fig. 18 and in Fig. 19 for a compressive load equal to $P = 160$ MN and $P = 192$ MN, respectively. It can be observed that a small change in e can result in a totally different buckling shape. The numerical values of deflection at mid-height of the column corresponding to various eccentricities are presented in Table 4 for the two different load levels.

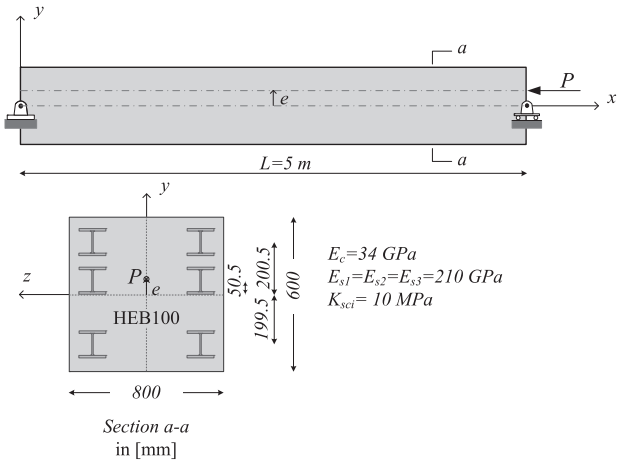

Fig. 16. Example 4. Pinned–pinned mega column with eccentric load.

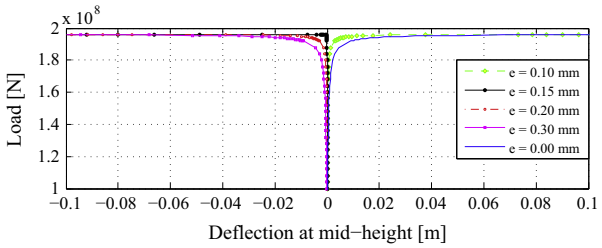

Fig. 17. Example 4. Load–deflection curve for various loading points.

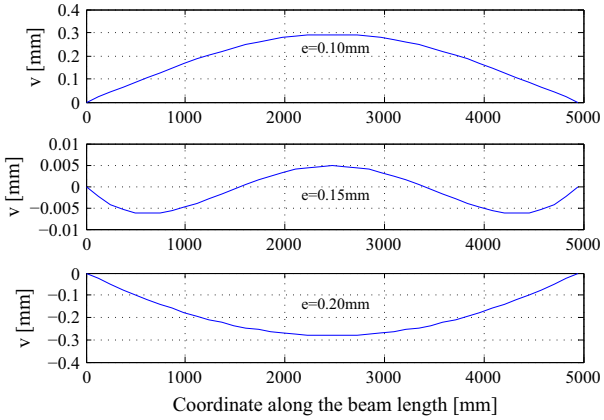

Fig. 18. Example 4. Deflection patterns for $P = 160$ MN.

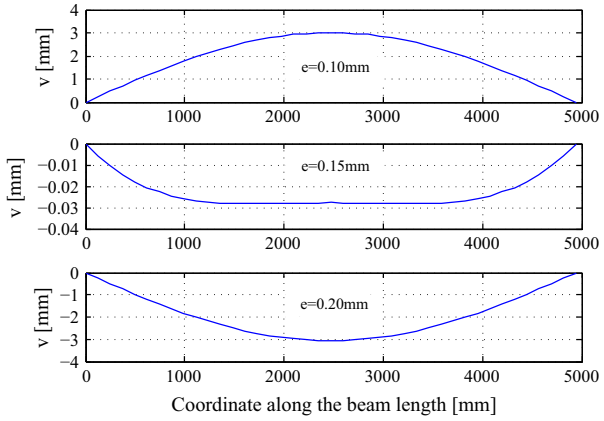

Fig. 19. Example 4. Deflection patterns for $P = 192$ MN.

Table 4
Example 4. Numerical results.

	$P = 160$ MN v (mm)	$P = 192$ MN v (mm)
$e = 0.1$ (mm)	0.2921	3.0110
$e = 0.15$ (mm)	0.0048	−0.0278
$e = 0.2$ (mm)	−0.2825	−3.0670

4.5. Example 5: Uniform bending of cantilever beam

In this classical problem (see Fig. 20), three cantilever steel beams (s_i) are embedded in beam (c). Those beams are subjected to an end moment M such that the deformed shape of the beam (c) is a quarter of circle.

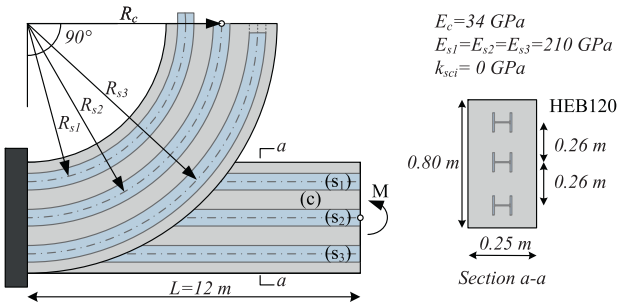

Fig. 20. Example 5. Uniform bending of cantilever beam.

Table 5
Example 5. Numerical results.

	Analytical	Present	Present/analytical
v_C (m)	7.6394	7.6473	1.0010
u_C (m)	−4.3606	−4.3527	0.9982
g_1 (m)	−0.4084	−0.4097	1.0031
g_2 (m)	0.0000	$-7.2905 \cdot 10^{-18}$	–
g_3 (m)	0.4084	0.4097	1.0031
M (MN m)	45.7204	45.7202	1.0000
$max\|\|V(x)\|\|$ (N)	0.0000	$9.4995 \cdot 10^{-7}$	–
$max\|\|N(x)\|\|$ (N)	0.0000	$1.6075 \cdot 10^{-6}$	–

The end moment required to deform the beam (c) is

$$M_c = \frac{(EI)_c}{R_c}, \quad R_c = \frac{2L}{\pi} \tag{102}$$

The beams (s_i) have to bend into the concentric arcs, which require the end moments

$$M_{si} = \frac{(EI)_{si}}{R_{si}}, \quad R_{si} = R_c - h_i \quad i = 1,2,3 \tag{103}$$

The required total moment is therefore $M = M_c + M_{s1} + M_{s2} + M_{s3}$ and the slip between those beams at the free end are

$$g_i = -(R_c - h_i)\frac{(R_c - R_{si})L}{R_c R_{si}} \quad i = 1,2,3 \tag{104}$$

The results obtained with 10 elements are presented in Table 5. Very good agreement with analytical solution is obtained.

5. Conclusion

In this paper, a new co-rotational finite element formulation for large displacement analysis of hybrid beam/column with several encased steel profiles in partial interaction has been presented. To describe the geometrical nonlinearity, the co-rotational framework was adopted and the motion of the element decomposed into a rigid body motion and a deformational part using a local co-rotational frame, which continuously translates and rotates with the element but does not deform with it. The treatment of geometric nonlinearity is effectively undertaken at the level of discrete nodal variables with the transformation matrix between the local and global nodal entities being independent of the assumptions made for the local element. To avoid curvature locking encountered in two-noded element (low order elements), the exact stiffness matrix was used for the local formulation. The performance of the formulation has been illustrated in five numerical examples. It was shown that this proposed formulation provides a robust and reliable option for large displacement analysis of hybrid beam. The developed formulation will serve for numerical investigation on the instability of hybrid column with the aim to derive practical design rules.

Appendix A. Transformation matrix

The matrix relating p_l and p_e is given by

$$\mathbf{B}_{le} = \begin{bmatrix} 0 & -h_1 & 0 & -1 & 0 & \cdots & 0 & 0 & 0 & \cdots & 0 \\ 0 & -h_2 & 0 & 0 & -1 & \cdots & 0 & 0 & 0 & \cdots & 0 \\ \vdots & \vdots & \vdots & \vdots & \vdots & \ddots & \vdots & \vdots & \vdots & \ddots & \vdots \\ 0 & -h_n & 0 & 0 & 0 & \cdots & -1 & 0 & 0 & \cdots & 0 \\ 0 & 0 & 0 & 0 & 0 & \cdots & 0 & 0 & 0 & \cdots & 0 \\ 0 & 0 & 0 & 0 & 0 & \cdots & 0 & 0 & 0 & \cdots & 0 \\ 0 & 1 & 0 & 0 & 0 & \cdots & 0 & 0 & 0 & \cdots & 0 \\ 1 & 0 & -h_1 & 0 & 0 & \cdots & 0 & -1 & 0 & \cdots & 0 \\ 1 & 0 & -h_2 & 0 & 0 & \cdots & 0 & 0 & -1 & \cdots & 0 \\ \vdots & \vdots & \vdots & \vdots & \vdots & \ddots & \vdots & \vdots & \vdots & \ddots & \vdots \\ 1 & 0 & -h_n & 0 & 0 & \cdots & 0 & 0 & 0 & \cdots & -1 \\ 1 & 0 & 0 & 0 & 0 & \cdots & 0 & 0 & 0 & \cdots & 0 \\ 0 & 0 & 0 & 0 & 0 & \cdots & 0 & 0 & 0 & \cdots & 0 \\ 0 & 0 & 1 & 0 & 0 & \cdots & 0 & 0 & 0 & \cdots & 0 \end{bmatrix} \tag{A.1}$$

Then, the matrix $\mathbf{H}_{le}$ is zero and can be written as

$$\mathbf{H}_{le} = \mathbf{0}_{(2n+3)\times(2n+3)} \tag{A.2}$$

The displacement vectors p_e and p_a are related by the matrix $\mathbf{B}_{ea}$ defined as

$$\mathbf{B}_{ea} = \begin{bmatrix} 1 & 0 & 0 & 0 & 0 & \cdots & 0 & 0 & 0 & \cdots & 0 \\ 0 & 1 & 0 & 0 & 0 & \cdots & 0 & 0 & 0 & \cdots & 0 \\ 0 & 0 & 1 & 0 & 0 & \cdots & 0 & 0 & 0 & \cdots & 0 \\ 0 & -g_{1i}\sin\bar{\theta}_i & 0 & \cos\bar{\theta}_i & 0 & \cdots & 0 & 0 & 0 & \cdots & 0 \\ 0 & -g_{2i}\sin\bar{\theta}_i & 0 & 0 & \cos\bar{\theta}_i & \cdots & 0 & 0 & 0 & \cdots & 0 \\ \vdots & \vdots & \vdots & \vdots & \vdots & \ddots & \vdots & \vdots & \vdots & \ddots & \vdots \\ 0 & -g_{ni}\sin\bar{\theta}_i & 0 & 0 & 0 & \cdots & \cos\bar{\theta}_i & 0 & 0 & \cdots & 0 \\ 0 & 0 & -g_{1j}\sin\bar{\theta}_j & 0 & 0 & \cdots & 0 & \cos\bar{\theta}_j & 0 & \cdots & 0 \\ 0 & 0 & -g_{2j}\sin\bar{\theta}_j & 0 & 0 & \cdots & 0 & 0 & \cos\bar{\theta}_j & \cdots & 0 \\ \vdots & \vdots & \vdots & \vdots & \vdots & \ddots & \vdots & \vdots & \vdots & \ddots & \vdots \\ 0 & 0 & -g_{nj}\sin\bar{\theta}_j & 0 & 0 & \cdots & 0 & 0 & 0 & \cdots & \cos\bar{\theta}_j \end{bmatrix} \tag{A.3}$$

The matrix $\mathbf{H}_{ea}^{\mathrm{T}}$ used for stiffness matrix transformation is then

$$\mathbf{H}_{ea}^{\mathrm{T}} = [\mathbf{H}_{ea}(1) \ \cdots \ \mathbf{H}_{ea}(2n+3)] \tag{A.4}$$

$$\mathbf{H}_{ea}(1) = \mathbf{0}_{1\times(2n+3)} \tag{A.5}$$

$$\mathbf{H}_{ea}^{\mathrm{T}}(2) = \begin{bmatrix} 0 \\ -\sum_{k=1}^{n}[g_{ki}f_e(k+3)]\cos\bar{\theta}_i \\ 0 \\ -\sin\bar{\theta}_i f_e(4) \\ -\sin\bar{\theta}_i f_e(5) \\ \vdots \\ -\sin\bar{\theta}_i f_e(n+3) \\ 0 \\ 0 \\ \vdots \\ 0 \end{bmatrix} \quad \mathbf{H}_{ea}^{\mathrm{T}}(3) = \begin{bmatrix} 0 \\ 0 \\ -\sum_{k=1}^{n}[g_{kj}f_e(k+n+3)]\cos\bar{\theta}_j \\ 0 \\ 0 \\ \vdots \\ 0 \\ -\sin\bar{\theta}_j f_e(n+4) \\ -\sin\bar{\theta}_j f_e(n+5) \\ \vdots \\ -\sin\bar{\theta}_j f_e(2n+3) \end{bmatrix} \tag{A.6}$$

$$\mathbf{H}_{ea}^{\mathrm{T}}(k+3) = \begin{bmatrix} 0 \\ -\sin\bar{\theta}_i f_e(k+3) \\ 0 \\ 0 \\ 0 \\ \vdots \\ 0 \\ 0 \\ 0 \\ \vdots \\ 0 \end{bmatrix} \quad \mathbf{H}_{ea}^{\mathrm{T}}(k+n+3) = \begin{bmatrix} 0 \\ 0 \\ -\sin\bar{\theta}_j f_e(k+n+3) \\ 0 \\ 0 \\ \vdots \\ 0 \\ 0 \\ 0 \\ \vdots \\ 0 \end{bmatrix}, \tag{A.7}$$

$k = 1,2,\ldots,n$

with

$$\mathbf{f}_e = [f_e(1) \ \cdots \ f_e(2n+3)]^{\mathrm{T}} \tag{A.8}$$

The matrices for the the last change of variables are as follows:

$$\mathbf{B}_{ag} = \begin{bmatrix} -c & -s & 0 & 0 & 0 & \cdots & 0 & c & s & 0 & 0 & 0 & \cdots & 0 \\ -s/l_n & c/l_n & 1 & 0 & 0 & \cdots & 0 & s/l_n & -c/l_n & 0 & 0 & 0 & \cdots & 0 \\ -s/l_n & c/l_n & 0 & 0 & 0 & \cdots & 0 & s/l_n & -c/l_n & 1 & 0 & 0 & \cdots & 0 \\ 0 & 0 & 0 & 1 & 0 & \cdots & 0 & 0 & 0 & 0 & 0 & 0 & \cdots & 0 \\ 0 & 0 & 0 & 0 & 1 & \cdots & 0 & 0 & 0 & 0 & 0 & 0 & \cdots & 0 \\ \vdots & \vdots & \vdots & \vdots & \vdots & \ddots & \vdots & \vdots & \vdots & \vdots & \vdots & \vdots & \ddots & \vdots \\ 0 & 0 & 0 & 0 & 0 & \cdots & 1 & 0 & 0 & 0 & 0 & 0 & \cdots & 0 \\ 0 & 0 & 0 & 0 & 0 & \cdots & 0 & 0 & 0 & 0 & 1 & 0 & \cdots & 0 \\ 0 & 0 & 0 & 0 & 0 & \cdots & 0 & 0 & 0 & 0 & 0 & 1 & \cdots & 0 \\ \vdots & \vdots & \vdots & \vdots & \vdots & \ddots & \vdots & \vdots & \vdots & \vdots & \vdots & \vdots & \ddots & \vdots \\ 0 & 0 & 0 & 0 & 0 & \cdots & 0 & 0 & 0 & 0 & 0 & 0 & \cdots & 1 \end{bmatrix} \tag{A.9}$$

and

$$\mathbf{H}_{ag} = \frac{\mathbf{z}\mathbf{z}^{\mathrm{T}}}{l_n} f_a(1) + \frac{1}{l_n^2}(\mathbf{r}\mathbf{z}^{\mathrm{T}} + \mathbf{z}\mathbf{r}^{\mathrm{T}})(f_a(2) + f_a(3)) \tag{A.10}$$

with

$$\mathbf{r} = [-c \ \ -s \ \ 0 \ \ 0 \ \ 0 \ \ \cdots \ \ 0 \ \ c \ \ s \ \ 0 \ \ 0 \ \ 0 \ \ \cdots \ \ 0]^{\mathrm{T}}$$
$$\mathbf{z} = [s \ \ -c \ \ 0 \ \ 0 \ \ 0 \ \ \cdots \ \ 0 \ \ -s \ \ c \ \ 0 \ \ 0 \ \ 0 \ \ \cdots \ \ 0]^{\mathrm{T}}$$

and c, s defined in Eqs. (7) and (8).

Appendix B. Auxiliary matrix

The force vectors are expressed as

$$\mathbf{D}(x) = [N_{s1} \ \ N_{s2} \ \ \cdots \ \ N_{sn} \ \ N_c \ \ M]^{\mathrm{T}} \tag{B.1}$$
$$\mathbf{D}_{sc}(x) = [D_{sc1} \ \ D_{sc2} \ \ \cdots \ \ D_{scn}]^{\mathrm{T}} \tag{B.2}$$
$$\mathbf{P}_e(x) = [0 \ \ 0 \ \ \cdots \ \ 0 \ \ 0 \ \ p_y(x)]^{\mathrm{T}} \tag{B.3}$$

and the matrix operation $\hat{\partial}$ and $\hat{\partial}_{sc}$ are as follows:

$$\hat{\partial} = \begin{bmatrix} \partial_x & 0 & \cdots & 0 & 0 & 0 \\ 0 & \partial_x & \cdots & 0 & 0 & 0 \\ \vdots & \vdots & \ddots & \vdots & \vdots & \vdots \\ 0 & 0 & \cdots & \partial_x & 0 & 0 \\ 0 & 0 & \cdots & 0 & \partial_x & 0 \\ 0 & 0 & \cdots & 0 & 0 & \partial_x^2 \end{bmatrix} \quad \hat{\partial}_{sc}^{\mathrm{T}} = \begin{bmatrix} -1 & 0 & \cdots & 0 & 1 & -h_1\partial_x \\ 0 & -1 & \cdots & 0 & 1 & -h_2\partial_x \\ \vdots & \vdots & \ddots & \vdots & \vdots & \vdots \\ 0 & 0 & \cdots & -1 & 1 & -h_n\partial_x \end{bmatrix} \tag{B.4}$$

The deformation and displacement fields are cast in the following compact forms:

$$\mathbf{e}^{\mathrm{T}} = [\epsilon_{s1} \ \ \epsilon_{s2} \ \ \cdots \ \ \epsilon_{sn} \ \ \epsilon_c \ \ \kappa] \tag{B.5}$$
$$\mathbf{d}^{\mathrm{T}} = [u_{s1} \ \ u_{s2} \ \ \cdots \ \ u_{sn} \ \ u_c \ \ v] \tag{B.6}$$
$$\mathbf{g}^{\mathrm{T}} = [g_1 \ \ g_2 \ \ \cdots \ \ g_n] \tag{B.7}$$

The tangent stiffness matrix of the section is

$$\mathbf{K} = \begin{bmatrix} (EA)_{s1} & 0 & \cdots & 0 & 0 & 0 \\ 0 & (EA)_{s2} & \cdots & 0 & 0 & 0 \\ \vdots & \vdots & \ddots & \vdots & \vdots & \vdots \\ 0 & 0 & \cdots & (EA)_{sn} & 0 & 0 \\ 0 & 0 & \cdots & 0 & (EA)_c & 0 \\ 0 & 0 & \cdots & 0 & 0 & (EI)_0 \end{bmatrix} \tag{B.8}$$

and

$$\mathbf{K}_{sc} = \begin{bmatrix} K_{sc1} & 0 & \cdots & 0 \\ 0 & K_{sc2} & \cdots & 0 \\ \vdots & \vdots & \ddots & \vdots \\ 0 & 0 & \cdots & K_{scn} \end{bmatrix} \tag{B.9}$$

The other auxiliary matrices used in the derivation of exact stiffness matrix are as follow

$$\mathbf{X}_\kappa = \int \left[-\frac{1}{(EI)_0} \mathbb{I}_{2n+6} - \chi \mathbf{X}_g(x) \right] \mathrm{d}x + \mathbb{I}_{2n+1}$$
$$\mathbf{X}_\theta = \int \mathbf{X}_\kappa \, \mathrm{d}x + \mathbb{I}_{2n+2}$$
$$\mathbf{X}_v = \int \mathbf{X}_\theta \, \mathrm{d}x + \mathbb{I}_{2n+3}$$
$$\mathbf{X}_{u_c} = \int \left[\int \left(\frac{1}{(EA)_c} [K_{sc1} \ \ K_{sc2} \ \ \cdots \ \ K_{scn}] \mathbf{X}_g \right) \mathrm{d}x \right] \mathrm{d}x + x\mathbb{I}_{2n+4} + \mathbb{I}_{2n+5}$$
$$\mathbf{X}_{u_{sk}} = \mathbf{X}_{u_c} - \mathbf{X}_{gk} - h_k \mathbf{X}_\theta, \ \ k = 1, 2, \ldots, n$$
$$\chi = \frac{1}{(EI)_0} [h_1 K_{sc1} \ \ h_2 K_{sc2} \ \ \cdots \ \ h_n K_{scn}]$$
$$\mathbb{I}_{2n+1} = [00 \cdots 000 \cdots 0100000] \tag{B.10}$$
$$\mathbb{I}_{2n+2} = [00 \cdots 000 \cdots 0010000]$$
$$\mathbb{I}_{2n+3} = [00 \cdots 000 \cdots 0001000]$$
$$\mathbb{I}_{2n+4} = [00 \cdots 000 \cdots 0000100]$$
$$\mathbb{I}_{2n+5} = [00 \cdots 000 \cdots 0000010]$$
$$\mathbb{I}_{2n+6} = [00 \cdots 000 \cdots 0000001]$$
$$\mathbf{Y}_{N_{sk}} = (EA)_{sk} \partial_x \mathbf{X}_{usk}, \ \ k = 1, 2, \ldots, n$$
$$\mathbf{Y}_{N_c} = (EA)_c \partial_x \mathbf{X}_{uc}(x)$$
$$\mathbf{Y}_M = (EI)_0 \mathbf{X}_\kappa$$
$$\mathbf{Y}_V = \mathbb{I}_{2n+6}$$

References

[1] Morino S. Recent developments in hybrid structures in Japan-research, design and construction. Eng Struct 1998;20(4):336–46.
[2] Newmark NM, Siess CP, Viest I, et al. Tests and analysis of composite beams with incomplete interaction. Proc Soc Exp Stress Anal 1951;9(1):75–92.
[3] Martinelli E, Nguyen Q-H, Hjiaj M. Dimensionless formulation and comparative study of analytical models for composite beams in partial interaction. J Construct Steel Res 2012;75:21–31.
[4] Schnabl S, Saje M, Turk G, Planinc I. Analytical solution of two-layer beam taking into account interlayer slip and shear deformation. J Struct Eng 2007;133(6):886–94.
[5] Girhammar U, Gopu V. Composite beam–columns with interlayer slip-exact analysis. J Struct Eng 1993;119(4):1265–82.
[6] Girhammar UA, Pan DH. Exact static analysis of partially composite beams and beam–columns. Int J Mech Sci 2007;49(2):239–55.
[7] Wu Y-F, Oehlers DJ, Griffith MC. Partial-interaction analysis of composite beam/column members. Mech Struct Mach 2002;30(3):309–32.
[8] Heinisuo M. An exact finite element technique for layered beams. Comput Struct 1988;30(3):615–22.
[9] Faella C, Martinelli E, Nigro E. Steel and concrete composite beams with flexible shear connection: exact analytical expression of the stiffness matrix and applications. Comput Struct 2002;80(11):1001–9.
[10] Xu R, Wu Y. Static, dynamic, and buckling analysis of partial interaction composite members using Timoshenko's beam theory. Int J Mech Sci 2007;49(10):1139–55.
[11] Nguyen Q-H, Martinelli E, Hjiaj M. Derivation of the exact stiffness matrix for a two-layer Timoshenko beam element with partial interaction. Eng Struct 2011;33(2):298–307.
[12] Ranzi G, Bradford M, Uy B. A direct stiffness analysis of a composite beam with partial interaction. Int J Numer Methods Eng 2004;61(5):657–72.
[13] Ayoub A. A force-based model for composite steel–concrete beams with partial interaction. J Construct Steel Res 2005;61(3):387–414.
[14] Salari MR, Spacone E, Shing PB, Frangopol DM. Nonlinear analysis of composite beams with deformable shear connectors. J Struct Eng 1998;124(10):1148–58.
[15] Dall'Asta A, Zona A. Slip locking in finite elements for composite beams with deformable shear connection. Finite Elem Anal Des 2004;40(13):1907–30.

[16] Ranzi G, Zona A. A steel–concrete composite beam model with partial interaction including the shear deformability of the steel component. Eng Struct 2007;29(11):3026–41.
[17] Zona A, Ranzi G. Finite element models for nonlinear analysis of steel–concrete composite beams with partial interaction in combined bending and shear. Finite Elem Anal Des 2011;47(2):98–118.
[18] Schnabl S, Saje M, Turk G, Planinc I. Locking-free two-layer Timoshenko beam element with interlayer slip. Finite Elem Anal Des 2007;43(9):705–14.
[19] Ranzi G. Locking problems in the partial interaction analysis of multi-layered composite beams. Eng Struct 2008;30(10):2900–11.
[20] Sousa Jr JBM. Exact finite elements for multilayered composite beam–columns with partial interaction. Comput Struct 2013;123:48–57.
[21] Pi Y-L, Bradford MA, Uy B. Second order nonlinear inelastic analysis of composite steel–concrete members. I: Theory. J Struct Eng 2006;132(5):751–61.
[22] Ranzi G, Dall'Asta A, Ragni L, Zona A. A geometric nonlinear model for composite beams with partial interaction. Eng Struct 2010;32(5):1384–96.
[23] Battini J-M, Nguyen Q-H, Hjiaj M. Non-linear finite element analysis of composite beams with interlayer slips. Comput Struct 2009;87(13):904–12.
[24] Hjiaj M, Battini J-M, Nguyen Q-H. Large displacement analysis of shear deformable composite beams with interlayer slips. Int J Non-Linear Mech 2012;47(8):895–904.
[25] Sousa Jr JBM, Oliveira CE, da Silva AR. Displacement-based nonlinear finite element analysis of composite beam–columns with partial interaction. J Construct Steel Res 2010;66(6):772–9.
[26] Hozjan T, Saje M, Srpcic S, Planinc I. Geometrically and materially non-linear analysis of planar composite structures with an interlayer slip. Comput Struct 2013;114–115(0):1–17.
[27] Nguyen Q-H, Hjiaj M, Lai V-A. Force-based fe for large displacement inelastic analysis of two-layer Timoshenko beams with interlayer slips. Finite Elem Anal Des 2014;85:1–10.
[28] Crisfield MA. Non-linear finite element analysis of solids and structures. Essentials, vol. 1. John Wiley & Sons, Inc.; 1991.
[29] Malvern LE. Introduction to the mechanics of a continuous medium, no. monograph; 1969.
[30] Wang T. Non-linear bending of beams with uniformly distributed loads. Int J Non-Linear Mech 1969;4(4):389–95.

ANNEXE 4

Q-H. Nguyen, E. Martinelli and M. Hjiaj. Derivation of the "exact" stiffness matrix for a two-layer Timoshenko composite beam element with partial interaction. *Engineering Structures* 2011 ; 33(2) : 298-307. (5-Year IF 2.152) http://dx.doi.org/10.1016/j.engstruct.2010.10.006.

Engineering Structures 33 (2011) 298–307

Contents lists available at ScienceDirect

Engineering Structures

journal homepage: www.elsevier.com/locate/engstruct

Derivation of the exact stiffness matrix for a two-layer Timoshenko beam element with partial interaction

Quang-Huy Nguyen [a], Enzo Martinelli [b], Mohammed Hjiaj [a,*]

[a] Structural Engineering Research Group, INSA de Rennes, 20 avenue des Buttes de Coësmes, CS 70839, F-35708 Rennes Cedex 7, France

[b] Department of Civil Engineering, University of Salerno, Via Ponte don Melillo - 84084 Fisciano (SA), Italy

ARTICLE INFO

Article history:
Received 31 March 2010
Received in revised form
23 August 2010
Accepted 4 October 2010
Available online 18 November 2010

Keywords:
Two-layer beam
Steel–concrete composite beam
Partial interaction
Shear deformation
Closed-form solution
Exact stiffness matrix

ABSTRACT

This paper presents the full closed-form solution of the governing equations describing the behaviour of a shear-deformable two-layer beam with partial interaction. Timoshenko's kinematic assumptions are considered for both layers, and the shear connection is modelled through a continuous relationship between the interface shear flow and the corresponding slip. The limiting cases of perfect bond and no bond are also considered. The effect of possible transversal separation of the two members has been neglected. With the above assumptions, the present work can be considered as a significant development beyond that available from Newmark et al.'s paper [4]. The differential equations derived considering the above key assumptions have been solved in closed form, and the corresponding "exact" stiffness matrix has been derived using the standard procedure basically inspired by the well-known direct stiffness method. This "exact" stiffness matrix has been implemented in a general displacement-based finite element code, and has been used to investigate the behaviour of shear-deformable composite beams. Both a simply supported and a continuous beam are considered in order to validate the proposed model, at least within the linear range. A parametric analysis has been carried out to study the influence of both shear flexibility and partial interaction on the global behaviour of composite beams. It has been found that the effect of shear flexibility on the deflection is generally more important for composite beams characterized by substantial shear interaction.

1. Introduction

For the last few decades, composite members and structures have often been used in civil engineering. Steel–concrete composite beams and nailed timber members are two possible technical solutions based on coupling two layers made up of different materials with the aim of optimizing their mechanical behaviour within a unique member. For these applications, relative displacements generally occur at the interface of the two layers, resulting in the so-called partial interaction. Whereas the transverse separation is often small and can be neglected [1,2], interface slips influence the behaviour of two-layer composite beams and must be considered. Several theoretical models characterized by different levels of approximation have been proposed and are currently available within the scientific literature. Timoshenko [3] developed a theory for composite beams with two bonded materials using the Bernoulli–Euler beam model for each component and assuming no relative displacement between them. The first formulation of an elastic theory for composite beams with partial interaction is commonly attributed to Newmark et al. [4]. They adopted the Euler–Bernoulli kinematic assumptions for both the concrete slab and the steel profile, and considered a continuous and linear relationship between the relative interface displacements (slips) and the corresponding interface shear stresses. This formulation is usually referred to as Newmark's model, which is the most cited work in the area of composite beams with continuous shear connection. In their paper, a closed-form solution is provided for elastic composite beams. Since then, this model has been used extensively by many authors to formulate analytical models for the static response of the composite beams in the linear-elastic range [5–11] as well as in the linear-viscoelastic range [12–16]. Buckling loads for composite members have been derived by Möhler [17]. Newmark's model was further developed to deal with the dynamic response of composite beams, which in some situations governs the design [18–20]. Besides these analytical works, several numerical models based on the basic assumptions of Newmark's model have been developed to investigate the behaviour of composite beams with partial interaction in the nonlinear range (for material nonlinear models, see, e.g., [21–25]; for geometric nonlinear models, see, e.g., [26–29]). Most of these papers are concerned with finite element (FE) formulations. A closed-form solution leading to an "exact" finite element, formally conceived under the so-called

* Corresponding author.
E-mail address: mohammed.hjiaj@insa-rennes.fr (M. Hjiaj).

0141-0296/$ – see front matter © 2010 Elsevier Ltd. All rights reserved.
doi:10.1016/j.engstruct.2010.10.006

"force-based" approach, has been proposed in [7]. Moreover, a space-exact time-discretized stiffness matrix has been proposed in [16] for the time-dependent analysis of continuous composite beams. A key extension of Newmark's model has been proposed in [30–32] by considering more general kinematic assumptions in which relative transverse displacement (uplift) is permitted.

Beyond the various alternative FE formulations proposed in the literature and based on the kinematic assumptions of Newmark's model, the most significant advances in the theory of two-layer beams in partial interaction moved recently toward the introduction of shear flexibility of both layers according to the well-known Timoshenko theory. To the best knowledge of the authors, the earliest Timoshenko beam theory with interlayer slip was developed by Murakami [33] for the analysis of the effect of interlayer slip on the stiffness degradation of laminated beams. This theory is superior to the Euler–Bernoulli beam theory with interlayer slip developed by Newmark et al. [4]. However, Murakami did not provide any analytical model for an elastic shear-deformable layered beam. Instead, he solved the governing equations of the problem using the FE method. Recent contributions on this subject have been proposed in [34–36]. Ranzi and Zona [34] developed a FE model which is obtained by coupling an Euler–Bernoulli beam for the reinforced concrete slab with a Timoshenko beam for the steel beam. Xu and Wu [35] proposed an analytical model considering the Timoshenko kinematic assumption for each component, but they imposed equal cross-section rotation for both components. A fully consistent shear-deformable two-layer beam model has been proposed by Schnabl et al. [37]. In their paper, no transverse separation is allowed, but completely independent shear strains and centroidal rotations of both layers are considered. The governing equations of the problem are provided, but only a solution strategy of these equations is outlined, and no analytical expressions are reported. Furthermore, applications were restricted to simply supported beams.

In this paper, the governing equations of a shear-deformable two-layer composite beam model with partial interaction, based on kinematic assumptions substantially similar to the analytical work reported in [37], are analytically solved. Furthermore, the limiting cases of perfect bond and no bond are also considered. Based on the full analytical solution, the expression for the "exact" stiffness matrix is derived. The proposed "exact" stiffness matrix may be utilized within the framework of a general FE numerical code (displacement-based procedure) for the analysis of any two-layer continuous beam with partial interaction. Two applications are considered in order to investigate the influence of shear flexibility and partial interaction on the overall behaviour of steel–concrete composite beams.

The paper is organized as follows. In Section 2, the governing field equations for a shear-deformable two-layer composite beam with partial interaction are presented. The governing equations of the problem are derived in Section 3. In Section 4, the full analytical solution of the governing equations is provided, regardless of the loading and the nature of the boundary conditions (support and end force). Having at hand the analytical expressions of the displacements and the stress resultants, the exact expression for the stiffness matrix is deduced for a generic shear-deformable two-layer composite beam element in Section 5. Two numerical examples dealing with a simply supported and a two-span continuous composite steel–concrete beam are presented in Section 6 in order to assess the performance of the proposed model and support the conclusions drawn in Section 7.

2. Field equations

This section introduces and outlines the field equations describing the mechanical behaviour of a shear-deformable two-layer composite beam with partial shear interaction in small displacements. Variables subscripted with *a* refer to layer *a* and those with *b* are related to layer *b*. Quantities with subscript *sc* are associated with the interface connection.

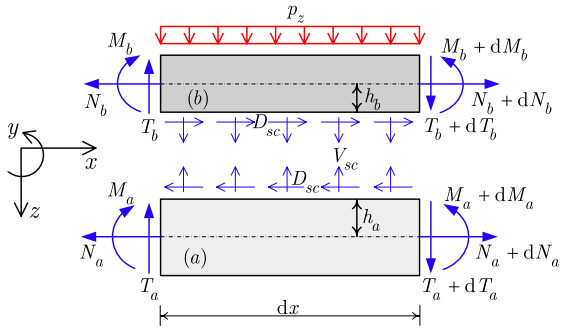

Fig. 1. Free body diagram of an infinitesimal two-layer composite beam segment.

2.1. Equilibrium

The equilibrium equations are derived by considering a differential element d*x* located at an arbitrary position *x* (see Fig. 1).

- Equilibrium equations for layer *a*:

$$\partial_x N_a - D_{sc} = 0 \tag{1}$$

$$\partial_x T_a - V_{sc} = 0 \tag{2}$$

$$\partial_x M_a - T_a + h_a D_{sc} = 0. \tag{3}$$

- Equilibrium equations for layer *b*:

$$\partial_x N_b + D_{sc} = 0 \tag{4}$$

$$\partial_x T_b + V_{sc} + p_z = 0 \tag{5}$$

$$\partial_x M_b - T_b + h_b D_{sc} = 0 \tag{6}$$

where
- $\partial_x^i \bullet = \mathrm{d}^i \bullet / \mathrm{d}x^i$;
- h_i is the distance between the centroid of layer i and the layer interface;
- N_i, T_i, M_i ($i = a, b$) are the axial forces, the shear forces, and bending moments at the centroid of layer i;
- D_{sc} is the shear bond force per unit length;
- V_{sc} is the uplift force per unit length; and
- p_z is the applied external load per unit length.

2.2. Compatibility

The transverse displacement for layer *a* and layer *b* are assumed to be the same. For each layer, the plane sections are supposed to remain planar, but not normal to the neutral axis (Timoshenko's assumption). Consequently, both layer *a* and layer *b* do not have the same rotation and curvature. Based on the above assumptions, the axial, shear, and flexural (curvature) deformations at any section are related to the beam displacements as follows (Fig. 2):

$$\varepsilon_i = \partial_x u_i \tag{7}$$

$$\gamma_i = \partial_x v + \theta_i \tag{8}$$

$$\kappa_i = \partial_x \theta_i, \tag{9}$$

where
- $i = a, b$;
- ε_i and u_i are the axial strain and the longitudinal displacement at the centroid of layer i;
- γ_i is the shear strain of layer i;
- v is the transverse displacement of two layers; and
- θ_i and κ_i are the rotation and curvature of layer i.

The interlayer slip g along the interface can be expressed as follows:

$$g = u_a - u_b - h_a\theta_a - h_b\theta_b. \tag{10}$$

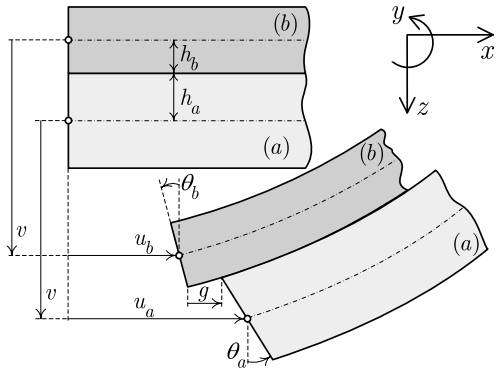

Fig. 2. Kinematics of a shear-deformable two-layer beam with interlayer slip.

2.3. Constitutive relations

The generalized stress–strain relationships for the transverse sections of the two layers are simply obtained by integrating over each cross-section the appropriate uniaxial constitutive model. For a linear-elastic material, these relationships lead to the following generalized relationships:

$$N_i = \int_{A_i} \sigma \, \mathrm{d}A = E_i A_i \varepsilon_i \tag{11}$$

$$T_i = \int_{A_i} \tau \, \mathrm{d}A = k_i^s G_i A_i \gamma_i \tag{12}$$

$$M_i = \int_{A_i} z\sigma \, \mathrm{d}A = E_i I_i \kappa_i, \tag{13}$$

where E_i, G_i, A_i, and I_i are the elastic modulus, the shear modulus, the area, and the second moment of area of layer i; k_i^s is the shear stiffness factor that depends on the cross-sectional shape of layer i. The above relations must be completed by the relationship between the shear bond force D_{sc} and the interlayer slip g:

$$D_{sc} = k_{sc} g, \tag{14}$$

where k_{sc} is the shear bond stiffness.

3. Derivation of the governing equations

The relationships introduced in Section 2 are now combined to derive the equations governing the behaviour of a shear-deformable two-layer composite beam with partial interaction. In particular, differentiating Eq. (8) twice, the following relation is obtained:

$$\partial_x^3 v = \partial_x^2 \gamma_a - \partial_x^2 \theta_a = \partial_x^2 \gamma_b - \partial_x^2 \theta_b, \tag{15}$$

which, in turn, is combined with relations (12) and (13) to obtain

$$\frac{\partial_x^2 T_a}{k_a^s G_a A_a} - \frac{\partial_x M_a}{E_a I_a} = \frac{\partial_x^2 T_b}{k_b^s G_b A_b} - \frac{\partial_x M_b}{E_b I_b}. \tag{16}$$

Moreover, the equilibrium Eqs. (2), (3), (5) and (6) can be introduced into (16) to derive the relationship between the shear forces and the interface stresses:

$$\frac{T_a}{E_a I_a} - \frac{T_b}{E_b I_b} = \frac{\partial_x V_{sc}}{GA} + \left(\frac{h_a}{E_a I_a} - \frac{h_b}{E_b I_b}\right) D_{sc}, \tag{17}$$

where

$$\frac{1}{GA} = \frac{1}{k_a^s G_a A_a} + \frac{1}{k_b^s G_b A_b}.$$

Next, the kinematic Eq. (10) is differentiated twice and then combined with the kinematic Eq. (9) and the constitutive relations (Eqs. (11), (13) and (14)) to provide

$$\frac{\partial_x^2 D_{sc}}{k_{sc}} = \frac{\partial_x N_a}{E_a A_a} - \frac{\partial_x N_b}{E_b A_b} - \frac{h_a \partial_x M_a}{E_a I_a} - \frac{h_b \partial_x M_b}{E_b I_b}. \tag{18}$$

Introducing the equilibrium Eqs. (3) and (6) into the above equation leads to

$$\frac{h_a T_a}{E_a I_a} + \frac{h_b T_b}{E_b I_b} = \left(\frac{1}{EA} + \frac{h_a^2}{E_a I_a} + \frac{h_b^2}{E_b I_b}\right) D_{sc} - \frac{\partial_x^2 D_{sc}}{k_{sc}}, \tag{19}$$

where

$$\frac{1}{EA} = \frac{1}{E_a A_a} + \frac{1}{E_b A_b}.$$

By using the equilibrium relationships (2) and (5), Eqs. (17) and (19) can be finally transformed as follows:

$$\left(\frac{h_a}{E_a I_a} - \frac{h_b}{E_b I_b}\right) \partial_x D_{sc} = \frac{p_z}{E_b I_b} + \frac{V_{sc}}{EI} - \frac{\partial_x^2 V_{sc}}{GA} \tag{20}$$

$$\left(\frac{h_a}{E_a I_a} - \frac{h_b}{E_b I_b}\right) V_{sc} = \frac{h_b p_z}{E_b I_b} + \left(\frac{1}{EA} + \frac{h_a^2}{E_a I_a} + \frac{h_b^2}{E_b I_b}\right) \partial_x D_{sc} - \frac{\partial_x^3 D_{sc}}{k_{sc}}, \tag{21}$$

where

$$\frac{1}{EI} = \frac{1}{E_a I_a} + \frac{1}{E_b I_b}.$$

4. Closed-form solution of the governing equations

In this section, we provide only the analytical solution of the governing equations for the general case of the interface connection (which means that $0 < k_{sc} < \infty$). The analytical formulation for two limiting cases, (1) perfect bond ($k_{sc} = \infty$) and (2) no bond ($k_{sc} = 0$), are presented in Appendix A.

Note that the differential equations (20) and (21) involve two unknown variables: the interface shear bond force D_{sc} and the uplift force V_{sc}. To solve these equations analytically, we need to consider two cases depending on the value of α:

$$\alpha = \frac{h_a}{E_a I_a} - \frac{h_b}{E_b I_b}. \tag{22}$$

4.1. Case 1: $\alpha \neq 0$

From Eq. (21), we obtain

$$V_{sc} = \frac{h_b p_z}{E_b I_b \alpha} + \frac{\beta^2}{\alpha} \partial_x D_{sc} - \frac{1}{k_{sc}\alpha} \partial_x^3 D_{sc}, \tag{23}$$

with

$$\beta^2 = \frac{1}{EA} + \frac{h_a^2}{E_a I_a} + \frac{h_b^2}{E_b I_b}. \tag{24}$$

Substituting Eq. (23) into (20) yields the governing differential equation expressed in terms of the shear bond force D_{sc}:

$$\frac{EI}{k_{sc} GA} \partial_x^5 D_{sc} - \left(\frac{EI}{GA}\beta^2 + \frac{1}{k_{sc}}\right) \partial_x^3 D_{sc} + \mu^2 \partial_x D_{sc} = -\frac{h p_z}{E_a I_a + E_b I_b}, \tag{25}$$

with

$$\mu^2 = \beta^2 - EI\alpha^2 = \frac{1}{EA} + \frac{h^2}{E_a I_a + E_b I_b} \tag{26}$$

$$h = h_a + h_b. \tag{27}$$

Remark. By taking the limit $GA \to \infty$, which corresponds to the Euler–Bernoulli assumption for both layers, Eq. (25) reduces to the governing equation of Newmark's model [4]:

$$\partial_x^3 D_{sc} - k_{sc}\mu^2 \partial_x D_{sc} = \frac{h k_{sc} p_z}{E_a I_a + E_b I_b}. \tag{28}$$

It is worth to mention that Eq. (25) also describes the behaviour of two-layer beams where one of the layers obeys the Bernoulli kinematic assumptions. Now let us prove that the characteristic equation of Eq. (25),

$$\frac{EI}{k_{sc}GA} r^5 - \left(\frac{EI}{GA}\beta^2 + \frac{1}{k_{sc}}\right) r^3 + \mu^2 r = 0, \tag{29}$$

has five real roots. Since

$$\Delta = \left(\frac{EI}{GA}\beta^2 + \frac{1}{k_{sc}}\right)^2 - \frac{4EI}{k_{sc}GA}\mu^2 = \left(\frac{EI}{GA}\beta^2 - \frac{1}{k_{sc}}\right)^2 + \frac{4EI^2\alpha^2}{k_{sc}GA} \geq 0, \tag{30}$$

we can write

$$\frac{EI}{GA}\beta^2 + \frac{1}{k_{sc}} = \frac{EI}{k_{sc}GA}\left(\lambda_1^2 + \lambda_2^2\right) \quad \text{and} \quad \mu^2 = \frac{EI}{k_{sc}GA}\lambda_1^2\lambda_2^2, \tag{31}$$

with

$$\lambda_1^2 = \frac{\frac{EI}{GA}\beta^2 + \frac{1}{k_{sc}} - \sqrt{\Delta}}{2\frac{EI}{k_{sc}GA}} \quad \text{and} \quad \lambda_2^2 = \frac{\frac{EI}{GA}\beta^2 + \frac{1}{k_{sc}} + \sqrt{\Delta}}{2\frac{EI}{k_{sc}GA}}. \tag{32}$$

Using (31), the characteristic Eq. (29) becomes

$$r\left(r^2 - \lambda_1^2\right)\left(r^2 - \lambda_2^2\right) = 0, \tag{33}$$

and it is rather clear that this equation has five real roots: 0, $\pm\lambda_1$, and $\pm\lambda_2$. Thus the solution of the fifth-order differential equation (25) can be expressed as

$$D_{sc} = C_1 e^{\lambda_1 x} + C_2 e^{-\lambda_1 x} + C_3 e^{\lambda_2 x} + C_4 e^{-\lambda_2 x} + C_5 + D_{sc}^0, \tag{34}$$

in which C_i $(i = 1, 5)$ are constants of integration and

$$D_{sc}^0 = -\frac{h p_z}{\mu^2 (E_a I_a + E_b I_b)} x \tag{35}$$

is a particular solution, corresponding to the case of uniformly distributed transverse load p_z. In order to avoid lengthy expressions, in the following development of the solution, we consider that $p_z = 0$ (i.e., $D_{sc}^0 = 0$). In fact, no further conceptual problems arise from taking p_z nonzero.

The following analytical expression for V_{sc} can be obtained by substituting (34) into (23):

$$V_{sc} = C_1\xi_1 e^{\lambda_1 x} - C_2\xi_1 e^{-\lambda_1 x} + C_3\xi_2 e^{\lambda_2 x} - C_4\xi_2 e^{-\lambda_2 x}, \tag{36}$$

where

$$\xi_i\ (i = 1, 2) = \frac{\lambda_i\left(k_{sc}\beta^2 - \lambda_i^2\right)}{k_{sc}\alpha}. \tag{37}$$

4.2. Case 2: $\alpha = 0$

It can be seen from Eqs. (26), (30) and (32) that in the present case we have

$$\lambda_1^2 = \frac{GA}{EI} \quad \text{and} \quad \lambda_2^2 = k_{sc}\beta^2 = k_{sc}\mu^2, \tag{38}$$

so the governing differential equations (20) and (21) are uncoupled:

$$\partial_x^2 V_{sc} - \lambda_1^2 V_{sc} = \frac{GA k_{sc} p_z}{E_b I_b} \tag{39}$$

$$\partial_x^3 D_{sc} - \lambda_2^2 \partial_x D_{sc} = \frac{h k_{sc} p_z}{E_a I_a + E_b I_b}, \tag{40}$$

and both unknowns V_{sc} and D_{sc} can be determined by solving each differential equation. As in case 1, in order to avoid lengthy expressions, we consider that $p_z = 0$. Thus, the solutions for V_{sc} and D_{sc} of the differential equations (46) and (40) can be expressed as

$$V_{sc} = C_1 e^{\lambda_1 x} - C_2 e^{-\lambda_1 x} \tag{41}$$

$$D_{sc} = C_3 e^{\lambda_2 x} + C_4 e^{-\lambda_2 x} + C_5, \tag{42}$$

where C_i $(i = 1, 5)$ are constants of integration.

4.3. Determination of the remaining mechanical variables

Once the analytical expressions for D_{sc} and V_{sc} are determined, those of the displacements and the internal forces can be obtained by using the equilibrium, compatibility, and constitutive equations. It can be observed from the expressions (34), (36), (47) and (42) that, for two cases ($\alpha \neq 0$ and $\alpha = 0$), the analytical expressions for D_{sc} and V_{sc} can be written as follows:

$$D_{sc} = \varrho C_1 e^{\lambda_1 x} + \varrho C_2 e^{-\lambda_1 x} + C_3 e^{\lambda_2 x} + C_4 e^{-\lambda_2 x} + C_5 \tag{43}$$

$$V_{sc} = C_1\xi_1 e^{\lambda_1 x} - C_2\xi_1 e^{-\lambda_1 x} + \varrho C_3\xi_2 e^{\lambda_2 x} - \varrho C_4\xi_2 e^{-\lambda_2 x}, \tag{44}$$

in which

$$\varrho = \begin{cases} 1 & \text{if } \alpha \neq 0 \\ 0 & \text{if } \alpha = 0. \end{cases} \tag{45}$$

D_{sc} and V_{sc} can also be expressed in vector form as follows:

$$D_{sc} = \mathbf{Y}_{D_{sc}}\mathbf{C} \tag{46}$$

$$V_{sc} = \mathbf{Y}_{V_{sc}}\mathbf{C}, \tag{47}$$

where the vectors $\mathbf{Y}_{D_{sc}}$, $\mathbf{Y}_{V_{sc}}$ and $\mathbf{C}$ have the following expressions:

$$\mathbf{Y}_{D_{sc}} = \begin{bmatrix} \varrho e^{\lambda_1 x} & \varrho e^{-\lambda_1 x} & e^{\lambda_2 x} & e^{-\lambda_2 x} & 1 & 0 & 0 & 0 & 0 & 0 \end{bmatrix} \tag{48}$$

$$\mathbf{Y}_{V_{sc}} = \begin{bmatrix} \xi_1 e^{\lambda_1 x} & -\xi_1 e^{-\lambda_1 x} & \varrho\xi_2 e^{\lambda_2 x} & -\varrho\xi_1 e^{-\lambda_2 x} & 0 & 0 & 0 & 0 & 0 & 0 \end{bmatrix} \tag{49}$$

$$\mathbf{C} = \begin{bmatrix} C_1 & C_2 & C_3 & C_4 & C_5 & C_6 & C_7 & C_8 & C_9 & C_{10} \end{bmatrix}^T. \tag{50}$$

Note that the vector $\mathbf{C}$ contains ten constants of integration, C_i $(i = 1, 10)$. At the present state, there are only five constants involved. The remaining constants will appear progressively as a result of the integration process needed for determinating the other force and displacement components (see expressions (59), (60), (65), (66) and (81)).

4.3.1. Determination of the shear forces T_a and T_b

The following expressions of the shear forces T_a and T_b can be derived by solving the system of equations (17) and (19):

$$T_a = \left(\frac{E_a I_a}{hEA} + h_a\right) D_{sc} - \frac{E_a I_a}{h k_{sc}} \partial_x^2 D_{sc} + \frac{h_b E_a I_a}{hGA} \partial_x V_{sc} \tag{51}$$

$$T_b = \left(\frac{E_b I_b}{hEA} + h_b\right) D_{sc} - \frac{E_b I_b}{h k_{sc}} \partial_x^2 D_{sc} - \frac{h_a E_b I_b}{hGA} \partial_x V_{sc}. \tag{52}$$

By introducing Eqs. (23) and (34) into above equations, they can be written in vector form as follows:

$$T_a = \mathbf{Y}_{T_a}\mathbf{C} \tag{53}$$

$$T_b = \mathbf{Y}_{T_b}\mathbf{C}, \tag{54}$$

where

$$\mathbf{Y}_{T_a} = \begin{bmatrix} a_1 e^{\lambda_1 x} & a_1 e^{-\lambda_1 x} & a_2 e^{\lambda_2 x} & a_2 e^{-\lambda_2 x} & a_3 & 0 & 0 & 0 & 0 & 0 \end{bmatrix} \quad (55)$$

$$\mathbf{Y}_{T_b} = \begin{bmatrix} b_1 e^{\lambda_1 x} & b_1 e^{-\lambda_1 x} & b_2 e^{\lambda_2 x} & b_2 e^{-\lambda_2 x} & b_3 & 0 & 0 & 0 & 0 & 0 \end{bmatrix}, \quad (56)$$

in which

$$\begin{aligned} a_i \ (i = 1, 2) &= \left(\frac{E_a I_a}{hEA} + h_a \right) \varrho - \frac{E_a I_a}{h k_{sc}} \varrho \lambda_i^2 + \frac{h_b E_a I_a}{hGA} \xi_i \lambda_i; \\ a_3 &= h_a + \frac{E_a I_a}{hEA} \end{aligned} \quad (57)$$

$$\begin{aligned} b_i \ (i = 1, 2) &= \left(\frac{E_b I_b}{hEA} + h_b \right) \varrho - \frac{E_b I_b}{h k_{sc}} \varrho \lambda_i^2 - \frac{h_a E_b I_b}{hGA} \xi_i \lambda_i; \\ b_3 &= h_b + \frac{E_b I_b}{hEA}. \end{aligned} \quad (58)$$

4.3.2. Determination of the axial forces N_a and N_b

The following analytical expressions for N_a and N_b are obtained from Eqs. (1) and (4) by direct integration:

$$N_a = \frac{\varrho C_1}{\lambda_1} e^{\lambda_1 x} - \frac{\varrho C_2}{\lambda_1} e^{-\lambda_1 x} + \frac{C_3}{\lambda_2} e^{\lambda_2 x} - \frac{C_4}{\lambda_2} e^{-\lambda_2 x} + C_5 x + C_6 \quad (59)$$

$$N_b = -\frac{\varrho C_1}{\lambda_1} e^{\lambda_1 x} + \frac{\varrho C_2}{\lambda_1} e^{-\lambda_1 x} - \frac{C_3}{\lambda_2} e^{\lambda_2 x} + \frac{C_4}{\lambda_2} e^{-\lambda_2 x} - C_5 x - C_7. \quad (60)$$

N_a and N_b can be expressed in vector form as follows:

$$N_a = \mathbf{Y}_{N_a} \mathbf{C} \quad (61)$$

$$N_b = \mathbf{Y}_{N_b} \mathbf{C}, \quad (62)$$

where

$$\mathbf{Y}_{N_a} = \begin{bmatrix} \varrho \frac{e^{\lambda_1 x}}{\lambda_1} & -\varrho \frac{e^{-\lambda_1 x}}{\lambda_1} & \frac{e^{\lambda_2 x}}{\lambda_2} & -\frac{e^{-\lambda_2 x}}{\lambda_2} & x & 1 & 0 & 0 & 0 & 0 \end{bmatrix} \quad (63)$$

$$\mathbf{Y}_{N_b} = -\begin{bmatrix} \varrho \frac{e^{\lambda_1 x}}{\lambda_1} & -\varrho \frac{e^{-\lambda_1 x}}{\lambda_1} & \frac{e^{\lambda_2 x}}{\lambda_2} & -\frac{e^{-\lambda_2 x}}{\lambda_2} & x & 0 & 1 & 0 & 0 & 0 \end{bmatrix}. \quad (64)$$

4.3.3. Determination of the axial displacements u_a and u_b

Once N_a and N_b are obtained, it follows from the compatibility relation (7) and constitutive relation (11) that the axial displacements u_a and u_b can be determined by direct integration. Their expressions are given by

$$u_a = \frac{1}{E_a A_a} \left(\frac{\varrho C_1}{\lambda_1^2} e^{\lambda_1 x} + \frac{\varrho C_2}{\lambda_1^2} e^{-\lambda_1 x} + \frac{C_3}{\lambda_2^2} e^{\lambda_2 x} + \frac{C_4}{\lambda_2^2} e^{-\lambda_2 x} + \frac{C_5}{2} x^2 + C_6 x + C_8 \right) \quad (65)$$

$$u_b = \frac{-1}{E_b A_b} \left(\frac{\varrho C_1}{\lambda_1^2} e^{\lambda_1 x} + \frac{\varrho C_2}{\lambda_1^2} e^{-\lambda_1 x} + \frac{C_3}{\lambda_2^2} e^{\lambda_2 x} + \frac{C_4}{\lambda_2^2} e^{-\lambda_2 x} + \frac{C_5}{2} x^2 + C_7 x + C_9 \right), \quad (66)$$

so u_a and u_b can be expressed in vector form as follows:

$$u_a = \mathbf{X}_{u_a} \mathbf{C} \quad (67)$$

$$u_b = \mathbf{X}_{u_b} \mathbf{C}, \quad (68)$$

with

$$\mathbf{X}_{u_a} = \frac{1}{E_a A_a} \begin{bmatrix} \varrho \frac{e^{\lambda_1 x}}{\lambda_1^2} & \varrho \frac{e^{-\lambda_1 x}}{\lambda_1^2} & \frac{e^{\lambda_2 x}}{\lambda_2^2} & \frac{e^{-\lambda_2 x}}{\lambda_2^2} & \frac{x^2}{2} & x & 0 & 1 & 0 & 0 \end{bmatrix} \quad (69)$$

$$\mathbf{X}_{u_b} = \frac{-1}{E_b A_b} \begin{bmatrix} \varrho \frac{e^{\lambda_1 x}}{\lambda_1^2} & \varrho \frac{e^{-\lambda_1 x}}{\lambda_1^2} & \frac{e^{\lambda_2 x}}{\lambda_2^2} & \frac{e^{-\lambda_2 x}}{\lambda_2^2} & \frac{x^2}{2} & 0 & x & 0 & 1 & 0 \end{bmatrix}. \quad (70)$$

4.3.4. Determination of the rotations θ_a and θ_b

By combining (8) with (12) and (10) with (14), the two following relations are obtained:

$$\theta_a - \theta_b = \frac{T_a}{k_a^s G_a A_a} - \frac{T_b}{k_b^s G_b A_b} \quad (71)$$

$$h_a \theta_a + h_a \theta_b = u_a - u_b - \frac{D_{sc}}{k_{sc}}. \quad (72)$$

It follows that once the expressions for T_a, T_b, u_a, u_b, and D_{sc} are known, the analytical expressions for both rotations are obtained by solving the system of equations (71) and (72) for θ_a and θ_b:

$$\theta_a = \mathbf{X}_{\theta_a} \mathbf{C} \quad (73)$$

$$\theta_b = \mathbf{X}_{\theta_b} \mathbf{C}, \quad (74)$$

where

$$\mathbf{X}_{\theta_a} = \frac{1}{h} \left(\mathbf{X}_{u_a} - \mathbf{X}_{u_b} - \frac{1}{k_{sc}} \mathbf{Y}_{D_{sc}} + \frac{h_b}{k_a^s G_a A_a} \mathbf{Y}_{T_a} - \frac{h_b}{k_b^s G_b A_b} \mathbf{Y}_{T_b} \right) \quad (75)$$

$$\mathbf{X}_{\theta_b} = \frac{1}{h} \left(\mathbf{X}_{u_a} - \mathbf{X}_{u_b} - \frac{1}{k_{sc}} \mathbf{Y}_{D_{sc}} - \frac{h_a}{k_a^s G_a A_a} \mathbf{Y}_{T_a} + \frac{h_a}{k_b^s G_b A_b} \mathbf{Y}_{T_b} \right). \quad (76)$$

4.3.5. Determination of the bending moments M_a and M_b

A direct definition of the bending moments can be obtained by using the analytical expressions for θ_a and θ_b. Moreover, introducing relation (9) into (13) leads to

$$M_a = \mathbf{Y}_{M_a} \mathbf{C} \quad (77)$$

$$M_b = \mathbf{Y}_{M_b} \mathbf{C}, \quad (78)$$

where

$$\mathbf{Y}_{M_a} = E_a I_a \partial_x \mathbf{X}_{\theta_a} \quad (79)$$

$$\mathbf{Y}_{M_b} = E_b I_b \partial_x \mathbf{X}_{\theta_b}. \quad (80)$$

4.3.6. Determination of the transversal displacement v

Finally, the transversal displacement v can be finally obtained by direct integration from Eqs. (8) and (12):

$$v = \int \left(\frac{T_a}{k_a^s G_a A_a} - \theta_a \right) \mathrm{d}x = \mathbf{X}_v \mathbf{C}, \quad (81)$$

where

$$\mathbf{X}_v = \int \left(\frac{\mathbf{Y}_{T_a}}{k_a^s G_a A_a} - \mathbf{X}_{\theta_a} \right) \mathrm{d}x + \begin{bmatrix} 0 & 0 & 0 & 0 & 0 & 0 & 0 & 0 & 0 & 1 \end{bmatrix}. \quad (82)$$

5. Exact stiffness matrix

The exact expression of the stiffness matrix can be easily obtained, starting from the general expressions of the internal force

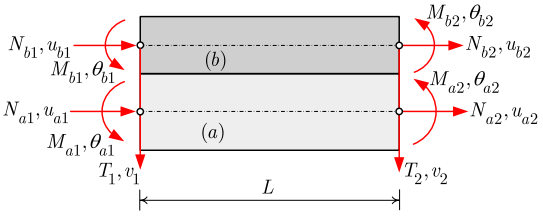

Fig. 3. Nodal forces and displacements of a composite beam element.

and displacement fields. Let a shear-deformable two-layer composite beam element of length L be considered (see Fig. 3). Since the same transverse displacement for the two layers is assumed (no uplift), this element has ten degrees of freedom. Applying the kinematic boundary conditions at $x = 0$ and $x = L$ leads to the relationship between the vector of constants of integration $\mathbf{C}$ and the vector of nodal displacements $\mathbf{q}$ as follows:

$$\mathbf{q} = \mathbf{XC}, \tag{83}$$

where

$$\mathbf{q} = \begin{bmatrix} u_{a1} & u_{b1} & v_1 & \theta_{a1} & \theta_{b1} & u_{a2} & u_{b2} & v_2 & \theta_{a2} & \theta_{b2} \end{bmatrix}^{\mathrm{T}} \tag{84}$$

$$\mathbf{X} = \begin{bmatrix} \mathbf{X}^{\mathrm{T}}_{u_a}(x=0) & \mathbf{X}^{\mathrm{T}}_{u_b}(x=0) & \mathbf{X}^{\mathrm{T}}_{v}(x=0) & \cdots & \mathbf{X}^{\mathrm{T}}_{\theta_b}(x=L) \end{bmatrix}^{\mathrm{T}}. \tag{85}$$

Next, by enforcing the static boundary conditions, the relationship between the vector of constants of integration $\mathbf{C}$ and the vector of nodal forces $\mathbf{Q}$ can be established:

$$\mathbf{Q} = \mathbf{YC}, \tag{86}$$

where

$$\mathbf{Q} = \begin{bmatrix} N_{a1} & N_{b1} & T_1 & M_{a1} & M_{b1} & N_{a2} & N_{b2} & T_2 & M_{a2} & M_{b2} \end{bmatrix}^{\mathrm{T}} \tag{87}$$

$$\mathbf{Y} = \begin{bmatrix} -\mathbf{Y}^{\mathrm{T}}_{N_a}(x=0) & -\mathbf{Y}^{\mathrm{T}}_{N_b}(x=0) & -\mathbf{Y}^{\mathrm{T}}_{T}(x=0) & \cdots & \mathbf{Y}^{\mathrm{T}}_{M_b}(x=L) \end{bmatrix}^{\mathrm{T}}, \tag{88}$$

in which $\mathbf{Y}_T = \mathbf{Y}_{T_a} + \mathbf{Y}_{T_b}$.

Since the nodal displacements are independent variables, the matrix $\mathbf{X}$ is always non-singular. Thus from Eq. (83) the following general expression for the constant vector $\mathbf{C}$ defined in (50) can be obtained:

$$\mathbf{C} = \mathbf{X}^{-1}\mathbf{q}. \tag{89}$$

Inserting this relation into (86) leads to a relationship between the vector of nodal forces and the vector of nodal displacements:

$$\mathbf{Q} = \mathbf{Kq}, \tag{90}$$

in which $\mathbf{K} = \mathbf{YX}^{-1}$ is the exact stiffness matrix for the shear-deformable two-layer composite beam model with interlayer slip and shear deformation.

6. Numerical examples

The purpose of this section is to assess the capability of the proposed "exact" finite element model to satisfactory predict the elastic structural behaviour of composite steel–concrete beams with partial interaction. For that, two composite steel–concrete beams are considered: the simply supported composite beam tested by Aribert et al. [38] and the two-span continuous composite beam tested by Ansourian [39].

6.1. Simply supported steel–concrete composite beam

In this section, the proposed "exact" finite element model is used to predict the elastic deflection of the simply supported

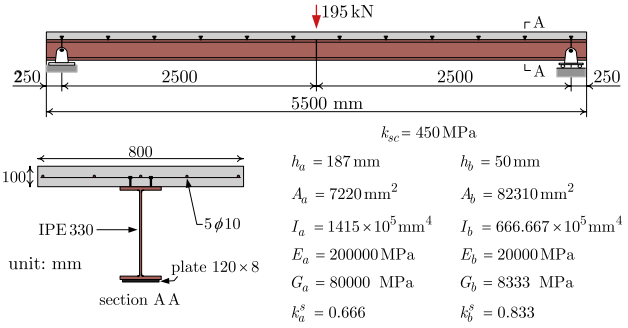

Fig. 4. Geometrical and mechanical characteristics of Aribert's beam [38].

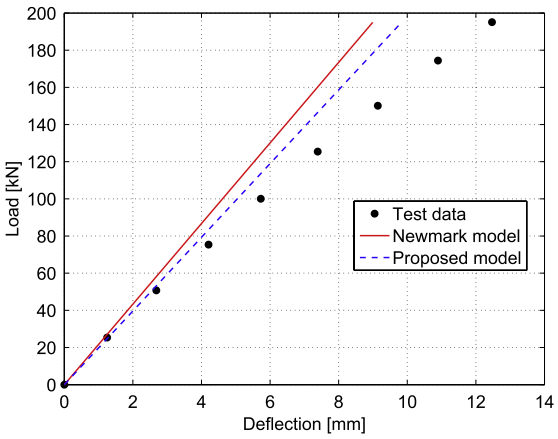

Fig. 5. Load–deflection curves.

composite beam tested by Aribert et al. [38]. This beam was a part of a series of tests aimed at investigating the effect of partial interaction on the behaviour of composite beams. The geometric characteristics and the material properties of the beam are shown in Fig. 4. The beam has a span length of 5000 mm loaded by a single concentrated force at mid-span. The steel section of the beam is IPE 330, reinforced at the bottom by a steel plate of dimensions 120 × 8 mm^2. The slab is 800 mm wide and 100 mm thick, longitudinally reinforced by five steel bars of 14 mm diameter at the mid-depth.

In order to compare the performance of the proposed model against the existing well-known Newmark model [4], the beam is modelled using four elements, which is the smallest number of elements needed for this simulation. Between the supports, two elements are used, and two more elements are placed at the beam ends. It is worth noting that since the model is based on "exact" stiffness matrix, considering more elements does not improve the results. Fig. 5 shows the load–deflection curve underneath the load point: the solid red line is the simulation by means of the proposed model; the dashed blue line corresponds to the calculation with Newmark's model; and the black dots are the experimental data under the considered load level. It can be observed that both analytical responses are slightly more flexible than the experimental response. However, the proposed model is closer to the experimental data than the corresponding simulation based on Newmark's model. This is because the proposed model is based on Timoshenko's beam theory, in which the shear flexibility of the cross-section is taken into account for each layer. Fig. 6 shows the analytical–experimental comparison for the slip distribution along the beam length for a value of concentrated load equal to 195 kN. It can be seen that both analytical models provide almost the same slip distribution and they are in reasonable agreement with the experimental data.

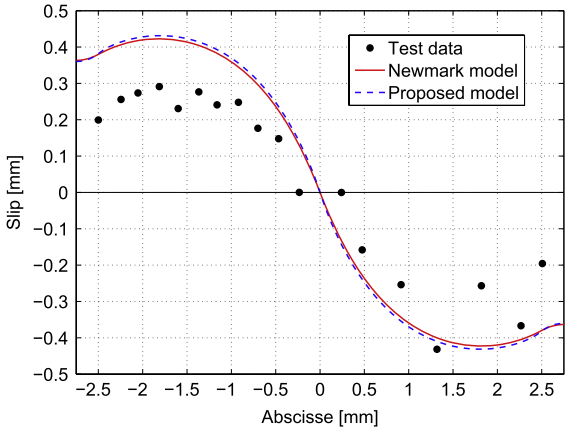

Fig. 6. Slip distribution along the beam length.

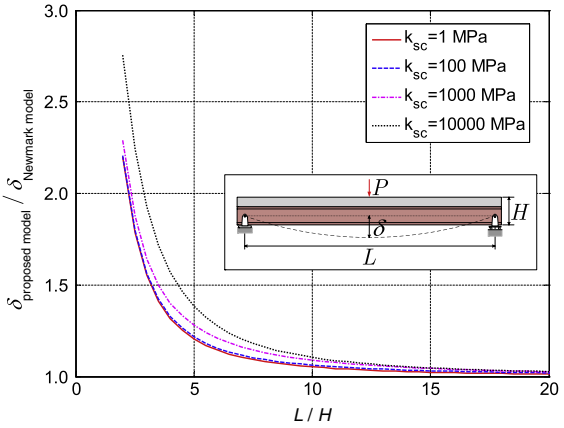

Fig. 7. Mid-span deflection ratio versus the span-to-depth ratio for different shear bond stiffness.

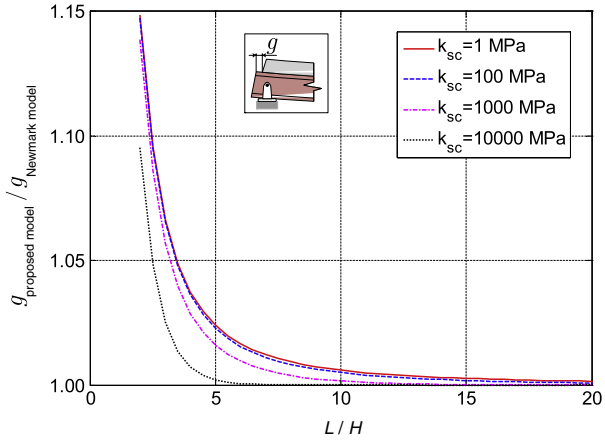

Fig. 8. End beam slip ratio versus the span-to-depth ratio for different shear bond stiffness.

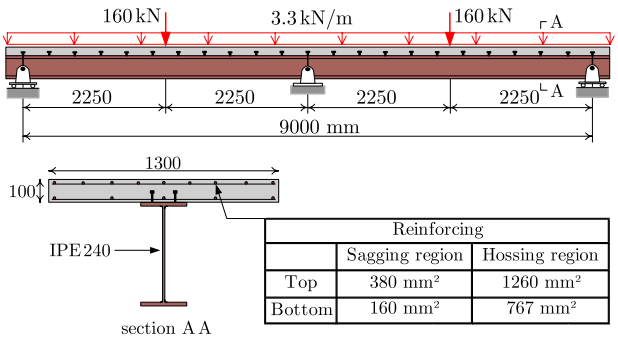

Reinforcing		
	Sagging region	Hossing region
Top	380 mm²	1260 mm²
Bottom	160 mm²	767 mm²

Fig. 9. Geometrical characteristics of Ansourian's beam CTB6 [39].

The role of shear flexibility of the two connected members can be analyzed by comparing the mechanical response obtained with the proposed model against the corresponding response predicted by the well-known Newmark model [4]. In particular, the comparison can be practically carried out in terms of mid-span deflections evaluated by means of the two above-mentioned models. Fig. 7 shows the mid-span deflections obtained with the proposed model compared with those obtained with Newmark's model for different span-to-depth ratios (L/H) and shear bond stiffness (k_{sc}). As expected, the deflection predicted by the proposed model is larger than the corresponding one evaluated according to Newmark's model, for any value of the ratio L/H. In particular, the black dotted line refers to the case of practically full interaction (rigid connection with $k_{sc} = 10\,000$ MPa): it is basically the same relationship that could have been derived by comparing the deflection obtained for solid beams modelled through the usual Timoshenko and Bernoulli theories, respectively. The other curves, related to cases of lower shear stiffness, monotonically reduce to the case of (practically) absent interaction (loose connection with $k_{sc} = 1$ MPa). It can be seen that partial interaction results in a reduction of the effect of shear flexibility of the connected members.

A further comparison is also proposed in terms of end beam slip (see Fig. 8). Since the slip basically depends on the degree of shear interaction, the influence of the shear deformations on the beam end slip is more pronounced for low value of the bond stiffness k_{sc}. As expected, the effect of shear flexibility of the connected members emerges for low L/H ratios. The other curves tend to the (almost) full interaction case ($k_{sc} = 10\,000$ MPa) as the interface shear bond stiffness k_{sc} increases. The curves in Fig. 8 approach the asymptotic value of 1 for $L/H \to \infty$ much more quickly than those represented in Fig. 7. This means that transverse displacements are more affected by shear flexibility than interface slip, whose value is more directly controlled by the interface stiffness k_{sc} considered by both the proposed model and the well-known Newmark model for composite beams in partial interaction.

6.2. Two-span continuous steel–concrete composite beam

The proposed model which was successfully applied above to the simply supported composite beam is now used to simulate a two-span continuous steel–concrete composite beam. Beam CTB6, which was a part of the experimental program carried out by Ansourian [39], is considered. The geometric definition of the beam is depicted in Fig. 9. Beam CTB6 has two equal spans of 4500 mm. It is subjected to its self-weight of 3.3 kN/m, and two concentrated loads are applied at the centre of each span. The steel beam section is IPE 240. The concrete slab is 1300 mm wide and 100 mm thick, longitudinally reinforced by steel bars at the top and bottom with different reinforcement ratio in the sagging and hogging region. The distances from the interface to the bottom and the top steel bars are 25 mm and 75 mm, respectively. Shear stiffness factors of 0.666 and of 0.833 are adopted for the steel beam section and concrete slab section, respectively. The material parameters used in the computer analysis are $E_a = 210\,000$ MPa; $G_a = 80\,769$ MPa; $E_b = 34\,000$ MPa; $G_b = 14\,167$ MPa. The shear bond stiffness (k_{sc}) is not given in [39], and a value of 10 000 MPa has been assumed for k_{sc}.

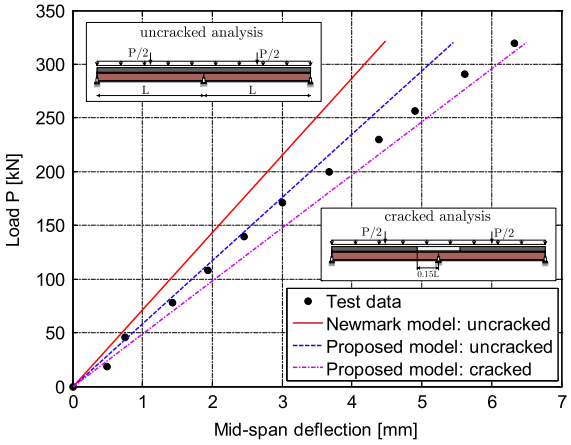

Fig. 10. Load versus deflection curves.

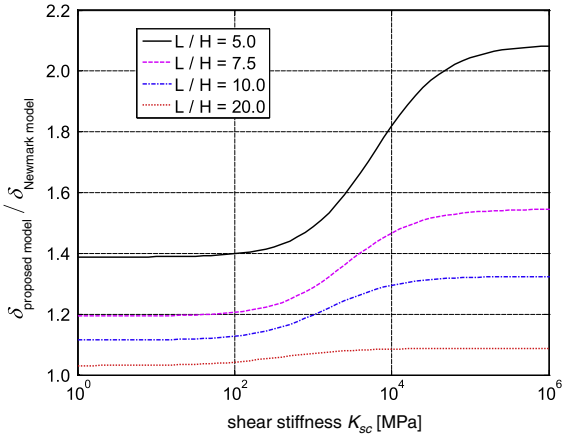

Fig. 11. Mid-span deflection ratio versus the shear bond stiffness for different span-to-depth ratio.

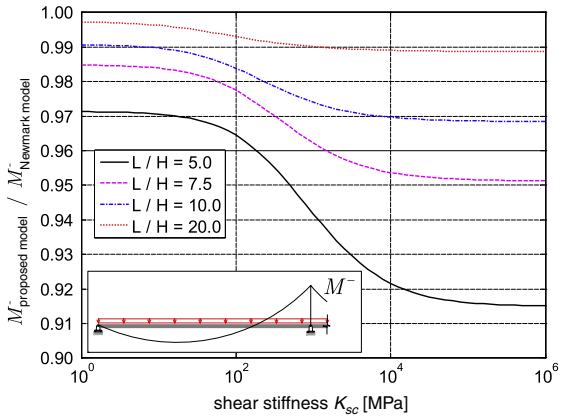

Fig. 12. Bending moment at internal support ratio versus the shear bond stiffness for different span-to-depth ratio.

Two analyses have been carried out using the proposed model. The first one includes an *uncracked analysis*, in which the concrete cracking in the slab is ignored. The second analysis comprises a "cracked analysis", as suggested by Eurocode 4 [40]. In this analysis, concrete cracking is taken into account by neglecting the concrete contribution along 15% of the span length on each side of the internal support. Due to the symmetry of the problem, only one half of the beam is considered in the numerical simulations. The mid-span deflections obtained by the proposed model, using two elements for the *uncracked analysis* and three elements for the *cracked analysis*, are compared against the experimental results in Fig. 10. As can be seen from this figure, the model predicts the deflection curve with the "cracked analysis" rather well. However, with the *uncracked analysis*, the model underestimates the mid-span deflection. These results indicate that the concrete cracking effects must be taken into account for continuous composite beams even under serviceability loads.

Fig. 11 reports on the vertical axis the same deflection ratio already introduced in Fig. 7. In this case, it is represented as a function of the interface modulus k_{sc} for four different values of the length-to-depth ratio L/H. These results are obtained by means of the *uncracked analysis*. The figure confirms that shear flexibility plays a more important role in the case of low L/H ratios and full connection. As shown in this figure, a significant increase of the mid-span deflection ratio is noted for small values of L/H when k_{sc} increases from 1 MPa (almost no interaction) to 10^6 MPa (nearly full interaction). This can be explained by the fact that full interaction amplify the effect of shear deformation which, in this case, is already important because of the small value of L/H. However, for large values of L/H, the mid-span deflection ratio is almost uninfluenced by k_{sc}. This is because the two single layers have a higher span-length-to-depth ratio.

Finally, the comparison between the proposed model and Newmark model is presented in terms of negative bending moment M^- achieved on the intermediate support of the analyzed continuous composite beams (see Fig. 12). The four curves tend to a clear asymptotic value as k_{sc} approaches infinity. Such a limit value could be derived by comparing the Timoshenko and Bernoulli solutions for the same composite beam in full interaction. As expected, it is lower for the "shortest" beam ($L/H = 0.5$) and tends to the unity as the beams get slenderer.

7. Conclusions

In this paper, the exact expression of the stiffness matrix has been developed for a two-layer Timoshenko composite beam with interlayer slip. This "exact" stiffness matrix has been obtained by deriving a closed-form solution of the governing equations of the problem. The proposed exact stiffness matrix can be used in a displacement-based procedure for the elastic analysis of shear-deformable two-layer continuous beams with interlayer slip and arbitrary loading and support conditions. Furthermore, the model is capable of performing both cracked and uncracked analyses for continuous composite steel–concrete beams, as defined in Eurocode 4 [40]. The influence of both shear flexibility and partial interaction can be covered by the present model, which is based on rather general kinematic assumptions within the framework of beam theory.

The performance of the proposed model has been assessed by comparing its predictions against experimental results considering simply supported and continuous steel–concrete composite beams. It has been found that, compared to Newmark model, the proposed model gives a better agreement between the predicted deflection and the measured deflection. Regarding the slip, it has been observed that both models provide the same slip distribution, which is fairly close to the measured one. Furthermore, this indicates also that by taking into account the shear deformations of each layer the present model is superior to Newmark model. The effect of concrete cracking in the hogging moment regions has been investigated by means of a well-known design-oriented methodology proposed by the European structural code for composite structures. The results indicated that the concrete cracking

must be taken into account in the calculation of the deflection of continuous composite beams even under serviceability loads.

Finally, the influence of shear flexibility and partial interaction on the overall behaviour of these two composite beams has been also investigated. A parametric analysis, based on various values of the length-to-depth ratio and of the shear bond stiffness, has been performed. It has been found that the effect of shear flexibility on the deflection is generally more important for composite beams characterized by substantial shear interaction. The results indicated that partial interaction results in a reduction of the effect of shear flexibility on the deflection of the connected members. Further, it has been observed that, in contrast with the deflection, the slip is almost unaffected by the shear flexibility.

Appendix. Analytical solution for the limiting cases of the interface connection

In this Appendix, the closed-form solution of the governing equations is derived for the two limiting cases of the interface connection (perfect bond and no bond). Only the analytical expressions for the primary variables (D_{sc} and V_{sc}) are given. Once these expressions are determined, the expressions for the remaining mechanical variables can be obtained by following the same steps as in Section 4.3.

A.1. Case of perfect bond

This case corresponds to an infinite value of the shear bond stiffness: $k_{sc} \rightarrow \infty$. The governing differential equation (21) becomes

$$\left(\frac{h_a}{E_aI_a} - \frac{h_b}{E_bI_b}\right) V_{sc} = \frac{h_b p_z}{E_bI_b} + \left(\frac{1}{EA} + \frac{h_a^2}{E_aI_a} + \frac{h_b^2}{E_bI_b}\right) \partial_x D_{sc}. \tag{A.1}$$

By eliminating $\partial_x D_{sc}$ in (20) and (A.1), one obtains

$$\frac{EI}{GA}\partial_x^2 V_{sc} - \frac{\mu^2}{\beta^2} V_{sc} = \frac{\left(\beta^2 + \alpha h_b\right) p_z EI}{\beta^2 E_bI_b}, \tag{A.2}$$

where α, β and μ are defined in (22), (24) and (26), respectively. The solution of the above equation is

$$V_{sc} = C_1 e^{\frac{\mu}{\beta}\lambda_1 x} + C_2 e^{-\frac{\mu}{\beta}\lambda_1 x} - \frac{\left(\beta^2 + \alpha h_b\right) p_z EI}{\mu^2 E_bI_b}, \tag{A.3}$$

where λ_1 is defined in (38) and C_1 and C_2 are constants of integration. After replacing V_{sc} in (A.1) by its expression (A.3), the following closed-form expression for D_{sc} can be obtained by direct integration:

$$D_{sc} = \frac{\alpha C_1}{\beta\mu} e^{\frac{\mu}{\beta}\lambda_1 x} - \frac{\alpha C_2}{\beta\mu} e^{-\frac{\mu}{\beta}\lambda_1 x} + C_3 - \left(\frac{\left(\beta^2 + \alpha h_b\right)\alpha EI}{\mu^2} + h_b\right) \frac{p_z x}{\beta^2 E_bI_b}, \tag{A.4}$$

where C_3 is a constant of integration.

Remark. It should be noted that the analytical expression of V_{sc} contains an exponential function and a polynomial function. As a result, the analytical expressions for the shear forces T_a and T_b as well as the rotations θ_a and θ_b will involve the same functions. In classical bi-material Timoshenko beam theory, the rotation is unique for the whole cross-section and is expressed with polynomial functions. This is in sharp contrast with the present model, in which the rotations of the layer are independent and therefore can have different values even for the perfect bond case.

A.2. Case of no bond

In this case, the governing differential equations (20) and (21) are reduced to the following single differential equation by setting $k_{sc} = 0$ and $D_{sc} = 0$:

$$\frac{\partial_x^2 V_{sc}}{GA} - \frac{V_{sc}}{EI} = \frac{p_z}{E_bI_b}. \tag{A.5}$$

The solution of the above equation is

$$V_{sc} = C_1 e^{\lambda_1 x} + C_2 e^{-\lambda_1 x} - \frac{p_z EI}{E_bI_b}, \tag{A.6}$$

where C_1 and C_2 are constants of integration; λ_1 is defined in (38).

References

[1] Abel-Aziz K, Aribert JM. Calcul des poutres mixtes jusqu'à l'état ultime avec un effet de soulèvement à l'interface acier–béton. Construction métallique. No. 4; 1985 [in French].
[2] Robinson H, Naraine KS. Slip and uplift effects in composite beams. In: Proceedings of the engineering foundation conference on composite construction. ASCE; 1988. p. 487–97.
[3] Timoshenko SP. Analysis of bi-metal thermostats. J Opt Soc Amer 1925;11: 233–55.
[4] Newmark MN, Siess CP, Viest IM. Tests and analysis of composite beams with incomplete interaction. Proc Soc Exp Stress Anal 1951;9(1):75–92.
[5] Heinisuo M. An exact finite element technique for layered beam. Comput Struct 1988;30(3):615–22.
[6] Girhammar UA, Gopu KA. Composite beam–column with interlayer slip exact analysis. J Struct Eng, ASCE 1993;119(4):2095–111.
[7] Faella C, Martinelli E, Nigro E. Steel and concrete composite beams: "exact" expression of the stiffness matrix and applications. Comput Struct 2002;80: 1001–9.
[8] Wu YF, Oehlers DJ, Griffith MC. Partial-interaction analysis of composite beam/column members. Mech Struct Mach 2002;30(3):309–32.
[9] Seracino R, Lee CT, Lim TC, Lim JY. Partial interaction stresses in continuous composite beams under serviceability loads. J Constr Steel Res 2004;60: 1525–43.
[10] Ranzi G, Bradford MA, Uy B. A direct stiffness analysis of a composite beam with partial interaction. Int J Numer Methods Eng 2004;61:657–72.
[11] Girhammar UA, Pan D. Exact static analysis of partially composite beams and beam–columns. Int J Mech Sci 2007;49:239–55.
[12] Bradford MA, Gilbert RI. Composite beams with partial interaction under sustained loads. J Struct Eng, ASCE 1992;118(7):1871–83.
[13] Gilbert RI, Bradford MA. Time-dependent behavior of continuous composite beams at service loads. J Struct Eng, ASCE 1995;121(2):319–27.
[14] Ranzi G, Bradford MA. Analytical solutions for the time-dependent behaviour of composite beams with partial interaction. Internat J Solids Structures 2006; 43(13):3770–93.
[15] Jurkiewiez B, Buzon S, Sieffert JG. Incremental viscoelastic analysis of composite beams with partial interaction. Comput Struct 2005;83(21–22): 1780–91.
[16] Nguyen QH, Hjiaj M, Uy B. Time-dependent analysis of composite beams with partial interaction based on a time-discrete exact stiffness matrix. Eng Struct 2010;32(9):2902–11.
[17] Möhler K. Über das Tragverhalten von BiegetrSgern und DruckstSben mit Zusammengesetzten Querschnitten und nachgiebigen Verwindungsmitteln. Technischen Hochschule Fridericiana zu Karlsruhe; 1956.
[18] Girhammar UA, Pan D. Dynamic analysis of composite members with interlayer slip. Internat J Solids Structures 1993;30(6):797–823.
[19] Adam C, Heuer R, Jeschko A. Flexural vibrations of elastic composite beams with interlayer slip. Acta Mech 1997;125(1–4):17–30.
[20] Girhammar UA, Pan D, Gustafsson A. Exact dynamic analysis of composite beams with partial interaction. Int J Mech Sci 2007;49:239–55.
[21] Gattesco N. Analytical modelling of nonlinear behaviour of composite beams with deformable connection. J Constr Steel Res 1999;52:195–218.
[22] Salari MR, Spacone E. Analysis of steel–concrete composite frames with bond–slip. J Struct Eng, ASCE 2001;127(11):1243–50.
[23] Ayoub A, Filippou FC. Mixed formulation of nonlinear steel–concrete composite beam element. J Struct Eng, ASCE 2000;126(3):371–81.
[24] Spacone E, El-Tawil S. Nonlinear analysis of steel–concrete composite structures: state-of-the-art. J Struct Eng, ASCE 2004;130(2):1901–12.
[25] Nguyen QH, Hjiaj M, Uy B, Guezouli S. Analysis of composite beams in the hogging moment regions using a mixed finite element formulation. J Constr Steel Res 2009;65(3):737–48.
[26] Saje M, Cas B, Planinc I. Non-linear finite element analysis of composite planar frames with an interlayer slip. Comput Struct 2004;82:1901–12.
[27] Krawczyk P, Rebora B. Large deflections of laminated beams with interlayer slips—part 2: finite element development. Eng Comput 2007;24(1):33–51.

[28] Battini JM, Nguyen QH, Hjiaj M. Non-linear finite element analysis of composite beams with interlayer slips. Comput Struct 2009;87(13–14):904–12.
[29] Ranzi G, Dall'Asta A, Ragni L, Zona A. A geometric nonlinear model for composite beams with partial interaction. Eng Struct 2010;32:1384–96.
[30] Adekola AO. Partial interaction between elastically connected elements of a composite beam. Internat J Solids Structures 1968;4:1125–35.
[31] Gara F, Ranzi G, Leoni G. Displacement-based formulations for composite beams with longitudinal slip and vertical uplift. Int J Numer Methods Eng 2006;65:1197–220.
[32] Kroflic A, Planinc I, Saje M, Turk G, Cas B. Non-linear analysis of two-layer timber beams considering interlayer slip and uplift. Eng Struct 2010;32:1617–30.
[33] Murakami H. A laminated beam theory with interlayer slip. J Appl Mech 1984;51:551–9.
[34] Ranzi Z, Zona A. A steel–concrete composite beam model with partial interaction including the shear deformability of the steel component. Eng Struct 2007;29(11):3026–41.
[35] Xu R, Wu Y. Static, dynamic, and buckling analysis of partial interaction composite members using Timoshenko's beam theory. Int J Mech Sci 2007;49:1139–55.
[36] Dezi L, Gara F, Leoni G. A shear deformable steel–concrete composite beam model. In: Proceedings of the ICSAS'07; 2007. p. 457–64.
[37] Schnabl S, Saje M, Turk G, Planinc I. Analytical solution of two-layer beam taking into account interlayer slip and shear deformation. J Struct Eng, ASCE 2007;133(6):886–94.
[38] Aribert JM, Labib AG, Rival JC. Etude numérique et expérimental de l'influence d'une connexion partielle sur le comportement de poutres mixtes. Communication présentée aux journées AFPC. Mars. Thème 1, sous-thème; 1983 [in French].
[39] Ansourian P. Experiments on continuous composite beams. Proc Inst Civ Eng 1982;73:25–51.
[40] Eurocode 4. Design of composite steel and concrete structures: general rules and rules for building. Part 1.1; 1994.

ANNEXE 5

Q-H. Nguyen, M. Hjiaj and S. Guezouli. Exact finite element model for shear-deformable two-layer beams with discrete shear connection. *Finite Element Analysis and Design* 2011 ; 47(7) : 718-727. (5-Year IF 1.967) http://dx.doi.org/10.1016/j.finel.2011.02.003.

Finite Elements in Analysis and Design 47 (2011) 718–727

Contents lists available at ScienceDirect

Finite Elements in Analysis and Design

journal homepage: www.elsevier.com/locate/finel

Exact finite element model for shear-deformable two-layer beams with discrete shear connection

Quang-Huy Nguyen *, Mohammed Hjiaj, Samy Guezouli

Structural Engineering Research Group, INSA de Rennes, 20 avenue des Buttes de Coësmes, CS 70839, F-35708 Rennes Cedex 7, France

ARTICLE INFO

Article history:
Received 11 October 2010
Received in revised form
17 February 2011
Accepted 18 February 2011
Available online 12 March 2011

Keywords:
Two-layer beam
Interlayer slip
Discrete shear connection
Transverse shear deformation
Closed-form solution
Exact stiffness matrix

ABSTRACT

This paper presents an exact finite element model for the linear static analysis of shear-deformable two-layer beams with interlayer slip. The layers are connected in a discontinuous way and therefore the shear connection is modeled using concentrated spring elements at each connector location. The Timoshenko beam theory is adopted for each layer in order to take into account the transverse shear deformations. It is assumed that no uplift can occur. Both layers have, thus, the same transversal deflection but different rotations and curvatures. The effect of friction at the interface has been accounted for by assuming that the friction force is proportional to the normal force at the interface. Based on the above key assumptions, the governing equations of the problem are established and an original closed-form solution is derived. From the analytical expressions for the displacement and force fields, the exact stiffness matrix for a generic two-layer beam element is deduced, which can be incorporated in any displacement-based F.E. code for the linear static analysis of two-layer beams with interlayer slip and arbitrary loading and support conditions. Finally, a parametric study, dealing with a two-span layered composite beam subjected to the uniformly distributed load, is carried out to study the effects of varying material and geometric parameters, such as connector spacing, interlayer friction coefficient, the connector stiffness, flexural-to-shear moduli ratios and span-to-depth ratios. The results indicated that the deflection is a quasi-linear function of the flexural-to-shear ratio (E/G) and the shear deformation begins to affect significantly the deflection when the length-to-depth ratio (L/H) is below 8. Further, the effect of the interlayer friction on the deflection becomes significant if the connector is rigid. Furthermore, the shear deformation effect on the cross-section rotation is more pronounced in the layer with low flexural stiffness.

1. Introduction

Composite members have been widely used in recent years, and this trend will continue to grow into the foreseeable future. The use of composite beams and/or columns has been spurred in part because composites exhibit a unique set of characteristics including being light weight, high strength and stiffness, and fire resistant. Steel–concrete composite beams and timber–concrete beams are two usual members obtained by coupling two layers made up of different materials. The shear force transfer at the connection between the layers is typically carried by two main mechanisms: mechanical interaction which is due to connectors; and friction which is assumed proportional to the normal force at the interface (incipient sliding). The mechanical behavior of composite members depends to a large extent on the behavior of the connecting devises. If the layers are connected continuously by means of strong adhesives, the mechanical assumption of a perfect bond between the layers is reasonable. However, the layers are often connected in a discrete way by means of connectors (shear studs, nails, etc.) which are not rigid. Therefore, slip and uplift can occur at the layer interface. Whereas the uplift is often small and can be neglected [1,2], interlayer slip influences significantly the behavior of two-layer beams and must be considered. This phenomenon is called partial interaction (or partial bond) which is an important issue in composite construction because of the implications it has on energy dissipation and local stress distributions, and inevitably increases the complexity of the composite beam analysis [3]. It can be found in the literature that the mechanical shear connection is modeled either using the concentrated springs at connector locations (namely discrete bond model) or using the distributed springs (namely continuous bond model). Indeed, the discrete bond model seems to describe the true nature of the connection of the usual two-layer beams. However, it requires a large number of elements, especially in the case of dense connection. In order to reduce the number of elements needed for the analysis, several researchers assumed that the bond stress is continuous along the layer interface and adopted the continuous bond model. The equivalent

* Corresponding author. Tel.: +33 2 23 23 86 83; fax: +33 2 23 23 84 48.
E-mail address: quang-huy.nguyen@insa-rennes.fr (Q.-H. Nguyen).

0168-874X/$ - see front matter © 2011 Elsevier B.V. All rights reserved.
doi:10.1016/j.finel.2011.02.003

distributed spring stiffness is actually computed by simply dividing the stiffness of a single row of the connectors by their distance along the beam length. However, using the continuous bond model for the layered beam with large connector spacing may lead to a significant underestimation of the transversal deflection as it will be shown in this paper.

At early stage of the use of layered beams, full interaction (perfect bond) was assumed in the design. It is until mid-fifties that Newmark and his co-authors [4] pointed out the influence of partial interaction on the overall elastic behavior of steel–concrete composite beams. In their seminal contribution, they proposed a new theory that accounts for partial interaction. The shear connection was modeled using continuous bond model. Both layers were assumed to follow the kinematic assumptions of Euler–Bernoulli beam theory. They derived the governing equations and solved the equilibrium equation expressed in terms of the axial force. Since, this solution was extensively used by many authors to formulate analytical models for the static response of the two-layer beams and columns with interlayer slip in the linear-elastic range (e.g. [5–12]) as well as in the linear-viscoelastic range (e.g. [13–16,18]). Newmark's model was further developed to deal with the dynamic response of composite beams (e.g. [19–22]). Recently, Faella et al. [8] presented an exact finite element model based on exact analytical expression of the stiffness matrix. Moreover, a space-exact time-discretized stiffness matrix has been proposed in [17,18] for the time-dependant analysis of continuous composite beams. An extension of Newmark's model has been proposed in [23] by considering more general kinematic assumptions where the uplift is permitted. Besides these analytical works, several numerical models, especially finite element models, based on the Euler–Bernoulli beam theory have been developed Qto investigate the behavior of composite beams with partial interaction in the nonlinear range (for material nonlinearity, see e.g. [24–29]; for geometric nonlinearity, see e.g. [30–33]; and for both material and geometric nonlinearity, see e.g. [34]).

Note that all the above-mentioned works adopt the continuous bond model for the interface connection. It can be seen in the literature that only few studies to date are concerned with the discrete bond model. To the best of our knowledge, the earliest numerical model dealing with discrete flexible connection was proposed by Aribert and Labib [35] for the nonlinear material analysis of composite beams. The model was next extended to take into account the uplift effects [1]. Note that in the Aribert and Labib's model, the transfer-matrix method was utilized as numerical solution technique and thus it may lead to numerical instability when the number of the computed sections (or connector) is important. Aribert et al. [36] later developed a displacement-based finite element model based for composite beams with discrete connection and taking into account the local bucking. Recently, Nguyen et al. [37] developed a mixed finite element model suitable for the nonlinear analysis of composite beams with discrete connection in the hogging moment regions where tension-stiffening has a significant influence.

Most contributions to date employed the classical Euler–Bernoulli beam theory with interlayer slip proposed by Newmark et al. [4]. It is well known that this theory neglects the transversal shear deformation by imposing the kinematic constraint of zero shear strain and infinite shear stiffness. Therefore, in the case of short and thick layered beams where span-to-depth ratio is small and the bending-to-shear stiffness ratio is large, the effect of shear deformation can be significant and therefore the Euler–Bernoulli beam theory with interlayer slip can be questioned. The most significant advances in the theory of two-layer beams with interlayer slip moved recently toward the introduction of shear deformation of both layers according to the Timoshenko beam theory. This theory is based on the assumption that, for each layer, the cross-sections remain plane and undistorted after deformation. Consequently, the transverse shear strain is constant through the layer cross-section. In fact, as early in 1984, Timoshenko's beam theory with interlayer slip has been developed by Murakami [38] for the analysis of the effect of interlayer slip on the stiffness degradation of laminated beams with distributed bond. However, Murakami did not provide the analytical solution for the linear elastic case. Instead, he solved the governing equations of the problem using the finite element method. Recent contributions on this subject have been proposed in [39–42]. Ranzi and Zona [39] developed a finite element model which is obtained by coupling an Euler–Bernoulli beam for the reinforced concrete slab with a Timoshenko beam for the steel beam. This model has been enhanced by the same authors [42] by considering the Timoshenko kinematics for both concrete slab and steel beam. Xu and Wu [40] proposed an analytical model considering the Timoshenko kinematic assumption for each component but they have imposed the constraint of equal cross-section rotation for both layers. Schnabl et al. [43] developed a fully consistent analytical model for the shear-deformable two-layer beams with distributed bond. In this model, completely independent shear strains and cross-section rotations of both layers are considered. The governing equations of the problem are provided but only a solution strategy of these equations is outlined and no analytical expressions are reported. Furthermore, applications were restricted to simply supported beams. Recently, Nguyen et al. [44] presented a full closed-form solution for shear-deformable two-layer beams with distributed bond where analytical expressions for all mechanical variables are derived. Based on this closed-form solution, the corresponding exact stiffness matrix was also deduced.

The goal of this paper is to develop a finite element model based on the exact stiffness matrix for the linear static analysis of two-layer beams which takes into account the effect of interlayer slip and transverse shear deformation. The paper focuses on two-layer beams connected in a discontinuous way by the connectors (discrete bond). The shear connection is modeled using concentrated spring elements at each connector location. The Timoshenko beam theory is adopted for each layer. The effect of friction at the interface is accounted for by assuming that the force of friction is proportional to the normal force at the interface. Firstly, the governing differential equations of the problem are formulated and then analytically solved from which analytical expressions for all mechanical variables are determined. Next, the corresponding "exact" stiffness matrix is derived for a shear-deformable two-layer beam element connected discontinuously at its ends. This stiffness matrix may be implemented into any finite element code for the exact static elastic analysis of two-layer beams with arbitrary boundary conditions. Finally, a parametric study dealing with a two-span layered beam is carried out with the aim to study the influence of varying material and geometric parameters on the deflection, such as connector spacing, interlayer friction coefficient, modulus of the connectors, flexural-to-shear moduli ratios and span-to-depth ratios.

2. Structural model

2.1. Field equations

In this section, we recall the field equations for a two-layer beam with discrete shear connection [36]. The following assumptions are made:

- No uplift occurs between the two layers; therefore both layers have the same transverse displacement.

- Frictional slip can occur at the interlayer (partial interaction).
- Timoshenko's kinematic assumptions hold for both layers.
- Concentrated springs are used to model the discrete shear connection.
- The displacements are small and all materials behave linear elastic.

All variables subscripted with i (i=1,2) belong to the layer i and those with st belong to the shear connectors.

2.1.1. Equilibrium

Due to the discrete nature of the shear connection, the stress resultants of the connected layer are discontinuous with jumps at each connector location. To derive the equilibrium conditions for a two-layer beam with discrete shear connection, we need to consider separately the equilibrium of an infinitesimal unconnected beam segment and the equilibrium at the cross-section containing shear connectors (see Fig. 1). The first set of equilibrium equations, which apply between two consecutive connectors, is readily obtained by expressing the equilibrium of an infinitesimal unconnected two-layer beam segment, of length dx, and subjected to an external distributed load (see Fig. 1a). The equilibrium conditions result in the following set of equations:

$$\partial_x N_i + (-1)^i \mu V_{sc} = 0 \tag{1}$$

$$\partial_x T_i + (-1)^i V_{sc} + (i-1) p_z = 0 \tag{2}$$

$$\partial_x M_i + (-1)^i T_i + h_i \mu V_{sc} = 0 \tag{3}$$

where i=1,2; $\partial_x^j \bullet = \mathrm{d}^j \bullet / \mathrm{d}x^j$; h_i is the distance between the centroid of the layer i and the layers interface; N_i, T_i, M_i are the axial forces, the shear forces and bending moments at the centroid of layer i; V_{sc} is the contact force per unit length; μ is the coefficient of friction at the layer interface; p_z is the applied external load per unit length.

The above equations must be completed by equilibrium equations at each cross-section containing shear connectors (see Fig. 1b). The resulting equation provides a relationship between the internal stress resultant jumps and the shear force acting on the connectors Q_{st}:

$$\begin{bmatrix} \Delta N_1 \\ \Delta M_1 \\ \Delta N_2 \\ \Delta M_2 \end{bmatrix} = \begin{bmatrix} 1 \\ -h_1 \\ -1 \\ -h_2 \end{bmatrix} Q_{st} \tag{4}$$

2.1.2. Compatibility

For each layer, the plane sections are supposed to remain plane, but not normal to the neutral axis. Consequently, both the layers do not have the same rotation and curvature. Based on the first-order shear deformation beam theory of Timoshenko, the axial, shear and flexural deformations at any section are related to the beam displacements as follows (see Fig. 2):

$$\varepsilon_i = \partial_x u_i \tag{5}$$

$$\gamma_i = \partial_x v + \theta_i \tag{6}$$

$$\kappa_i = \partial_x \theta_i \tag{7}$$

where ε_i and u_i are the axial strain and displacement at the centroid of layer i; γ_i is the shear strain of layer i; v is the transverse displacement of two layers; θ_i and κ_i are the rotation and curvature of layer i.

The interlayer slip g along the interface can be expressed as follows:

$$g = u_1 - u_2 - h_1\theta_1 - h_2\theta_2 \tag{8}$$

2.1.3. Constitutive relations

The generalized stress–strain relationships for the transverse sections of the two layers are simply obtained by integrating over each cross-section the appropriate uniaxial constitutive model. For a linear elastic material, these relationships lead to the following generalized relationships:

$$N_i = \int_{A_i} \sigma \, \mathrm{d}A = EA_i \varepsilon_i \tag{9}$$

$$T_i = \int_{A_i} \tau \, \mathrm{d}A = GA_i \gamma_i \tag{10}$$

$$M_i = \int_{A_i} z\sigma \, \mathrm{d}A = EI_i \kappa_i \tag{11}$$

where $AE_i = E_i A_i$, $GA_i = k_i^s G_i A_i$ and $I_i = E_i I_i$ in which E_i, G_i, A_i and I_i are the elastic modulus, the shear modulus, the area and the second moment of area of the layer i; k_i^s is the shear correction factor that depends on the cross-sectional shape of layer i. The relationship between the interlayer slip and the shear force acting on the connector Q_{st} is given by

$$Q_{st} = k_{st} g \tag{12}$$

where k_{st} is the stiffness of the connector.

2.2. Governing equations: derivation and analytical solution

The relationships introduced in Section 2.1 can be combined to derive the differential equations that govern the behavior of the shear-deformable two-layer beams with discrete shear connection. To do so, we consider separately an unconnected two-layer beam segment and a connector element in order to keep the continuous quantities of the variables within each element. In what follows, we present the full derivation of the analytical

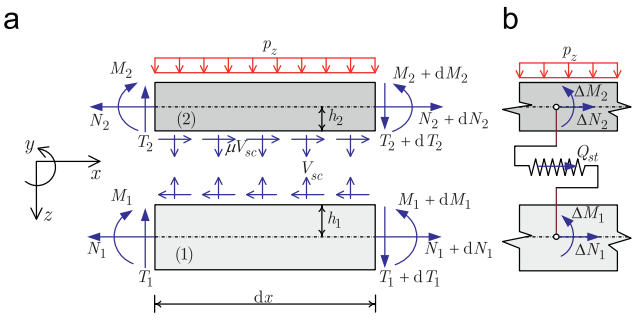

Fig. 1. (a) Infinitesimal unconnected two-layer beam segment. (b) Connector location.

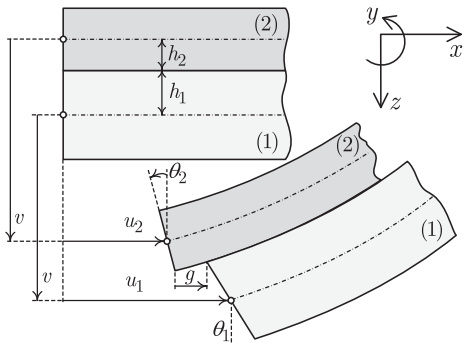

Fig. 2. Kinematics of a two-layer beam with interlayer slip.

solution for an unconnected two-layer beam segment under bending. The governing equations for a connector as well as the corresponding stiffness matrix are presented in Section 2.2.2.

Eq. (6) is differentiated twice to obtain

$$\partial_x^3 v = \partial_x^2 \gamma_i - \partial_x^2 \theta_i \quad \text{with } i = 1,2 \tag{13}$$

where the shear deformations γ_i and the cross-section rotations θ_i are eliminated using relations (7), (10) and (11) to give

$$\partial_x^3 v = \frac{\partial_x^2 T_1}{GA_1} - \frac{\partial_x M_1}{EI_1} = \frac{\partial_x^2 T_2}{GA_2} - \frac{\partial_x M_2}{EI_2} \tag{14}$$

Next, the equilibrium equations (2) and (3) are used to eliminate the layer bending moments M_i from (14) to obtain

$$\frac{T_1}{EI_1} - \frac{T_2}{EI_2} = \left(\frac{1}{GA_1} + \frac{1}{GA_2}\right)\partial_x V_{sc} + \mu\left(\frac{h_1}{EI_1} - \frac{h_2}{EI_2}\right)V_{sc} \tag{15}$$

By combining the derivative of the above relation with the equilibrium equation (2), one obtains a differential equation involving only the contact force V_{sc}, which is the primary unknown of the problem:

$$\frac{\partial_x^2 V_{sc}}{GA} + \mu\left(\frac{h_1}{EI_1} - \frac{h_2}{EI_2}\right)\partial_x V_{sc} - \frac{V_{sc}}{EI} = \frac{p_z}{EI_2} \tag{16}$$

where

$$\frac{1}{GA} = \frac{1}{GA_1} + \frac{1}{GA_2} \quad \text{and} \quad \frac{1}{EI} = \frac{1}{EI_1} + \frac{1}{EI_2} \tag{17}$$

It can be clearly seen that the characteristic equation of the second-order differential equation (16)

$$\frac{1}{GA}r^2 + \mu\left(\frac{h_1}{EI_1} - \frac{h_2}{EI_2}\right)r - \frac{1}{EI} = 0 \tag{18}$$

has two real roots since

$$\Delta = \mu^2\left(\frac{h_1}{EI_1} - \frac{h_2}{EI_2}\right)^2 + \frac{4}{GA\,EI} > 0 \tag{19}$$

Thus the solution of the second-order differential equation (16) can be expressed as

$$V_{sc} = C_1 e^{\lambda_1 x} + C_2 e^{\lambda_2 x} + V_{sc}^0 \tag{20}$$

where

$$\lambda_{1,2} = \frac{GA}{2}\left[\mu\left(\frac{h_1}{EI_1} - \frac{h_2}{EI_2}\right) \pm \sqrt{\Delta}\right] \tag{21}$$

$C_{1,2}$ are constants of integration and

$$V_{sc}^0 = -\frac{EIp_z}{EI_2} \tag{22}$$

is a particular solution, derived in the case of uniformly distributed transverse load p_z. V_{sc} can also be expressed in vector form as follows:

$$V_{sc} = \mathbf{Y}_{V_{sc}}\mathbf{C} + V_{sc}^0 \tag{23}$$

where

$$\mathbf{Y}_{V_{sc}} = [e^{\lambda_1 x} \;\; e^{\lambda_2 x} \;\; 0 \;\; 0 \;\; 0 \;\; 0 \;\; 0 \;\; 0 \;\; 0 \;\; 0] \tag{24}$$

$$\mathbf{C} = [C_1 \;\; C_2 \;\; C_3 \;\; C_4 \;\; C_5 \;\; C_6 \;\; C_7 \;\; C_8 \;\; C_9 \;\; C_{10}]^{\mathrm{T}} \tag{25}$$

Note that the vector $\mathbf{C}$ contains 10 constants of integration C_i (i=1,10). At the present stage, there are only two constants, but the other constants will appear as a result of the integration process needed for the determination of the other internal force and displacement unknowns.

- *Analytical expressions for shear forces T_1 and T_2*
  The following expression for the shear forces T_1 can be obtained from Eq. (2) by direct integration:

  $$T_1 = \mathbf{Y}_{T_1}\mathbf{C} + T_1^0 \tag{26}$$

  where

  $$\mathbf{Y}_{T_1} = \left[\frac{e^{\lambda_1 x}}{\lambda_1} \;\; \frac{e^{\lambda_2 x}}{\lambda_2} \;\; 1 \;\; 0 \;\; 0 \;\; 0 \;\; 0 \;\; 0 \;\; 0 \;\; 0\right] \tag{27}$$

  $$T_1^0 = -\frac{EIp_z}{EI_2}x \tag{28}$$

  By introducing (26) into (15), one obtains

  $$T_2 = \mathbf{Y}_{T_2}\mathbf{C} + T_2^0 \tag{29}$$

  where

  $$\mathbf{Y}_{T_2} = \frac{EI_2}{EI_1}\mathbf{Y}_{T_1} - \frac{EI_2}{GA}\partial_x \mathbf{Y}_{V_{sc}} - \mu\left(\frac{h_1 EI_2}{EI_1} - h_2\right)\mathbf{Y}_{V_{sc}} \tag{30}$$

  $$T_2^0 = \frac{EI_2}{EI_1}T_1^0 - \mu\left(\frac{h_1 EI_2}{EI_1} - h_2\right)V_{sc}^0 \tag{31}$$

- *Analytical expression for transversal displacement v*
  Eliminating M_1 from (14) using Eq. (3) gives the following differential equation for v:

  $$\partial_x^3 v = \frac{\partial_x^2 T_1}{GA_1} - \frac{T_1 - h_1\mu V_{sc}}{EI_1} \tag{32}$$

  which is integrated twice to give the following expression:

  $$v = \mathbf{X}_v\mathbf{C} + v^0 \tag{33}$$

  where

  $$\mathbf{X}_v = \left[\varsigma_1 e^{\lambda_1 x} \;\; \varsigma_2 e^{\lambda_2 x} \;\; \frac{x}{GA_1} - \frac{x^3}{6EI_1} \;\; x^2 \;\; x \;\; 1 \;\; 0 \;\; 0 \;\; 0 \;\; 0\right] \tag{34}$$

  $$v^0 = \frac{p_z x(GA_1 x^3 - 12EI_1 x - 4\mu h_1 GA_1)}{24GA_1(EI_1 + EI_2)} \tag{35}$$

  in which

  $$\varsigma_i = \frac{1}{GA_1\lambda_i^2} + \frac{\mu h_1 \lambda_i - 1}{EI_1\lambda_i^4} \quad \text{with } i = 1,2 \tag{36}$$

- *Analytical expressions for axial displacements u_1 and u_2*
  Combining the constitutive relation (9), the compatibility relation (5) and the equilibrium relation (1), one obtains

  $$\partial_x^2 u_1 = \frac{\mu}{EA_1}V_{sc} \tag{37}$$

  $$\partial_x^2 u_2 = \frac{-\mu}{EA_2}V_{sc} \tag{38}$$

  By substituting the expression (23) into the above equations, the following expressions for u_1 and u_2 are obtained by direct integration:

  $$u_1 = \mathbf{X}_{u_1}\mathbf{C} + u_1^0 \tag{39}$$

  $$u_2 = \mathbf{X}_{u_2}\mathbf{C} + u_2^0 \tag{40}$$

  where

  $$\mathbf{X}_{u_1} = \frac{\mu}{EA_1}\left[\frac{e^{\lambda_1 x}}{\lambda_1^2} \;\; \frac{e^{\lambda_2 x}}{\lambda_2^2} \;\; 0 \;\; 0 \;\; 0 \;\; 0 \;\; x \;\; 1 \;\; 0 \;\; 0\right], \quad u_1^0 = \frac{-\mu EIp_z}{2EA_1EI_2}x^2 \tag{41}$$

  $$\mathbf{X}_{u_2} = \frac{-\mu}{EA_2}\left[\frac{e^{\lambda_1 x}}{\lambda_1^2} \;\; \frac{e^{\lambda_2 x}}{\lambda_2^2} \;\; 0 \;\; 0 \;\; 0 \;\; 0 \;\; 0 \;\; 0 \;\; x \;\; 1\right], \quad u_2^0 = \frac{\mu EIp_z}{2EA_2EI_2}x^2 \tag{42}$$

- *Analytical expressions for the remaining unknowns*
  So far, we know how to obtain the analytical expressions for the shear forces T_i ($i=1,2$), the common transversal displacement v of the two layers and the axial displacements u_i ($i=1,2$) which are expressed as a function of 10 constants of integration. Once these expressions are determined, the analytical expressions for the remaining mechanical variables can be derived by inserting them back into the governing equations. Finally, one obtains:

$$\theta_i = \mathbf{X}_{\theta_i}\mathbf{C} + \theta_i^0 \tag{43}$$

$$M_i = \mathbf{Y}_{M_i}\mathbf{C} + M_i^0 \tag{44}$$

$$N_i = \mathbf{Y}_{N_i}\mathbf{C} + N_i^0 \tag{45}$$

where $i=1,2$ and

$$\mathbf{X}_{\theta_i} = \frac{\mathbf{Y}_{T_i}}{EA_i} - \partial_x \mathbf{X}_v, \quad \theta_i^0 = \frac{T_i^0}{EA_i} - \partial_x v^0 \tag{46}$$

$$\mathbf{Y}_{M_i} = EI_i \partial_x \mathbf{X}_{\theta_i}, \quad M_i^0 = EI_i \partial_x \theta_i^0 \tag{47}$$

$$\mathbf{Y}_{N_i} = EA_i \partial_x \mathbf{X}_{u_i}, \quad N_i^0 = EA_i \partial_x u_i^0 \tag{48}$$

It is noted that the expressions of all mechanical variables presented above involve 10 constants of integrations, which is fully consistent with the problem of an arbitrary shear-deformable two-layer beam under bending where there are always 10 boundary conditions (five at both ends).

2.2.1. Exact stiffness matrix for unconnected two-layer beam element

The exact expression of the stiffness matrix can be easily obtained starting from the general expressions of the force and displacement fields. Let us consider an unconnected two-layer beam element of length L (see Fig. 3). Since the same transverse displacement for two layers is assumed (no uplift), this element has 10 degrees of freedom. Applying the kinematic boundary conditions at $x=0$ and $x=L$ leads to a relationship between the vector of constants of integration $\mathbf{C}$ and the vector of nodal displacements $\mathbf{q}$ as follows:

$$\mathbf{q} = \mathbf{X}\mathbf{C} + \mathbf{q}^0 \tag{49}$$

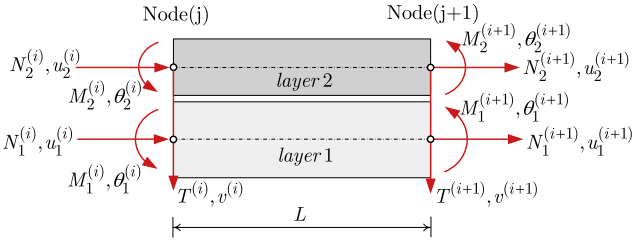

Fig. 3. Nodal forces and displacements of an unconnected composite beam element.

where

$$\mathbf{q} = [u_1^{(j)}\ u_2^{(j)}\ v^{(j)}\ \theta_1^{(j)}\ \theta_2^{(j)}\ u_1^{(j+1)}\ u_2^{(j+1)}\ v^{(j+1)}\ \theta_1^{(j+1)}\ \theta_2^{(j+1)}]^{\mathrm{T}} \tag{50}$$

$$\mathbf{X} = [\mathbf{X}_{u_1}^{\mathrm{T}}(x=0)\ \mathbf{X}_{u_2}^{\mathrm{T}}(x=0)\ \mathbf{X}_v^{\mathrm{T}}(x=0)\ \cdots\ \mathbf{X}_{\theta_2}^{\mathrm{T}}(x=L)]^{\mathrm{T}} \tag{51}$$

$$\mathbf{q}^0 = [u_1^0(x=0)\ u_2^0(x=0)\ v^0(x=0)\ \cdots\ \theta_2^0(x=L)]^{\mathrm{T}} \tag{52}$$

Next, by enforcing the static boundary conditions, the relationship between the vector of constants of integration $\mathbf{C}$ and the vector of nodal forces $\mathbf{Q}$ is established

$$\mathbf{Q} = \mathbf{Y}\mathbf{C} + \mathbf{Q}^0 \tag{53}$$

where

$$\mathbf{Q} = [N_1^{(j)}\ N_2^{(j)}\ T^{(j)}\ M_1^{(j)}\ M_2^{(j)}\ N_1^{(j+1)}\ N_2^{(j+1)}\ T^{(j+1)}\ M_1^{(j+1)}\ M_2^{(j+1)}]^{\mathrm{T}} \tag{54}$$

$$\mathbf{Y} = [-\mathbf{Y}_{N_1}^{\mathrm{T}}(x=0)\ -\mathbf{Y}_{N_2}^{\mathrm{T}}(x=0)\ -\mathbf{Y}_T^{\mathrm{T}}(x=0)\ \cdots\ \mathbf{Y}_{M_2}^{\mathrm{T}}(x=L)]^{\mathrm{T}} \tag{55}$$

$$\mathbf{Q}^0 = [-N_1^0(x=0)\ -N_2^0(x=0)\ -T^0(x=0)\ \cdots\ M_2^0(x=L)]^{\mathrm{T}} \tag{56}$$

in which $\mathbf{Y}_T = \mathbf{Y}_{T_1} + \mathbf{Y}_{T_2}$ and $T^0 = T_1^0 + T_2^0$.

Since the nodal displacements are independent variables, the matrix $\mathbf{X}$ is always non-singular. Thus from Eq. (49) the following general expression for the constant vector $\mathbf{C}$ defined in (24) can be obtained:

$$\mathbf{C} = \mathbf{X}^{-1}(\mathbf{q} - \mathbf{q}^0) \tag{57}$$

Inserting this relation into (53) leads to a relationship between the vector of nodal forces and the vector of nodal displacements

$$\mathbf{K}\mathbf{q} = \mathbf{Q} + \mathbf{Q}_z \tag{58}$$

in which $\mathbf{K} = \mathbf{Y}\mathbf{X}^{-1}$ is the exact stiffness matrix of the unconnected two-layer beam and $\mathbf{Q}_z = \mathbf{K}\mathbf{q}^0 - \mathbf{Q}^0$ represents the nodal force vector due to the external distributed load p_z.

2.2.2. Stiffness matrix for a connector element

The connector element is a specific element with no length which, according to its stiffness, allows a certain amount of sliding between two layer but prevents any separation. This element has four degrees of freedom: the axial displacements, u_1 and u_2, and the cross-section rotations, θ_1 and θ_2 (see Fig. 4). Combining Eqs. (4), (8) and (12) leads to the relationship between the element displacement vector $\mathbf{q}_{st} = [u_1\ u_2\ \theta_1\ \theta_2]^{\mathrm{T}}$ and the element force vector $\mathbf{Q}_{st} = [\Delta N_1\ \Delta N_2\ \Delta M_1\ \Delta M_2]^{\mathrm{T}}$ as follows:

$$\mathbf{K}_{st}\mathbf{q}_{st} = \mathbf{Q}_{st} \tag{59}$$

where

$$\mathbf{K}_{st} = k_{st}\begin{bmatrix} 1 & -1 & -h_1 & -h_2 \\ -1 & 1 & h_1 & h_2 \\ -h_1 & h_1 & h_1^2 & h_1 h_2 \\ -h_2 & h_2 & h_1 h_2 & h_2^2 \end{bmatrix} \tag{60}$$

is the stiffness matrix of the connector element.

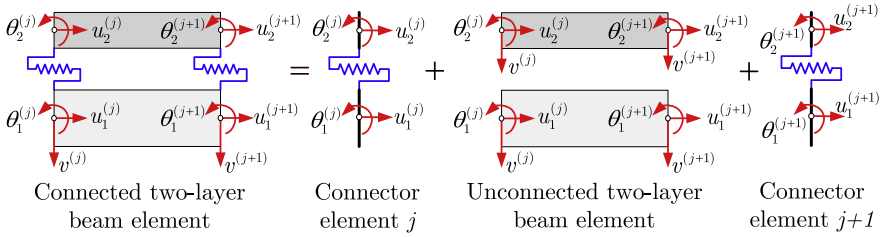

Fig. 4. Illustration of the two-layer beam finite element.

2.2.3. Exact stiffness matrix for a connected two-layer beam element

Let us consider a two-layer beam element connected discontinuously at its ends, as shown in Fig. 4. The stiffness matrix of such an element, namely $\mathbf{K}_e$, is obtained by assembling the stiffness matrix of an unconnected element $\mathbf{K}$ with the stiffness matrix $\mathbf{K}_{st}$ of the connector element:

$$\mathbf{K}_e = [\mathbf{T}^{(j)}]^{\mathrm{T}}\mathbf{K}_{st}^{(j)}\mathbf{T}^{(j)} + \mathbf{K} + [\mathbf{T}^{(j+1)}]^{\mathrm{T}}\mathbf{K}_{st}^{(j+1)}\mathbf{T}^{(j+1)} \tag{61}$$

where

$$\mathbf{T}^{(j)} = \begin{bmatrix} 1 & 0 & 0 & 0 & 0 & 0 & 0 & 0 & 0 & 0 \\ 0 & 1 & 0 & 0 & 0 & 0 & 0 & 0 & 0 & 0 \\ 0 & 0 & 0 & 1 & 0 & 0 & 0 & 0 & 0 & 0 \\ 0 & 0 & 0 & 0 & 1 & 0 & 0 & 0 & 0 & 0 \end{bmatrix} \quad \text{and}$$

$$\mathbf{T}^{(j+1)} = \begin{bmatrix} 0 & 0 & 0 & 0 & 0 & 1 & 0 & 0 & 0 & 0 \\ 0 & 0 & 0 & 0 & 0 & 0 & 1 & 0 & 0 & 0 \\ 0 & 0 & 0 & 0 & 0 & 0 & 0 & 0 & 1 & 0 \\ 0 & 0 & 0 & 0 & 0 & 0 & 0 & 0 & 0 & 1 \end{bmatrix} \tag{62}$$

The above stiffness matrix may be implemented into any finite element code for the exact static elastic analysis of shear-deformable two-layer beams with arbitrary support and loading conditions.

3. Comparison with existing models

The purpose of this section is to compare the predictions of proposed model against calculations obtained with three existing models which consider different kinematic and/or bond model assumptions. The first model, denoted as EB-C model, is the well-known Newmark's model which employs Euler–Bernoulli's theory and considers a continuous connection model [4]. The second one, denoted as EB-D model, adopt Euler–Bernoulli's beam theory with a discrete connection (see [45]). The last one, denoted as T–C model, which has been recently proposed by Nguyen et al.'s model [44], consider Timoshenko's beam theory with a continuous connection model. The present model is denoted as T–D model. The comparison is performed on a two-layer beam continuous over two equal spans with equal uniformly distributed load $p=100$ kN/m. The geometric characteristics and the material properties of the beam are shown in Fig. 5. The shear correction factor k^s for rectangular cross-section is taken equal to $\frac{5}{6}$ [46]. The layers are connected by a set of connectors. For the continuous connection model, equivalent distributed bond stiffness is calculated by dividing the stiffness of a single connector by their spacing along the beam.

Fig. 6 depicts the deflection distribution along the first span for each model. It can be seen that the maximum deflection obtained with the continuous shear connection model is very close to the one obtained with the discrete with ($\simeq 0.6\%$ difference). It can be explained by the fact that the connector spacing in the present case is small compared to the span length ($L_{st}=L/5$) so discrete connection can be replaced by continuous connection without

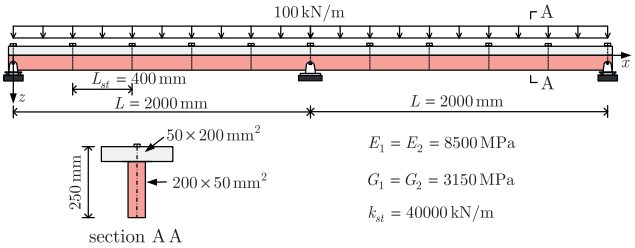

Fig. 5. Two-span two-layer beam.

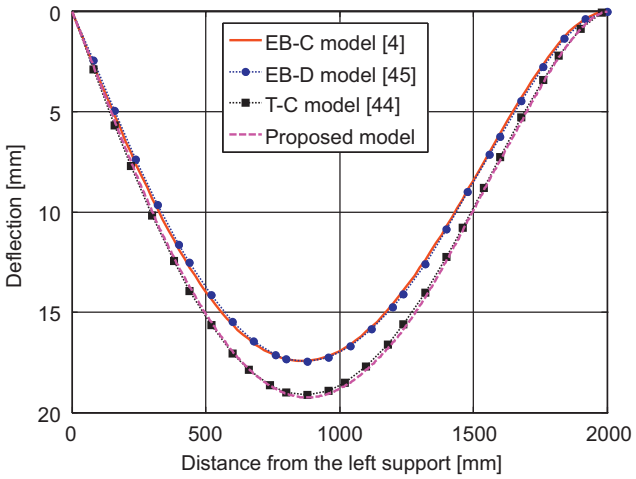

Fig. 6. Deflection distributions along the beam length.

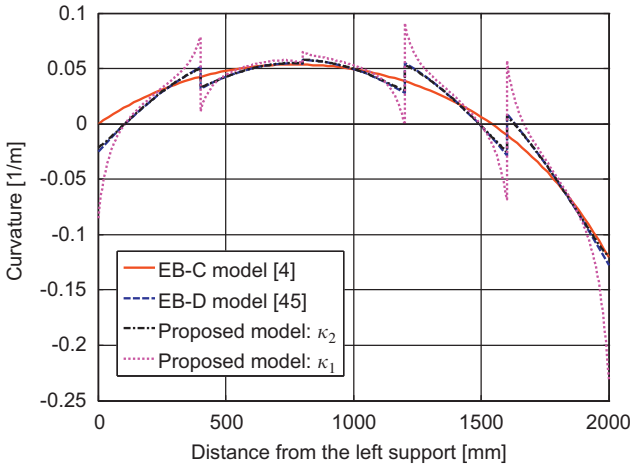

Fig. 7. Curvature distributions along the beam length.

any significant error on the deflection calculation. The influence of the connector spacing on the deflection is pointed out in the next section. Further, it can be also observed that, due to the shear deformations of the layers, the maximum deflection increases by about 6%.

Fig. 7 compares the curvature distributions along the first span. With the discrete shear connection model, the distribution is discontinuous with a jump at each connector location, regardless of the beam theory adopted. In fact, the discrete nature of the shear connection causes jumps of the axial force in each layer at the connector locations. Since the total bending moment is continuous, we conclude that the bending moment in each layer is discontinuous as well as the corresponding curvature. Further, it can be seen from Fig. 7 that, with the present model, the curvature of layer 1 is rather different from the curvature of layer 2. This is in sharp contrast with the model proposed by [40] where both layers are enforced to have the same curvature. Furthermore, it can be seen that curvature of layer 1 is very close to the curvature distribution predicted by the EB-D model. It seems that the transverse shear deformation has a stronger effect on layer 2, probably due to its very low flexural stiffness compared to layer 1 ($EI_1 = 16EI_2$) while the transverse shear stiffness is the same for both layers ($GA_1 = GA_2$). The same conclusion can be reached when looking at the rotation distributions shown in Fig. 8. Moreover, this figure indicates that the rotation distribution curve

associated with a discrete shear connection model is not smooth (discontinuity of the derivative) at the connector locations. This is an immediate consequence of the discontinuous nature of the curvature distribution since the curvature is the derivative of the rotation.

The slip distributions along the first span, obtained with different models, are plotted in Fig. 9. It can be observed that the transverse shear deformation does not affect significantly the slip distribution. Indeed, the curves almost do not change with the beam theory for both connection models. Further, the non-smooth slip curve observed is effectively related to the non-smooth rotation curve (see Eq. (8)). Table 1 provide the value of mechanical variables obtained with the four aforementioned models.

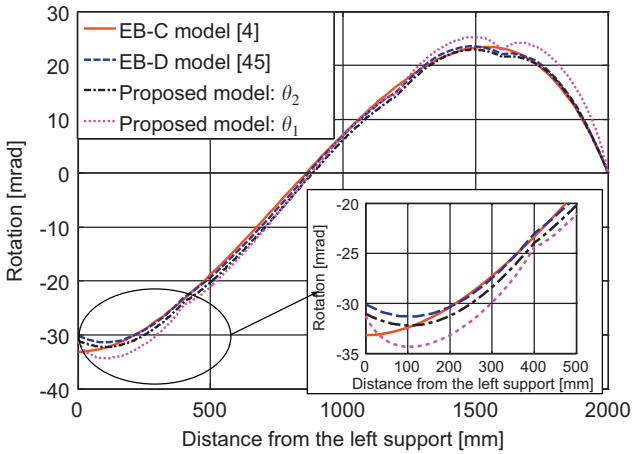

Fig. 8. Rotation distributions along the beam length.

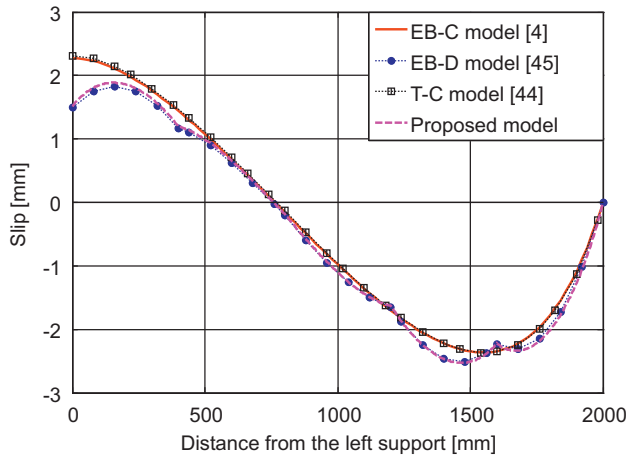

Fig. 9. Slip distributions along the beam length.

4. Parametric study

In this section, the proposed exact finite element model is used to conduct a parametric study in order to investigate the influence of material and geometric parameters, such as connector spacing, interlayer friction coefficient, stiffness of the connectors, flexural-to-shear moduli ratios and span-to-depth ratios, on the global structural behavior of the two-span layered beam discussed in the previous section.

Fig. 10 compares the defections at mid-span calculated with the proposed model against those obtained with the T–C model for various connector stiffness and connector spacing. It is worth mentioning that the continuous connection (employed in T–C model) can be considered as an asymptotic case of the discrete connection (employed in present model) with connector spacing equal to zero. It can be observed that the connector spacing has no influence on the deflection for low level of shear connection ($k_{st} < 10^4$). This indicates that for a certain range of shear connection stiffness, making use of the continuous connection model instead of the discrete one, whatever the connector spacing is, would not cause any underestimation of deflection. However, when the shear connection stiffness becomes important, it may lead to a significant underestimation of the deflection. Fig. 10 shows that the deflection depends indeed on the connector spacing for high level of shear connection. As can be seen, the deflection can be underestimated by about 52% ($k_{st} = 10^8$ kN/m and $L_{st} = L/2$).

The influence of connector spacing and connector stiffness on slips at the first support is illustrated in Fig. 11. It can be observed that unlike the deflection, the slip decreases with increasing connector spacing. In other words, replacing a discrete connection by a continuous one overestimates the slip. For rigid connection ($k_{st} = 10^8$ kN/m), this overestimation is 114% when $L_{st} = L/16$ and can be up to 233% when $L_{st} = L/2$. The results indicate that the influence of connector spacing and connector stiffness is more pronounced on the slips than the deflections.

Fig. 12 shows the effect of interlayer friction on the deflection at midspan for several values of connector stiffness. The vertical axis represents the ratio of the deflection with interlayer friction over the one without friction. As can be seen, for connector stiffness $k_{st} \leq 1000$ kN/m, the deflection is nearly not affected by friction. However, with increasing value of the connector stiffness we have a pronounced effect of friction on the beam deflection. The results indicate that, for rigid connection ($k_{st} = 10^8$ kN/m) with a friction coefficient μ equal to 0.4, the deflection decreases by about 18% which is not negligible in the practical design.

Table 1
Comparison against existing model.

	Discrete connection		Continuous connection	
	Timoshenko's theory (present model)	Euler–Bernoulli's theory (Nguyen et al. [2])	Timoshenko's theory (Nguyen et al. [4])	Euler–Bernoulli's theory (Newmark et al. [3])
$v(x=L/2)$,mm	18.8 (11.2%)	17.0 (0.6%)	18.7 (10.6%)	16.9
$\theta_1(x=0)$,mrad	−31.0 (−6.6%)	−30.1 (−9.3%)	−33.9 (2.1%)	−33.2
$\theta_2(x=0)$,mrad	−31.3 (−5.7%)	–	−36.1 (8.7%)	–
$\kappa_1(x=L)$,m^{-1}	−0.12 (0%)	−0.13 (8.3%)	−0.11 (−8.3%)	−0.12
$\kappa_2(x=L)$,m^{-1}	−0.23 (91.6%)	–	−0.22 (83.3%)	–
$g(x=0)$,mm	1.5 (−34.7%)	1.5 (−34.7%)	2.3 (0%)	2.3

Note: The percent variations are computed in comparison to the results obtained with Newmark's model.

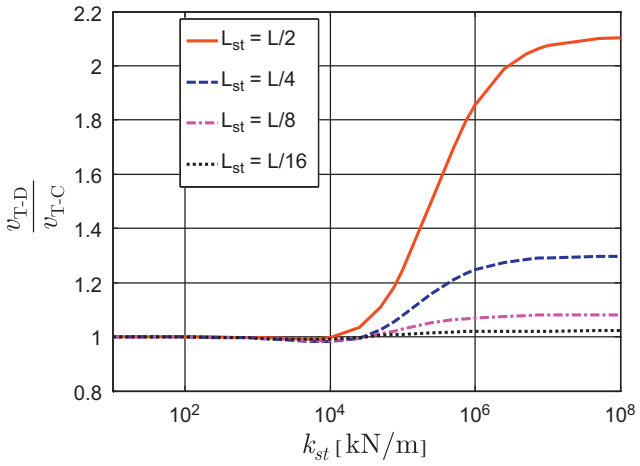

Fig. 10. Influence of connector spacing and connector stiffness on deflections.

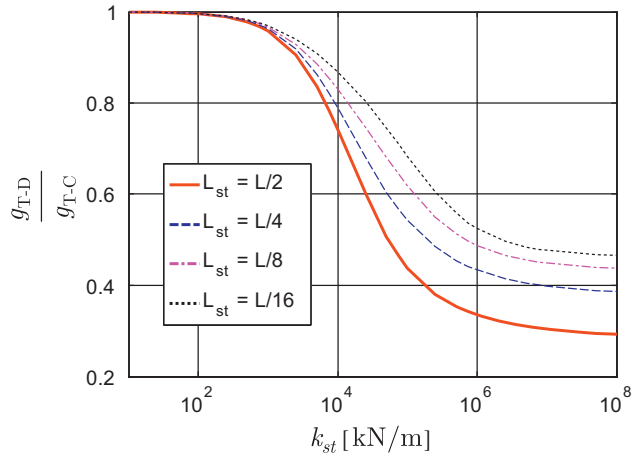

Fig. 11. Influence of connector spacing and connector stiffness on slips.

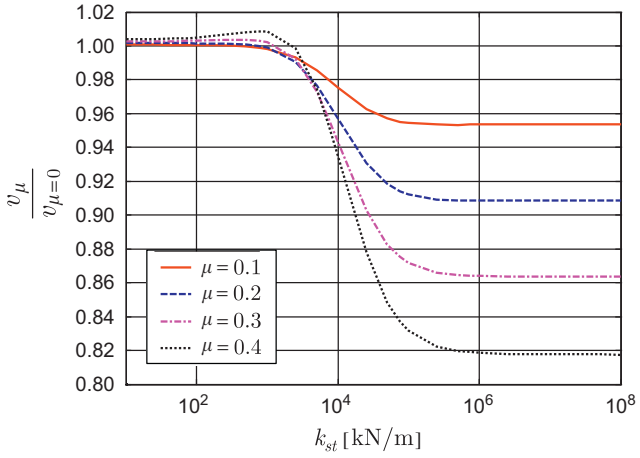

Fig. 12. Influence of friction coefficient on deflections.

The influence of transverse shear deformations on the mechanical variables is investigated in this study by varying firstly the flexural-to-shear modulus ratio (E/G) and secondly

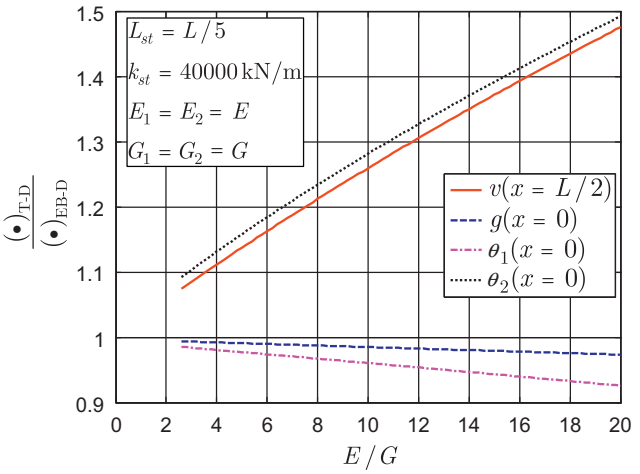

Fig. 13. Influence of E/G ratio on the deflection, the slip and the rotations.

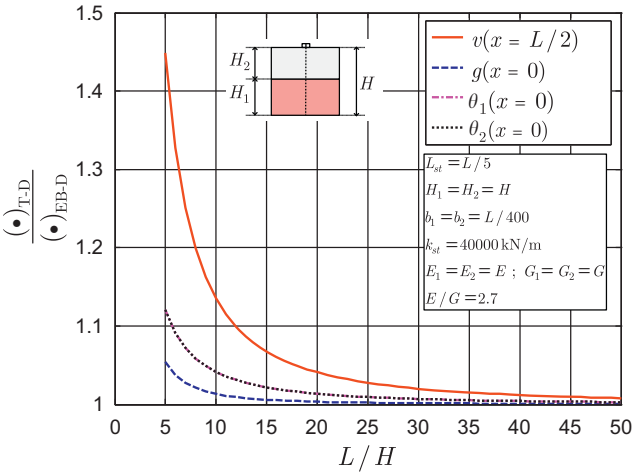

Fig. 14. Influence of length–dept ratio on the deflection, the slip and the rotations.

the span-to-depth (L/H) ratio. The evolution of the ratios between the deflections, slips and rotations obtained with present (T–D) model and those obtained with EB–D model for various realistic value of E/G (2.6–20) is shown in Fig. 13. It can be observed that deflection, slip and rotations are quasi-linear functions of the flexural-to-shear modulus ratio. More precisely, the deflection increases with E/G while the slip at the left support decreases with E/G. Further, compared to slip, the deflection is more influenced by the E/G ratio. Furthermore, the shear deformations have different effect on the layer rotations. Indeed, it can be seen that the rotation of the layer 2 increases significantly with E/G while the rotation of the layer 1 slightly decreases. This indicates that, when two layers have the same shear stiffness, the shear deformability affects more the layer with weak flexural stiffness.

By considering two identical layers, the influence of the length-to-depth ratio on the deflection, slip and rotations is depicted in Fig. 14. The results show that shear deformations start to have a pronounced effect on the deflection when $L/H \leq 8$ (20% increase of deflection for $L/H = 8$). Nevertheless, the influence on the rotations and slip is not strong. In particular, for $L/H = 5$, the increase of deflection, rotations and slip are 45%, 12% and 5%, respectively.

5. Conclusions

We have proposed a finite element model based on the exact stiffness matrix for the linear static analysis of shear-deformable layered beams with interlayer slip. The beams considered are the usual two-layer beams connected discontinuously by shear connectors such as steel–concrete composite beams and nailed timber beams. The shear connection has been modeled using concentrated spring elements at each connector location. The transverse shear deformations has been taken into account by adopting Timoshenko beam theory for each layer. The effect of friction at the interface has been also accounted for in the model. Based on the closed-form solution of the governing equations of the problem, the exact stiffness matrix has been derived for a shear-deformable two-layer beam element connected discontinuously at its ends with the aim of using the displacement method (F.E. method) for the exact static elastic analysis of two-layer continuous beams with arbitrary loading/boundary conditions.

The predictions of the proposed model have been compared against calculations obtained with three existing models which consider different kinematic assumptions and/or bound model. These models includes the well-known Newmark model, the EB-D model (Euler–Bernoulli's theory with discrete connection) and the T–C model (Timoshenko's assumptions with continuous connection). A parametric study dealing with a two-span layered beam has been undertaken. The following conclusions can be drawn:

- Regardless of the kinematic assumptions, a discrete connection model leads to slip and rotation distributions that are not smooth (discontinuous derivative) at the connector locations. Consequently, the curvatures are discontinuous with more or less pronounced jumps at each connector.
- As expected, adopting Timoshenko kinematics' assumptions for each layer increases the deflection. More precisely, the deflection is a quasi-linear function of the flexural-to-shear ratio (E/G). Furthermore, the shear deformation starts to affect significantly the deflection when the length-to-depth ratio (L/H) is below 8 (20% increase of deflection for $L/H=8$).
- For composite beams with sparse shear connection (i.e. large connector spacing), replacing a discrete shear connection by an equivalent continuous one causes an underestimation of the deflection which can be substantial in very loose connection. For example, in our parametric study, the results indicate that the deflection can be underestimated by about 52% with a connector stiffness $k_{st}=10^8$ kN/m and a connector spacing $L_{st}=L/2$.
- Unlike the deflection, the slip decreases with increasing connector spacing. It has been observed that, in the case of rigid connector ($k_{st}=10^8$), the influence of connector spacing is more pronounced on the slips than the deflections.
- The effect of the interlayer friction on the deflection is not significant if the connector is very flexible ($k_{st}\leq 1000$ kN/m). However, we have a pronounced effect of friction on the beam deflection when the shear connection becomes rigid. The results indicate that, for ($k_{st}=10^8$ kN/m) with a friction coefficient μ equal to 0.4, the deflection decreases by about 18% which is not negligible in the practical design.
- The shear deformation effect on the cross-section rotation depends on the flexural stiffness of the layer. If the layers have different flexural stiffness then shear deformability will have an opposite effect on each layer. Indeed, it can be observed that the cross-section rotation of the less stiff layer (bottom layer) increases with shear-deformability whereas the cross-section rotation of the stiffer layer (top layer) decreases with shear-deformability.
- The slip is nearly not affected by the shear deformations

References

[1] K. Abel-Aziz, J.M. Aribert, Calcul des poutres mixtes jusqu'à l'état ultime avec un effet de soulèvement à l'interface acier-béton, Construction métallique, No. 4, 1985 (in French).
[2] H. Robinson, K.S. Naraine, Slip and uplift effects in composite beams, in: Proceedings of the Engineering Foundation Conference on Composite Construction (ASCE), 1988, pp. 487–497.
[3] R.P. Johnson, Composite Structures of Steel and Concrete: Beams, Slabs, Columns, and Frames for Buildings, third ed., Wiley–Blackwell, September 2004.
[4] M.N. Newmark, C.P. Siess, I.M. Viest, Tests and analysis of composite beams with incomplete interaction, Proceedings of the Society for Experimental Stress Analysis 9 (1) (1951) 75–92.
[5] J.R. Goodman, Layered wood systems with interlayer slip, Doctoral Dissertation, University of California, Berkley, 1967.
[6] M. Heinisuo, An exact finite element technique for layered beam, Computer and Structures 30 (3) (1988) 615–622.
[7] U.A. Girhammar, K.A. Gopu, Composite beam-column with interlayer slip exact analysis, Journal of Structural Engineering (ASCE) 119 (4) (1993) 2095–2111.
[8] C. Faella, E. Martinelli, E. Nigro, Steel and concrete composite beams: "exact" expression of the stiffness matrix and applications, Computer and Structures 80 (2002) 1001–1009.
[9] Y.F. Wu, D.J. Oehlers, M.C. Griffith, Partial-interaction analysis of composite beam/column members, Mechanics of Structures and Machines 30 (3) (2002) 309–332.
[10] R. Seracino, C.T. Lee, T.C. Lim, J.Y. Lim, Partial interaction stresses in continuous composite beams under serviceability loads, Journal of Constructional Steel Research 60 (2004) 1525–1543.
[11] G. Ranzi, M.A. Bradford, B. Uy, A direct stiffness analysis of a composite beam with partial interaction, International Journal for Numerical Methods in Engineering 61 (2004) 657–672.
[12] U.A. Girhammar, D. Pan, Exact static analysis of partially composite beams and beam-columns, International Journal of Mechanical Sciences 49 (2007) 239–255.
[13] M.A. Bradford, R.I. Gilbert, Composite beams with partial interaction under sustained loads, Journal of Structural Engineering (ASCE) 118 (7) (1992) 1871–1883.
[14] R.I. Gilbert, M.A. Bradford, Time-dependent behavior of continuous composite beams at service loads, Journal of Structural Engineering (ASCE) 121 (2) (1995) 319–327.
[15] G. Ranzi, M.A. Bradford, Analytical solutions for the time-dependent behaviour of composite beams with partial interaction, International Journal of Solids and Structures 43 (13) (2006) 3770–3793.
[16] B. Jurkiewiez, S. Buzon, J.G. Sieffert, Incremental viscoelastic analysis of composite beams with partial interaction, Computers and Structures 83 (21–22) (2005) 1780–1791.
[17] G. Ranzi, M.A. Bradford, Analysis of composite beams with partial interaction using the direct stiffness approach accounting for time effects, International Journal for Numerical Methods in Engineering 78 (5) (2009) 564–586.
[18] Q.H. Nguyen, M. Hjiaj, B. Uy, Time-dependent analysis of composite beams with partial interaction based on a time-discrete exact stiffness matrix, Engineering Structures 32 (9) (2010) 2902–2911.
[19] W.M. Henghold, Layered beam vibrations including slip, Doctoral Dissertation, Fort Collins: Civil Engineering Department, Colorado State University, 1972.
[20] U.A. Girhammar, D. Pan, Dynamic analysis of composite members with interlayer slip, International Journal of Solids and Structures 30 (6) (1993) 797–823.
[21] C. Adam, R. Heuer, A. Jeschko, Flexural vibrations of elastic composite beams with interlayer slip, Acta Machanica 125 (1–4) (1997) 17–30.
[22] U.A. Girhammar, D. Pan, A. Gustafsson, Exact dynamic analysis of composite beams with partial interaction, International Journal of Mechanical Sciences 49 (2007) 239–255.
[23] A.O. Adekola, Partial interaction between elastically connected elements of a composite beam, International Journal of Solids and Structures 4 (1968) 1125–1135.
[24] L.C.P. Yam, J.C. Chapman, The inelastic behaviour of simply supported composite beams of steel and concrete, Proceedings of the Institution of Civil Engineers 41 (1968) 651–683.
[25] Y. Arizumi, S. Hamada, Elastic–plastic analysis of composite beams with incomplete tnteraction by finite element method, Computers and Structures 14 (5–6) (1981) 453–462.
[26] N. Gattesco, Analytical modelling of nonlinear behaviour of composite beams with deformable connection, Journal of Constructional Steel Research 52 (1999) 195–218.
[27] M.R. Salari, E. Spacone, Analysis of steel–concrete composite frames with bond-slip, Journal of Structural Engineering (ASCE) 127 (11) (2001) 1243–1250.
[28] A. Ayoub, F.C. Filippou, Mixed formulation of nonlinear steel-concrete composite beam element, Journal of Structural Engineering (ASCE) 126 (3) (2000) 371–381.
[29] E. Spacone, S. El-Tawil, Nonlinear analysis of steel–concrete composite structures: state-of-the-art, Journal of Structural Engineering (ASCE) 130 (2) (2004) 1901–1912.
[30] M. Saje, B. Cas, I. Planinc, Non-linear finite element analysis of composite planar frames with an interlayer slip, Computers and Structures 82 (2004) 1901–1912.

[31] P. Krawczyk, B. Rebora, Large deflections of laminated beams with interlayer slips—part 2: finite element development, Engineering with Computers 24 (1) (2007) 33–51.
[32] J.M. Battini, Q.H. Nguyen, M. Hjiaj, Non-linear finite element analysis of composite beams with interlayer slips, Computers and Structures 87 (13–14) (2009) 904–912.
[33] G. Ranzi, A. Dall'Asta, L. Ragni, A. Zona, A geometric nonlinear model for composite beams with partial interaction, Engineering Structures 32 (2010) 1384–1396.
[34] P. Boeraeve, Contribution à l'analyse statique non linéaire des structures mixtes planes formées de poutres avec prise en compte des effets différés et des phases de construction, Doctoral Dissertation, University of Liège, Belgium, 1991 (in French).
[35] J.M. Aribert, A.G. Labib, Modèle de calcul élasto-plastique de poutres mixtes à connexion partielle, Construction Métallique 4 (1982) 3–51.
[36] J.M. Aribert, E. Ragneau, H. Xu, Développement d'un élément fini de poutre mixte acier-béton intégrant les phénomènes de glissement et de semi-continuité avec éventuellement voilement local, Construction Métallique 2 (1993) 31–49.
[37] Q.H. Nguyen, M. Hjiaj, B. Uy, S. Guezouli, Analysis of composite beams in the hogging moment regions using a mixed finite element formulation, Journal of Constructional Steel Research 65 (3) (2009) 737–748.
[38] H. Murakami, A laminated beam theory with interlayer slip, Journal of Applied Mechanics 51 (1984) 551–559.
[39] Z. Ranzi, A. Zona, A steel–concrete composite beam model with partial interaction including the shear deformability of the steel component, Engineering Structures 29 (11) (2007) 3026–3041.
[40] R. Xu, Y. Wu, Static, dynamic, and buckling analysis of partial interaction composite members using Timoshenko's beam theory, International Journal of Mechanical Sciences 49 (2007) 1139–1155.
[41] L. Dezi, F. Gara, G. Leoni, A shear deformable steel–concrete composite beam model, in: Proceedings of the ICSAS'07, Oxford, UK, 24–27 July 2007, pp. 457–464.
[42] A. Zona, G. Ranzi, Finite element models for nonlinear analysis of steel–concrete composite beams with partial interaction in combined bending and shear, Finite Elements in Analysis and Design 47 (2) (2011) 98–118.
[43] S. Schnabl, M. Saje, G. Turk, I. Planinc, Analytical solution of two-layer Beam taking into account interlayer slip and shear deformation, Journal of Structural Engineering (ASCE) 133 (6) (2007) 886–894.
[44] Q.H. Nguyen, E. Martinelli, M. Hjiaj, Derivation of the "exact" stiffness matrix for a two-layer Timoshenko beam element with continuous shear connection, Engineering Structures 33 (2) (2011) 298–307.
[45] Q.H. Nguyen, M. Hjiaj, J.M. Aribert, A space-exact beam element for time-dependent analysis of composite members with discrete shear connection, Journal of Constructional Steel Research 66 (2010) 1330–1338.
[46] G.R. Cowper, The shear coefficient in Timoshenko's beam theory, Journal of Applied Mechanics 33 (2) (1966) 335–340.

ANNEXE 6

P. Keo, M. Hjiaj, **Q-H. Nguyen** and H. Somja. Derivation of the exact stiffness matrix of shear-deformable multi-layered beam element in partial interaction. *Finite Elements in Analysis and Design* 2016. 112 :40-49. (5-Year IF 1.967) http://dx.doi.org/10.1016/j.finel.2015.12.004.

Finite Elements in Analysis and Design 112 (2016) 40–49

Contents lists available at ScienceDirect

Finite Elements in Analysis and Design

journal homepage: www.elsevier.com/locate/finel

Derivation of the exact stiffness matrix of shear-deformable multi-layered beam element in partial interaction

Pisey Keo, Quang-Huy Nguyen, Hugues Somja, Mohammed Hjiaj *

Université Européenne de Bretagne - INSA de Rennes, LGCGM/Structural Engineering Research Group, 20 avenue des Buttes de Coësmes, CS 70839, F-35708 Rennes Cedex 7, France

ARTICLE INFO

Article history:
Received 20 July 2015
Received in revised form
10 November 2015
Accepted 8 December 2015

Keywords:
Multi-layered beam
Interlayer slips
Shear-flexibility
Exact stiffness
Finite elements

ABSTRACT

This paper presents the exact finite element formulation for the analysis of partially connected shear-deformable multi-layered beams. Timoshenko's kinematic assumptions are considered for each layer or component, and the shear connection is modeled through a continuous relationship between the interface shear flow and the corresponding slip. The effect of possible transversal separation of the two adjacent layers has not been considered. The governing equations describing the behavior of a shear-deformable multi-layered beam in partial interaction consist of a set of coupled system of differential equations in which the primary variables are the slips and the shear deformations. This coupled system has been solved in closed form, and the "exact" stiffness matrix has been derived using the direct stiffness method. The latter has been implemented in a general displacement-based finite element code, and has been used to investigate the behavior of shear-deformable multi-layered beams. Both a simply supported and two continuous beams have been considered in order to assess the capability of the proposed formulation and to investigate the influence of the shear connection stiffness and span-to-depth ratios on mechanical responses of the beams. It has been found that the transverse displacement is more affected by shear flexibility than the interlayer slips.

1. Introduction

The analysis of members consisting of semi-rigidly connected layers is complicated due to the partial transfer of shear force at the interface. Over the years, there has been a great deal of research conducted on elastic two-layered composite beams in partial interaction. The first contribution is commonly attributed to Newmark et al. [1] who investigated the behavior of a two-layered beam considering that both layers are elastic and deform according to the Eurler–Bernoulli kinematics. In their paper, a closed-form solution is provided for a simply supported elastic composite beam. Since then, numerous analytical models were developed to study different aspects of the behavior of two-layered composite beams in more complicated situations. To investigate the behavior of elastic two-layered beam, several analytical formulations were proposed [2–10]. Significant development beyond that available from Newmark et al.'s paper [1] has been made in [9] by considering Timoshenko's kinematic assumptions for both layers. Besides these analytical works, several numerical models, mostly FE formulations have been developed to investigate the nonlinear behavior of both Bernoulli and Timoshenko two-layered beams with interlayer slip [11–22]. Most of the papers on layered beams in partial interaction are restricted to the case of two-layered beams and, multi-layered beams have received less attention. Chui and Barclay [23] and Schnabl et al. [24] proposed an exact analytical model for the case of three-layered members where the thickness as well as the material of the individual layers is arbitrary. Sousa et al. [25] developed an analytical solution for statically determinate multi-layered beams with the assumption that the cross-section rotation of each layer is the same although Timoshenko's kinematic is considered (cross-section rotations are the same for Bernoulli multi-layered beam). The governing equations describing the behavior of such multi-layered beam consist of a coupled system of differential equations in which the slips are considered as the primary variables. Skec et al. [26] proposed mathematical models with analytical solutions for the analysis of linear elastic Reissner multi-layered beams. The models take into account the interlayer slip and uplift of the adjacent layers, different material properties, independent transverse shear deformations, and different boundary conditions for each layer. Ranzi [27] proposed two types of displacement-based finite elements to evaluate locking problems in partial interaction of multi-layered beam based on Euler–Bernoulli kinematics. For classical polynomial shape functions, it is shown that elements without internal node suffer from the curvature locking problems. On the

* Corresponding author.
E-mail address: mohammed.hjiaj@insa-rennes.fr (M. Hjiaj).

http://dx.doi.org/10.1016/j.finel.2015.12.004
0168-874X/

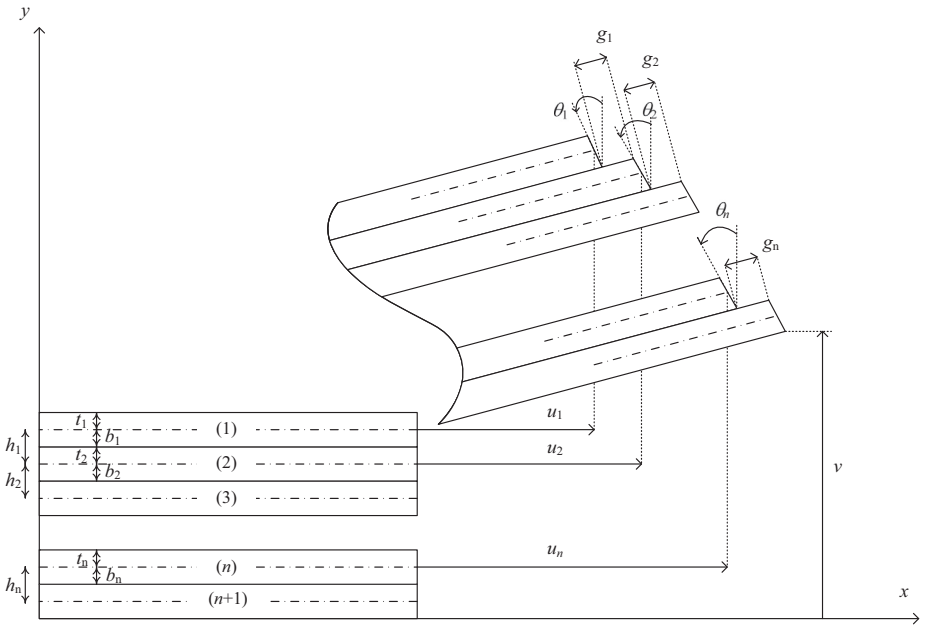

Fig. 1. Displacement field of a multi-layered beam.

contrary, adding an internal node remove locking problems, improve the representation of the axial displacement of each layer and better characterizes the partial interaction behavior of multi-layered beam.

A formulation based on the exact stiffness matrix offers the possibility of generating a locking-free model. These elements are highly attractive due to their precision, computational efficiency and mesh independency. Heinisuo [28] proposed a finite element formulation using exact stiffness matrix for uniform, straight, linearly elastic beams with two faces and one core and with three symmetric faces and two identical cores. Based on the analytical solution given in [25], Sousa [29] derived the exact flexibility matrix for partially connected multi-layered beams with the assumption that both transverse displacement and rotation are the same for all layers. The model is based on the derivation of flexibility matrix obtained from a statically determinate coordinate system.

The purpose of this paper is to present a new exact FE formulation for the analysis of shear-deformable multi-layered beams in partial interaction based on the exact stiffness matrix derived from the governing equations of the problem. The features of the formulation presented in this paper are as follows: (i) longitudinal partial interaction of the layers is considered which provides a general description of the stresses and strains in the layers; (ii) different rotations of cross-sections of each layer are considered; (iii) exact stiffness matrix is used which provide accurate and stable results. The present model provides, therefore, an efficient tool for linear elastic analysis of shear-deformable multi-layered beam with arbitrary support and loading conditions. The rest of the paper is organized as follows. In Section 2, the field equations for a shear-deformable multi-layered beam in partial interaction are presented. The governing equations of the problem are derived in Section 3. In Section 4, the full analytical solution of the coupled differential governing equations is provided, regardless of the loading and the nature of the boundary conditions (support and end force). Special care has been taken while dealing with the constants of integration. The exact expression for the stiffness matrix is deduced for a generic shear-deformable multi-layered beam element in Section 5. Numerical examples are presented in Section 6 in order to assess the performance of the formulation and to support the conclusions drawn in Section 7.

2. Field equations

The field equations describing the geometrically linear behavior of an elastic multi-layered beam with $n+1$ layers in partial interaction are briefly outlined in this section. The following assumptions are commonly accepted in the model to be discussed in this paper:

- connected members are made out of elastic, homogenous and isotropic materials;
- the cross-sections of all components remain plane but not orthogonal to beam axis after deformation;
- adjacent layers are connected at their interfaces where relative slips can develop;
- transverse displacement v is assumed to be the same for all layers;
- discretely located shear connectors are regarded as continuous.

Quantities with subscript sc are associated with the interface connection.

2.1. Compatibility

With the above assumptions, the layer has independent cross-section rotation and curvature, see Fig. 1. Kinematic equations relating the displacement components (u_i, v, θ_i) to the corresponding strain components $(\epsilon_i, \theta_i, \kappa_i)$ are as follows:

$$\epsilon_i = \partial u_i \tag{1}$$

$$\theta_i = \partial v - \gamma_i \tag{2}$$

$$\kappa_i = \partial \theta_i \tag{3}$$

where

- $\partial \bullet = \mathrm{d}\bullet/\mathrm{d}x$;

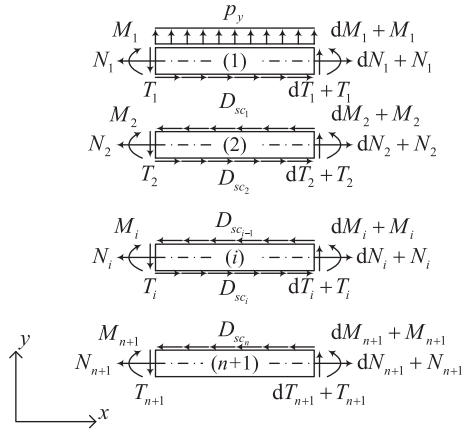

Fig. 2. Equilibrium of a multi-layered beam.

- $i = 1, 2, \ldots, n+1$;
- ϵ_i and u_i are the axial strain and the longitudinal displacement at the centroid of layer i, respectively;
- γ_i is the shear strain of layer i;
- v is the transverse displacement;
- θ_i and κ_i are the cross-section rotation and the curvature (flexural deformation) of layer i, respectively; and
- t_i and b_i are the distances from the layer axis i to its top and bottom surfaces, respectively.

The interlayer slip corresponds to the difference between axial displacements of adjacent layers at their connected interface which is expressed as:

$$g_i = u_{i+1} - u_i - b_i\,\theta_i - t_{i+1}\,\theta_{i+1}, \quad i = 1, 2, \ldots, n \tag{4}$$

2.2. Equilibrium

The equilibrium equations are derived by considering the free body diagram of a differential element dx located at an arbitrary point x on a multi-layered beam, see Fig. 2. The shear connector connecting the adjacent layers "i" and "$i+1$" transmits the longitudinal shear flow D_{sc_i}. The equilibrium conditions result in the following set of equations:

$$\partial N_i - D_{sc_{i-1}} + D_{sc_i} = 0 \tag{5}$$

$$\partial M_i + T_i + t_i\,D_{sc_{i-1}} + b_i\,D_{sc_i} = 0 \tag{6}$$

$$\sum_{j=1}^{n+1} \partial T_j + p_y = 0 \tag{7}$$

$$T = \sum_{j=1}^{n+1} T_j \tag{8}$$

where

- $i = 1, 2, \ldots, n+1$;
- N_i: normal force acting on layer "i";
- M_i: bending moments acting on layer "i";
- T_i: shear force acting on layer "i";
- T: total shear force; and
- D_{sc_i}: shear stress at connected interface between layer "i" and "$i+1$" ($D_{sc_0} = 0$; $D_{sc_{n+1}} = 0$).

2.3. Constitutive relations

The generalized stress–strain relationships are simply obtained by integrating the appropriate uniaxial constitutive model over each cross-section. For a linear elastic material, these relationships lead to the following set of equations:

$$N_i = \int_{A_i} \sigma\,\mathrm{d}A_i = (EA)_i\,\epsilon_i \tag{9}$$

$$M_i = -\int_{A_i} y\,\sigma\,\mathrm{d}A_i = (EI)_i\,\kappa_i \tag{10}$$

$$T_i = \int_{A_i} \tau\,\mathrm{d}A_i = (GA)_i\,\gamma_i \tag{11}$$

where

- $i = 1, 2, \ldots, n+1$;
- $(EA)_i = E_i\,A_i$ is the axial stiffness of layer "i";
- $(EI)_i = E_i\,I_i$ is the flexural stiffness of layer "i"; and
- $(GA)_i = G_i\,A_i$ is the shear stiffness of layer "i".

E_i, G_i, A_i and I_i are the elastic modulus, the shear modulus, the area, and the second moment of area of layer "i", respectively. The above relations must be completed by the relationship between the shear stress D_{sc_i} and the interlayer slip g_i. The assumption of linear and continuous shear connection can be expressed by the following simple relationship between interface slip and shear stress:

$$D_{sc_i} = k_{sc_i}\,g_i \tag{12}$$

where k_{sc_i} is the shear connector stiffness.

3. Derivation of the governing equations

The relationships introduced in Section 2 are now combined to derive the equations governing the behavior of shear-deformable multi-layered beam in partial interaction. Combining the kinematic relations (Eqs. (1) and (2)) with the elastic behavior equations (9)–(12) and inserting the outcome into the equilibrium equations (5)–(8) produce the following set of differential equations:

$$\partial^2 u_i = \frac{1}{(EA)_i}\left(k_{sc_{i-1}}\,g_{i-1} - k_{sc_i}\,g_i\right), \quad i = 1, 2, \ldots, n+1 \tag{13}$$

$$\partial^2 \theta_i = -\frac{1}{(EI)_i}\left(t_i\,k_{sc_{i-1}}\,g_{i-1} + b_i\,k_{sc_i}\,g_i\right) - \frac{(GA)_i}{(EI)_i}\gamma_i, \quad i = 1, 2, \ldots, n+1 \tag{14}$$

$$\partial^3 v = -\frac{T}{(\mathrm{EI})_0} - \sum_{j=1}^{n} \frac{h_j}{(\mathrm{EI})_0} k_{sc_j}\,g_j + \sum_{j=1}^{n+1} \frac{(\mathrm{EI})_j}{(\mathrm{EI})_0}\partial^2\gamma_j \tag{15}$$

where $(EI)_0 = \sum_{j=1}^{n+1} E_j\,I_j$ and h_j is the distance between the reference axes of adjacent layers j and $j+1$. Taking the derivative of the slip distribution equation (4) and making use of Eqs. (13) and (14), one arrives at the following equation:

$$\partial^2 g_i = \beta_i\,k_{sc_{i-1}}\,g_{i-1} + \alpha_i\,k_{sc_i}\,g_i + \beta_{i+1} k_{sc_{i+1}}\,g_{i+1} + \frac{b_i (GA)_i}{(EI)_i}\gamma_i + \frac{t_{i+1}(GA)_{i+1}}{(EI)_{i+1}}\gamma_{i+1} \tag{16}$$

in which

$$\alpha_i = \frac{1}{(EA)_i} + \frac{1}{(EA)_{i+1}} + \frac{b_i^2}{(EI)_i} + \frac{t_{i+1}^2}{(EI)_{i+1}} \tag{17}$$

$$\beta_i = -\frac{1}{(EA)_i} + \frac{t_i\, b_i}{(EI)_i} \tag{18}$$

The above differential equations can be cast in a compact form as follows:

$$\partial^2 \mathbf{g}_t = \mathbf{A}_t\, \mathbf{g}_t + \mathbf{A}_s\, \mathbf{g}_s + \mathbf{H}_t \frac{T}{(EI)_{n+1}} \tag{19}$$

where

$$\mathbf{H}_t = [\overbrace{0\ 0\ \cdots\ 0}^{n-1}\quad t_{n+1}]^{\mathrm{T}} \tag{20}$$

$$\mathbf{g}_t = [g_1\ g_2\ \cdots\ g_n]^{\mathrm{T}} \tag{21}$$

$$\mathbf{g}_s = [\gamma_1\ \gamma_2\ \cdots\ \gamma_n]^{\mathrm{T}} \tag{22}$$

$$\mathbf{A}_t = \begin{bmatrix} k_{sc_1}\,\alpha_1 & k_{sc_2}\,\beta_2 & 0 & \cdots & 0 & 0 \\ k_{sc_1}\,\beta_2 & k_{sc_2}\,\alpha_2 & k_{sc_3}\,\beta_3 & \cdots & 0 & 0 \\ 0 & k_{sc_2}\,\beta_3 & k_{sc_3}\,\alpha_3 & \ddots & 0 & 0 \\ \vdots & \vdots & \ddots & \ddots & \ddots & \vdots \\ 0 & 0 & 0 & \ddots & k_{sc_{n-1}}\,\alpha_{n-1} & k_{sc_n}\,\beta_n \\ 0 & 0 & 0 & \cdots & k_{sc_{n-1}}\,\beta_n & k_{sc_n}\,\alpha_n \end{bmatrix}$$

and

$$\mathbf{A}_s = \begin{bmatrix} \frac{h_1(GA)_1}{(EI)_1} & \frac{h_2(GA)_2}{(EI)_2} & 0 & \cdots & 0 & 0 \\ 0 & \frac{h_1(GA)_1}{(EI)_1} & \frac{h_2(GA)_2}{(EI)_2} & \ddots & 0 & 0 \\ \vdots & \ddots & \ddots & \ddots & \ddots & \vdots \\ 0 & 0 & 0 & \cdots & \frac{h_{n-1}(GA)_{n-1}}{(EI)_{n-1}} & \frac{h_n(GA)_n}{(EI)_n} \\ -\frac{h_{n+1}(GA)_1}{(EI)_{n+1}} & -\frac{h_{n+1}(GA)_2}{(EI)_{n+1}} & -\frac{h_{n+1}(GA)_3}{(EI)_{n+1}} & \cdots & -\frac{h_{n+1}\,(GA)_{n-1}}{(EI)_{n+1}} & \frac{h_n(GA)_n}{(EI)_n} - \frac{h_{n+1}(GA)_n}{(EI)_{n+1}} \end{bmatrix} \tag{24}$$

Next, we derive a second system of differential equations by eliminating the shear deformation of the $(n+1)$th layer. We start by considering equilibrium equations (6) for $i=k$ and $i=n+1$ with $k=1,\ldots,n$. Then, we use the constitutive relations (Eqs. (10)–(12)) to eliminate the internal forces and the longitudinal shear stresses from these two equilibrium equations. Taking the derivative of the cross-section rotation in equation (2) and inserting the outcome into Eq. (3), we obtain the expression of the curvature as a function of the transverse displacement and the shear deformation. The latter is inserted into the equilibrium equations (6) (for $i=k$ and $i=n+1$) from which the transverse displacement is eliminated as unknown by subtracting the kth equilibrium equation from the $(n+1)$th. Finally, γ_{n+1} is expressed in terms of γ_k using Eqs. (8) and (11), and the following differential equation is obtained

$$\partial^2\gamma_k + \sum_{j=1}^{n} \frac{(GA)_j}{(GA)_{n+1}} \partial^2\gamma_j = \frac{t_k}{(EI)_k} k_{sc_{k-1}}\, g_{k-1} + \frac{b_k}{(EI)_k} k_{sc_k}\, g_k - \frac{t_{n+1}}{(EI)_{n+1}} k_{sc_n}\, g_n$$

$$+ \frac{(GA)_k}{(EI)_k}\gamma_k + \sum_{j=1}^{n} \frac{(GA)_j}{(EI)_{n+1}}\gamma_j - \frac{T}{(EI)_{n+1}} \tag{25}$$

which can be written in the following matrix form:

$$\partial^2 \mathbf{g}_s = \mathbf{B}^{-1}\,\mathbf{R}_t\,\mathbf{g}_t + \mathbf{B}^{-1}\,\mathbf{R}_s\,\mathbf{g}_s - \mathbf{B}^{-1}\,\mathbb{I}\,\frac{T}{(EI)_{n+1}} \tag{26}$$

where

$$\mathbf{B} = \begin{bmatrix} 1+\frac{(GA)_1}{(GA)_{n+1}} & \frac{(GA)_2}{(GA)_{n+1}} & \cdots & \frac{(GA)_n}{(GA)_{n+1}} \\ \frac{(GA)_1}{(GA)_{n+1}} & 1+\frac{(GA)_2}{(GA)_{n+1}} & \cdots & \frac{(GA)_n}{(GA)_{n+1}} \\ \vdots & \vdots & \ddots & \vdots \\ \frac{(GA)_1}{(GA)_{n+1}} & \frac{(GA)_2}{(GA)_{n+1}} & \cdots & 1+\frac{(GA)_n}{(GA)_{n+1}} \end{bmatrix} \tag{27}$$

$$\mathbf{R}_t = \begin{bmatrix} \frac{b_1\,k_{sc_1}}{(EI)_1} & 0 & \cdots & & 0 & -\frac{t_{n+1}\,k_{sc_n}}{(EI)_{n+1}} \\ \frac{t_2\,k_{sc_1}}{(EI)_2} & \frac{b_2\,k_{sc_2}}{(EI)_2} & 0 & \cdots & 0 & -\frac{t_{n+1}\,k_{sc_n}}{(EI)_{n+1}} \\ 0 & \frac{t_3\,k_{sc_2}}{(EI)_3} & \frac{b_3\,k_{sc_3}}{(EI)_3} & \cdots & 0 & -\frac{t_{n+1}\,k_{sc_n}}{(EI)_{n+1}} \\ \vdots & \vdots & \ddots & \ddots & \vdots & \vdots \\ 0 & 0 & 0 & \ddots & \frac{b_{n-1}\,k_{sc_{n-1}}}{(EI)_{n-1}} & -\frac{t_{n+1}\,k_{sc_n}}{(EI)_{n+1}} \\ 0 & 0 & 0 & \cdots & \frac{t_n\,k_{sc_{n-1}}}{(EI)_n} & \frac{b_n\,k_{sc_n}}{(EI)_n} - \frac{t_{n+1}\,k_{sc_n}}{(EI)_{n+1}} \end{bmatrix} \tag{28}$$

$$\mathbf{R}_s = \begin{bmatrix} \frac{(GA)_1}{(EI)_1} + \frac{(GA)_1}{(EI)_{n+1}} & \frac{(GA)_2}{(EI)_{n+1}} & \cdots & \frac{(GA)_n}{(EI)_{n+1}} \\ \frac{(GA)_1}{(EI)_{n+1}} & \frac{(GA)_2}{(EI)_2} + \frac{(GA)_2}{(EI)_{n+1}} & \cdots & \frac{(GA)_n}{(EI)_{n+1}} \\ \vdots & \vdots & \ddots & \vdots \\ \frac{(GA)_1}{(EI)_{n+1}} & \frac{(GA)_2}{(EI)_{n+1}} & \cdots & \frac{(GA)_n}{(EI)_n} + \frac{(GA)_n}{(EI)_{n+1}} \end{bmatrix} \tag{29}$$

$$\mathbb{I} = [1\ \ 1\ \ \cdots\ \ 1]^{\mathrm{T}} \tag{30}$$

Combining Eq. (19) with Eq. (26), one arrives at the following coupled second-order system of differential equations:

$$\partial^2 \mathbf{g} - \mathbf{A}\,\mathbf{g} = \mathbf{H}\frac{T}{(EI)_{n+1}} \tag{31}$$

where

$$\mathbf{g} = [\mathbf{g}_t^{\mathrm{T}}\ \ \mathbf{g}_s^{\mathrm{T}}]^{\mathrm{T}} \tag{32}$$

$$\mathbf{A} = \begin{bmatrix} \mathbf{A}_t & \mathbf{A}_s \\ \mathbf{B}^{-1}\,\mathbf{R}_t & \mathbf{B}^{-1}\,\mathbf{R}_s \end{bmatrix} \tag{33}$$

$$\mathbf{H} = \begin{bmatrix} \mathbf{H}_t \\ -\mathbf{B}^{-1}\,\mathbb{I} \end{bmatrix} \tag{34}$$

A diagonalization of the matrix $\mathbf{A}$ will uncouple the above system

of differential equations (31) and produce a set of $2n$ second-order ordinary equations. Let $\mathbf{A}_v$ and $\mathbf{A}_\lambda$ be the matrix collecting unit eigenvectors and eigenvalues of $\mathbf{A}$, respectively. Then, the following relationship holds:

$$\mathbf{A}_\lambda = \mathbf{A}_v^{-1}\,\mathbf{A}\,\mathbf{A}_v. \tag{35}$$

Subsequently, we insert the vector $\mathbf{g}$ obtained by pre-multiplying the vector $\tilde{\mathbf{g}}$ by the matrix $\mathbf{A}_v$

$$\mathbf{g} = \mathbf{A}_v\tilde{\mathbf{g}} \tag{36}$$

into Eq. (31) and make use of Eq. (35) to produce an uncoupled differential equation system:

$$\partial^2\tilde{\mathbf{g}} - \mathbf{A}_\lambda\,\tilde{\mathbf{g}} = \overline{\mathbf{H}}\frac{T}{(\mathrm{EI})_{n+1}} \tag{37}$$

where $\overline{\mathbf{H}} = \mathbf{A}_v^{-1}\mathbf{H}$. By denoting $\overline{H}_i$ the component "i" of vector $\overline{\mathbf{H}}$, one arrives at a set of ordinary differential equations in terms of $2n$ variables ($\tilde{g}_k$):

$$\partial^2\tilde{g}_i - \lambda_i\,\tilde{g}_i = \overline{H}_i\frac{T}{(\mathrm{EI})_{n+1}}, \qquad i = 1,2,\ldots,2n \tag{38}$$

where λ_i is the eigenvalue of the matrix $\mathbf{A}$.

4. Closed-form solution of the governing equations

In this section, we provide the analytical solution of the governing equations for the general case of flexible interface connection that is $0 < k_{sck} < \infty$. The governing differential equation involves the single unknown variable vector $\tilde{\mathbf{g}}$. It is worth to point out that the exact solution of the governing differential equations (38) requires the distribution of the shear force $T(x)$ to be known. In order to simplify the development of the solution, we assume that the externally distributed load applied to the element is constant. As a result, the distribution of shear force must be linear to ensure the overall transverse equilibrium:

$$T(x) = -p_y\,x + C_{4n+6} \tag{39}$$

where C_{4n+6} is the shear force on the left-hand side of the beam and is considered to be a constant of integration. All kinematic variables can be determined once the expression of $\tilde{g}_i$ is found by solving the differential equations (Eq. (38)). Let $P_i(x)$ be the particular solution for non-homogeneous differential equation (Eq. (38)). Hence, the general solution of Eq. (38) is given by

- For $\lambda_i > 0$

$$\tilde{g}_i = \tilde{C}_{2i-1}e^{\sqrt{\lambda_i}x} + \tilde{C}_{2i}e^{-\sqrt{\lambda_i}x} + P_i(x), \quad i = 1,2,\ldots,2n \tag{40}$$

- For $\lambda_i < 0$

$$\tilde{g}_i = C_{2i-1}\cos\sqrt{-\lambda_i}x + C_{2i}\sin\sqrt{-\lambda_i}x + P_i(x), \quad i = 1,2,\ldots,2n \tag{41}$$

- For $\lambda_i = 0$

$$\tilde{g}_i = C_{2i-1} + C_{2i}\,x + P_i(x), \quad i = 1,2,\ldots,2n \tag{42}$$

The expression of $\tilde{g}_i$ in case $\lambda_i > 0$ involves exponential terms which may take very large values. To avoid numerical ill-conditioning of the stiffness matrix, we replace the actual expressions of the constants of integration with the following ones:

$$\tilde{C}_{2i-1} = e^{-\sqrt{\lambda_i}L}\,C_{2i-1}, \quad i = 1,2,\ldots,2n \tag{43}$$

$$\tilde{C}_{2i} = C_{2i}, \quad i = 1,2,\ldots,2n \tag{44}$$

in which L is the length of the beam.

All $\tilde{g}_i$ are collected in a vector so the analytical solution can be written in a matrix form as follows:

$$\tilde{\mathbf{g}} = \mathbf{X}_{\tilde{g}}\mathbf{C} + \mathbf{Z}_{\tilde{g}} \tag{45}$$

with

$$\tilde{\mathbf{g}} = \left[\,\tilde{g}_1\;\;\tilde{g}_2\cdots\tilde{g}_{2n}\,\right]^{\mathrm{T}} \tag{46}$$

and

$$\mathbf{C} = [C_1\;\;C_2\;\;\cdots\;\;C_{4n+6}]^{\mathrm{T}} \tag{47}$$

The coefficients $C_{1,\ldots,4n+6}$ are constants of integration that will be determined by enforcing the kinematic boundary conditions at both beam ends. The components of matrix $\mathbf{X}_{\tilde{g}}$ and $\mathbf{Z}_{\tilde{g}}$ involve the eigenvalues of $\mathbf{A}$ and the external load p_y. In case $\mathbf{A}$ is positive definite i.e. $\lambda_i > 0$, we obtain the following expression for $\mathbf{X}_{\tilde{g}}$ and $\mathbf{Z}_{\tilde{g}}$:
and

$$\mathbf{Z}_{\tilde{g}} = \frac{p_y\,x}{(EI)_{n+1}}\left[\frac{\overline{H}_1}{\lambda_1}\;\;\frac{\overline{H}_2}{\lambda_2}\;\;\cdots\;\;\frac{\overline{H}_{2n}}{\lambda_{2n}}\right]^{\mathrm{T}} \tag{49}$$

$$\mathbf{X}_{\tilde{g}} = \begin{bmatrix} e^{\sqrt{\lambda_1}(x-L)} & e^{-\sqrt{\lambda_1}x} & 0 & 0 & \cdots & 0 & 0 & 0 & 0 & 0 & 0 & \dfrac{-\overline{H}_1}{\lambda_1(EI)_{n+1}} \\ 0 & 0 & e^{\sqrt{\lambda_2}(x-L)} & e^{-\sqrt{\lambda_2}x} & \cdots & 0 & 0 & 0 & 0 & 0 & 0 & \dfrac{-\overline{H}_2}{\lambda_2(EI)_{n+1}} \\ \vdots & \vdots & \vdots & \vdots & \ddots & \vdots & \vdots & \vdots & \vdots & \vdots & \vdots & \vdots \\ 0 & 0 & 0 & 0 & \cdots & e^{\sqrt{\lambda_{2n}}(x-L)} & e^{-\sqrt{\lambda_{2n}}x} & 0 & 0 & 0 & 0 & \dfrac{-\overline{H}_n}{\lambda_{2n}(EI)_{n+1}} \end{bmatrix} \tag{48}$$

Having at hand the analytical expression for $\tilde{g}_i$, it is straightforward to derive the slip distributions g_i and shear deformations γ_i. Substituting Eq. (44) into Eq. (36), one gets

$$\mathbf{g} = \mathbf{X}_g\mathbf{C} + \mathbf{Z}_g \tag{50}$$

in which

$$\mathbf{X}_g = \mathbf{A}_v\,\mathbf{X}_{\tilde{g}} \quad \mathbf{Z}_g = \mathbf{A}_v\,\mathbf{Z}_{\tilde{g}} \tag{51}$$

The vector $\mathbf{Z}_g$ and the matrix $\mathbf{X}_g$ are decomposed into two sub-vectors and two sub-matrices, respectively, in order to separate the slip distribution g_i from the shear deformation distribution. The first bloc collects the slip distribution g_i and the second one gathers the shear deformation γ_i:

$$\mathbf{g}_t = \mathbf{X}_{gt}\mathbf{C} + \mathbf{Z}_{gt} \tag{52}$$

$$\mathbf{g}_s = \mathbf{X}_{gs}\mathbf{C} + \mathbf{Z}_{gs} \tag{53}$$

where $\mathbf{X}_g = [\mathbf{X}_{gt}^{\mathrm{T}}\;\mathbf{X}_{gs}^{\mathrm{T}}]^{\mathrm{T}}$ and $\mathbf{Z}_g = [\mathbf{Z}_{gt}^{\mathrm{T}}\;\mathbf{Z}_{gs}^{\mathrm{T}}]^{\mathrm{T}}$ with $\mathbf{X}_{gt} = [\mathbf{X}_{g_1}^{\mathrm{T}}\;\mathbf{X}_{g_2}^{\mathrm{T}}\cdots\mathbf{X}_{g_n}^{\mathrm{T}}]^{\mathrm{T}}$, $\mathbf{Z}_{gt} = [Z_{g_1}\;Z_{g_2}\cdots Z_{g_n}]^{\mathrm{T}}$, $\mathbf{X}_{gs} = [\mathbf{X}_{\gamma_1}^{\mathrm{T}}\;\mathbf{X}_{\gamma_2}^{\mathrm{T}}\cdots\mathbf{X}_{\gamma_n}^{\mathrm{T}}]^{\mathrm{T}}$ and $\mathbf{Z}_{gs} = [Z_{\gamma_1}\;Z_{\gamma_2}\cdots$

$Z_{\gamma_n}]^{\mathrm{T}}$. The shear deformation distribution of $(n+1)$th layer can be determined by combining Eqs. (8) and (11) with Eq. (53):

$$\gamma_{n+1} = \mathbf{X}_{\gamma_{n+1}}\,\mathbf{C} + Z_{\gamma_{n+1}} \tag{54}$$

where

$$\mathbf{X}_{\gamma_{n+1}} = -\frac{1}{(GA)_{n+1}}\sum_{j=1}^{n}(GA)_j\,\mathbf{X}_{\gamma_j} + \frac{\mathbb{I}_{4n+6}}{(GA)_{n+1}} \tag{55}$$

$$Z_{\gamma_{n+1}} = -\frac{1}{(GA)_{n+1}}\sum_{j=1}^{n}(GA)_j\,Z_{\gamma_j} - \frac{p_y\,x}{(GA)_{n+1}} \tag{56}$$

4.1. Determination of displacement fields

We use the differential equations expressing the cross-section displacements of each layer and their derivatives as a function of the interlayer slips, the shear deformations and the second derivative of the shear deformation that have been derived in Section 3 to determine the displacement fields. By back substituting the above expressions of the slip distribution and shear deformation distribution (Eqs. (52)–(53)) into Eqs. (13) and (15), the analytical expressions for the displacement v and u_i $(i=1,2,\ldots,n+1)$ can be obtained. Making use of the kinematic relationships (Eqs. (2) and (3)), the analytical expressions for cross-section rotation and curvature can be established. All these kinematic variables depend on $4n+6$ constants of integration.

Combining Eqs. (52)–(54) with Eq. (39) and performing three successive integrations of the outcome give the distribution of vertical displacement as follows:

$$v = \mathbf{X}_v\mathbf{C} + Z_v \tag{57}$$

where

$$\mathbf{X}_v = \int\left(\int\left(\int\left(-\frac{\mathbb{I}_{4n+6}}{(EI)_0} - \sum_{j=1}^{n}\frac{h_j}{(EI)_0}k_{sc_j}\,\mathbf{X}_{g_j} + \sum_{j=1}^{n+1}\frac{(EI)_j}{(EI)_0}\,\partial^2\mathbf{X}_{\gamma_j}\right)\mathrm{d}x\right)\mathrm{d}x\right)\mathrm{d}x + \mathbb{I}_{4n+1}\frac{x^2}{2} + \mathbb{I}_{4n+2}\,x + \mathbb{I}_{4n+3} \tag{58}$$

$$Z_v = \int\left(\int\left(\int\left(\frac{p_y\,x}{(EI)_0} - \sum_{j=1}^{n}\frac{h_j}{(EI)_0}k_{sc_j}\,Z_{g_j} + \sum_{j=1}^{n+1}\frac{(EI)_j}{(EI)_0}\,\partial^2 Z_{\gamma_j}\right)\mathrm{d}x\right)\mathrm{d}x\right)\mathrm{d}x \tag{59}$$

$$\mathbb{I}_{4n+1} = \left[\overbrace{0\;0\;\cdots\;0}^{4n}\;1\;0\;0\;0\;0\;0\right] \tag{60}$$

$$\mathbb{I}_{4n+2} = [0\;0\;\cdots\;0\;0\;1\;0\;0\;0\;0] \tag{61}$$

$$\mathbb{I}_{4n+3} = [0\;0\;\cdots\;0\;0\;0\;1\;0\;0\;0] \tag{62}$$

$$\mathbb{I}_{4n+4} = [0\;0\;\cdots\;0\;0\;0\;0\;1\;0\;0] \tag{63}$$

$$\mathbb{I}_{4n+5} = [0\;0\;\cdots\;0\;0\;0\;0\;0\;1\;0] \tag{64}$$

$$\mathbb{I}_{4n+6} = [0\;0\;\cdots\;0\;0\;0\;0\;0\;0\;1] \tag{65}$$

The expression of the cross-section rotation distribution for each layer is obtained by taking the derivative of the transverse displacement and subtracting the shear deformation distribution according to Eq. (4):

$$\theta_i = \mathbf{X}_{\theta_i}\,\mathbf{C} + Z_{\theta_i}, \quad i=1,2,\ldots,n+1 \tag{66}$$

The expression of the curvature distribution for each layer is obtained by taking the derivative of the cross-section rotation distribution according to Eq. (3):

$$\kappa_i = \mathbf{X}_{\kappa_i}\,\mathbf{C} + Z_{\kappa_i}, \quad i=1,2,\ldots,n+1 \tag{67}$$

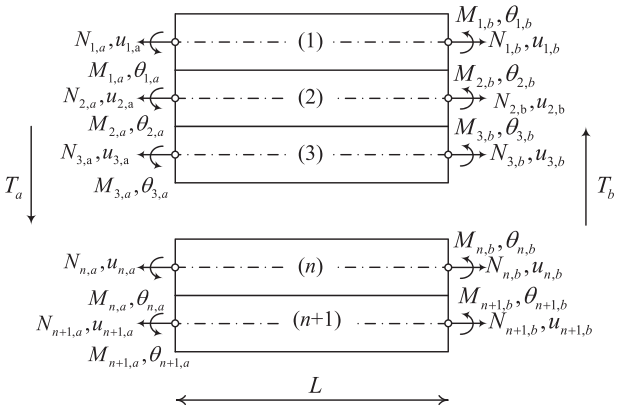

Fig. 3. Nodal forces and displacements of a multi-layered beam element.

in which

$$\mathbf{X}_{\theta_i} = \partial\mathbf{X}_v - \mathbf{X}_{\gamma_i}, \quad Z_{\theta_i} = \partial Z_v - Z_{\gamma_i} \tag{68}$$

$$\mathbf{X}_{\kappa_i} = \partial\mathbf{X}_{\theta_i}, \quad Z_{\kappa_i} = \partial Z_{\theta_i} \tag{69}$$

The axial displacement of the first layer can be determined by integrating twice the right-hand side of Eq. (13) for $i=1$. This gives

$$u_1 = \mathbf{X}_{u_1}\mathbf{C} + Z_{u_1} \tag{70}$$

where

$$\mathbf{X}_{u_1} = -\frac{k_{sc_1}}{(EA)_1}\int\left(\int\mathbf{X}_{g_1}\,\mathrm{d}x\right)\mathrm{d}x + x\,\mathbb{I}_{4n+4} + \mathbb{I}_{4n+5} \tag{71}$$

$$Z_{u_1} = -\frac{k_{sc_1}}{(EA)_1}\int\left(\int Z_{g_1}\,\mathrm{d}x\right)\mathrm{d}x \tag{72}$$

Once the axial displacement of the first layer is known, Eq. (4) is used to derive the axial displacement for the remaining layers. Indeed, at this stage we have $4n+6$ constants of integration which correspond to the number of degrees of freedom. Consequently, the remaining kinematic variables must be determined by using the kinematic relations. Inserting Eqs. (52), (66) and (70) into Eq. (4) and solving consecutively for the axial displacement of layer $i+1$, one gets

$$u_{i+1} = \mathbf{X}_{u_{i+1}}\mathbf{C} + Z_{u_{i+1}}, \quad i=1,2,\ldots,n \tag{73}$$

where

$$\mathbf{X}_{u_{i+1}} = \mathbf{X}_{g_i} + \mathbf{X}_{u_i} + h_i\,\mathbf{X}_{\theta_i} + h_{i+1}\,\mathbf{X}_{\theta_{i+1}} \tag{74}$$

$$Z_{u_{i+1}} = Z_{g_i} + Z_{u_i} + h_i\,Z_{\theta_i} + h_{i+1}\,Z_{\theta_{i+1}} \tag{75}$$

4.2. Determination of internal forces

Once the displacement fields are defined, one can use the linear elastic relationship equations (9) and (10) to obtain the nodal forces

$$N_i = \mathbf{Y}_{N_i}\mathbf{C} + R_{N_i}, \quad i=1,2,\ldots,n+1 \tag{76}$$

$$M_i = \mathbf{Y}_{M_i}\mathbf{C} + R_{M_i}, \quad i=1,2,\ldots,n+1 \tag{77}$$

$$T = \mathbf{Y}_T\mathbf{C} + R_T \tag{78}$$

where

$$\mathbf{Y}_{N_i} = (EA)_i\partial\mathbf{X}_{u_i}, \quad R_{N_i} = (EA)_{s_i}\partial Z_{us_i}, \quad i=1,2,\ldots,n+1 \tag{79}$$

$$\mathbf{Y}_{M_i} = (EI)_i\,\mathbf{X}_{\kappa_i}, \quad R_{M_i} = (EI)_i Z_{\kappa_i}, \quad i=1,2,\ldots,n+1 \tag{80}$$

$$\mathbf{Y}_T = \mathbb{I}_{4n+6}, \quad R_T = -p_y\,x \tag{81}$$

5. Exact stiffness matrix

The direct stiffness method is used to derive the exact stiffness of the multi-layered beam with $n+1$ layers. It can be obtained starting from the general expressions of the internal force and displacement fields. Let a multi-layered beam element of length L be considered. Since the same transverse displacement is assumed, this element has $(4n+6)$ degrees of freedom. Applying the kinematic boundary conditions at $x=0$ and $x=L$ leads to the relationship between the vector of constants of integration $\mathbf{C}$ and the vector of nodal displacements $\mathbf{q}$:

$$\mathbf{q}=\mathbf{X}\,\mathbf{C}+\mathbf{Z} \tag{82}$$

where

$$\mathbf{q}=[u_{1,0}\ \cdots\ u_{n+1,0}\ v_0\ \theta_{1,0}\ \cdots\ \theta_{n+1,0}\ u_{1,L}\ \cdots\ u_{n+1,L}\ v_L\ \theta_{1,L}\ \cdots\ \theta_{n+1,L}]^{\mathrm{T}} \tag{83}$$

$$\mathbf{X}=[\mathbf{X}_{u_{1,0}}\ \cdots\ \mathbf{X}_{\theta_{n+1,0}}\ \mathbf{X}_{u_{1,L}}\ \cdots\ \mathbf{X}_{\theta_{n+1,L}}]^{\mathrm{T}} \tag{84}$$

$$\mathbf{Z}=[Z_{u_{1,0}}\ \cdots\ Z_{\theta_{n+1,0}}\ Z_{u_{1,L}}\ \cdots\ Z_{\theta_{n+1,L}}]^{\mathrm{T}} \tag{85}$$

The nodal displacements being independent, see Fig. 3, the matrix $\mathbf{X}$ is invertible. Thus, the constants C_i are obtained as a function of the nodal displacements q_i.

$$\mathbf{C}=\mathbf{X}^{-1}(\mathbf{q}-\mathbf{Z}) \tag{86}$$

The nodal forces can be expressed in compact form as:

$$\mathbf{Q}=\mathbf{Y}\,\mathbf{C}+\mathbf{R} \tag{87}$$

where

$$\mathbf{Q}=[-N_{1,0}\ \cdots\ -M_{n+1,0}\ N_{1,L}\ \cdots\ M_{n+1,L}]^{\mathrm{T}} \tag{88}$$

$$\mathbf{Y}=[-\mathbf{Y}_{N_{1,0}}\ \cdots\ -\mathbf{Y}_{M_{n+1,0}}\ \mathbf{Y}_{N_{1,L}}\ \cdots\ \mathbf{Y}_{M_{n+1,L}}]^{\mathrm{T}} \tag{89}$$

$$\mathbf{R}=[-R_{N_{1,0}}\ \cdots\ -R_{M_{n+1,0}}\ R_{N_{1,L}}\ \cdots\ R_{M_{n+1,L}}]^{\mathrm{T}} \tag{90}$$

Inserting Eq. (86) into Eq. (87), one obtains:

$$\mathbf{K}\,\mathbf{q}=\mathbf{Q}+\mathbf{Q}_0 \tag{91}$$

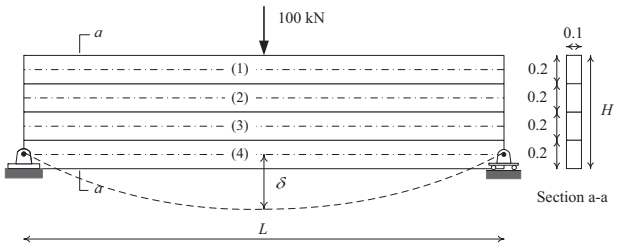

Fig. 4. Simply supported four-layered beam (dimension in [m]).

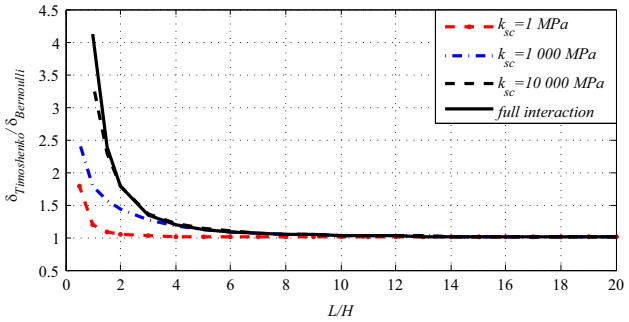

Fig. 5. Mid-span deflection ratio versus span-to-depth ratio for different shear connector stiffnesses.

where

$$\mathbf{K}=\mathbf{Y}\,\mathbf{X}^{-1} \tag{92}$$

represents the exact stiffness of the element and

$$\mathbf{Q}_0=\mathbf{K}\,\mathbf{Z}-\mathbf{R} \tag{93}$$

represents the nodal force due to the uniform external load p_y.

6. Numerical application

The purpose of this section is to assess the capabilities of the proposed formulation in reproducing the linear elastic behavior of shear-deformable multi-layered beams with interlayer slips and to investigate the influence of the shear connection stiffness, the cross-section shear deformability and the span-to-depth ratio on the mechanical response of the beams. To do so, the predictions of the exact finite element model for multi-layered beams with shear-rigid are compared against the results obtained with the present exact model. The investigation is carried out considering three examples: a simply supported four-layered beam, a two-span continuous three-layered beam and a dissymmetric continuous four-layered beam. The governing equations for deriving the exact stiffness matrix of shear-rigid multi-layered beam can be found in [29].

6.1. Simply supported four-layered beam

A simply supported four-layered beam of span L is analyzed with the proposed formulation. The beam consists of four identical connected layers with a total depth equal to H, see Fig. 4. The elastic modulus is 8000 MPa and the Poisson coefficient is 0.3 for each layer. The shear correction factor is taken equal to 5/6 for all layer cross-sections. For this example, we assume that the shear connector stiffness (k_{sc}) is identical for each slipping plane. The

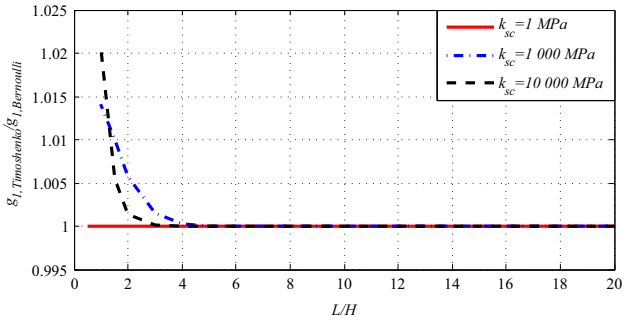

Fig. 6. End beam slip strain (g_1) ratio versus span-to-depth ratio for different shear connector stiffnesses.

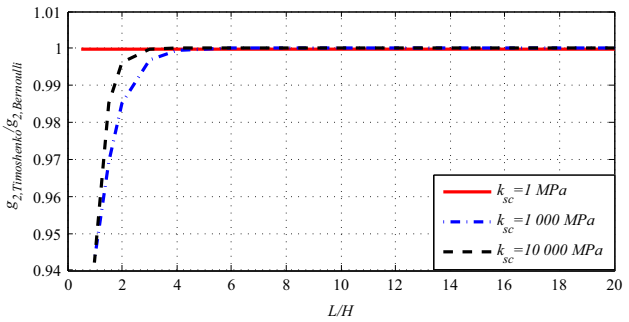

Fig. 7. End beam slip strain (g_2) ratio versus span-to-depth ratio for different shear connector stiffnesses.

beam is modeled using two elements, which is the smallest number of elements needed for simply supported beam subjected to a concentrated load. It is worth mentioning that since the model is based on exact stiffness matrix, considering more elements does not improve the results. The effect of the shear flexibility on the mechanical response of the beam is analyzed by comparing the mechanical response obtained with the shear-flexible model (Timoshenko) against the corresponding response predicted by shear-rigid model (Bernoulli). In particular, the comparison is carried out in terms of the deflection underneath the load point (100 kN) at mid-span evaluated by means of the two above-mentioned models. Fig. 5 shows the mid-span deflections obtained with both models for different span-to-depth ratios (L/H) and shear connector stiffness (k_{sc}). As expected, the deflection predicted by shear-flexible model is larger than the corresponding one evaluated according to shear-rigid model, for any value of the ratio L/H. Moreover, the deflection ratio tends to infinity when the span-to-depth ratio tends to zero, and to unity when span-to-depth ratio tends to infinity. In particular, the black dash line refers to the case of significantly high rigid connection with $k_{sc} = 10\,000$ MPa (close to the full interaction curve which corresponds to the solid black line). The other curve representing partial interaction ($k_{sc} = 1000$ MPa) monotonically reduces to the case of loose connection with $k_{sc} = 1$ MPa. It can be seen that partial interaction results in a reduction of the effect of shear flexibility of the connected members on the transverse displacement.

Further comparisons are also proposed in terms of end beam slips (see Fig. 6 between the 1st and 2nd layer (g_1), and between 2nd and 3rd layer (g_2), Fig. 7). It is worth mentioning that by symmetry, the interlayer slips g_1 and g_3 are equal in magnitude. As a result, only the distributions of g_1 and g_2 are discussed here. In particular, one can observe that the interlayer slip g_2 given by the shear-flexible model is smaller than the one given by shear-rigid model. Besides, the curves in Figs. 6 and 7 approach the asymptotic value of 1 for large value of L/H much more quickly than those represented in Fig. 5. This means that the transverse displacement

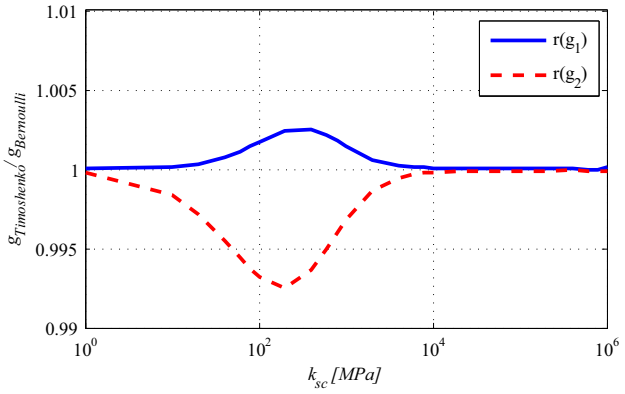

Fig. 8. End beam slip strain ratio versus shear connector stiffness for span-to-depth ratio $L/H = 3$.

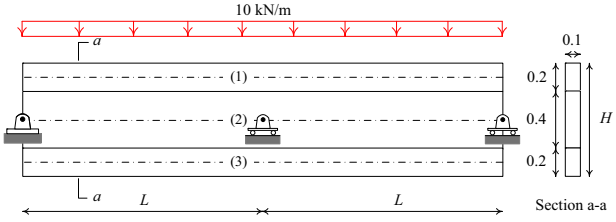

Fig. 9. Two-span continuous three-layered beam (dimension in (m)).

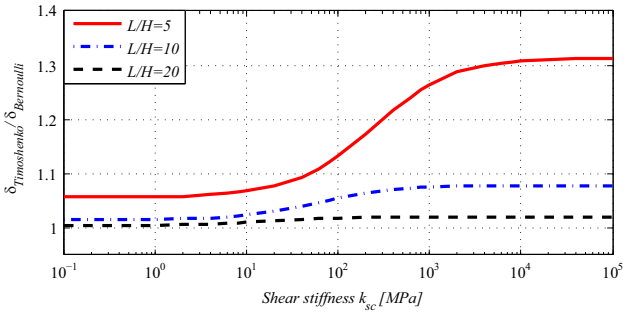

Fig. 10. Deflection ratio versus shear connector stiffness for different span-to-depth ratios.

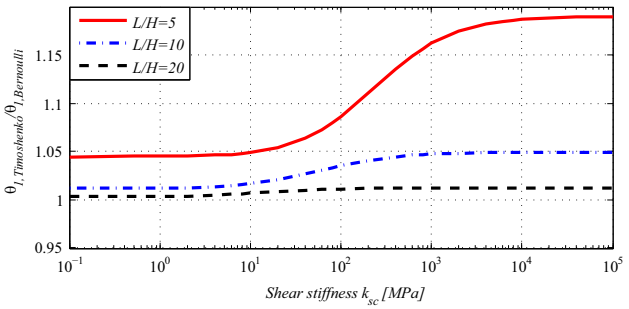

Fig. 11. End beam rotation (θ_1) ratio versus shear connector stiffness for different span-to-depth ratios.

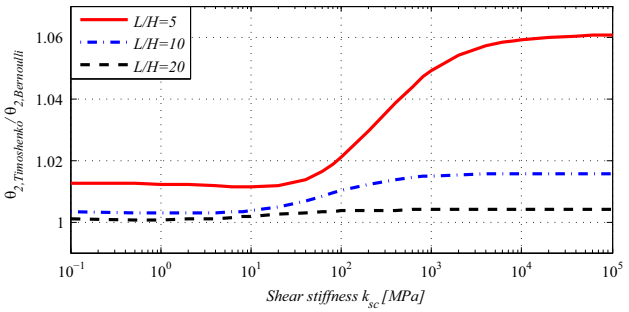

Fig. 12. End beam rotation (θ_2) ratio versus shear connector stiffness for different span-to-depth ratios.

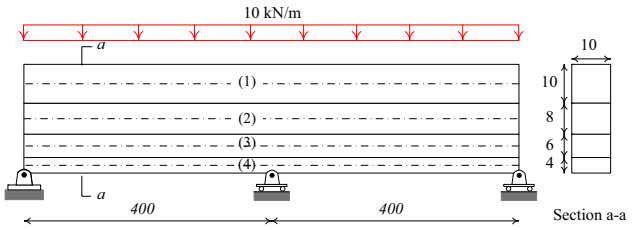

Fig. 13. Two-span continuous four-layered beam (dimension in [cm]).

is more affected by shear flexibility than interface slip, whose value is directly controlled by the interface stiffness k_{sc} considered in both shear-flexible and shear-rigid model for multi-layered beams in partial interaction. Since the interlayer slip basically depends on the shear connector stiffness, the influence of the shear deformations on the beam end slips is also contingent on k_{sc} and is more pronounced for low value of L/H. The geometry and the mechanical properties of the layers being identical, the interlayer slip ratios of both models are equal to unities for $k_{sc} = 1$ MPa

Table 1
End slips and maximum moment in mm and kN m.

	Sousa [29]	Present
M_{max}	19.03058820	19.02883046
g_1	1.44496919	1.44498441
g_2	1.14888312	1.14974670
g_3	0.79506892	0.79618523

Table 2
End slips and maximum moment in mm and kN m

M_{max}	19.26696216
g_1	1.46135402
g_2	1.17957176
g_3	0.85443617

Table 3
Processing time in function of number of elements.

Number of element	2	4	8	16	32
Total time (s)	0.4680	0.4680	0.4840	0.5150	0.5930

which corresponds to what has been expected for the case without interaction. Fig. 8 shows the distributions of interlayer slip ratios in function of shear connector stiffness. One can observe that for notably low value of L/H, the distribution ratios vary significantly and they tend to asymptotic values for large value of k_{sc}.

6.2. Two-span continuous three-layered beam

The shear-flexible model which was successfully applied to the above simply supported four-layered beam is now used to simulate a two-span continuous three-layered beam. Only two elements are needed for the analysis. The geometric characteristics of the beam is shown in Fig. 9 where H is the total height of the section. The beam section is composed of two equal layers with 10 cm wide and 20 cm thick attached to the core of the same width and a depth of 40 cm. The beam has two equal spans (L) and is subjected to a uniformly distributed load of 10 kN/m. Like previous example, we analyze a three-layered beam with the same elastic modulus, Poisson coefficient and shear correction factor for each layer. Those values are respectively 8000 MPa, 0.3 and 5/6. Moreover, the shear connector stiffness (k_{sc}) for each slipping plane is considered to have the same value. The beam is analyzed using both shear-flexible and shear-rigid model. Fig. 10 represents the ratio of maximum deflection obtained with both models. In this case, the ratio is given as a function of the interface shear modulus k_{sc} for three different values of the length-to-depth ratio L/H. The curves illustrated in Fig. 10 confirm the important role played by the shear flexibility in the case of low L/H ratios and full connection. One can observe that the deflection ratio significantly increases, particularly for low L/H ratio, when the value of k_{sc} varies from 0.1 MPa (almost no interaction) to 10^5 MPa (nearly full interaction). Nevertheless, increasing the value of k_{sc} has little effect on the deflection ratio for large values of L/H.

Furthermore, comparison in terms of cross-section rotation at beam end is also performed. Due to symmetry, only cross-section rotations of the first and the second layers are presented (see, respectively, Figs. 11 and 12). Obviously, the rotation of each layer is the same for shear-rigid model (Bernoulli). Since the shear deformation is different for each layer, the cross-section rotations θ_1 and θ_2 are not the same for shear-flexible model. However, the influence of L/H ratio and k_{sc} on $\theta_{1,2}$ is similar.

6.3. Four-layered beam with dissymmetric distribution of layers

Consider a 4-layered continuous beam with rectangular cross-section for each layer depicted in Fig. 13. This problem was considered in [29] using exact flexibility matrix in which an equal cross-section rotation is assumed for all layers. A connection stiffness equal to 5 MPa is used for each slipping plane. The elastic modulus for all layers is 50,000 MPa, the Poisson coefficient is taken as 0.3 and the shear correction factor is assumed equal to unity. The results for the end slips and maximum bending moment are presented in Table 1. It can be seen that there is a good agreement between the results of both models.

To further assess the present model, we consider more complex situation with a dissymmetric connection stiffness k_{sc} taken equal to 5 MPa for the first interlayer, to 3 MPa for the second interlayer and to 1 MPa for the last slipping plane. The results of the analysis with 2 elements are reported in Table 2. The connection being more flexible, the slips are larger compared to the previous case.

To evaluate the computing time, we perform the analysis with different number of elements. The analysis was run on the PC Machine with CPU @3.20 GHz and 8Go RAM. The actual total computing time as a function of the number of elements is presented in Table 3. We can see that the computing time of the FE analysis using the present exact stiffness matrix is within a second.

7. Conclusion

In this paper, the exact expression of the stiffness matrix for a shear-deformable multi-layered beam in partial interaction has been developed. This stiffness matrix is obtained from the closed-form solution of the governing equations of the problem consisting in a coupled system of differential equations where the slips and shear deformations are considered as primary variables. Particular care was given to the determination of the constants of integration. The proposed exact stiffness matrix can be used in a displacement-based procedure for the elastic analysis of shear-deformable multi-layered beams in partial interaction with arbitrary loading and support conditions. The influence of the shear flexibility and the partial interaction on the overall behavior of multi-layered beams has been investigated. A parametric analysis considering various values of the length-to-depth ratio and of the shear connection stiffness has been performed. It has been found that the transverse displacement is more affected by shear flexibility than the interface slip. It has been observed that the partial interaction results in a reduction of the shear flexibility effect on the transverse displacement. Moreover, the interlayer slip given by the shear-flexible beam element is not always larger than the one given by shear-rigid beam element. It has been shown that the computation time when using the present exact finite element is reasonable.

References

[1] N.M. Newmark, C.P. Siess, I. Viest, et al., Tests and analysis of composite beams with incomplete interaction, Proc. Soc. Exp. Stress Anal. 9 (1) (1951) 75–92 , URL http://refhub.elsevier.com/S0045-7949(13)00110-7/h0005.
[2] U. Girhammar, V. Gopu, Composite beam-columns with interlayer slip-exact analysis, J. Struct. Eng. 119 (4) (1993) 1265–1282 , URL http://dx.doi.org/10.1061/(ASCE)0733-9445(1993)119:4(1265).
[3] Y.-F. Wu, D.J. Oehlers, M.C. Griffith, Partial-interaction analysis of composite beam/column members, Mech. Struct. Mach. 30 (3) (2002) 309–332 , URL http://dx.doi.org/10.1081/SME-120004420.
[4] C. Faella, E. Martinelli, E. Nigro, Steel and concrete composite beams with flexible shear connection: exact analytical expression of the stiffness matrix

and applications, Comput. Struct. 80 (11) (2002) 1001–1009 , URL http://dx.doi.org/10.1016/S0045-7949(02)00038-X.
[5] G. Ranzi, M. Bradford, B. Uy, A direct stiffness analysis of a composite beam with partial interaction, Int. J. Numer. Methods Eng. 61 (5) (2004) 657–672 , URL http://dx.doi.org/10.1002/nme.1091.
[6] U.A. Girhammar, D.H. Pan, Exact static analysis of partially composite beams and beam-columns, Int. J. Mech. Sci. 49 (2) (2007) 239–255 , URL http://dx.doi.org/10.1016/j.ijmecsci.2006.07.005.
[7] R. Xu, Y. Wu, Static, dynamic, and buckling analysis of partial interaction composite members using Timoshenko's beam theory, Int. J. Mech. Sci. 49 (10) (2007) 1139–1155 , URL http://dx.doi.org/10.1016/j.ijmecsci.2007.02.006.
[8] S. Schnabl, M. Saje, G. Turk, I. Planinc, Analytical solution of two-layer beam taking into account interlayer slip and shear deformation, J. Struct. Eng. 133 (6) (2007) 886–894 , URL http://dx.doi.org/10.1061/(ASCE)0733-9445(2007)133:6(886).
[9] Q.-H. Nguyen, E. Martinelli, M. Hjiaj, Derivation of the exact stiffness matrix for a two-layer Timoshenko beam element with partial interaction, Eng. Struct. 33 (2) (2011) 298–307 , URL http://dx.doi.org/10.1016/j.engstruct.2010.10.006.
[10] R. Xu, G. Wang, Variational principle of partial-interaction composite beams using timoshenko's beam theory, Int. J. Mech. Sci. 60 (1) (2012) 72–83 , URL http://dx.doi.org/10.1016/j.ijmecsci.2012.04.012.
[11] M.R. Salari, E. Spacone, P.B. Shing, D.M. Frangopol, Nonlinear analysis of composite beams with deformable shear connectors, J. Struct. Eng. 124 (10) (1998) 1148–1158 , URL http://dx.doi.org/10.1061/(ASCE)0733-9445(1998)124:10(1148).
[12] A. Ayoub, F.C. Filippou, Mixed formulation of nonlinear steel-concrete composite beam element, J. Struct. Eng. 126 (3) (2000) 371–381 , URL http://dx.doi.org/10.1061/(ASCE)0733-9445(2000)126:3(371).
[13] A. Dall'Asta, A. Zona, Non-linear analysis of composite beams by a displacement approach, Comput. Struct. 80 (27) (2002) 2217–2228 , URL http://dx.doi.org/10.1016/S0045-7949(02)00268-7.
[14] A. Dall'Asta, A. Zona, Slip locking in finite elements for composite beams with deformable shear connection, Finite Elements Anal. Des. 40 (13–14) (2004) 1907–1930 , URL http://dx.doi.org/10.1016/j.finel.2004.01.007.
[15] A. Ayoub, A force-based model for composite steel–concrete beams with partial interaction, J. Constr. Steel Res. 61 (3) (2005) 387–414 , URL http://dx.doi.org/10.1016/j.jcsr.2004.08.004.
[16] F. Gara, G. Ranzi, G. Leoni, Displacement-based formulations for composite beams with longitudinal slip and vertical uplift, Int. J. Numer. Methods Eng. 65 (8) (2006) 1197–1220 , URL http://dx.doi.org/10.1002/nme.1484.
[17] G. Ranzi, A. Zona, A steel–concrete composite beam model with partial interaction including the shear deformability of the steel component, Eng. Struct. 29 (11) (2007) 3026–3041 , URL http://dx.doi.org/10.1016/j.engstruct.2007.02.007.
[18] S. Schnabl, M. Saje, G. Turk, I. Planinc, Locking-free two-layer Timoshenko beam element with interlayer slip, Finite Elements Anal. Des. 43 (9) (2007) 705–714 , URL http://dx.doi.org/10.1016/j.finel.2007.03.002.
[19] J.-M. Battini, Q.-H. Nguyen, M. Hjiaj, Non-linear finite element analysis of composite beams with interlayer slips, Comput. Struct. 87 (13–14) (2009) 904–912 , URL http://dx.doi.org/10.1016/j.compstruc.2009.04.002.
[20] A. Zona, G. Ranzi, Finite element models for nonlinear analysis of steel–concrete composite beams with partial interaction in combined bending and shear, Finite Elements Anal. Des. 47 (2) (2011) 98–118 , URL http://dx.doi.org/10.1016/j.finel.2010.09.006.
[21] E. Martinelli, Q.-H. Nguyen, M. Hjiaj, Dimensionless formulation and comparative study of analytical models for composite beams in partial interaction, J. Constr. Steel Res. 75 (2012) 21–31 , URL http://dx.doi.org/10.1016/j.jcsr.2012.02.016.
[22] M. Hjiaj, J.-M. Battini, Q.-H. Nguyen, Large displacement analysis of shear deformable composite beams with interlayer slips, Int. J. Non-Linear Mech. 47 (8) (2012) 895–904 , URL http://dx.doi.org/10.1016/j.ijnonlinmec.2012.05.001.
[23] Y.H. Chui, D.W. Barclay, Analysis of three-layer beams with non-identical layers and semi-rigid connections, Can. J. Civil Eng. 25 (2) (1998) 271–276 , URL http://www.nrcresearchpress.com/doi/pdf/10.1139/l97-093.
[24] S. Schnabl, I. Planinc, M. Saje, B. Čas, G. Turk, An analytical model of layered continuous beams with partial interaction, Struct. Eng. Mech. 22 (3) (2006) 263–278 , URL ⟨http://drugg.fgg.uni-lj.si/3375/⟩.
[25] J.B.M. Sousa Jr, C.E. Oliveira, A.R. da Silva, Displacement-based nonlinear finite element analysis of composite beam–columns with partial interaction, J. Constr. Steel Res. 66 (6) (2010) 772–779 , URL http://dx.doi.org/10.1016/j.jcsr.2009.12.015.
[26] L. Škec, S. Schnabl, I. Planinc, G. Jelenic, Analytical modelling of multilayer beams with compliant interfaces, Struct. Eng. Mech. 44 (4) (2012) 465 , URL http://dx.doi.org/10.12989/sem.2012.44.4.465.
[27] G. Ranzi, Locking problems in the partial interaction analysis of multi-layered composite beams, Eng. Struct. 30 (10) (2008) 2900–2911 , URL http://dx.doi.org/10.1016/j.engstruct.2008.04.006.
[28] M. Heinisuo, An exact finite element technique for layered beams, Comput. Struct. 30 (3) (1988) 615–622 , URL http://dx.doi.org/10.1016/0045-7949(88)90297-0.
[29] J.B.M. Sousa Jr., Exact finite elements for multilayered composite beam-columns with partial interaction, Comput. Struct. 123 (2013) 48–57 , URL http://dx.doi.org/10.1016/j.compstruc.2013.04.008.

ANNEXE 7

P. Le Grognec, **Q-H. Nguyen** and M. Hjiaj. Exact buckling solution for two-layer Timoshenko beams with interlayer slip. International *Journal of Solids and Structures* 2012 ; 49 : 143-150. (5-Year IF 2.483) http://dx.doi.org/10.1016/j.ijsolstr.2011.09.020.

International Journal of Solids and Structures 49 (2012) 143–150

Contents lists available at SciVerse ScienceDirect

International Journal of Solids and Structures

journal homepage: www.elsevier.com/locate/ijsolstr

Exact buckling solution for two-layer Timoshenko beams with interlayer slip

Philippe Le Grognec [a,*], Quang-Huy Nguyen [b], Mohammed Hjiaj [b]

[a] Ecole des Mines de Douai, Polymers and Composites Technology & Mechanical Engineering Department, 941 rue Charles Bourseul – BP 10838, 59508 Douai Cedex, France
[b] Université Européenne de Bretagne – INSA de Rennes, LGCGM – Structural Engineering Research Group, 20 avenue des Buttes de Coësmes – CS 70839, 35708 Rennes Cedex 7, France

ARTICLE INFO

Article history:
Received 22 April 2011
Received in revised form 23 August 2011
Available online 5 October 2011

Keywords:
Two-layer beam
Partial interaction
Buckling
Transverse shear
Closed-form solution

ABSTRACT

This paper deals with the buckling behavior of two-layer shear-deformable beams with partial interaction. The Timoshenko kinematic hypotheses are considered for both layers and the shear connection (no uplift is permitted) is represented by a continuous relationship between the interface shear flow and the corresponding slip. A set of differential equations is obtained from a general 3D bifurcation analysis, using the above assumptions. Original closed-form analytical solutions of the buckling load and mode of the composite beam under axial compression are derived for various boundary conditions. The new expressions of the critical loads are shown to be consistent with the ones corresponding to the Euler–Bernoulli beam theory, when transverse shear stiffnesses go to infinity. The proposed analytical formulae are validated using 2D finite element computations. Parametric analyses are performed, especially including the limiting cases of perfect bond and no bond. The effect of shear flexibility is particularly emphasized.

1. Introduction

Composite beams are widely used in civil engineering. Such structures involve two layers composed of different materials, like steel and concrete, in order to optimize the global mechanical behavior. Due to the technical solutions employed to assemble the two layers, relative displacements generally occur at the interface resulting in the so-called partial interaction. Whereas the transverse separation is often small in practice and can thus be neglected, the interface slip may often influence the behavior of the composite beams insomuch it must be considered for a more reliable modeling analysis.

For about 60 years, numerous analytical and numerical models characterized by different levels of approximation have been proposed in the literature. The first formulation of an elastic theory for composite beams with partial interaction is commonly attributed to Newmark et al. (1951). These authors adopted the Euler–Bernoulli kinematic assumptions for both layers and considered a continuous and linear relationship between the relative interface displacements (slips) and the corresponding interface shear stresses. This formulation is usually referred to as the Newmark's model, and was extensively used from that time by many authors to formulate theoretical models for the static and/or dynamic response of composite beams in the linear elastic range (Heinisuo, 1988; Girhammar and Gopu, 1993; Faella et al., 2002; Wu et al., 2002; Ranzi et al., 2004; Girhammar and Pan, 2007) as well as in the linear visco-elastic range (Nguyen et al. 2010a,b). In addition, several numerical models based on the same basic assumptions have been developed to investigate the behavior of composite beams with partial interaction in the non-linear range (for material non-linearities, see e.g. Gattesco (1999), Salari and Spacone (2001a,b) and Nguyen et al. (2009), for geometric non-linearities, see e.g. Battini et al. (2009)). Most of these papers are concerned with finite element formulations, based on either a displacement-based or the so-called "force-based" approach, most often providing the exact stiffness matrix, among other things. For instance, a space-exact time-discretized stiffness matrix has been proposed in Nguyen et al. (2010a,b) for the time-dependent analysis of continuous composite beams.

The most significant advances in the theory of two-layer beams in partial interaction moved recently toward the introduction of shear flexibility of both layers according to the well-known Timoshenko theory. The earliest use of the Timoshenko beam hypotheses in the analysis of composite beams with interlayer slip has been performed by Murakami (1984). He analyzed the effect of interlayer slip on the stiffness degradation of laminated beams, by means of the finite element method. A few contributions, dealing with composite beams with partial interaction and including transverse shear effects, have been proposed recently (Ranzi and Zona, 2007; Dezi et al., 2007; Schnabl et al., 2007; Nguyen et al., 2011). Ranzi and Zona (2007) developed a finite element model for the analysis of steel–concrete two-layer beams coupling a Euler–Bernoulli beam for the reinforced concrete slab with a Timoshenko beam for the steel member. A fully consistent shear-deformable two-layer beam model has been proposed by Schnabl et al. (2007), allowing for completely independent shear strains and centroidal rotations of both layers. Lastly, Nguyen et al. (2011) derived the exact stiffness matrix of a two-layer shear-deformable

* Corresponding author.
E-mail addresses: philippe.le.grognec@mines-douai.fr (P. Le Grognec), quang-huy.nguyen@insa-rennes.fr (Q.-H. Nguyen), mohammed.hjiaj@insa-rennes.fr (M. Hjiaj).

0020-7683/$ - see front matter © 2011 Elsevier Ltd. All rights reserved.
doi:10.1016/j.ijsolstr.2011.09.020

beam element, using kinematic assumptions similar to the analytical work reported in Schnabl et al. (2007).

Among the references above, the buckling problem of such two-layer beams with interlayer slip has been little-studied. The numerical model developed by Battini et al. (2009) was specially employed to investigate the non-linear buckling of composite beams, using bisection methods along the fundamental path to detect the singularity of the tangent stiffness matrix in an incremental way. Čas et al. (2007) studied the buckling of layered wood columns with a non-linear load-slip law, also involving numerical indirect methods for the calculation of critical loads and mode shapes. Besides, a general analytical study of the buckling behavior of two-layer beams with interlayer slip was recently performed (Kryžanowski et al., 2009; Schnabl and Planinc, 2010; Schnabl and Planinc, 2011). The authors first considered the case of Bernoulli beams and conducted a detailed parametric analysis (Kryžanowski et al., 2009; Schnabl and Planinc, 2010). The boundary conditions were naturally shown to have a great influence on the critical loads and the corresponding buckling modes, whereas the pre-critical shortening (axial deformations) could be neglected in the analysis. In Schnabl and Planinc (2011), the previous theoretical analysis was generalized to the case of Timoshenko beams, including the transverse shear effects in the model. The governing equations of the problem were provided but only a solution strategy of these equations was outlined and no closed-form expressions were reported. At last, Xu and Wu (2007) also proposed an analytical model considering the Timoshenko kinematic assumption for each component and derived explicit solutions for the buckling loads of partial interaction composite members in the particular case of simply-supported end conditions. However, they have imposed an equal cross-section rotation for both components.

In this paper, a bifurcation analysis of a shear-deformable two-layer beam with interlayer slip is carried out, based on the same general kinematic assumptions as in Schnabl and Planinc (2011), giving rise to original closed-form solutions for classical boundary conditions. The paper is organized as follows. In Section 2, the bifurcation equation of the problem is first written in a 3D framework. Next this equation is linearized and particularized, using the appropriate kinematic assumptions and considering a uniaxial stress state with small pre-critical displacements. This approach is a general and efficient way to cope with the buckling of structures subjected to a uniform uniaxial pre-critical stress state. It was successfully applied to the case of compressed elastoplastic plates and cylinders (Le Grognec and Le van, 2009) and beams (Le Grognec and Le van, 2011), in earlier studies. The final set of differential equations is analytically solved as far as the boundary conditions make it possible. In Section 3, the new solution is compared to the ones obtained with the Bernoulli hypotheses and the simplified Timoshenko assumptions used in Xu and Wu (2007), respectively. Furthermore, the limiting cases of perfect bond and no bond are also considered. Numerical finite element computations are performed in order to validate the analytical results and show the importance of shear flexibility in such a buckling analysis. A parametric analysis is finally achieved to show the relative influence of various geometric and material parameters.

2. Critical buckling load of a two-layer shear-deformable beam with interlayer slip

2.1. Problem definition

Let us consider a straight composite beam with two sub-elements of possibly different cross-sections and materials and including shear connectors at the interface which are uniformly distributed along the longitudinal direction, as shown in Fig. 1. In the reference configuration, the beam m ($m = a,b$) occupies a cylindrical volume Ω_m of constant cross-section area A_m, second moment of area I_m, height $2h_m$ and length L. In the linear elastic regime, the material m (of the beam m) is assumed to be isotropic, defined by the fourth-order elasticity tensor $\mathbf{D}^m$ whose components in an orthonormal basis are $D^m_{ijkl} = \Lambda_m\delta_{ij}\delta_{kl} + \mu_m(\delta_{ik}\delta_{jl} + \delta_{il}\delta_{kj})$, where δ_{ij} is the Kronecker symbol, and Λ_m and μ_m are the Lamé constants. Use is also made of the Young's modulus E_m, the Poisson's ratio ν_m and the shear modulus G_m related to Λ_m and μ_m by the standard relations $\Lambda_m = \dfrac{E_m\nu_m}{(1+\nu_m)(1-2\nu_m)}$ and $\mu_m = G_m = \dfrac{E_m}{2(1+\nu_m)}$. The shear bond stiffness density by unit length of the continuous shear connectors is constant and denoted by k_{sc}.

The composite beam is subjected to an axial compressive force which leads to buckling. The critical load and the bifurcation mode are derived from a 3D framework: the theory is developed using a total Lagrangian formulation where the beams are seen as 3D bodies (Le Grognec and Le van, 2011).

2.2. Theoretical formulation

The critical load λ_c and the bifurcation mode $\mathbf{X}$ of a 3D body are obtained by solving the following bifurcation equation:

$$\forall \delta\mathbf{U}, \quad \int_\Omega \nabla^T\delta\mathbf{U} : \mathbf{K}(\lambda_c) : \nabla\mathbf{X}\, d\Omega = 0 \tag{1}$$

The fourth-order nominal tangent elastic tensor $\mathbf{K}$ can be written as follows:

$$\mathbf{K} = \frac{\partial\mathbf{\Pi}}{\partial\mathbf{F}} = \mathbf{F}\cdot\frac{\partial\mathbf{\Sigma}}{\partial\mathbf{E}}\cdot\mathbf{F}^T + (\mathbb{I}\cdot\mathbf{\Sigma})^T = \mathbf{F}\cdot\mathbf{D}\cdot\mathbf{F}^T + (\mathbb{I}\cdot\mathbf{\Sigma})^T \tag{2}$$

In the above equation, $\mathbf{E}$ denotes the Green strain tensor and $\mathbf{\Sigma}$ the second Kirchhoff stress tensor (symmetric). $\mathbf{F}$ is the deformation gradient and $\mathbf{\Pi} = \mathbf{F}\cdot\mathbf{\Sigma}$ the first Kirchhoff stress tensor (non-symmetric). $\mathbb{I}$ represents the fourth-order unit tensor ($I_{ijkl} = \delta_{il}\delta_{kj}$) and the superscript ^{T} the transposition of a second-order tensor and the major transposition of a fourth-order tensor ($(\mathbf{A}^T)_{ijkl} = A_{klij}$), respectively. Use is also made of the fourth-order material tangent elastic tensor $\mathbf{D}$ which has been already introduced.

We shall now derive more explicit expressions of the above tensors by exploiting the uniaxial stress state in the compressed beams at hand. Let the beams be subjected in the pre-critical state to a nominal axial compressive stress $\Pi_{xx} = -P < 0$, so that the first Kirchhoff stress tensor $\mathbf{\Pi}$ is expressed in the orthonormal basis $(\mathbf{e}_x, \mathbf{e}_y, \mathbf{e}_z)$ as:

$$\mathbf{\Pi} = -P\mathbf{e}_x\otimes\mathbf{e}_x = \begin{bmatrix} -P & 0 & 0 \\ 0 & 0 & 0 \\ 0 & 0 & 0 \end{bmatrix} \quad (P > 0) \tag{3}$$

Let us make the assumption that the pre-critical deformations are small, which is usually satisfied in practice:

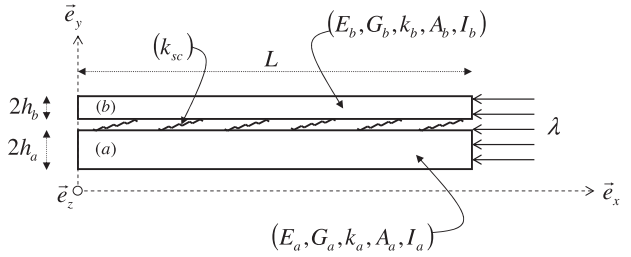

Fig. 1. Two-layer shear-deformable beam with shear connectors under axial compression.

$$\|\nabla \mathbf{U}\| \ll 1 \tag{4}$$

Thus, the stress tensor $\boldsymbol{\Sigma}$ writes:

$$\boldsymbol{\Sigma} = \mathbf{F}^{-1} \cdot \boldsymbol{\Pi} \approx \boldsymbol{\Pi} \tag{5}$$

The nominal tangent elastic tensor in Eq. (2) becomes:

$$\mathbf{K} \approx \frac{\partial \boldsymbol{\Sigma}}{\partial \mathbf{E}} + (\mathbb{I} \cdot \boldsymbol{\Sigma})^T = \mathbf{D} - P\mathbf{e}_i \otimes \mathbf{e}_x \otimes \mathbf{e}_x \otimes \mathbf{e}_i \tag{6}$$

which is independent of the spatial coordinates (the implicit summation convention on repeated indices is used with $i = x, y, z$).

Furthermore, when dealing with 1D models like beams, ad hoc assumptions are usually added in order to enforce some specific stress state in the body. Namely, the transverse normal material stresses are assumed to be zero: $\Sigma_{yy} = \Sigma_{zz} = 0$. Taking into account these assumptions leads one to replace tensor $\mathbf{D}$ with the reduced tensor $\mathbf{C}$ defined as:

$$C_{ijkl} = D_{ijkl} + \frac{D_{ijyy}\left(D_{yyzz}D_{zzkl} - D_{zzzz}D_{yykl}\right) + D_{ijzz}\left(D_{zzyy}D_{yykl} - D_{yyyy}D_{zzkl}\right)}{D_{yyyy}D_{zzzz} - D_{yyzz}D_{zzyy}}$$
$$(i,j) \neq (y,y),(z,z), \quad (k,l) \neq (y,y),(z,z) \tag{7}$$

It can be readily checked that tensor $\mathbf{C}$ has the major and both minor symmetries. In the sequel, we only need the following reduced moduli (and their equivalents obtained by major or minor symmetries):

$$C_{xxxx} = E, \quad C_{xyxy} = C_{xzxz} = C_{yzyz} = \mu = G \tag{8}$$

Eventually, the bifurcation equation (1) of a single beam writes in the uniaxial stress case:

$$\forall \delta \mathbf{U}, \quad \int_\Omega \nabla^T \delta \mathbf{U} : (\mathbf{C} - P_c \mathbf{e}_i \otimes \mathbf{e}_x \otimes \mathbf{e}_x \otimes \mathbf{e}_i) : \nabla \mathbf{X}\, d\Omega = 0 \tag{9}$$

As far as the composite beam is concerned, one has to consider two similar integrals (like the one in Eq. (9)) in the global bifurcation equation (one for each beam), together with a special term for the contribution of the connectors, which will be formulated in the sequel. Moreover, in order to ensure an homogeneous pre-critical state in the composite beam, we assume that a uniform displacement is applied all over the two different cross-sections of the composite beam at end $x = L$ whereas the axial displacement is prevented at end $x = 0$ (see Fig. 1). The corresponding compressive stresses ($P_m > 0$ for the beam m) are related to the enforced displacement $\lambda > 0$ (which will act as the bifurcation parameter) by the following relation:

$$P_m = \frac{E_m \lambda}{L} \tag{10}$$

Let us now consider the bending problem of the two-layer beam in the xy-plane. The Timoshenko theory is employed, as it includes transverse shear effects which may be non negligible in practice. Dealing with a single beam, the Timoshenko kinematics is defined by two scalar displacement fields $u(x)$ and $v(x)$, respectively the axial and transverse displacements of the centroid axis of the beam, and the cross-section rotation $\theta(x)$, independent of deflection v since the plane sections are supposed to remain plane but not normal to the neutral axis. When the beam buckles from the straight position (the fundamental solution) to a bent shape, the expressions for the bifurcation mode $\mathbf{X}$ and the displacement variation $\delta\mathbf{U}$ are both chosen according to the Timoshenko kinematics:

$$\mathbf{X} = \begin{vmatrix} \mathcal{U} - y\Theta \\ \mathcal{V} \\ 0 \end{vmatrix}, \quad \delta\mathbf{U} = \begin{vmatrix} \delta u - y\delta\theta \\ \delta v \\ 0 \end{vmatrix} \tag{11}$$

The two sub-elements of the composite beam are interconnected in such a way that they present the same deflection (no uplift). Conversely, layers a and b do not have the same longitudinal displacement and rotation. Consequently, the 3D modal displacement field of the whole system involves the five following scalar functions $\mathcal{U}_a(x)$, $\mathcal{U}_b(x)$, $\mathcal{V}(x)$, $\Theta_a(x)$ and $\Theta_b(x)$. The modal interlayer slip $\mathcal{G}$ along the interface can be expressed as follows:

$$\mathcal{G} = \mathcal{U}_a - h_a\Theta_a - \mathcal{U}_b - h_b\Theta_b \tag{12}$$

The global bifurcation equation then writes:

$$\forall \delta\mathbf{U}_a, \delta\mathbf{U}_b, \quad \int_{\Omega_a} \nabla^T \delta\mathbf{U}_a : \mathbf{K}_c^a : \nabla\mathbf{X}_a\, d\Omega + \int_{\Omega_b} \nabla^T \delta\mathbf{U}_b : \mathbf{K}_c^b : \nabla\mathbf{X}_b\, d\Omega + \int_0^L \delta g k_{sc} \mathcal{G}\, dx = 0 \tag{13}$$

that is to say:

$$\begin{aligned}
&\forall \delta u_a, \delta u_b, \delta v, \delta\theta_a, \delta\theta_b, \quad \int_{\Omega_a} \Big[E_a(\mathcal{U}_{a,x} - y_a\Theta_{a,x})(\delta u_{a,x} - y_a\delta\theta_{a,x}) - G_a\mathcal{V}_{,x}\delta\theta_a - G_a\Theta_a\delta v_{,x} + G_a\mathcal{V}_{,x}\delta v_{,x} + G_a\Theta_a\delta\theta_a \\
&- \frac{E_a\lambda_c}{L}(\mathcal{U}_{a,x} - y_a\Theta_{a,x})(\delta u_{a,x} - y_a\delta\theta_{a,x}) - \frac{E_a\lambda_c}{L}\mathcal{V}_{,x}\delta v_{,x} \Big] d\Omega + \int_{\Omega_b} \Big[E_b(\mathcal{U}_{b,x} - y_b\Theta_{b,x})(\delta u_{b,x} - y_b\delta\theta_{b,x}) - G_b\mathcal{V}_{,x}\delta\theta_b - G_b\Theta_b\delta v_{,x} + G_b\mathcal{V}_{,x}\delta v_{,x} \\
&+ G_b\Theta_b\delta\theta_b - \frac{E_b\lambda_c}{L}(\mathcal{U}_{b,x} - y_b\Theta_{b,x})(\delta u_{b,x} - y_b\delta\theta_{b,x}) - \frac{E_b\lambda_c}{L}\mathcal{V}_{,x}\delta v_{,x} \Big] d\Omega + \int_0^L (\delta u_a - h_a\delta\theta_a - \delta u_b - h_b\delta\theta_b) k_{sc}(\mathcal{U}_a - h_a\Theta_a - \mathcal{U}_b - h_b\Theta_b) dx = 0
\end{aligned} \tag{14}$$

where y_m stands for the y-coordinate of a current point relative to the centroid axis of the corresponding beam m.

First, integrating over the cross-sections S_a and S_b, then integrating by parts with respect to x and eliminating negligible higher-order terms (presupposing that $\lambda_c \ll L$) yields five local differential equations for the components $\mathcal{U}_a$, $\mathcal{U}_b$, $\mathcal{V}$, Θ_a and Θ_b of the eigenmode:

$$\begin{aligned}
&E_aA_a\mathcal{U}_{a,xx} - k_{sc}\mathcal{G} = 0 \\
&E_bA_b\mathcal{U}_{b,xx} + k_{sc}\mathcal{G} = 0 \\
&k_aG_aA_a(\Theta_{a,x} - \mathcal{V}_{,xx}) + k_bG_bA_b(\Theta_{b,x} - \mathcal{V}_{,xx}) + (E_aA_a + E_bA_b)\frac{\lambda_c}{L}\mathcal{V}_{,xx} = 0 \\
&E_aI_a\Theta_{a,xx} + k_aG_aA_a(\mathcal{V}_{,x} - \Theta_a) + k_{sc}h_a\mathcal{G} = 0 \\
&E_bI_b\Theta_{b,xx} + k_bG_bA_b(\mathcal{V}_{,x} - \Theta_b) + k_{sc}h_b\mathcal{G} = 0
\end{aligned} \tag{15}$$

where k_a and k_b are introduced as the transverse shear correction factors depending on the cross-sectional shapes of the beams a and b, respectively.

At this stage, one has to specify the boundary conditions in order to solve the previous system. Let us first assume, as an example, that both beams are clamped at end $x = 0$ and guided at end $x = L$ (see Fig. 2(a)). This particular choice of boundary conditions will be retained in the sequel for the numerical validation, as it allows one to keep the same uniform prescribed displacements at both ends of the beams for the buckling mode calculation as in the pre-critical stage, and makes thus the numerical computations easier. The components of the eigenmode must satisfy the

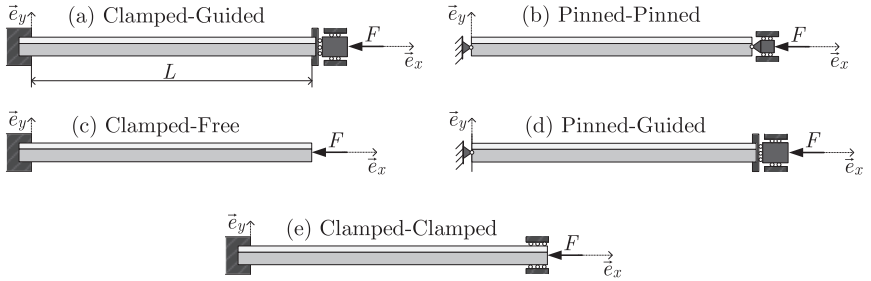

Fig. 2. Boundary conditions.

above-mentioned displacement boundary conditions, that is to say $\mathcal{U}_a(0)=\mathcal{U}_b(0)=\mathcal{V}(0)=\Theta_a(0)=\Theta_b(0)=\Theta_a(L)=\Theta_b(L)=0$.

Taking into account $\delta u_a(0)=\delta u_b(0)=\delta v(0)=\delta\theta_a(0)=\delta\theta_b(0)=\delta\theta_a(L)=\delta\theta_b(L)=0$ in the bifurcation equation (14) leads one, after integration by parts, to the remaining stress boundary conditions at the end $x=L:\mathcal{U}_{a,x}(L)=0,\mathcal{U}_{b,x}(L)=0$ and $k_aG_aA_a(\Theta_a(L)-\mathcal{V}_{,x}(L))+k_bG_bA_b(\Theta_b(L)-\mathcal{V}_{,x}(L))+(E_aA_a+E_bA_b)\frac{\lambda_c}{L}\mathcal{V}_{,x}(L)=0$.

2.3. Solution procedure

The bifurcation mode of a single Timoshenko beam under axial compression with the boundary conditions defined above takes the following form:

$$\begin{cases}\mathcal{U}=0\\ \mathcal{V}=\alpha\left(1-\cos\dfrac{\pi x}{L}\right)\\ \Theta=\beta\sin\dfrac{\pi x}{L}\end{cases}\tag{16}$$

where α and β are constants which are dependent one from the other.

In the case of the composite beam, we assume that the presence of connectors does not affect the transverse displacements and the cross-section rotations, and we denote the following modal components:

$$\begin{cases}\mathcal{V}=\alpha\left(1-\cos\dfrac{\pi x}{L}\right)\\ \Theta_a=\beta_a\sin\dfrac{\pi x}{L}\\ \Theta_b=\beta_b\sin\dfrac{\pi x}{L}\end{cases}\tag{17}$$

which are consistent with the corresponding boundary conditions.

Then, combining the two first local equations with the four corresponding boundary conditions concerning the longitudinal displacements $(\mathcal{U}_a(0)=\mathcal{U}_b(0)=0$ and $\mathcal{U}_{a,x}(L)=\mathcal{U}_{b,x}(L)=0)$ leads to the simple relationship:

$$\mathcal{U}_a=-\frac{E_bA_b}{E_aA_a}\mathcal{U}_b\tag{18}$$

Using Eqs. (17) and (18), the first differential equation in (15) can be solved for the function $\mathcal{U}_b$. Accounting for the associated boundary conditions, it gives rise to the solution:

$$\mathcal{U}_b=-\frac{h_a\beta_a+h_b\beta_b}{1+\dfrac{E_bA_b}{E_aA_a}+\dfrac{\pi^2E_bA_b}{k_{sc}L^2}}\sin\frac{\pi x}{L}\tag{19}$$

By the way, one can notice that the axial components of the buckling mode are not zero, contrary to the case of a single Timoshenko beam.

All the modal fields depend only on the three constants α, β_a and β_b. The last three equations in (15) write finally:

$$\begin{aligned}&\pi^2[(E_aA_a+E_bA_b)\lambda_c-(k_aG_aA_a+k_bG_bA_b)L]\alpha+\pi k_aG_aA_aL^2\beta_a\\&\quad+\pi k_bG_bA_bL^2\beta_b=0\\&\pi k_aG_aA_aL\xi\alpha-\left[(\pi^2E_aI_a+k_aG_aA_aL^2)\xi+\pi^2E_aA_aE_bA_bk_{sc}L^2h_a^2\right]\beta_a\\&\quad-\pi^2E_aA_aE_bA_bk_{sc}L^2h_ah_b\beta_b=0\\&\pi k_bG_bA_bL\xi\alpha-\pi^2E_aA_aE_bA_bk_{sc}L^2h_ah_b\beta_a\\&\quad-\left[(\pi^2E_bI_b+k_bG_bA_bL^2)\xi+\pi^2E_aA_aE_bA_bk_{sc}L^2h_b^2\right]\beta_b=0\end{aligned}\tag{20}$$

with $\xi=(E_aA_a+E_bA_b)k_{sc}L^2+\pi^2E_aA_aE_bA_b$.

One obtains the critical displacement by setting the determinant of the linear equation system (20) to zero:

$$\lambda_c=\frac{L}{\overline{EA}}\frac{\dfrac{\pi^2\overline{EI}_\infty}{L^2}\left(\dfrac{\pi^2\widetilde{EI}^2\overline{GA}}{L^2\overline{EI}_\infty\widetilde{GA}^2}+\dfrac{\overline{EI}}{\overline{EI}_\infty}+\dfrac{k_{sc}\widetilde{EI}^2\widehat{EI}_\infty\overline{GA}}{\widehat{EA}\widehat{EI}\overline{EI}_\infty\widetilde{GA}^2}+\dfrac{k_{sc}L^2}{\pi^2\widehat{EA}}\right)}{\dfrac{\pi^4\widetilde{EI}^2}{2L^4\widetilde{GA}^2}\left(1+\dfrac{k_{sc}L^2\widehat{EI}_\infty}{\pi^2\widehat{EA}\widehat{EI}}\right)+\left(1+\dfrac{\pi^2}{L^2}\overline{\left(\dfrac{EI}{GA}\right)}\right)\left(1+\dfrac{k_{sc}L^2}{\pi^2\widehat{EA}}\right)+\dfrac{k_{sc}\bar{h}^2}{\widehat{GA}}}\tag{21}$$

with:

$$\begin{aligned}&\bar{h}=h_a+h_b,\quad\overline{EA}=E_aA_a+E_bA_b,\quad\widehat{EA}=\frac{E_aA_aE_bA_b}{E_aA_a+E_bA_b}\\&\overline{EI}=E_aI_a+E_bI_b,\quad\overline{EI}_\infty=\overline{EI}+\bar{h}^2\widehat{EA},\quad\widetilde{EI}=\sqrt{E_aI_aE_bI_b}\\&\overline{GA}=k_aG_aA_a+k_bG_bA_b,\quad\widetilde{GA}=\sqrt{k_aG_aA_ak_bG_bA_b}\\&\widehat{EI}=\bar{h}^2\left(\frac{h_a^2}{E_aI_a}+\frac{h_b^2}{E_bI_b}\right)^{-1},\quad\widehat{GA}=\bar{h}^2\left(\frac{h_a^2}{k_aG_aA_a}+\frac{h_b^2}{k_bG_bA_b}\right)^{-1}\\&\widehat{EI}_\infty=\widehat{EI}+\bar{h}^2\widehat{EA},\quad\overline{\left(\frac{EI}{GA}\right)}=\frac{E_aI_a}{k_aG_aA_a}+\frac{E_bI_b}{k_bG_bA_b}\end{aligned}\tag{22}$$

Then, the buckling load can be written as follows:

$$F_c=\frac{\overline{EA}}{L}\lambda_c=\frac{\dfrac{\pi^2\overline{EI}_\infty}{L^2}\left(\dfrac{\pi^2\widetilde{EI}^2\overline{GA}}{L^2\overline{EI}_\infty\widetilde{GA}^2}+\dfrac{\overline{EI}}{\overline{EI}_\infty}+\dfrac{k_{sc}\widetilde{EI}^2\widehat{EI}_\infty\overline{GA}}{\widehat{EA}\widehat{EI}\overline{EI}_\infty\widetilde{GA}^2}+\dfrac{k_{sc}L^2}{\pi^2\widehat{EA}}\right)}{\dfrac{\pi^4\widetilde{EI}^2}{L^4\widetilde{GA}^2}\left(1+\dfrac{k_{sc}L^2\widehat{EI}_\infty}{\pi^2\widehat{EA}\widehat{EI}}\right)+\left(1+\dfrac{\pi^2}{L^2}\overline{\left(\dfrac{EI}{GA}\right)}\right)\left(1+\dfrac{k_{sc}L^2}{\pi^2\widehat{EA}}\right)+\dfrac{k_{sc}\bar{h}^2}{\widehat{GA}}}\tag{23}$$

Alternatively, focusing on the transverse modal displacement, the five differential equations in (15) may be combined with each other in order to provide one single differential equation involving only the transverse component of the buckling mode $\mathcal{V}$. The procedure is not straightforward, but for clarity purposes, no details are given here (see Nguyen et al. (submitted for publication) for a more detailed explanation of the procedure). Using the previous notations (22), the sought equation takes the following form:

$$\frac{\widetilde{EI}^2}{\widetilde{GA}^2}(F_c-\overline{GA})\mathcal{V}_{,xxxxxxxx}-\left[\frac{k_{sc}\widetilde{EI}^2\widehat{EI}_\infty}{\widehat{EA}\widehat{EI}\widetilde{GA}^2}(F_c-\overline{GA})+\overline{\left(\frac{EI}{GA}\right)}F_c-\overline{EI}\right]\mathcal{V}_{,xxxxxx}$$
$$+\left[\left(1+\frac{k_{sc}\bar{h}^2}{\widehat{GA}}+\frac{k_{sc}}{\widehat{EA}}\overline{\left(\frac{EI}{GA}\right)}\right)F_c-\frac{k_{sc}\overline{EI}_\infty}{\widehat{EA}}\right]\mathcal{V}_{,xxxx}-\frac{k_{sc}}{\widehat{EA}}F_c\mathcal{V}_{,xx}=0 \tag{24}$$

The critical load F_c is then deduced from Eq. (24) either by solving the eighth-order differential equation together with the required boundary conditions, or by simply introducing the modal shape $\mathcal{V}(x)$ (once it has been proved to be the same as in the case of a single beam) and solving a linear equation. For instance, one can readily check that the critical load (23) derived for clamped–guided boundary conditions also stands for pinned–pinned (simply-supported) boundary conditions because both cases correspond to the same wavelength $2L$ of the buckling mode (see Fig. 2(b)). In the same way, another critical load is obtained for clamped–free (cantilever) and pinned–guided boundary conditions where the wavelength of the buckling mode is equal to $4L$ (see Fig. 2(c) and (d)):

$$F_c=\frac{\dfrac{\pi^2\overline{EI}_\infty}{L^2}\left(\dfrac{\pi^2\widetilde{EI}^2\overline{GA}}{16L^2\overline{EI}_\infty\widetilde{GA}^2}+\dfrac{\overline{EI}}{4\overline{EI}_\infty}+\dfrac{k_{sc}\widetilde{EI}^2\widehat{EI}_\infty\overline{GA}}{4\widehat{EA}\widehat{EI}\overline{EI}_\infty\widetilde{GA}^2}+\dfrac{k_{sc}L^2}{\pi^2\widehat{EA}}\right)}{\dfrac{\pi^4\widetilde{EI}^2}{16L^4\widetilde{GA}^2}\left(1+\dfrac{4k_{sc}L^2\widehat{EI}_\infty}{\pi^2\widehat{EA}\widehat{EI}}\right)+\left(1+\dfrac{\pi^2}{4L^2}\overline{\left(\dfrac{EI}{GA}\right)}\right)\left(1+\dfrac{4k_{sc}L^2}{\pi^2\widehat{EA}}\right)+\dfrac{k_{sc}\bar{h}^2}{\widehat{GA}}} \tag{25}$$

Finally, the clamped–clamped boundary conditions (giving rise to a wavelength of L) provide another critical load (see Fig. 2(e)):

$$F_c=\frac{\dfrac{\pi^2\overline{EI}_\infty}{L^2}\left(\dfrac{16\pi^2\widetilde{EI}^2\overline{GA}}{L^2\overline{EI}_\infty\widetilde{GA}^2}+\dfrac{4\overline{EI}}{\overline{EI}_\infty}+\dfrac{4k_{sc}\widetilde{EI}^2\widehat{EI}_\infty\overline{GA}}{\widehat{EA}\widehat{EI}\overline{EI}_\infty\widetilde{GA}^2}+\dfrac{k_{sc}L^2}{\pi^2\widehat{EA}}\right)}{\dfrac{16\pi^4\widetilde{EI}^2}{L^4\widetilde{GA}^2}\left(1+\dfrac{k_{sc}L^2\widehat{EI}_\infty}{4\pi^2\widehat{EA}\widehat{EI}}\right)+\left(1+\dfrac{4\pi^2}{L^2}\overline{\left(\dfrac{EI}{GA}\right)}\right)\left(1+\dfrac{k_{sc}L^2}{4\pi^2\widehat{EA}}\right)+\dfrac{k_{sc}\bar{h}^2}{\widehat{GA}}} \tag{26}$$

Eqs. (23), (25) and (26) can be reformulated in a unified way, using the following general expression:

$$F_c=\frac{\dfrac{\pi^2\overline{EI}_\infty}{\rho^2L^2}\left(\dfrac{16\pi^2\widetilde{EI}^2\overline{GA}}{\rho^2L^2\overline{EI}_\infty\widetilde{GA}^2}+\dfrac{4\overline{EI}}{\overline{EI}_\infty}+\dfrac{4k_{sc}\widetilde{EI}^2\widehat{EI}_\infty\overline{GA}}{\widehat{EA}\widehat{EI}\overline{EI}_\infty\widetilde{GA}^2}+\dfrac{k_{sc}\rho^2L^2}{\pi^2\widehat{EA}}\right)}{\dfrac{16\pi^4\widetilde{EI}^2}{\rho^4L^4\widetilde{GA}^2}\left(1+\dfrac{k_{sc}\rho^2L^2\widehat{EI}_\infty}{4\pi^2\widehat{EA}\widehat{EI}}\right)+\left(1+\dfrac{4\pi^2}{\rho^2L^2}\overline{\left(\dfrac{EI}{GA}\right)}\right)\left(1+\dfrac{k_{sc}\rho^2L^2}{4\pi^2\widehat{EA}}\right)+\dfrac{k_{sc}\bar{h}^2}{\widehat{GA}}} \tag{27}$$

In the general formula (27), the so-called effective length factor ρ has been introduced. It may be defined as the ratio between the buckling mode wavelength and the true length of the beam. One has thus to take $\rho = 1,2,4$ to find again the expressions (26), (23), (25), respectively.

3. Validation and applications

3.1. Special cases

3.1.1. Euler–Bernoulli assumption

From the general solution (27) for the critical loads, one can deduce simplified expressions by taking the limit $k_mG_mA_m \to \infty$ for $m = a$ and/or b, considering that the corresponding beam(s) obey(s) the Euler–Bernoulli kinematic theory. In the most simple case where transverse shear effects are neglected in both layers, the critical forces take the following form:

$$F_c^{EB}=\frac{4\pi^2\left(4\pi^2\widehat{EA}\overline{EI}+k_{sc}\rho^2L^2\overline{EI}_\infty\right)}{\rho^2L^2\left(4\pi^2\widehat{EA}+k_{sc}\rho^2L^2\right)} \tag{28}$$

Eq. (28) is consistent with the solution obtained by Xu and Wu (2007), among others, for simply-supported boundary conditions ($\rho = 2$) with the same hypotheses.

3.1.2. Timoshenko assumption with one rotation field

As previously mentioned, Xu and Wu (2007) also derived an intermediate formula for the buckling load of such a composite beam, taking into account the transverse shear effects with the Timoshenko theory, but considering only one rotation field for both layers, thus simplifying the kinematics in comparison with our own solution. The two Timoshenko models will be compared to each other by means of numerical applications in the next subsection. As far as analytical closed-form expressions are concerned, one can check that the two solutions are identical in the particular case where the two beams are alike in all respects, from both the geometric and material points of view, as the two rotation fields are then similar, due to symmetry conditions. The corresponding buckling loads write:

$$F_c^{sym}=\frac{8\pi^2kGAE\left(2\pi^2EAI+k_{sc}\rho^2L^2(I+Ah^2)\right)}{8\pi^4E^2AI+2\pi^2\rho^2L^2kGA^2E+4\pi^2k_{sc}\rho^2L^2E(I+Ah^2)+k_{sc}\rho^4L^4kGA} \tag{29}$$

using the same notations as before, without subscripts as the beams are identical.

3.1.3. Limiting cases of the interface connection

In this paragraph, the buckling loads of the composite beam are derived for the two limiting cases of the interface connection, namely the case of a perfect bond and the case of no bond.

The case of a loose connection corresponds to a null shear bond stiffness ($k_{sc} = 0$), and thus the critical loads write:

$$F_c^{nb}=\frac{4\pi^2\left(4\pi^2\widetilde{EI}^2\overline{GA}+\rho^2L^2\overline{EI}\widetilde{GA}^2\right)}{16\pi^4\widetilde{EI}^2+4\pi^2\rho^2L^2\widetilde{GA}^2\overline{\left(\frac{EI}{GA}\right)}+\rho^4L^4\widetilde{GA}^2}$$
$$=\frac{4\pi^2E_aI_a}{\rho^2L^2\left(1+\dfrac{4\pi^2E_aI_a}{k_aG_aA_a\rho^2L^2}\right)}+\frac{4\pi^2E_bI_b}{\rho^2L^2\left(1+\dfrac{4\pi^2E_bI_b}{k_bG_bA_b\rho^2L^2}\right)} \tag{30}$$

They are proved to be the sum of the buckling loads of each Timoshenko beam considered separately, with the same boundary conditions.

The opposite case of a rigid connection corresponds to an infinite value of the shear bond stiffness: $k_{sc} \to \infty$. From Eq. (27), the following simplified expression is then obtained:

$$F_c^{pb}=\frac{4\pi^2\widehat{GA}\left(4\pi^2\widetilde{EI}^2\widehat{EI}_\infty\overline{GA}+\rho^2L^2\widehat{EI}\overline{EI}_\infty\widetilde{GA}^2\right)}{16\pi^4\widetilde{EI}^2\widehat{EI}_\infty\widehat{GA}+4\pi^2\rho^2L^2\widehat{EI}\widetilde{GA}^2\left(\widehat{GA}\overline{\left(\frac{EI}{GA}\right)}+\bar{h}^2\widehat{EA}\right)+\rho^4L^4\widehat{EI}\widehat{GA}\widetilde{GA}^2} \tag{31}$$

Due to the kinematic hypotheses, the composite beam displays two cross-section rotation fields, which generally differ from each other, even in the case of a full interaction. It can therefore not identify with a single Timoshenko beam, except in the particular case of two identical beams where the buckling loads of the composite beam are the ones of a Timoshenko beam:

Table 1
Geometry and material parameters for the numerical validation.

Beam	Length (m)	Width (mm)	Height (mm)	Young's modulus (MPa)	Poisson's ratio
(*a*)	1	100	20	200,000	0.3
(*b*)	1	100	200	5000	0.3

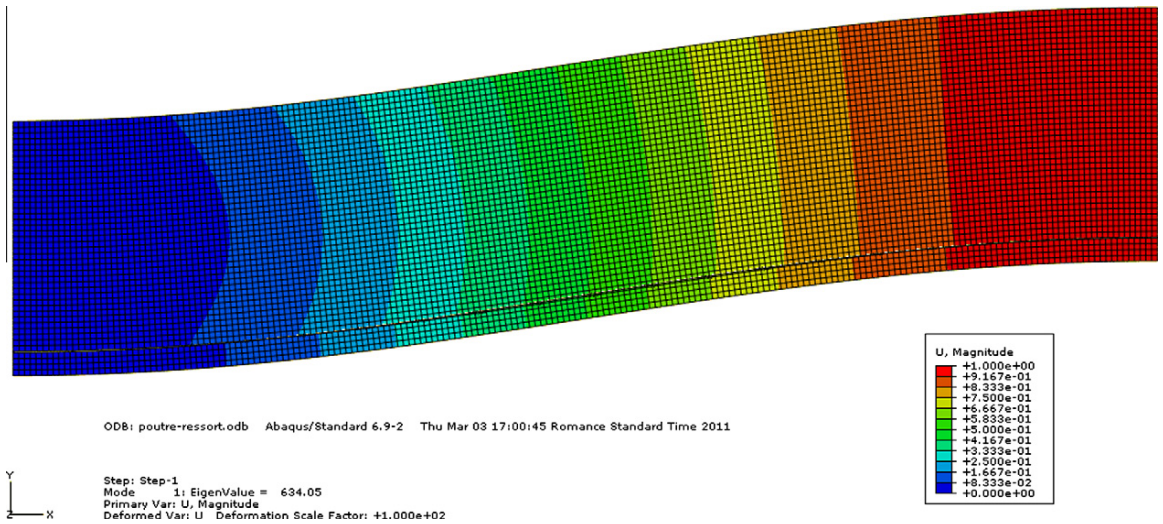

Fig. 3. Buckling mode shape of the two-layer beam with no bond.

$$F_c^{pb\text{-}sym} = \frac{4\pi^2 (EI)_{eq}}{\rho^2 L^2 \left(1 + \dfrac{4\pi^2 (EI)_{eq}}{(kGA)_{eq} \rho^2 L^2}\right)} \tag{32}$$

where $(EI)_{eq}$ and $(kGA)_{eq}$ represent the effective flexural and transverse shear stiffnesses of the composite beam, respectively, in the special case of two identical beams without interlayer slip. Due to the rigid connection, the effective flexural stiffness takes the general well-known value $\overline{EI}_\infty$, and thus $(EI)_{eq} = 2EI + 2EAh^2$. In the perfect bond case, an effective transverse shear stiffness can be defined as the sum of the transverse shear stiffnesses of each separate beam ($\overline{GA}$), as long as shear strains are the same in the two beams. For two identical beams, the equivalent transverse shear stiffness is thus $(kGA)_{eq} = 2kGA$.

3.2. Numerical validation

In order to validate the analytical expression (23) for the buckling load of the composite beam with interlayer slip, finite element computations have been performed. A linearized stability analysis is achieved using Abaqus software, and a 2D plane stress model is retained for the sake of simplicity, considering the particular case of rectangular cross-sections without any loss of generality. 2D eight-node rectangular elements are chosen, involving quadratic shape functions with reduced integration. The displacements in both directions are prevented at the left end of the beams ($x = 0$), what corresponds to the clamped condition for the beam model. On the right-hand side ($x = L$), only the longitudinal displacements (along $\mathbf{e}_x$) are uniformly prescribed in order to yield homogeneous compressive stresses in each beam at the pre-critical stage and let the beams buckle with transverse displacements at this end. The geometry and material parameters are summarized in Table 1. The cross-section areas A_m and second moments of area I_m are simply deduced from the width and height $2h_m$ of the beams. The shear moduli G_m are also calculated using Young's moduli E_m and Poisson's ratios ν_m. The shear correction factors k_m both take the classical value 5/6, usually chosen for homogeneous rectangular sections. At last, the interface shear bond stiffness varies from 0 (no bond) to 10,000 MPa which practically corresponds to the case of a rigid connection. The buckling mode obtained by the 2D finite element computation is depicted in Fig. 3 in the particular case of no bond.

The role of shear flexibility of the two connected members is simultaneously analyzed by comparing the buckling load obtained by the present model to the solution obtained with the Bernoulli hypotheses (neglecting the transverse shear effects) and the one reported in Xu and Wu (2007) with the simplified Timoshenko theory (considering that both layers have the same shear strains). Fig. 4 displays four curves representing the evolution of the buckling load versus the interface shear bond stiffness: the green dotted line[1] stands for the Bernoulli solution; the red dashed line refers to the intermediate solution of Xu and Wu (2007); the solid blue line corresponds to our own analytical results; and the black dots are finite element values.

In the example in hand, the composite beam has a very small length-to-height ratio (for the thickest beam b, $L/2h_b = 5$) so that Bernoulli and Timoshenko solutions naturally differ from each other. The relative difference between the buckling loads deriving from the two theories is about 10% in the case of no bond ($k_{sc} = 0$) and grows up to more than 30% when the interface shear bond stiffness tends to infinity (all the curves tend to asymptotic values corresponding to the full interaction case as the interface shear bond stiffness increases). Let us note in passing that the shear flexibility plays a more important role when the interaction is stronger, as expected. In the particular case of a full interaction, the composite beam can be considered as a single beam of height $2(h_a + h_b)$ and the influence of shear deformations is maximum. The results obtained in Xu and Wu (2007) lie between the Bernoulli and Timoshenko solutions. It has been already mentioned that these results perfectly coincide with ours as soon as the two beams are identical. In the example considered, the two beams have voluntarily been provided with different Young's moduli and heights in order to see the possible deviation between the two kinematic assumptions. As a consequence, the solutions with the simplified kinematics are about 20% higher than the ones obtained with the general hypotheses. Above all, the numerical results turn out to be very close to our analytical predictions (with a maximum relative error of 6.5%). The proposed model is thus proved to be in much better agreement with numerical calculations than the other analytical solutions previously issued in the literature, even for drastically dissimilar beams.

[1] For interpretation of color in Figs. 4 and 5, the reader is referred to the web version of this article.

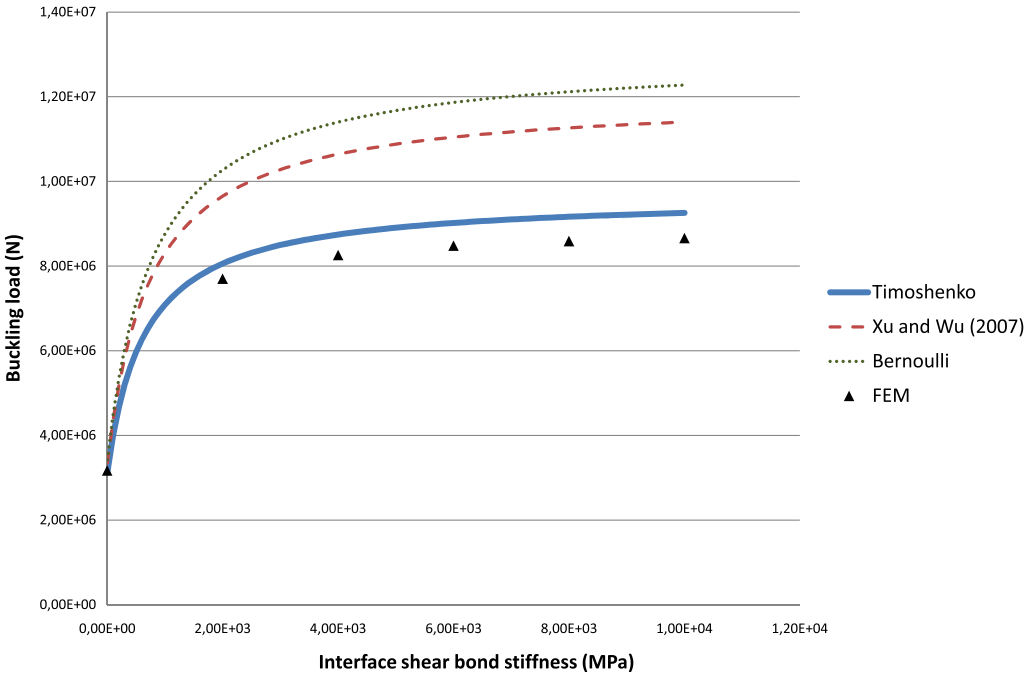

Fig. 4. Comparison between numerical and analytical critical loads (with different kinematic hypotheses) for various interface shear bond stiffnesses.

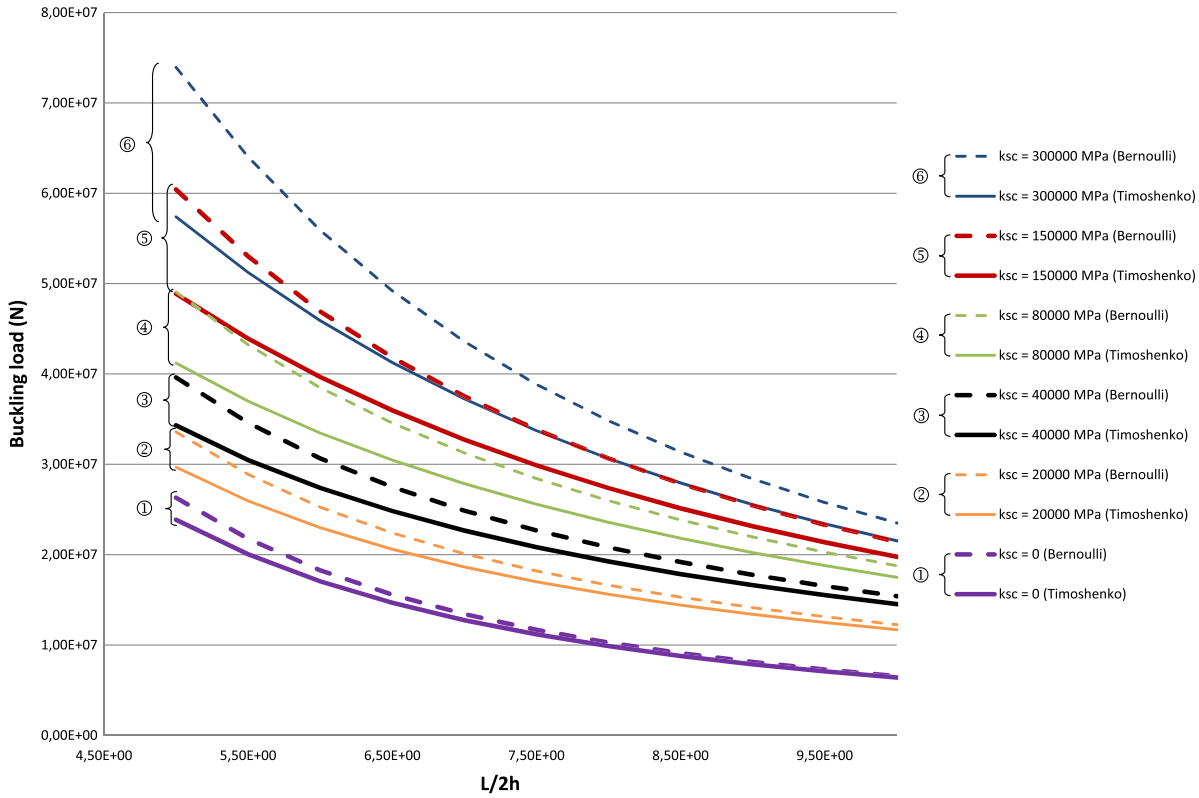

Fig. 5. Influence of the shear flexibility on the buckling load in relation to the length-to-height ratio for different interface shear bond stiffnesses.

3.3. Parametric study

A parametric analysis is finally performed by depicting the influence of the length-to-height ratio on the buckling loads for several interface shear bond stiffnesses with the same boundary conditions as in the previous subsection (only the present model and the Bernoulli solution are plotted here in order to evaluate the transverse shear effects). For simplicity purposes, the two

beams are identical here and the same parameters as for the beam *a* in the previous numerical validation are assigned to both beams (see Table 1). Fig. 5 shows the buckling loads versus the length-to-height ratio $L/2h$ where h represents the half-height of any of the beams indifferently.

It clearly appears that for large values of the length-to-height ratio (say $L/2h > 10$), the results hardly depend on the kinematic theory. The Bernoulli and Timoshenko solutions do not differ from more than 9%, even in the case of an almost full interaction. Conversely, for the smallest value considered $L/2h = 5$, the shear flexibility strongly affects the buckling behavior, especially when k_{sc} is maximum, as observed in Fig. 4. In this particular case, the maximum discrepancy between the two theories reaches again the relative value of 30% approximately. To illustrate the idea, let us remark that the red dashed line ($k_{sc} = 150{,}000$ MPa with the Bernoulli assumption) nearly coincides with the solid blue line ($k_{sc} = 300{,}000$ MPa with the Timoshenko assumption).

4. Conclusions

In this paper, original closed-form expressions of the elastic buckling loads of a two-layer shear-deformable beam with interlayer slip under axial compression have been derived for various boundary conditions, assuming that both beams verify the Timoshenko hypotheses. The analytical solutions arise from a 3D linearized bifurcation analysis of the composite beam under a uniaxial stress state. The critical loads are consistent with the ones previously obtained by other authors with the more classical Bernoulli theory, as long as transverse shear stiffnesses approach infinity. The general expressions for any interface shear bond stiffness also allow one to recover some well-known buckling loads in the particular cases of no bond and full interaction.

The validity of the proposed formulae has been assessed thanks to finite element computations (using 2D eight-node rectangular elements). It has been shown that our own results are in much better agreement with the numerical values than the solutions obtained with simplified kinematic assumptions. In particular, in the framework of the Timoshenko theory, the importance of considering two independent rotation fields for the cross-sections of the two beams (as if to distinguish the shear strains of the two beams) has been emphasized in the case of two distinct beams.

Finally, the combined influence of shear flexibility and partial interaction on the overall behavior of such a composite beam has been investigated. A parametric analysis, based on various values of the length-to-height ratio and of the interface shear bond stiffness, has been performed. It has been found that the effect of shear deformations on the buckling load is generally more important for composite beams characterized by a substantial shear interaction.

References

Battini, J.M., Nguyen, Q.H., Hjiaj, M., 2009. Non-linear finite element analysis of composite beams with interlayer slips. Computers & Structures 87 (13–14), 904–912.

Čas, B., Saje, M., Planinc, I., 2007. Buckling of layered wood columns. Advances in Engineering Software 38 (8–9), 586–597.

Dezi, L., Gara, F., Leoni, G., 2007. A shear deformable steel-concrete composite beam model. In: 6th International Conference on Steel and Aluminium Structures Oxford, UK, July 24–27, 2007.

Faella, C., Martinelli, E., Nigro, E., 2002. Steel and concrete composite beams with flexible shear connection: "exact" analytical expression of the stiffness matrix and applications. Computers & Structures 80 (11), 1001–1009.

Gattesco, N., 1999. Analytical modeling of nonlinear behavior of composite beams with deformable connection. Journal of Constructional Steel Research 52 (2), 195–218.

Girhammar, U.A., Gopu, V.K.A., 1993. Composite beam-columns with interlayer slip – exact analysis. ASCE Journal of Structural Engineering 119 (4), 1265–1282.

Girhammar, U.A., Pan, D.H., 2007. Exact static analysis of partially composite beams and beam-columns. International Journal of Mechanical Sciences 49 (2), 239–255.

Heinisuo, M., 1988. An exact finite element technique for layered beams. Computers & Structures 30 (3), 615–622.

Kryžanowski, A., Schnabl, S., Turk, G., Planinc, I., 2009. Exact slip-buckling analysis of two-layer composite columns. International Journal of Solids and Structures 46 (14–15), 2929–2938.

Le Grognec, P., Le van, A., 2009. Some new analytical results for plastic buckling and initial post-buckling of plates and cylinders under uniform compression. Thin-Walled Structures 47 (8–9), 879–889.

Le Grognec, P., Le van, A., 2011. On the plastic bifurcation and post-bifurcation of axially compressed beams. International Journal of Non-Linear Mechanics 46 (5), 693–702.

Murakami, H., 1984. A laminated beam theory with interlayer slip. ASME Journal of Applied Mechanics 51, 551–559.

Newmark, N.M., Siess, C.P., Viest, I.M., 1951. Tests and analysis of composite beams with incomplete interaction. Proceedings of the Society of Experimental Stress Analysis 9 (1), 75–92.

Nguyen, Q.H., Hjiaj, M., Uy, B., Guezouli, S., 2009. Analysis of composite beams in the hogging moment regions using a mixed finite element formulation. Journal of Constructional Steel Research 65 (3), 737–748.

Nguyen, Q.H., Hjiaj, M., Aribert, J.M., 2010a. A space-exact beam element for time-dependent analysis of composite members with discrete shear connection. Journal of Constructional Steel Research 66 (11), 1330–1338.

Nguyen, Q.H., Hjiaj, M., Uy, B., 2010b. Time-dependent analysis of composite beams with continuous shear connection based on a space-exact stiffness matrix. Engineering Structures 32 (9), 2902–2911.

Nguyen, Q.H., Martinelli, E., Hjiaj, M., 2011. Derivation of the exact stiffness matrix for a two-layer Timoshenko beam element with partial interaction. Engineering Structures 33 (2), 298–307.

Nguyen, Q.H., Hjiaj, M., Le Grognec, P., submitted for publication. Analytical approach for free vibration analysis of two-layer Timoshenko beams with interlayer slip. Journal of Sound and Vibration.

Ranzi, G., Bradford, M.A., Uy, B., 2004. A direct stiffness analysis of a composite beam with partial interaction. International Journal for Numerical Methods in Engineering 61 (5), 657–672.

Ranzi, G., Zona, A., 2007. A steel-concrete composite beam model with partial interaction including the shear deformability of the steel component. Engineering Structures 29 (11), 3026–3041.

Salari, M.R., Spacone, E., 2001a. Finite element formulations of one-dimensional elements with bond-slip. Engineering Structures 23 (7), 815–826.

Salari, M.R., Spacone, E., 2001b. Analysis of steel-concrete composite frames with bond-slip. ASCE Journal of Structural Engineering 127 (11), 1243–1250.

Schnabl, S., Saje, M., Turk, G., Planinc, I., 2007. Analytical solution of two-layer beam taking into account interlayer slip and shear deformation. ASCE Journal of Structural Engineering 133 (6), 886–894.

Schnabl, S., Planinc, I., 2010. The influence of boundary conditions and axial deformability on buckling behavior of two-layer composite columns with interlayer slip. Engineering Structures 32 (10), 3103–3111.

Schnabl, S., Planinc, I., 2011. The effect of transverse shear deformation on the buckling of two-layer composite columns with interlayer slip. International Journal of Non-Linear Mechanics 46 (3), 543–553.

Wu, Y.F., Oehlers, D.J., Griffith, M.C., 2002. Partial interaction analysis of composite beam/column members. Mechanics of Structures and Machines 30 (3), 309–332.

Xu, R., Wu, Y., 2007. Static, dynamic, and buckling analysis of partial interaction composite members using Timoshenko's beam theory. International Journal of Mechanical Sciences 49 (10), 1139–1155.

ANNEXE 8

P. Le Grognec, **Q-H. Nguyen** and M. Hjiaj. Plastic bifurcation analysis of a two-layer shear-deformable beam-column with partial interaction. *International Journal of Non-Linear Mechanics* 2014 ; 67 : 85-94. (5-Year IF 1.870) http://dx.doi.org/10.1016/j.ijnonlinmec.2014.08.010.

International Journal of Non-Linear Mechanics 67 (2014) 85–94

Contents lists available at ScienceDirect

International Journal of Non-Linear Mechanics

journal homepage: www.elsevier.com/locate/nlm

Plastic bifurcation analysis of a two-layer shear-deformable beam–column with partial interaction

Philippe Le Grognec [a,*], Quang-Huy Nguyen [b], Mohammed Hjiaj [b]

[a] Mines Douai, Polymers and Composites Technology & Mechanical Engineering Department, 941 rue Charles Bourseul, CS 10838, F-59508 Douai Cedex, France

[b] Structural Engineering Research Group - LGCGM, Université Européenne de Bretagne – INSA de Rennes, 20 avenue des Buttes de Coësmes, CS 70839, F-35708 Rennes Cedex 7, France

ARTICLE INFO

Article history:
Received 26 February 2014
Received in revised form
3 July 2014
Accepted 16 August 2014
Available online 26 August 2014

Keywords:
Plastic buckling
Two-layer beam–column
Partial interaction
Transverse shear
Closed-form expressions
Finite element validation

ABSTRACT

This paper deals with the plastic buckling behavior of two-layer shear-deformable beam–columns with partial interaction. The Timoshenko kinematic hypotheses are considered for both layers and the shear connection (no uplift is permitted) is represented by a continuous relationship between the interface shear flow and the corresponding slip. A set of differential equations is obtained from a general 3D plastic bifurcation analysis, using the above assumptions. Original closed-form expressions of the buckling loads and the corresponding modes of the composite beams under axial compression are derived for various boundary conditions, considering that both layers (or possibly only one) behave plastically at the critical point. The particular case of Euler–Bernoulli beams can be deduced from these general expressions by neglecting the influence of shear deformability. The proposed analytical solutions are favorably compared against the predictions of a FE model based on a co-rotational two-layer beam formulation which accounts for interlayer slip and inelasticity. Parametric analyses are performed and the effect of the elastoplastic moduli is particularly emphasized.

1. Introduction

Composite beams are widely used in civil engineering. Such structures involve two layers composed of different materials, like steel and concrete, in order to optimize the global mechanical behavior. Due to the technical solutions employed to assemble the two layers, relative displacements generally occur at the interface resulting in the so-called partial interaction. Whereas the transverse separation is often small in practice and can thus be neglected, the interface slip may often influence the behavior of the composite beams insomuch it must be considered for a more reliable modeling analysis.

For about 60 years, numerous analytical and numerical models characterized by different levels of approximation have been proposed in the literature. The first formulation of an elastic theory for composite beams with partial interaction is commonly attributed to Newmark et al. [1]. They adopted the Euler–Bernoulli kinematic assumptions for both layers and considered a continuous and linear relationship between the relative interface displacements (slips) and the corresponding interface shear stresses. This formulation is usually referred to as Newmark's model, and was extensively used from that time by many authors to formulate theoretical models for the static and/or dynamic response of elastic composite beams [2–7]. Most of these papers are concerned with finite element formulations based on the exact stiffness/flexibility matrix. The use of exact stiffness matrix was extended to time-dependent analysis of continuous composite beams in an approximate way using the age-adjusted modulus and the mean stress method [8] but also in a more general fashion by constructing a space-exact but time-discretized stiffness matrix [9,10]. Significant advances in the theory of two-layer beams in partial interaction have been achieved through introducing the shear flexibility of both layers according to the well-known Timoshenko theory. Xu and Wu [11] proposed an analytical model considering the Timoshenko kinematic assumption for each component, but they imposed equal cross-section rotation for both components. The governing equations for shear-deformable two-layer beams have been derived by Schnabl et al. [12] assuming independent shear strains and cross-section rotations for each layer. Nguyen et al. [13] derived the exact stiffness matrix of a two-layer shear-deformable beam element, using kinematic assumptions similar to the analytical work reported in Schnabl et al. [12]. Analytical

* Corresponding author.
E-mail address: philippe.le.grognec@mines-douai.fr (P. Le Grognec).

http://dx.doi.org/10.1016/j.ijnonlinmec.2014.08.010
0020-7462/

solutions for the free vibration behavior of two-layer Timoshenko beams with interlayer slip have been derived by Nguyen et al. [14].

The aforementioned theoretical models have been the driving force behind the development of various advanced formulations such as force-based and mixed FE formulations which have been used to investigate the inelastic behavior of shear-rigid composite beams as well as fully or partly shear-flexible composite beams (see [15–22], among others). For geometrically non-linear problems, most contributions consider composite beams made of two Euler–Bernoulli layers and both total Lagrangian and co-rotational beam/column elements have been developed [23–25]. In Čas et al. [26], a large displacement total Lagrangian formulation for composite beams in partial interaction was developed (see also [27]). Each layer was considered separately and internal constraints were applied, using Lagrange multipliers, so as to enforce contact between the layers. Large displacement analysis of elastic shear-deformable two-layer beams has been addressed in Hjiaj et al. [28] using the co-rotational framework and the exact local stiffness matrix to prevent shear and curvature locking.

The non-linear buckling of two-layer beam–columns with interlayer slip has been less studied. Linearized buckling loads have been computed by Girhammar and Gopu [3] using a modified second-order theory for two-layer beams with longitudinal slips. Exact expressions for buckling length coefficients of elastic composite beams with particular boundary conditions have been derived by Girhammar and Pan [4]. The total Lagrangian formulation for shear-rigid composite beams in partial interaction proposed by Čas et al. [26] was employed to perform the bucking analysis of layered wood columns (see [29]). A general analytical study of the buckling behavior of two-layer beams with interlayer slip was recently performed [30–32]. The authors first considered the case of Euler–Bernoulli beams and conducted a detailed parametric analysis [30,31]. As expected, it was observed a strong influence of the boundary conditions on the critical loads and the corresponding buckling modes, whereas the pre-critical shortening (axial deformations) could be neglected in the analysis. In Schnabl and Planinc [32], the previous theoretical analysis was generalized to the case of Timoshenko beams, including the transverse shear effects in the model. The governing equations of the problem were provided but only a solution strategy of these equations was outlined and no closed-form expressions were reported. Xu and Wu [11] also proposed an analytical model considering the Timoshenko kinematic assumption for each component and derived explicit solutions for the buckling loads of partial interaction composite members in the particular case of simply-supported end conditions. However, they have imposed an equal cross-section rotation for both components. Le Grognec et al. [33] provided closed-form analytical solutions for the buckling behavior of two-layer shear-deformable beams with various boundary conditions, considering two independent shear strains in both layers, as was the case in Schnabl and Planinc [32]. At last, the numerical model developed by Battini et al. [34] and Hjiaj et al. [28] was employed to investigate the non-linear buckling of composite beams, using bisection methods along the fundamental path to detect the singularity of the tangent stiffness matrix in an incremental way.

To the authors' best of knowledge, the buckling analysis of inelastic shear-deformable composite beams with partial interaction was not addressed. The pioneering works on the plastic buckling of a regular beam under axial compression were conducted by Considère [35] and Engesser at the end of the nineteenth century, and later by von Karman. Yet, the early results before the 1940s were not quite correct or properly justified. The first significant result is due to Shanley [36], who provided a rational explanation for the plastic buckling of the so-called Shanley's column, which had been introduced by von Karman in elasticity. This discrete model (a rigid rod supported by two elastoplastic springs) is supposedly able to reproduce the behavior of a beam cross-section and it led to results which are qualitatively similar to those of a continuum structure under plastic buckling. Shanley thus showed that, in plasticity, the first bifurcation occurs at the tangent modulus critical load, giving rise to an incipient unloaded zone and an increasing load during the initial post-bifurcation. Hill [37] extended these results to a 3D continuum by using the concept of "comparison elastic solid". He examined the uniqueness and stability criteria, and pointed out the difference between bifurcation and stability. The existence of continua of bifurcation points in plastic buckling problems was discovered by Cimetière [38] when dealing with the case of compressed rectangular plates. These continua enable the structure to bifurcate within intervals of critical loads, by continuously modifying the unloaded zone and the structural stiffness. Each continuous range of bifurcation points (one per mode) observed in plasticity spreads from the tangent modulus critical value λ_T to the elastic one λ_E, and contains a particular intermediate value (the reduced modulus critical load λ_R) corresponding to a constant loading bifurcation.

The plastic buckling problem can be formulated using either the J_2 deformation or flow theories. Each theory has its own advantages and drawbacks and may yield different critical values. The deformation theory, although it does not take into account elastic unloading, provides critical loads that compare best with the experiments, whereas the flow theory generally overpredicts the critical values. The discrepancy – known as the plastic buckling paradox – can be accounted for and quantified through an analysis of imperfection sensitivity, as can be found in Durban [39]. Among others, Durban and Zuckerman [40] illustrated this plastic buckling paradox in the case of rectangular plates under biaxial compression/tension. They derived semi-analytical solutions for various boundary conditions and particularly showed the possible discrepancy between the results provided by the J_2 flow and deformation theories. Ore and Durban [41,42] also derived semi-analytical values for the critical loads of elastoplastic annular plates in pure shear and cylinders under axial compression, and showed again the discrepancy between the results provided by the flow and deformation theories of plasticity. Here, we shall adopt the physically more correct flow plasticity theory, keeping in mind that both flow and deformation theories may give rise to nearly similar results in case of beams under axial compression. Our goal is not to compare the merits of the different theories but rather to evaluate the ability of the theoretical tools developed to predict plastic bifurcations of composite beams.

In this paper, a plastic bifurcation analysis of a two-layer beam–column with interlayer slip is thus carried out, following the method already adopted in Le Grognec et al. [33]. In contrast with the elastic case, buckling is supposed here to occur while one (or both) layer(s) deform(s) plastically. Among all the possible critical values in the first continuum of bifurcation points, our attention focuses on the minimum value, namely the tangent modulus critical load. The paper is organized as follows. In Section 2, the bifurcation equation of the problem is given in a 3D context. Next, this equation is linearized and particularized, using the appropriate kinematic assumptions and considering a uniaxial pre-critical stress state with small pre-critical displacements. This approach is a general and efficient way to cope with the elastic/plastic buckling of structures subjected to uniform pre-critical stress/strain states. It was successfully applied to the case of compressed elastic/plastic beams [43], plates and cylinders [44], reinforced sandwiches under through-thickness compression [45] and sandwich beam–columns under longitudinal compression and pure bending [46]. The final set of differential equations is analytically solved as far as the boundary conditions make it possible, giving rise to original closed-form expressions. The general case of two shear-deformable beams with

independent shear strains is first considered and particular expressions are then provided in the case of Euler–Bernoulli beams, thus neglecting the transverse shear effects. In Section 3, a large displacement finite element formulation for inelastic composite beams with partial interaction based on the co-rotational approach is briefly presented. An incremental calculation procedure is developed, allowing for the detection of critical buckling loads in a non-linear context. In Section 4, a few examples are discussed and the analytical and numerical results are compared, for validation purposes. A parametric study is finally achieved so as to show the influence of various material parameters.

2. Critical buckling load of an elastoplastic two-layer shear-deformable beam–column with interlayer slip

2.1. Problem definition

Let us consider a straight elastoplastic composite beam with two sub-elements of possibly different cross-sections and materials. The layers are joined using shear connectors at the interface which are uniformly distributed along the longitudinal direction, as shown in Fig. 1. In the reference configuration, the layer m ($m=a,b$) occupies a cylindrical domain Ω_m of constant cross-section area A_m, second moment of area I_m, height $2h_m$ and length L.

In the linear elastic regime, the material m (of the layer m) is assumed to be isotropic, defined by the fourth-order elasticity tensor $\mathbf{D}^m$ whose components in an orthonormal basis are $D^m_{ijkl}=\Lambda_m\delta_{ij}\delta_{kl}+\mu_m(\delta_{ik}\delta_{jl}+\delta_{il}\delta_{kj})$, where δ_{ij} is the Kronecker symbol, and Λ_m and μ_m are the Lamé constants. Use is also made of Young's modulus E_m, Poisson's ratio ν_m and the shear modulus G_m related to Λ_m and μ_m by the standard relations $\Lambda_m=E_m\nu_m/(1+\nu_m)(1-2\nu_m)$ and $\mu_m=G_m=E_m/2(1+\nu_m)$.

In the plastic regime, we adopt the J_2 flow theory and assume that the plastic threshold of the material m is defined by the von Mises yield function with a linear isotropic hardening:

$$f(\boldsymbol{\Sigma},B)=\sqrt{\tfrac{3}{2}\boldsymbol{\Sigma}^d:\boldsymbol{\Sigma}^d}-\sigma_0^m-B,\quad B=H_m p \tag{1}$$

where $\boldsymbol{\Sigma}$ denotes the second Kirchhoff stress tensor (symmetric), $\boldsymbol{\Sigma}^d$ its deviatoric part, p is the equivalent plastic strain, and σ_0^m and H_m stand for the initial yield stress and the isotropic hardening modulus (constant) of material m, respectively.

The constitutive behavior of the continuous shear connection is characterized by a linear elastic relationship between the interface shear stresses and the corresponding slip. With the loading and boundary conditions applied in the present analysis, a perfectly homogeneous pre-critical strain state is supposed to be achieved in the whole composite beam (with piecewise uniform stresses) and the relative longitudinal displacement between the two layers is then zero at the critical time. As far as buckling is concerned, there is thus no need for a detailed description of the possibly non-linear constitutive law of the shear connection, since only the initial shear bond stiffness is necessary, whose value per unit length is constant and denoted by k_{sc}.

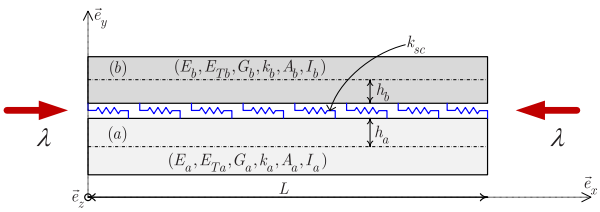

Fig. 1. Two-layer shear-deformable elastoplastic beam–column with shear connectors under axial compression.

The composite beam is subjected to an axial compressive force which leads to buckling. The critical load and the bifurcation mode are derived from a 3D framework: the theory is developed using a total Lagrangian formulation where the beams are seen as 3D bodies.

2.2. Theoretical formulation

Let us first consider a single 3D body and make the two following assumptions concerning plastic bifurcation:

- The whole solid (or possibly just one layer in the present analysis) is assumed to be plastified on the fundamental branch at critical time (the yield stress(es) σ_0 involved in the analysis is (are) assumed to be small enough for the plastic strains to appear before the critical load is reached, in such a way that the buckling phenomenon occurs in the plastic regime).
- At critical time, the plastic zone corresponding to the bifurcated solution is supposed to be equal to that of the fundamental solution (namely to the whole solid or possibly just to one layer in the present analysis), i.e. the bifurcation takes place at the tangent modulus critical load with incipient unloading.

With the above assumptions, the critical load $\lambda_c=\lambda_T$ and the bifurcation mode $\mathbf{X}$ of the 3D body are obtained by solving the following bifurcation equation [47]:

$$\forall\delta\mathbf{U},\quad \int_\Omega \nabla^T\delta\mathbf{U}:\mathbf{K}^p(\lambda_T):\nabla\mathbf{X}\,d\Omega=0 \tag{2}$$

The fourth-order nominal tangent elastoplastic tensor $\mathbf{K}^p$ can be written as follows:

$$\mathbf{K}^p=\frac{\partial\boldsymbol{\Pi}}{\partial\mathbf{F}}=\mathbf{F}\cdot\frac{\partial\boldsymbol{\Sigma}}{\partial\mathbf{E}}\cdot\mathbf{F}^T+(\mathcal{I}\cdot\boldsymbol{\Sigma})^T=\mathbf{F}\cdot\mathbf{D}^p\cdot\mathbf{F}^T+(\mathcal{I}\cdot\boldsymbol{\Sigma})^T \tag{3}$$

In the above equation, $\mathbf{E}$ denotes the Green strain tensor, $\mathbf{F}$ is the deformation gradient and $\boldsymbol{\Pi}=\mathbf{F}\cdot\boldsymbol{\Sigma}$ the first Kirchhoff stress tensor (non-symmetric). $\mathcal{I}$ represents the fourth-order unit tensor ($\mathcal{I}_{ijkl}=\delta_{il}\delta_{kj}$) and the superscript T is the transposition of a second-order tensor and the major transposition of a fourth-order tensor ($(\mathbf{Z}^T)_{ijkl}=Z_{klij}$), respectively. Use is also made of the fourth-order material tangent elastoplastic tensor $\mathbf{D}^p$ which can be defined as follows:

$$\mathbf{D}^p=\frac{\partial\boldsymbol{\Sigma}}{\partial\mathbf{E}}=\mathbf{D}-\frac{\mathbf{D}:\dfrac{\partial f}{\partial\boldsymbol{\Sigma}}\otimes\dfrac{\partial f}{\partial\boldsymbol{\Sigma}}:\mathbf{D}}{H+\dfrac{\partial f}{\partial\boldsymbol{\Sigma}}:\mathbf{D}:\dfrac{\partial f}{\partial\boldsymbol{\Sigma}}} \tag{4}$$

where the tensor product $\otimes$ of two second-order tensors $\mathbf{S}$ and $\mathbf{T}$ is defined by $(\mathbf{S}\otimes\mathbf{T})_{ijkl}=S_{ij}T_{kl}$. Relation (4) can be recast as

$$\mathbf{D}^p=\mathbf{D}-\mathbf{N}\otimes\mathbf{N} \tag{5}$$

where the symmetric tensor $\mathbf{N}$ has the following expression:

$$\mathbf{N}=\frac{\mathbf{D}:\dfrac{\partial f}{\partial\boldsymbol{\Sigma}}}{\sqrt{H+\dfrac{\partial f}{\partial\boldsymbol{\Sigma}}:\mathbf{D}:\dfrac{\partial f}{\partial\boldsymbol{\Sigma}}}} \tag{6}$$

Likewise, Eq. (3) takes the following form:

$$\mathbf{K}^p=\mathbf{K}^e-\mathbf{M}^T\otimes\mathbf{M} \tag{7}$$

where $\mathbf{K}^e$ and $\mathbf{M}$ are tensors defined as

$$\mathbf{K}^e=\mathbf{F}\cdot\mathbf{D}\cdot\mathbf{F}^T+(\mathcal{I}\cdot\boldsymbol{\Sigma})^T,\quad \mathbf{M}=\mathbf{N}\cdot\mathbf{F}^T \tag{8}$$

We shall now derive more explicit expressions of the above tensors by exploiting the uniform uniaxial stress state in the compressed beams at hand. Let the beams be subjected, in the pre-critical state, to a nominal axial compressive stress

$\Pi_{xx} = -P < 0$. Consequently, the components of the first Kirchhoff stress tensor $\mathbf{\Pi}$ relative to the orthonormal basis $(\mathbf{e}_x, \mathbf{e}_y, \mathbf{e}_z)$ can be computed as

$$\mathbf{\Pi} = -P\mathbf{e}_x \otimes \mathbf{e}_x = \begin{bmatrix} -P & 0 & 0 \\ 0 & 0 & 0 \\ 0 & 0 & 0 \end{bmatrix} \quad (P > 0) \tag{9}$$

Let us assume that the pre-critical deformations are small, which is usually satisfied in practice:

$$\| \nabla \mathbf{U} \| \ll 1 \tag{10}$$

Thus, the stress tensor $\mathbf{\Sigma}$ can be approximated by $\mathbf{\Pi}$:

$$\mathbf{\Sigma} = \mathbf{F}^{-1} \cdot \mathbf{\Pi} \approx \mathbf{\Pi} \tag{11}$$

and the expression of tensor $\mathbf{N}$ (Eq. (6)) can then be simplified as follows:

$$\mathbf{N} = \frac{\mu}{\sqrt{H+3\mu}}(\mathbf{I} - 3\mathbf{e}_x \otimes \mathbf{e}_x) = \frac{\mu}{\sqrt{H+3\mu}} \begin{bmatrix} -2 & 0 & 0 \\ 0 & 1 & 0 \\ 0 & 0 & 1 \end{bmatrix} \tag{12}$$

Hence the material tangent elastoplastic tensor (Eq. (5)) reads

$$\mathbf{D}^p = \mathbf{D} - \frac{\mu^2}{H+3\mu}(\mathbf{I} - 3\mathbf{e}_x \otimes \mathbf{e}_x) \otimes (\mathbf{I} - 3\mathbf{e}_x \otimes \mathbf{e}_x) \tag{13}$$

In the orthonormal basis $(\mathbf{e}_x, \mathbf{e}_y, \mathbf{e}_z)$, the components of $\mathbf{D}^p$ are

$$\begin{aligned} &D^p_{xxxx} = \Lambda + 2\mu - \frac{4\mu^2}{H+3\mu}, \quad D^p_{yyzz} = \Lambda - \frac{\mu^2}{H+3\mu} \\ &D^p_{yyyy} = \Lambda + 2\mu - \frac{\mu^2}{H+3\mu}, \quad D^p_{xxzz} = \Lambda + \frac{2\mu^2}{H+3\mu} \\ &D^p_{zzzz} = \Lambda + 2\mu - \frac{\mu^2}{H+3\mu}, \quad D^p_{xxyy} = \Lambda + \frac{2\mu^2}{H+3\mu} \\ &D^p_{xyxy} = D^p_{xzxz} = D^p_{yzyz} = \mu \end{aligned} \tag{14}$$

The other components are either zero or derived from Eq. (14) using both major and minor symmetries of tensor $\mathbf{D}^p$ ($D^p_{ijkl} = D^p_{klij} = D^p_{jikl} = D^p_{ijlk}$).

The nominal tangent elastoplastic tensor in Eq. (3) becomes

$$\mathbf{K}^p \approx \frac{\partial \mathbf{\Sigma}}{\partial \mathbf{E}} + (\mathcal{I} \cdot \mathbf{\Sigma})^T = \mathbf{D}^p - P\mathbf{e}_i \otimes \mathbf{e}_x \otimes \mathbf{e}_x \otimes \mathbf{e}_i \tag{15}$$

which is independent of the spatial coordinates (the implicit summation convention on repeated indices is used with $i = x, y, z$).

Furthermore, when dealing with 1D models such as beams, constraints are placed on the deformation map. In particular, the plane-sections hypothesis imposes that plane sections do not distort in their own planes. Rigorously speaking the rigid cross-section kinematic constraint induces normal stresses in the plane of the cross-section (Poisson's effect). Nevertheless, the behavior of beams indicates that these stresses tend to be rather small so that we will assume that the transverse normal material stresses are equal to zero: $\Sigma_{yy} = \Sigma_{zz} = 0$. These constraints on the stress field lead one to replace tensor $\mathbf{D}^p$ with the reduced tensor $\mathbf{C}^p$ defined as

$$C^p_{ijkl} = D^p_{ijkl} + \frac{D^p_{ijyy}(D^p_{yyzz}D^p_{zzkl} - D^p_{zzzz}D^p_{yykl}) + D^p_{ijzz}(D^p_{zzyy}D^p_{yykl} - D^p_{yyyy}D^p_{zzkl})}{D^p_{yyyy}D^p_{zzzz} - D^p_{yyzz}D^p_{zzyy}}$$

$$(i,j) \neq (y,y),(z,z), \quad (k,l) \neq (y,y),(z,z) \tag{16}$$

It can be readily checked that tensor $\mathbf{C}^p$ enjoys both major and minor symmetries. In the sequel, we only need the following reduced moduli (and their equivalents obtained by major or minor symmetries):

$$C^p_{xxxx} = E_T, \quad C^p_{xyxy} = C^p_{xzxz} = C^p_{yzyz} = \mu = G \tag{17}$$

where E_T is the tangent elastoplastic modulus related to Young's modulus E and the isotropic hardening modulus H by $1/E_T = 1/E + 1/H$.

The bifurcation equation (2) for a single beam writes in the uniaxial stress case:

$$\forall \delta\mathbf{U}, \quad \int_\Omega \nabla^T \delta\mathbf{U} : (\mathbf{C}^p - P_c \mathbf{e}_i \otimes \mathbf{e}_x \otimes \mathbf{e}_x \otimes \mathbf{e}_i) : \nabla\mathbf{X} \, d\Omega = 0 \tag{18}$$

As far as the composite beam is concerned, one has to consider two similar integrals (like the one in Eq. (18)) in the global bifurcation equation (one for each layer), together with a specific term for the contribution of the connectors, which will be formulated in the sequel.

Let us now consider the bending problem of the two-layer beam in the xy-plane. The Timoshenko theory is employed, as it includes transverse shear effects which may be non-negligible in practice. The plane-sections hypothesis suggests that a cross-section will move as a rigid body, neither changing in shape nor deviating from flatness. To track the motion of a 2D beam, it is necessary to specify the longitudinal and transverse displacements of the centroidal axis of the beam $u(x)$ and $v(x)$, as well as the cross-section rotation $\theta(x)$. The latter is independent of the deflection v since the plane sections are supposed to remain plane but not normal to the neutral axis. When the beam buckles from the straight position (the fundamental solution) to a bent shape, the expressions for the bifurcation mode $\mathbf{X}$ and the displacement variation $\delta\mathbf{U}$ are both chosen according to the Timoshenko kinematics:

$$\mathbf{X} = \begin{vmatrix} \mathcal{U}(x) - y\Theta(x) \\ \mathcal{V}(x) \\ 0 \end{vmatrix}, \quad \delta\mathbf{U} = \begin{vmatrix} \delta u(x) - y\delta\theta(x) \\ \delta v(x) \\ 0 \end{vmatrix} \tag{19}$$

The two sub-elements of the composite beam are interconnected in such a way that they present the same deflection (no uplift). Conversely, layers a and b do not have the same longitudinal displacement and rotation. Consequently, the 3D modal displacement field of the whole system involves the five following scalar functions $\mathcal{U}_a(x)$, $\mathcal{U}_b(x)$, $\mathcal{V}(x)$, $\Theta_a(x)$ and $\Theta_b(x)$. The modal interlayer slip $\mathcal{G}$ along the interface can be expressed as follows:

$$\mathcal{G} = \mathcal{U}_a - h_a\Theta_a - \mathcal{U}_b - h_b\Theta_b \tag{20}$$

The global bifurcation equation then writes

$$\begin{aligned} &\forall \delta\mathbf{U}_a, \delta\mathbf{U}_b, \quad \int_{\Omega_a} \nabla^T \delta\mathbf{U}_a : \mathbf{K}^p_a(P_{ca}) : \nabla\mathbf{X}_a \, d\Omega \\ &+ \int_{\Omega_b} \nabla^T \delta\mathbf{U}_b : \mathbf{K}^p_b(P_{cb}) : \nabla\mathbf{X}_b d\Omega + \int_0^L \delta g \; k_{sc} \; \mathcal{G} \, dx = 0 \end{aligned} \tag{21}$$

that is to say

$$\begin{aligned} &\forall \delta u_a, \delta u_b, \delta v, \delta\theta_a, \delta\theta_b, \quad \int_{\Omega_a} [E_{Ta}(\mathcal{U}_{a,x} - y_a\Theta_{a,x})(\delta u_{a,x} - y_a\delta\theta_{a,x}) \\ &- G_a\mathcal{V}_{,x}\delta\theta_a - G_a\Theta_a\delta v_{,x} + G_a\mathcal{V}_{,x}\delta v_{,x} + G_a\Theta_a\delta\theta_a \\ &- P_{ca}(\mathcal{U}_{a,x} - y_a\Theta_{a,x})(\delta u_{a,x} - y_a\delta\theta_{a,x}) - P_{ca}\mathcal{V}_{,x}\delta v_{,x}] \, d\Omega \\ &+ \int_{\Omega_b} [E_{Tb}(\mathcal{U}_{b,x} - y_b\Theta_{b,x})(\delta u_{b,x} - y_b\delta\theta_{b,x}) \\ &- G_b\mathcal{V}_{,x}\delta\theta_b - G_b\Theta_b\delta v_{,x} + G_b\mathcal{V}_{,x}\delta v_{,x} + G_b\Theta_b\delta\theta_b \\ &- P_{cb}(\mathcal{U}_{b,x} - y_b\Theta_{b,x})(\delta u_{b,x} - y_b\delta\theta_{b,x}) - P_{cb}\mathcal{V}_{,x}\delta v_{,x}] \, d\Omega \\ &+ \int_0^L (\delta u_a - h_a\delta\theta_a - \delta u_b - h_b\delta\theta_b)k_{sc}(\mathcal{U}_a - h_a\Theta_a - \mathcal{U}_b - h_b\Theta_b) \, dx = 0 \end{aligned} \tag{22}$$

where y_m stands for the y-coordinate of a current point relative to the centroid axis of the corresponding layer m.

First, integrating over the cross-sections S_a and S_b, then integrating by parts with respect to x and eliminating negligible higher-order terms (assuming that $P_{ca} \ll E_{Ta}$ and $P_{cb} \ll E_{Tb}$) yield five local differential equations for the components $\mathcal{U}_a$, $\mathcal{U}_b$, $\mathcal{V}$, Θ_a

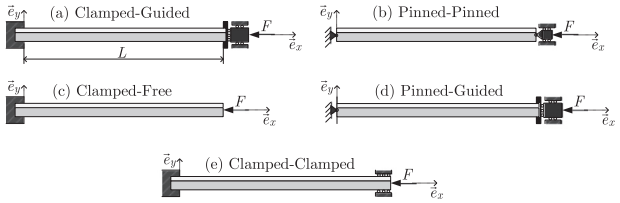

Fig. 2. Boundary conditions.

and Θ_b of the eigenmode:

$$
\begin{aligned}
&E_{Ta}A_a\mathcal{U}_{a,xx}-k_{sc}\mathcal{G}=0\\
&E_{Tb}A_b\mathcal{U}_{b,xx}+k_{sc}\mathcal{G}=0\\
&k_aG_aA_a(\Theta_{a,x}-\mathcal{V}_{,xx})+k_bG_bA_b(\Theta_{b,x}-\mathcal{V}_{,xx})+\lambda_T\mathcal{V}_{,xx}=0\\
&E_{Ta}I_a\Theta_{a,xx}+k_aG_aA_a(\mathcal{V}_{,x}-\Theta_a)+k_{sc}h_a\mathcal{G}=0\\
&E_{Tb}I_b\Theta_{b,xx}+k_bG_bA_b(\mathcal{V}_{,x}-\Theta_b)+k_{sc}h_b\mathcal{G}=0
\end{aligned}
\tag{23}
$$

where k_a and k_b are the transverse shear correction factors depending on the cross-sectional shapes of the layers a and b, respectively, and $\lambda_T=P_{ca}A_a+P_{cb}A_b$ is the sought tangent modulus critical force.

At this stage, one has to specify the boundary conditions in order to solve the previous system of differential equations. Let us first assume, as an example, that both layers are clamped at end $x=0$ and guided at end $x=L$ (see Fig. 2(a)). The components of the eigenmode must satisfy the above-mentioned displacement boundary conditions, that is to say $\mathcal{U}_a(0)=\mathcal{U}_b(0)=\mathcal{V}(0)=\Theta_a(0)=\Theta_b(0)=\Theta_a(L)=\Theta_b(L)=0$.

Taking into account $\delta u_a(0)=\delta u_b(0)=\delta v(0)=\delta\theta_a(0)=\delta\theta_b(0)=\delta\theta_a(L)=\delta\theta_b(L)=0$ in the bifurcation equation (22) leads one, after integration by parts, to the remaining stress boundary conditions at the beam end $x=L:\mathcal{U}_{a,x}(L)=0$, $\mathcal{U}_{b,x}(L)=0$ and $k_aG_aA_a(\Theta_a(L)-\mathcal{V}_{,x}(L))+k_bG_bA_b(\Theta_b(L)-\mathcal{V}_{,x}(L))+\lambda_T\mathcal{V}_{,x}(L)=0$.

2.3. Solution procedure

The bifurcation mode of a single Timoshenko beam under axial compression with the boundary conditions defined above takes the following form:

$$
\begin{cases}
\mathcal{U}=0\\
\mathcal{V}=\alpha\left(1-\cos\dfrac{\pi x}{L}\right)\\
\Theta=\beta\ \sin\dfrac{\pi x}{L}
\end{cases}
\tag{24}
$$

where α and β are constants which are dependent one from the other.

In the case of the composite beam, we assume that the presence of connectors does not affect the transverse displacements and the cross-section rotations, and we denote the following modal components:

$$
\begin{cases}
\mathcal{V}=\alpha\left(1-\cos\dfrac{\pi x}{L}\right)\\
\Theta_a=\beta_a\ \sin\dfrac{\pi x}{L}\\
\Theta_b=\beta_b\ \sin\dfrac{\pi x}{L}
\end{cases}
\tag{25}
$$

which are consistent with the corresponding boundary conditions.

Then, combining the two first local equations with the four corresponding boundary conditions concerning the longitudinal displacements ($\mathcal{U}_a(0)=\mathcal{U}_b(0)=0$ and $\mathcal{U}_{a,x}(L)=\mathcal{U}_{b,x}(L)=0$) leads to the simple relationship:

$$
\mathcal{U}_a=-\frac{E_{Tb}A_b}{E_{Ta}A_a}\mathcal{U}_b \tag{26}
$$

Using Eqs. (25) and (26), the first differential equation in (23) can be solved for the function $\mathcal{U}_b$. Accounting for the associated boundary conditions, it gives rise to the following solution:

$$
\mathcal{U}_b=-\frac{h_a\beta_a+h_b\beta_b}{1+\dfrac{E_{Tb}A_b}{E_{Ta}A_a}+\dfrac{\pi^2E_{Tb}A_b}{k_{sc}L^2}}\ \sin\frac{\pi x}{L} \tag{27}
$$

It is worth to notice that the axial components of the buckling mode are not null which is the case for a regular Timoshenko beam.

All the modal displacement fields depend only on the three constants α, β_a and β_b. The last three equations in (23) write finally

$$
\begin{aligned}
&\pi^2[\lambda_TL-(k_aG_aA_a+k_bG_bA_b)L]\alpha+\pi k_aG_aA_aL^2\beta_a+\pi k_bG_bA_bL^2\beta_b=0\\
&\pi k_aG_aA_aL\xi\alpha-[(\pi^2E_{Ta}I_a+k_aG_aA_aL^2)\xi+\pi^2E_{Ta}A_aE_{Tb}A_bk_{sc}L^2h_a^2]\beta_a\\
&\quad-\pi^2E_{Ta}A_aE_{Tb}A_bk_{sc}L^2h_ah_b\beta_b=0\\
&\pi k_bG_bA_bL\xi\alpha-\pi^2E_{Ta}A_aE_{Tb}A_bk_{sc}L^2h_ah_b\beta_a\\
&\quad-[(\pi^2E_{Tb}I_b+k_bG_bA_bL^2)\xi+\pi^2E_{Ta}A_aE_{Tb}A_bk_{sc}L^2h_b^2]\beta_b=0
\end{aligned}
\tag{28}
$$

with $\xi=(E_{Ta}A_a+E_{Tb}A_b)k_{sc}L^2+\pi^2E_{Ta}A_aE_{Tb}A_b$.

One obtains the critical force by setting the determinant of the linear equation system (28) equal to zero:

$$
\lambda_T=\frac{\dfrac{\pi^2\overline{E_TI}_\infty}{L^2}\left(\dfrac{\pi^2\widetilde{E_TI}^2\overline{GA}}{L^2\overline{E_TI}_\infty\widetilde{GA}^2}+\dfrac{\overline{E_TI}}{\overline{E_TI}_\infty}+\dfrac{k_{sc}\widetilde{E_TI}^2\widehat{E_TI}_\infty\overline{GA}}{\widehat{E_TA}\widehat{E_TI}\overline{E_TI}_\infty\widetilde{GA}^2}+\dfrac{k_{sc}L^2}{\pi^2\widehat{E_TA}}\right)}{\dfrac{\pi^4\widetilde{E_TI}^2}{L^4\widetilde{GA}^2}\left(1+\dfrac{k_{sc}L^2\widehat{E_TI}_\infty}{\pi^2\widehat{E_TA}\widehat{E_TI}}\right)+\left(1+\dfrac{\pi^2}{L^2}\overline{\left(\dfrac{E_TI}{GA}\right)}\right)\left(1+\dfrac{k_{sc}L^2}{\pi^2\widehat{E_TA}}\right)+\dfrac{k_{sc}\overline{h}^2}{\widehat{GA}}}
\tag{29}
$$

with

$$
\begin{aligned}
&\overline{h}=h_a+h_b,\quad \widehat{E_TA}=\frac{E_{Ta}A_aE_{Tb}A_b}{E_{Ta}A_a+E_{Tb}A_b}\\
&\overline{E_TI}=E_{Ta}I_a+E_{Tb}I_b,\quad \overline{E_TI}_\infty=\overline{E_TI}+\overline{h}^2\widehat{E_TA},\quad \widetilde{E_TI}=\sqrt{E_{Ta}I_aE_{Tb}I_b}\\
&\overline{GA}=k_aG_aA_a+k_bG_bA_b,\quad \widetilde{GA}=\sqrt{k_aG_aA_ak_bG_bA_b}\\
&\widehat{E_TI}=\overline{h}^2\left(\frac{h_a^2}{E_{Ta}I_a}+\frac{h_b^2}{E_{Tb}I_b}\right)^{-1},\quad \widehat{GA}=\overline{h}^2\left(\frac{h_a^2}{k_aG_aA_a}+\frac{h_b^2}{k_bG_bA_b}\right)^{-1}\\
&\widehat{E_TI}_\infty=\widehat{E_TI}+\overline{h}^2\widehat{E_TA},\quad \overline{\left(\frac{E_TI}{GA}\right)}=\frac{E_{Ta}I_a}{k_aG_aA_a}+\frac{E_{Tb}I_b}{k_bG_bA_b}
\end{aligned}
\tag{30}
$$

One can readily check that the critical load (29) derived for clamped-guided boundary conditions also stands for pinned–pinned (simply-supported) boundary conditions because both cases correspond to the same wavelength $2L$ of the buckling mode (see Fig. 2(b)). In the same way, another critical load is obtained for clamped–free (cantilever) and pinned-guided boundary conditions where the wavelength of the buckling mode is equal to $4L$ (see Fig. 2(c) and (d)):

$$
\lambda_T=\frac{\dfrac{\pi^2\overline{E_TI}_\infty}{L^2}\left(\dfrac{\pi^2\widetilde{E_TI}^2\overline{GA}}{16L^2\overline{E_TI}_\infty\widetilde{GA}^2}+\dfrac{\overline{E_TI}}{4\overline{E_TI}_\infty}+\dfrac{k_{sc}\widetilde{E_TI}^2\widehat{E_TI}_\infty\overline{GA}}{4\widehat{E_TA}\widehat{E_TI}\overline{E_TI}_\infty\widetilde{GA}^2}+\dfrac{k_{sc}L^2}{\pi^2\widehat{E_TA}}\right)}{\dfrac{\pi^4\widetilde{E_TI}^2}{16L^4\widetilde{GA}^2}\left(1+\dfrac{4k_{sc}L^2\widehat{E_TI}_\infty}{\pi^2\widehat{E_TA}\widehat{E_TI}}\right)+\left(1+\dfrac{\pi^2}{4L^2}\overline{\left(\dfrac{E_TI}{GA}\right)}\right)\left(1+\dfrac{4k_{sc}L^2}{\pi^2\widehat{E_TA}}\right)+\dfrac{k_{sc}\overline{h}^2}{\widehat{GA}}}
\tag{31}
$$

Finally, the clamped–clamped boundary conditions (giving rise to a wavelength of L) provide another critical load (see Fig. 2(e)):

$$
\lambda_T=\frac{\dfrac{\pi^2\overline{E_TI}_\infty}{L^2}\left(\dfrac{16\pi^2\widetilde{E_TI}^2\overline{GA}}{L^2\overline{E_TI}_\infty\widetilde{GA}^2}+\dfrac{4\overline{E_TI}}{\overline{E_TI}_\infty}+\dfrac{4k_{sc}\widetilde{E_TI}^2\widehat{E_TI}_\infty\overline{GA}}{\widehat{E_TA}\widehat{E_TI}\overline{E_TI}_\infty\widetilde{GA}^2}+\dfrac{k_{sc}L^2}{\pi^2\widehat{E_TA}}\right)}{\dfrac{16\pi^4\widetilde{E_TI}^2}{L^4\widetilde{GA}^2}\left(1+\dfrac{k_{sc}L^2\widehat{E_TI}_\infty}{4\pi^2\widehat{E_TA}\widehat{E_TI}}\right)+\left(1+\dfrac{4\pi^2}{L^2}\overline{\left(\dfrac{E_TI}{GA}\right)}\right)\left(1+\dfrac{k_{sc}L^2}{4\pi^2\widehat{E_TA}}\right)+\dfrac{k_{sc}\overline{h}^2}{\widehat{GA}}}
\tag{32}
$$

Eqs. (29), (31) and (32) can be reformulated in a unified way, using the following general expression:

$$\lambda_T = \frac{\dfrac{\pi^2\overline{E_T I}_\infty}{\rho^2 L^2}\left(\dfrac{16\pi^2\widetilde{E_T I}^2\overline{GA}}{\rho^2L^2\overline{E_T I}_\infty\widetilde{GA}^2}+\dfrac{4\overline{E_T I}}{\overline{E_T I}_\infty}+\dfrac{4k_{sc}\widetilde{E_T I}^2\widehat{E_T I}_\infty\overline{GA}}{\widehat{E_T A}\widehat{E_T I}\overline{E_T I}_\infty\widetilde{GA}^2}+\dfrac{k_{sc}\rho^2L^2}{\pi^2\widehat{E_T A}}\right)}{\dfrac{16\pi^4\widetilde{E_T I}^2}{\rho^4L^4\widetilde{GA}^2}\left(1+\dfrac{k_{sc}\rho^2L^2\widehat{E_T I}_\infty}{4\pi^2\widehat{E_T A}\widehat{E_T I}}\right)+\left(1+\dfrac{4\pi^2}{\rho^2L^2}\left(\dfrac{\overline{E_T I}}{\overline{GA}}\right)\right)\left(1+\dfrac{k_{sc}\rho^2L^2}{4\pi^2\widehat{E_T A}}\right)+\dfrac{k_{sc}\overline{h}^2}{\widehat{GA}}} \tag{33}$$

In the general formula (33), the so-called effective length factor ρ has been introduced. It may be defined as the ratio between the buckling mode wavelength and the beam length. One has thus to take $\rho = 2, 4, 1$ to find again the expressions (29), (31) and (32), respectively.

Similar differential equations and solutions for the J_2 deformation theory can be obtained from the above results, provided the tangent moduli are replaced by the equivalent secant moduli. The same expressions may also be used in the case where one of the layers (or both) remain(s) elastic before the occurrence of buckling, provided the tangent elastoplastic moduli are replaced with the elastic moduli in the concerned layer(s).

By taking the limit $k_m G_m A_m \to \infty$ for $m = a$ and/or b, we recover, from the general solution (33), the expressions for the critical loads of two-layer beams where one or both layers deform according to the Euler–Bernoulli kinematics. In the most simple case where transverse shear effects are neglected in both layers, the critical force has the following expression:

$$\lambda_T^{EB} = \frac{4\pi^2(4\pi^2\widehat{E_T A}\overline{E_T I}+k_{sc}\rho^2L^2\overline{E_T I}_\infty)}{\rho^2L^2(4\pi^2\widehat{E_T A}+k_{sc}\rho^2L^2)} \tag{34}$$

3. Numerical computation of the true plastic bifurcation loads

In this section, a finite element model for elastoplastic shear-deformable composite beams together with an incremental calculation procedure for bifurcation points are briefly presented. The computational tool will serve for the numerical evaluation of the elastoplastic buckling loads of shear-deformable composite beams which will be compared against analytical solutions developed in the previous section.

3.1. Finite element formulation of a composite beam with partial interaction

The finite element formulation, developed for the quasi-static response of shear-deformable two-layer composite beams with material and geometric non-linearities, is based on the co-rotational approach. This approach relies on the following kinematic assumptions: displacements and rotations may be arbitrarily large, but deformations must remain small. In co-rotational formulation, the motion of the element is decomposed into rigid-body motion and deformational part using a local co-rotational frame which continuously translates and rotates with the element, but does not deform with it. It requires the definition of nodal variables relative to the local system and the transformation matrix relating local and global kinematic variables. The geometric non-linearity induced by element large rigid-body motion is incorporated in this transformation matrix. The main advantage of this approach is that the formulation of the element in local coordinate system is completely independent of the transformation, i.e., the material non-linearity can be treated in the local system where element can be formulated as geometrically linear. However, when considering composite beams with interlayer slip, it is necessary to select pertinent kinematic local and global variables.

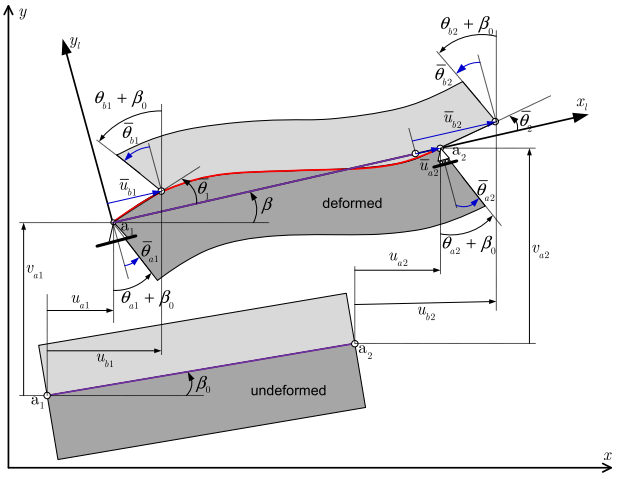

Fig. 3. Degrees of freedom in the global and local coordinate systems.

3.1.1. Local displacement-based element

The geometrically linear element is derived in the local system (x_l, y_l) without rigid-body modes. The latter translates and rotates with the element as deformation proceeds. To ease the derivation, we select the nodal interlayer slips instead of displacements of the layer b along the x_l-axis as local degrees of freedom (see Fig. 3). This choice allows us to easily construct the transformation matrix relating the global nodal displacements and the local ones. Quadratic shape functions are used to approximate the layer rotations $\overline{\theta}_a$ and $\overline{\theta}_b$, the axial displacement $\overline{u}_a$ and the slip $\overline{g}$, while the transverse displacement $\overline{v}$ is interpolated using cubic shape functions. Thus, in this local system, the element has 13 degrees of freedom which are statically condensed thereafter to obtain the local displacement vector containing only the degrees of freedom at the element ends. The material non-linearity is taken into account by adopting the distributed plasticity model with fiber section discretization along with consistent integration. The details of the derivation of the local plastic element can be found in Lai [22].

3.1.2. Co-rotational formulation

The central idea of the co-rotational approach is to decompose the motion of the element into a rigid-body and a pure deformational part, through the use of a local coordinate system (x_l, y_l) which continuously rotates and translates with the element (see Fig. 3). The origin of the local coordinate system is taken at node a_1 and the x_l-axis of the local coordinate system is defined by the line connecting the nodes a_1 and a_2. The y_l-axis is perpendicular to the x_l-axis so that the result is a right-handed orthogonal coordinate system. The motion of the element from the original undeformed configuration to the actual deformed one can thus be separated in two parts. The first one, which corresponds to the rigid motion of the local frame, is described by the translation of the node a_1 and the rigid rotation of the axes. The deformational part of the motion is always small relative to the local coordinate system.

According to the notations defined in Fig. 3, the components of the local displacement vector can be computed from those of the global displacement vector as

$$\overline{u}_{a2} = l_n - l_0 \tag{35}$$

$$\overline{u}_{b1} = g_1 \cos\left(\frac{\theta_{a1}+\theta_{b1}}{2}+\beta_0-\beta\right) \tag{36}$$

$$\overline{u}_{b2} = g_2 \cos\left(\frac{\theta_{a2}+\theta_{b2}}{2}+\beta_0-\beta\right) \tag{37}$$

$$\overline{\theta}_{a1} = \theta_{a1}+\beta_0-\beta \tag{38}$$

$$\overline{\theta}_{b1} = \theta_{b1}+\beta_0-\beta \tag{39}$$

$$\overline{\theta}_{a2} = \theta_{a2}+\beta_0-\beta \tag{40}$$

$$\overline{\theta}_{b2} = \theta_{b2}+\beta_0-\beta \tag{41}$$

where l_0 and l_n are, respectively, the undeformed and deformed element length, and g_1 and g_2 denote the global slips at interface which are assumed as perpendicular to the average end cross-section rotations. An overbar indicates a local quantity.

As can be seen from Eqs. (35) to (41), the local displacement vector $\mathbf{p}_l$ can be expressed as functions of the global one $\mathbf{p}_g$, i.e.

$$\mathbf{p}_l = \mathbf{p}_l(\mathbf{p}_g) \tag{42}$$

Then, $\mathbf{p}_l$ is used to compute the internal force vector $\mathbf{f}_l$ and the tangent stiffness matrix $\mathbf{K}_l$ in the local system. Note that $\mathbf{f}_l$ and $\mathbf{K}_l$ depend only on the definition of the local strains and not on the particular form of Eq. (42). The transformation matrix $\mathbf{B}_{lg}$ between the local and global displacements is defined by

$$\delta\mathbf{p}_l = \mathbf{B}_{lg}\delta\mathbf{p}_g \tag{43}$$

and is obtained by differentiation of Eq. (42). The global internal force vector $\mathbf{f}_g$ and the global tangent stiffness matrix $\mathbf{K}_g$, consistent with $\mathbf{p}_g$, can be obtained by equating the internal virtual work in both the global and the local system, i.e.

$$\mathbf{f}_g = \mathbf{B}_{lg}^{\mathrm{T}}\mathbf{f}_l, \quad \mathbf{K}_g = \mathbf{B}_{lg}^{\mathrm{T}}\mathbf{K}_l\mathbf{B}_{lg}+\mathbf{H}_{lg}, \quad \mathbf{H}_{lg} = \left.\frac{\partial(\mathbf{B}_{lg}^{\mathrm{T}}\mathbf{f}_l)}{\partial\mathbf{p}_g}\right|_{\mathbf{f}_l} \tag{44}$$

Eqs. (42) and (43) and transformations (44) are explained in detail in Hjiaj et al. [28].

3.2. Indirect method for the estimation of the elastoplastic buckling loads

Due to the geometric and material non-linearities, the finite element problem is numerically solved in an incremental way. A specific technique is implemented within this numerical procedure (see [48]) in order to detect the bifurcation points along the fundamental equilibrium path. At the end of each increment, it must be checked whether one has gone across one or several critical points. The detection of critical points is based on the singularity of the tangent stiffness matrix, which may be factorized following the Crout formula $\mathbf{K}_g = \mathbf{LdL}^T$, where $\mathbf{L}$ is a lower triangular matrix with unit diagonal elements and $\mathbf{d}$ is a diagonal matrix. Since the number of negative eigenvalues of $\mathbf{K}_g$ is equal to the number of negative diagonal elements (pivots) of $\mathbf{d}$, the critical points are determined by counting the negative pivot number and comparing its value between the successive increments.

Each critical point detected has to be isolated in order to specify the corresponding critical value. To do this, the prescribed force or displacement, or the current arc-length (depending on the control parameter used), may be re-estimated in one shot by interpolation of the appropriate eigenvalue, or several times using a dichotomy-like method. The step increment is then renewed so as to reach a point just behind the current bifurcation point, and so on for the next bifurcation points.

Table 1
Geometry and material parameters.

Length	Width	Height	Young's modulus	Poisson's ratio	Tangent modulus
2 m	300 mm	150 mm	8000 MPa	0.25	80 MPa

4. Validation and analysis

4.1. Comparisons between analytical and numerical critical values

The aim of this subsection is to validate the closed-form expressions of the elastoplastic buckling loads derived in Section 2 by comparing the analytical solutions against the predictions of the numerical model presented in Section 3. The comparison is performed on a two-layer column with the following three classical Euler boundary conditions: (a) clamped–free, (b) pinned–pinned and (c) clamped–clamped. For simplicity purposes, both layers have the same cross-section dimensions as well as the same material properties (see Table 1). The interface shear bond law of the connection is taken to be linear (elastic behavior) and three values of interface shear bond stiffness are considered: $k_{sc} = 10$ MPa, 100 MPa, and 1000 MPa. The shear correction factors k_a and k_b take both the classical value 5/6, usually retained for homogeneous rectangular sections. Finally, it is worth mentioning that the initial compression yield stress is chosen very small so as to trigger numerically the plastic buckling phenomenon.

The analytical plastic buckling loads are given in Table 2 together with the critical values obtained with the FE model using 40 finite elements. It should be noted that the same kinematic assumptions have been adopted for both analytical and FE models. Therefore, by increasing the number of elements, the numerical critical load should tend towards the analytical value. In the present validation procedure, a quite dense mesh (40 finite elements) is used and therefore, as can be seen from Table 2, the analytical solutions and the numerical predictions are in very good agreement.

4.2. Parametric study

In this section, the proposed analytical expressions of the critical load which were successfully validated above are used to conduct parametric studies so as to investigate the influence of various geometric and material parameters on the buckling load of

Table 2
Comparisons between analytical and numerical plastic buckling loads.

Boundary conditions	$k_{sc}=10$ MPa			$k_{sc}=100$ MPa			$k_{sc}=1000$ MPa		
	Buckling loads (kN)		Relative error (%)	Buckling loads (kN)		Relative error (%)	Buckling loads (kN)		Relative error (%)
	Analytical	Numerical		Analytical	Numerical		Analytical	Numerical	
Clamped–free	30.8	31.1	0.97	33.0	33.2	0.61	33.3	33.5	0.60
Pinned–pinned	102.4	102.9	0.49	128.9	129.4	0.39	132.7	133	0.23
Clamped–clamped	276.9	277.3	0.14	471.7	472.3	0.13	524.8	525.1	0.06

the two-layer column. The conclusions reported in Le Grognec et al. [33] can also be drawn for the present analyses. Indeed, it can be seen that transverse shear effects have more influence on the buckling response if the slenderness ratio of the composite beam is lower and/or the interface shear bond stiffness is larger. Instead, our attention focuses here on the elastoplastic nature of the buckling phenomenon.

4.2.1. *Influence of the elastoplastic tangent modulus*

First, the influence of the elastoplastic tangent modulus on the critical buckling load is investigated. For this purpose, the composite beam defined above is again considered (with pinned–pinned boundary conditions). The layer b is supposed here to behave elastically and the tangent modulus of the elastoplastic layer a is varied from 0 to 80 MPa so as to evaluate its influence on the critical load. The yield stress of layer a is always chosen sufficiently small to ensure that the composite beam plastically deforms before the occurrence of the buckling point. In Fig. 4, the analytical buckling load is plotted versus the modulus ratio E_T/E for different values of the shear bond stiffness k_{sc} ranging from 0 to 1000 MPa. The critical load only slightly increases with the tangent modulus. This increase reduces with decreasing shear bond stiffness. Furthermore, for a given tangent modulus, the critical load generally depends on the value of k_{sc}, but less and less as the tangent modulus tends to zero. In the particular case of a null tangent modulus (corresponding to perfect plasticity), the critical load no longer depends on the interface stiffness. Indeed, it is just as if the composite beam was replaced by layer b, and since layer a does not contribute to the global force, the interface does not influence any more the general buckling behavior.

4.2.2. *Elastic, partially plastic or totally plastic buckling*

Finally, one considers again the composite beam of the previous section with similar boundary conditions. The same elastoplastic material as before is considered for both layers, except for the tangent modulus which takes here a higher value (namely $E_T = 2000$ MPa) for convenience (such a great value allows one to describe all the sought behaviors by only modifying the beam length in a realistic way). The shear bond stiffness k_{sc} is set to 500 MPa.

In the case of a compressed regular elastoplastic beam, it has already been widely demonstrated that, due to the presence of continua of bifurcation points, three buckling behaviors are likely to occur in practice, depending on the relative position of the yield force λ_0 and the elastic and tangent modulus plastic critical loads (see [43], for example). For a yield force higher than the elastic critical load ($\lambda_0 \geq \lambda_E$), buckling occurs elastically at the classical elastic critical load. Conversely, for a yield force lower than the

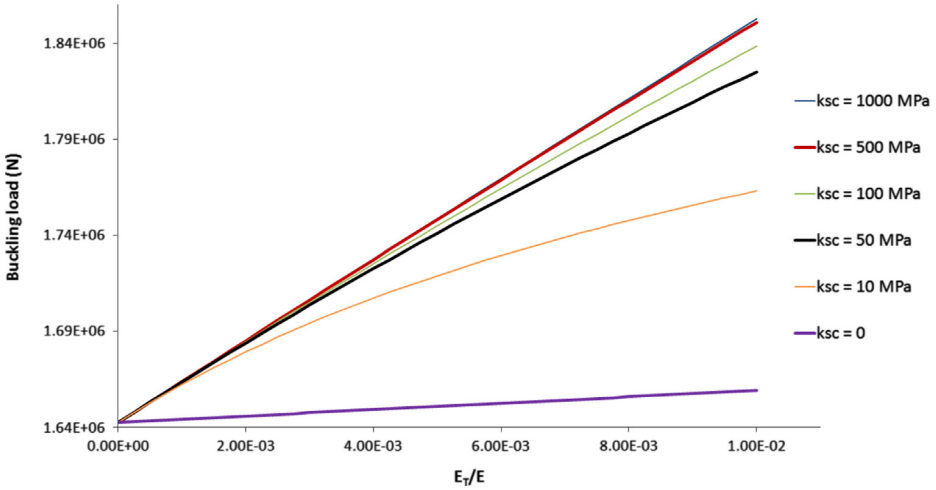

Fig. 4. Critical buckling loads versus modulus ratio for various interface shear bond stiffnesses.

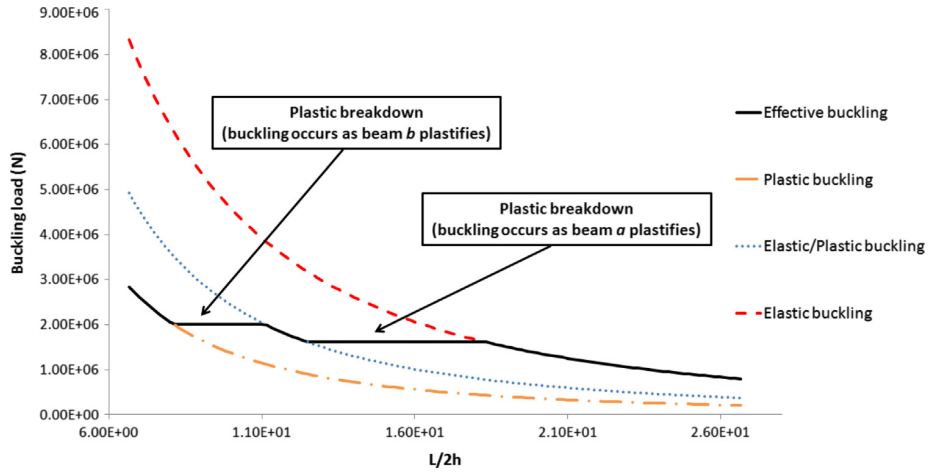

Fig. 5. Effective buckling loads for a large range of slenderness ratio.

tangent modulus critical load ($\lambda_0 \leq \lambda_T$), plasticity occurs before the tangent modulus critical load is reached, at which plastic buckling may occur. In the intermediate case where the yield force lies in the continuum of bifurcation points (between the two previous extreme critical loads), namely $\lambda_T \leq \lambda_0 \leq \lambda_E$, plasticity occurs at a point where buckling is likely to occur, so that both phenomena take place at the same time, which is commonly referred to the plastic breakdown.

In the present case of a composite beam, the same phenomenon may happen successively for each layer. For illustrative purposes, two different yield stresses are retained (namely $\sigma_0^a = 18$ MPa and $\sigma_0^b = 25$ MPa). Consequently, two different yield forces can be derived ($\lambda_0^a = 1.62$ MN and $\lambda_0^b = 2.01$ MN), at which plasticity occurs in layers a and b, respectively. The length of the composite beam is then varied so as to change the buckling behavior from elastic buckling to plastic buckling through plastic breakdown successively for each layer. Fig. 5 plots the three possible buckling curves in absolute terms (using Eq. (33) with either the elastic or the elastoplastic moduli, depending on the behavior of each layer), with respect to the slenderness ratio: a purely elastic one, a partially plastic one (corresponding to the case where only layer a behaves plastically at the critical point), and a totally plastic one. A last curve is finally plotted, corresponding to the effective buckling loads, which is related to the yield stress values at hand. As expected, for particularly high or low slenderness ratios, the composite beam buckles respectively in an elastic or a plastic fashion. For intermediate values of the slenderness ratio, the beam is partially elastic and plastic at the critical point, due to the difference between the yield stresses of layers a and b. Even more interesting are the two horizontal plateaus in the effective curve that represent the plastic breakdown transition of layers a and b. Whilst the elastic/plastic buckling load increases with decreasing value of the slenderness ratio, the critical force remains constant within the two particular intervals of slenderness ratio corresponding to plastic breakdown, as it coincides with the yield force at which plasticity occurs in the layer involved.

5. Conclusions

In this paper, closed-form expressions of the elastoplastic buckling loads of shear-deformable two-layer beam–columns with interlayer slip under axial compression have been derived. For this purpose, a 3D plastic bifurcation analysis has been performed and then particularized to the case of 1D beams under uniaxial stress states. The analytical expressions appear to be very similar to their elastic counterpart, provided that some elastic moduli are conveniently replaced by the corresponding tangent elastoplastic ones. The critical loads are first obtained in the general case of a shear-deformable composite column (assuming that both layers deform according to the Timoshenko hypotheses). The particular case of Euler–Bernoulli beams is then recovered by making the transverse shear stiffness of each layer tend to infinity.

The proposed formulae have been validated by comparing the analytical solutions against the numerical predictions obtained with a sophisticated FE model based on a co-rotational two-layer beam formulation (including the interlayer slip). The materially and geometrically non-linear calculations are performed in an incremental way. Along the equilibrium paths, the true elastoplastic bifurcation loads are numerically identified as singular points for the tangent stiffness matrix. Comparisons are performed for various boundary conditions and different interface shear bond stiffnesses (from the case of quasi-null bond to the case of full interaction), in order to check the broad applicability of the present solutions. The good agreement between the analytical and numerical results demonstrates that the analytical solutions derived in this paper can be used with confidence to accurately determine the elastoplastic buckling loads of shear-deformable composite columns in partial interaction.

The influence of the elastoplastic tangent modulus of one layer on the buckling behavior is investigated. In the limit case of perfect plasticity (provided that the other layer remains elastic or elastoplastic with non-zero hardening), the behavior of the two-layer beam is governed by only one layer without any influence of the interface, whatever the corresponding shear bond stiffness is. The critical load in this limit case is therefore the classical elastic or plastic buckling load of a regular beam. Finally, in a particular case (when both layers are elastoplastic but with different yield stresses), five different behaviors can be successively identified by only varying the length of the composite beam: purely elastic buckling, plastic breakdown (for the layer with minimum yield stress), elastic/plastic buckling, plastic breakdown (for the layer with maximum yield stress) and totally plastic buckling.

References

[1] N.M. Newmark, C.P. Siess, I.M. Viest, Tests and analysis of composite beams with incomplete interaction, Proc. Soc. Exp. Stress Anal. 9 (1) (1951) 75–92.
[2] C. Faella, E. Martinelli, E. Nigro, Steel and concrete composite beams with flexible shear connection: “exact” analytical expression of the stiffness matrix and applications, Comput. Struct. 80 (11) (2002) 1001–1009.
[3] U.A. Girhammar, V.K.A. Gopu, Composite beam–columns with interlayer slip—exact analysis, ASCE J. Struct. Eng. 119 (4) (1993) 1265–1282.
[4] U.A. Girhammar, D.H. Pan, Exact static analysis of partially composite beams and beam–columns, Int. J. Mech. Sci. 49 (2) (2007) 239–255.
[5] M. Heinisuo, An exact finite element technique for layered beams, Comput. Struct. 30 (3) (1988) 615–622.
[6] Y.F. Wu, D.J. Oehlers, M.C. Griffith, Partial interaction analysis of composite beam/column members, Mech. Struct. Mach. 30 (3) (2002) 309–332.
[7] G. Ranzi, M.A. Bradford, B. Uy, A direct stiffness analysis of a composite beam with partial interaction, Int. J. Numer. Methods Eng. 61 (5) (2004) 657–672.
[8] G. Ranzi, M.A. Bradford, Analytical solutions for the time-dependent behaviour of composite beams with partial interaction, Int. J. Solids Struct. 43 (13) (2006) 3770–3793.
[9] Q.H. Nguyen, M. Hjiaj, J.M. Aribert, A space-exact beam element for time-dependent analysis of composite members with discrete shear connection, J. Constr. Steel Res. 66 (11) (2010) 1330–1338.
[10] Q.H. Nguyen, M. Hjiaj, B. Uy, Time-dependent analysis of composite beams with continuous shear connection based on a space-exact stiffness matrix, Eng. Struct. 32 (9) (2010) 2902–2911.
[11] R. Xu, Y. Wu, Static, dynamic, and buckling analysis of partial interaction composite members using Timoshenko's beam theory, Int. J. Mech. Sci. 49 (10) (2007) 1139–1155.
[12] S. Schnabl, M. Saje, G. Turk, I. Planinc, Analytical solution of two-layer beam taking into account interlayer slip and shear deformation, ASCE J. Struct. Eng. 133 (6) (2007) 886–894.
[13] Q.H. Nguyen, E. Martinelli, M. Hjiaj, Derivation of the exact stiffness matrix for a two-layer Timoshenko beam element with partial interaction, Eng. Struct. 33 (2) (2011) 298–307.
[14] Q.H. Nguyen, M. Hjiaj, P. Le Grognec, Analytical approach for free vibration analysis of two-layer Timoshenko beams with interlayer slip, J. Sound Vib. 331 (12) (2012) 2949–2961.
[15] M.R. Salari, E. Spacone, Finite element formulations of one-dimensional elements with bond-slip, Eng. Struct. 23 (7) (2001) 815–826.
[16] M.R. Salari, E. Spacone, Analysis of steel-concrete composite frames with bond-slip, ASCE J. Struct. Eng. 127 (11) (2001) 1243–1250.
[17] Q.H. Nguyen, M. Hjiaj, B. Uy, S. Guezouli, Analysis of composite beams in the hogging moment regions using a mixed finite element formulation, J. Constr. Steel Res. 65 (3) (2009) 737–748.
[18] A. Ayoub, A two-field mixed variational principle for partially connected composite beams, Finite Elem. Anal. Des. 37 (11) (2001) 929–959.
[19] A. Dall'Asta, A. Zona, Non-linear analysis of composite beams by a displacement approach, Comput. Struct. 80 (27–30) (2002) 2217–2228.
[20] E. Spacone, S. El-Tawil, Nonlinear analysis of steel–concrete composite structures: state of the art, ASCE J. Struct. Eng. 130 (2) (2004) 159–168.
[21] G. Ranzi, A. Zona, A steel-concrete composite beam model with partial interaction including the shear deformability of the steel component, Eng. Struct. 29 (11) (2007) 3026–3041.
[22] V.A. Lai, Nonlinear analysis of steel-concrete beams taking into account the shear deformability of the steel joist (Ph.D. thesis), INSA de Rennes, 2012.
[23] C. Tort, J.F. Hajjar, A mixed finite element for 3D nonlinear dynamic analysis of rectangular concrete-filled steel tube beam–columns, ASCE J. Eng. Mech. 136 (11) (2010) 1329–1339.

[24] Y.L. Pi, M.A. Bradford, B. Uy, Second order nonlinear inelastic analysis of composite steel-concrete members. I: theory, ASCE J. Struct. Eng. 132 (5) (2006) 751–761.
[25] G. Ranzi, A. Dall'Asta, L. Ragni, A. Zona, A geometric nonlinear model for composite beams with partial interaction, Eng. Struct. 32 (5) (2010) 1384–1396.
[26] B. Čas, M. Saje, I. Planinc, Non-linear finite element analysis of composite planar frames with an interlayer slip, Comput. Struct. 82 (23–26) (2004) 1901–1912.
[27] P. Krawczyk, B. Rebora, Large deflections of laminated beams with interlayer slips. Part 2: finite element development, Eng. Comput. 24 (1) (2007) 33–51.
[28] M. Hjiaj, J.M. Battini, Q.H. Nguyen, Large displacement analysis of shear deformable composite beams with interlayer slips, Int. J. Non-Linear Mech. 47 (8) (2012) 895–904.
[29] B. Čas, M. Saje, I. Planinc, Buckling of layered wood columns, Adv. Eng. Softw. 38 (8–9) (2007) 586–597.
[30] A. Kryžanowski, S. Schnabl, G. Turk, I. Planinc, Exact slip-buckling analysis of two-layer composite columns, Int. J. Solids Struct. 46 (14–15) (2009) 2929–2938.
[31] S. Schnabl, I. Planinc, The influence of boundary conditions and axial deformability on buckling behavior of two-layer composite columns with interlayer slip, Eng. Struct. 32 (10) (2010) 3103–3111.
[32] S. Schnabl, I. Planinc, The effect of transverse shear deformation on the buckling of two-layer composite columns with interlayer slip, Int. J. Non-Linear Mech. 46 (3) (2011) 543–553.
[33] P. Le Grognec, Q.H. Nguyen, M. Hjiaj, Exact buckling solution for two-layer Timoshenko beams with interlayer slip, Int. J. Solids Struct. 49 (1) (2012) 143–150.
[34] J.M. Battini, Q.H. Nguyen, M. Hjiaj, Non-linear finite element analysis of composite beams with interlayer slips, Comput. Struct. 87 (13–14) (2009) 904–912.
[35] A. Considère, Résistance des pièces comprimées, in: Congrès International des Procédés de Construction, vol. 3, Librairie Polytechnique, Paris, 1891, pp. 371–397.
[36] F.R. Shanley, Inelastic column theory, Int. J. Aeronaut. Sci. 14 (5) (1947) 261–267.
[37] R. Hill, A general theory of uniqueness and stability in elastic–plastic solids, J. Mech. Phys. Solids 6 (1958) 236–249.
[38] A. Cimetière, On the modelling and buckling of elastoplastic plates (Sur la modélisation et le flambage des plaques élastoplastiques) (Ph.D. thesis), University of Poitiers, 1987.
[39] D. Durban, Plastic buckling of plates and shells, in: Stability Analysis of Plates and Shells (NASA CP-1998-206280), 1998, pp. 293–311.
[40] D. Durban, Z. Zuckerman, Elastoplastic buckling of rectangular plates in biaxial compression/tension, Int. J. Mech. Sci. 41 (1999) 751–765.
[41] E. Ore, D. Durban, Elastoplastic buckling of annular plates in pure shear, ASME J. Appl. Mech. 56 (3) (1989) 644–651.
[42] E. Ore, D. Durban, Elastoplastic buckling of axially compressed circular cylindrical shells, Int. J. Mech. Sci. 34 (9) (1992) 727–742.
[43] P. Le Grognec, A. Le van, On the plastic bifurcation and post-bifurcation of axially compressed beams, Int. J. Non-Linear Mech. 46 (5) (2011) 693–702.
[44] P. Le Grognec, A. Le van, Some new analytical results for plastic buckling and initial post-buckling of plates and cylinders under uniform compression, Thin-Walled Struct. 47 (8–9) (2009) 879–889.
[45] C. Lainé, P. Le Grognec, S. Comas Cardona, C. Binetruy, Analytical, numerical and experimental study of the bifurcation and collapse behavior of a 3D reinforced sandwich structure under through-thickness compression, Int. J. Mech. Sci. 67 (2013) 42–52.
[46] M.A. Douville, P. Le Grognec, Exact analytical solutions for the local and global buckling of sandwich beam–columns under various loadings, Int. J. Solids Struct. 50 (16–17) (2013) 2597–2609.
[47] Q.S. Nguyen, Stability and Non-Linear Solid Mechanics, Wiley, London, 2000.
[48] E. Riks, An incremental approach to the solution of snapping and buckling problems, Int. J. Solids Struct. 15 (7) (1979) 529–551.

ANNEXE 9

Q-H. Nguyen, M Hjiaj and P. Le Grognec. Analytical approach for free vibration analysis of two-layer Timoshenko beams with interlayer slip. *Journal of Sound and Vibration* 2012 ; 331 : 2902-2911. (5-Year IF 2.223) http://dx.doi.org/10.1016/j.jsv.2012.01.034.

Journal of Sound and Vibration 331 (2012) 2949–2961

Contents lists available at SciVerse ScienceDirect

Journal of Sound and Vibration

journal homepage: www.elsevier.com/locate/jsvi

Analytical approach for free vibration analysis of two-layer Timoshenko beams with interlayer slip

Quang-Huy Nguyen [a,*], Mohammed Hjiaj [a], Philippe Le Grognec [b]

[a] Université Européenne de Bretagne – INSA de Rennes, 20 avenue des Buttes de Coësmes, CS 70839, F-35708 Rennes Cedex 7, France
[b] Ecole des Mines de Douai, Polymers and Composites Technology & Mechanical Engineering Department, 941 rue Charles Bourseul – BP 10838, 59508 Douai Cedex, France

ARTICLE INFO

Article history:
Received 6 October 2011
Received in revised form
29 December 2011
Accepted 27 January 2012
Handling Editor: W. Lacarbonara
Available online 14 February 2012

ABSTRACT

In this paper, an analytical procedure for free vibrations of shear-deformable two-layer beams with interlayer slip is developed. The effect of transverse shear flexibility of two layers is taken into account in a general way by assuming that each layer behaves as a Timoshenko beam element. Therefore, the layers have independent shear strains that depend indeed on their own shear modulus. This is the main improvement of the proposed model compared to existing models where the transverse shear flexibility is ignored or taken into account in a simplified way in which the shear strains of both layers are assumed to be equal whatever the shear modulus of the layers. In the proposed model, the two layers are connected continuously and the partial interaction is considered by assuming a continuous relationship between the interface shear flow and the corresponding slip. Based on these key assumptions, the governing differential equation of the problem is derived using Hamilton's principle and is analytically solved. The solutions for the eigenfrequencies and eigenmodes of four single span two-layer beams with classical Euler boundary conditions, i.e. *pinned-pinned*, *clamped-clamped*, *clamped-pinned* and *clamped-free*, are presented. Next, some numerical applications dealing with these four beams are carried out in order to compare the eigenfrequencies obtained with the proposed model against two existing models which consider different kinematic assumptions. Finally, a parametric study is conducted with the aim to investigate the influence of varying material and geometric parameters on the eigenfrequencies, such as shear stiffness of the connectors, span-to-depth ratios, flexural-to-shear moduli ratios and layer shear moduli ratios.

1. Introduction

Two-layer composite members are widely used in civil engineering. Steel-concrete composite beams and nailed timber members are two possible technical solutions based on coupling two layers made up of different materials with the aim of optimizing their mechanical behaviour within a unique member. The mechanical behavior of composite members depends to a large extent on the behavior of the connecting devises. If the layers are connected by means of strong adhesives, the mechanical assumption of a perfect bond between the layers is reasonable. However, the layers are often connected by mean of connectors (shear studs, nails, etc.) which are not rigid. Therefore, relative displacements (interlayer slip)

* Corresponding author. Tel.: +33 223238394.
E-mail address: quang-huy.nguyen@insa-rennes.fr (Q.-H. Nguyen).

0022-460X/$ - see front matter © 2012 Elsevier Ltd. All rights reserved.
doi:10.1016/j.jsv.2012.01.034

generally occur at the interface of the two layers, resulting in the so-called partial interaction. Whereas the transverse separation is often small in practice and can thus be neglected [1], the interface slip will often influence the behavior of the composite beams in so much it must be considered for a more reliable modeling analysis.

Several theoretical and numerical models characterized by different levels of approximation have been proposed. At the early stage of the use of two-layer beams, full interaction (perfect bond) was assumed in the design and, accordingly, such beams have been analyzed using classical 1-D model based on Euler–Bernoulli beam theory as homogeneous beams. A review of several beam and plate theories for vibration, wave propagations, buckling and post-buckling can be found in [2,3]. Particular attention was given to models that account for transverse shear deformation. It is well-known that, in the Euler–Bernoulli model, the transverse shear effects on cross-section deformation are not accounted for and therefore this model yields better results for slender beams than for short beams. Timoshenko developed a first-order shear deformation theory which assumes a constant shear deformation distribution over the cross-section [4,5]. However, according to 3-D elasticity theory, the shear strains vary at least quadratically over the cross-section depth and therefore the so-called shear correction factors are needed in order to get the structural responses closer to the exact solutions. Several refined higher-order beam theories were proposed in which transverse shear deformations have been considered without any shear correction factor (see for example [6–8]). A review on different higher-order shear deformation theories for the analysis of isotropic and laminated beams was presented by Ghugal and Shimpi [9]. The higher-order theories are often used for the analysis of multilayered laminated composite beams without interlayer slip but these theories have not been applied to two-layer composite beams with partial interaction.

It is until mid-fifties that Newmark et al. [10] pointed out the influence of partial interaction on the overall elastic behaviour of steel-concrete composite beams. In their seminal contribution, they proposed the first formulation of an elastic theory for composite beams with partial interaction in which both layers were assumed to follow the kinematic assumptions of Euler–Bernoulli beam theory. This formulation is usually referred to as Newmark's model, and was extensively used from that time by many authors to formulate theoretical models for the static response of two-layer beams in the linear elastic range [11–15] as well as in the linear visco-elastic range [16–19]. In addition, several numerical models based on the same basic assumptions of Newmark's model have been developed to investigate the behavior of composite beams with partial interaction in the nonlinear range (for material nonlinearity, see, e.g. [20–24], for geometric nonlinearity, see, e.g. [25–28]). The Newmark's model was further developed to deal with the dynamic response of composite beams [29,30,15].

By employing the Euler–Bernoulli beam theory, Newmark's model neglects the transverse shear deformation of the layers. Therefore, the beam stiffness is overestimated which leads to underestimation of the deflection and overestimation of the natural frequencies. This overestimation is significantly pronounced in the case of short and thick layered beams where span-to-depth ratio is small and the bending-to-shear stiffness ratio is large. The theory of two-layer beams with interlayer slip recently moved towards the introduction of transverse shear deformation of both layers according to the Timoshenko beam theory. The earliest use of the Timoshenko beam hypotheses in the analysis of composite beams with interlayer slip has been proposed by Murakami [31]. Few contributions, dealing with two-layer beams with partial interaction and including transverse shear effects, have been recently proposed [32–37]. In the work of Xu and Wu [33], the transverse shear effects were taken into account using Timoshenko kinematic assumption for each layer. However, to simplify the problem and in order to provide a closed-form solution for static, dynamic and buckling behaviours, they imposed a kinematic constraint where both layers are assumed to have the same transverse shear strain. Schnabl et al. [34] developed a consistent analytical model for linear static behaviour of layered beams. In their model, each layer is assumed to behave as a Timoshenko beam element therefore the cross-section rotations of the layers are generally different from each other. Whereas, the governing equations of the problem are provided, only a solution strategy of these equations is outlined and no analytical expressions are reported. Recently, Nguyen et al. [18] presented a full closed-form solution for linear static response of two-layer beams where analytical expressions for all mechanical variables are derived. Lastly, the exact buckling solution for two-layer Timoshenko beams has been developed by Le Grognec et al. [38].

While the transversal shear effects have been taken into account in the calculation of deflection and buckling load of two-layer Timoshenko beam as mentioned in the references above, there are only few investigations concerning the influence of transversal shear on the natural frequencies of such beams. To the best knowledge of the authors, there are two models available in the literature. The first one is developed by Berczyński and Wróblewski [39]. In this model, the authors considered the Timoshenko beam theory for each layer and derived an implicit twelfth order equation for the determination of the eigenvalues. However, the solution for the eigenvalues has been presented in a general form without any details. The second one is developed by Wu et al. [32] where Timoshenko kinematic assumptions are adopted but the same transverse shear strain for both layers is imposed. The authors derived explicit solutions for the eigenfrequencies of two-layer beams with partial interaction. Note that imposing equal transverse shear strain seems to be a strong assumption especially in the case when a large difference between the shear stiffness of the two layers exists. This will be pointed out and discussed in Section 3.

In this paper, an exact dynamic analysis procedure for the free vibration of shear-deformable two-layer beams with interlayer slip is developed. The effect of transverse shear deformation of two layers is taken into account in a general way by assuming that each layer behaves as a Timoshenko beam element. Accordingly, the main improvement of the proposed model, compared to Wu et al. model [32], is that allows the layers to have independent shear strains which depend indeed on their shear modulus. The two layers are connected continuously and the partial interaction is modeled by assuming

a respective continuous relationship between the interface shear flow and the corresponding slip. Based on these key assumptions, the governing differential equations of the problem are derived using Hamilton's principle and are analytically solved. The solution procedure for the determination of the eigenfrequencies and eigenmodes of four single span two-layer beams with classical Euler boundary conditions, i.e. *pinned-pinned*, *clamped-clamped*, *clamped-pinned* and *clamped-free*, is presented. Next, some numerical applications dealing with these four beams are carried out in order to compare the eigenfrequencies obtained by the proposed model against two existing models which consider different kinematic assumptions, i.e. Girhammar and Pan model [29] and Wu et al. model [32]. Finally, a parametric study is conducted with the aim to study the influence of varying material and geometric parameters on the eigenfrequencies, such as the shear stiffness of the connectors, span-to-depth ratios, flexural-to-shear moduli ratios and layer shear moduli ratios.

2. Free vibration of two-layer Timoshenko beams with interlayer slip

The transverse vibration of two-layer composite beams with partial interaction is considered. Fig. 1 shows a two-layer composite beam of length L with shear connectors which are supposed to be uniformly distributed along the longitudinal direction. Each layer has its own geometric and material properties with a subscript i denoting the layer i ($i=a, b$). Thus each layer has constant cross-section A_i, second moment of area I_i, mass per unit length m_i, Young's modulus E_i, shear modulus G_i, shear correction factor k_i and distance between modulus-weight centroid and layer interface h_i. The shear bond stiffness of the continuous connections is constant and denoted by k_{sc}.

The following general assumptions are made when developing the governing differential equations of motion of a two-layer beam:

(i) The rotational inertia is neglected.
(ii) Slip can occur at the contact interface but no transverse separation, i.e. two layers have the same transverse displacement.
(iii) Kinematic assumptions of Timoshenko beam theory are adopted for each layer. Therefore, both layers do not have the same rotation and curvature (This is the main difference compared to Wu et al. model [32] where the rotations and curvatures are enforced to be equal.)
(iv) All displacements and strains are small so that the theory of linear elasticity applies.
(v) In the case of concentrated mechanical shear connections like shear studs, bolts and nails, it is assumed that the discrete connection can be replaced by a continuous connection with an equivalent distributed bond stiffness calculated by dividing the stiffness of a single concentrated connector by their spacing along the beam.

It worth to mention that the first assumption is adopted considering the conclusions of a recent paper by Xu and Wu [33] where after several parametric studies, they pointed out that the effect of shear deformation on the frequency is more significant that of rotatory inertia.

Based on the assumptions (ii), (iii) and (iv), the interlayer slip, denoted by g (cf. Fig. 2), can be expressed as follows:

$$g = u_a - u_b - h_a\theta_a - h_b\theta_b \tag{1}$$

where u_i and θ_i ($i=a, b$) are the axial displacement of the modulus-weighted centroid and the rotation of layer i, respectively.

2.1. Theoretical formulation

The total elastic energy U of the studied two-layer beam is expressed as

$$U = \sum_{i=a,b} \frac{1}{2}\int_L (EA_i(u_{i,x})^2 + EI_i(\theta_{i,x})^2 + GA_i(\theta_i + v_{,x})^2)\,\mathrm{d}x + \frac{1}{2}\int_L k_{sc}g^2\,\mathrm{d}x \tag{2}$$

where $EA_i = E_iA_i$; $EI_i = E_iI_i$; $GA_i = k_iG_iA_i$; and $(\,)_{,x}$ stands for the spatial derivative.

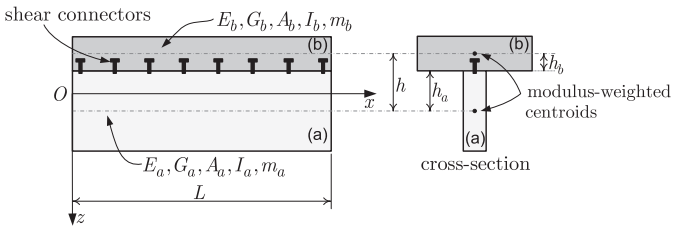

Fig. 1. The coordinate system and notation for a two-layer composite beam.

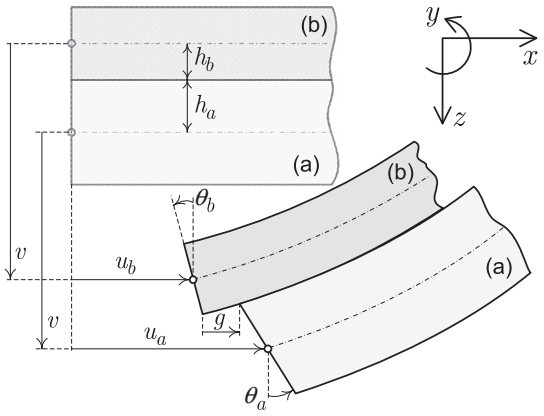

Fig. 2. Kinematic of a two-layer beam.

The total kinetic energy T of the studied two-layer beam is given by

$$T = \frac{1}{2}\int_L m\dot{v}^2 \, \mathrm{d}x \tag{3}$$

where $m = m_a + m_b$; v is the common flexural displacement of the two layers; and the dot denotes the differentiation with respect to the time t.

The problem of free vibration can now be formulated using Hamilton's principle, i.e.

$$\int_{t_1}^{t_2} (\delta T - \delta U)\, \mathrm{d}t = 0 \tag{4}$$

Introducing Eqs. (2) and (3) in the above equation and integrating by parts lead to

$$\begin{aligned}\int_{t_1}^{t_2}\int_L \{&(EA_a u_{a,xx} - k_{sc}g)\delta u_a + (EA_b u_{b,xx} + k_{sc}g)\delta u_b + [EI_a\theta_{a,xx} + GA_a(v_{,x} + \theta_a) + h_a k_{sc}g]\delta\theta_a \\ &+ [EI_b\theta_{b,xx} + GA_b(v_{,x} + \theta_b) + h_b k_{sc}g]\delta\theta_b + [GA_a(v_{,xx} + \theta_{a,x}) + GA_b(v_{,xx} + \theta_{b,x}) - m\ddot{v}]\delta v\}\, \mathrm{d}x\, \mathrm{d}t \\ &= \int_{t_1}^{t_2} [N_a\delta u_a + N_b\delta u_b + M_a\delta\theta_a + M_b\delta\theta_b + (T_a + T_b)\delta v]_0^L \, \mathrm{d}t\end{aligned} \tag{5}$$

It should be noted that the variations δu_i, $\delta\theta_i$ and δv must vanish at the bounds of integration t_1 and t_2 according to Hamilton's principle. Since the variations δu_i, $\delta\theta_i$ and δv are arbitrary, the governing differential equations of motion in free vibration follow from Eq. (5) as

$$EA_a u_{a,xx} - k_{sc}g = 0 \tag{6a}$$

$$EA_b u_{b,xx} + k_{sc}g = 0 \tag{6b}$$

$$EI_a\theta_{a,xx} + GA_a(v_{,x} + \theta_a) + h_a k_{sc}g = 0 \tag{6c}$$

$$EI_b\theta_{b,xx} + GA_b(v_{,x} + \theta_b) + h_b k_{sc}g = 0 \tag{6d}$$

$$GA_a(v_{,xx} + \theta_{a,x}) + GA_b(v_{,xx} + \theta_{b,x}) - m\ddot{v} = 0 \tag{6e}$$

2.2. Derivation of the governing differential equation of motion in free vibration and solution

Eqs. (1) and (6) may be combined together in order to provide one single differential equation involving only the transverse displacement v. For instance, from the relations (6c), (6d) and (6e) we can write $\theta_{i,x}$ ($i = a,b$) as a function of v, g and their derivatives as follows:

$$\theta_{a,x} = \frac{k_{sc}\left(\dfrac{h_a GA_a}{EI_a} + \dfrac{h_b GA_b}{EI_b}\right)g_{,x} - GA_\infty v_{,xxxx} + m\ddot{v}_{,xx} - \dfrac{GA_b}{EI_b}m\ddot{v}}{GA_a\left(\dfrac{GA_a}{EI_a} - \dfrac{GA_b}{EI_b}\right)} - v_{,xx} \tag{7}$$

$$\theta_{b,x}=\frac{k_{sc}\left(\frac{h_aGA_a}{EI_a}+\frac{h_bGA_b}{EI_b}\right)g_{,x}-GA_\infty v_{,xxxx}+m\ddot{v}_{,xx}-\frac{GA_a}{EI_a}m\ddot{v}}{GA_b\left(\frac{GA_b}{EI_b}-\frac{GA_a}{EI_a}\right)}-v_{,xx} \tag{8}$$

where $GA_\infty=GA_a+GA_b$ (shear stiffness of cross-section with full interaction). By inserting Eqs. (7) and (8) into (6c), we obtain:

$$\frac{k_{sc}}{GA_\infty}\left(\frac{h_aGA_a}{EI_a}+\frac{h_bGA_b}{EI_b}\right)g_{,xxx}-\frac{hk_{sc}GA}{EI_aEI_b}g_{,x}=v_{,xxxxxx}-\frac{GA}{EI}v_{,xxxx}-\frac{m}{GA_\infty}\ddot{v}_{,xxxx}+\frac{m}{GA_\infty}\left(\frac{GA_a}{EI_a}+\frac{GA_b}{EI_b}\right)\ddot{v}_{,xx}-\frac{m\,GA}{EI_aEI_b}\ddot{v} \tag{9}$$

in which $GA=GA_aGA_b/(GA_a+GA_b)$ and $EI=EI_aEI_b/(EI_a+EI_b)$.

Next, Eq. (1) is differentiated twice and combined with (6a) and (6b) to provide

$$g_{,xx}=\frac{k_{sc}}{EA}g-h_a\theta_{a,xx}-h_b\theta_{b,xx} \tag{10}$$

where $EA=EA_aEA_b/EA_a+EA_b$. Introducing Eqs. (7) and (8) into the above equation leads to

$$\begin{aligned}&\left[\frac{GA_a}{EI_a}-\frac{GA_b}{EI_b}+k_{sc}\left(\frac{h_aGA_a}{EI_a}+\frac{h_bGA_b}{EI_b}\right)\left(\frac{h_a}{GA_a}-\frac{h_b}{GA_b}\right)\right]g_{,xx}-\frac{k_{sc}}{EA}\left(\frac{GA_a}{EI_a}-\frac{GA_b}{EI_b}\right)g\\&=\left(\frac{h_a}{GA_a}-\frac{h_b}{GA_b}\right)(GA_\infty v_{,xxxxx}-m\ddot{v}_{,xxx})+\left(\frac{h_aGA_b}{GA_aEI_b}-\frac{h_bGA_a}{GA_bEI_a}\right)m\ddot{v}_{,x}+h\left(\frac{GA_a}{EI_a}-\frac{GA_b}{EI_b}\right)v_{,xxx}\end{aligned} \tag{11}$$

Note that the differential Eqs. (9) and (11) involve both interlayer slip g and the flexural displacement v. By eliminating $g_{,xxx}$ and $g_{,x}$ from these two equations, we obtain one single differential equation involving only v. The sought equation takes the following form:

$$v_{,xxxxxxxx}-\xi_1v_{,xxxxxx}+\xi_2v_{,xxxx}-\xi_3\ddot{v}_{,xxxxxx}+\xi_4\ddot{v}_{,xxxx}-\xi_5\ddot{v}_{,xx}+\xi_6\ddot{v}=0 \tag{12}$$

where

$$\xi_1=k_{sc}\left(\frac{1}{EA}+\frac{h_a^2}{EI_a}+\frac{h_b^2}{EI_b}\right)+\frac{GA}{EI} \tag{13}$$

$$\xi_2=\frac{k_{sc}GA\left(EI_a+EI_b+h^2EA\right)}{EAEI_aEI_b} \tag{14}$$

$$\xi_3=\frac{m}{GA_\infty} \tag{15}$$

$$\xi_4=\frac{m}{GA_\infty}\left[\frac{GA_a}{EI_a}+\frac{GA_b}{EI_b}+k_{sc}\left(\frac{1}{EA}+\frac{h_a^2}{EI_a}+\frac{h_b^2}{EI_b}\right)\right] \tag{16}$$

$$\xi_5=\frac{mk_{sc}}{GA_\infty EA}\left(\frac{GA_a}{EI_a}+\frac{GA_b}{EI_b}\right)+\frac{mGA}{EI_aEI_b}\left[k_{sc}\left(\frac{h_a^2}{GA_a}+\frac{h_b^2}{GA_b}\right)+1\right] \tag{17}$$

$$\xi_6=\frac{mk_{sc}GA}{EAEI_aEI_b} \tag{18}$$

According to the method of separation of variables, the general solution of Eq. (12) is assumed to take the following form:

$$v(x,t)=\sum_n\phi_n(x)\varphi_n(t) \tag{19}$$

where ϕ_n are the eigenmodes which depend on the boundary conditions, and φ_n are the time functions of the free vibration. Introducing (19) in (12) leads to

$$\left(\frac{d^8\phi_n}{dx^8}-\xi_1\frac{d^6\phi_n}{dx^6}+\xi_2\frac{d^4\phi_n}{dx^4}\right)\varphi_n-\left(\xi_3\frac{d^6\phi_n}{dx^6}-\xi_4\frac{d^4\phi_n}{dx^4}+\xi_5\frac{d^2\phi_n}{dx^2}-\xi_6\phi_n\right)\frac{d^2\varphi_n}{dt^2}=0 \tag{20}$$

from which the following ordinary differential equations are obtained:

$$\frac{d^2\varphi_n}{dt^2}+\omega_n^2\varphi_n=0 \tag{21}$$

$$\frac{d^8\phi_n}{dx^8}-(\xi_1-\omega_n^2\xi_3)\frac{d^6\phi_n}{dx^6}+(\xi_2-\omega_n^2\xi_4)\frac{d^4\phi_n}{dx^4}+\omega_n^2\xi_5\frac{d^2\phi_n}{dx^2}-\omega_n^2\xi_6\phi_n=0 \tag{22}$$

Eq. (21) represents harmonic vibration, i.e.

$$\varphi_n(t) = e^{i\omega_n t} \tag{23}$$

which is consistent with the fact that a conservative system has a constant energy [29]. The general solution of the homogenous differential Eq. (22) is based on the root characteristic of its eigenequation:

$$(\lambda^2)^4 - (\xi_1 - \omega_n^2\xi_3)(\lambda^2)^3 + (\xi_2 - \omega_n^2\xi_4)(\lambda^2)^2 + \omega_n^2\xi_5\lambda^2 - \omega_n^2\xi_6 = 0 \tag{24}$$

Note that this is a quartic equation of λ^2 which can indeed be solved in an analytical way (see Appendix A). Furthermore, it can be proved that for the ordinary values of geometrical and material parameters and whatever the value of ω^2, this quartic equation has four real roots of which one is negative ($\lambda_1^2 < 0$) while the other three are positives ($\lambda_2^2 > 0$, $\lambda_3^2 > 0$ and $\lambda_4^2 > 0$). While the proof is not straightforward, for sake of brevity, no details are given here. The general solution of the differential Eq. (22), consequently, has the form:

$$\phi_n(x) = c_1 \sin(\lambda_1 x) + c_2 \cos(\lambda_1 x) + c_3 e^{\lambda_2 x} + c_4 e^{-\lambda_2 x} + c_5 e^{\lambda_3 x} + c_6 e^{-\lambda_3 x} + c_7 e^{\lambda_4 x} + c_8 e^{-\lambda_4 x} \tag{25}$$

where c_i $(i = 1, 2, \ldots, 8)$ are constants of integration determined by the boundary conditions. In the following, three classical boundary conditions at the beam ends, which are pinned supported (P), clamped (C) and free (F), are considered.

(a) For the *pinned end*, the boundary conditions $v = M_a = M_b = N_a = 0$ yield

$$\left.\begin{aligned} &\phi_n = 0 \\ &\frac{d^2\phi_n}{dx^2} = 0 \\ &\frac{d^4\phi_n}{dx^4} = 0 \\ &\frac{d^6\phi_n}{dx^6} = 0 \end{aligned}\right\} \tag{26}$$

(b) For the *clamped end*, the boundary conditions $v = \theta_a = \theta_b = g = 0$ yield

$$\left.\begin{aligned} &\phi_n = 0 \\ &GA_\infty \frac{d^3\phi_n}{dx^3} + (\varsigma_1 + m\omega_n^2)\frac{d\phi_n}{dx} = 0 \\ &GA_\infty \frac{d^5\phi_n}{dx^5} + (\varsigma_1 + m\omega_n^2)\frac{d^3\phi_n}{dx^3} + \varsigma_2\frac{d\phi_n}{dx} = 0 \\ &GA_\infty \frac{d^7\phi_n}{dx^7} + (\varsigma_1 + m\omega_n^2)\frac{d^5\phi_n}{dx^5} + \varsigma_2\frac{d^3\phi_n}{dx^3} + \varsigma_3\frac{d\phi_n}{dx} = 0 \end{aligned}\right\} \tag{27}$$

where

$$\varsigma_1 = \frac{GA_a^2}{EI_a} + \frac{GA_b^2}{EI_b}$$

$$\varsigma_2 = \frac{GA_a^3}{EI_a^2} + \frac{GA_b^3}{EI_b^2} + k_{sc}\left(\frac{h_a GA_a}{EI_a} + \frac{h_b GA_b}{EI_b}\right)^2$$

$$\varsigma_3 = \frac{GA_a^4}{EI_a^3} + \frac{GA_b^4}{EI_b^3} + 2k_{sc}\left(\frac{h_a GA_a^2}{EI_a^2} + \frac{h_b GA_b^2}{EI_b^2}\right)\left(\frac{h_a GA_a}{EI_a} + \frac{h_b GA_b}{EI_b}\right) + k_{sc}^2\left(\frac{1}{EA} + \frac{h_a^2}{EI_a} + \frac{h_b^2}{EI_b}\right)\left(\frac{GA_a h_a}{EI_a} + \frac{GA_b h_b}{EI_b}\right)^2$$

(c) For the *free end*, the boundary conditions $M_a = M_b = N_a = N_b = T_a = T_b = 0$ yield

$$\left.\begin{aligned} &GA_\infty \frac{d^2\phi_n}{dx^2} + m\omega_n^2\phi_n = 0 \\ &GA_\infty \frac{d^4\phi_n}{dx^4} + (\varsigma_1 + m\omega_n^2)\frac{d^2\phi_n}{dx^2} = 0 \\ &GA_\infty \frac{d^6\phi_n}{dx^6} + (\varsigma_1 + m\omega_n^2)\frac{d^4\phi_n}{dx^4} + \varsigma_2\frac{d^2\phi_n}{dx^2} = 0 \\ &GA_\infty \frac{d^5\phi_n}{dx^5} + (\varsigma_1 + m\omega_n^2)\frac{d^3\phi_n}{dx^3} + \varsigma_4\left(GA_\infty \frac{d^3\phi_n}{dx^3} + m\omega_n^2\frac{d\phi_n}{dx}\right) = 0 \end{aligned}\right\} \tag{28}$$

where

$$\varsigma_4 = \frac{\frac{GA_a^2 h_a}{EI_a^2} + \frac{GA_b^2 h_b}{EI_b^2}}{\frac{h_a GA_a}{EI_a} + \frac{h_b GA_b}{EI_b}} + k_{sc}\left(\frac{1}{EA} + \frac{h_a^2}{EI_a} + \frac{h_b^2}{EI_b}\right)$$

In this paper, four classical Euler boundary conditions, which are pinned-pinned (PP), clamped-clamped (CC), clamped-pinned (CP) and clamped-free (CF), are considered. Indeed, eight boundary conditions are necessary to determinate the integration constants c_i $(i=1,2,\ldots,8)$ which lead to the frequencies and modes shapes for free vibrations. By substituting Eq. (25) into the boundary conditions (26), (27) and (28), the following homogeneous algebraic equation is obtained:

$$\mathbf{A}\mathbf{c} = \mathbf{0} \tag{29}$$

where $\mathbf{c} = [c_1\ c_2\ c_3\ c_4\ c_5\ c_6\ c_7\ c_8]^{\mathrm{T}}$; and the elements of the matrix $\mathbf{A}$ depend on the specified boundary conditions. For example, in case of pinned-pinned beam (simply supported), $\mathbf{A}$ takes the following form

$$\mathbf{A} = \begin{bmatrix} 0 & 1 & 1 & 1 & 1 & 1 & 1 & 1 \\ 0 & -\lambda_1^2 & \lambda_2^2 & \lambda_2^2 & \lambda_3^2 & \lambda_3^2 & \lambda_4^2 & \lambda_4^2 \\ 0 & \lambda_1^4 & \lambda_2^4 & \lambda_2^4 & \lambda_3^4 & \lambda_3^4 & \lambda_4^4 & \lambda_4^4 \\ 0 & -\lambda_1^6 & \lambda_2^6 & \lambda_2^6 & \lambda_3^6 & \lambda_3^6 & \lambda_4^6 & \lambda_4^6 \\ \sin(\lambda_1 L) & \cos(\lambda_1 L) & e^{\lambda_2 L} & e^{-\lambda_2 L} & e^{\lambda_3 L} & e^{-\lambda_3 L} & e^{\lambda_4 L} & e^{-\lambda_4 L} \\ -\lambda_1^2 \sin(\lambda_1 L) & -\lambda_1^2 \cos(\lambda_1 L) & \lambda_2^2 e^{\lambda_2 L} & \lambda_2^2 e^{-\lambda_2 L} & \lambda_3^2 e^{\lambda_3 L} & \lambda_3^2 e^{-\lambda_3 L} & \lambda_4^2 e^{\lambda_4 L} & \lambda_4^2 e^{-\lambda_4 L} \\ \lambda_1^4 \sin(\lambda_1 L) & \lambda_1^4 \cos(\lambda_1 L) & \lambda_2^4 e^{\lambda_2 L} & \lambda_2^4 e^{-\lambda_2 L} & \lambda_3^4 e^{\lambda_3 L} & \lambda_3^4 e^{-\lambda_3 L} & \lambda_4^4 e^{\lambda_4 L} & \lambda_4^4 e^{-\lambda_4 L} \\ -\lambda_1^6 \sin(\lambda_1 L) & -\lambda_1^6 \cos(\lambda_1 L) & \lambda_2^6 e^{\lambda_2 L} & \lambda_2^6 e^{-\lambda_2 L} & \lambda_3^6 e^{\lambda_3 L} & \lambda_3^6 e^{-\lambda_3 L} & \lambda_4^6 e^{\lambda_4 L} & \lambda_4^6 e^{-\lambda_4 L} \end{bmatrix} \tag{30}$$

In order to obtain a non-trivial solution for the constants c_i $(i=1,2,\ldots,8)$, the determinant of the matrix $\mathbf{A}$ needs to vanish:

$$\det \mathbf{A} = 0 \tag{31}$$

Eq. (31) is the so-called frequency equation which enables us to compute the eigenfrequencies of the four Euler beam cases considered in this paper. However, it should be noted that this equation is transcendental with respect to the frequency ω_n. Therefore, an iterative procedure is necessary to find the roots. The iteration is conveniently carried out in the following way:

(1) assume a frequency increment $\Delta\omega_n$ and set $\omega_n^j = \omega_n^{j-1} + \Delta\omega_n$ in which $\omega_n^0 = 0$;
(2) determinate λ_1, λ_2, λ_3 and λ_4 by solving Eq. (20) according to Appendix A;
(3) calculate $\det \mathbf{A}^j$ and if $(\det \mathbf{A}^{j-1} \det \mathbf{A}^j) < 0$ then $\Delta\omega_n = -\Delta\omega_n/2$;
(4) check for convergence: if $|\det \mathbf{A}^j| \leq$ specified tolerance then end iteration. Else set $j = j+1$ and go back to step (1).

Once an eigenfrequency for a defined set of boundary conditions is known, its associated eigenmode can be determined. This is done by removing one of the eight equations for boundary conditions. This leaves seven equations with eight unknowns which may be solved by assuming the value of one of the constants c_i $(i=1,2,\ldots,8)$.

3. Numerical examples

The aim of this section is to validate the solution procedure for the determination of the eigenfrequencies proposed above. To do so, some numerical applications dealing with four single-span two-layer beams are carried out in order to compare the eigenfrequencies obtained by the proposed model against two existing models which consider different kinematic assumptions. The first model, which employs Euler–Bernoulli kinematic for both layers, has been proposed by Girhammar and Pan [29]. The second one, which adopts Timoshenko kinematic and imposes equal shear strains for two layers, is Wu et al. model [32]. Next, a parametric analysis is performed to study the influence of both shear flexibility and partial interaction on the eigenfrequencies of the two-layer beams.

3.1. Comparison with existing models

The comparison is performed on four single-span two-layer beams which correspond to four classical Euler boundary conditions, i.e. pinned-pinned (PP), clamped-clamped (CC), clamped-pinned (CF) and clamped-free (CF) (cf. Fig. 3). The geometrical and mechanical properties of the two-layer beams are characterized by the following parameters: L=4000 mm; $h_a = 75$ mm; $b_a = 50$ mm; $h_b = 25$ mm; $b_b = 300$ mm; $E_a = 8000$ MPa; $G_a = 5000$ MPa; $E_b = 12,000$ MPa; $G_b = 8000$ MPa; $m_a = 6$ kg/m; $m_b = 37.5$ kg/m; and $k_{sc} = 50$ MPa. Note that, except for the shear modulus G_a and G_b, these parameters are taken from the numerical example in [30].

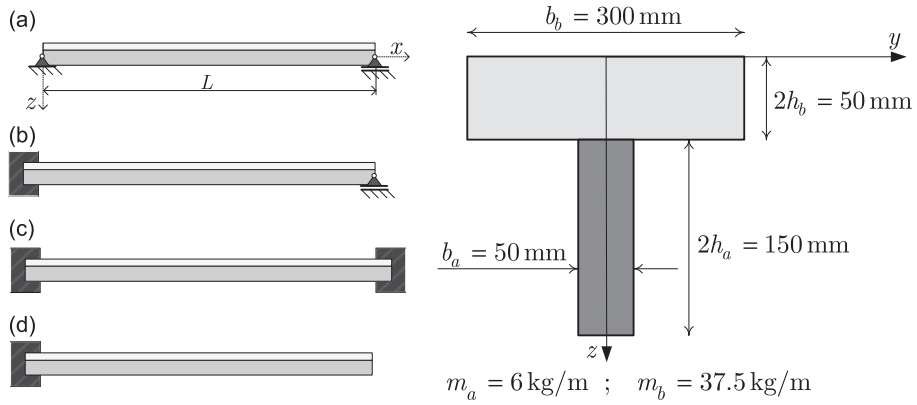

Fig. 3. Four considered single-span two-layer beams; dimensions of cross-section.

Table 1
Comparison of eigenfrequencies of simply supported two-layer beam.

	Eigenfrequency [rad/s] (relative error)		
	Proposed model	Girhammar and Pan model	Wu et al. model
Mode 1	1.9368	1.9640 (1.4%)	1.9584 (1.1%)
Mode 2	6.1730	6.3678 (3.2%)	6.3505 (2.9%)
Mode 3	11.9821	12.6273 (5.4%)	12.5676 (4.9%)
Mode 4	19.3632	20.9251 (8.1%)	20.7729 (7.3%)
Mode 5	28.2310	31.3910 (11.2%)	31.0638 (10.0%)
Mode 6	49.9397	59.0374 (18.2%)	57.9406 (16.0%)
Mode 7	62.3059	76.2604 (22.4%)	74.4643 (19.5%)
Mode 8	75.7420	95.7622 (26.4%)	92.9761 (22.7%)
Mode 9	90.0801	117.5471 (30.5%)	113.4126 (25.9%)
Mode 10	105.2750	141.6176 (34.5%)	135.7039 (28.9%)

In Table 1, the first ten eigenfrequencies of the simply supported two-layer beam obtained with the proposed model are compared against those obtained with Girhammar and Pan model [29] as well as Wu et al. model [32]. It should be noted that the relative errors presented in this table are computed with respect to the frequencies obtained with our model. The reason is simply that our model is based on the general Timoshenko kinematic assumption for two layers. That is to say that the other two models are particular cases of the present one when one more kinematic constraint is imposed. As can be seen from Table 1, Girhammar and Pan model [29] predicts the largest eigenfrequencies. This is practically due to the fact that the shear flexibility of the cross-section is neglected (Euler–Bernoulli assumption). Indeed, we can see that when the shear flexibility of the cross-section is taken into account, the eigenfrequencies decrease. Further, by imposing the same shear strains for the two layers, Wu et al. model [32] gives eigenfrequencies which are closer to those of Girhammar and Pan model [29] than to our model. It must be pointed out that, in the present example, the two layers have completely different shear modulus and geometrical characteristics therefore the assumption of identical shear strains and rotations is too strong. We will see later in the parametric studies that when the two layers are geometrically and materially identical Wu et al. model [32] predicts the same results than our model because in this case the kinematic constraint added by Wu and his co-authors is automatically satisfied. Furthermore, the relative error is increasing with higher eigenmodes. For example, the tenth eigenfrequency is overestimated by 34.5% with Girhammar and Pan model [29] and by 28.9% with Wu et al. model [32] which seems to be important in our option. Finally, from the numerical results we can conclude that the proposed model predicts correctly the eigenfrequencies of the two-layer simply supported beams with interlayer slip taking into account the shear flexibility.

3.2. Parametric studies

In this section, the proposed model, which was validated above, is used to conduct the parametric studies to, firstly compare with two aforementioned models considering various beam end conditions, geometrical and material characteristics, secondly investigate the effects of shear bond stiffness and shear modulus on the eigenfrequency.

3.2.1. Influence of span-to-depth ratio on the eigenfrequency

In the present parametric study, except for the span length L which varies from 600 mm to 4000 mm, the other parameters are kept the same as in Section 3.1. The relative eigenfrequencies of the first eigenmode versus span-to-depth

ratio for PP, CF, CP and CC are plotted in Fig. 4. In fact, we are investigating the effect of transverse shear deformation on eigenfrequencies of the two-layer beams by varying the span-to-depth ratio. Therefore, the eigenfrequencies obtained by Girhammar and Pan model [29], denoted $\omega^{\mathrm{G-P}}$ in Fig. 4, are chosen as the reference values to compare with since this model ignores the transverse shear deformation as aforementioned. As can be seen from Fig. 4, whatever the value of L/h from 3 to 20, the first eigenfrequencies predicted by the proposed model are always smaller than the ones obtained with Wu et al. model [32]. That is to say that the effect of transverse shear deformation on eigenfrequencies is more pronounced in the proposed model. It can be explained by the fact that Wu et al. model [32] is less flexible compared to our model because of the imposed kinematic constraint. Further, for a given value of span-to-depth ratio, the eigenfrequency of the CC beam is more influenced by the transverse shear deformation than the other three beams. For example, for $L/h=3$, compared to Girhammar and Pan model [29], the proposed model gives the first eigenfrequency of CC, CP, CC and CF beams about 13.7%, 8.9%, 4% and 3.5% smaller, respectively.

3.2.2. *Influence of shear bond stiffness on the eigenfrequency*

In the present parametric study, except for the shear bond stiffness k_{sc} which varies from 0.01 MPa (no bond) to 100,000 MPa (perfect bond), the other parameters are kept the same as in Section 3.1. The relative eigenfrequencies of the first eigenmode versus shear stiffness of connectors for PP, CP, CC and CF are plotted in Fig. 5. Note that, the relative eigenfrequencies are computed with respect to the eigenfrequency of the regular Euler–Bernoulli beam (full interaction), noted $\omega_{\mathrm{full}}^{\mathrm{E-B}}$. For the sake of clarity, we give in the following, the formula of $\omega_{\mathrm{full}}^{\mathrm{E-B}}$ for the four classical Euler cases:

$$\omega_{\mathrm{full}}^{\mathrm{E-B}}=\left(\frac{\lambda}{L}\right)^2\sqrt{\frac{EI_{\mathrm{full}}}{m}}\quad\text{with }\lambda=\begin{cases}\pi & \text{For Pinned-Pinned}\\ 4.694 & \text{For Clamped-Pinned}\\ 7.43 & \text{For Clamped-Clamped}\\ 1.875 & \text{For Clamped-Free}\end{cases}\tag{32}$$

It can be observed from Fig. 5 that when two layers are not connected, the three models give almost the same first eigenfrequency which is nearly half of $\omega_{full}^{\mathrm{E-B}}$. Further, the shear flexibility does not influence on the eigenfrequency when

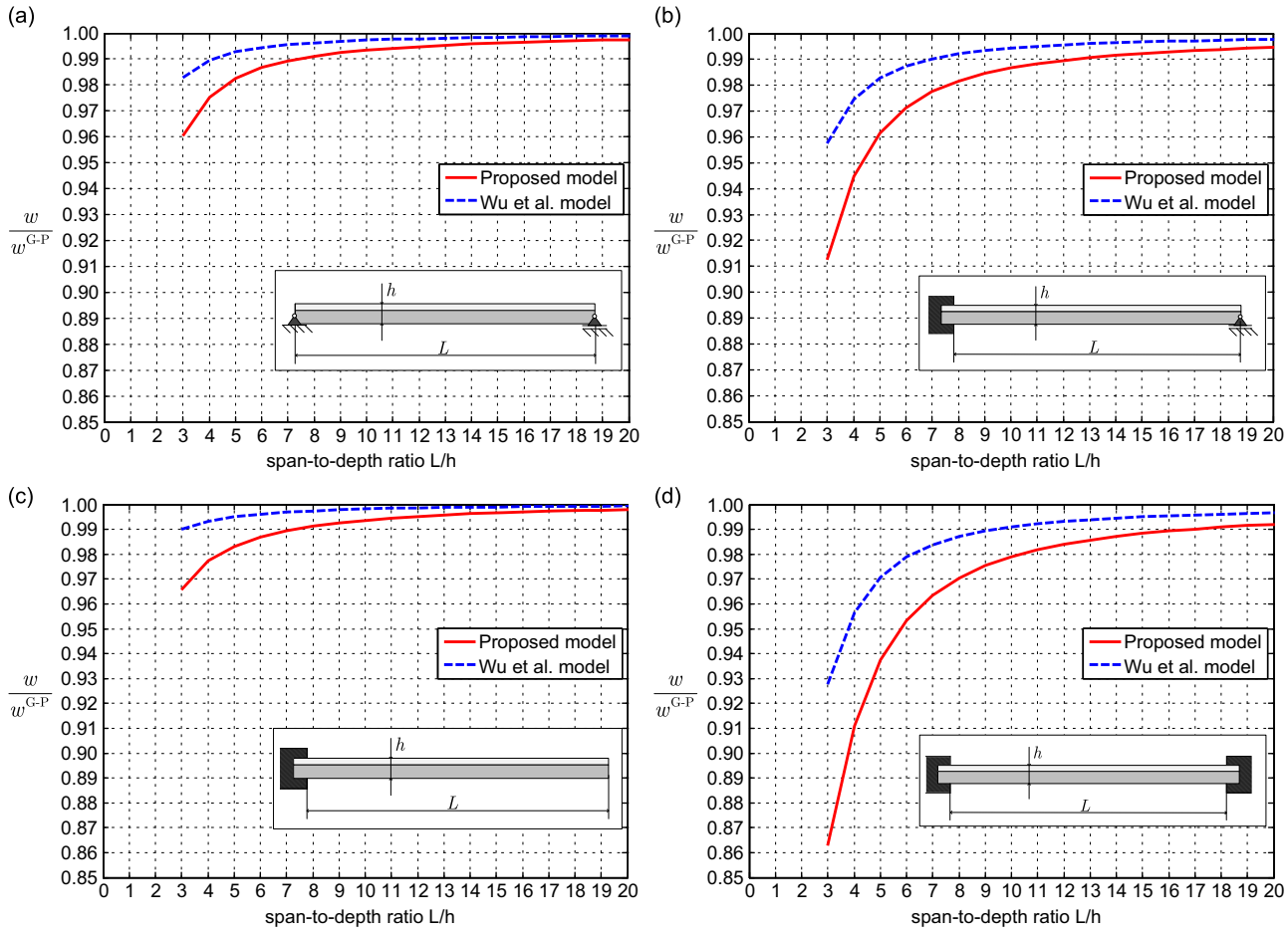

Fig. 4. Relative eigenfrequencies versus span-to-depth ratio for: (a) PP beam; (b) CP beam; (c) CF beam; and (d) CC beam.

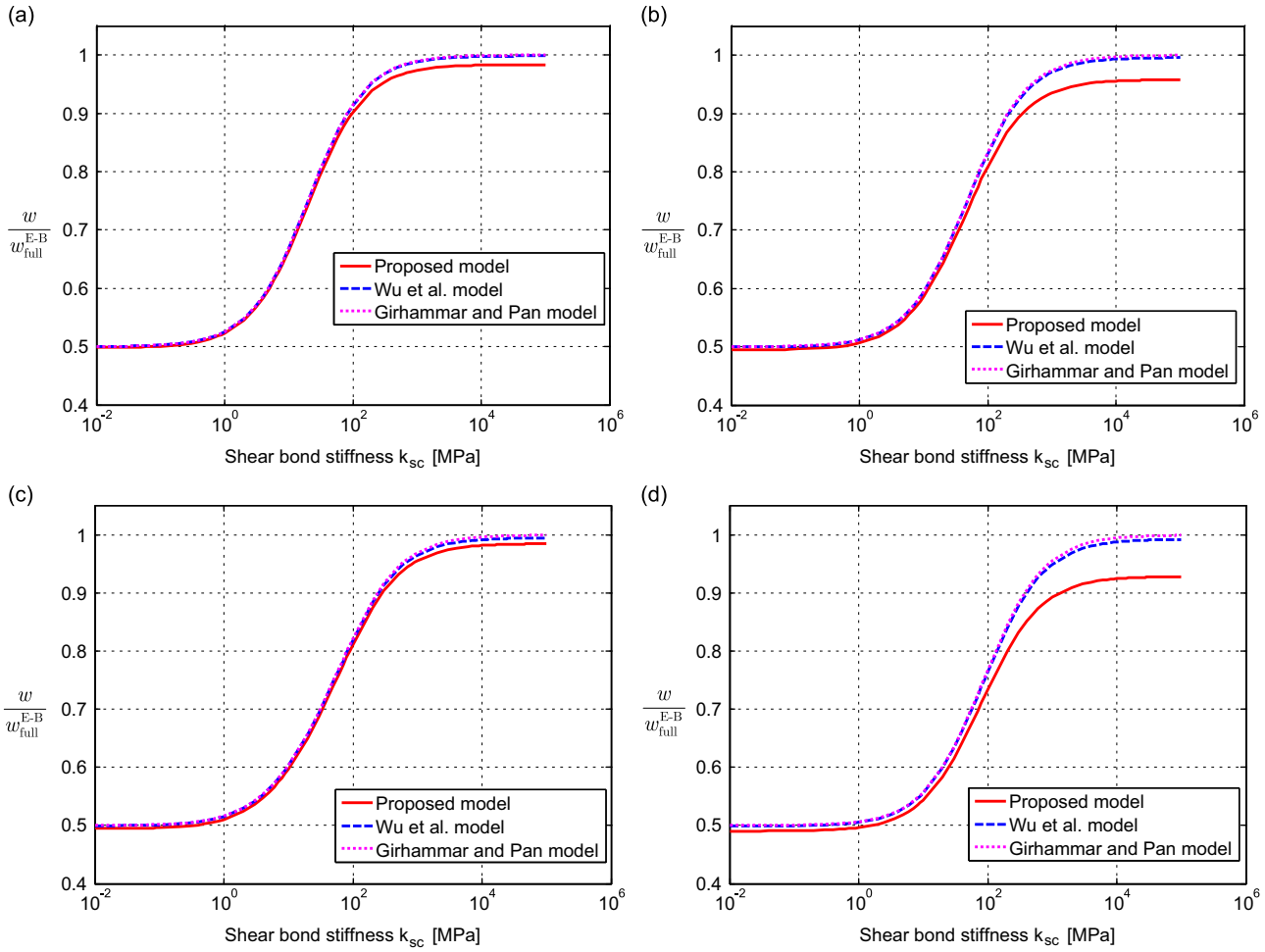

Fig. 5. Relative eigenfrequencies versus shear stiffness of connectors for: (a) PP beam; (b) CP beam; (c) CF beam; and (d) CC beam.

the layers are weakly connected, especially in case of PP and CF beams. Furthermore, the eigenfrequency predicted by Wu et al. model [32] remains close to the one predicted by Girhammar and Pan model [29] whatever the value of shear bond stiffness. This underlines the conclusion which was drawn previously that the assumption of equal shear strains, therefore rotations, of two layers is too strong. This makes the model close to Girhammar and Pan model [29] and the effect of transverse shear deformation is underestimated. However, in the proposed model, the shear flexibility starts to have more effects with strong bond, especially in case of CP and CC beams (cf. Fig. 5b and d). It is worth noting that although in case of perfect bond, the rotations of the layers obtained with the proposed model generally differ from each other, whenever we have the different geometrical and material characteristics of the layers. This is to say that it can therefore not identify with a single Timoshenko beam, except in the particular case of two identical layers.

3.2.3. *Influence of shear modulus on the eigenfrequency*

The influence of shear modulus on the eigenfrequency of a two-layer beam is now investigated. To do so, the geometrical parameters are kept the same as in Section 3.1 and we assume that two layers have identical material characteristics. Therefore in the present parametric study, the shear modulus G varies from 2400 MPa to 160,000 MPa and we set $E_a = E_b = E = 8000$ MPa. The relative eigenfrequencies of the first eigenmode versus G/E ratio for PP and CC are plotted in Fig. 6. As aforementioned, in order to study the effect of the shear flexibility, we decided to choose the eigenfrequency obtained with the Girhammar and Pan model [29] as a reference because the transverse shear deformation is not taken into account in this model. Thus, in Fig. 6, the symbol $\omega^{\text{G-P}}$ means the first eigenfrequency obtained with the Girhammar and Pan model [29]. As can be seen from Fig. 6a, with regard to Wu et al. model [32] and ours, the shear modulus does not much influence the eigenfrequency of the simply supported beam. For example, in the ordinary case where $G/E = 0.43$, the relative difference of the eigenfrequencies obtained are smaller than 1%. Further, as can be observed previously the proposed model gives a smaller eigenfrequency than the Wu et al. model [32]. Furthermore, when the G/E ratio tends towards to infinity, it has been found that the relative eigenfrequencies tend to 1. Regarding the CC beam, as in the case of the PP beam the same conclusions can be drawn when observing the Fig. 6b. However, the effect of transverse

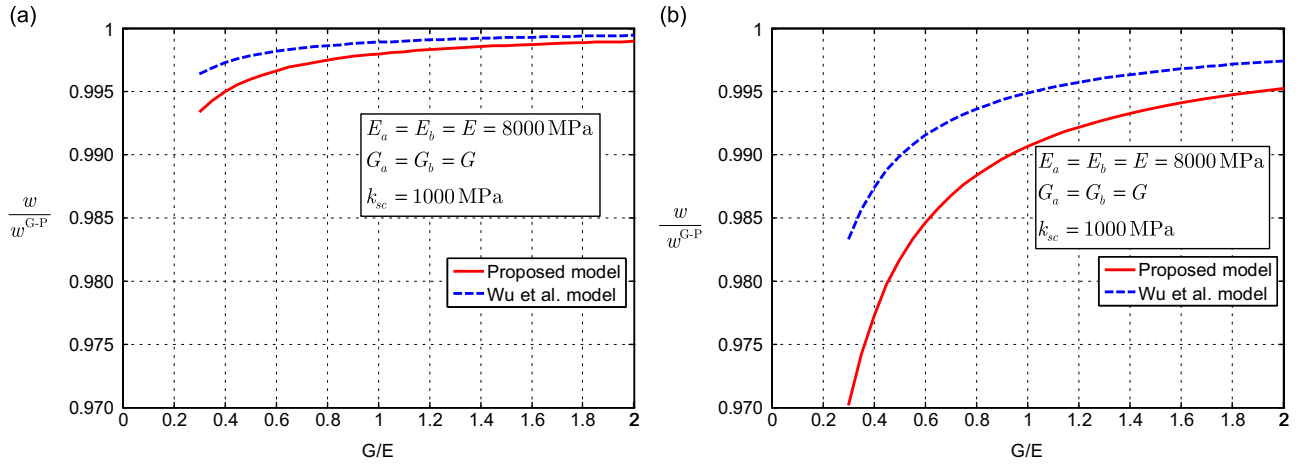

Fig. 6. Relative eigenfrequencies versus G/E ratio: (a) PP beam and (b) CC beam.

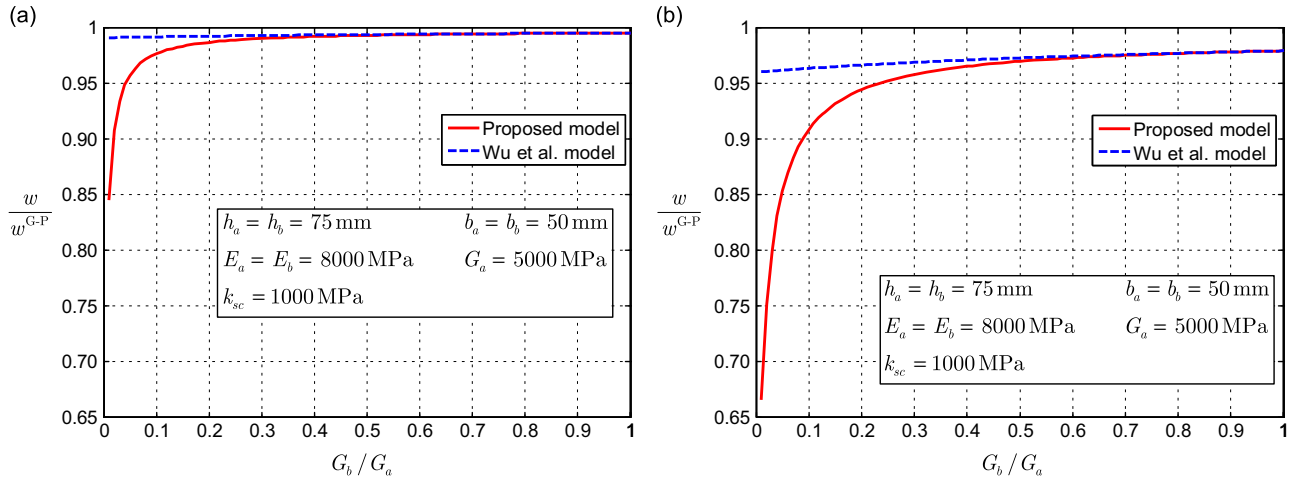

Fig. 7. Relative eigenfrequencies versus shear modulus ratio: (a) PP beam and (b) CC beam.

shear deformation is a bit more pronounced with a relative difference of the eigenfrequencies up to 3%. Further, it should be noted that the relative difference of the eigenfrequencies may become important for higher eigenmodes as can been seen in Table 1.

3.2.4. Influence of shear modulus ratio on the eigenfrequency

It is worth mentioning that the main improvement of our model compared to Wu et al. model [32] is to allow the layers to have independent shear strains from each other, which depend indeed on each shear modulus. Thus, it would be very interesting to see the results obtained with these two models when the shear moduli of the two layers are completely different. This why we conducted a parametric study in which two layers are chosen to be geometrically and materially identical except for the shear modulus. Therefore in the present parametric study, the other parameters are: $h_a = h_b = 75$ mm; $b_a = b_b = 50$ mm; $E_a = E_b = E = 8000$ MPa; $G_a = 5000$ MPa; $m_a = m_b = 6$ kg/m; and $k_{sc} = 1000$ MPa.

In Fig. 7, we present the relative eigenfrequencies of the first eigenmode versus the layer shear modulus ratio G_b/G_a ratio for PP and CC. It can be clearly observed that when the shear modulus ratio G_b/G_a becomes small, i.e. a big gap of shear modulus between two layers exists, the eigenfrequencies predicted by the proposed model are much lower than those predicted by Wu et al. model [32]. However, the two models give the same results when the shear modulus ratio G_b/G_a is equal to one. This can be explained by the fact that the shear strains and the cross-section rotations of the layers become increasingly different with increasing differences in the the shear modulus. Then the assumption of identical layer shear strains becomes inaccurate. The fact of imposing the same shear strains leads to the eigenfrequencies to stay close to the ones of Girhammar and Pan model [29], hence overestimate them. It seems that in the Wu et al. model [32], the effect of transverse shear deformation is governed by the bigger shear modulus of the two layers. However, the proposed model gives the eigenfrequencies that are strongly influenced by the shear modulus ratio G_b/G_a. That is to say that the effect of shear flexibility is governed by the smaller shear modulus of the two layers which, in our point of view, makes sense.

4. Conclusions

In this paper, an analytical model for flexural free vibration analysis of shear-deformable two-layer beams with interlayer slip has been presented. In the present work, the effect of transverse shear deformation has been taken into account by considering each layer behaves as a Timoshenko beam. The partial interaction has been also considered by assuming a linear continuous bond model at the layer interface. Based on these key assumptions, the governing differential equations of the problem have been derived and an original analytical solution has been developed. Based on this solution, results eigenfrequencies and eigenmodes of four single span two-layer beams with classical Euler boundary conditions, i.e. *pinned-pinned*, *clamped-clamped*, *clamped-pinned* and *clamped-free*, have been presented. Our approach has been validated by comparing the eigenfrequencies obtained by it against two existing analytical models by Girhammar and Pan [29] and Wu et al. [32]. While the effect of shear-flexibility is ignored in Girhammar and Pan model [29], it is taken into account in Wu et al. model [32] by using the Timoshenko beam theory and imposing a kinematic constraint of equal cross-section shear strains. It is worth mentioning that the main improvement of our model compared to that of Wu et al. model [32] is in taking into account the shear flexibility in a general way which allows the layers to have independent shear strains which depend indeed on their own shear modulus. Thus the eigenfrequencies predicted by the proposed model are always smaller than the ones obtained with Girhammar and Pan model [29] and Wu et al. model [32] as confirmed by the results. Furthermore, the relative differences are increasingly significant with higher eigenmode. Finally, the influence of the transverse shear deformation and the partial interaction on the eigenfrequencies of four classical Euler beams has been also investigated by performing a parametric studies with varying material and geometric parameters, such as span-to-depth ratio, shear bond stiffness at the interface and layer shear modulus ratio. The results show that the shear flexibility does not effect on the eigenfrequency when the layers are weakly connected. Regarding the influence of the shear modulus ratio, it has been found that when there is a big gap of shear modulus between two layers in such cases, the eigenfrequencies predicted by the proposed model are much more lower than those of Wu et al. model [32]. That shows that the fact of imposing the same layer shear strains is a strong assumption in this case.

Appendix A. Solving a quartic equation

Let us consider a quartic equation which has the standard form

$$x^4+ax^3+bx^2+cx+d=0 \tag{A.1}$$

where a, b and c are real. Eq. (A.1) can be rewritten as

$$\left(x^2+\frac{ax}{2}\right)^2=\left(\frac{a^2}{4}-b\right)x^2-cx-d \tag{A.2}$$

By adding $(x^2+ax/2)y+y^2/4$ to both sides of the above equation, one obtains

$$\left(x^2+\frac{ax}{2}+\frac{y}{2}\right)^2=\left(\frac{a^2}{4}-b+y\right)x^2-\left(c-\frac{ay}{2}\right)x+\frac{y^2}{4}-d \tag{A.3}$$

The objective now is to choose a value for y such that the right hand side of the equation becomes a perfect square. This can be done by letting the discriminant of the quadratic function become zero, i.e.

$$\Delta=\left(c-\frac{ay}{2}\right)^2-4\left(\frac{a^2}{4}-b+y\right)\left(\frac{y^2}{4}-d\right)=0 \tag{A.4}$$

This leads to a cubic equation for y:

$$y^3-by^2+(ac-4d)y-c^2-d(a^2-4b)=0 \tag{A.5}$$

It is well-known that a cubic equation can be easy analytically solved and always has at least one real root, namely y_0. Consequently, Eq. (A.3) can be rewritten as

$$\left(x^2+\frac{ax}{2}+\frac{y_0}{2}\right)^2=\left(\frac{a^2}{4}-b+y_0\right)\left(x-\frac{c-\frac{ay_0}{2}}{\frac{a^2}{4}-b+y_0}\right)^2 \tag{A.6}$$

Finally, four roots (real and/or complex) of the quartic equation can be found by solving the two following quadratic equations for x:

$$x^2+\frac{ax}{2}+\frac{y_0}{2}=\pm\sqrt{\frac{a^2}{4}-b+y_0}\left(x-\frac{c-\frac{ay_0}{2}}{\frac{a^2}{4}-b+y_0}\right) \tag{A.7}$$

References

[1] H. Robinson, K. Naraine, Slip and uplift effects in composite beams, *Proceedings of the Engineering Foundation Conference on Composite Construction*, American Society of Civil Engineers, 66(11), 1988, pp. 487–497.
[2] K. Kapania, S. Raciti, Recent advances in analysis of laminated beams and plates. Part i: shear effects and buckling, *AIAA Journal* 27 (7) (1989) 923–935.
[3] K. Kapania, S. Raciti, Recent advances in analysis of laminated beams and plates. Part ii: vibrations and wave propagation, *AIAA Journal* 27 (7) (1989) 935–946.
[4] S. Timoshenko, On the corrections for shear of the differential equation for transverse vibrations of prismatic bars, *Philosophical Magazine* 41 (1921) 744–746.
[5] S. Timoshenko, On the transverse vibrations of bars of uniform cross section, *Philosophical Magazine* 43 (1922) 125–131.
[6] J. Reddy, A simple higher-order theory for laminated composite plates, *Journal of Applied Mechanics, Transactions of the ASME* 51 (4) (1984) 745–752.
[7] E. Carrera, G. Giunta, Refined beam theories based on a unified formulation, *International Journal of Applied Mechanics* 2 (1) (2010) 117–143.
[8] R. Batra, S. Vidoli, F. Vestroni, Plane wave solutions and modal analysis in higher order shear and normal deformable plate theories, *Journal of Sound and Vibration* 257 (1) (2002) 63–88.
[9] Y. Ghugal, R. Shimpi, A review of refined shear deformation theories for isotropic and anisotropic laminated beams, *Journal of Reinforced Plastics and Composites* 20 (3) (2001) 225–271.
[10] M. Newmark, C. Siess, I. Viest, Tests and analysis of composite beams with incomplete interaction, *Proceedings of Society of Experimental Stress Analysis* 9 (1) (1951) 75–92.
[11] M. Heinisuo, An exact finite element technique for layered beam, *Computers and Structures* 30 (3) (1988) 615–622.
[12] U. Girhammar, K. Gopu, Composite beam-column with interlayer slip exact analysis, *Journal of Structural Engineering (ASCE)* 119 (4) (1993) 2095–2111.
[13] C. Faella, E. Martinelli, E. Nigro, Steel and concrete composite beams: ''exact'' expression of the stiffness matrix and applications, *Computers and Structures* 80 (2002) 1001–1009.
[14] G. Ranzi, M. Bradford, B. Uy, A direct stiffness analysis of a composite beam with partial interaction, *International Journal for Numerical Methods in Engineering* 61 (5) (2004) 657–672.
[15] U. Girhammar, D. Pan, A. Gustafsson, Exact dynamic analysis of composite beams with partial interaction, *International Journal of Mechanical Sciences* 51 (8) (2009) 565–582.
[16] R. Gilbert, M. Bradford, Time-dependent behavior of continuous composite beams at service loads, *Journal of Structural Engineering (ASCE)* 121 (2) (1995) 319–327.
[17] G. Ranzi, M. Bradford, B. Uy, Analytical solutions for the time-dependent behaviour of composite beams with partial interactions, *International Journal of Solids and Structures* 43 (13) (2006) 3770–3793.
[18] Q.-H. Nguyen, M. Hjiaj, J.-M. Aribert, A space-exact beam element for time-dependent analysis of composite members with discrete shear connection, *Journal of Constructional Steel Research* 66 (11) (2010) 1330–1338.
[19] Q.-H. Nguyen, M. Hjiaj, B. Uy, Time-dependent analysis of composite beams with partial interaction based on a time-discrete exact stiffness matrix, *Engineering Structures* 32 (9) (2010) 2902–2911.
[20] N. Gattesco, Analytical modelling of nonlinear behaviour of composite beams with deformable connection, *Journal of Constructional Steel Research* 52 (2) (1999) 195–218.
[21] A. Ayoub, F. Filippou, Mixed formulation of nonlinear steel-concrete composite beam element, *Journal of Structural Engineering (ASCE)* 126 (3) (2000) 371–381.
[22] M. Salari, E. Spacone, Analysis of steel-concrete composite frames with bond-slip, *Journal of Structural Engineering (ASCE)* 127 (11) (2001) 1243–1250.
[23] E. Spacone, S. El-Tawil, Nonlinear analysis of steel-concrete composite structures: state-of-the-art, *Journal of Structural Engineering (ASCE)* 130 (2) (2004) 1901–1912.
[24] Q.-H. Nguyen, M. Hjiaj, B. Uy, S. Guezouli, Analysis of composite beams in the hogging moment regions using a mixed finite element formulation, *Journal of Constructional Steel Research* 65 (3) (2009) 737–748.
[25] M. Saje, B. Cas, I. Planinc, Non-linear finite element analysis of composite planar frames with an interlayer slip, *Computers and Structures* 82 (23–26) (2004) 1901–1912.
[26] P. Krawczyk, B. Rebora, Large deflections of laminated beams with interlayer slips—part 2: finite element development, *Engineering with Computers* 24 (1) (2007) 33–51.
[27] J. Battini, Q.-H. Nguyen, M. Hjiaj, Non-linear finite element analysis of composite beams with interlayer slips, *Computers and Structures* 87 (13–14) (2009) 904–912.
[28] G. Ranzi, A. Dall'Asta, L. Ragni, A. Zona, A geometric nonlinear model for composite beams with partial interaction, *Engineering Structures* 32 (5) (2010) 1384–1396.
[29] U. Girhammar, D. Pan, Dynamic analysis of composite members with interlayer slip, *International Journal of Solids and Structures* 30 (6) (1993) 797–823.
[30] C. Adam, R. Heuer, A. Jeschko, Flexural vibrations of elastic composite beams with interlayer slip, *Acta Mechanica* 125 (1–4) (1997) 17–30.
[31] H. Murakami, A laminated beam theory with interlayer slip, *Journal of Applied Mechanics* 51 (3) (1984) 551–559.
[32] Y. Wu, R. Xu, W. Chen, Free vibrations of the partial-interaction composite members with axial force, *Journal of Sound and Vibration* 299 (4–5) (2007) 1074–1093.
[33] R. Xu, Y. Wu, Static, dynamic, and buckling analysis of partial interaction composite members using timoshenko's beam theory, *International Journal of Mechanical Sciences* 49 (10) (2007) 1139–1155.
[34] S. Schnabl, M. Saje, G. Turk, I. Planinc, Analytical solution of two-layer beam taking into account interlayer slip and shear deformation, *Journal of Structural Engineering (ASCE)* 133 (6) (2007) 886–894.
[35] Q.-H. Nguyen, E. Martinelli, M. Hjiaj, Derivation of the exact stiffness matrix for a two-layer Timoshenko beam element with partial interaction, *Engineering Structures* 33 (2) (2011) 298–307.
[36] A. Zona, G. Ranzi, Finite element models for nonlinear analysis of steel-concrete composite beams with partial interaction in combined bending and shear, *Finite Elements in Analysis and Design* 47 (2) (2011) 98–118.
[37] P. Le Grognec, A. Le van, On the plastic bifurcation and post-bifurcation of axially compressed beams, *International Journal of NonLinear Mechanics* 47 (8–9) (2011) 693–702.
[38] P. LeGrognec, Q.-H. Nguyen, M. Hjiaj, Exact buckling solution for two-layer Timoshenko beams with interlayer slip, *International Journal of Solids and Structures* 49 (1) (2012) 143–150.
[39] S. Berczyński, T. Wróblewski, Vibration of steel-concrete composite beams using the Timoshenko beam model, *Journal of Vibration and Control* 11 (6) (2005) 829–848.

ANNEXE 10

M. Manthey, **Q-H. Nguyen**, H. Somja, J. Duchêne and M. Hjiaj. Experimental Study of the Composite Timber-Concrete SBB Connection under Monotonic and Reversed-Cyclic Loadings. *Materials and Joints in Timber Structures*. 2014 ; S. Aicher, H. W. Reinhardt and H. Garrecht, Springer Netherlands. 9 : 433-442. http://dx.doi.org/10.1007/978-94-007-7811-5_39

Experimental Study of the Composite Timber-Concrete SBB Connection under Monotonic and Reversed-Cyclic Loadings

Manuel Manthey[1,2,*], Quang Huy Nguyen[1], Hugues Somja[1], Jérôme Duchêne[2], and Mohammed Hjiaj[1]

[1] Laboratory of Structural Mechanics INSA, Rennes, France
Manuel.Manthey@insa-rennes.fr, m.manthey@a-i-a.fr
[2] AIA Ingénierie, Angers, France

Abstract. The present paper investigates the mechanical behavior of a novel dowel-type Timber-Concrete Composite system, namely SBB, under monotonic and reversed-cyclic loadings. This system consists of timber beams connected to a concrete slab using a dowel type connection. Because the structural behavior of timber-concrete composite slabs is mainly governed by the shear connection between concrete and timber, an extensive experimental program was carried out in order to assess its behavior under both monotonic (serviceability design) and cyclic loadings (seismic design) and to identify failure modes for each possible configuration. In order to fully characterize the load-slip behavior of the SBB connection under both monotonic and reversed cyclic loading, 24 Push-Out tests (12 under monotonic loading, 12 under reversed cyclic loading) were performed. The experimental program and the results (parameters and phenomenology) are discussed in this paper.

Keywords: Composite structures, Timber, Concrete, Push-Out tests, SBB shear connector, cyclic loading.

1 Introduction

1.1 Timber Concrete Composite Structures

Timber-Concrete Composite systems are competitive technical solution in refurbishment as well as in new building construction. With this system, the best properties of timber and concrete materials can be exploited since tensile stresses induced by gravity loads are resisted primarily by the timber beam and compression by the concrete slab. Timber-Concrete Composite (=TCC) Structures offers

* Corresponding author.

S. Aicher et al. (eds.), *Materials and Joints in Timber Structures*, RILEM Bookseries 9, DOI: 10.1007/978-94-007-7811-5_39, © RILEM 2014

many advantages over traditional floors. Yeoh [14] presents a non-exhaustive list of these advantages. Currently, there are no standards for the design of Timber-Concrete Composite structure. Nevertheless, design methods have been proposed in the technical literature [3, 6, 7, 8, 14]. The design of TCC must account for two main phenomena: the partial composite action resulting from the flexibility of the shear connection and the time dependant properties of the component material (creep, concrete shrinkage, mechano-sorption, thermal strains and hygroscopic strains).

1.2 SBB Timber-Concrete Connection System

Various connectors are available in the market with a wide range of stiffnesses and load capacities which are crucial design parameters for TCC and empirically determined by Push-Out tests. Ceccotti [2] summarizes the most commonly used methods for joining concrete to timber. Dias [4] describes the typical load-slip behavior for different types of joints. The "dowel type fasteners" used in his work (see Figure 1) are dowels with a 10mm diameter, so it cannot be directly compared to SBB shear-connectors which have diameters from 21 to 26 mm. The joints made with dowel type fasteners have smaller strengths and stiffness but much higher plastic deformation capacity.

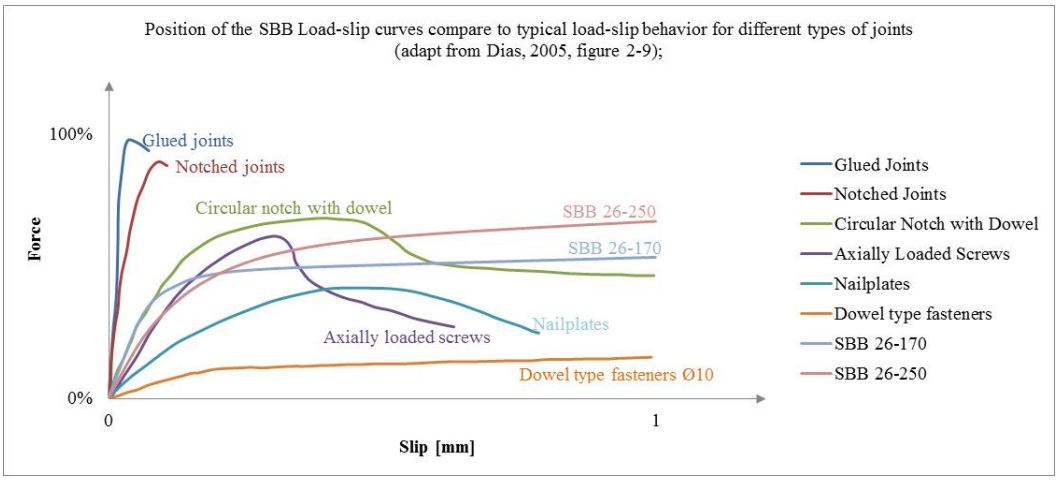

Fig. 1 Position of the SBB Load-slip curves compare to the typical behavior of different type of joints (adapt from Dias, 2005, Figure 2-9)

SBB Timber-Concrete System (see Figure 2) has been developed by the French company AIA Ingénierie for the last decade and now is widely used in the country. The SBB system consists of timber beams connected to a concrete slab using a large diameter dowel type connection patented at the French patent bureau. Two SBB configurations will be investigated in this paper SBB 26-170 (170 mm length) and SBB 26-250 (250 mm length).

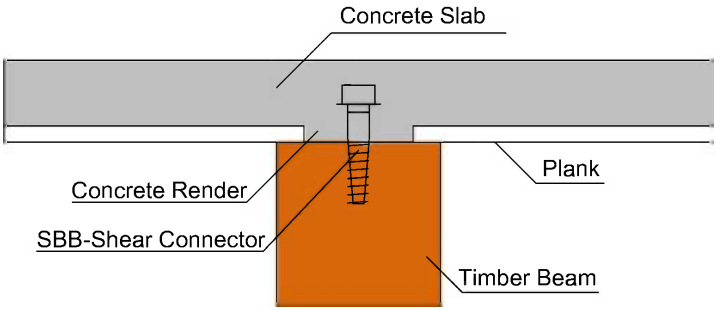

Fig. 2 SBB Timber-Concrete System

For seismic design purposes, AIA Ingénierie decided to fully characterize the load-slip behavior of the SBB connection under reversed-cyclic loading. Under seismic loads, the relative stiffness of the diaphragm and its connectors has implications on the seismic response of a building and affects how the floor system can be modeled. Studies at the University of Canterbury [10] showed that for TCC floor unit under diaphragm action, the diaphragm displacement was less than 5% of the total displacement, so TCC can be modeled as a rigid unit. Eurocode 8 [3] requires that the concrete slab depth is at least equal to 7 cm to consider that the slab act as a rigid unit. TCC floors with SBB system are built with a minimum concrete slab depth of 7 cm in seismic area. Others considerations from Eurocode 8 [3] concerning floors dimensions should be respected. Under seismic action, all the TCC floor (concrete slab + timber beam) moves as a rigid unit, so only the connectors between TCC floor and LLRS are subjected to reversed cyclic action.

2 Experimental Set-up and Loadings

2.1 Experimental Set-up

As the aim of this study is to analyze the mechanical behavior of timber-concrete connections, a particular attention has to be paid to the parameters that may affect it, specifically in the experimental shear test set-up. In their paper, Monteiro et al. [9] identified different shear test set-ups with a database based on a literature survey. The database showed that three types of experimental test set-ups exist for Timber-Concrete Connections: Double Shear tests, Asymmetric-Shear tests and Pure Shear tests. Others SBB configurations were already tested in double shear Push-Out test in the past. In 2011, complementary Push-Out tests were performed with Glue Laminated Timber Beam (GL24h) and two SBB dowel dimensions (26-170 and 26-250). As SBB 26-250 do have a 250 mm dowel length without the head (compare to the 170 mm for SBB 26-170), and considering the 70 mm thickness of the concrete flange, a 60 mm concrete render was necessary for the SBB 26-250 tests. This concrete render was deliberately not reinforced with steel. Concerning the concrete, minimal class on site is C25/30. According to Eurocode 4 (Annex B – Clause 2.3.), Push Out tests need to be performed with a reduced

concrete class, which in the present case is C16/20. Concreting of slab 2 was done two days after concreting of slab 1. A plastic foil was applied between timber and concrete in order to prevent the bleeding of concrete in the timber member during the concreting phase. These layers also allowed minimizing the friction forces between timber and concrete during the shear test. Concerning measures the three points of interests were: a) the relative slip between the concrete slab and the timber member measured near the connectors, in load direction; b) the separation between the timber beam and the concrete slab; c) the load applied on the specimen. Those measurements allowed calculating the relevant mechanical properties of the connection such as slip moduli and shear strengths. Concerning boundaries conditions (see Figure 3), timber beam was clamped thanks to a thick steel plate placed on the top of it and restrained with four pre-stressed steel links. In order to apply cyclic loading, a steel device was designed for the campaign. This device allowed achieving a reversed-cyclic vertical loading directly on the concrete flanges.

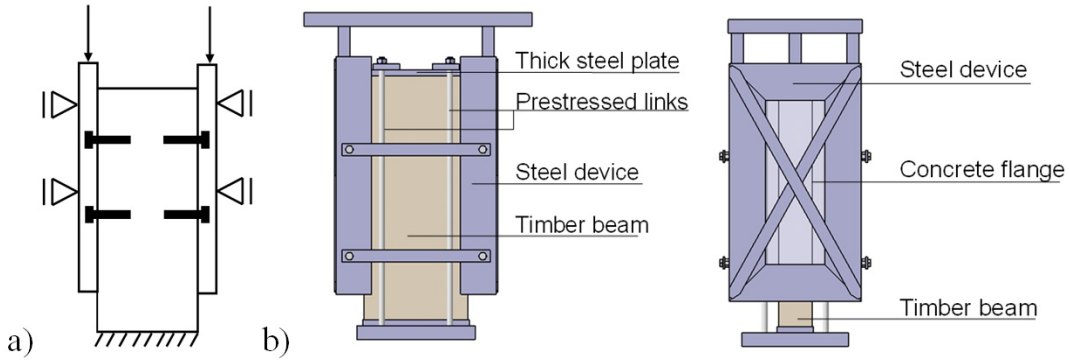

Fig. 3 a) Test set up and b) Views of the designed Push-Out Device

2.2 Loading

As unfortunately, the design of TCC is not addressed by standards, a combination of timber standards and composite steel-concrete structure was used to determine the loading program. Monotonic Push-Out tests were carried out according to European Standard EN 26891 [12], and Eurocode 4 [3] (Annex B). Considering Reversed-cyclic loadings, two references were used: the European Standards EN 12512 [11] and the ECCS n°45 [5]. Both references offer the possibility to define the reversed-cyclic displacement path according to δ_y, with δ_y being the conventional limit of elastic range measured in preliminary classical monotonic tests. Many procedures exist to deduce the limit of elastic range from a load-slip curve; the one chosen is discussed later in this paper. The specimens considered here do have the same behavior in compression and tension, if this is not the case, two limits of elastic range should be investigated, one in compression and one in

tension [5]. The reversed-cyclic load program has been developed according to EN 12512 [11]. Nevertheless some modifications were made: (1) three cycles were made at the +/-0,25.δ_y step and at the +/-0,5.δ_y step instead of one, (2) additional intermediate steps were added, basically one intermediate step between each steps of the standard, for example a +/-0.375. δ_y step was added between the +/-0,25.δ_y step and the +/-0,5.δ_y step, a +/-3.δ_y step was added between the +/-2.δ_y step and the +/-4.δ_y step (see Figure 4). The cyclic loadings were carried out till failure of the system (in tensile and compression). The tests were performed under load control during the elastic part and then under displacement control for the plastic range.

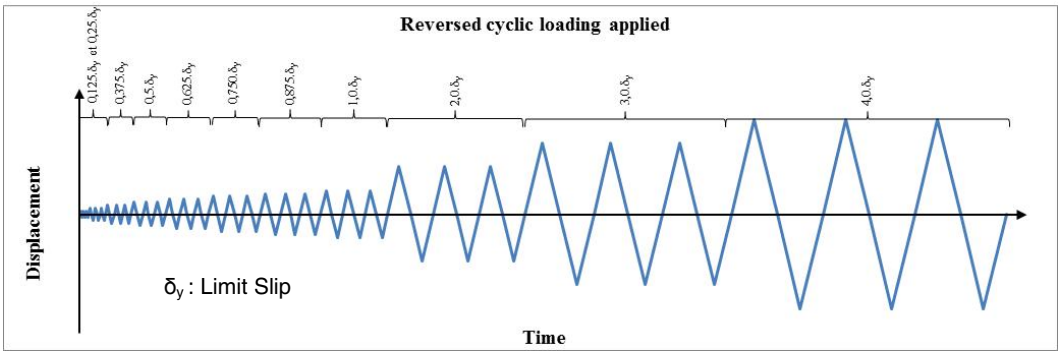

Fig. 4 Reversed-cyclic loading defined for the SBB Push-Out tests

3 Results for the Monotonic Push-Out Tests

From the values measured during the monotonic Push-Out tests, particular emphasis is put on the ultimate load (P_{max}) and on the slip moduli ($K_{0,4}$ and $K_{0,6}$) because they are the parameters usually considered to design a Timber Concrete Composite structure. Limit slip, ultimate slip and static ductility ratio are also quantified. Strength is quantified as the maximum load applied when failure occurs in the Push-Out specimen. However designers need to know the design shear strength, $P_{Rd,}$ which is obtained as a 5% fractile value of the maximum load according to Eurocode 0 [3], (Annex D-clause D.7.2) and then divided by 1,25 as recommended in the Eurocode 5-2 [3], (clause 2.4.1.-[3]). Stiffness is quantified by the slip modulus at two different load levels: 40% and 60% of the mean maximum load corresponding to the service and ultimate load levels, as recommended by Ceccotti [2]. Limit slip δ_y and yield load P_y are values of the slip and the load corresponding to the transition from elastic behavior to plastic range. To determine these values, two methods were used, the one from the EN 12512 [11] and the one proposed by Lachal and Aribert [1] for steel concrete shear connector.

As both methods showed similar results, for normative consideration, the EN 12512 method was adopted. According methods previously described, shear connector properties were determined for monotonic tests series, the one with SBB 26-170 Shear Connectors in Glue Laminated Timber and the one with SBB 26-250 Shear Connectors in Glue Laminated Timber. Key parameters are listed in Table 1. It is worth to mention that Push-Out tests with the SBB 26-250 were built deliberately with unreinforced concrete render. As most of the degradation during the test was observed on the concrete render, it can be assumed that with a reinforced concrete render, higher strength and stiffness should be achieved. The Push-Out tests with the 26-250 SBB Shear connectors are showing a lower stiffness than the Push-Out tests with the 26-170 SBB Shear connectors. This can be explained by the lower flexibility of shorter connector.

Table 1 Monotonic Push-Out tests, key parameters. (*: EN 12512 limit)

	SBB 26-170	SBB 26-250
Maximum load applied per connector P_{max} [daN]	3075	4676
Design shear strength P_{Rd} [daN]	2460	3741
Stiffness $K_{0,4}$ (service load level) [daN/mm]	3516	1942
Stiffness $K_{0,6}$ (ultimate load level) [daN/mm]	2321	1282
Ultimate slip δ_u [mm]	30*	30*
Limit slip δ_y [mm]	1,32	2,17
Ductility ratio δ_u/δ_y	22,73	13,83

Having analyzed the test results, concerning monotonic loading, SBB connection exhibits an excellent ductile behavior (see Figure 5). Even at a 40 mm slip the system is showing high remaining shear strength. Moreover stiffness and shearstrength were experimentally characterized for the SBB, providing all parameters needed for TCC floors design in serviceability uses. Timber-Concrete separation measured during the tests was not significant, less than 1 mm before failure and about 8 mm at the failure. They were monitored during the Push-Out tests to control the relative out-of-plane movement of the timber-concrete composite structures. Figure 5 summarizes the phenomenological observations from the Push-Out tests under monotonic loading with SBB 26-170 and SBB 26-250. Until P_y, the shear connector is considered to behave elastically. After P_y, the shear connector behavior becomes plastic with a positive hardening. Plastic hinge appears on Shear Connector in timber part only for SBB 26-170 and in timber and concrete parts for SBB 26-250.Once maximal shear resistance is reached, concrete degradation is clearly observed.

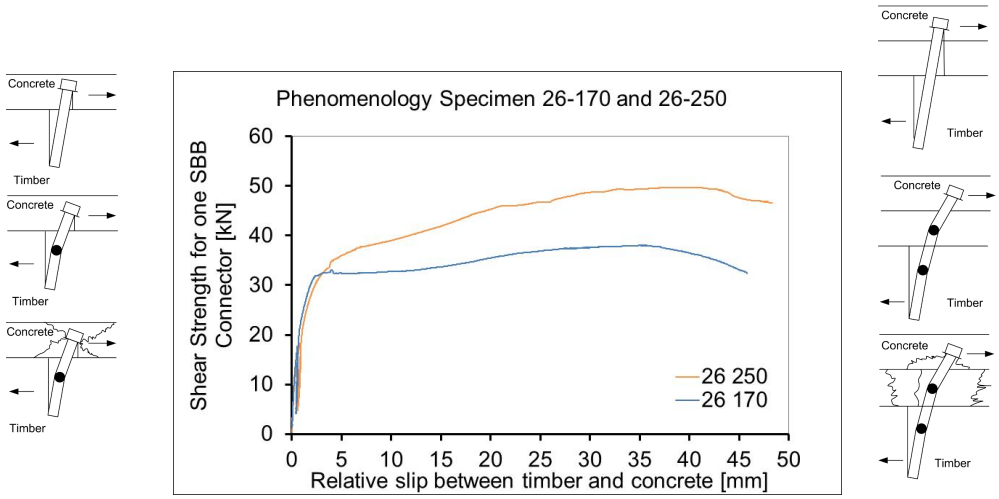

Fig. 5 Load-slip curves and Phenomenology for the SBB 26-170 Push-Out tests and the SBB 26-250

4 Results Reversed-Cyclic Push-Out Tests

In reversed-cyclic Push-Out tests, main features highlighted are yield point of the connection, maximal strength and ultimate displacement as well as ductility. A particular attention is paid to the strength degradation after 3 load-cycles at the same displacement level, the so-called Action Reduction Factors. From the Push-Out tests, load-slip curves showing hysteresis curves are obtained (see Figure 6). Properties are determined following EN 12512 (see [3]). Analysis should be done on the backbones curves of the reversed-cyclic tests. Parameters should be quantified in tension and compression to check the symmetrical behavior of the system. Maximum strength is quantified as the maximum load applied during the Push-Out test. According to EN 12512, ultimate slip δ_u is defined as the lowest displacement value between: a) Displacement at failure; b) Displacement at 80 % of the maximal strength, post peak; c) 30mm. Ultimate strength, P_u, is the corresponding strength to the ultimate displacement. Limit slip δ_y and yield load P_y define the transition zone between elastic and plastic behavior. To determine those, EN 12512 method [11] was used. Action Reduction Factor was evaluated for both tests series, in compression and tension for two displacement levels: $4.\delta_y$ and $6.\delta_y$. Indeed, according Eurocode 8-1 [3], Clause 8.3, Action Reduction Factor shouldn't exceed 20% within 3 cycles at the same displacement level. When this condition is satisfied for a ductility ratio from 4, the connection system can be used as a dissipative element in a DCM structure and when this condition is satisfied for a ductility ratio from 6, the connection system can be used as a dissipative element in a DCH structure. Under reversed-cyclic loading, the SBB connection shows

a ductile behavior without a significant reduction in the shear strength with large displacements values. According to the Action Reduction Factor and to the Eurocode 8 [3], connection with SBB 26-170 could be used as dissipative element in DCH structures. Due to the unreinforced concrete render and to the large length of SBB 26-250, an important degradation of the connection with SBB 26-250 was observed so that SBB 26-250 could be only used as dissipative element in DCM structures. It is important to notice that Timber-Concrete Diaphragm are primary element in seismic design and are considered as non dissipative element in a structure under seismic solicitations. The high ductility of the connection under cyclic loading is still a comforting fact even though it is not a mandatory point for TCC floors diaphragm design in seismic area. SBB Shear Connectors do have a dissipative role when connecting the floor diaphragm to the lateral resisting system. If SBB shear connectors have a dissipative role, as for example connecting the floor diaphragm to the lateral resisting system, accidental "cyclic" design shear strength ($=P_{Rd,ACC}$) should be used. Cyclic design strength can be defined as a 5% fractile value of the ultimate load P_u (=80% P_{max}) applied on the specimen under reversed-cyclic loading, according to Eurocode 0 [3] (Annex D-Clause D.7.2), and then divided by 1,0 considering accidental solicitations. As well as monotonic Push-Out tests, Timber-Concrete separation measured during the tests was not significant. They were monitored during the Push-Out tests to control the relative out-of-plane movement of the timber-concrete composite structures. The Equivalent Viscous Damping Ratio (EVDR) as specified in CEN-EN 12512 [11] (2000) is used to compare the energy dissipation capacity between different types of connections. This non-dimensional parameter expresses the hysteresis damping properties of the connection. It is determined as the ratio between the dissipated energy in one half cycle and the work performed by the applied force. In the elastic stage, SBB 26-170 show EVDR values twice as high as the EVDR values obtained with SBB 26-250. In the plastic stage, both connections show similar EVDR values. Those EVDR values indicate a quite high energy dissipation capacity of the SBB connectors with EVDR values from 5% to 12% in the elastic stage and, for both test series, an increased value for plastic deformations with EVDR values of 17% and 22% for SBB 26-170 and SBB 26-250 connections, respectively. Initial behavior of the shear connector is elastic. Nevertheless, one cycle after another, reversed-cyclic loading gradually damage timber and concrete material near the SBB shear connector. Irreversible deteriorations occur, in timber, the hole is ovalised and in concrete, cracks appear. Those deformations depict the particular shape of the load-slip curves. On Figure 7, three consecutive hysteresis loops at an advanced loading stage can be seen, on which critical points from the hysteretic response are represented. Concrete and wood have already been damaged earlier, that's why no loop starts from the origin.

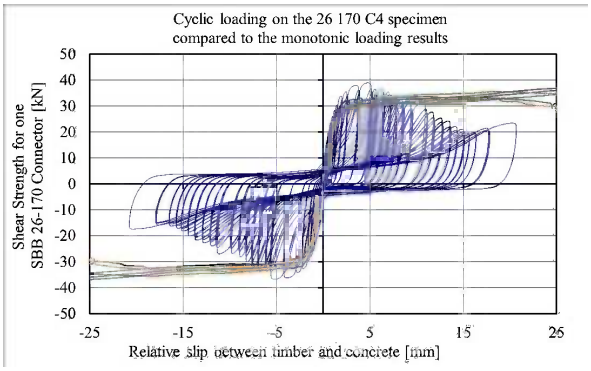

	SBB 26-170	SBB 26-250
P_y [daN]	2742	2774
δ_y [mm]	0,70	1,01
P_u [daN]	3095	2964
δ_u [mm]	7,80	9,00
Ductility δ_u / δ_y	11,81	9,29
Ductility class	DCH	DCM

Fig. 6 Load-slip curve for one of the six reversed cyclic loading with the SBB 26-170 connector and comparison to the monotonic loading tests. Table 4.1: Principle parameters for the reversed-cyclic loading (mean values).

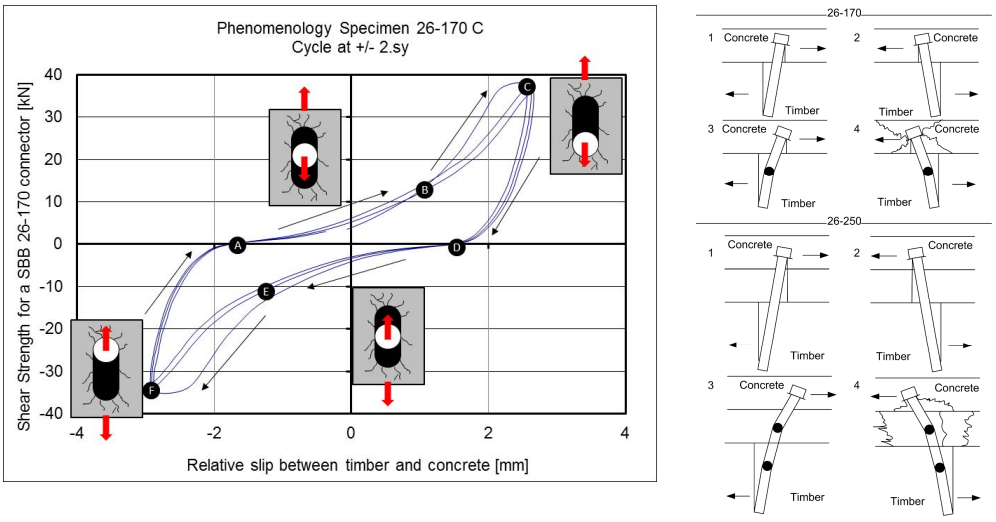

Fig. 7 Load-slip curve for a 3 load-cycles at the same displacement level; Phenomenology for SBB26-170 and SBB26-250 Shear connector under reversed-cyclic loading

5 Conclusion

Concerning Push-Out under monotonic loading, having analyzed the test results, SBB connection shows an excellent ductile behavior with all SBB References tested. Stiffness and shear strength were experimentally characterized for the SBB configurations, providing all parameters needed for TCC floors design in "normal" uses.

For Push-Out tests under reversed-cyclic loading, the SBB connection with both SBB 26-170 and SBB 26-250 shows a ductile behavior without a significant reduction in the shear strength with high displacements values. Concerning EVDR (Equivalent Viscous Damping Ratio), EVDR values from 5% to 12% are observed in the elastic stage. For both test series, the EVDR values increase for plastic deformations with EVDR values of 17% and 22% for SBB 26-170 and SBB 26-250

connections, respectively. According to the ARF (Action Reduction Factor) and to the Eurocode 8, connection with SBB 26-170 can be used as dissipative element in DCH structures and SBB 26-250 can be used as dissipative element in DCM structures. The high ductility of the connection under cyclic loading is a comforting fact, allowing SBB system use in seismic area without any beam-slab connection brittle failure risk.

Acknowledgments. AIA Ingénierie is acknowledged for providing funds for the realization of the test program. A special word of thanks to D. Cvetkovic, C. Garand and F. Marie of the INSA Rennes for assisting in all stages of the tests.

References

[1] Aribert, J.-M., Lachal, A.: Formulation de la rupture par fatigue de connecteurs acier-béton pour des sollicitations de type sismique, revue. Construction Métallique 4 (2002)
[2] Ceccotti, A.: Composite concrete-timber structures. Structural Engineering Material 4, 264–275 (2002)
[3] CEN Eurocode 0; 4;5; 8, European Committee for Standardization, Brussels
[4] Dias, A.: Thesis: Mechanical Behaviour of timber-concrete joints, Technische Universiteit Delft, Universidade de Coimbra (2005)
[5] ECCS: European Convention for Constructional Steelwork, n°45 Recommended Testing Procedure for Assessing the Behavior of Structural Steel Elements under Cyclic Loads (1986)
[6] Fragiacomo, M., Yeoh, D.: The Design of a Semi-Prefabricated LVL-Concrete Composite Floor. Hindawi Publishing Coroporation, Advances in Civil Engineering (2012)
[7] Girhammar, U.A.: A Simplified analysis method for composite beams with interlayer slip. International Journal of Mechanical Sciences 51, 515–530 (2009)
[8] Lukaszewska, E.: Thesis: Development of Prefabricated Timber-Concrete Composite Floors. Luleå University of Technology (2009)
[9] Monteiro, Dias, Negrao: Assessment of Timber-Concrete Connections Made with Glued Notches: Test Set-Up and Numerical Modelling, Society for Experimental Mechanics (2011)
[10] Newcombe, M.P., Carradine, D., Pampanin, S., Buchanan, A.H., Deam, B.L., Van Beerschoten, W.A., Fragiacomo, M.: In-Plane Experimental Testing of Timber-Concrete Composite Floor Diaphragms. In: NZSEE Conference 2009 (2009)
[11] NF EN 12512:2002: Timer structures – Tests methods – Cyclic testing of joints made with mechanical fasteners, CEN Brussels (2002)
[12] NF EN 26891:2000: Timber structures – Joints made with mechanical fasteners – General principles for the determination of strength and deformation characteristics, CEN Brussels (2000)
[13] SBB SAS (2000) SBB website, `http://bois-beton.fr` (accessed March 13, 2013)
[14] Yeoh, D.: Thesis: Behaviour and Design of Timber-Concrete Composite Floor System. University of Canterbury (2010)

ANNEXE 11

Q-H. Nguyen, V-T. Tran and M. Hjiaj. Development of design method for composite columns with several encased steel profiles under combined shear and bending. *7th European Conference on Steel and Composite Structures*. Napoli, Italia, September 10-12, 2014.

DEVELOPMENT OF DESIGN METHOD FOR COMPOSITE COLUMNS
with several encased steel profiles under combined shear and bending

Quang-Huy NGUYEN, Mohammed Hjiaj, Van-Toan TRAN

National Institute of Applied Sciences Rennes, Dept. Civil Engineering and Urban, France
Quang-Huy.Nguyen@insa-rennes.fr, Mohammed.Hjiaj@insa-rennes.fr, Van-Toan.Tran@insa-rennes.fr,

INTRODUCTION

Nowadays, the composite framing systems are used frequently in practice for tall buildings. The design of a framing system that combines structural steel and reinforced concrete produces a building having the advantages of each material, namely, the inherent mass, stiffness, damping, and economy of reinforced concrete, and the speed of construction, strength, long-span capability, and light weight of structural steel. One of the key elements is the composite column, where the practice of encasing structural steel shapes encased in reinforced concrete is common. The use of encased composite columns is actually more or less limited to the simple encased steel profile because this kind of composite columns is covered by standard rules of Eurocode 4 [1]. Regarding the concrete columns reinforced by more than one steel profile, namely “hybrid” column, although a number of researchers have focused on its various aspects [2-5], they are currently not covered by standards because they are neither reinforced concrete structures in the sense of Eurocode 2 [6] or ACI318 [7], nor composite steel-concrete structures in the sense of Eurocode 4 or AISC 2010 [8]. Gaps in knowledge are mostly related to the problem of force transfer between concrete and embedded steel profiles, a situation in which it is neither known how to combine the resistances provided by bond, by stud connectors and by plate bearings, nor how to reinforce the transition zones between classical reinforced concrete and concrete reinforced by steel profiles. AISC allows engineers to design composite sections built-up from two or more encased steel. But, it doesn’t explain how to perform and check the design.

The present paper aims to develop a design method for “hybrid” columns with several encased steel profiles. Particular attention will be paid to shear (longitudinal and transversal) resistances because preventing shear failure is one of the major concerns when designing a composite structural member. Experiments conducted with simple encased steel profile shown that the shear failure generally involves two possible failure modes: (1) the diagonal shear failure, which closely resembles the shear failure of an ordinary reinforced concrete structural member; and (2) the shear bond failure, which results in cracks along the interface of the steel flange and concrete. For a composite member, the shear bond failure can be critical when the steel flange width is large and approaching the overall width of the composite section [9]. Some tests carried out in Japan have shown that shear bond cracks along the interface of the steel flange and concrete are responsible for early failure [10]. For this reason, in this paper a method for the calculation of the number of connector to ensure the full interaction between steel profiles and concrete around is firstly proposed. Then a strut-and-tie model is developed to evaluate the transverse shear resistance taking into account the contribution of the steel profiles. Finally, a hybrid column with three steel profiles is designed using the proposed method and the design resistance values are compared to the ones obtained by an Abaqus FE model.

1 DESIGN MODEL

1.1 Details of considered hybrid column

For the sake of simplicity, the hybrid column considered in this paper is a composite column with three fully encased steel profiles (see Figure 1). The three steel profiles are oriented such that they are summited to weak axis bending. The connection is made by headed studs. It is assumed that the second order effect is negligible.

1.2 Design of shear connection

In the proposed design model, the number of headed shear studs will be calculated to assure full interaction between steel profiles and concrete. That mean that the full plastic bending moment of the composite cross-section (in sense of Eurocode 4) can be reached. Therefore, the shear studs must be able to transfer the maximum tensile force from the lower steel profile to cracked concrete.

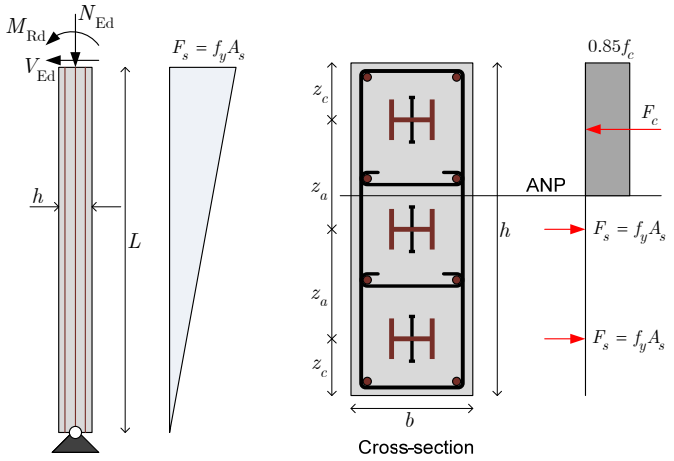

Fig. 1. Tensile force distribution of steel profile in case of full interaction

Figure 1 shows the tensile force distribution of bottom steel profile when the full plastic bending moment is reached. Thus, the longitudinal shear force, namely V_L, acting on the shear studs from the cross-section where the full plastic bending moment is reached to the cross-section where the bending moment vanishes is

$$V_L = A_s f_y \tag{1}$$

where A_s is area of one steel profile and f_y is yield stress. The minimum number of shear stud needed for bottom steel profile to ensure the full interaction is

$$n_{\min} = V_L / P_{Rd} \tag{2}$$

where P_{Rd} is design shear resistance of one stud given in EC4-1§6.6.3.1(1). The same number of shear stud is needed for middle steel profile. Because the plastic neutral axis is certainly above the profile (see Figure 1) so the determination of number of shear stud of middle profile is exactly the same as the one of lower profile. For the upper profile, less number of shear studs is needed because of the presence of concrete this profile cannot be yielded in compression so that the force transferred from steel to concrete via the studs is less than the one in the lower and middle profiles. However, the same number of shear stud will be implemented for three profiles.

1.3 Resistance of cross-section to combined compression and bending

There is nowadays no design standard providing the guidance on how to determine properly the plastic resistances of composite section with more than one encased steel profile. However, once the full interaction between steel profiles and concrete is ensured, the resistances of the hybrid cross-sections to combined compression and bending and the corresponding interaction curve may be calculated using the simplified method of design of Eurocode 4 (clause 6.7.3.2(2)). Furthermore, the interaction curve may be also drawn by performing a classical fiber cross-section analysis and using pivot method of Eurocode 2 for yielding criteria.

1.4 Strut-and-tie model for shear resistance

In order to evaluate the transverse shear resistance, a strut-and-tie model is proposed. In this model the complete section is divided into two sub-sections. The first sub-section has a width limited to

the width of the steel shape h_a. The second sub-section is the RC part that has a width: $b_c=b-h_a$ where b being the width of complete section (*see Figure 2*). The repartition of the total shear force V_{Ed} into the sub-sections 1 and 2 can be determined according to EC4-1 §6.7.3.2(4) in which the shear force acting on each sub-section is proportional to total shear force by plastic bending moment ratio:

$$V_{\mathrm{Ed1}} = V_{\mathrm{Ed}} \frac{M_{\mathrm{pl,Rd1}}}{M_{\mathrm{pl,Rd}}} \qquad (3)$$
$$V_{\mathrm{Ed2}} = V_{\mathrm{Ed}} - V_{\mathrm{Ed1}}$$

where $M_{\mathrm{pl,Rd1}}$ is the plastic resistance moment of sub-section 1; $M_{\mathrm{pl,Rd}}$ is the plastic resistance moment of compete section.
Having at hand the transverse shear distribution, to evaluate the transverse shear resistance of total section, the transverse shear resistances of each sub-section are need to be evaluated.

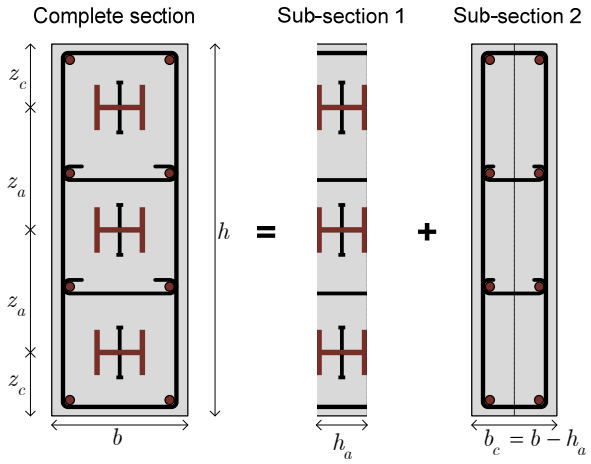

Fig. 2. Decomposition of complete cross-section

1.4.1 Transverse shear resistance of sub-section 1

The transverse shear resistance of sub-section 1 is estimated using strut-and-tie model which is illustrated in Figure 3. It should be noted that in this model the "transverse tie" resistance is not studied because the stirrups represented the "transverse tie" are in sub-element 2.
The equilibrium of vertical forces leads:

$$V_{\mathrm{Ed1}} = 3V_{\mathrm{a}} + \sqrt{2}F_{\mathrm{c}} \qquad (4)$$

where V_{a} is the shear force acting on each steel profile and F_{c} is the compression force in concrete strut.

The transverse shear resistance of sub-section 1 depends on resistance en concrete strut $F_{\mathrm{c,Rd}}$ and shear resistance of steel profile $V_{\mathrm{a,Rd}}$. Therefore, it is necessary to know the distribution of transverse shear in sub-section 1. To do so, a stiffness approach is used. Let us consider a reference cantilever beam containing two elements mentioned above as shown in Figure 3. We assume that under the action of shear force V_{Ed1} the beam end deflection is δ. This deflection can be expressed in term of steel profile shear force V_{a} as:

$$V_{\mathrm{a}} = G_a A_{\mathrm{a}} \delta / z_a \qquad (5)$$

where A_{a} is the shear area of a profile; G_{a} is the shear modulus of steel.

Furthermore, according to the kinematic scheme in Figure 5 the shortening of the concrete compression strut, namely δ_{strut}, is related to the deflection δ by:

$$\delta_{\mathrm{strut}} = \delta / \sqrt{2} \tag{6}$$

This shortening is due to the compression force F_{c} thus:

$$F_{\mathrm{c}} = E_c A_{\mathrm{strut}} \delta_{\mathrm{strut}} / L_{\mathrm{strut}} \tag{7}$$

Where E_{c} is concrete modulus; $A_{\mathrm{struts}} = h_a z_a / \sqrt{2}$ is the total area of concrete strut; $L_{\mathrm{strut}} = z_a \sqrt{2}$ is the length of concrete strut. Finally, F_{c} is expressed in function of δ as:

$$F_{\mathrm{c}} = E_c h_a \delta / 2\sqrt{2} \tag{8}$$

From equation (5) and (8) we have:

$$V_{\mathrm{a}} = \frac{2\sqrt{2} G_a A_{\mathrm{a}}}{E_c h_a z_a} F_{\mathrm{c}} \tag{9}$$

Substituting equation (9) into (4) leads to:

$$F_{\mathrm{c}} = \frac{\sqrt{2} E_c h_a z_a}{2\left(6 G_a A_{\mathrm{a}} + E_c h_a z_a\right)} V_{\mathrm{Ed1}} \text{ and } V_{\mathrm{a}} = \frac{G_a A_{\mathrm{a}}}{6 G_a A_{\mathrm{a}} + E_c h_a z_a} V_{\mathrm{Ed1}} \tag{10}$$

The transverse shear resistance of sub-section 1 is:

$$V_{\mathrm{Rd1}} = \min \begin{cases} \dfrac{2\left(6 G_a A_{\mathrm{a}} + E_c h_a z_a\right)}{\sqrt{2} E_c h_a z_a} F_{\mathrm{Rd},c} = \dfrac{6 G_a A_{\mathrm{a}} + E_c h_a z_a}{E_c h_a^2} \upsilon_1 f_c \\ \dfrac{6 G_a A_{\mathrm{a}} + E_c h_a z_a}{G_a A_{\mathrm{a}}} V_{\mathrm{Rd,a}} = \dfrac{6 G_a A_{\mathrm{a}} + E_c h_a z_a}{\sqrt{3} G_a \gamma_{Mo}} f_y \end{cases} \tag{11}$$

where $\upsilon_1 = 0.6$ is a strength reduction factor for concrete cracked in the shear and $\gamma_{Mo} = 1.0$ is partial factor for resistance of sub-section 1.

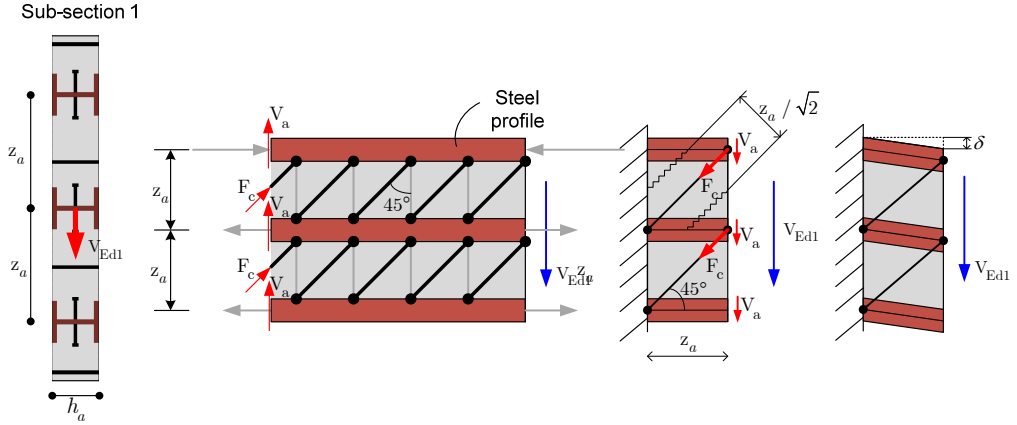

Fig. 3. Strut-and-tie model for sub-section 1

1.4.2 Transverse shear resistance of sub-section 2

This sub-section can be considered as RC section so the transverse shear resistance can be computed according to EC2:

$$V_{\mathrm{Rd,max}} = \frac{\alpha_{\mathrm{cw}} b_{\mathrm{c}} 0.81 h \upsilon_1 f_{\mathrm{c}}}{\cot\theta + \tan\theta} \tag{12}$$

$$V_{\mathrm{Rd,s}} = \frac{A_{\mathrm{sw}}}{s} z\, f_{\mathrm{ywd}} \cot\theta \qquad (13)$$

It should be noted that the stirrups are supposed to play a role of transverse "tie" in strut-and-tie model for both sub-sections. That means that they are subjected to the total transverse shear force V_{Ed}. Therefore, for instant we suppose that the transverse shear resistance of sub-section 2 is deduced from resistance of concrete compression strut $V_{\mathrm{Rd2}} = V_{\mathrm{Rd,max}}$.

Transverse shear resistance of total section: The transverse shear resistance of total section is indeed deduced from:

- Shear resistance of sub-section 1.
- Resistance of concrete compression strut of sub-section 2.
- Resistance of transverse tie (stirrups).

2 NUMERICAL APPLICATION

The proposed design model is now used to evaluate the resistance to combined bending and shear of a composite column reinforced by three encased steel profile. The geometric and material characteristics are presented in Figure 4.

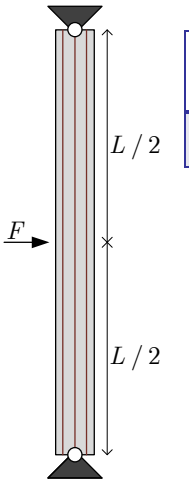

Steel profile	Rebar	Stirrups and pins	Stirrup spacing (mm)	Connector	Connector spacing (mm)
3 HEB100	8 HA20	HA16	200	40 Nelson H3L16mm	200

- Distance between two axes of supports: L = 3750 mm
- Design concrete resistance: $f_c = f_{ck}$ = 40 MPa ;
- Steel profile resistance: f_y = 460 MPa (S460);
- Steel rebar resistance: f_{yk} = 500 MPa;
- Dimensions of the cross-section: height h = 820 mm and width b = 200 mm.

Fig. 4. Geometric and material characteristics of studied hybrid column

Table 1: Summary of design resistances

$n_{\min}$	$M_{\mathrm{pl,Rd}}$ (kNm)	$V_{\mathrm{Ed1}} / V_{\mathrm{Ed}}$	$V_{\mathrm{Ed2}} / V_{\mathrm{Ed}}$	V_{Rd1} (kN)	V_{Rd2} (kN)	$V_{\mathrm{Rd,s}}$ (kN)	V_{Rd} (kN)
19	1488	0.694	0.306	1332	797	668	668

Table 1 shows the bending and shear resistances estimated with the proposed method. The force applied at mid-height to reach the resistance of the column can be deduced from the shear and bending resistances as

$$F_{\mathrm{Rd}} = \min\left(\frac{4M_{\mathrm{pl,Rd}}}{L};\ 2V_{\mathrm{Rd}}\right) = 1336\ \mathrm{kN} \qquad (14)$$

3 CALIBRATION OF PROPOSED DESIGN MODEL BY NUMERICAL 3D MODEL

Until the experimental test is done, we tried to calibrate the proposed design model by a numerical 3D model. The hybrid column considered in the previous section is now simulated by Abaqus FE software where solid elements are adopted for concrete, steel profiles and connectors and truss

elements are used for steel reinforcement. Regarding the material models, concrete damaged plasticity model is used. The model parameters are selected to provide more or less the same stress-strain curve for uniaxial compression given in EC2. In this numerical model, steel reinforcement is embedded in concrete while “Hard contact” and “Frictionless” interactions are used to connect steel profiles and shear stud to concrete around. Figure 5 shows the load-displacement curve obtained by the numerical model. As can be seen, the design value is quiet well calibrated by the numerical results.

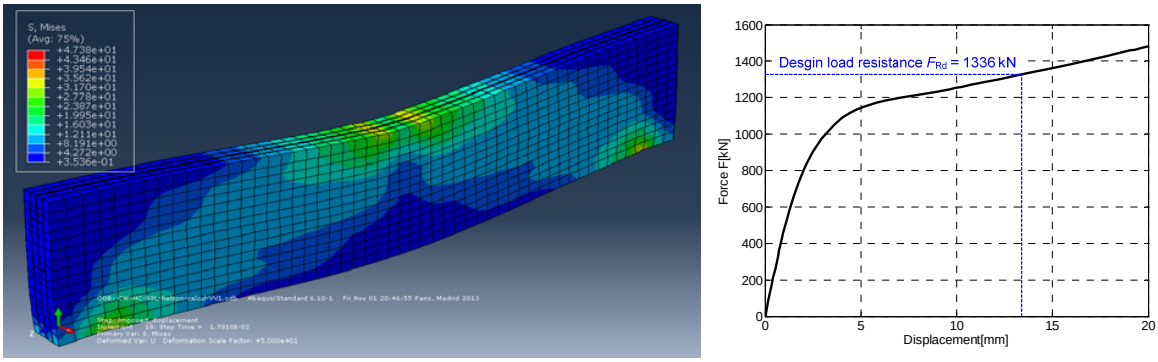

Fig. 5. Numerical results

4 CONCLUSIONS

In this paper, a design model for “hybrid” columns with several encased steel profiles subjected to combined compression, bending and shear has been proposed. A simple method for the calculation of the number of connector to ensure the full interaction between steel profiles and concrete around has been developed. Particular attention has been paid to transverse shear resistance for which a strut-and-tie model has been developed taking into account the contribution of the steel profiles. The proposed design model has been more or less calibrated by 3D numerical model. However, the experimental tests need to be conducted to validate this method.

REFERENCES

[1] European Committee for Standardization, "Design of composite steel and concrete structures-Part 1.1: General rules and rules for buildings. EN 1994-1-1", Eurocode-4, 2005.
[2] Echigo, S, Y. Tachibana, A. Kitajima, "New type hybrid structure and practical analysis method of creep and shrinkage", Construction and Building Materials, Vol 12, No.2–3, pp. 93-103, 1998.
[3] Morino, S, "Recent developments in hybrid structures in Japan—research, design and construction", Engineering Structures, Vol 20, No. 4–6, pp. 336-346, 1998.
[4] Kim, S.E , H.T. Nguyen, "Finite element modeling and analysis of a hybrid steel–PSC beam connection", Engineering Structures, Vol 32, No. 9, pp. 2557-2569, 2010.
[5] Dan, D, A. Fabian, V. Stoian, "Theoretical and experimental study on composite steel–concrete shear walls with vertical steel encased profiles", Journal of Constructional Steel Research, Vol 67, No.5, pp. 800-813, 2011.
[6] European Committee for Standardization, "Design of concrete structures-Part 1: General rules and rules for buidings. EN1992-1-1", Eurocode-2, 2004.
[7] American Concrete Institute, "Building code requirements for reinforced concrete", ACI-318, 2005.
[8], American Institute for Steel Construction, "Specifications for Structural Steel Buildings", *ANSI/AISC 360-05*, AISC, 2010.
[9] Weng, C, S. Yen, C. Chen, "Shear Strength of Concrete-Encased Composite Structural Members", Journal of Structural Engineering, Vol 127, No. 10, pp. 1190-1197, 2001.
[10] Zhang, F, M. Yamada, "Composite Columns Subjected to Bending and Shear", in *Composite Construction in Steel and Concrete II*, D. Darwin and D. Buckner, (ASCE), United States, 1993.

ANNEXE 12

P. Keo, H. Somja, **Q-H. Nguyen** and M. Hjiaj. Simplified design method for slender hybrid columns. *Journal of Constructional Steel Research* 2015 ; 110 :101-120. (5-Year IF 1.699) http://dx.doi.org/10.1016/j.jcsr.2015.03.006.

Journal of Constructional Steel Research 110 (2015) 101–120

Contents lists available at ScienceDirect

Journal of Constructional Steel Research

Simplified design method for slender hybrid columns

Pisey Keo, Hugues Somja, Quang-Huy Nguyen *, Mohammed Hjiaj

Université Européenne de Bretagne-INSA de Rennes, 20 avenue des Buttes de Coësmes, CS 70839, F-35708 Rennes Cedex 7, France

ARTICLE INFO

Article history:
Received 30 October 2014
Accepted 7 March 2015
Available online 2 April 2015

Keywords:
Hybrid column
Second-order effects
Moment magnification approach
Eurocodes
FE model
Co-rotational formulation

ABSTRACT

This paper deals with numerical investigations on second-order effects in slender RC columns reinforced by several steel sections, namely hybrid columns, subjected to combined axial load and uniaxial bending moment. A FE model is developed in which geometrical and material nonlinearities as well as the partial interaction effect between the steel profiles and the surrounding concrete are taken into account. This model is then used to perform an extensive numerical parametric study on the ultimate load of hybrid columns considering 1140 different data sets. The comparison between the results obtained with FE analysis and Eurocode simplified methods (moment magnification approach) shows that EC2 and EC4 methods give wide discrepancies where half of case-studies are unsafe. The aim of the paper is to extend the use of the Eurocode moment magnification method to slender hybrid column design. In this method, the second-order bending moment is calculated by multiplying the first-order one by a magnification factor k that depends on the flexural stiffness EI and the equivalent moment distribution. New expressions for the correction factors involved in the determination of the effective flexural stiffness EI are proposed and calibrated by the results of the extended parametric study with 2960 data sets. The comparison of the predictions given by the new expressions against the FE analysis shows that the proposed new expressions of correction factors for moment magnification method provides largely safe designs for slender hybrid columns.

1. Introduction

Hybrid structures (also called Steel-Reinforced Concrete structures) composed of steel members encased in reinforced concrete have been used at an increasing rate for mid-to-high rise buildings as they effectively combine structural steel and reinforced concrete members to their best advantage. These hybrid frames possess several advantages from structural, economical and construction view points compared to either traditional reinforced concrete or steel frames. Engineering practices show that beams and columns made of two different materials may fully develop the merits of each of them. For instance, composite columns have significant economic advantages over either pure structural steel or reinforced concrete (RC) alternatives. For a given cross sectional dimension, composite columns also have higher strength and stiffness therefore leading to reduced slenderness and increased buckling resistance. In the early time of hybrid construction, these systems were built by first erecting a steel skeleton and selected columns or entire bays of the steel framing were encased in reinforced concrete to increase, at minimal cost, their strength, stiffness as well as their fire resistance. Sooner these systems became very popular in seismic prone area and nowadays it is commonly accepted within the engineering community that composite and hybrid systems offer an economical method to develop the required strength and stiffness. Several hybrid systems have been developed and for some design rules need to be devised.

In high-rise buildings, slender RC columns containing multiple encased profiles as reinforcement are often used to resist horizontal loads by bending about their strong axes when standard reinforcement with rebars is not sufficient to sustain such large loads. Those composite steel–concrete columns are called “hybrid column” because they are neither RC columns in the sense of EC2 [1], nor composite columns in the sense of EC4 [2]. In the latter, the design rules are provided only for a single encased steel profile. Nevertheless, it is legitimate to raise the following question: can we use design rules given in EC2 or EC4 to design such column? For columns being sensitive to instability, both EC2 and EC4 propose simplified design methods based on moment magnification approach. The latter can be written as $M_{Ed,2} = kM_{Ed,1}$ where $M_{Ed,2}$ is second-order bending moment; $M_{Ed,1}$ is first-order bending moment; and k is the so-called moment magnification factor. Different expressions for the factor k have been proposed in the technical literature (see for example [1–5]). A large number of expressions for k found in the technical literature can be written as: $k = \beta / (1 - N_{Ed} / N_{cr})$ where N_{Ed} is the design axial load; N_{cr} the elastic critical normal force; and β the equivalent uniform moment factor. The accuracy of moment magnification method strongly depends on the effective flexural stiffness EI involved in the expression of N_{cr} which depends on, among other factors, the nonlinearity of the concrete stress-strain curve, creep and cracking along the column length, and on the factor β. The

* Corresponding author.
E-mail address: qnguyen@insa-rennes.fr (Q.-H. Nguyen).

http://dx.doi.org/10.1016/j.jcsr.2015.03.006
0143-974X/

expression for *EI* used to design reinforced concrete and composite columns has been studied for decades. There is a vast amount of expressions for the effective flexural stiffness *EI* in the literature. Mavichak and Furlong [6] considered the relative normal force as a single parameter in their expression for *EI*. Mirza [7] suggested to take into account the eccentricity, the slenderness ratio, and the creep factor related to the sustained load. The latter was further enhanced by Tikka and Mirza [8–11] taking into account the reinforcement ratio in their proposed *EI* equation. The abovementioned factors including the strength of concrete are also considered in [3,12]. Bonet et al. [4] extended their work to propose a new equation for *EI* valid for arbitrary cross-section shape. Similarly, many authors proposed an expression for the equivalence uniform moment factor β. The most adopted expression by the codes was proposed by Austin [13] which is a linear function of the ratio between the eccentricities at the extremities of the column. This expression was deduced from the solution of a linear elastic analysis. Robinson et al. [14] proposed to replace the linear expression with a quadratic function of (r_m). Trahair [15] and Duan et al. [16] considered the eccentricity ratio and axial force level in their expression for β. Sarker and Rangan [17] explained that the expression provided by Austin [13] is unsafe for low to medium column slenderness and they proposed another expression for β which is valid for short-term load and for normal to high strength concrete. Tikka and Mirza [18] maintained that the expression proposed by Austin [13] which is used in ACI-318 [5] is safe. ACI-318 [5] suggest to adopt β equal to 1.0 for column subjected to transverse load, and EC2 [1] does not define the β factor explicitly.

This paper deals with numerical investigations on second-order effects in slender RC columns reinforced by several steel sections subjected to combined axial load and uniaxial bending moment about strong axis. The first objective of this study is to point out that a straightforward application of the bending moment magnification method proposed in EC2 or EC4 to hybrid columns may lead to unsafe results in several situations. To remain consistent with the Eurocodes, a new version of bending moment magnification method for slender hybrid columns is proposed. To do so, a FE model is developed in which the geometrical/material nonlinearities as well as the partial interaction effect between steel profiles and the surrounding concrete are taken into account. This model is validated for standard composite columns (due to lack of experimental results) and will serve as reference for an extensive parametric study (1140 data sets) in which the applicability of the simplified methods proposed in EC2 and EC4 are evaluated in case of hybrid columns. Based on the extensive parametric study with 2960 data sets, new expressions for the coefficient *k*, β, *and EI* are proposed. The organization of this paper is as follows. In Section 2, the FE model is briefly presented. Next, the recommendations for the design of columns in EC2 and EC4 are briefly recalled. Section 4 is devoted to the parametric study in which the hypotheses considered for material laws and geometrical and material imperfections are deduced from Eurocode recommendations for FE analysis and from the background of these methods. Finally, a design method for slender hybrid column is proposed and validated based on the results obtained from FE analysis in Section 5.

2. Finite Element model for hybrid members in partial interaction

In order to analyze the behavior of slender hybrid columns, a two-dimensional beam-column finite element formulation was developed based on Euler–Bernoulli kinematics and fiber cross-section discretization. The corotational approach was adopted. In this context, the element displacements are separated into rigid-body and deformational degrees of freedom. The element rigid-body motion is handled separately via the mapping from the corotational frame to global coordinate system. The developed FE model is capable to consider the following aspects: a cross-section with more than one steel section in partial interaction; geometrical and material nonlinearities; initial imperfection; residual stresses; and concrete confinement. For the sake of clarity the FE formulation is presented for a hybrid column with two encased steel profiles. However, the concepts are also applicable to general case of several encased steel profiles. A more detailed description can be found in [19].

Let us consider a planar element with two steel sections fully encased in concrete with shear connectors at the contact interface uniformly distributed along the element length, as shown in Fig. 3. It is assumed that the interlayer slip can occur at the interface but there is no uplift.

For the present case, the element has 10 global degrees of freedom in the fixed global coordinate system: global displacements and rotation of the nodes (c_i and c_j) and slips (g_{ki}, g_{kj}) between the steel node s_k and concrete node $c_{i;j}$. Since all component are bent according to Euler–Bernoulli kinematics, the cross-section rotations of each component (steel sections and concrete section) are equal and the slips (g_{ki}, g_{kj}) are perpendicular to the end cross-sections. The vector of global nodal displacements is defined by

$$\mathbf{p}_g = \left[u_{ci}\, v_{ci}\, \theta_i\, g_{1i}\, g_{2i}\, u_{cj}\, v_{cj}\, \theta_j\, g_{1j}\, g_{2j}\right]^{\mathrm{T}}. \tag{1}$$

Due to the presence of the three rigid body modes in the global coordinate system, the corresponding element stiffness matrix is singular. Therefore, the linear local element is derived in the local system (x_l,y_l) without rigid body modes. The latter translates and rotates with the element as the deformation proceeds. In this local system, the element has seven degrees of freedom and the vector of local displacements is defined as

$$\mathbf{p}_l = \left[\overline{u}_{s1i}\, \overline{u}_{s2i}\, \overline{\theta}_i\, \overline{u}_{s1j}\, \overline{u}_{s2j}\, \overline{u}_{cj}\, \overline{\theta}_j\right]. \tag{2}$$

2.1. Co-rotational formulation

The origin of the local coordinate system is taken at node c_i and the x_l-axis of the local coordinate system is defined by the line connecting nodes c_i and c_j. These nodes are chosen to be at the centroid of concrete section in order to easily derive the kinematic relationships between the global nodal displacements and the local ones. The y_l-axis is perpendicular to the x_l-axis so that the result is a right-handed orthogonal coordinate system. The motion of the element from the original undeformed configuration to the actual deformed one can thus be separated in two parts. The first one, which corresponds to the rigid motion of the local frame, is described by the translation of the node c_i and the rigid rotation of the axes. The deformational part of the motion is always small in the local coordinate system and a geometrical linear element will be used.

According to the notations defined in Fig. 1, the components of the local displacement vector $\mathbf{p}_l$ can be computed from those of the global vector $\mathbf{p}_g$ as

$$\overline{u}_{cj} = l_n - l_o \tag{3}$$

$$\overline{\theta}_i = \theta_i + \beta_o - \beta \tag{4}$$

$$\overline{\theta}_j = \theta_j + \beta_o - \beta \tag{5}$$

$$\overline{u}_{ski} = g_{ki}cos\overline{\theta}_i - h_k\overline{\theta}_i \text{ with } k = 1 \text{ or } 2 \tag{6}$$

$$\overline{u}_{skj} = g_{kj}cos\overline{\theta}_j - h_k\overline{\theta}_j \text{ with } k = 1 \text{ or } 2 \tag{7}$$

where

$$cos\beta_o = \frac{1}{l_o}\left(x_{cj} - x_{ci}\right) \tag{8}$$

$$sin\beta_o = \frac{1}{l_o}\left(y_{cj} - y_{ci}\right) \tag{9}$$

$$cos\beta = \frac{1}{l_n}\left(x_{cj} + u_{cj} - x_{ci} - u_{ci}\right) \tag{10}$$

$$sin\beta = \frac{1}{l_n}\left(y_{cj} + v_{cj} - y_{ci} - v_{ci}\right) \tag{11}$$

and l_o and l_n being the element length in initial and deformed configuration, respectively:

$$l_o = \sqrt{\left(x_{cj} - x_{ci}\right)^2 + \left(y_{cj} - y_{ci}\right)^2} \tag{12}$$

$$l_n = \sqrt{\left(x_{cj} + u_{cj} - x_{ci} - u_{ci}\right)^2 + \left(y_{cj} + v_{cj} - y_{ci} - v_{ci}\right)^2}. \tag{13}$$

As can be seen from Eqs. (3) to (7), the local displacement vector $\mathbf{p}_l$ can be expressed as a function of the global one $\mathbf{p}_g$, i.e.:

$$\mathbf{p}_l = \mathbf{p}_l\left(\mathbf{p}_g\right). \tag{14}$$

Then, $\mathbf{p}_l$ is used to compute the internal force vector $\mathbf{f}_l$ and the tangent stiffness matrix $\mathbf{K}_l$ in the local system. Note that $\mathbf{f}_l$ and $\mathbf{K}_l$ depend only on the definition of the local strains and not on the particular form of Eq. (14). The transformation matrix $\mathbf{B}_{lg}$ between the local and global displacements is defined by:

$$\delta\mathbf{p}_l = \mathbf{B}_{lg}\delta\mathbf{p}_g \tag{15}$$

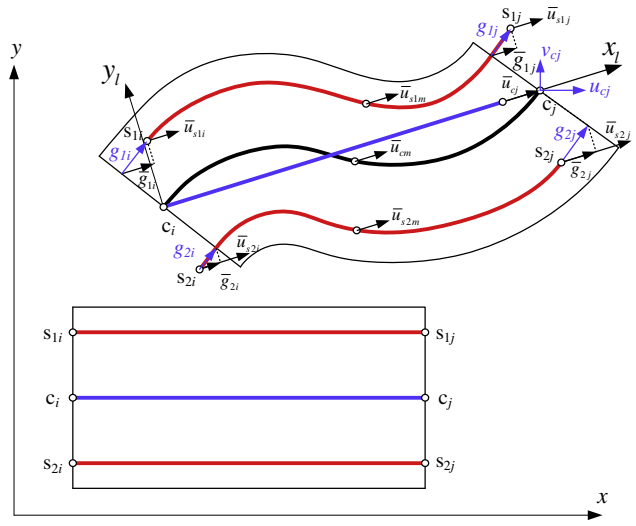

Fig. 1. Degrees of freedom and co-rotational kinematics.

and is obtained by differentiation of Eq. (14). The global internal force vector $\mathbf{f}_g$ and the global tangent stiffness matrix $\mathbf{K}_g$, consistent with $\mathbf{p}_g$, can be obtained by equating the internal virtual work in both the global and the local system, i.e.:

$$\mathbf{f}_g = \mathbf{B}_{lg}^{\mathrm{T}}\mathbf{f}_l \qquad \mathbf{K}_g = \mathbf{B}_{lg}^{\mathrm{T}}\mathbf{K}_l\mathbf{B}_{lg} + \mathbf{H}_{lg} \qquad \mathbf{H}_{lg} = \left.\frac{\partial\left(\mathbf{B}_{lg}^{\mathrm{T}}\mathbf{f}_l\right)}{\partial\mathbf{p}_g}\right|_{\mathbf{f}_l} \tag{16}$$

$$B_{lg}^{\mathrm{T}} = \begin{bmatrix} \frac{-s\lambda_{1i}}{l_n} & \frac{-s\lambda_{2i}}{l_n} & \frac{-s}{l_n} & \frac{c}{l_n} & \frac{-s\lambda_{1i}}{l_n}-c & \frac{-s\lambda_{2i}}{l_n}-c & -c & \frac{-s}{l_n} \\ \frac{c\lambda_{1i}}{l_n} & \frac{c\lambda_{2i}}{l_n} & \frac{c\lambda_{1i}}{l_n}-s & \frac{c\lambda_{2i}}{l_n}-s & -s & \frac{c}{l_n} & & \\ \lambda_{1i} & \lambda_{2i} & 1 & 0 & 0 & 0 & 0 & \\ -cos(\theta_i-\alpha) & 0 & 0 & 0 & 0 & 0 & 0 & \\ 0 & -cos(\theta_i-\alpha) & 0 & 0 & 0 & 0 & 0 & \\ \frac{s\lambda_{1i}}{l_n} & \frac{s\lambda_{2i}}{l_n} & \frac{s}{l_n} & \frac{s\lambda_{1j}}{l_n}+c & \frac{s\lambda_{2l}}{l_n}+c & c & \frac{s}{l_n} & \\ \frac{-c\lambda_{1i}}{l_n} & \frac{-c\lambda_{2i}}{l_n} & \frac{-c}{l_n} & \frac{-c\lambda_{1j}}{l_n}+s & \frac{-c\lambda_{2j}}{l_n}+s & s & \frac{-c}{l_n} & \\ 0 & 0 & 0 & \lambda_{1j} & \lambda_{1j} & 0 & 1 & \\ 0 & 0 & 0 & -cos\left(\theta_j-\alpha\right) & 0 & 0 & 0 & \\ 0 & 0 & 0 & 0 & -cos\left(\theta_j-\alpha\right) & 0 & 0 & \end{bmatrix} \tag{17}$$

$$\mathbf{H}_{lg} = \frac{\omega_1 z^{\mathrm{T}}}{l_n} + \omega_2 r^{\mathrm{T}} + \omega_3 t_{1i}^{\mathrm{T}} + \omega_3 t_{2i}^{\mathrm{T}} + \omega_5 t_{1j}^{\mathrm{T}} + \omega_6 t_{2j}^{\mathrm{T}} + \omega_7 l_3^{\mathrm{T}} + \omega_8 l_8^{\mathrm{T}} \tag{18}$$

where

$$\omega_1 = \left[\xi_1 \quad \xi_2 \quad 0 \quad -sin(\theta_i-\alpha)f_l(1) \quad -sin(\theta_i-\alpha)f_l(2) \quad -\xi_1 \quad -\xi_2 \quad 0 \quad -sin(\theta_i-\alpha)f_l(4) \quad -sin(\theta_i-\alpha)f_l(5)\right] \tag{19}$$

$$\omega_2 = \left[\xi_1 \quad \xi_2 \quad 0 \quad 0 \quad 0 \quad \xi_1 \quad \xi_2 \quad 0 \quad 0 \quad 0\right] \tag{20}$$

$$\omega_3 = \left[-\frac{s}{l_n} \quad \frac{c}{l_n} \quad 1 \quad 0 \quad 0 \quad \frac{s}{l_n} \quad -\frac{c}{l_n} \quad 0 \quad 0 \quad 0\right] f_l(1) \tag{21}$$

$$\omega_4\left[-\frac{s}{l_n} \quad \frac{c}{l_n} \quad 1 \quad 0 \quad 0 \quad \frac{s}{l_n} \quad -\frac{c}{l_n} \quad 0 \quad 0 \quad 0\right] f_l(2) \tag{22}$$

$$\omega_5 = \left[-\frac{s}{l_n} \quad \frac{c}{l_n} \quad 0 \quad 0 \quad 0 \quad \frac{s}{l_n} \quad -\frac{c}{l_n} \quad 1 \quad 0 \quad 0\right] f_l(4) \tag{23}$$

$$\omega_6 = \left[-\frac{s}{l_n} \quad \frac{c}{l_n} \quad 0 \quad 0 \quad 0 \quad \frac{s}{l_n} \quad -\frac{c}{l_n} \quad 1 \quad 0 \quad 0\right] f_l(5) \tag{24}$$

$$\omega_7 = \left[0 \quad 0 \quad 0 \quad sin(\theta_i-\alpha)f_l(1) \quad sin(\theta_i-\alpha)f_l(2) \quad 0 \quad 0 \quad 0 \quad 0 \quad 0\right] \tag{25}$$

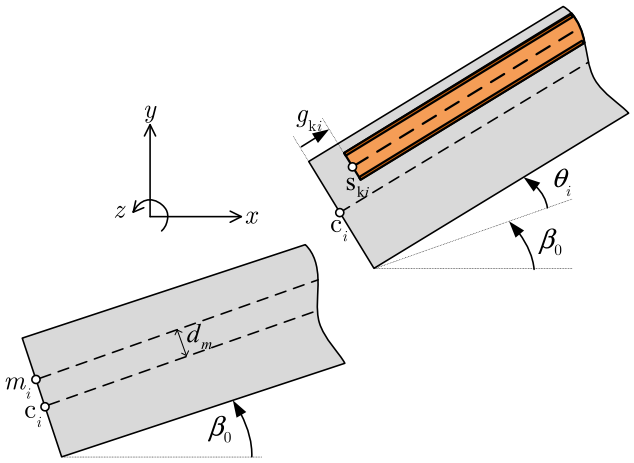

Fig. 2. Eccentric nodes in co-rotational frame.

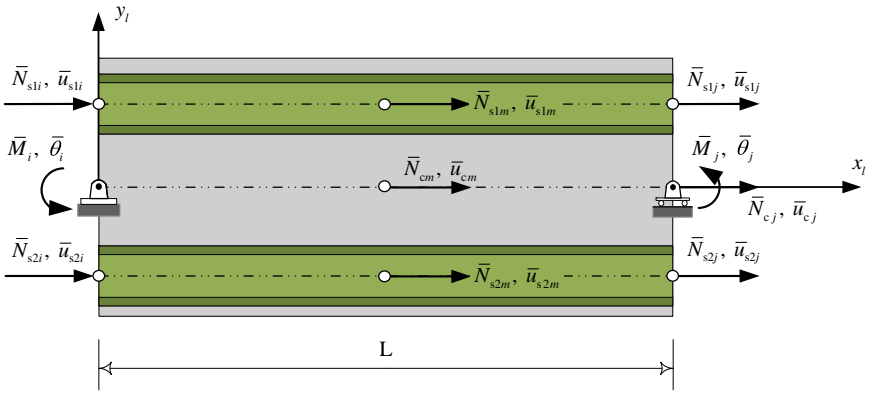

Fig. 3. Degrees of freedom of local linear element with two encased steel profiles.

$$\omega_8\left[0\ \ 0\ \ 0\ \ 0\ \ 0\ \ 0\ \ 0\ \ 0\ \ sin\left(\theta_j-\alpha\right)f_l(4)\ \ \ sin\left(\theta_j-\alpha\right)f_l(5)\right] \tag{26}$$

$$t_{1i} = [0\ \ 0\ \ g_{1i}cos(\theta_i-\alpha)\ \ \ \sin(\theta_i-\alpha)\ \ 0\ \ 0\ \ 0\ \ 0\ \ 0\ \ 0] - g_{1i}cos(\theta_i-\alpha)\frac{z}{l_n} \tag{27}$$

$$t_{2i} = [0\ \ 0\ \ g_{2i}cos(\theta_i-\alpha)\ \ 0\ \ \sin(\theta_i-\alpha)\ \ 0\ \ 0\ \ 0\ \ 0\ \ 0] - g_{2i}cos(\theta_i-\alpha)\frac{z}{l_n} \tag{28}$$

$$t_{1j} = \left[0\ \ 0\ \ 0\ \ 0\ \ 0\ \ 0\ \ 0\ \ g_{1j}cos\left(\theta_j-\alpha\right)\ \ \ \sin(\theta_i-\alpha)\ \ \ 0\right] - g_{1j}cos\left(\theta_j-\alpha\right)\frac{z}{l_n} \tag{29}$$

$$t_{2j} = \left[0\ \ 0\ \ 0\ \ 0\ \ 0\ \ 0\ \ 0\ \ g_{2j}cos\left(\theta_j-\alpha\right)\ \ \ 0\ \ \ \sin(\theta_i-\alpha)\right] - g_{2j}cos\left(\theta_j-\alpha\right)\frac{z}{l_n} \tag{30}$$

$$z = [s\ \ \ -c\ \ \ 0\ \ \ 0\ \ \ 0\ \ \ -s\ \ \ c\ \ \ 0\ \ \ 0\ \ \ 0] \tag{31}$$

$$r = [-c\ \ \ -s\ \ \ 0\ \ \ 0\ \ \ 0\ \ \ c\ \ \ s\ \ \ 0\ \ \ 0\ \ \ 0] \tag{32}$$

$$I_3 = [0\ \ 0\ \ 1\ \ 0\ \ 0\ \ 0\ \ 0\ \ 0\ \ 0\ \ 0] \tag{33}$$

$$I_8 = [0\ \ 0\ \ 0\ \ 0\ \ 0\ \ 0\ \ 0\ \ 1\ \ 0\ \ 0]. \tag{34}$$

The choice of the interlayer slips as the degrees of freedom is indispensable for the robustness of the FE formulation. Due to this choice (see Eq. (1)) the boundary conditions require a special treatment in case external concentrated loads are not applied to the node located at the centroid of the column cross-section (origin of the local frame) but somewhere else on the cross-section.

Let us consider (see Fig. 2) that prescribed displacement or rotation is applied at node m_i. This situation requires a rigid link between the nodes c_i and m_i and a change of degrees of freedom from $\mathbf{p}_g$ to $\mathbf{p}_m$ with

$$\mathbf{p}_m = \left[u_{mi}\ \ \ v_{mi}\ \ \ \theta_i\ \ \ g_{1i}\ \ \ g_{2i}\ \ \ u_{cj}\ \ \ v_{cj}\ \ \ \theta_j\ \ \ g_{1j}\ \ \ g_{2j}\right]^{\mathrm{T}}. \tag{35}$$

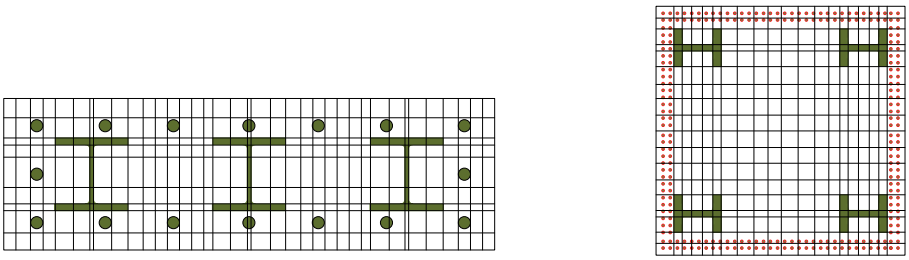

a) Hybrid column with three encased steel profiles.

b) Mega column with four encased steel profiles.

Fig. 4. Fiber discretization of sections.

Table 1
Specimen dimensions and material properties.

Specimen	B × D (mm)	kL (mm)	Structural steel	Long. bar	e/D	f_c (MPa)	f_y (MPa)	f_s (MPa)
CESC1	230 × 230	2000	H100 × 96 × 5 × 8	4ϕ12	0.3	20.5[a]	337	459
CESC2	230 × 230	2000	H100 × 96 × 5 × 8	4ϕ12	0.3	13.7[a]	337	459
CESC3	230 × 230	2000	H140 × 133 × 5.5 × 8	4ϕ12	0.3	20.5[a]	307	459
CESC4	230 × 230	2000	H140 × 133 × 5.5 × 8	4ϕ12	0.3	28.2[a]	307	459
CESC5	230 × 230	3000	H140 × 133 × 5.5 × 8	4ϕ12	0.3	28.2[a]	307	459
CESC6	230 × 230	3000	H100 × 96 × 5 × 8	4ϕ12	0.17	20.5[a]	337	459
CESC7	230 × 230	3000	H100 × 96 × 5 × 8	4ϕ12	0.17	13.7[a]	337	459
CESC8	160 × 160	960	H100 × 100 × 6 × 8	4ϕ6	0.25	21.1[a]	345	460
CESC9	160 × 160	2400	H100 × 100 × 6 × 8	4ϕ6	0.25	23.4[a]	345	460
CESC10	160 × 160	3600	H100 × 100 × 6 × 8	4ϕ6	0.25	23.3[a]	345	460
SCESC1	280 × 280	1200	H150 × 150 × 7 × 10	12ϕ16	0.0	29.5[b]	296	350
SCESC2	280 × 280	1200	H150 × 150 × 7 × 10	12ϕ16	0.0	28.1[b]	296	350
SCESC3	280 × 280	1200	H150 × 150 × 7 × 10	12ϕ16	0.0	29.8[b]	296	350
SCESC4	280 × 280	1200	H150 × 75 × 5 × 7	12ϕ16	0.0	28.1[b]	303	350
SCESC5	280 × 280	1200	H150 × 75 × 5 × 7	12ϕ16	0.0	26.4[b]	303	350
SCESC6	280 × 280	1200	H150 × 75 × 5 × 7	12ϕ16	0.0	29.8[b]	303	350

[a] Concrete cube strength.
[b] Concrete cylinder strength.

The internal force vector and tangent stiffness matrix consistent with $\mathbf{p}_m$ are then obtained by using the transformation matrix $\mathbf{B}_{gm}$. This gives

$$\delta\mathbf{p}_g = \mathbf{B}_{gm}\,\delta\mathbf{p}_m \quad \mathbf{f}_m = \mathbf{B}_{gm}^{\mathrm{T}}\,\mathbf{f}_g \quad \mathbf{K}_m = \mathbf{B}_{gm}^{\mathrm{T}}\,\mathbf{K}_g\,\mathbf{B}_{gm} + \mathbf{H}_{gm} \tag{36}$$

with

$$\mathbf{B}_{gm\,(k,k)} = 1 \ \text{ with } \ k = 1, 2, \cdots, 10 \tag{37}$$

$$\mathbf{B}_{gm\,(1,3)} = cos(\beta_o + \theta_i)\,d_{\mathrm{m}} \tag{38}$$

$$\mathbf{B}_{gm\,(2,3)} = sin(\beta_o + \theta_i)\,d_{\mathrm{m}} \tag{39}$$

and the only non-zero term in the matrix $\mathbf{H}_{gm}$ is

$$\mathbf{H}_{gm\,(3,3)} = -sin(\beta_o + \theta_i)\,d_{\mathrm{m}} f_g(1) + cos(\beta_o + \theta_i)\,d_{\mathrm{m}} f_g(2). \tag{40}$$

2.2. Local displacement-based element

The geometrically linear element is derived in the local system (x_l, y_l). The local element has ten degrees of freedom (see Fig. 3). The transverse displacement $\bar{v}$ is approximated using cubic Hermite interpolations. In order to avoid the curvature locking, three internal nodes (one for each component) are added in order to use quadratic shape function for axial displacement interpolation. However, to save computation time, three degrees of freedom corresponding to the internal nodes will be statically condensed out thereafter to obtain the local displacement vector containing only the degrees of freedom at the element ends. The material non-linearity is taken into account by adopting the distributed plasticity model with fiber section discretization (see Fig. 4). Each fiber is fed with a uniaxial constitutive model.

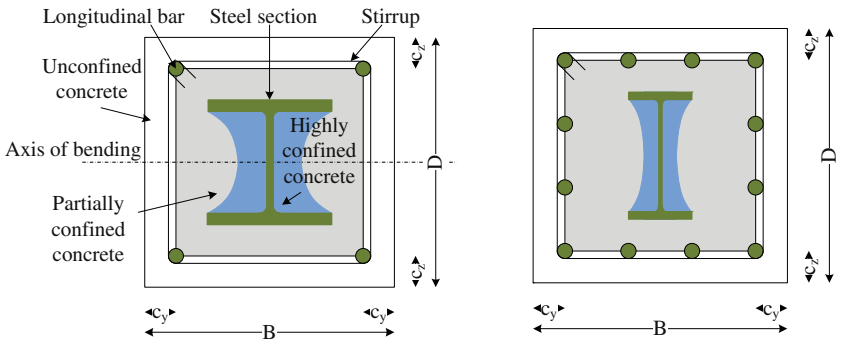

a) Specimen CESC1-CESC10. b) Specimen SCESC1-SCESC6.

Fig. 5. Specimen dimension and regions for unconfined, partially confined and highly confined concrete.

2.3. Indirect method for the estimation of the elastoplastic buckling loads

Due to the geometric and material non-linearities, the finite element problem is numerically solved in an incremental way. A specific technique is implemented within this numerical procedure, following Riks [20], in order to detect the bifurcation points along the fundamental equilibrium path. At the end of each increment, it must be checked whether one has gone across one or several critical points. The detection of critical points is based on the singularity of the tangent stiffness matrix, which may be factorized following the Crout formula $\mathbf{K}_g = \mathbf{LdL}^T$, where $\mathbf{L}$ is a lower triangular matrix with unit diagonal elements and $\mathbf{d}$ is a diagonal matrix. Since the number of negative eigenvalues of $\mathbf{K}_g$ is equal to the number of negative diagonal elements (pivots) of $\mathbf{d}$, the critical points are determined by counting the negative pivot number and comparing their values between the successive increments. Each detected critical point has to be isolated in order to specify the corresponding critical value. To do this, the prescribed force or displacement, or the current arc-length (depending on the control parameter used), may be re-estimated in one shot by interpolation of the appropriate eigenvalue, or several times using a dichotomy-like method. The step increment is then renewed so as to reach a point just behind the current bifurcation point, and so on for the next bifurcation points.

2.4. Validation

To the best of our knowledge, there is no available experimental result for buckling test on RC column with multi-embedded steel profiles (hybrid columns) in technical literature. Nevertheless, a couple of experimental compression-bending tests on steel-concrete shear walls with vertical steel encased profiles were conducted by Dan et al. [21] and by Zhou et al. [22]. The dimensions of the tested specimens are such that they cannot be considered as slender columns. Therefore, the developed finite element model is validated by comparing its prediction against ten test results of

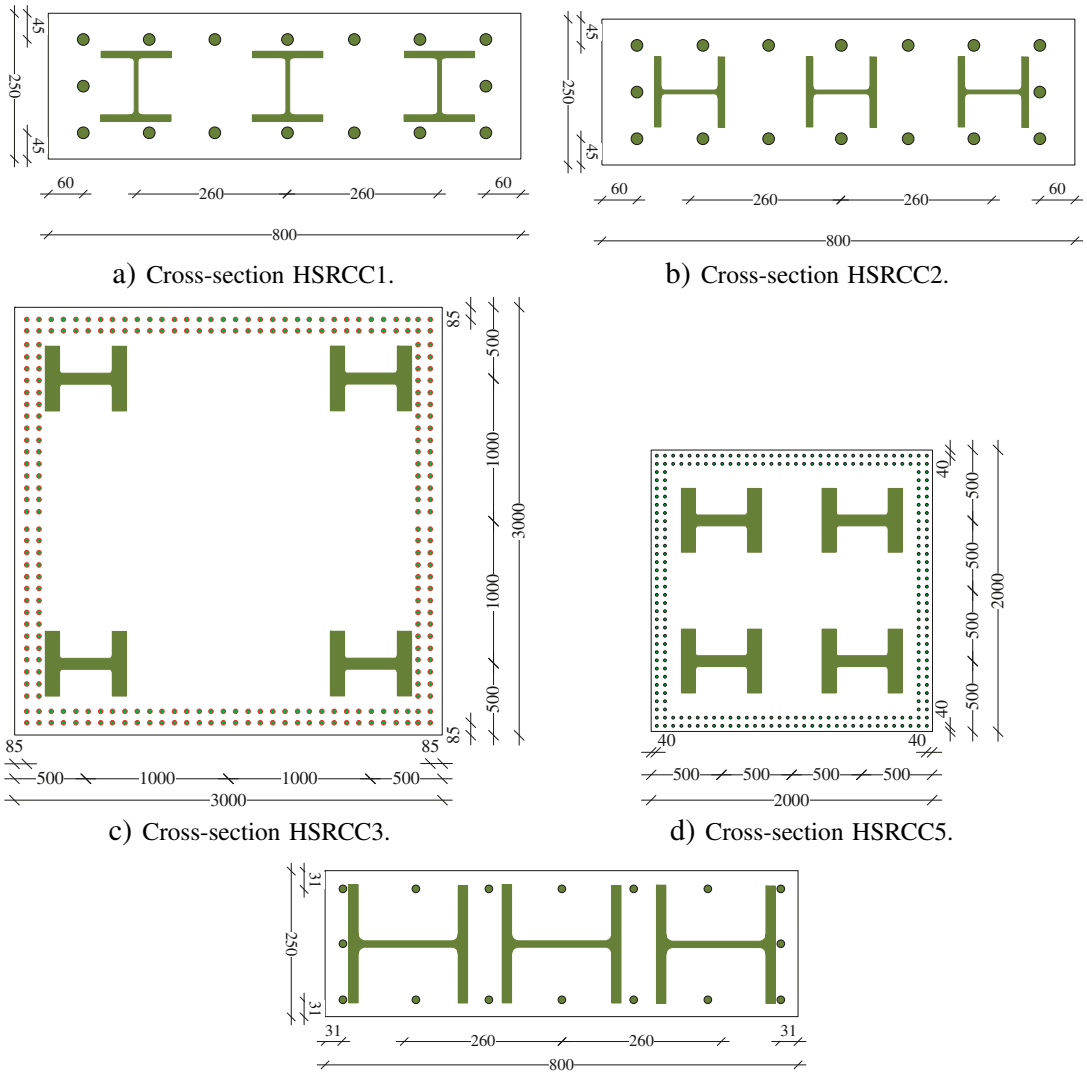

Fig. 6. Cross-sections considered in parametric study.

eccentrically loaded slender composite columns [23,24] and six test results of short composite columns [25]. For the sake of clarity, in this study we denote the seven specimens tested by Al-Shahari et al. [23] as CESC1–CESC7, the three specimens tested by Morino et al. [24] as CESC8–CESC10, and the six concrete encased steel composite short columns tested by Chen and Yeh [25] as SCESC1–SCESC6. The geometrical and material properties of the abovementioned specimens are summarized in Table 1.

All composite column specimens are pinned at both ends. Columns CESC1–CESC10 are loaded with the same eccentricity at both extremities. The concrete region is subdivided into three parts as suggested by Mirza et al. [26]. The highly confined concrete zone is taken from the web of the steel section to each flange, and the partially confined concrete zone is from the parabolic border of the highly confined concrete zone to the centerlines of the transverse reinforcement as illustrated in Fig. 5. The confinement factor varies from 1.10 to 1.97 for highly confined concrete and from 1.08 to 1.50 for partially confined concretedepending on spacing of the stirrups, as given by [27]. The concrete outside the ties is not confined. The effect of residual stresses in structural steel is included and the initial imperfection is taken equal to l_0 / 1000 in which l_0 is the effective length.

For all numerical simulations, the modified concrete stress–strain model proposed by Kent and Park [28] in compression is adopted. For concrete in tension, linear stress–strain relationship up to the tensile strength and linear tensile softening with fracture energy 0.12 N/mm are assumed. The stress–strain relationships of structural steel recommended by EC3 [29] and reinforcing bar recommended by EC2 [1] are adopted. All test specimens are modeled with the developed FE model using 6 elements. In Table 2, the predictions of the model are compared against test results. A good agreement between numerical and experimental results can be observed. Indeed, the mean value of numerical–experimental load capacity ratio for sixteen cases is very close to 1 and the corresponding standard deviation is only 6%. Furthermore, it is worth to mention that, in most cases, the FE model predictions are on the safe side.

3. Eurocode design methods for slender columns

In the design of slender structures, the second-order effects need to be considered. Eurocodes provide guidance on how to consider these effects in structural analysis using either a first-order analysis with appropriate amplification factors or a more precise second-order analysis. Nevertheless, second-order effects may be ignored if they are significantly less than the corresponding first-order ones, for instance less than 10% as stated in EN 1992-1-1: 5.8.2(6) and in EN 1994-1-1: 5.2.1(3). This implies that the designer would first check the second-order effects before ignoring them. EC2 and EC4 provide simplified criteria to verify if a global second-order analysis of the structure must be carried out in global structural analysis. If the answer to the question is “yes”, EC2 refers to its Appendix H for the evaluation of the global second-order effects using magnified horizontal forces, where the rigidity of bracing elements is determined by taking into account concrete cracking. Members sensitive to second-order effects will then be checked separately using the internal forces given by the global structural analysis. EN 1994-1-1: 5.2.2(3) states that individual stability checks of composite columns can be ignored if their individual imperfection and their reduced stiffness are fully accounted for in the global structural analysis.

Once the second-order effects (including cracking, material nonlinearity and creep) need to be accounted for, EC2 and EC4 propose both a simplified method, called “moment magnification method”, in which the first-order bending moment M_{Ed} is modified by a magnification factor k to obtain the second-order bending moment. The factor k largely depends on the flexural stiffness and the equivalent moment distribution. Hence, the procedure involves two steps. The first stage is to compute the effective stiffness EI and the second one is to estimate the first-order moment magnification factor based on the shape of the bending moment diagram. In general, not only the factors mentioned previously influence the flexural stiffness of the columns but also the column slenderness, the eccentricity, the magnitude of the normal force and the reinforcement ratio. The expression of EI can be written in the following form:

$$EI = K_c E_c I_c + K_s E_s I_s + K_a E_a I_a \tag{41}$$

where the contribution of concrete, rebars and steel sections with subscript c, s and a, respectively are multiplied by a correction factor and summed up. The correction factors K_c, K_s and K_a can be calibrated using more or less sophisticated models, to ensure agreement between the proposed method and FE analysis.

Table 2
Comparison between tests and finite element results.

Specimen	$\bar{\lambda}$	P_{Test} [kN]	P_{FE} [kN]	P_{FE}/P_{Test}
CESC1	0.36	654	641	0.98
CESC2	0.34	558	553	0.99
CESC3	0.34	962	813	0.85
CESC4	0.36	949	924	0.97
CESC5	0.55	900	822	0.91
CESC6	0.54	813	764	0.94
CESC7	0.51	704	646	0.92
CESC8	0.25	740	600	0.81
CESC9	0.63	504	493	0.98
CESC10	0.95	412	378	0.92
SCESC1	0.19	4220	4261	1.01
SCESC2	0.19	4228	4239	1.00
SCESC3	0.19	4399	4641	1.06
SCESC4	0.19	3788	3606	0.95
SCESC5	0.18	3683	3615	0.98
SCESC6	0.19	3893	3873	0.99
Mean	–	–	–	0.95
Cov	–	–	–	0.06

3.1. The moment magnification method in Eurocode 2

According to EC2, the first-order bending moment can be magnified using two different simplified methods. The first one, based on the nominal stiffness, can be applied in all situations. The second one is based on the nominal curvature and is primarily suitable for isolated members with constant normal force. Since EC4 also proposes an approach based on the nominal stiffness for the moment magnification method, this method could be a good candidate for hybrid column designs.

The total design moment, including second order moment, may be determined by multiplying the first-order moment including the effect of imperfections by the magnification factor k which is expressed as (EN1992−1−1:5.8.7.31)

$$k = 1 + \frac{\beta}{\frac{N_B}{N_{Ed}} - 1} \tag{42}$$

where

- β is a factor which depends on distribution of 1st and 2nd order moments. For isolated columns with constant cross section and axial load, $\beta = 1.233$ for a constant first order moment distribution, 1.028 for a parabolic distribution and 0.822 for a symmetric triangular distribution;
- N_{Ed} is the design value of the axial load; and
- $N_B = \frac{\pi^2 EI}{l_0^2}$ is the buckling load based on nominal stiffness EI which is defined by the following expression (EN1992−1−1:5.8.7.21)

$$EI = K_c E_{cd} I_c + K_s E_s I_s \tag{43}$$

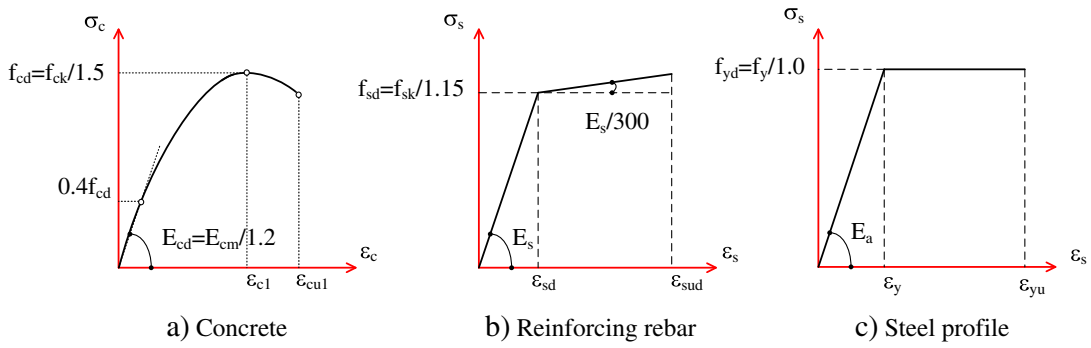

Fig. 7. Material constitutive laws used for FE analysis.

in which l_0 is the effective length of the column; K_c a factor to account for the effects of cracking, creep and material nonlinearity; and K_s a factor related to the contribution of reinforcement. Providing that the geometric reinforcement ratio is greater than 0.2%, they are determined by the following expressions (EN1992−1−1:5.8.7.22):

$$K_c = \sqrt{\frac{f_{ck}}{20}}\min\left(\frac{N_{Ed}}{A_c f_{cd}}\frac{\lambda}{170};0.2\right)\frac{1}{1+\varphi_{ef}} \text{ and } K_s = 1 \tag{44}$$

where φ_{ef} is the effective creep ratio and λ is the slenderness ratio.

3.2. The moment magnification method in Eurocode 4

According to EC4, the second-order effects in composite columns can be accounted for by multiplying the largest first-order design bending moment M_{Ed} by a magnification factor k given by:

$$k = \frac{\beta}{1-\dfrac{N_{Ed}}{N_{cr,eff}}} \tag{45}$$

where

- $\beta = 1$ if the 1st order maximum bending moment M_{Ed} is in the column. Otherwise $\beta = \max(0.66 + 0.44r_m; 0.44)$ in which r_m is the ratio between bending moments acting at the column extremities $(-1 \le r_m \le 1)$;
- N_{Ed} is the total design normal force;
- $N_{cr,eff}$ is the buckling load computed with the effective stiffness $(EI)_{eff,II}$ defined by the following expression (EN1994−1−1:6.7.3.42)

$$(EI)_{eff,II} = 0.9(E_a I_a + E_s I_s) + 0.45E_{cm}I_c \tag{46}$$

In order to take into account the influence of long-term effects on the effective elastic flexural stiffness, EC4 proposes to reduce the modulus of elasticity of concrete E_{cm} to the value $E_{c,eff}$ in accordance with the following expression:

$$E_{c,eff} = E_{cm}\frac{1}{1+\left(N_{G,Ed}/N_{Ed}\right)\varphi_t} \tag{47}$$

where φ_t is the creep coefficient; and $N_{G,Ed}$ is the part of total design normal force N_{Ed} that is permanent.

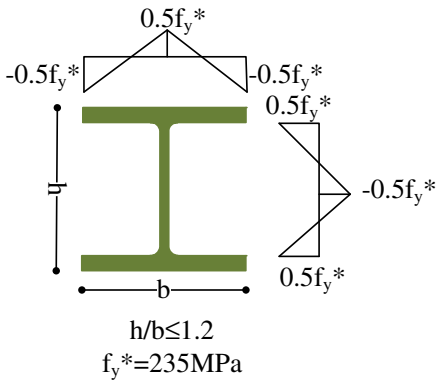

Fig. 8. Residual stress distribution of steel profile.

4. Parametric study and assessment of simplified methods of EC2 and EC4

In this section, the developed FE model which was successfully validated is used to conduct an extensive parametric study in order to assess the applicability of moment magnification methods of EC2 and EC4 to hybrid column designs. To do so, the ultimate load of slender hybrid columns with different types of cross-sections are computed using our FE model and the Eurocode simplified methods. The results obtained with Eurocode methods are compared against each other to assess the applicability of these simplified methods to hybrid column design. Five different hybrid cross-section configurations (HSRCC1–5) are considered. The cross-sections HSRCC1 and HSRCC2 are built with 3 steel profiles HEB120. In the first configuration (HSRCC1) the weak-axis of the profiles is parallel to the bending axis whereas in the second configuration (HSRCC2) they are orthogonal (see Fig. 6a and b). Hybrid cross-

Table 3
Summary of case-studies.

Section	S1; S2; S3; S4; S5
Concrete	C35/45; C60/75; C90/105
f_{yk}	500 MPa
f_a	355 MPa
$\bar{\lambda}$	0.5; 1.0; 2.0
e/h	0.0–3.0
δ	0.2–0.62
ϕ_{ef}	0; 1.5

Table 4
Material properties.

Concrete		
$f_{ck} = 60$ MPa	$E_{cm} = 39.10$ GPa	$\varphi_{ef} = 1.5$
$\gamma_c = 1.5$	$\gamma_{cE} = 1.2$	
Reinforcing rebar		
$f_{sk} = 500$ MPa	$E_s = 210$ GPa	$\gamma_s = 1.15$
Steel profile		
$f_y = 355$ MPa	$E_a = 210$ GPa	$\gamma_a = 1.0$
Connector stiffness		
$K_{sc} = 8$ MPa	$K_{sc} = 800$ MPa	$K_{sc} = 3000$ MPa
$K_{sc} = 7000$ MPa	$K_{sc} = \infty$ MPa	

sections HSRCC3 and HSRCC5 correspond to the so-called mega-column which contains 4 steel profiles located at each corner of the cross-section (see Fig. 6c and d). The cross-section (HSRCC4) has also 3 steel profiles but with larger steel cross-section.

The diameter of the rebars is 20 mm for HSRCC1, HSRCC2 and HSRCC5, 32 mm for HSRCC3, and 12 mm for HSRCC4. Due to symmetry, only half-section of mega-column (HSRCC3 and HSRCC5) is modeled. For all cases considered in this study, the limit of elasticity for steel profile is 355 MPa and 500 MPa for reinforcement bar. Three concrete classes are considered: C35, C60 and C90. Note that hybrid columns HSRCC4 and HSRCC5 with a significantly high value of steel contribution ratio δ are modeled with concrete class C35. Although the hybrid column HSRCC4 is not totally realistic, it is considered here as a limit case with a large value of δ.

In high-rise buildings, there is a significant amount of long term loads (approximately 75% of total loads). Therefore, the effect of sustained loads has to be considered. In this work, the effective creep ratio is taken equal to 1.5. As a consequence, the concrete stress–strain curve is modified following EC2 recommendations.

For columns subjected to axial compression and bending moment, three different relative slenderness $\overline{\lambda}$ are considered for each cross-section configuration. To access the effect of creep on the ultimate load, both situations (with and without creep) are considered for each case. From the value of relative slenderness and geometry of the cross-section, the column length can be deduced. For columns subjected to compressive load only, the whole range of possible relative slenderness is covered. The parametrical study is summarized in Table 3.

In this study, we consider that the column is experiencing bending about the strong axis. This situation corresponds to the case where the extreme load produced by wind or seismic load in that direction and the motion of the column is restrained on the other direction.

4.1. Material laws

In order to evaluate the accuracy of the safety level when applying the simplified design methods proposed in EC2 and EC4 for hybrid column design, the general design methods (using nonlinear FE analysis) suggested by the Eurocodes should be adopted. Nonlinear material models as well as the safety format have to be properly described. The comparison of the results provided by simplified method of EC2 against FE analysis is readily achieved by using the stress–strain relationship based on the design values of the constitutive model parameters as it is clearly defined in EN 1992-1-1: 5.8.6. Regarding the safety format for nonlinear FE analysis, the Eurocode for composite structures recommends to use the stress–strain relationships defined in EC2 and EC3 as stated in EN 1994-1-1: 6.7.2(8). Therefore, the material constitutive laws and the partial factors recommended by EC2 and EC3 are adopted (Fig. 7). The descriptions of the stress–strain relationships are recalled in the following. The code suggests to adopt a bilinear stress–strain relationship for reinforcing bar. EN 1992-1-1: 5.8.6(3) recommends using the concrete stress–strain relationship expressed by Eq. (48) where the tension part of concrete is ignored.

$$\frac{\sigma_c}{f_{cm}} = \frac{k\eta - \eta^2}{1 + (k-2)\eta} \tag{48}$$

where

- $\eta = \epsilon_c / \epsilon_{c1}$;
- ϵ_{c1} is the strain at peak stress according to EN 1992-1-1; and
- $k = 1.05E_{cm} \times |\epsilon_{c1}| / f_{cm}$ (f_{cm} according to EN 1992-1-1).

Eq. (48) is valid for $0 < |\epsilon_c| < |\epsilon_{cu1}|$ where ϵ_{cu1} is the nominal ultimate strain. According to EN 1992-1-1: 5.8.6(4), creep can be taken into account by multiplying all strain values in the concrete stress–strain diagram with a factor $(1 + \varphi_{ef})$, where φ_{ef} is the effective creep ratio. According to EN 1994-1-1: 3.2(2), the design value of the modulus of elasticity E_s of reinforcing rebar may be taken equal to the value for structural steel given in EN 1993-1-1: 3.2.6.

Incremental FE model based on fiber discretization requires appropriate uniaxial stress–strain relationships for each material with the design values of strengths. This requirement is consistent with the stress–strain relationship given by the code. The stiffness of the element is then derived from these stress–strain curves. Since there is dependency between strength and stiffness in FE analysis, the partial factors for concrete, rebar reinforcement and steel profile are taken respectively equal to 1.5, 1.15 and 1; and the partial factor for design modulus of elasticity of concrete is taken equal to 1.2 (following EN 1992-1-1: 5.8.6(3)). The design stress–strain curves for each material are illustrated in Fig. 7.

4.2. Geometric imperfection and residual stresses

Second-order analysis requires the definition of an imperfection. Those imperfections found their sources in both the geometric imperfection as well as the residual stresses. The definition of this initial deformed shape strongly affects the behavior of slender columns. For concrete columns, EC2 recommends to consider a geometric imperfection equal to $l_0 / 400$ whereas for steel columns EC3 not only suggests to adopt a geometric imperfection equal to $l_0 / 1000$ but also to take into account the effects of the residual stress distribution. The imperfect shape of composite columns is governed by the steel component and therefore by the residual stress distribution within this component (see Fig. 8). Accordingly, an initial imperfection $l_0 / 1000$ has to be considered and the geometric effects of the residual stress distribution must be considered. To simplify the calculation, EC4 suggests to replace the residual stresses by an equivalent initial bow imperfection. However, Bergmann et al. [30] have shown that this simplification produces an approximate value of the ultimate resistance in axial compression. The hybrid column being built as a concrete column; we adopt an initial imperfection w_0 equal to $l_0 / 400$ combined with an explicit representation of the residual stress distribution in order to ensure the best accuracy of the results.

Table 5
The ratio of bearing capacity of the column P_u to $P_{u,\infty}$.

$P_u/P_{u,\infty}$	Case A			Case B		
	$\overline{\lambda} = 0.5$	$\overline{\lambda} = 1.0$	$\overline{\lambda} = 2.0$	$\overline{\lambda} = 0.5$	$\overline{\lambda} = 1.0$	$\overline{\lambda} = 2.0$
$K_{sc} = 8$ MPa	0.72	0.72	0.76	0.98	0.96	0.92
$K_{sc} = 8000$ MPa	0.90	0.99	1.00	1.00	1.00	1.00
$K_{sc} = 3000$ MPa	0.95	1.00	1.00	1.00	1.00	1.00
$K_{sc} = 7000$ MPa	1.00	1.00	1.00	1.00	1.00	1.00

4.3. Shear connection

Eurocode 4 design rules for composite columns assume full interaction between the steel section and the surrounding concrete, i.e. the slips at steel–concrete interfaces can be ignored. To remain consistent with Eurocode rules, the same hypothesis is retained for hybrid columns although the latter may be viewed as a fairly strong assumption for both composite and hybrid columns, particularly with deformable shear connector. The consequence of this assumption on the ultimate load of hybrid columns will be evaluated by carefully analyzing the effect of the connection stiffness on the ultimate load using the nonlinear finite element model developed in Section 2 which takes into account the partial interaction.

The shear connection stiffness K_{sc} can be determined by $K_{sc} = k_{sc0} / d$ where k_{sc0} is the stiffness of a shear stud and d is the spacing between the connectors. It is varied from low to high stiffness. For a certain value of the stiffness, the load-bearing capacity does not vary with increasing value of the connection stiffness and slips become very small so that we can assume full interaction. The value of this critical stiffness will be used for the parametric study in order to remain consistent with EC4.

The investigation on the effect of the stiffness K_{sc} and the slip distribution has been carried out on the pinned–pinned hybrid column with cross-section HSRCC1. Three different lengths corresponding to three different values of the relative slenderness $\overline{\lambda}$ (0.5, 1 and 2) are considered. The column is subjected to an eccentric load causing a symmetric single curvature bending about the strong axis of the cross-section. The eccentricity ratio e/h is equal to 0.3 at both column extremities. It is worth to mention that the axial load is applied through an eccentric node linked rigidly to concrete node. The material properties are summarized in Table 4.

In this case, a linear elastic behavior of the connector is considered; the confinement of concrete is ignored and the residual stress distribution in the steel section is assumed to follow the diagram given in Fig. 8. The column is supposed to have an initial geometrical imperfection of l_0 / 400. The ultimate design capacity of the column is obtained by performing a nonlinear analysis using material laws and safety concept described in Section 4.1. The finite element results with a mesh consisting of 10 elements are shown in Table 5. The ratio between the bearing capacity of the column in partial interaction P_u and the one in full interaction $P_{u,\infty}$ is computed considering several values of connection stiffness K_{sc} and relative slenderness $\overline{\lambda}$. Regarding the boundary conditions for the interlayer slip at the column ends, two cases have been considered. In case A, interlayer slips are permitted at both ends of the column whereas in case B, the slips are prevented. It can be observed from Table 5 that when the interlayer slips at extremities are prohibited (case B), the ultimate load in full interaction can be achieved for a moderate shear connection stiffness. However, with a low value of K_{sc} and no slips at the column ends (case B) the ultimate load is slightly below the one in full interaction. On the contrary, the ultimate load drops significantly for a column with low slenderness ratio and free slips at the column ends. In both cases (A and B), the ultimate load in full interaction can be achieved for columns with medium-to-high relative slenderness with a moderate shear connection stiffness.

4.4. Assessment of the EC2 moment magnification method

In the present section, the applicability of the EC2 version of the moment magnification method to hybrid columns is assessed by comparing its predictions against FE analysis results for hybrid column with cross-section HSRCC1 (see Fig. 6a). The concrete class is C60 and the effect of creep is taken into account ($\phi_{ef} = 1.5$). It can be seen from Fig. 9a that in case of pure compression, the moment magnification method of EC2 gives unsafe results for low-to-moderate relative slenderness whereas the method provides conservative results for high relative slenderness. For column subjected to single curvature bending and regardless of the load eccentricity (see Fig. 9b and c), EC2 method overestimates the ultimate load for low-to-moderate relative slenderness ($\overline{\lambda} = 0.5$ to 1.0). The same conclusion applies for columns bent in double curvature under antisymmetric bending moment (see Fig. 9d) except for very high load eccentricities (close to pure bending). For high relative slenderness, EC2 method gives safe results except for columns bent in single curvature under large bending moment.

Since this simplified method is based on the effective stiffness of the column *EI*, it can be concluded that the expression for the effective stiffness proposed by EC2 cannot be applied in a straightforward fashion to hybrid column design. This effective stiffness should be modified by adjusting the factor K_c (see Eq. (44)) which depends on the relative slenderness of the column so that it becomes applicable to hybrid column. Moreover, the factor K_s which is applied to the stiffness can also be modified in order to account for the plastification of the steel section.

4.5. Assessment of the EC4 variant of the moment magnification method

In this section we pursue our study by an assessment of the performance of the EC4 version of the moment magnification method when applied to hybrid columns. Again a comparison of the predictions of the EC4 method against FE analysis results for hybrid column with cross-section HSRCC1 (see Fig. 6a) is carried out. The concrete class and effective creep ratio are the same as previous case (C60 and $\phi_{ef} = 1.5$). Quite surprisingly, the EC4 version of the moment magnification method seems to perform less well. Indeed, for a hybrid column subjected to pure compression (see Fig. 10a) where the ultimate load of the column is characterized by the resistance in axial compression, the simplified method of EC4 gives safe results regardless of column relative slenderness. Apart from the later case, this method gives unsafe results for a large number of cases. For low load eccentricity, the ultimate load given by EC4 formulation is safe regardless of column relative slenderness (see Fig. 10b to d). For moderate load eccentricity, EC4 method always overestimates the ultimate load. Under large bending moment, EC4 method gives safe results, particularly for column under symmetric single curvature bending in the zone of nearly pure bending. The conservative nature of the results can be attributed to the equivalent moment factor β, which, in the present case, is equal to 1.1.

Since this moment magnification method is based on the effective stiffness of the column *EI*, it can also be concluded that the expression for effective stiffness given in EC4 cannot be applied in a straightforward fashion to hybrid column design. This effective stiffness should be modified by reformulating the factor $K_{e,II}$ as well as K_0. These factors should be minimized to reduce the value of the effective stiffness and as a result the ultimate load will be decreased. This modification is proposed in Section 5.

4.6. Results of the parametric study

The ultimate load for isolated hybrid columns with five different cross-section configurations (see Fig. 6) has been evaluated using both the finite element model and the moment magnification method proposed in EC2 and EC4. The accuracy of moment magnification method should be evaluated according to Appendix D of EN 1990 [31]. The application of the method given in this Appendix is rather straightforward provided that a large number of ultimate loads are available with the magnitude of the latter being influenced by a single parameter. It is much more complicated to apply this method for members subjected to axial load and bending moment where additionally, a large number of key parameters have to be taken into account. Because of this difficulty, an exact implementation of EN 1990-Appendix D cannot be rigorously followed while assessing the moment magnification method of EC2 and EC4. To evaluate the EC3 variant of the method for steel beam-column member, the ratio of the experimental or numerical failure load to the corresponding theoretical load has been used in [32].

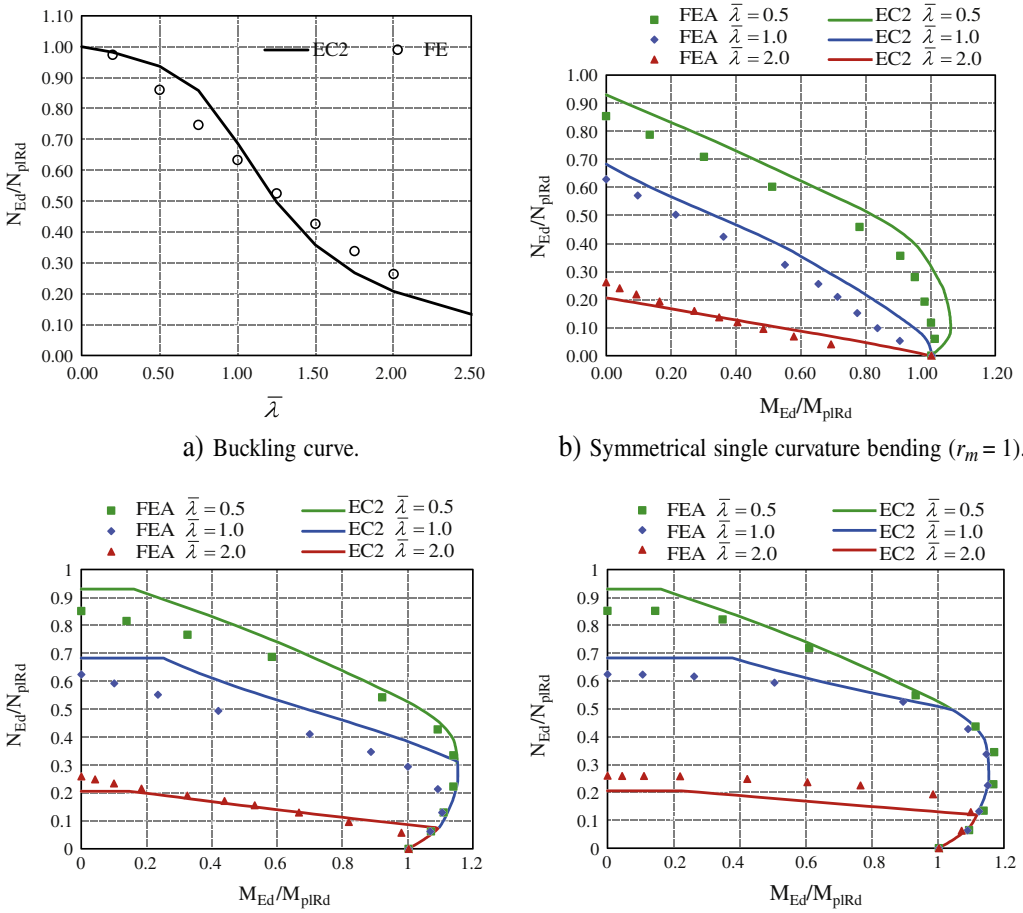

a) Buckling curve.

b) Symmetrical single curvature bending ($r_m = 1$).

c) Single curvature bending ($r_m = 0$).

d) Double symmetrical curvature bending ($r_m = -1$).

Fig. 9. Comparison of simplified method of EC2 against FE analysis results.

Similarly, the ratio between the first order bending moment obtained via numerical simulation $(M1)_{FE}$ and the ones obtained with the simplified method $(M1)_{FE}$ was used to calibrate the simplified method of EC2 in [33]. However, this procedure is not appropriate in case the column is subjected to axial load only which makes this ratio go to infinity. To overcome this difficulty, the ratio R expressed in Eq. (49) has been selected by Bonnet et al. [4] as a reference value to evaluate the accuracy of their own proposal. This ratio Eq. (49) is also adopted in our investigation.

$$R = \frac{R_{FE}}{R_{SM}} \tag{49}$$

where: $R_{FE} = \sqrt{\left(\frac{N_{FE}}{N_{pl.Rd}}\right)^2 + \left(\frac{M_{FE}}{M_{pl.Rd}}\right)^2}$ and $R_{SM} = \sqrt{\left(\frac{N_{SM}}{N_{pl.Rd}}\right)^2 + \left(\frac{M_{SM}}{M_{pl.Rd}}\right)^2}$.

Figs. 11 and 12 give a summary of the results obtained with both EC2 and EC4 version of the moment magnification approach which are compared against FE analyses. In order to evaluate the contribution of the various parameters governing the ultimate load, the R ratio is first computed for all the considered cases (1140 data sets). The value of the R ratio is given as a function of each key variables: relative slenderness $\bar{\lambda}$, eccentricity e/h, steel contribution ratio δ, reinforcement ratio ρ, concrete characteristic strength f_{ck}, effective creep ratio ϕ_{ef} and the ratio r_m between the bending moment applied at the column ends. For every value of each parameter all corresponding values of R are given as discrete points.

To analyze the relative performance of the EC2 and EC4 variants of the moment magnification method, the graphs for the R ratio computed for each method for a given parameter are put as a pair. Regarding the contribution of the relative slenderness on variant of the method, two different graphs are provided. The first graph is for columns subjected to pure compression and the other for columns subjected combined compression and bending. The statistical distribution of R is represented along with its mean value r and the interval ($r + s$ and $r - s$) where s is the standard deviation. Both simplified methods show a rather wide discrepancy compared to FE analysis results. The most significant parameters are the slenderness of the column, the steel section contribution to the cross-section strength under pure compression (δ) as well as the geometrical reinforcement ratio (ρ). Fig. 11 shows that for column subjected to an axial load only (zero eccentricity), both simplified methods give unsafe results for low relative slenderness. In case the latter is moderate, the predictions of EC2 moment magnification method are unsafe while the EC4 one gives conservative results. Nevertheless, EC2 method provides reasonable results compared to EC4 method for high relative slenderness. For column subjected to combined compression and bending moment, both codes provide unsafe results in most cases. In particular, the interaction curve given by EC2 moment magnification method without considering the creep effect ($\varphi_{ef} = 0$) is close to FE analysis results. However, EC2 becomes un-conservative if creep is considered ($\varphi_{ef} = 1.5$). Looking at all cases, it was found that the mean value r and the standard deviation s are respectively equal to

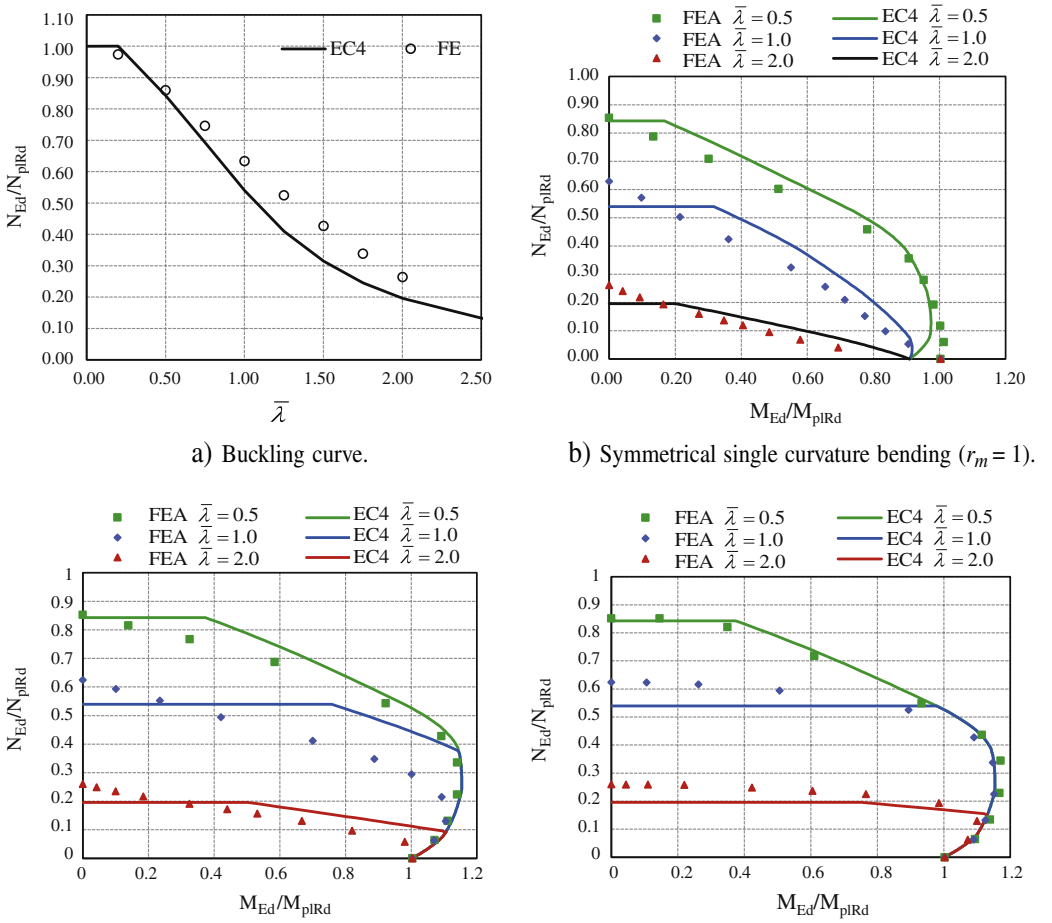

a) Buckling curve.

b) Symmetrical single curvature bending ($r_m = 1$).

c) Single curvature bending ($r_m = 0$).

d) Double symmetrical curvature bending ($r_m = -1$).

Fig. 10. Comparison of simplified method of EC4 against FE analysis results.

0.996 and 0.104 for EC2 simplified method and 1.010 and 0.112 for EC4 simplified method. The percentage of R below 0.97 is 41.84% and 34.86% for EC2 and EC4 simplified method, respectively. As a general conclusion, it can be pointed out that mean estimations of both design codes seem to be correct but that their shortcomings lead to a large scatter of the results.

5. Proposal of a moment magnification design method for hybrid column

5.1. Further insight into the physical behavior of hybrid column

Before suggesting new expressions for correction factors involved in the moment magnification method for hybrid column design, some effects are analyzed to get further insight into the physical behavior of hybrid column.

5.1.1. Effect of sustained loads

The reduction of the load-bearing capacity due to creep is illustrated in Fig. 13a and b for different load eccentricities. The interaction curve of hybrid column with cross-section HSRCC2 subjected to eccentric load and bent in a symmetric single curvature is depicted in Fig. 13c where $N_{pl,Rd0}$ stands for the plastic design normal force and $M_{pl,Rd0}$ for the plastic bending moment of the cross-section, both being considered without creep effect. Two values of the effective creep ratio are considered ($\delta_{ef} = 0$ and $\delta_{ef} = 1.50$). The concrete strength used in this study is C35. It can be seen that the plastic design moment of the cross-section with $\delta_{ef} = 1.50$ is larger than that with $\delta_{ef} = 0$. This difference comes from the ductility of the concrete which allows the compressed part of the steel section to yield before concrete crushes.

5.1.2. Effect of the residual stresses in the steel section

The buckling behavior of steel member is governed by the residual stresses. The distribution of the latter is shown in Fig. 8 for standard I-sections. The hybrid column with cross-section HSRCC1-3 are considered as well as the hybrid column with two steel profiles (HEB120) that are very close to each other (see Fig. 17a). The diameter of the rebar used for this column is ϕ12. The columns are modeled with concrete strength C35, structural steel yield stress 355 MPa and reinforcement yield stress 500 MPa. The column is subjected to the same eccentric loads at both ends. The comparison of buckling and interaction curves considering and disregarding the residual stresses is given in Figs. 14 to 17b. The dash line (– ◦ –) corresponds to the interaction curve when the residual stresses within the steel profile are not considered whereas the solid line (—) corresponds to the interaction curve with residual stresses. It can be seen that the residual stresses have a marginal effect on the behavior of hybrid columns and they can be ignored. Therefore, it can be concluded that the structural steels behave as large rebars. Considering the above comments, it can be concluded that the new

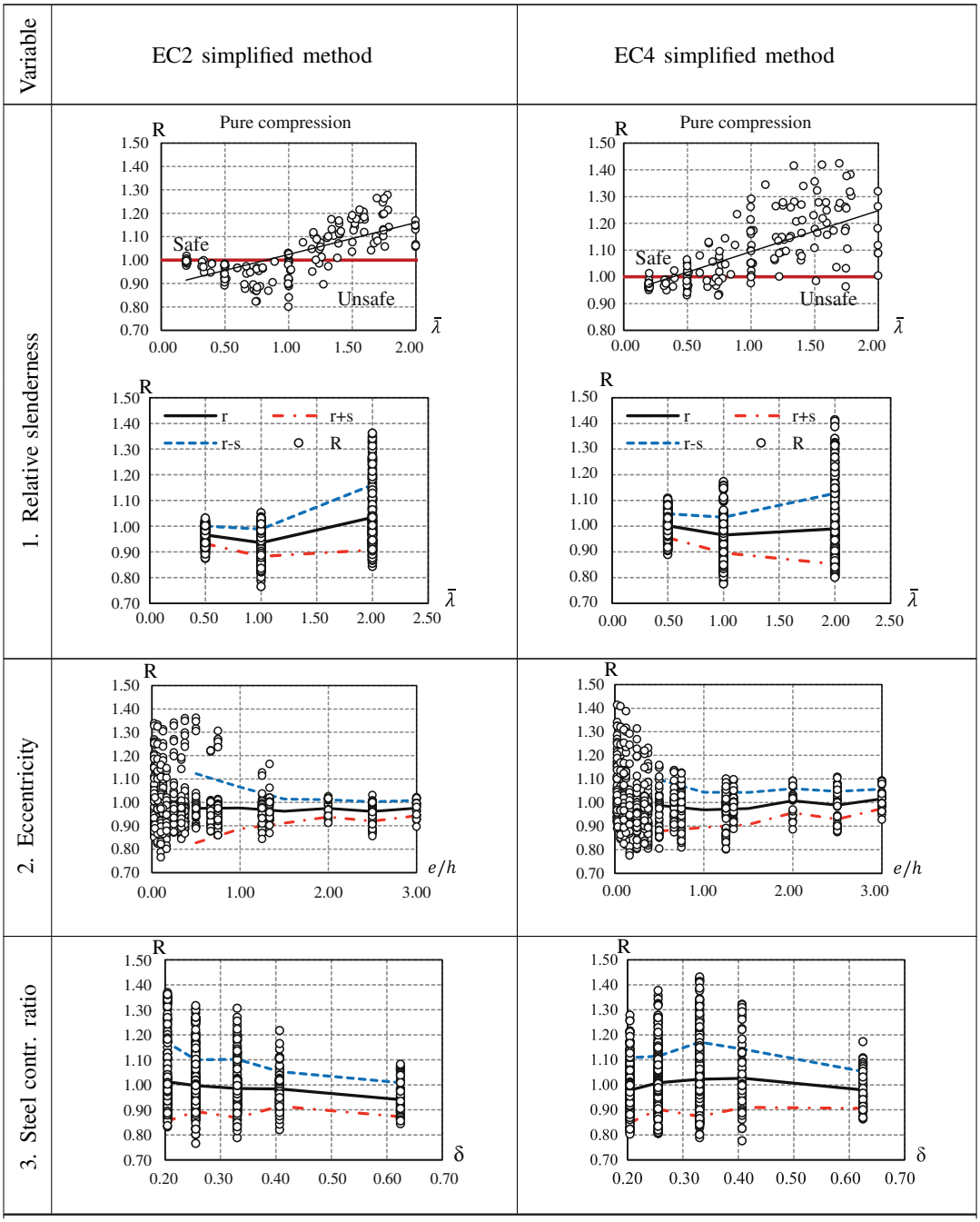

Fig. 11. Results of parametric study of EC2 and EC4 version of moment magnification method: Part 1.

method for hybrid columns should be inspired from the EC2 variant rather than from the EC4 version.

5.2. A proposal for the expression of the flexural stiffness EI applicable to hybrid columns subjected to combined axial load and uniaxial bending

The parametric study with 1140 data sets presented previously shows that both EC2 and EC4 versions of the moment magnification method lead to unsafe results in half of the case-studies (Table 3). It means that the effective flexural stiffness *EI* given in EC2 and EC4 are not appropriate for slender hybrid column design. Based on the outcome of the parametric study with 2960 cases including different yield stress of steel section, new expressions for β and the correction factors (K_s,K_a,K_c) involved in the definition of the effective flexural stiffness *EI* are proposed. By doing so, we are able to make the moment magnification method given in Eurocodes suitable for hybrid column design. The proposed simplified method based on moment magnification approach is summarized in the following.

The total design moment is determined by multiplying the first-order moment (including the effect of geometric imperfection) by the magnification factor *k* which is defined as

$$k = \frac{\beta}{1-\frac{N_{Ed}}{N_{cr}}} \tag{50}$$

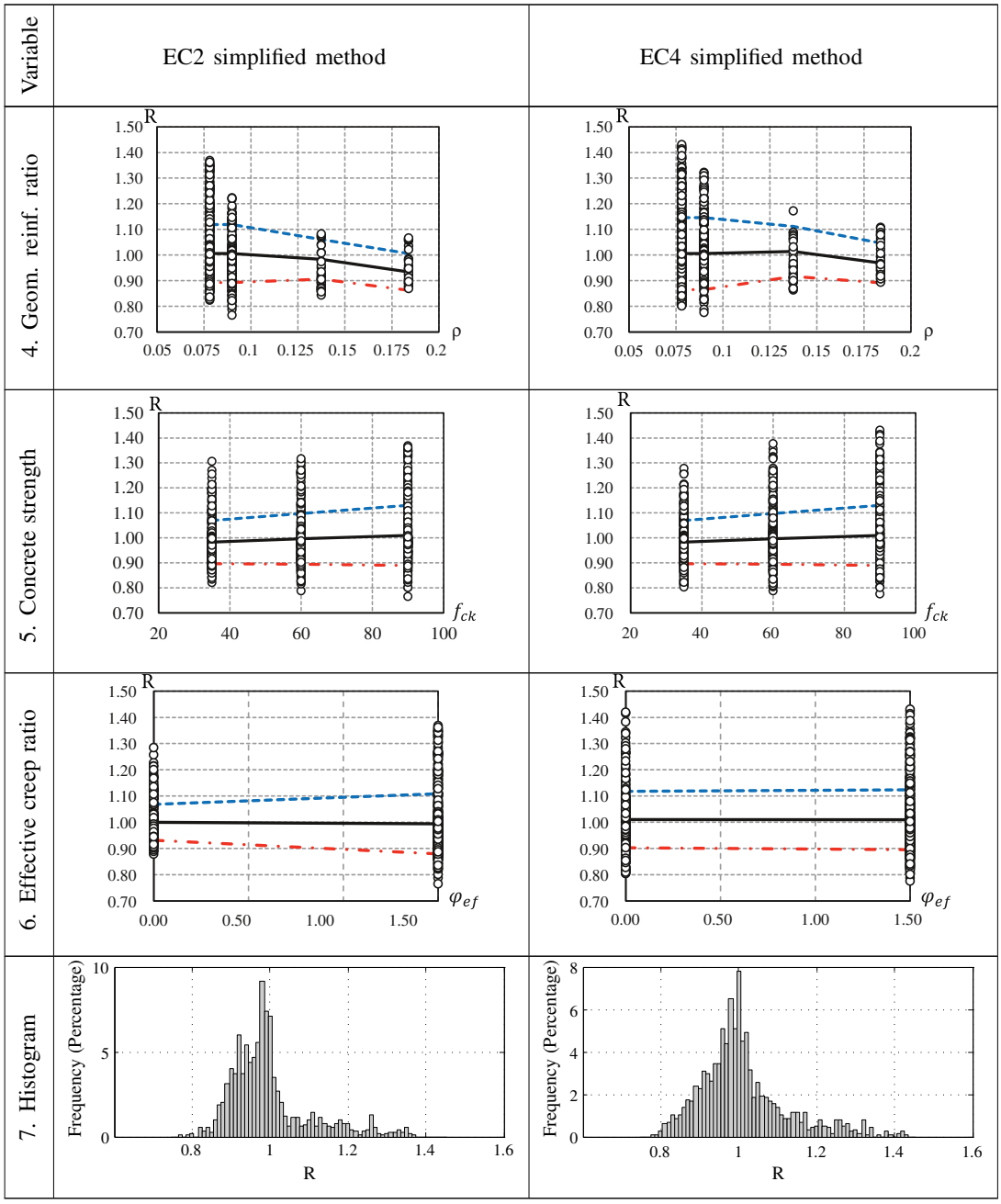

Fig. 12. Results of parametric study of EC2 and EC4 version of moment magnification method: Part 2.

where $\beta = 0.6r_m + 0.4 \geq 0.4$; and N_{cr} is buckling load which is calculated by using the following expression for the flexural stiffness EI

$$EI = K_c E_{cd} I_c + K_s E_s I_s + K_a E_a I_a \tag{51}$$

with

$$K_c = k_1 k_2 / \left(1 + \varphi_{ef}\right) \tag{52}$$

$$K_s = 1 \tag{53}$$

$$K_a = \frac{0.76\left(\frac{f_y}{f_{ck}}\right)^{0.0124}}{1 + 105\varphi_{ef}\exp(-0.078\lambda)} \leq 1 \tag{54}$$

$$k_1 = \sqrt{\frac{f_{ck}}{20}} \tag{55}$$

$$k_2 = n\frac{\lambda}{170} \leq 0.2 \tag{56}$$

$$n = \frac{N_{Ed}}{N_{pl,Rd}} \tag{57}$$

where the expressions of the correction factors K_c and K_s recommended in EC2 have been used. Further, since there is no steel profile in a reinforced concrete section, the correction factor K_a does not exist in EC2. If one compares these correction factors to those in EC4, they are totally

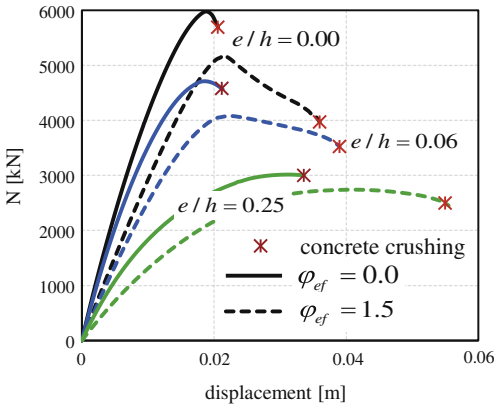

b) Reduction of ultimate load due to creep for slenderness ratio $\bar{\lambda}$ = 1 .0.

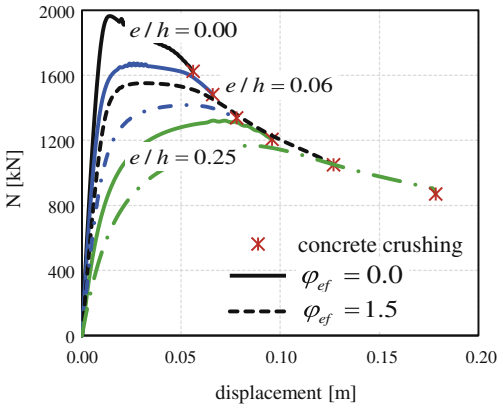

b) Reduction of ultimate load due to creep for slenderness ratio $\bar{\lambda}$ = 2 .0.

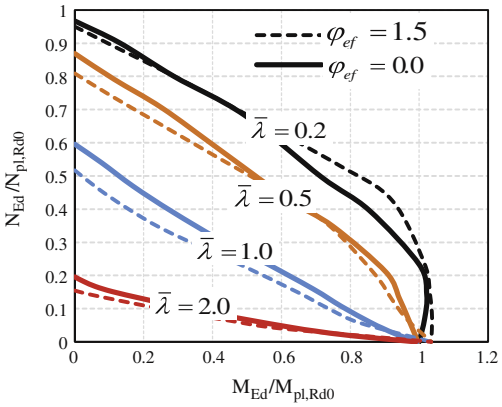

c) Interaction curve.

Fig. 13. Illustration of creep effect on slender hybrid column.

different. In fact, due to compressive creep strains, as shown in Section 5.1.2, longitudinal steel compressive strains can exceed the yield strain. This implies that the steel modulus that collaborates in the effective stiffness *EI* of the hybrid column could not be the elastic modulus but should rather be the secant modulus which varies with concrete creep. Moreover, for slender columns, plastification in the compression zone of the steel section may not develop before instability. Hence, the secant modulus of steel should be a function of the creep coefficient ϕ_{ef} and the geometric slenderness λ. For higher values of the creep coefficient, the value of the secant modulus of the steel section

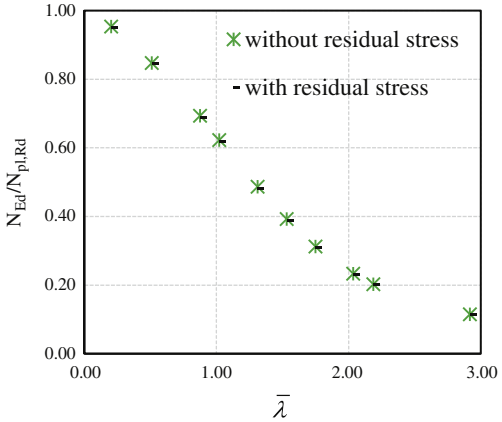

a) Buckling curve.

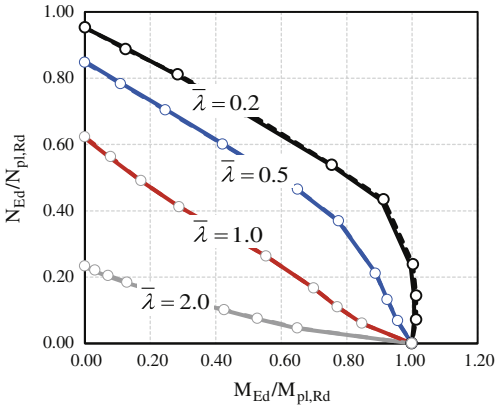

b) Interaction curve.

Fig. 14. Effect of residual stress in buckling behavior of HSRCC1.

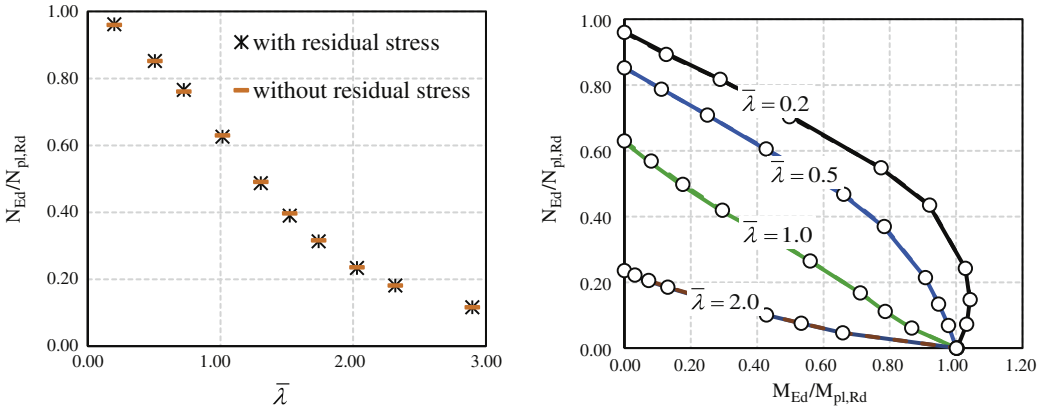

a) Buckling curve. b) Interaction curve.

Fig. 15. Effect of residual stress in buckling behavior of HSRCC2.

will be rather lower. However, for higher values of slenderness this modulus will be higher. Therefore, in addition to the previous cases already analyzed, we need to investigate the effect of the steel yield stress on the ultimate load of hybrid columns. All cases previously analyzed with $f_y = 355$ MPa are now recalculated with $f_y = 235$ MPa and $f_y = 460$ MPa. The objective is to analyze the effect of plastification of the steel sections, particularly for low yield stress. As a result, the correction factor K_a of EC4 is modified to take into account the effect of plastification of the steel section. This factor is calibrated based on the results of a parametric study with 2960 parameter sets (cross-sections, column effective slenderness and creep coefficient) performed by using our FE model.

The procedure employed to establish the expression of K_a is as follows. Let us consider a slender hybrid column with an initial imperfection w_0 subjected to axial loads and uniaxial bending, bent in a symmetric single curvature ($r_m = 1$), the ultimate first-order bending moment $M_{Ed,1}$ can be obtained with a nonlinear FE analysis for a particular axial load N_{Ed}. Likewise, it is also possible to compute the ultimate bending moment $M_{pl,N,Rd}$ of the column cross-section for the same axial force. By equating the second-order bending moment calculated with the moment magnification method to the ultimate bending moment of the column cross-section, the moment magnification factor k can be obtained. Finally, by making use of the critical buckling load formulation and the proposed form of the effective stiffness expression, the correction factor K_a can be derived. This procedure has also been adopted in [4].

- First, the magnification factor is calculated:

$$k = \frac{M_{pl,N,Rd}}{M_{Ed,1}} \tag{58}$$

- This value allows the critical buckling load of the column to be computed:

$$N_{cr} = \frac{N_{FE}}{1 - \dfrac{M_{Ed,1}}{M_{pl,N,Rd}}}. \tag{59}$$

- The flexural stiffness of the column can be computed from

$$EI = \frac{N_{cr} L^2}{\pi^2}. \tag{60}$$

- Finally, the calibration factor K_a can be obtained as

$$K_a = \frac{EI - K_c E_{cd} I_c + E_s I_s}{E_a I_a}. \tag{61}$$

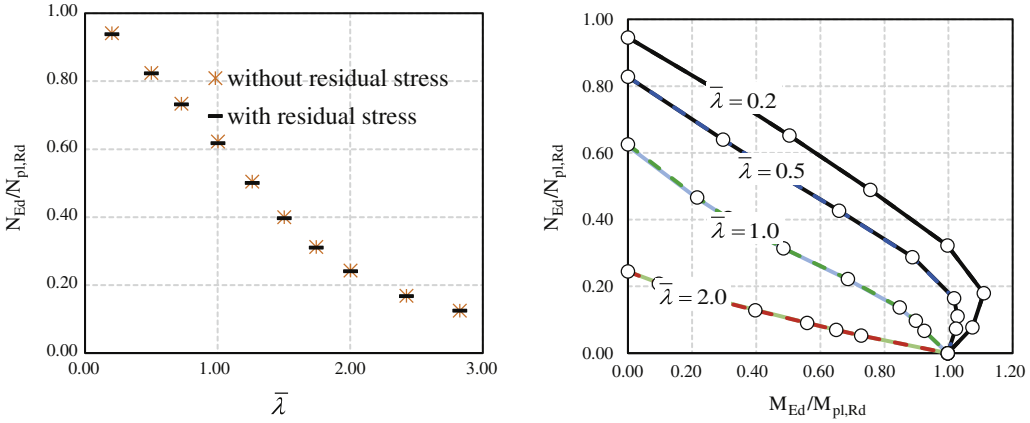

a) Buckling curve. b) Interaction curve.

Fig. 16. Effect of residual stress in buckling behavior of HSRCC3.

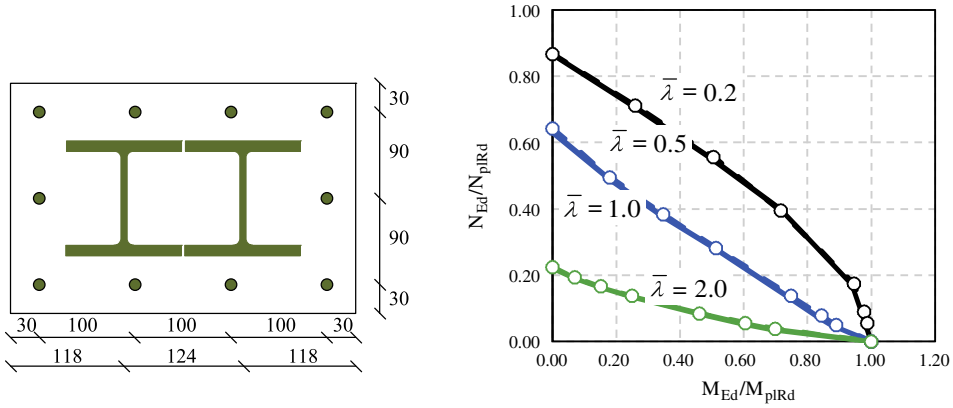

a) Hybrid cross-section HSRCC6. b) Effect of residual stress on interaction curve.

Fig. 17. Effect of residual stress in buckling behavior of hybrid column where the cross-section has two steel profiles very close to each other.

5.3. Comparisons between proposed simplified method and FEA

In order to evaluate the contribution of the various parameters governing the ultimate load, the *R* ratio has been computed for all the considered cases (2960 data sets). The value of the *R* ratio is given as a function of the main variables: eccentricity e/h, geometric slenderness ratio λ and relative slenderness $\bar{\lambda}$, the latter being calculated according to EC4 formulation. For every value of each parameter all corresponding value of *R* are given as discrete points. In Fig. 18c, *R* is given with the mean value *r*, $r + s$ and $r - s$, where *s* is standard deviation. It can be seen that despite the wide dispersion at high relative slenderness ratio, the proposed formulation gives a relatively low scatter compared to FE analysis results. The standard deviations are equal to 0.0147, 0.0325 and 0.0712 for relative slenderness ratio $\bar{\lambda}$ equal to 0.5, 1 and 2, respectively. The frequency histogram shown in Fig. 18d was constructed using the proposed formulation. With a 0.005 precision, the percentage of the *R* ratio equal to 1 is 50.9%, and less than 1 is cumulatively 23.72% as can be seen on the histogram. The percentage of *R* below 0.97 is 10.34%. Its overall variability gives a good estimation of the mean value of the ultimate load with relatively small deviation. The mean value *r* and the standard deviation *s* provided by the proposed simplified method are respectively equal to 1.0022 and 0.0459 which have been improved compared to the ones given by EC2 simplified method ($r = 0.996$, $s = 0.104$) and EC4 simplified method ($r = 1.010$,

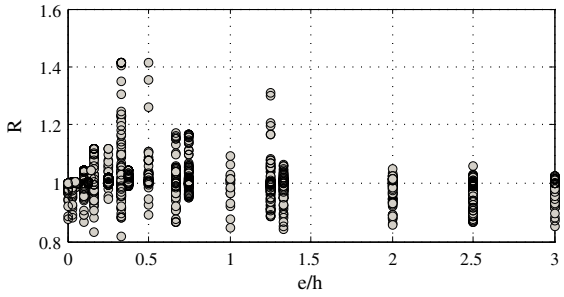

(a) Influence of eccentricity on the ultimate load of the hybrid column.

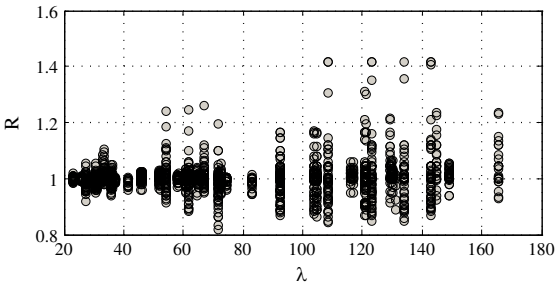

b) Influence of geometric slenderness on the ultimate load of the hybrid column.

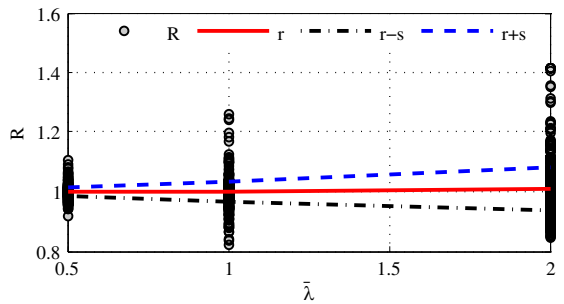

c) Influence of relative slenderness on the ultimate load of the hybrid column.

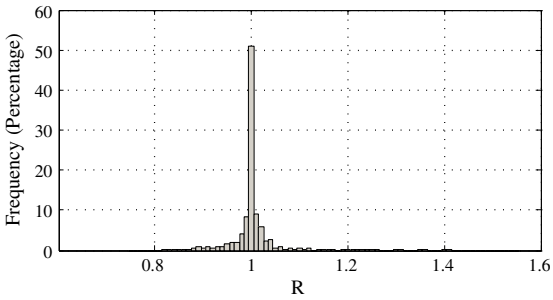

d) Histogram of frequency of the *R* ratio.

Fig. 18. Performance of the results given by the new simplified method.

$s = 0.112$). Based on these numerical results, we can conclude that the developed method gives the ultimate load of a slender hybrid column subjected to combined axial force and bending moment with sufficient precision.

6. Conclusion

Numerical investigations on the second-order effects in slender hybrid column subjected to combined axial load and uniaxial bending moment have been performed. One of the main objectives of this study was to evaluate the bending moment magnification method proposed in EC2 and EC4 when applied to hybrid columns. To do so, a FE model has been developed in which the geometrical/material nonlinearities as well as the partial interaction effect between the steel profiles and the surrounding concrete are taken into account. The FE model has been validated by comparing its predictions against experimental results for standard composite columns. To thoroughly analyze the applicability of EC2 and EC4 variants of the moment magnification method to hybrid columns, an extensive parametric study with 1140 data sets (cross-sections, column effective slenderness and creep coefficient) has been carried out. The comparison between the results obtained with Eurocode simplified methods and with FE analyzes shows that simplified method of EC2 and EC4 leads to a wide scatter where half of case-studies are unsafe. It means that the proposed effective flexural stiffness *EI* of EC2 and EC4 are not appropriate for the hybrid column design. It was observed that the secant modulus of compressed part of the steel section varies as a function of the creep coefficient φ_{ef} and the geometric slenderness λ. Therefore, in addition to the previous cases already analyzed, a further investigation of the effect of the steel yield stress on the ultimate load of hybrid columns has been carried out. This later investigation was based on an extensive numerical parametric study with 2960 data sets. A simplified method has been proposed for hybrid column design. This method is developed within the context of Eurocodes, i.e. moment magnification approach. In the proposed method, new expressions for the correction factors (for the determination of effective flexural stiffness (*EI*)) are proposed in order to take into account the creep effect and the effect of plastification of the steel profiles. The comparisons between proposed simplified method and FE analyzes show that the developed method provides the ultimate load for typical slender hybrid column with adequate accuracy.

Nomenclature

$M_{Ed,1}$	design first-order bending moment
$M_{Ed,2}$	design second-order bending moment
N_{Ed}	design axial load
$N_{pl,Rd}$	design value of the plastic resistance of the cross-section to compressive normal force
$M_{pl,N,Rd}$	design value of the plastic resistance moment of the cross-section taking into account the compressive normal force
N_{cr}	elastic critical normal force
l_0	effective column length
β	equivalent moment factor
k	moment magnification factor
EI	flexural stiffness of the compression member
E_c	elastic modulus of concrete
E_a	elastic modulus of structural steel
E_s	elastic modulus of reinforcement
I_c	moment of inertia of concrete cross section
I_a	moment of inertia of structural steel about the axis through the center of hybrid section
I_s	moment of inertia of longitudinal reinforcing bars about the axis through the center of hybrid section
E_{cd}	design modulus of elasticity of concrete: $E_{cd} = E_{cm}/\gamma_{cE}$
λ	geometric slenderness ratio
ρ	geometrical reinforcement ratio
f_{ck}	characteristic compressive cylinder strength of concrete at 28 days
φ_{ef}	effective creep ratio
n	relative axial force
$N_{pl,Rk}$	characteristic plastic resistance of cross-section
E_{cm}	secant modulus of elasticity of concrete
ϕ_t	creep coefficient according to EN 1994-1-1:5.4.2.2(2)
$N_{G,Ed}$	part of normal force that is permanent
r_m	ratio of both end moments
δ	steel contribution ratio
$\overline{\lambda}$	relative slenderness

Acknowledgments

The authors gratefully acknowledge financial support by the European Commission (Research Fund for Coal and Steel) through the project SMARTCOCO (SMART COmposite COmponents: concrete structures reinforced by steel profiles) under grant agreement RFSR-CT-2012-00039.

References

[1] EN 1992-1-1. Eurocode 2: Design of Concrete Structures: Part 1-1: General Rules and Rules for Buildings; 2004.
[2] EN 1994-1-1. Eurocode 4: Design of composite steel and concrete structures: Part 1-1: General Rules and Rules for Buildings; 2004.
[3] Bonet J, Miguel P, Fernandez M, Romero M. Biaxial bending moment magnifier method. Eng Struct 2004;26(13):2007–19.
[4] Bonet J, Romero M, Miguel P. Effective flexural stiffness of slender reinforced concrete columns under axial forces and biaxial bending. Eng Struct 2011;33(3):881–93.
[5] A. Committee, A. C. Institute, I. O. for Standardization. Building Code Requirements for Structural Concrete (aci 318-08) and Commentary. American Concrete Institute; 2008.
[6] Mavichak V, Furlong RW. Strength and stiffness of reinforced concrete columns under biaxial bending. Tech. rep., Center for Highway Research. University of Texas at Austin; 1976.
[7] Mirza S. Flexural stiffness of rectangular reinforced concrete columns. ACI Structural Journal 1990;87(4).
[8] Tikka TK, Mirza SA. Nonlinear EI equation for slender reinforced concrete columns. ACI structural journal 2005;102(6).
[9] Tikka TK, Mirza SA. Nonlinear equation for flexural stiffness of slender composite columns in major axis bending. J Struct Eng 2006;132(3):387–99.
[10] Tikka TK, Mirza SA. Nonlinear EI equation for slender composite columns bending about the minor axis. J Struct Eng 2006;132(10):1590–602.
[11] Tikka TK, Mirza SA. Effective flexural stiffness of slender structural concrete columns. Can J Civ Eng 2008;35(4):384–99.
[12] Westerberg B. Slender column with uniaxial bending, international federation for structural concrete (fib). Design examples for 1996 FIP recommendations practical design of structural concrete, 16. Tech. rep., Technical Report, Bulletin; 2002.
[13] Austin W. Strength and design of metal beam-columns. J Struct Div 1961;87(4):1–32.
[14] Robinson J, Fouré B, Bourghli A. Le flambement des poteaux en béton armé chargé avec des excentricités différentes à leurs extrémités. Tech. rep., Institut Technique du Bâtiment et des Travaux Publics 1975; no. supplément au no. 333:74; 1975.
[15] Trahair NS. Design strengths of steel beam-columns. Tech. rep., Structural Engineering Report No 132. Department of Civil Engineering, University of Alberta; 1985.
[16] Duan L, Sohal IS, Chen W-F. On beam-column moment amplification factor. Eng J 1989;26(4):130–5.
[17] Sarker PK, Rangan BV. Reinforced concrete columns under unequal load eccentricities. ACI Structural Journal 2003;100(4).
[18] Tikka TK, Mirza SA. Equivalent uniform moment diagram factor for reinforced concrete columns. ACI Structural Journal 2004;101(4).
[19] Keo P, Nguyen Q-H, Somja H, Hjiaj M. Geometrical nonlinear analysis of hybrid beam-column with several encased steel profiles in partial interaction. J Eng Struct 2015 [submitted for publication].
[20] Riks E. An incremental approach to the solution of snapping and buckling problems. Int J Solids Struct 1979;17(7):529–51.
[21] Theoretical and experimental study on composite steel–concrete shear walls with vertical steel encased profiles. J Constr Steel Res 2011;67(5):800–13.
[22] Zhou Y, Lu X, Dong Y. Seismic behaviour of composite shear walls with multi-embedded steel sections. Part i: experiment. Struct Des Tall Special Build 2010;19(6):618–36.
[23] Al-Shahari A, Hunaiti Y, Ghazaleh B. Behavior of lightweight aggregate concrete-encased composite columns. Steel Compos Struct 2003;3(2):97–110.
[24] Morino S, Matsui C, Watanabe H. Strength of biaxially loaded src columns. Composite and Mixed Construction: Proceedings of the U.S./Japan Joint Seminar. ASCE; 1985. p. 185–94.

[25] Chen C, Yeh S. Ultimate strength of concrete encased steel composite columns. Proceedings of the Third National Conference on Structural Engineering; 1996. p. 2197–206.
[26] Mirza S, Skrabek B. Reliability of short composite beam-column strength interaction. J Struct Eng 1991;117(8):2320–39.
[27] Chen C-C, Lin N-J. Analytical model for predicting axial capacity and behavior of concrete encased steel composite stub columns. J Constr Steel Res 2006;62(5):424–33.
[28] Kent DC, Park R. Flexural members with confined concrete. J Struct Div 1971;97(7):1969–90.
[29] EN 1993-1-1: Eurocode 3: Design of steel structures: Part 1-1: General Rules and Rules for Buildings.
[30] Bergmann R, Hanswille G. New design method for composite columns including high strength steel. Composite Construction in Steel and Concrete V. ASCE; 2006. p. 381–9.
[31] EN 1990: Eurocode: Basic of structural design. Annex D: Design by Tests Results; 2002.
[32] Boissonnade N, Greiner R, Jaspart J-P, Lindner J. Rules for member stability in en 1993-1-1: background documentation and design guidelines. European Convention for Constructional Steelwork, Technical Committee 8-Stability; 2006.
[33] Westerberg B. Second Order Effects in Slender Concrete Structures: Background to Chapters 5.8, 5.9 and Annex H in EN 1992-1-1; 2002.

ANNEXE 13

Q-H. Nguyen, X.H. Nguyen, D.D Le and O. Mirza. Experimental investigation on seismic response of exterior RCS beam-column connection. *11th International Conference on Advances in Steel Concrete Composite and Hybrid Structures*. Beijing, China, 3-5 December 2015.

11th International Conference on
Advances in Steel and Concrete Composite Structures
Tsinghua University, Beijing, China, December 3-5, 2015

EXPERIMENTAL INVESTIGATION ON SEISMIC RESPONSE OF EXTERIOR RCS BEAM-COLUMN CONNECTION

Q-H. Nguyen[a], X.H. Nguyen[b], D.D. Le[b] & O. Mirza[c]

[a] INSA de Rennes, 20 avenue des Buttes de Coësmes, CS 70839, F-35708 Rennes Cedex 7, France
E-mails: qnguyen@insa-rennes.fr

[b] University of Transport and Communications, 3 Cau Giay Street, Hanoi, Vietnam
E-mails: nguyenxuanhuy@utc.edu.vn; ledangdung@utc.edu.vn

[c] Institute for Infrastructure Engineering, University of Western Sydney, Penrith, NSW 2751, Australia
E-mail: O.Mirza@uws.edu.au

Keywords:
International conference; Composite structures; Beam-column connection; RCS joint; experimentation.

A B S T R A C T

This paper presents an experimental study on seismic performance of a new type of exterior RCS connection to which steel profile encased in RC column is directly welded to the steel beam. A full scale exterior hybrid joint was tested under reversed-cyclic loading. Seismic performance in term of load bearing capacity, story drift capacity, ductility, energy dissipation and stiffness degradation were evaluated. The test specimen showed a stable overall response to cyclic load reversals. The experimental results indicated that the test specimen performed in a ductile manner and the stiffness degradation during the cycles performed was gradual. It was concluded that the studied RCS joint could be used as dissipative element in the structures of ductility class medium (DCM).

1 INTRODUCTION

Hybrid RCS frames consisting of reinforced concrete (RC) column and steel (S) beam have been used at an increasing rate for mid-to-high-rise buildings for the last 30 years. RCS frames possess several advantages from structural, economical and construction view points compared to either traditional RC or steel frames. As described by Grisffis (1986), RCS frames effectively combine structural steel and reinforced concrete members to their best advantage. Due to the advantages offered by RCS frame systems, a large number of research programs have been conducted in US and Japan to study the interaction between steel and concrete members in RCS frames (Deierlein & Noguchi 2004). A primary challenge in design of RCS frames was the connection between steel beam and RC column. In an attempt to identify the in-plane behaviour of composite RCS beam-column joint connections, a comprehensive testing program was conducted at the University of Texas at Austin (Sheikh et al. 1989 & Deierlein et al. 1989). From these research work, design guidelines for both interior and exterior RCS joints in buildings located in low to moderate seismic risk zones were developed by the American Society of Civil Engineers. In a review of ASCE Guidelines (1994), Kanno & Deierlein (1996) cited several areas where the ASCE Guidelines could be improved. Based on results from the forty-four data, they reported that the joint strength model in the ASCE Guidelines is somewhat over-conservative and there is room to improve its accuracy, especially for bearing failure condition. Conservatism evident in the comparison is due to the fact that the ASCE Guidelines do not recognise some of the strength and stiffness enhancements provided by certain joint details. Kanno & Deierlein (2000) then proposed a refined and more accurate design model for RCS joints.

A large number of connection details have been proposed for RCS connections. This makes the applicability of RCS construction difficult since design recommendations need to be available for each joint detail (Bahman et al. 2012). In 2004, Nishiyama et al. (2004) have developed "Guidelines: Steel-Concrete Composite Structures for Seismic Design". The guidelines are for ordinary steel beam-reinforced concrete columns (RCS) buildings, structural system comprising relatively regular-shaped frame, with or without multistory reinforced concrete shear walls; the height is not more than 60 m, design strength of concrete ranging from 21 to 60 MPa; and reinforcing bars and structural steel standardised in the Japan Industrial Standards, and the design follows the

"strong column-weak beam" philosophy. The joint failure modes are similar to the design guidelines of the ASCE 1994, for the shear failure and bearing failure. Design equations for the ultimate shear strength of the joint panels and associated hysteretic models for 12 different details of RCS joints, including through-beam and through-column types, are included, which can be used in advanced analysis that considers the inelastic behaviour of beam-column joints.

A new type of exterior RCS connection, namely "hybrid joint", in which a steel profile totally encased inside RC column is directly welded to the steel beam (Fig. 1), is recently proposed within European RCFS project SMARTCOCO (2013). The most important advantage of this hybrid joint is to offer a very easy and simple steel beam to RC column connection. However, this kind of joint detail is not covered by the existing design guidelines. Based on Eurocodes (2, 3 and 4) and existing research works in the literature, a design method was proposed within European RCFS project SMARTCOCO. So far, the seismic behaviour of this type of connection is not yet been experimentated.

This paper deals with an experimental study on seismic performance of the above-mentioned hybrid joint. A full scale exterior hybrid joint was tested under reversed-cyclic loading. Seismic performance in terms of load bearing capacity, story drift capacity, ductility, energy dissipation and stiffness were evaluated.

2 EXPERIMENTAL PROGRAM

2.1 *Test specimen*

The specimen is a full-scale exterior RCS connection, in which a steel profile embedded inside RC column is directly welded to the steel beam. Geometric and reinforcement details of specimen is shown in Figure 1.

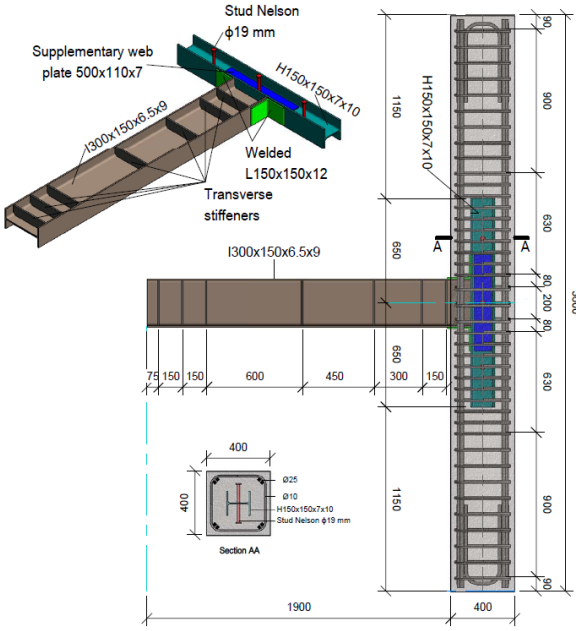

Figure 1. Description of specimen

2.2 *Material properties*

The concrete compressive strength at test day and the properties of structural and reinforcement steels are given in Table 1.

Table 1. Measured material strengths.

Item	Strength [MPa]	
Concrete	f_c = 31.3 MPa	
I300x150x6.5x9	f_y = 285 MPa	f_u = 420 MPa
H150x150x7x10	f_y = 294 MPa	f_u = 436 MPa
ϕ25 bars	f_y = 310 MPa	f_u = 490 MPa
ϕ16 bars	f_y = 352 MPa	f_u = 496 MPa

2.3 *Instrumentation, test setup and procedure*

The instrumentation consists of load cells to measure applied forces and reactions, displacement transducers (LVDTs) to measure displacements and strain gauge to record the strains. At the joint region, in order to identify the failure mode, eleven strain gauges (from G1 to G11) were placed on both transverse and longitudinal reinforcements of the column as shown in Figure 2. There are also four strain gauge rosettes (from R1 to R4) arranged in the encased steel profile.

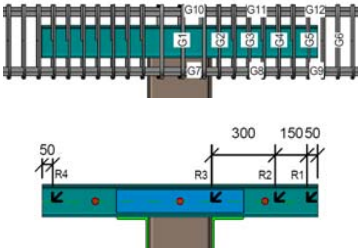

Figure 2. Strain gauge locations

The experimental test setup is shown in Figure 3. As shown, a hydraulic actuator of 1000 kN capacity with a stroke length of 75 mm was used to apply the cyclic lateral displacements at the top of the column. This actuator was horizontally held to the strong wall and the bottom of the column was pinned to the strong floor of the laboratory. A steel plate was used in the space between the specimen and the actuator for smooth transfer of actuator load at the column level. The beam was restrained by a vertical steel rod. If second order effects are neglected, it can be considered that the restraint is a pin support.

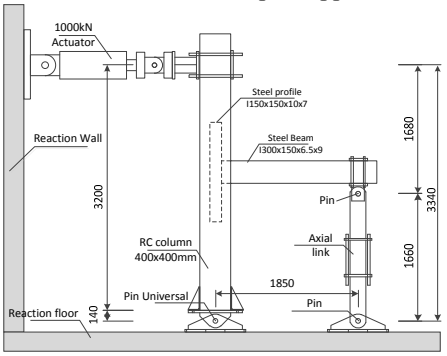

Figure 3. Test setup

Figure 4 presents the loading sequence adopted for the test. The loading procedure is built based on Issue 45 of ECCS "Recommended Testing Procedure for Assessing the Behaviour of Structural Steel Elements under Cyclic Loads". The displacement amplitudes are presented in terms of story drift which is defined as the ratio between the imposed lateral displacement and the column height. The specimen were loaded with displacement control until a significant reduction of specimen strength was observed.

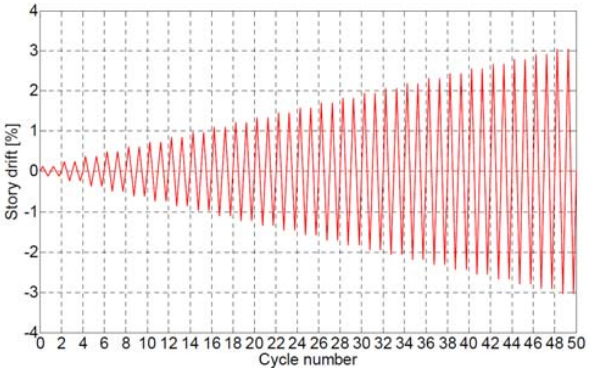

Figure 4. Cyclic displacement pattern.

3 EXPERIMENTAL RESULTS

The experimental results obtained from the test are presented in this Section. The overall response of the specimen during the test is discussed and the force-drift curve is given. Then the ductility, energy dissipation and stiffness degradation are presented and discussed.

3.1 *Concrete cracking observation*

During the test, the critical concrete cracks were identified. These include diagonal shear cracks in the joint region due to joint panel shear deformations and various cracks on the columns face due to the local force transmission between embedded steel profile and concrete surrounding. Figure 5 shown the cracking pattern of the specimen at the different displacement levels. Four basic types of cracks are diagonal cracks on the two lateral faces at the center of the joint region, diagonal and horizontal cracks on the front face starting from the flanges of the steel beam, vertical cracks on the front face, and horizontal flexural cracks on the side face which extend onto the front face. At 0.8% drift, the first diagonal crack appeared. After the formation of the first diagonal crack in the joint, it was observed at 0.9% drift that two horizontal cracks appeared which were originated at the steel beam flanges and were followed by the above-mentioned diagonal crack. A second diagonal crack in the joint was observed at 1.7% drift along with some flexural cracks in the column. A vertical crack starting from the top flange was formed at 1.8% drift and propagated upward in the RC column zone where there is the embedded steel profile. At 2.7% drift, this crack was connected with two inclined quasi symmetric cracks inclined 45° relative to the vertical. It is noted that the connection point of these cracks is located at the same level of the end point of the embedded profile in the RC column as can be seen in Figure 5. With progressive increase in drift, the cracks propagated and widened gradually. Deterioration of joint strength was observed from about 1.6% drift.

Figure 5. Cracking pattern.

3.2 *Load-drift response*

The specimen behaviour is described by a plot of the horizontal load at the upper column against story drift. Figure 6 shows the lateral load versus story drift response. As can be seen, the hysteresis behaviour is a bit unsymmetrical in term of applied force. It is because the cracking was more pronounced in the upper joint region.

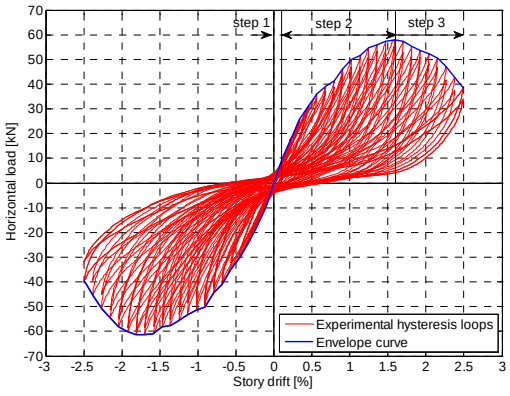

Figure 6. Load-drift curve.

The load-drift response of the joint can be subdivided in three steps. The first step is represented by the behaviour of the joint prior to significant cracking in concrete and characterized by elastic deformations. At low load levels, concrete is uncracked and adhesive bond and contact

transfer force between steel profile and concrete. At the end of this region the adhesive bond breaks and microcracks in concrete cause initial mobilizing of the lateral reinforcing ties (stirrups). Step 2 starts from 0.3% drift with surface cracking of the concrete which results in decreasing stiffness and increasing of participation of lateral reinforcing ties. Step 3 was marked by steel web yielding from 1.6% drift and represented by a deterioration of joint strength. During this step, crack widths increase as there is a greater mobilization of the concrete shear mechanisms.

3.3 *Ductility*

The displacement ductility of the specimen is represented by the displacement ductility factor μ which is defined as the ratio of ultimate displacement δ_u to the yield displacement δ_y. These displacements are determined from the envelope curve of the hysteresis loops. The ultimate displacement is defined as displacement corresponding to 15% drop of loading capacity. The yield displacement of specimen is determined based on the general yielding method presented in Li et al. (2013).

Table 2. Force and drift at different characteristic points.

	Yielding point		Limit point		Ultimate point		Ductility
	P_y [kN]	δ_y [%]	P_{max} [kN]	δ_{max} [%]	$P_{85\%}$ [kN]	δ_u [%]	$\mu = \frac{\delta_u}{\delta_y}$
Push	48.81	0.976	57.90	1.587	49.20	2.187	2.24
Pull	-51.12	-1.028	-61.27	-1.813	-51.90	-2.227	2.17
Mean	**49.96**	**1.002**	**59.58**	**1.70**	**50.55**	**2.202**	**2.20**

Table 2 shows the drifts and corresponding horizontal applied loads at yielding, limit and ultimate points. A displacement ductility factor μ=2.2 is obtained. According to Eurocode 8, it can be concluded that the studied RCS joint could be used as dissipative element in DCM structures. It can be also observed from Table 2 that the ratio between the maximum force P_{max} and the yielding force P_y is about 1.2. It means that after yielding the strength of the specimen increased by about 20%.

3.4 *Energy dissipation*

The energy dissipation characteristics of a member are an important measure of its seismic performance. Energy dissipation at each cycle is calculated from the enclosed area within the hysteresis loop at this cycle. Cumulative energy dissipation is computed by summing energy dissipated in previous cycles. Figure 7 presents the energy dissipation ratio at each displacement level where two loading cycles were performed. The energy dissipation ratio was calculated as the ratio between the effective dissipated energy during each loading cycle and the maximum dissipated energy that could theoretically be dissipated. It can be observed that there are no major differences in energy dissipation ratio during each displacement level except the last level of displacement (74.8mm). From the displacement level of 13.6 mm to the end of the test the energy dissipation ratio appears to be more or less stable between 7.6% and 10.6%.

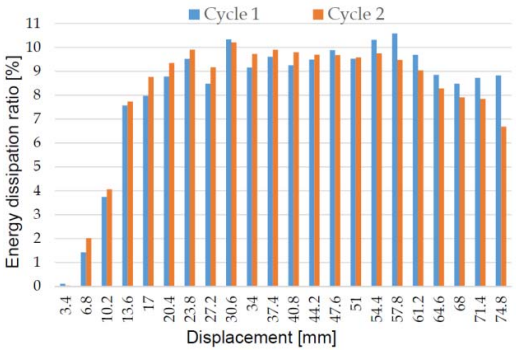

Figure 7. Load-drift curve.

3.5 *Stiffness degradation*

The stiffness of an element is defined as the load which induces a unit deflection in a specified point and in a given direction. This definition is based on a linear relationship between load and deflection. In civil engineering the stiffness of a structural member (K) is defined as the ratio between the applied load and the resulting deflection. Due to concrete cracking and material yielding during the cyclic loading, the stiffness of the elements decreases, phenomenon known also as stiffness degradation. In this paper herein, the stiffness degradation is assessed using the secant stiffness determined from each complete hysteresis loop. The secant stiffness was determined as the slope of a line passing through the peak loads at both directions. It represents the ability to resist deformation.

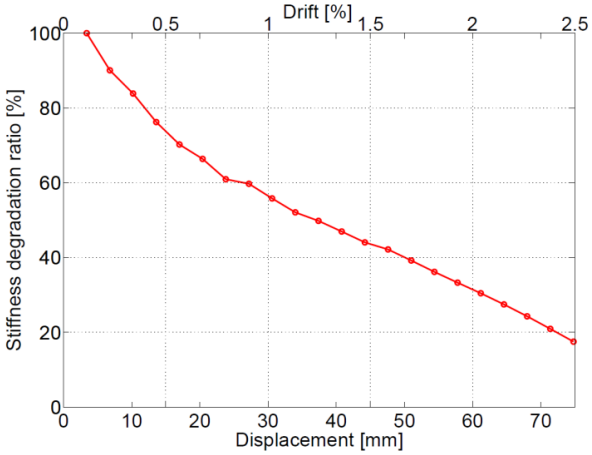

Figure 8. Stiffness degradation.

The stiffness degradation ratio versus horizontal displacement and drift is plotted in Figure 8. The stiffness degradation ratio was calculated as the ratio between the secant stiffness at the first cycle of displacement level and the initial stiffness of the specimen which is defined at a displacement level of 3.4 mm. It can be observed that at yielding the stiffness of the specimen related to the initial stiffness is approximate 56%. At failure (the load bearing capacity decreases to 85% of the maximum capable force) the stiffness degradation ratio was about 25.6% which

indicates that the stiffness is significantly degraded at this stage of loading. Furthermore, it can be seen from Figure 8 that from the drift level of 0.85% the secant stiffness decreases quasi linearly.

4 CONCLUSION

In this paper, an experimental study on seismic performance of a new type of exterior RCS beam-column connection has been presented. The studied "hybrid" joint consist of a steel profile encased inside RC column which is directly welded to the steel beam. A full scale hybrid joint specimen has been tested under reversed-cyclic loading. The seismic performance of the test specimen has been analyzed in term of load bearing capacity, story drift capacity, ductility, energy dissipation and stiffness degradation. During cyclic loading a stable behaviour of the specimen was observed with minor capacity degradation. The experimental results indicated that the stiffness degradation during the cycles performed was gradual. It has been found that after yielding the strength of the specimen still increased by about 20%. The test specimen performed in a ductile manner with ductility factor μ=2.2. However, further experimental studies are needed to extend the range of the test data and to investigate other variables such as the length of encased steel profiles, stirrup density, and concrete strength.

5 ACKNOWLEDGEMENTS

This research is funded by Vietnam National Foundation for Science and Technology Development (NAFOSTED) under grant number 107.01-2011.11.

6 REFERENCES

Bahman, F.A., Hosein, G. & Nima, T. 2012. Seismic performance of composite RCS special moment frames. *KSCE Journal of Civil Engineering* 2(2): 450-457.

Deierlein, G., Sheikh, T. M., Yura, J. A. & Jirsa, J. O. 1989. Beam-column moment connections for composite frames: Part 2. *Journal of Structural Engineering, ASCE* 115(11): 2877-2896.

Deierlein, G. & Noguchi, H. 2004. Overview of U.S. -Japan research on seismic design of composite reinforced concrete and steel moment frame. *Journal of Structural Engineering, ASCE* 130(2): 361-367.

Eurocode 2, EN1992-1-1 Design of concrete structures-Part 1: General rules and rules for buildings.

Eurocode 3, EN1993-1-8 Design of steel structures-Part 1-8: Design of joint.

Eurocode 4, EN1994-1-1 Design of composite steel and concrete structures-Part 1: General rules and rules for buildings.

Eurocode 8, EN1998-1 Design of structures for earthquake resistance – Part 1: General rules, seismic actions and rules for buildings.

European Convention for Constructional Steelwork. Working Group 1.3, Seismic Design. 2007. *Recommended testing procedure for assessing the behaviour of structural steel elements under cyclic loads*. Issue 45. ECCS.Grisffis, L.G. 1986. Some design considerations for composite-frame structures. *Engineering Journal* 23(2): 59-64.

Kanno, R. & Deierlein, G. 1996. Seismic behavior of composite (RCS) beam-column joint assemblies. *Composite Construction in Steel and Concrete III, ASCE* : 236-249.

Kanno, R. & Deierlein, G. 2000. Design Model of Joints for RCS Frames. *Composite Construction in Steel and Concrete IV*: 947-958.

Li, B., Lam, E.S., Wu, B. & Wang, Y. 2013. Experimental investigation on reinforced concrete interior beam-column joints rehabilitated by ferrocement jackets. *Engineering Structures* 56: 897-909.

Nishiyama, I., Kuramoto, H. & Noguchi, H. 2004. Guidelines: seismic design of composite reinforced concrete and steel buildings, *J Struct Eng ASCE* 130(2): 336-342.

Smart Composite Components - Concrete Structures Reinforced by Steel Profiles 2013. Mid-Term Report. *Research Program of the Research Fund for Coal and Steel*.

Sheikh, T. M., Deierlein, G.G., Yura, J. A. & Jirsa, J. O. 1989. Beam-column moment connections for composite frames: Part 1. *Journal of Structural Engineering, ASCE* 115(11): 2858-2876.

The ASCE Task Committee on Design Criteria for Composite Structures in Steel and Concrete 1994. Guidelines for design of joints between steel beam and reinforced concrete columns. *Journal of Structural Engineering, ASCE* 120(8): 2330-2357.

ANNEXE 14

Q-H. Nguyen, M. Hjiaj, X.H. Nguyen and D.D Le. Finite Element analysis of a hybrid RCS beam-column connection. *The 3rd International Conference CIGOS 2015 on « Innovations in Construction »*. Paris, France, 11-12 May 2015.

International Conference
INNOVATIONS IN CONSTRUCTION
ENS CACHAN, FRANCE MAY 11th & 12th, 2015 CIGOS - PARIS 2015

Finite Element analysis of a hybrid RCS beam-column connection

Quang-Huy Nguyen[a,1], Mohammed Hjiaj[a], Xuan Huy Nguyen[b], Huy Cuong Nguyen[b]

[a] *INSA de Rennes, 20 avenue des Buttes de Coësmes, CS 70839, F-35708 Rennes Cedex 7, France*
[b] *University of Transport and Communications, 3 Cau Giay Street, Hanoi, Vietnam*

Abstract

A new type of exterior RCS connection, in which a steel profile totally embedded inside RC column is directly welded to the steel beam, is recently proposed within European RCFS project SMARTCOCO. This kind of joint detail is not covered by the existing design guidelines. Indeed, Eurocodes 2, 3 and 4 give some provisions that can partly be used for the design of such a joint. There remains however a real lack of knowledge relatively to the issue of the force transmission from the embedded steel profile to the surrounding concrete of the column. Questions that can rise when designing such a connection are about the optimal anchorage length to embed the steel profile or about the design of reinforcements in the connection zone of the RC column and in the transition zone at each end of the embedded steel profile. Based on Eurocodes and existing research works in the literature, a design method is proposed within European RCFS project SMARTCOCO. However, experimental tests and numerical simulations need to be conducted to valid this method. This paper deals with nonlinear finite element model for this type of exterior RCS beam-column connection. The material nonlinearities of concrete, steel beam, stud and rebar are included in the finite element model. Four RCS joints with different anchorage lengths and concrete classes are modeled. The failure modes and loads are analyzed and compared to the predicted ones of the design model.

Keywords: RCS joint, hybrid structures, Finite Element model, ABAQUS.

1. Introduction

Hybrid RCS frames consisting of reinforced concrete (RC) column and steel (S) beam have been used at an increasing rate for mid- to highrise buildings during the last 30 years. RCS frames posses several advantages from structural, economical and construction view points compared to either traditional RC or steel frames. As described by Griffis (1986),

*Corresponding author
Email address: qnguyen@insa-rennes.fr (Quang-Huy Nguyen)

RCS frames effectively combine structural steel and reinforced concrete members to their best advantage. From the construction view point, these systems are usually built by first erecting a steel skeleton, which allows the performance of different construction tasks along the height of the building. Engineering practices show that beams and columns made of two different materials may fully develop the merits of each of them, and thus combine rationality with economy in terms of material selection. RC columns are approximately 10 times more cost-effective than steel columns in terms of axial strength and stiffness (Sheikh et al. (1987)). RC columns also offer superior damping properties to a structure, especially in tall buildings. In addition, steel floor systems are significantly lighter compared to RC floor systems, leading to substantial reductions in the weight of the building, foundation costs, and inertial forces.

Due to the advantages offered by RCS frame systems, a large number of research programs have been conducted in US and Japan to study the interaction between steel and concrete members in RCS frames (Deierlein and Noguchi (2004)). A primary challenge in design of RCS frames was the connection between steel beam and RC column. In an attempt to identify the in-plane behavior of composite RCS beam-column joint connections, a comprehensive testing program was conducted at the University of Texas at Austin (Sheikh et al. (1989); Deierlein et al. (1989)). 15 interior RCS connections with various joint details were tested under monotonic and cyclic loading. Specimens consisted of a single structural steel beam passing through an RC column (without a slab), and were tested under both inelastic monotonic and cyclic loading conditions. Two joint failure modes were identified as panel shear failure and vertical bearing failure. Panel shear failure is similar to joint shear failure mechanisms in structural steel or RC joints; however, in composite RCS joints both the structural steel and RC elements participate in joint shear resistance. Vertical bearing failure occurs when concrete in the column directly above and below the steel beam is crushed, allowing rigid body rotations of the beam within the RC column (Sheikh et al. (1989)). From these research work, design guidelines for both interior and exterior RCS joints in buildings located in low to moderate seismic risk zones were developed by the American Society of Civil Engineers ASCE Task Committee (1994). This research was extended by Kanno and Deierlein (1993) who tested a series of 19 interior RCS connection specimen (without a slab) subjected to cyclic loading at Cornell University. The test objective was to investigate joint failure modes, the performance of highstrength concrete joints, joint aspect ratio, the effect of column axial load on the joint. Various joint details were studied, included face bearing plates, extended face bearing plates, steel columns, band plates wrapping around the columns regions just above and below steel beams, and the shear studs vertical joint reinforcement. Experimental data showed that joint details had a direct influence on the joint strength and ductility, but did not affect the overall stiffness of the specimen. In a review of ASCE Guidelines, Kanno and Deierlein (1996) cited several areas where the ASCE Guidelines could be improved. Based on the comparing results from forty-four data, they reported that the joint strength model in the ASCE Guidelines is somewhat over-conservative and there is room to improve its accuracy, especially for bearing failure condition. Conservatism evident in the comparison is due in part to the fact that the ASCE Guidelines do not recognize some of the strength and stiffness enhancements provided by certain joint details. Then, Kanno and Deierlein (2002) proposed a refined and more accurate design model for RCS joints. In their model, the major improvements are to more accurately evaluate joint failure modes that are unique to RCS

joints, and be able to consider the joint details illustrated in Figure 1.

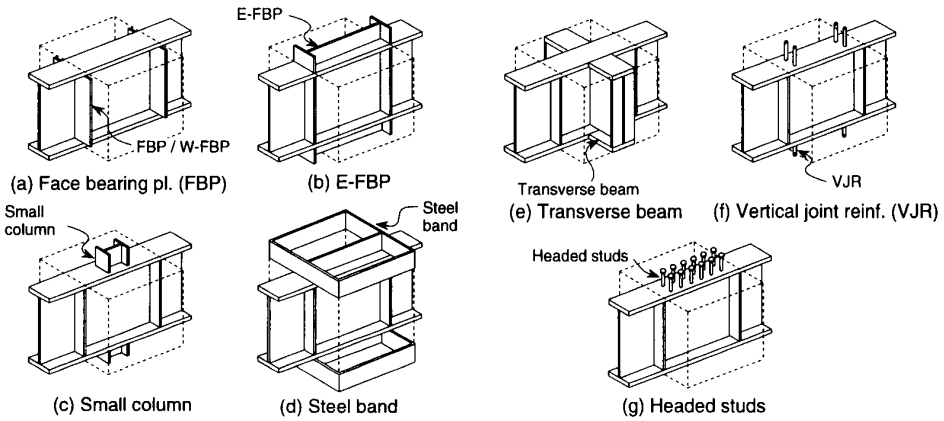

Figure. 1. Joint details considered in Kanno and Deierlein (2002) model

Since 1997, various researchers in the U.S. and Japan conducted extensive studies on RCS systems as of the U.S.-Japan cooperative research program on composite and hybrid construction (see for example Kim and Noguchi (1997); Noguchi and Kim (1998); Sakaguchi et al. (1998); Nishiyama et al. (1998); Uchida and Noguchi (1998); Parra-Montesinos and Wight (2000); Baba and Nishimura (2000); Bugeja et al. (2000)). In 1998, Noguchi and Kim (1998) studied the analytical of exterior RCS connections based on experimental results from tests performed at Chiba University and the Building Research Institute in Japan. In 2000, Parra-Montesinos and Wight (2000) performed an experimental study on seismic response of exterior RCS beam column connections. They pointed out that RCS frames were suitable for use in high seismic risk zones. However, test results also indicated that large discrepancies between predicted and the experimental shear strength in exterior RCS joints when using the ASCE design guidelines, and thus Parra-Montesinos and Wight (2001) developed a new model, based on joint shear deformation, and design equations. This design model is capable of predicting the shear force, and stirrup and concrete strains at any level of joint shear distortion for exterior joints.

Despite the extensive research conducted on RCS connections, research methods are mainly through experiments and analyses of RCS connections using finite element method still remain in the beginning stage. Compared to the experiment, finite element method is more effective from an economical viewpoint, and can also gain important data that could not be measured in experiment. El-Tawil and Deierlein (2001) have presented the formulation for a plasticity-based distributed beamŰcolumn element that can be used for the seismic analysis of three-dimensional mixed frame structures comprised of steel, reinforced concrete, and composite members. Cheng and Chen (2005) have simulated the force-deformation behavior of RCS joint sub-assemblages by a non-linear analysis program, DRAIN-2DX, with consideration of composite effects of the beam and slab as well as shear distortion in the panel zone. Noguchi and Uchida (2004) utilized the nonlinear three-dimensional finite element method (FEM) to analyze two frame specimens with reinforced

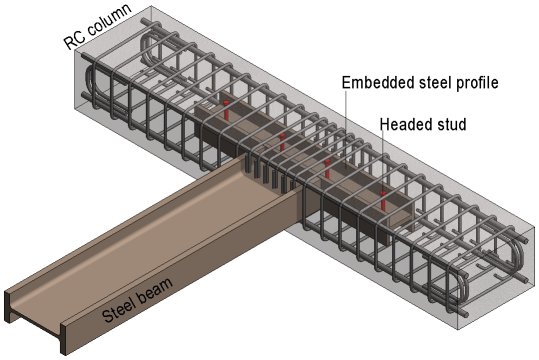

Figure. 2. New RCS connection detail.

concrete columns and steel beams, which had different beam-column joint detailing. Li et al. (2012) studied the influence of different parameters on the behavior of composite frame structures by finite element software ABAQUS.

A new type of exterior RCS connection, in which a steel profile totally embedded inside RC column is directly welded to the steel beam (Figure 2), is recently proposed within European RCFS project SMARTCOCO (Smartcoco Report (2013)). As can be seen, this kind of joint detail is not covered by the existing design guidelines. Indeed, Eurocodes 2, 3 and 4 give some provisions that can partly be used for the design of such a joint. There remains however a real lack of knowledge relatively to the issue of the force transmission from the embedded steel profile to the surrounding concrete of the column. Questions that can rise when designing such a connection are about the optimal anchorage length to embed the steel profile or about the design of reinforcements in the connection zone of the RC column and in the transition zone at each end of the embedded steel profile. Based on Eurocodes (2,3 and 4) and existing research works in the literature, a design method is proposed within European RCFS project SMARTCOCO (Smartcoco Report (2013)). However, experimental tests and numerical simulations need to be conducted to valid this method. Therefore, in this paper, the main objective is to develop a reliable nonlinear three-dimensional finite element model to investigate the behavior of the new RCS joint detail illustrated in Figure 2. The finite element ABAQUS software is employed. Four RCS joints with different concrete strengths are modeled. The failure modes and load are analyzed and compared to the predicted ones of the design model proposed in Smartcoco Report (2013).

2. Design of test specimen

To evaluate the effectiveness of the design method proposed in Smartcoco Report (2013), four exterior RSC specimens are designed. These specimens will be constructed and tested under static loading at the Structures Laboratory of INSA Rennes during 2015. The specimens consist of a 3000 mm long RC column with 400 x 600 mm^2 cross-section reinforced 8 HA25 steel bars (1.63% steel ratio) and of a 2000 mm long of steel beam. The steel beam cross-section is modified HEM450 in which the flange widths are reduced to 200 mm. A HEM200 steel profile of 1000 mm long is totally embedded in the RC column and

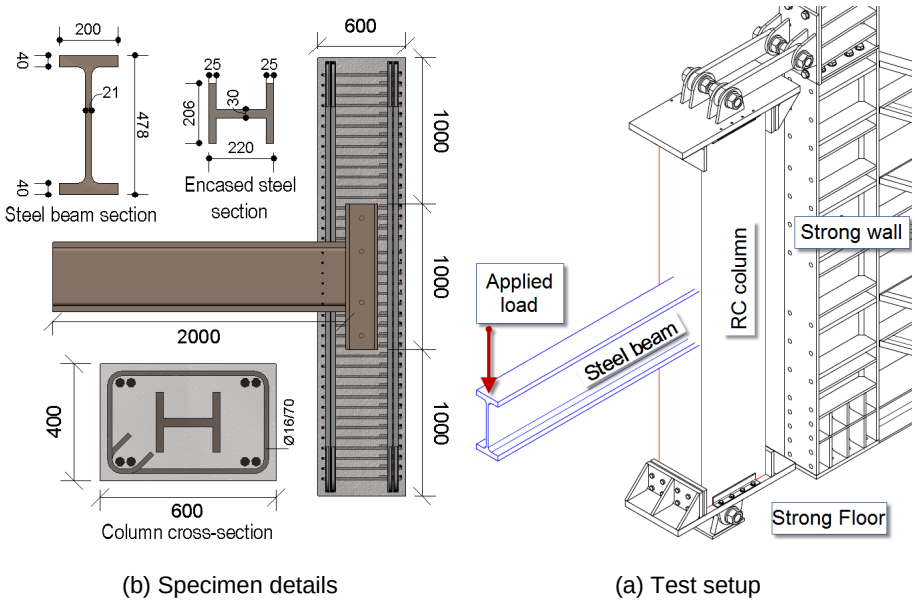

Figure. 3. Specimen details and test setup.

connected to the steel beam by welding. The specimen details are given in Figure 3. Note that the specimens differs from each other only by their concrete strength. Four concrete strengths, i.e. 30 MPa, 40 MPa, 50 MPa and 60 MPa, are considered.

According to the design method proposed in Smartcoco Report (2013), the design resistance of the studied RCS joint may be deduced from the resistance of the constituted components which are:

- Composite joint (in sense of Eurocode 4 (2005)), namely Inner joint element, consisting of embedded steel profile, concrete encased in between the flanges of the steel profile and steel beam which is welded to the embedded profile;
- Reinforced concrete part around the embedded profile, namely outer joint element;
- Local strut and tie mechanism due to the force transmission from steel beam and embedded steel profile to concrete;
- Reinforced concrete part located outside the region of joint;
- Steel beam;
- Connection between encased steel profile and surrounding concrete;

The design load and the corresponding failure mode for each specimen are summarized in Table 1. Note that the the details of specimen design are not presented here. They can be found in Smartcoco Report (2013). It can be seen that regardless of concrete strength all specimens have the same design load value. The latter corresponds to the applied load

Table. 1. Summary of design loads of specimens.

Specimen	Concrete strength	Design Load	Design failure mode
HJS30	f_{cm} = 30 MPa	505 kN	Web panel of Inner joint in tension
HJS40	f_{cm} = 40 MPa	505 kN	Web panel of Inner joint in tension
HJS50	f_{cm} = 50 MPa	505 kN	Web panel of Inner joint in tension
HJS60	f_{cm} = 60 MPa	505 kN	Web panel of Inner joint in tension

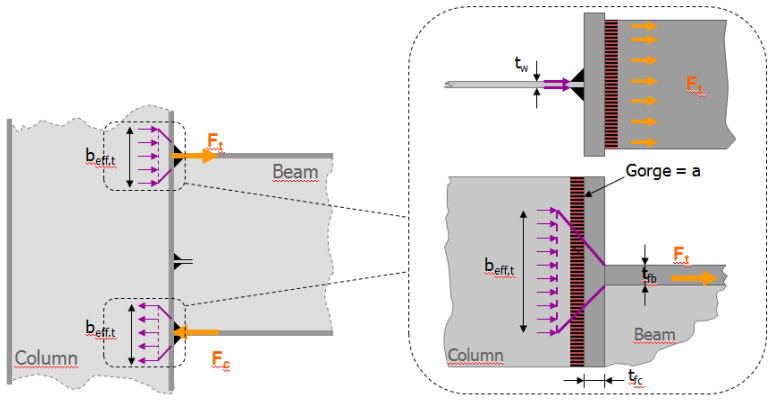

Figure. 4. Force transmission from steel beam to column through beam flanges.

which causes the yielding of the column web panels in tension (i.e. yielding of of inner joint element). As can be observed from beam-column force transmission scheme illustrated in Figure 4, the mechanism of the column web panel in tension is not affected by the concrete. So far it can be concluded that for the studied RSC joint specimens the connection between the steel beam and embedded steel column is dominant and the joint resistance can be simply evaluated according to clause 6.2.6.3 of Eurocode 3 (2005)).

3. Finite element model

3.1. General

Advances in computational features and software have brought the finite element method within reach of both academic research and engineers in practice by means of general-purpose nonlinear finite element analysis packages, with one of the most used nowadays being ABAQUS (2013) software. The program offers a wide range of options regarding element types, material behavior and numerical solution controls, as well as graphic user interfaces, auto-meshers, and sophisticated post-processors and graphics to speed the analyses. In this paper, this commercial software is employed to develop reliable three-dimensional finite element model for the RCS joint specimen.

Due to the symmetry of the specimen geometry and loading, in order to save the calculation time, only half of the specimen was modeled. A full view of specimen is shown in Figure 2 for reference. Five components of specimen (concrete column, rebars, steel beam, embedded steel profile and headed studs) are modeled separately and assembled to make a complete specimen model. In addition, the interaction between components influences

greatly the analysis results. Thus, the interface and contact between the concrete in joint region and the structural steel, the interface and contact between the headed studs and concrete, the interaction of reinforcement and concrete need also to be modeled. Furthermore, the choice of element types, mesh sizes, boundary conditions and load applications that provide accurate and reasonable results are also important in simulating the behavior of the RCS joint. Displacements are assumed to be small therefore the nonlinear geometric effect is not considered. However, the material nonlinearity is included in the finite element analysis.

3.2. Material modeling of concrete

The Concrete Damaged Plasticity (CDP) model, developed by Lee and Fenves (1998), available in ABAQUS material library is used to model the concrete material. This model consists of the combination of non-associated multi-hardening plasticity and scalar damaged elasticity to describe the irreversible damage that occurs during the fracturing process.

For compressive behavior, the uniaxial stress-strain curve of Eurocode 2 (2004) is selected for the determination of yield stress and inelastic strain. The compressive stress is assumed to increase linearly with respect to the total strain until the initial yield/damage stress which is taken equal to $0.4f_{cm}$ where f_{cm} is the mean compressive cylinder strength. The initial Young's modulus is calculated according to Eurocode 2 (2004). The Poisson's ratio is taken as 0.2. Then, the compressive stress grows until failure strength f_{cm}. The strain (ε_{c1}) associated with f_{cm} is equal to 0.0022, given by Eurocode 2 (2004). After exceeding the compression strain ε_{c1}, localization of damage occurs and the compressive stress decreases with the softening strain.

For tensile behavior of concrete, the effects of the reinforcement interaction with concrete is considered and the tension stiffening is specified by means of a post-failure stress-displacement relationship. As stated in the ABAQUS manual, in cases with little or no reinforcement, the stress-strain tension stiffening approach often causes mesh-sensitive results. Therefore, the fracture energy cracking criterion was used in this study. With this approach, the brittle behavior of concrete is characterized by a stress-displacement response rather than a stress-strain response. The displacement is determined primarily by the crack opening, and it does not depend on the element length or the mesh size.

The damage parameters in compression as in tension are determined by assuming that the split of inelastic strains into plastic and damaging parts by the scalar parameter as proposed by Krätzig and Pölling (2004).

3.3. Material modeling of steel

The von Mises yield criterion with isotropic hardening rule is used for the structural steel, reinforcing steel and headed stud. An elastic-linear-work-hardening material, available in ABAQUS material library, is considered with tangent hardening modulus being equal to 1/10000 of elastic modulus, in order to avoid numerical problems. The yielding stress and elastic modulus are taken equal to 460 MPa and 210000 MPa for structural steel, respectively, while 500 MPa and 200000 MPa for reinforcing steel and headed stud.

3.4. Selection of element type and meshing

The concrete column, steel beam and headed stud are modeled with solid C3D8R element available in Abaqus library. The C3D8R-element is an 8-node linear brick element

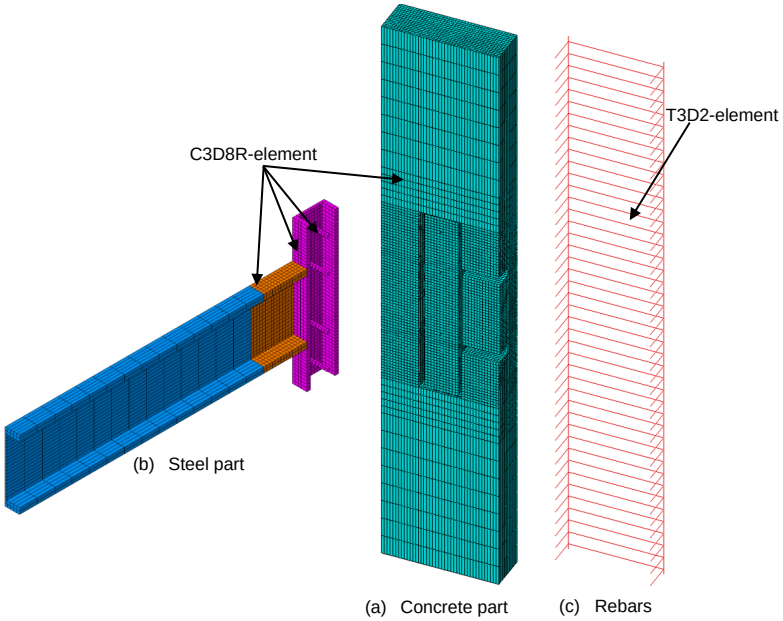

Figure. 5. FE type and mesh of components of the exterior RSC joint specimen

with reduced integration stiffness and with hour-glass enhanced. Note that compared to the quadratic brick C3D20R element (20-node element), the accuracy of this element is slightly lower but using this element leads to a significant reduction of degree of freedom therefore computational cost. Furthermore, according to ABAQUS manual, this element is suitable for nonlinear analysis including contact, large deformation, plasticity, and failure. The reinforcement bars can be modeled using solid, beam or truss elements. The use of solid elements is computationally expensive and therefore not chosen. Because the reinforcing bars do not provide a very high bending stiffness, the 2-node linear 3-D truss elements, namely T3D2, are used.

Figure 5 shows the meshing of the FE model for the concrete column, rebars, steel beam and headed studs. In order to achieve the reliable results, the fine mesh was used in the connection zone. Reasonable convergence was achieved with such a mesh size, and refinement of the mesh was studied only up to the point where the change in the mesh size did not have an impact on the results.

3.5. Interaction conditions between components

Contact interactions between components may significantly affect the complete specimen behavior and need to be carefully conditioned. Improper definition of contact interactions may introduce nonphysical into the simulation. In fact, the reinforcing bars are fully anchored in concrete so that embedded constraint can be used for the interaction between rebars and concrete surrounding. This constraint implies an infinite bond strength at the interface between the concrete and the reinforcement. In the present case, the truss elements representing the reinforcement are the embedded region while the concrete slab is the host region.

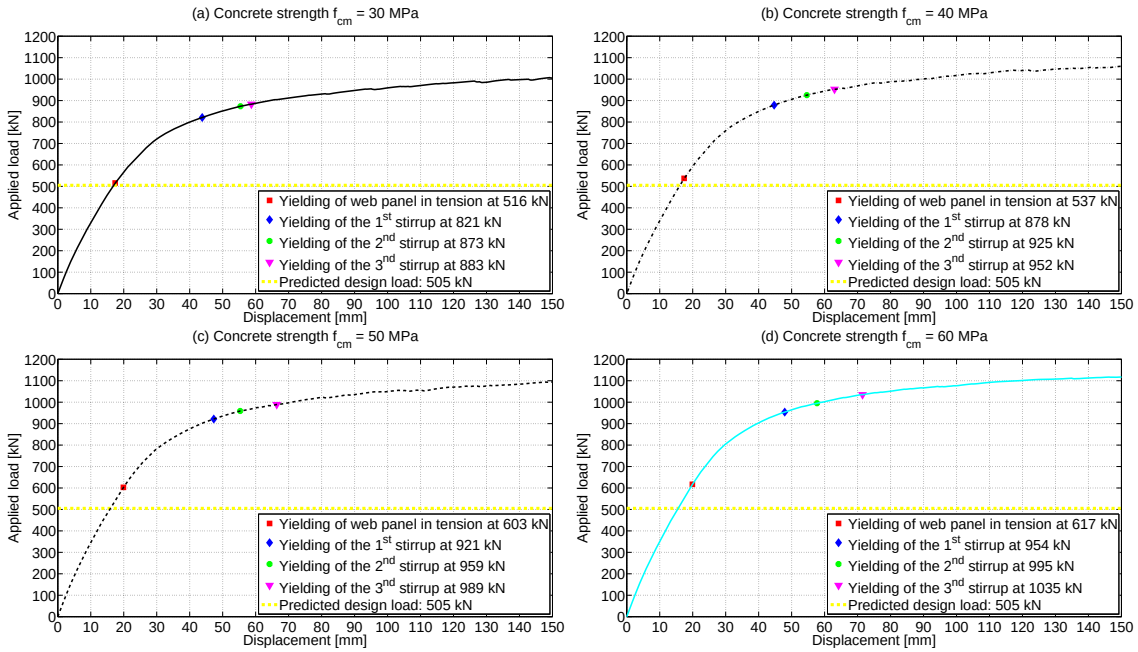

Figure. 6. Load-displacement curves for different values of concrete strengths

Surface-to-surface contact elements (available in Abaqus library) are used to model the interaction between concrete column and steel profile. The interaction properties are defined by the behaviour normal and tangential to the surfaces. For the normal behavior, surface "hard" contact constraint is assumed. This type of normal behaviour implies that no penetration is allowed at each constraint location. For the tangential behaviour, the penalty frictional formulation is used and the coefficient of friction between the steel profile and the concrete column is assumed to be 0.5.

3.6. Loading and boundary conditions

As shown in Figure 3, in the experimental test setup, the ends of the RC column are pinned and the steel beam is subjected to a vertical concentrated load at its end. In the FE model, the RC column is restrained at its lower and upper ends in vertical and horizontal directions by means of hinges. The loading is applied continuously in the form of the displacement control manner. The displacement of 150 mm is imposed on the whole cross-section at the beam end in vertical direction.

4. Results and discussion

The load-displacement curves obtained from the FE analysis are presented in Figure 6. The predicted design loads are also reported in order to make the comparisons. The first yielding observed numerically is about the encased steel web panel in tension as it is shown in Figure 7 for the case of concrete strength $f_{cm} = 40$ MPa. As can be seen, at the applied load of 537 kN a small zone of plastification appears in the web panel at the level of upper steel beam flange. Then, with the increase of the load, the plastic strain

develops more in this area than anywhere else. The yielding of web panel in tension is also numerically depicted by the Von Mises stress distribution as shown in Figure 8. It is noted that some plastification zones are indeed observed in concrete before reaching the yielding of web panel in tension as shown by the equivalent plastic strain distribution in concrete in Figure 9. They are identified as "local" plastification and not avoided in steel-concrete structures. Therefore, this kind of plastification is not considered as yielding mode of the specimens. It can be observed from Figure 6 that the first failure mode, i.e. embedded steel web panel in tension, obtained numerically is in good agreement with the design one. The numerical results show that after reaching the yielding of web panel in tension the specimens do not lost much in stiffness and still withstand a applied load up to 1.6 times of the load causing the first yielding. This can be explained by the fact that the concrete contribution on the resistance is activated after reaching the "steel" yielding. However, this numerical observation needs to be confirmed by the experimental one.

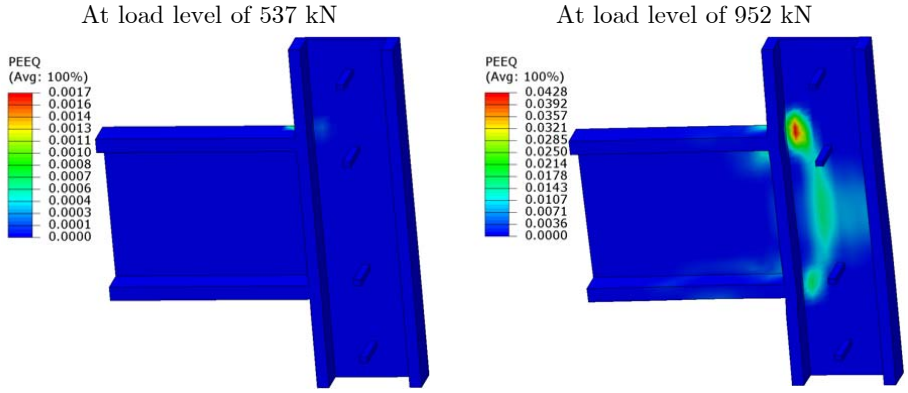

Figure. 7. Equivalent plastic strain distribution in steel for the case of $f_{cm} = 40$ MPa

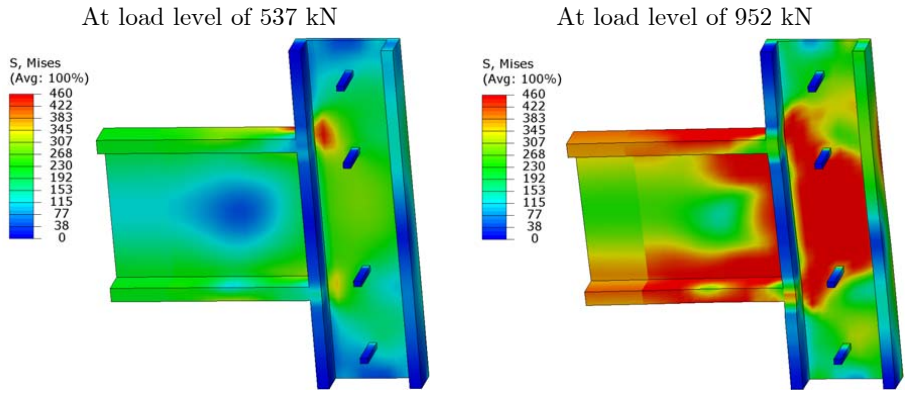

Figure. 8. Von Mises stress distribution in steel for the case of $f_{cm} = 40$ MPa

The second yielding observed numerically is at the stirrups as shown in Figure 10 for

the specimen HJS40. The load levels corresponding to the yielding of the 1st, 2nd and 3nd stirrups are reported in Figure 6. Unlike the first yielding (web panel in tension) caused by the bending moment transmission from steel beam to encased steel column, the yielding of the stirrups probably results from the transmission of the vertical applied force (shear force) to the concrete column. This force transmission principally occurs at the interface contact between steel beam lower flange and the concrete below. It formes a "local strut and tie" mechanism in which two concrete struts start from the lower flange to the longitudinal reinforcement and the stirrups play a role of tie element. That explains more or less by the plastification zone in concrete as shown in Figure 9 at the applied load of 952 kN and also by the fact that the first stirrup yielded is the one who is just below lower flange of the steel beam as can be seen in Figure 10.

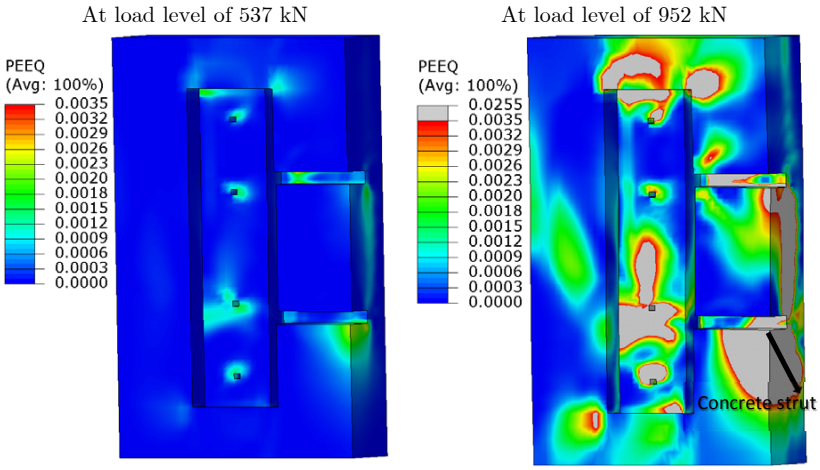

Figure. 9. Equivalent plastic strain distribution in concrete for the case of $f_{cm} = 40$ MPa

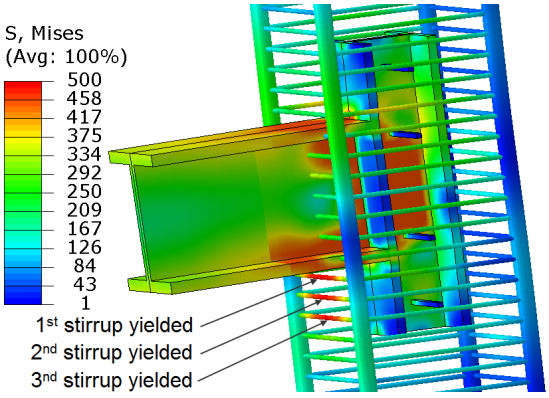

Figure. 10. Von Mises stress distribution at 952 kN for the case of $f_{cm} = 40$ MPa

5. Conclusions

In this paper, a numerical analysis of the behavior of a new type of exterior RCS joint subjected to static loading has been presented. The considered exterior RCS connection consists of a steel profile totally encased inside RC and welded to the steel beam. This type of beam-to-column joint has been recently proposed and studied within European RCFS project SMARTCOCO (Smartcoco Report (2013)) because it seems to presents some advantages compared to the existing RCS joint in term of resistance and construction methods. A 3D finite element model has been created using ABAQUS software. This model takes into account the material nonlinearities, interaction and the contact between steel and concrete. Four RCS joints with different concrete strengths have been simulated. The failure modes and load have been analyzed and compared to the predicted ones of the design model proposed in Smartcoco Report (2013).

It has been found that the predicted design failure mode is quiet well simulated by the FE model. The numerical results indicated that for the studied RCS joint the failure mode firstly reached is caused by the bending moment transmission from steel beam to encased steel column. As a result the concrete does not affect much on the load value corresponding to this "steel joint" yielding. However, it has been shown that the concrete contribution in the joint resistance starts to be activated when "steel joint" yielding is reached and results in the hardening load-displacement curves. Furthermore, the numerical simulations presented in this paper allow to bring out the local strut and tie mechanism which has been based to develop the design method in Smartcoco Report (2013). Finally, the present FE model is useful to predict more or less the failure modes that shall be observed in the experimental tests.

6. Acknowledgements

The authors gratefully acknowledge financial support by the European Commission (Research Fund for Coal and Steel) through the project SMARTCOCO (SMART COmposite COmponents: concrete structures reinforced by steel profiles) under grant agreement RFSR-CT-2012-00039.

7. References

Griffis, L.G., Some design considerations for composite-frame structures, *Engineering Journal* **23** Issue 2 (1986) 59-64.

Griffis, L.G., Composite frame construction, *Constructional Steel Design* **23** Issue 2 (1986) 59-64.

Sheikh, T. M.; Yura, J. A.; and Jirsa, J. O., Moment Connections between Steel Beams and Concrete Columns, *PMFSEL Report* No. 87-4, University of Texas at Austin, Austin, Tex.

Deierlein, D. D.; Noguchi, H., Overview of U.S. -Japan research on seismic design of composite reinforced concrete and steel moment frame, *Journal of Structural Engineering, ASCE* **130** Issue 2 (2004) 361-367.

Sheikh, T. M., Deierlein, G. G., Yura, J. A., and Jirsa, J. O., Beam-column moment connections for composite frames: Part 2., *Journal of Structural Engineering, ASCE* **115** Issue 11 (1989) 2858-2876.

Deierlein, G. G., Sheikh, T. M., Yura, J. A., and Jirsa, J. O., Beam-column moment connections for composite frames: Part 2., *Journal of Structural Engineering, ASCE* **115** Issue 11 (1989) 2877-2896.

The ASCE Task Committee on Design Criteria for Composite Structures in Steel and Concrete, Guidelines for design of joints between steel beam and reinforced concrete columns, *Journal of Structural Engineering, ASCE* **120** Issue 8 (1994) 2330-2357.

Kanno, R., and Deierlein, D.D., Strength, deformation, and seismic resistance of joints between steel beams and reinforced concrete columns, *Structural Engrg* Report No.93-6, Cornell University.

Kanno, R., and Deierlein, D.D., Seismic behavior of composite (RCS) beam-column joint assemblies, Composite Construction in Steel and Concrete III, ASCE, pp. 236-249 (1996).

Kanno, R., and Deierlein, D.D., Design Model of Joints for RCS Frames, Composite Construction in Steel and Concrete IV: pp. 947-958 (2002).

Sakaguchi, N., Tominaga, H., Murai, Y., Takase, Y., and Shuto, K., Strength and ductility of steel beam-RC column joint, *World Conf. on Earthquake Engrg.* **4** (1998), 713-718.

Nishiyama, I., Itadani, H., and Sugihiro, K., Bi-directional seismic response of reinforced concrete column and structural steel beam subassemblages, *Proc., Struct. Engrg. World Conf.(1998),* Elvesier Sciences, New York.

Uchida, K., and Noguchi, H., Nonlinear three-dimensional finite element analysis of RCS frame, *Proc., 5th Joint Tech. Coordinating Com. Meeting,* U.S.-Japan Cooperative Earthquake Research Program on Composite and Hybrid Structures, Tokyo.

Baba, N., and Nishimura, Y., Stress transfer on through beam type steel beam-reinforced concrete column joints, Proc. of 6th ASCCS conference. 2000. p. 753-60.

Kim, K. and Noguchi, H., An analytical study on the shear strength of RCS joints, 4th JTCC meeting. 1997.

Noguchi, H., and Kim, K., Shear strength of beam-to-column connections in RCS system, *Proc., Struct. Engrs. World Congr. (1998),* Elsevier Science, Oxford, England.

Parra-Montesinos, G. and Wight, J.K., Seismic response of exterior RC column-to-steel beam connections, *Journal of Structural Engineering, ASCE* **126** Issue 10 (2000) 1113-1121.

Bugeja, M.N., Bracci, J.M., Moore, W.P., Seismic behavior of composite RCS frame systems, *Journal of Structural Engineering, ASCE* **126** Issue 4 (2000) 429-436.

Parra-Montesinos, G. and Wight, J.K., Modeling shear behavior of hybrid RCS beam-column connections, *Journal of Structural Engineering, ASCE* **127** Issue 1 (2001) 3-11.

BahmanFarahmand, A., Hosein,G., and Nima, T., Seismic performance of composite RCS special moment frames, *KSCE Journal of Civil Engineering* **2** number 2 (2012) 450-457.

Li, W., Li, Q-N., Jiang, W-S., and Jiang, L., Seismic performance of composite reinforced concrete and steel moment frame structures - state-of-the-art, *Composites Part B: Engineering* **42** Issue 2 (2011) 190-206.

Fargier-Gabaldon, L., Design of moment connections for composite framed structures, PhD dissertation, The University of Michigan, USA; 2005.

Nishiyama, I., Kuramoto, H., and Noguchi, H., Guidelines: seismic design of composite reinforced concrete and steel buildings, *J Struct Eng ASCE* **130** Issue 2 (2004) 336-342.

El-Tawil, S., Deierlein, G.G., Nonlinear analysis of mixed steel-concrete frames. I: element formulation, *J Struct Eng ASCE* **127** Issue 6 (2001) 647-655.

Cheng, C.T., and Chen, C.C., Seismic behavior of steel beam and reinforced concrete column connections, *J Constr Steel Res* **61** (2005) 587-606.

Noguchi, H., and Uchida, K., Finite Element Method Analysis of Hybrid Structural Frames with Reinforced Concrete Columns and Steel Beams, *J Struct Eng ASCE* **130** (2004) 328-335.

Li, W., Li, Q.N., and Jiang, W.S., Parameter study on composite frames consisting of steel beams and reinforced concrete columns, *J Constr Steel Res* **77** (2012) 145-162.

Smart Composite Components - Concrete Structures Reinforced by Steel Profiles, *Research Programme of the Research Fund for Coal and Steel* Mid-Term Report (2013).

Lee, J., and Fenves, G.L., Plastic-damage model for cyclic loading of concrete structures, *Journal of enginerring mechanics* **124** (1998) 892-900.

Lee, J., and Fenves, G.L., A plastic-damage concrete model for earthquake analysis of dams, *Earthquake Engineering & Structural Dynamics* **27** Issue 9 (1998) 937-956.

Users Manual V.6.13 (2013), *Dassault Systems Simula Corp.*

EN1992-1-1: Design of concrete structures-Part 1: General rules and rules for buidings.

EN 1993-1-8: Design of steel structures: Part 1-8: Design of joint.

EN 1994-1-1: Design of composite steel and concrete structures: Part 1-1: General Rules and Rules for Buildings.

Krätzig, W.B., and Pölling, R., An elasto-plastic damage model for reinforced concrete with minimum number of material parameters, *Computers and Structures* **82** (2004) 1201Ű1215.

Kim, S.E., and Nguyen, H.T., Finite element modeling and analysis of a hybrid steel-PSC beam connection, *Engineering Structures* **32** (2010) 2557-2569.

Partie IV

Rapport de soutenance et des rapporteurs

UNIVERSITÉ DE RENNES 1
Sections Sciences et Philosophie - HDR
Campus de Beaulieu CS 74205 35042 RENNES cedex

Habilitation à **D**iriger les **R**echerches – mention Sciences de la Vie

par **Mr NGUYEN Quang Huy** soutenue le 22 Avril 2016

-=-=-=-=-=-=-=-=-=-=-

RAPPORT DE SOUTENANCE (Signature obligatoire de tous les membres du jury)

Président de jury : Ferrier Emmanuel

Rapporteur du jury :

Monsieur NGUYEN Quang Huy a présenté, dans un excellent français, ses travaux de recherche portant sur la modélisation numérique et expérimentale des structures multi-matériaux acier/béton et bois/béton.

Sa présentation orale, dynamique, a su montrer la cohérence, la richesse et la diversité des résultats obtenus. L'exposé particulièrement pédagogique a parfaitement retracé le parcours du candidat et a très bien illustré les activités de recherche à caractère numérique et expérimentale. Il a développé une stratégie de recherche intéressante et originale qu'il a su mettre en œuvre en combinant la modélisation et l'expérimentation. Ses travaux sont publiés dans les meilleures revues du domaine.

Le jury souligne que les compétences scientifiques du candidat sont autant dans le domaine de l'expérimentation sur structures que dans la modélisation des structures multi-couches. Les réponses aux questions du jury ont montré la grande maîtrise du sujet du candidat et sa curiosité scientifique. La discussion scientifique qui a suivie la présentation ouvre des perspectives intéressantes pour la suite de la carrière de M. NGUYEN.

Le candidat a montré son aptitude à encadrer et développer des recherches dans le domaine de la mécanique des structures hétérogènes.

Le jury lui décerne donc, à l'unanimité, le diplôme d'habilitation à diriger des recherches de l'Université de Rennes.

E. Ferrier.

M. HJIAJ

Luc TAERWE. Oreste S. Bursi Cristina Câmpian Panayiotis Kotronis

Department of **Structural Engineering**
MAGNEL LABORATORY FOR CONCRETE RESEARCH
Director: Prof. dr. ir. L. Taerwe

Rapport sur le mémoire d'habilitation à diriger des recherches de Dr Quang Huy NGUYEN
Titre: "Modélisation numérique et expérimentale des structures mixtes acier-béton et bois-béton "

Rapporteur : Professeur Luc TAERWE

Monsieur Quang Huy NGUYEN est maître de conférences à l'INSA de Rennes dans le département de Génie Civil, il effectue sa recherche dans le laboratoire de Génie Civil et Génie Mécanique (LGCGM) de l'INSA de Rennes. En 2005 il obtient le diplôme d'ingénieur en Génie Civil et Urbanisme de l'INSA de Rennes et le diplôme de Master Recherche en Ingénierie Mécanique et Génie Civil. En 2009 il présente sa thèse de doctorat intitulée « Modélisation du comportement non-linéaire des poutres mixtes acier-béton avec prise en compte des effets différés». Il s'agit d'une thèse en cotutelle internationale entre l'INSA de Rennes et l'Université de Wollongong (Australie) qui résulte dans un double diplôme de Doctorat en Génie Civil. De 2006 à 2009, un poste de PAST à mi-temps lui permet de rajouter l'enseignement à ses compétences et d'allier enseignement, recherche et ingénierie.

Entre 2008 et 2009 il occupe des positions de ATER et ingénieur d'études à l'INSA de Rennes. En 2010 il est recruté comme Maître de conférences à l'INSA de Rennes, ce qui lui permet de rajouter l'enseignement (cours sur le Béton Armé et la Mécanique) à ses compétences et d'allier enseignement, recherche et ingénierie. Il a co-encadré 4 thèses et encadre en ce moment 2 thèses. Il a publié 19 articles dans des revues à comité de lecture, et 17 actes de congrès internationaux. Il s'agit d'un dossier de recherche de très bonne qualité, avec un parcours qui montre de plus une excellente capacité d'adaptation et d'évolution tout en conservant en ligne de mire le fil conducteur du thème retenu pour l'activité de recherche.

Monsieur Quang Huy NGUYEN a été responsable d'un projet industriel SBB et coordinateur interne d'un projet Européen. Les dernières années il a reçu des bourses pour des collaborations scientifiques internationales avec l' Université de Western Sydney et l' Université de Transport et Communication de Hanoi. Depuis 2013 il est actif dans de Comité Technique « Composite Structures TC11 » de la Convention Européenne de la Construction Métallique.

Les travaux de recherche menés, outre des aspects scientifiques riches, comportent un intérêt applicatif manifeste et présentent de très forts potentiels de valorisation en ingénierie pour le Génie Civil. Le sujet est vaste et pluridisciplinaire (mécanique des structures mixtes et méthodes numériques en non linéaire géométrique et matériau) et bénéficie d'un couplage fort entre les démarches expérimentales et une modélisation au niveau de complexité appropriée. Mr Quang Huy NGUYEN construit méthodiquement un panel d'outils expérimentaux et numériques sophistiqués et performants, nécessaires à cette démarche, et par ses solides compétences est tout à fait en état de

guider de jeunes thésards dans le domaine de la mécanique de structures mixtes acier-béton et bois-béton dédiées au Génie Civil.
Mr Quang Huy NGUYEN a acquis au fil des années un rôle d'expert, ce qui lui permet de présenter ce mémoire en vue de l'habilitation à diriger des recherches dont la forme diffère d'un mémoire universitaire classique. Dans la deuxième partie du mémoire il donne un aperçu clair des résultats scientifiques obtenus où il distingue trois grands thèmes.

Le premier thème est la modélisation des poutres multicouches de Timoshenko. Pour ces structures, qui sont largement utilisées dans le secteur de la construction, la connexion entre les différentes couches, est le point le plus critique dans le comportement et le dimensionnement. Le candidat a développé deux outils bien distincts d'un niveau scientifique très solide: une méthode de résolution analytique et un modèle des éléments finis.

Le deuxième thème s'agit du comportement des planchers mixtes bois-béton sous sollicitations sismiques et d'incendie. Ce thème contient une grande partie expérimentale qui a été menée de façon très rigoureuse. Une modélisation numérique permet d'isoler l'influence de la dilatation thermique gênée du béton.

Le troisième thème est l'étude prénormative des structures hybrides béton-acier. Il s'agit ici d'une combinaison originale de recherches expérimentales et de simulations numériques en vue d'obtenir de résultats utilisables en pratique.

Quelques perspectives sont données sur les trois sujets principaux. Le rapporteur regrette que cette partie soit cependant un peu prudente, sans doute dans la mesure où le choix des axes de travail de recherche dépendent ici fortement aussi de cadres contractuels. Cette partie devra être discutée plus amplement lors de la soutenance.

Pour conclure, je rappelle que l'habilitation à diriger des recherches sanctionne, d'après les textes, « un haut niveau scientifique, une démarche originale dans un domaine scientifique, une aptitude à maitriser une stratégie de recherche et une capacité à encadre de jeunes chercheurs ». Dans le cas de NGUYEN, je considère que ces quatre points sont largement attestés par les éléments suivants :
(a) Le haut niveau scientifique apparait dans les publications denses en contributions, dans des revues de haut niveau.
(b) La démarche originale dans un domaine scientifique est visible sur chaque sujet : un nouveau regard et de nouveaux outils ont été apportés. On note une forte implication dans le domaine numérique basée sur une connaissance théorique de très haut niveau. Le candidat fait aussi preuve d'une capacité certaine de mettre au point des essais pertinents et fiables, dont la définition des programme expérimentaux est de qualité en adéquation avec les verrous mis en exergue.
(c) L'aptitude à maitriser une stratégie de recherche est aussi évidente, dont certains sujets ont nécessité une combinaison de plusieurs approches. Le candidat a montré qu'il réunit les conditions d'autonomie, de maturité, de vision stratégique et de capacité à l'encadrement de jeunes chercheurs .

Je rajouterai qu'en plus Mr Quang Huy NGUYEN a toujours eu le sens de l'utilité de ses recherches. On note au travers des nombreux contrats en lien avec la profession une reconnaissance certaine par le milieu professionnel. Il fait passer son savoir au travers d'enseignements appropriés, assume des responsabilités pédagogiques et collectives, et point d'importance, il a su bénéficier d'un réseau de collaborations au niveau national et international autour de ses thèmes de recherche.

En conclusion, sur la base de la qualité et l'originalité des sujets et résultats obtenus, j'émets un avis très favorable pour la présentation en soutenance des travaux de recherche de Mr Quang Huy NGUYEN en vue d'obtenir le diplôme d'habilitation à diriger des recherches de l'Université de Rennes 1.

Fait à Gand, le 27 mars 2016

Prof.dr.ir. Luc TAERWE

MINISTRY OF EDUCATION AND SCIENTIFIC RESEARCH

TECHNICAL UNIVERSITY
OF CLUJ-NAPOCA

Rapport du Professeur des Universités CRISTINA MIHAELA CAMPIAN, Faculté de Génie Civil, Université Technique de Cluj-Napoca, Roumanie

sur le dossier d'Habilitation à diriger des Recherches de **Nguyen Quang Huy**, intitulé

"Modélisation numérique et expérimentale des structures mixtes acier-béton et bois-béton"

Je connais M. **Nguyen Quang Huy** dans le cadre des échanges internationaux avec INSA de Rennes où il a encadré des étudiants en Master de l'Université Technique de Cluj, ainsi que par ses articles scientifiques apparus dans diverses publications de spécialité.

Ses activités de recherche sont riches en résultats, sans doute basés sur son expérience au sein de l'université.

Le présent rapport concerne principalement des publications réunies dans le dossier d'Habilitation.

A. Contenu

A.1. Généralités

Le dossier scientifique présenté par Monsieur **Nguyen Quang Huy** porte sur la modélisation expérimentale, théorique et numérique des structures mixtes et hybrides (acier-béton et bois-béton).

Son mémoire est composé de trois parties. Dans la première partie il présente son parcours professionnel (son CV, le résumé de la carrière, avec aussi les activités de recherche et d'encadrement, d'enseignement et des responsabilités administratives assumées).

Sa deuxième partie est articulée autour de trois thèmes. La première porte sur la modélisation des poutres multicouches de Timoshenko, le seconde sur l'étude expérimentale et numérique du comportement des planchers mixtes bois-béton sous sollicitations accidentelles et la troisième sur l'étude prénormative des structures hybrides béton-acier.

Les recherches effectuées et en cours sont présentées par un parcours logique: positionner le problème, les résultats essentiels et les perspectives.

Dans la troisième partie, Monsieur NGUYEN une sélection d'articles publiés en vue de permettre aux lecteurs d'avoir accès aux détails de ses recherches.

A.2. Détails

Dans la deuxième partie, pour **le première thème**, le candidat déclare son objectif principal de développer des outils numériques afin d'analyser le comportement mécanique en flexion, du comportement vibratoire et du comportement au flambement des poutres multicouches avec prise en compte de la déformation de cisaillement des couches.

Ses recherches sont présentées sur le parcours : présentation/formulation du problème, résultats essentiels, publications (références dans l'annexes).

Dans l'ensemble des ses travaux, Monsieur NGUYEN développe une méthode de résolution analytique d'une part et un modèle des éléments finis d'autre part.

La résolution analytique s'appuie sur la théorie des poutres de Timoshenko et la cinématique de glissement à l'interface du modèle de Newmark et al., en aboutissant à une

str. Memorandumului nr.28, 400114 Cluj-Napoca, România
tel. +40-264-401200, fax +40-264-592055, secretariat tel. +40+264-202209, fax +40-264-202280
http://www.utcluj.ro/

solution des équations du problème de flexion en petits déplacement. La matrice de rigidité obtenue a été introduite dans un programme d'éléments finis. dans l'hypothèse de faibles déformations précritiques il obtient ainsi des expressions simples de la charge critique. la solution du problème de vibration libre a été développée en négligeant l'inertie de rotation des composants. Comme perspectives, Monsieur NGUYEN déclare l'étude de l'influence de cette inertie sur les fréquences propres de poutre multicouche de Timochenko.

Le second thème concerne les planchers mixtes bois-béton sous sollicitations sismiques et incendie.

Les travaux présentés apportent des éléments pour les problèmes posés d'une part par le comportement global, et d'autre part pour ceux du comportement local, conduites dans le cadre des programmes expérimentales faites à INSA de Rennes, avec des partenaires de l'industrie.

C'est vrais, il y a peut des recherches sur ce sujet des planchers mixtes bois-béton. planchers utilisées dans des constructions neuve comme dans des réhabilitations. Le comportement sous séisme de ces types de planchers est gouvernée par le glissement relatif à l'interface entre le bois et le béton, compte tenu de la connexion. soumis évidement au cisaillement. Le propriétés mécanique de la connexion sont en général caractérisées par des essais Push-Out, faites à INSA Rennes aussi en régime statique qu'en régime cyclique alterné. Les objectifs de ce travail ont été : la caractérisation de la résistance au cisaillement de la connexion, la capacité de déformation de la connexion d'un système bois-béton sous sollicitations cycliques alternées et la détermination de la ductilité, du coefficient d'amortissement visqueux et de la dissipation d'énergie de la connexion et enfin l'évaluation de la perte de résistance au cisaillement sous trois cycles consécutifs de même amplitude.

C'est évident que le rôle de planchers, sous les sollicitations sismique et celui de diaphragme horizontal, diaphragme classé en fonction des rigidités latérales des systèmes verticaux comme rigide, semi-rigide ou souple. Cette encadrement est une simplification. faite pour des raisons de calculs, mais qui n'est pas vraiment exactement le phénomène réel. L'Eurocode 8-1 ne donne une définition que pour le diaphragme rigides, qui semble être assurée par le plancher en béton, qui a son tour aussi est imposé d'être d'une épaisseur d'au moins 7 cm. armée dans les deux directions horizontales, et en respectant bien sur les exigences de l'Eurocode 2-1.

Les essais expérimentales portées sur ce types de planchers ont contribue au renouvèlement de l'avis technique sur le type de système bois-béton analysée, en justifiant aussi son utilisation dans des zones sismiques de la France métropolitaine (ou l'action verticale sismique n'est pas à prendre en compte).

Dans la même aire de recherche, le comportement sous incendie a été étudié à l'aide des modèle numériques sur Abaqus. La modélisation thermique des sections mixtes bois-béton permet ainsi de juger le dégrée d'échauffement des différents éléments constitutifs de la section du plancher soumis a l'incendie (section bois, section béton et connecteur).

L'objectif des travaux de recherche du candidat dans l**e troisième thème** concerne les structures hybrides, alors de participer à un effort international européen en vue d'aboutir à une méthode de dimensionnement pour les éléments hybrides béton-acier (Projet Smart cocc, Comite technique TC11).

Celle ci concerne premièrement les poteaux hybrides, qui présentent des systèmes assez variés, domaine dans lequel Monsieur NGUYEN analyse les types des éléments poteaux renforces par plusieurs profils acier noyés. Le problème est que les calculs de ces types de poteaux ne sont couverts par aucune norme des Eurocodes. En vue d'aboutir a une norme qui les concerne, le candidat a amélioré la méthode de l'Eurocode 2 en intégrant les effets d'une plastification partielle ou complète des profils lorsque les déformations augmentent. en principal sur l'effet du fluage. Un modèle en éléments finis, dans lequel les non linéarités géométriques et de matériaux, ainsi que l'effet de l'interaction partielle acier-béton sont pris en compte. validé par des essais. Un étude paramétrique très conséquent sur 1140 cas différents de poteaux hybrides a été réalisée. Le candidat a a amélioré la méthode de l'Eurocode 2 en intégrant les effets d'une plastification partielle ou complète des profils lorsque les déformations augmentent. en principal

sur l'effet du fluage. Un modèle en éléments finis, dans lequel les non linéarités géométriques et de matériaux, ainsi que l'effet de l'interaction partielle acier-béton sont pris en compte, validé par des essais.

Par la suite, une méthode simplifiée, a été proposée pour ces types de poteaux, tout en restant dans le contexte des Eurocodes.

Dans la deuxième partie, une méthode de dimensionnement pour les murs hybrides a été développée. Les résultats obtenus ont été traités et analysés avec pour objectif essentiel la mise en évidence des différents mécanismes de transfert de charge et de ruine des murs hybrides soumis à la flexion simple. La poursuite de ce travail consisterait à étudier le comportement des murs hybrides sous sollicitations sismiques et d'incendie.

Un autre thème de recherche présentée a été celle d'un nouvel assemblage hybride poteau BA/poutre acier, nommée assemblage RCS. Cet assemblage a été étudié par un parcours expérimental sous chargement statique et cyclique, et une étude analytique sur un modèle en éléments finis, en proposant une méthode de calcul pour estimer la résistance de l'assemblage. Le modèle de l'assemblage développé a pris en compte plusieurs aspects qui conditionnent le comportement global de celui-ci. Il a servi à une étude paramétrique ou les paramètres étudiés ont été la longueur du profil noyé et la classe de résistance du béton.

Plusieurs articles des revues à comité de lectures fournissent la synthèse des recherches pour chaque thème.

B. Forme

Le dossier scientifique et les annexes sont clairement structurés, dans une succession logique, avec des résumés succincts.

C. Conclusions

J'ai lu avec intérêt le mémoire de Monsieur **Nguyen Quang Huy**, mémoire qui par son contenu et sa présentation témoigne une excellente formation professionnelle et des remarquables capacités analytiques et descriptives, qui le recommandent comme un très bon spécialiste dans son domaine. Il a sans doute la capacité de diriger de recherches et de maîtriser des aspects numériques et théoriques difficiles.

En conclusion, je donne un avis très favorable pour que Monsieur **Nguyen Quang Huy** puisse soutenir en public son travail en vue de l'obtention de l'habilitation à diriger des recherches.

Cluj-Napoca, le 18 mars 2019

Cristina Mihaela Campian, Professeur des universités

str. Memorandumului nr.28, 400114 Cluj-Napoca, Romania
tel. +40-264-401200, fax +40-264-592055, secretariat tel. +40-264-202209, fax +40-264-202214
http://www.utcluj.ro/

Rapport de M. KOTRONIS Panagiotis

Professeur à l'École Centrale Nantes

sur le mémoire de

Mr NGUYEN Quang Huy

intitulé :

Modélisation numérique et expérimentale des structures mixtes acier-béton et bois-béton

Le document présenté par Mr NGUYEN Quang Huy se compose d'une présentation générale du candidat, une synthèse de ses travaux de recherche et une sélection de quatorze (14) publications scientifiques. Il contient quatre-vingt huit (88) pages (sans les annexes), il est très bien rédigé et comporte des illustrations de qualité. Comme c'est l'habitude pour les mémoires d'Habilitation à Diriger des Recherches, l'écriture est synthétique, sans trop s'attarder sur les détails des développements théoriques et/ou les résultats des expérimentations et des simulations numériques effectuées par l'auteur. Beaucoup plus d'informations sont fournies dans les publications scientifiques sélectionnées et présentées à la fin du mémoire.

Synthèse des travaux

La synthèse des travaux comporte trois (3) thèmes structurés en une brève introduction, un bilan et des perspectives.

Le premier thème concerne le développement d'outils analytiques et numériques novateurs pour l'analyse du comportement mécanique en flexion, du comportement vibratoire et du comportement au flambement des poutres multicouches avec prise en compte de la déformation de cisaillement des couches. Ce chapitre présente des approches originales pouvant trouver des applications tant dans la recherche académique qu'industrielle. Par poutres multicouches on entend ici des poutres mixtes de sections de matériaux différents avec des connecteurs de cisaillement qui sont supposés répartis le long de l'interface. A fin de trouver la matrice de raideur exacte et la matrice de masse, à l'instar d'autres travaux existants dans la littérature, l'auteur identifie les fonctions d'interpolation en combinant les équations d'équilibre, de compatibilité et des lois constitutives. Quelques questions s'imposent ici: si les fonctions de forme dépendent des propriétés matériaux, comment l'auteur prévoit leur utilisation dans le domaine non-linéaire? Quelle est la performance de l'outil numérique proposé pour la prise en compte du couplage non-linéaire effort normal (N) - moment de flexion (M)? Une comparaison de l'approche avec des éléments finis utilisant des fonctions de forme plus "classiques" serait d'un grand intérêt. De la même façon, la mise en lumière des similitudes et des différences avec des poutres "multifibres" avec ou sans discontinuités intégrées pourrait être très éducative.

Le deuxième chapitre concerne le comportement des planchers mixtes bois-béton sous sollicitations sismiques et d'incendie. L'auteur propose des essais Push-Out sous chargement

Ecole Centrale Nantes, Institut de Recherche en Génie Civil et Mécanique (GeM)
1 Rue de la Noë, BP 92101, 44321 Nantes, Cedex 3, France
Tel: +33 - (0) 240 376 893 - Fax: +33 - (0) 240 372 535

statique et cyclique alterné et une modélisation thermique et/ou thermo-mécanique avec des outils existants dans Abaqus. Ce travail présente l'intérêt d'être lié avec une problématique industrielle concrète et vise à identifier la capacité d'un type spécifique de planchers bois-béton à dissiper de l'énergie lors d'une sollicitation sismique et à assurer un fonctionnement minimal en situation d'incendie. Même si la solution technologique proposée présente une force résiduelle importante, une chute significative apparait après quelques cycles de chargement. Le comportement de la structure étant dominé par le comportement de ses connections, on pourrait imaginer une modélisation simplifiée de type macro-élément afin d'optimiser le temps de calcul. On peut regretter que dans le document il n'y a pas de modélisation purement mécanique sous chargement cyclique ou sismique et le fait que la question de la localisation des déformations n'est pas abordée.

Le troisième chapitre concerne une étude pré-normative des structures hybrides béton-acier avec comme objectif le développement d'une méthode de dimensionnement. Une méthode simplifiée originale est proposée pour des poteaux hybrides intégrant les effets d'une plastification partielle ou complète des profilés. Comment l'auteur envisage-t-il de combiner cette méthode avec l'utilisation du coefficient de comportement préconisé dans l'Eurocode 8? Pour le cas des murs en béton armé renforcés par des profilés métalliques un modèle bielle-tirant est adopté pour la résistance à l'effort tranchant. Le choix des sections de bielles et de l'angle mériterait une discussion plus détaillée.

Bilan quantitatif

Le curriculum vitae et la présentation générale présentés dans la première partie du document permet de mesurer l'évolution de Mr NGUYEN Quang Huy, sa maitrise scientifique, son investissement pédagogique et collectif. Il a co-encadré six (6) thèses de doctorat (dont quatre (4) soutenues) et six (6) master recherche. Il a vingt (20) publications dans des revues internationales à comité de lecture (dont une (1) en révision) avec une activité régulière depuis l'obtention de la thèse de doctorat. Mr NGUYEN Quang Huy a été responsable scientifique d'un projet industriel d'envergure et coordinateur interne de son laboratoire d'un projet Européen. Il a également expertisé des articles pour plusieurs revues internationales et il bénéficie de la PEDR depuis 2014.

Mr NGUYEN Quang Huy présente un très bon bilan, particulièrement bien équilibré entre recherche (analytique, expérimental et numérique), encadrement et implication collective. Par conséquent, c'est sans hésitation que je donne un **avis très favorable** à ce que Mr NGUYEN Quang Huy présente ses travaux en vue de l'obtention du diplôme d'Habilitation à Diriger des Recherches (HDR).

Fait à Nantes, le 06 avril 2016
Panagiotis KOTRONIS
Professeur Ecole Centrale de Nantes

Ecole Centrale Nantes, Institut de Recherche en Génie Civil et Mécanique (GeM)
1 Rue de la Noë, BP 92101, 44321 Nantes, Cedex 3, France
Tel: +33 - (0) 240 376 893 - Fax: +33 - (0) 240 372 535